Measurement of Single Spin Asymmetry in $n^{\uparrow}(e, e'\pi^{\pm})X$ on Transversely Polarized ^{3}He

by

Xin Qian

Department of Physics
Duke University

Date: _____

Approved:

_____
Prof. Haiyan Gao, Advisor

_____
Prof. Steffen A Bass

_____
Prof. Albert M Chang

_____
Prof. Ronen M Plesser

_____
Prof. Henry R Weller

Dissertation submitted in partial fulfillment of the requirements for the degree of
Doctor of Philosophy in the Department of Physics
in the Graduate School of Duke University
2010

Abstract

(Nuclear Physics)

Measurement of Single Spin Asymmetry in $n^{\uparrow}(e, e'\pi^{\pm})X$ on Transversely Polarized ^{3}He

by

Xin Qian

Department of Physics
Duke University

Date: _____

Approved:

_____
Prof. Haiyan Gao, Advisor

_____
Prof. Steffen A Bass

_____
Prof. Albert M Chang

_____
Prof. Ronen M Plesser

_____
Prof. Henry R Weller

An abstract of a dissertation submitted in partial fulfillment of the requirements for the degree of Doctor of Philosophy in the Department of Physics in the Graduate School of Duke University

2010

Abstract

Parton distribution functions (PDFs) provide important information about the flavor and spin structure of nucleon, which is one of the most fundamental building blocks of nature. Furthermore, they can also shed light on quantum chromodynamics (QCD) in the confinement region. Inclusive deep inelastic scattering (DIS) has been one of the most common tools in accessing PDFs through the measurement of structure functions. Moreover, the cross section in semi-inclusive deep inelastic scattering (SIDIS), which is the product of PDFs and fragmentation functions (FF), which describe the parton hadronization process due to the color force, provides additional information about PDFs. With recent theoretical developments in the framework of the transverse momentum dependent parton distribution functions (TMDs), the importance of SIDIS process have been widely recognized and accepted, since the inclusive DIS will not be able to attain the information of parton transverse momentum.

JLab experiment E06-010 is measuring the target single spin asymmetry (SSA) in SIDIS from the $\overrightarrow{n}(e, e'\pi^{+,-})X$ reaction with a transversely polarized ^{3}He (effective polarized neutron) target at JLab Hall A with a 5.89 GeV incident electron beam. The kinematic coverage is $0.13 < \mathrm{x} < 0.41$ and $1.31 < Q^2 < 3.1$ (GeV^2). This experiment represents the first SSA measurement from the SIDIS $\overrightarrow{n}(e, e'\pi^{\pm})X$ process. One of the main objectives of the experiment is to measure the Collins asymmetry, which in turn constrains the "transversity", one of the PDFs whose direct physical

interpretation is the probability of finding a transversely polarized parton inside a transversely polarized nucleon. The other main objective of the experiment is to measure the Sivers asymmetry which reveals important information about correlations between the parton transverse momentum and the nucleon spin. The Sivers asymmetry is closely linked to the parton's orbital angular momentum, which is one important piece in understanding the nucleon spin in terms of quark and gluon degrees of freedom.

This dissertation will first give an introduction to QCD, SIDIS and current theoretical and the experimental status of SSA. Next the experimental setup of E06-010 will be described, followed by the data analysis procedure to extract the Collins/Sivers asymmetries. In the end, the preliminary results from the data analysis will be shown and discussed.

To my lovely wife Shudan Shen

Contents

List of Tables

List of Figures

List of Abbreviations and Symbols

Symbols

$\mathbf{k}$,$\vec{k}$	3-vector of k.
$\otimes$	A convolution integral.
Λ_{QCD}	The scale of QCD: 217^{+25}_{-23} MeV in the MS scheme [5].
$A^{\pm}$	Light-cone variables: $A^{\pm} = \frac{1}{\sqrt{2}}(A^0 \pm A^3)$.
$\not{k}$	$\not{k} = k^{\mu}\gamma_{\mu}$
$\mathcal{G}$	Math mode of G.
$\mathcal{L}$	Math mode of L.
$\mathcal{P}$	Math mode of P.
α_S	Strong Interaction Coupling Constant.
α	E&M Interaction Coupling Constant.

Abbreviations

A/D	Analog to Digital
AC	Alternating Current
ADC	Analog to Digital Converter
AFP	Adiabatic Fast Passage
BCM	Beam Current Monitor
BNC	Bayonet Neill-Concelman
BPM	Beam Positron Monitor

CEBAF	Continuous Electron Beam Accelerator Facility
CT	Color Transparency
CW	Continuous-Wave
CODA	CEBAF Online Data Acquisition
CRL	CODA readout list
DAQ	Data Acquisition
DC	Direct Current
DGLAP	Dokshitzer-Gribov-Lipatov-Altarelli-Parisi
DIS	Deep Inelastic Scattering
DY	Drell-Yan Process
E&M	Electromagnetic
ECL	Emitter Coupled Logic
EDT	Electronic dead time
EMF	Electromotive Forced
EPICS	Experimental Physics and Industrial Control System
EPR	Electron Paramagnetic Resonance
FAP	Fiber Array Package
FWHM	Full Width Half Maximum
FSI	Final State Interaction
GPD	Generalized Parton Distribution Functions
GPIB	General Purpose Interface Bus
HRS	High Resolution Spectrometer
HV	High Voltage
IPD	Impact Parameter Distribution Functions
JLab	Jefferson Lab
IA	Impulsed Approximation

L1A	Level-1 Accept
Linac	linear accelerator
LO	Leading-order
MC	Monte Carlo
MLE	Maximum Likelihood Estimation
MWDC	Multi-Wire Drift Chamber
NIM	Nuclear Instrument Module
NMR	Nuclear Magnetic Resonance
NLO	Next-to-leading-order
OPE	Operator Product Expansion
PDF	Parton Distribution Functions
PHP	Hypertext PreProcessor
PID	Particle Identification
PLC	Point Like Configuration
PMT	Photo-multiplier Tube
QCD	Quantum Chromodynamics
RF	Radio Frequency
RICH	The Ring Imaging Cerenkov Detector
RMS	Root Mean Square
ROC	Read-out Controller
RTD	Resistive Temperature Device
SEOP	Spin Exchange Optical Pumping
SIDIS	Semi-Inclusive Deep Inelastic Scattering
SQL	Structured Query Language
SRC	Short Range Correlation
SSA	Single Spin Asymmetry

TDC	Time to Digital Converter
TMC	Target Mass Correction
TMD	Transverse Momentum Dependent Parton Distribution Functions
TOF	Time-of-flight
TTL	Transistor-Transistor Logic
TS	Trigger Supervisor
TSUM	Total hardware sum
VDC	Vertical Drift Chamber
	VMD Vector Meson Dominance
	VME Versa Module Europa
u1,u3,u10	upstream BCMs
d1,d3,d10	downstream BCMs
ppm	part per million
Vp, V+	HRS's polarity is positive and ^{3}He target is vertically polarized.
Vn, V-	HRS's polarity is negative and ^{3}He target is vertically polarized.
Tp, T+	HRS's polarity is positive and ^{3}He target is transversely polarized.
Tn, T-	HRS's polarity is negative and ^{3}He target is transversely polarized.

Conventions

Hall Coordinate System (Target Coordinate System)

- Longitudinal Direction: Along the beam line.
- Vertical Direction: Along the gravity direction.
- Transverse or Horizontal Direction: Perpendicular to both longitudinal and vertical direction.

- x: beam left.
- y: vertical up.
- z: beam direction.

Magnet Coordinate System

- x: To the right, when stand facing the magnet.
- y: Anti-gravity direction.
- z: x $\times$ y.

BigBite Detector Coordinate System

- z: point into the chamber, toward the calorimeter.
- x: point to the bottom of the chamber from the center of the chamber, also referred to the dispersive direction.
- y: z $\times$ x, also referred to as the non-dispersive direction.

Left HRS Coordinate System

- z: anti-gravity direction.
- dispersive direction: The vector of dispersive direction is in the dipole bending plane. The VDC's long edge is along the dispersive direction.
- non-dispersive direction: The vector of non-dispersive direction is perpendicular to the dipole bending plane and the z direction.

Notations

ϵ is the totally antisymmetric tensor $\epsilon^{0123} = -\epsilon_{0123} = 1$. And

$$g_{\mu nu} = g^{\mu\nu} = \begin{pmatrix} 1 & 0 & 0 & 0 \\ 0 & -1 & 0 & 0 \\ 0 & 0 & -1 & 0 \\ 0 & 0 & 0 & -1 \end{pmatrix} \tag{1}$$

is the metric tensor with Greek indices running over 0, 1, 2, 3, or t, x, y, z. γ_μ is the Dirac matrices. In the light-cone frame, any four-vector $A_\mu = (A^0, \mathbf{A}) = (A^0, A^1, A^2, A^3)$ in the rest frame can be rewritten as $(A^+, A^-\mathbf{A}_\perp)$, where

$$A^\pm = \frac{1}{\sqrt{2}}(A^0 \pm A^3). \tag{2}$$

Acknowledgements

During the past seven years as a Duke graduate student, I received endless support and help from countless people both in research and in life. I'd like to take this opportunity to thank these people who made this thesis possible.

I owe my deepest gratitude to my advisor, Haiyan Gao, without whom I wouldn't even be here at Duke. In 2003, I was still a naive undergraduate in China, trying to find my way in life. I wasn't the brightest, nor was I the one with the most accolades. Haiyan saw something in me that even I myself wasn't able to see, and she trusted me to have the potential to grow. For that, I am forever grateful. From the very beginning, Haiyan showed an extraordinary amount of patience with me, guiding me through every step of research and tolerating many of my mistakes. As I became more competent and mature, she granted me plenty of academic freedom and encouraged me to grow as an independent physicist. Haiyan really was a wonderful advisor, and I cannot imagine where I would be in my career without her guidance. When I came here, I had promised myself not to let Haiyan down. Seven years later, I can only hope that I have also made her proud.

My experiences in graduate school were a bit different from many of my peers, because I spent four years doing research not at Duke but in Jefferson Lab, Virginia. In those years, while Haiyan continued to support me through emails and telecommunication, it was my JLab supervisor Jian-ping Chen who had the most influence on me on a daily basis. As a nuclear physicist, Jian-ping is one of the

most knowledgeable people I have ever met. Yet, what I admire the most about him is the rigorous, no-nonsense way he approaches research. Never the one to tolerate scientific carelessness, Jian-ping routinely challenged me with tough and pointed questions. His strictness forced me to realize many of my shortcomings and therefore made me into a better physicist. Even though I have left JLab, what I have learned from Jian-ping will always accompany me in my future career.

I would also like to thank the spokespersons of E06-010: Jian-ping Chen, Evaristo Cisbani, Haiyan Gao, Xiaodong Jiang, and Jen-Chieh Peng. Without their scientific vision, there wouldn't have been E06-010 for me to work on as a thesis project. I'd like to particularly thank Xiaodong, who had worked with me on many projects and whose enthusiasm for Physics had always been my inspiration. Moreover,I want to thank all the collaborating scientists and the entire staff of JLab Hall A, whose diligent work made the successful running of E06-010 possible. Furthermore, many post-docs and fellow students worked together with me on E06-010. They are Yi Qiang, Brad Sawatzky, Bryan Moffit, Alexandre Camsonne, Seamus Riordan, Bo Zhao, Vicent Sulkosky, Xiaofeng Zhu, Kalyan Allada, Chiranjib Dutta, Joe Katich, Jin Huang, Youcai Wang, and Yi Zhang. It was an honor to work with these bright scientists, and the journey we took together was unforgettable.

I am grateful to Dipangkar Dutta for guiding me through my first data analysis on E01-107 and supporting my work over the years. Being the spokesperson of E01-107, Dipangkar was always willing to answer my questions and explain the experimental details to me. I also want to thank Benjamin Clasie for his patience in explaining the analysis details and his constant encouragement which helped me out of frustration many times. In addition, I would like to thank Rolf Ent, Dave Gaskell, Peter Bosted, Garth Huber and all the other collaborating scientists who mentored me on E01-017 data analysis; as well as Stepan Stepanyan, Tsutomu Mibe, Jean-Marc Laget and many other collaborating scientists who helped me on the CLAS ϕ data analysis.

I want to thank Wei Chen, a great colleague and even better friend, for the countless times he rescued me from all kinds of computer or coding problems. I'd also like to thank Xiaofeng Zhu and Yi Qiang, who worked with me on E06-010 as post-docs, for their constant help and inspiration, and for simply being two of my best friends. Additionally, I want to acknowledge all the current and past members of duke MEP group who I had been working with; as well as many friends at Duke and JLab who made my life outside the research colorful and enjoyable.

I would like to thank all my committee members: my advisor Haiyan Gao, Steffen A Bass, Albert M Change, Ronen M Plessor, and Henry R Weller for taking time to read this thesis. I also would like to thank my wife Shudan Shen, my classmate James H. Esterline, my JLab supervisor Jian-ping Chen, Xiaodong Jiang, Evaristo Cisbani, Bryan Moffit, Vincent Sulkosky for carefully reading my thesis and giving me many great suggestions.

I would like to acknowledge the MEP group's U.S. Department of Energy and the National Science Foundation grant under the contract number DE-FG02-03ER41231. I would also like to thank the fellowship support from Jefferson Lab/SURA during my stay at the Jefferson Lab.

I'd like to thank my parents for their unconditional love. My father, Yanfang Qian, and my mother, Huiling Zhao, are probably the biggest fans of me in this world. No matter what decisions I make about career or life, they always give me 100% of understanding and support. Knowing that I will never be able to repay their love and sacrifice, I only hope to achieve as much as I can and make them proud.

Last but not the least important, my wife. Our love endured the test of four-year separation, yet still blossomed with the nourishment of patience, understanding, and trust. With her taking care of my life, I was able to focus on my research; with her confidence and encouragement, I was able to pursue bigger and higher aims; and with her standing firmly beside me, I will have the courage to weather any storm in

life. Therefore, I dedicate this thesis to my beloved wife, Shudan.

1

Summary of Non-thesis Analysis Work

In addition to the subject of this thesis on experiment E06-010 (neutron transversity experiment), I also played leading roles in data analyses of two other experiments at Jefferson Lab. The first analysis was on the Jefferson Lab experiment E01-107, the pion Color Transparency experiment (πCT), which was carried out in Hall C in 2004. The second was a CLAS-approved analysis (CAA) of Hall B g10 data (ϕ analysis). The following two sections provides a summary of the current status of these two analyses.

1.1 πCT

The goal of this experiment was to search for the CT effect through electroproduction of positively charged pions from nuclei at different values of 4-momentum transfer squared Q^2. The detailed description of the πCT experiment can be found in B. Clasie's Ph.D. thesis [6]. The nuclear transparency results were reported in Ref. [7], to which I contributed as the second author, and Physical Review Focus [8]. The results of the Rosenbluth (Longitudinal/Transverse, hereafter L/T) separation on

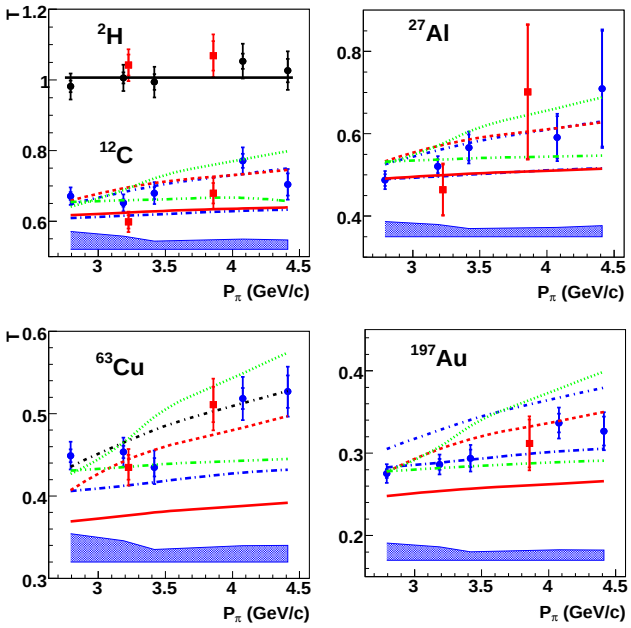

FIGURE 1.1: The redefined nuclear transparencies $T_D = \frac{\sigma_A}{\sigma_D}$ are plotted versus P_π for ^{12}C, ^{27}Al, ^{63}Cu, and ^{197}Au. The solid circles (blue) are the high ϵ points while the solid squares (red) are low ϵ points. The dashed and solid lines (red) are Glauber calculations from Larson *et al.* [11], with and without CT respectively. Similarly, the dot-short dash and dot-long dash lines (blue) are Glauber calculations with and without CT from Cosyn*et al.* [12]. The effects of short-range correlations are included in these latter calculations. The dotted and dot-dot-dashed lines (green) are microscopic+ BUU transport calculations from Kaskulov et al. [13], with and without CT respectively.

the hydrogen cross sections were published in Ref. [9] (second author). In addition, the results of the hydrogen and nuclear cross sections and the nuclear cross section L/T separation have been summarized in an archive paper, which was accepted by PRC [10].

1.1.1 Nuclear Transparency

Color Transparency (CT) was first proposed by Brodsky and Mueller [15] in 1982. It refers to the decrease of the hadron-nucleon interaction for hadrons produced in a point-like configuration (PLC) in exclusive processes inside a nucleus at large

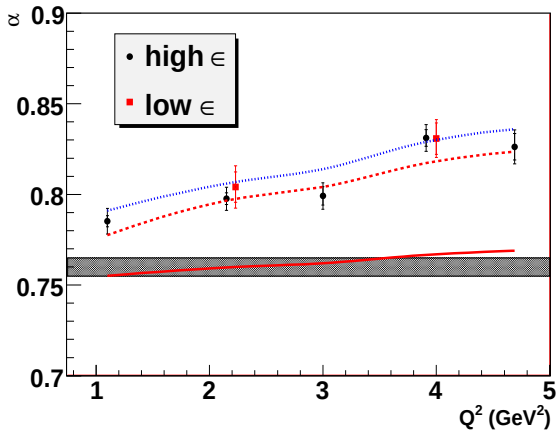

FIGURE 1.2: The parameter α, as extracted from the global nuclear data set of this experiment (from $T = A^{\alpha-1)}$) is plotted versus Q^2 (solid black circles). The hatched band is the value of α extracted from pion-nucleus scattering data [14]. The solid, dashed and dotted lines are α obtained from fitting the A-dependence of the theoretical calculations: the Glauber and Glauber+CT calculations of Ref. [11], and the Glauber + CT (including short-range correlation effects) calculations of Ref. [12], respectively. The red solid squares in addition show the α value extracted at low ϵ value at two values of Q^2.

momentum transfer. An intuitive way to understand the CT is to treat the hadron as a color dipole. Therefore, the smaller the dipole is, the smaller the interaction is. As CT is quite natural at high energies, the search of the onset of CT is more interesting at low energies. To search for the onset of the CT, a natural experimental observable is the nuclear transparency, which is defined as the ratio of the cross section per nucleon for a process on a bound nucleon inside a nucleus to that on a free nucleon. Color transparency will lead to an increase in nuclear transparency as a function of momentum transfer and hadron momentum. In addition, the A-dependence of the nuclear transparency will deviate from that found in pion-nucleus total cross section data, and will also depend on values of Q^2. The search of CT was first carried out in $A(e, e'p)$ channel. The results for deuterium, carbon, iron and gold nuclei from $Q^2 \approx 2$ GeV^2 to 8.1 GeV^2 [16, 17, 18, 19] are consistent with the absence of CT

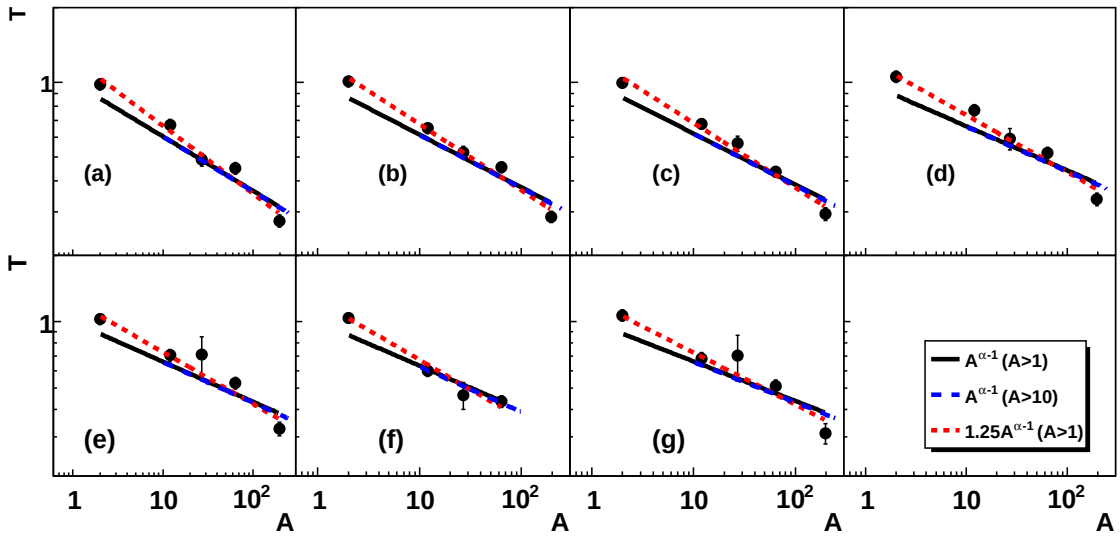

FIGURE 1.3: The nuclear transparency vs. the nucleon number, A for (a) $\epsilon = 0.5$, $Q^2 = 1.1$ GeV^2, (b) $\epsilon = 0.56$, $Q^2 = 2.15$ GeV^2, (c) $\epsilon = 0.45$, Q^2=3.0 Gev^2, (d) $\epsilon = 0.39$, $Q^2 = 3.9$ Gev^2, (e) $\epsilon = 0.26$, $Q^2 = 4.7$ Gev^2, (f) $\epsilon = 0.27$, $Q^2 = 2.16$ Gev^2, and, (g) $\epsilon = 0.25$, $Q^2 = 4.01$ Gev^2. The lines are fits to the experimental data using the parametrization T $= A^{\alpha-1}$ for $A > 1$ (solid black), $A > 10$ (long-dashed blue) and T $= 1.25A^{\alpha-1}$ (short-dashed red). Only the statistical uncertainties of the data are shown. The value of the parameter α is listed in Table. 1.1.

effect, which has been interpreted as an indication that the proton formation length may only have been as large as internucleonic distance in these experiments [20]. In this case, it would be much easier to search for onset of CT in the meson system, since the formation length of meson is longer due to smaller mass than proton and the PLC is more likely formed in a quark-antiquark pair compared to a three quark baryon [21]. Fig. 1.1 shows the nuclear transparency vs. P_π for $p(e, e'\pi^+)n$ process from ^{12}C, ^{27}Al, ^{63}Cu and ^{197}Au. The full nuclear transparency data set was fitted to $T = A^{\alpha-1}$ for $A > 1$ (Fig. 1.3), where A is the mass number of the target. α is plotted as a function of Q^2 in Fig. 1.2. The total uncertainties in α are determined by fitting the experimental data with the statistical and overall (point-to-point, normalization and model) systematic uncertainties added in quadrature. The uncertainties in α are dominated by systematics, and include fitting uncertainties and model uncertainties.

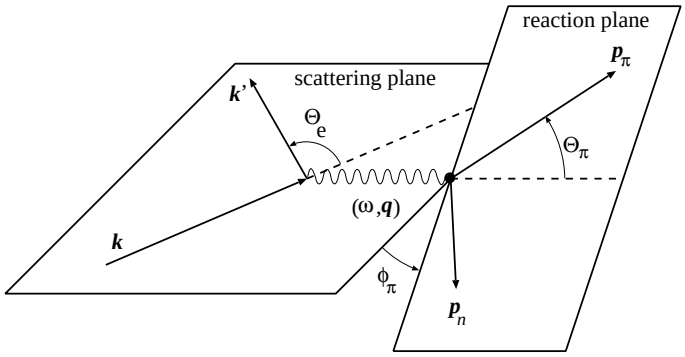

FIGURE 1.4: Kinematic variables of the p$(e, e'\pi^+)$n reaction in the laboratory frame.

Even though the single-parameter fit T $= A^{\alpha-1}$ is simple and neglects local A-dependent shell or density effects, this does not affect the final conclusion that the A-dependence changes with Q^2. We have verified this with two methods: (i) We find an almost identical increase of α with Q^2 when fitting only the data from medium-heavy nuclei, $A > 10$, as shown by the blue dashed curves in Fig. 1.3 and listed in the third column of Table. 1.1. (ii) The increase of α with Q^2 also remains when we change from a single-parameter fit to a two-parameter fit to $T = \beta A^{\alpha-1}$, as indicated by the red dotted curves in Fig. 1.3 and listed in the fourth column in Table. 1.1. Although the quality of the fit is better for the two-parameter form, the best fit is obtained for $\beta = 1.25$ which is unphysical for $A = 1$ since it does not satisfy the condition $T(A = 1) = 1$. Moreover, the single-parameter fit describes the hadron-nucleus cross-sections for a wide range of hadrons [14], which is our motivation for comparing the electroproduction data with the same form. Thus, even though the exact value of α may come with a variety of nuclear physics uncertainties, given the simplistic form of the A dependence, we find that the empirical Q^2 dependence is well established. In summary, our results, together with the previous meson transparency measurements [22, 23], are consistent with the predicted CT effect.

1.1.2 Kinematics and Cross Sections

The kinematic variables of the pion electroproduction reaction are shown in Fig. 1.4. The incident and scattered electron have 3-vector momenta $\mathbf{k}$ and $\mathbf{k}'$, respectively. The polar angle θ_e of the scattered momentum is defined in the lab frame, and $\theta_e = 0$ for the incident electron direction. The scattering plane is defined by the 3-vector momenta of the incoming and outgoing electron. The corresponding four-momenta are $k \equiv (E, \mathbf{k})$ and $k' \equiv (E', \mathbf{k}')$. The virtual photon carries a four-momentum $q \equiv (\omega, \mathbf{q}) \equiv k - k'$. The reaction plane is defined by the 3-vector momenta $\mathbf{P}_\pi$ of the produced pion and $\mathbf{q}$. The angle between the two planes is ϕ_π, while the angle between $\mathbf{p}_\pi$ and $\mathbf{q}$ is θ_π.

The pion electroproduction reaction can be described using three Lorentz invariants. In addition to $Q^2 = -q^2$, the Mandelstam variable $t = (P_\pi - q)^2$ and the invariant mass of the virtual photon-nucleon system (W) are also used. Here $W = \sqrt{M_p^2 + 2M_p\omega - Q^2}$, where M_p is the proton mass.

The pion electroproduction cross section from a stationary proton in the one photon-exchange approximation is [24]:

$$\frac{d^5\sigma}{d\Omega_{e'} dE_{e'} d\Omega_\pi} = \Gamma_\nu \frac{d^2\sigma}{d\Omega_\pi}, \tag{1.1}$$

where

$$\Gamma_\nu = \frac{\alpha}{2\pi^2} \frac{E_{e'}}{E_e} \frac{K_{eq}}{Q^2} \frac{1}{1-\epsilon} \tag{1.2}$$

is the virtual photon flux, and α is the fine structure constant. The factor $K_{eq} = (W^2 - M_p^2)/(2M_p)$ is the equivalent photon energy, and

$$\epsilon = (1 + \frac{2|\mathbf{q}|^2}{Q^2} \tan^2 \frac{\theta_e}{2})^{-1} \tag{1.3}$$

is the longitudinal polarization of the virtual photon. The two-fold differential cross

section for a stationary proton target can be written as

$$\frac{d^2\sigma}{d\Omega_\pi} = J\frac{d^2\sigma}{dtd\phi_\pi}. \tag{1.4}$$

The solid angle of the pion, Ω_π, is determined in the lab frame. J is the Jacobian matrix for the transformation from Ω_π to t, ϕ_π. The two-fold cross section can be separated into four structure functions, which correspond to the polarization states of the virtual photon, a longitudinal (L), a transverse (T), and two interference terms (LT and TT):

$$\begin{aligned} 2\pi\frac{d^2\sigma}{dtd\phi_\pi} &= \epsilon\frac{d\sigma_{\rm L}}{dt} + \frac{d\sigma_{\rm T}}{dt} + \sqrt{2\epsilon(\epsilon+1)}\,\frac{d\sigma_{\rm LT}}{dt}\cos\phi_\pi \\ &\quad + \epsilon\frac{d\sigma_{\rm TT}}{dt}\cos 2\phi_\pi, \end{aligned} \tag{1.5}$$

The interference terms vanish in parallel kinematics ($\theta_\pi = 0$) due to their dependence on θ_π [25, 26].

The four structure functions can be separated if measurements at different values of ϵ and ϕ_π are performed (L/T separation) while W, Q^2 and t are kept constant. The photon polarization ϵ is varied by changing the incident electron energy and the angle of the scattering electron.

For nuclei, there is a new degree of freedom due to the Fermi momentum of the struck nucleon. Therefore, the differential pion electroproduction cross section becomes:

$$\frac{d^6\sigma}{d\Omega_{e'}dE_{e'}d\Omega_\pi dP_\pi} = \Gamma_\nu\frac{d^3\sigma}{d\Omega_\pi dP_\pi}. \tag{1.6}$$

The three-fold differential cross section, $\frac{d^3\sigma}{d\Omega_\pi dP_\pi}$, is also separated into longitudinal, transverse, and interference terms as in Eqns. (1.4) and (1.5).

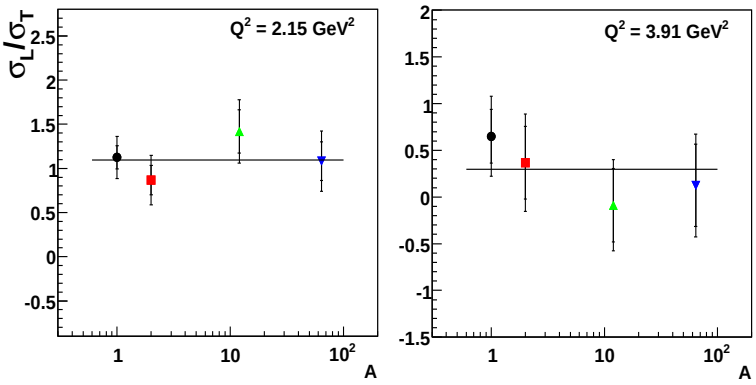

FIGURE 1.5: The ratio of longitudinal to transverse cross sections for pion electroproduction from ^{1}H, ^{2}H, ^{12}C, and ^{63}Cu targets, at fixed $Q^2 = 2.15$ (left) and 3.91 (right) GeV^2. The inner error bars represent the statistical uncertainties, while the outer error bars are the sum in quadrature of the statistical and systematic uncertainties. The curves represent constant-value fits to all nuclear data at a fixed Q^2. The probability of these constant-value fits assuming Gaussian statistics is 69% and 70%, respectively. The statistics at $Q^2 = 3.91$ GeV^2 is limited.

1.1.3 Nuclear L/T Separation

The motivation of the nuclear L/T separation is to verify the quasi-free reaction mechanism in the pion electroproduction data taken from nuclear targets in the πCT experiment. If the quasi-free mechanism is correct, one would expect that the longitudinal-transverse characters for pion electroproduction are equivalent between the nuclear and hydrogen targets. In this case, the ratio of longitudinal to transverse cross sections should be independent of the nuclear mass number A. The ratio of longitudinal to transverse cross sections at fixed $Q^2 = 2.15$ and 3.91 GeV^2 for the various targets in this experiment are shown in Fig. 1.5. The fact that the A-dependence of the σ_L/σ_T ratio agrees with fit to a straight line within the experimental uncertainties is consistent with the quasi-free assumption.

1.1.4 Extraction of Hydrogen and Nuclear Cross Sections

The hydrogen differential cross sections are shown in Fig. 1.6. They are compared with the predictions of two different models of pion electroproduction, the VGL-Regge model [27], and the more recent "KGM" model [28]. The VGL-Regge calculations use a gauge invariant model with π and ρ Regge trajectory exchanges incorporated. They significantly underestimate the measured differential cross sections. Most of the discrepancies may be attributed to the fact that the model underestimates σ_T as shown in Ref. [9] while agreeing well with σ_L. The recent KGM model [28] agrees much better with the measured differential cross sections. The longitudinal cross section of this model is dominated by hadronic degrees of freedom and the pion electromagnetic form factor, while the transverse cross section includes the deep-inelastic scattering (DIS) Ansatz.

The differential cross sections for all four nuclear targets (deuterium, carbon, copper and gold) were extracted and are shown in Fig. 1.7. In this case, an additional complication, due to the added degree of freedom induced by the Fermi-motion (or more generally, the nuclear binding) of the struck proton, is taken into account by extracting the double-differential cross sections $\frac{d^2\sigma}{dtdP_\pi^{CM}}$. Here, P_π^{CM} is the pion momentum in the center-of-mass frame of the virtual photon and the nucleus.

The local variations in the nuclear cross sections as illustrated in Fig. 1.7 indicate effects of Fermi motion. These local variations are more pronounced for the deuterium target, because of its narrower Fermi distribution. Although the general trend of the nuclear cross section is similar to that of the hydrogen cross section, the fall-off of the nuclear cross sections with P_π is steeper than that found for the hydrogen cross sections.

1.2 ϕ Analysis

This analysis was performed to improve the current understanding of ϕ-nucleon interaction. Detailed information about this CLAS approved analysis can be found in Ref. [29]. The analysis note [30] passed the CLAS internal review and the extracted ϕ-N total cross sections were reported in Ref [31] (first author). Moreover, a letter has been written reporting on the first measurement of the cross sections of sub-threshold ϕ production on deuterium [32]. It is currently under the CLAS Collaboration review. The results of the ϕ photoproduction on hydrogen and deuterium at quasi-free kinematics have been drafted into an archive paper [33]. In the following, we will briefly describe the physics motivation and results.

1.2.1 The Extraction of the ϕ-N Total Cross Section

Multi-gluon exchange between hadrons, known as Pomeron exchange, is a fundamental process and plays an important role in high-energy interactions. Studying multi-gluon exchange at low energies is challenging since at low energies the hadron-hadron interactions are dominated by quark exchange. However, multi-gluon exchange is expected to be dominant in the interaction between two hadrons when they have no common quarks. The ϕ-meson is unique in that it is nearly an $s\bar{s}$ state and hence gluon exchange is expected to dominate the ϕ-N scattering process.

Direct measurement of the ϕ-N cross section is not possible due to the lack of a ϕ-meson beam. Previously, an upper limit of $\sigma_{\phi N} \simeq 11$ mb was obtained using the ϕ photoproduction data on the proton and the vector meson dominance (VMD) model [34]. However, from the observed A-dependence of nuclear ϕ photoproduction, a larger value (inelastic $\sigma_{\phi N}^{inelas} \simeq 35$ mb, which is part of the total $\sigma_{\phi N}$), is obtained [35].

The ϕ-meson photoproduction from deuterium offers an additional tool to clarify

this situation. The reaction $\gamma + d \rightarrow \phi + p + n$ can be used to extract the ϕ-N interaction cross section through the Final State Interaction (FSI) at large missing momenta. The reaction $\gamma(d, \phi p)n$ was measured by detecting kaons from the ϕ-meson decay ($\phi \rightarrow K^+K^-$, branching ratio about 0.5) in coincidence with the proton. Our results [31] show that the extracted ϕ-N cross section from deuterium is larger than that obtained from the ϕ photoproduction data on the proton using the VMD. The cross-section ratios between the high and the low missing momentum regions are shown in the top panels of Fig. 1.8. The bottom two panels of Fig. 1.8 show the confidence level analysis for both results from the $\gamma + d \rightarrow \phi + p + (n)$ channel and the $\gamma + d \rightarrow \phi + d$ coherent channel [36].

1.2.2 The Extraction of Subthreshold ϕ Production Cross Section

The presence of the attractive QCD van der Waals interaction, proposed by Brodsky, Schmidt and de Téramond [37], is a manifestation of the role of gluons in the confinement region. The QCD van der Waals interaction, mediated by multi-gluon exchanges, is dominant when two interacting color singlet hadrons have no common valence quarks. Gao, Lee, and Marinov [38] predicted the existence of a bound state of ϕ-N. Such a bound state was also predicted by Huang, Zhang, and Yu [39]. To form such a ϕ-N bound state, the relative velocity between the ϕ-meson and the nucleon needs to be low, so that the QCD van der Waals interaction is enhanced [40]. Thus, the experimental search of a ϕ-N bound state can be performed with a quasi-free subthreshold ϕ-meson photoproduction inside a nucleus and the subsequent formation of the bound state of the ϕ-meson with another nucleon inside the nucleus [38]. The presence of the ϕ-N bound state may lead to a signal in a triple coincidence detection of kinematically correlated K^+, K^-, and the proton in the final state from its decay [38, 41]. In this analysis, we extracted for the first time the subthreshold production of ϕ-mesons from a deuterium target for the photon energy of 1.65-1.75

GeV (Fig. 1.9). The extracted cross-sections are in reasonable agreement with the simple quasi-free calculation within the experimental uncertainties, which will help provide reliable information on the expected production rate of the ϕ-N bound state. These data also provide important information on various physical backgrounds, for example, the direct K^+K^- production from nucleons.

1.2.3 The Extraction of "Proton" ϕ Photoproduction Cross Sections from Deuteron at Quasi-Free Kinematics

Early photoproduction measurements of ϕ-mesons are consistent with the assumption that the cross section is dominated by the diffractive production via Pomeron exchange [42]. The differential cross sections for this reaction channel peak in the forward kinematics and vary slowly with the photon energy away from threshold [43, 44, 45]. In addition, early polarization data also agree with the vector dominance model which predicts that the incoming photon first fluctuates into an $s\bar{s}$ pair before interacting with the nucleon [46, 47]. Theoretical predictions [48, 49] and new data from CLAS [50], LEPS [51], and SAPHIR [52] Collaborations indicate that there is much more to learn from this reaction. Recently, a "resonance-like" structure has been observed in the π photo-production channel from both the neutron and the proton at $\sqrt{s}$ around 2.2 GeV [53]. Such phenomenon is possibly caused by a group of strange quark resonances, in which case the cross sections in the similar photon energy range should also deviate from the predictions of the simple Pomeron exchange reaction mechanism. In this analysis, the "proton" ϕ photoproduction cross-sections have been extracted from the deuterium data at E_γ = 1.75-3.59 GeV, with a low spectator nucleon momentum cut to ensure the quasi-free kinematics. Fig. 1.10 shows that the results deviate from the calculations based on Pomeron exchange.

setting	$A^{\alpha-1}$				$A>1$		$A^{\alpha-1}$		$A>10$	$1.25A^{\alpha-1}$		$A>1$
Q^2 GeV^2	α	stat.	sys.	χ^2/N_{dof}	norm.	tot.	α	χ^2/N_{dof}	norm.	α	χ^2/N_{dof}	norm.
1.1	0.785	0.003	0.006	5.54	1	0	0.784	5.56	1	0.731	2.05	1
2.15	0.798	0.003	0.006	6.15	1.017	0.012	0.795	5.14	1.014	0.739	1.45	1.011
2.23*	0.804	0.008	0.008	3.68	1.024	0.017	0.797	0.29	1.017	0.730	1.06	0.999
3.0	0.799	0.005	0.005	5.53	1.018	0.013	0.796	4.84	1.015	0.740	1.12	1.012
3.91	0.831	0.006	0.006	7.47	1.059	0.013	0.827	6.52	1.055	0.775	1.84	1.062
4.0*	0.831	0.009	0.006	4.09	1.059	0.016	0.827	2.59	1.055	0.769	1.11	1.052
4.69	0.826	0.007	0.006	4.61	1.052	0.015	0.822	4.04	1.048	0.770	1.61	1.053

Table 1.1: The α parameter extracted from three different fits. * represents the data taken at low ϵ values. The fit quality χ^2/N_{dof} (chi-square per degree of freedom) for each fit is also listed. The first fit is to T $= A^{\alpha-1}$ for data with $A > 1$. The obtained α values along with the uncertainties are listed. To indicate the increase in α with Q^2, we also show the ratio $\frac{\alpha(Q^2)}{\alpha(Q^2=1.1)}$ and its uncertainty. The second fit is to $A^{\alpha-1}$, but only for data with $A > 10$. The third fit is to T $= \beta A^{\alpha-1}$ for data with $A > 1$. The quality of fit was best for $\beta = 1.25$ however, it does not satisfy the condition T $= 1$ for $A = 1$. The parameter α shows a similar and consistent increase with Q^2 for all three fits. The total uncertainties for the $A > 10$ and the two parameter fit are very similar to the ones shown for the first fit and hence they are not shown.

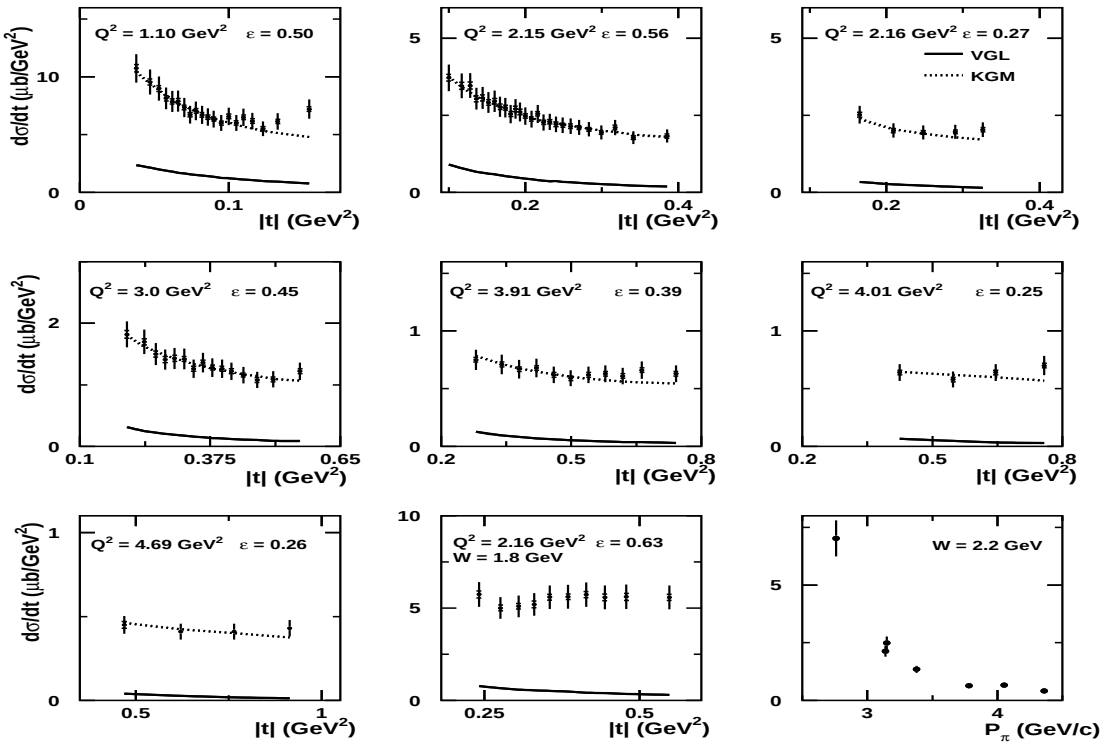

FIGURE 1.6: Differential cross sections $\frac{d\sigma}{dt}$ for pion electroproduction from hydrogen target versus $|t|$. The last panel (bottom right) shows the differential cross section versus the pion momentum in the lab frame (only the seven points at W =2.2 GeV are shown here). For each of the points in the last panel, the data were averaged over the respective t range shown in the previous panels. For the panels showing differential cross section versus $|t|$, the center of mass energy W is 2.2 GeV for all except one kinematic setting where W = 1.8 GeV (bottom middle). The data are compared with both the VGL-Regge [27] and the KGM [28] calculations where available.

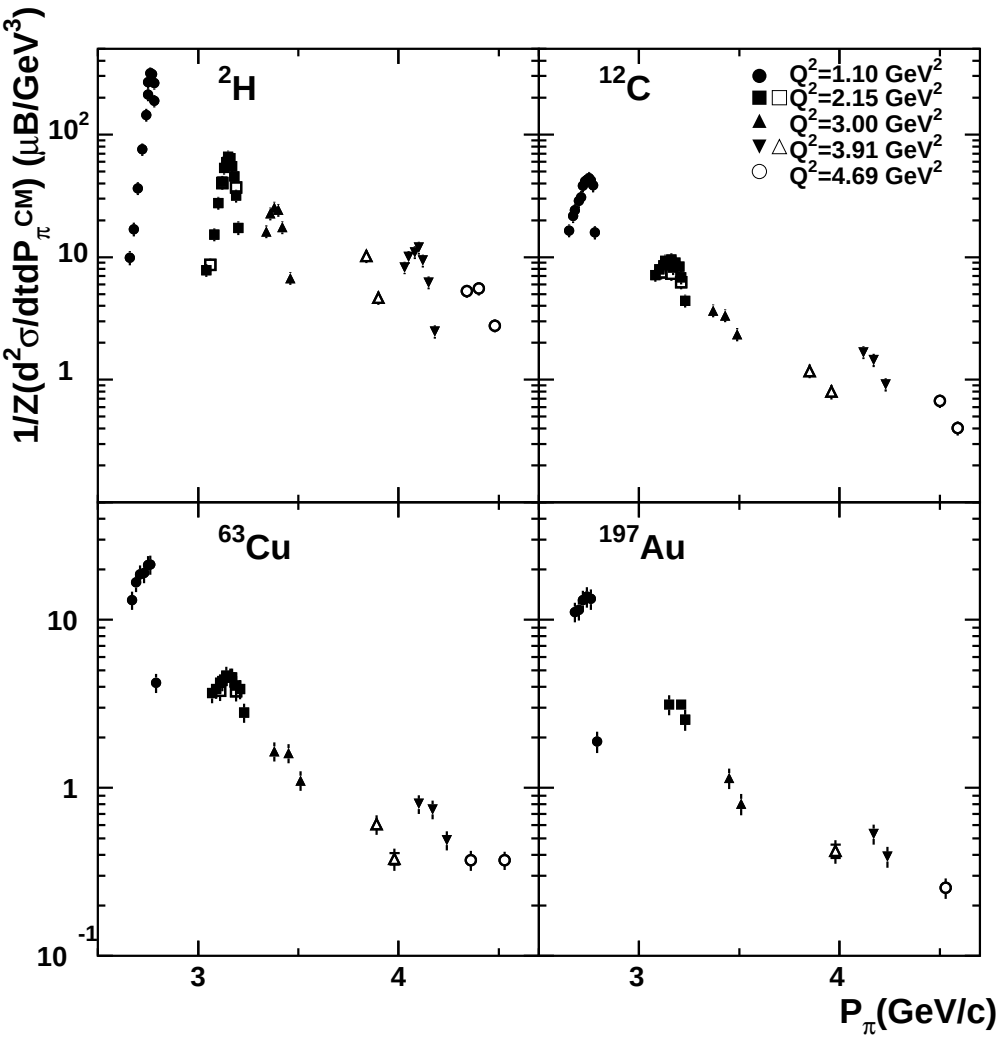

FIGURE 1.7: The extracted double differential cross sections $\frac{1}{Z}\frac{d\sigma}{dtdP_\pi^{CM}}$ versus the pion momentum P_π for the deuterium, carbon, copper, and gold targets. The cross sections are normalized by the atomic number Z, since π^+ can only be generated from a proton in this channel. For each target at Q^2 =2.15 GeV^2 and Q^2 = 3.91 GeV^2 the solid symbols represent the high ϵ kinematics while the open symbols represent the low ϵ kinematics.

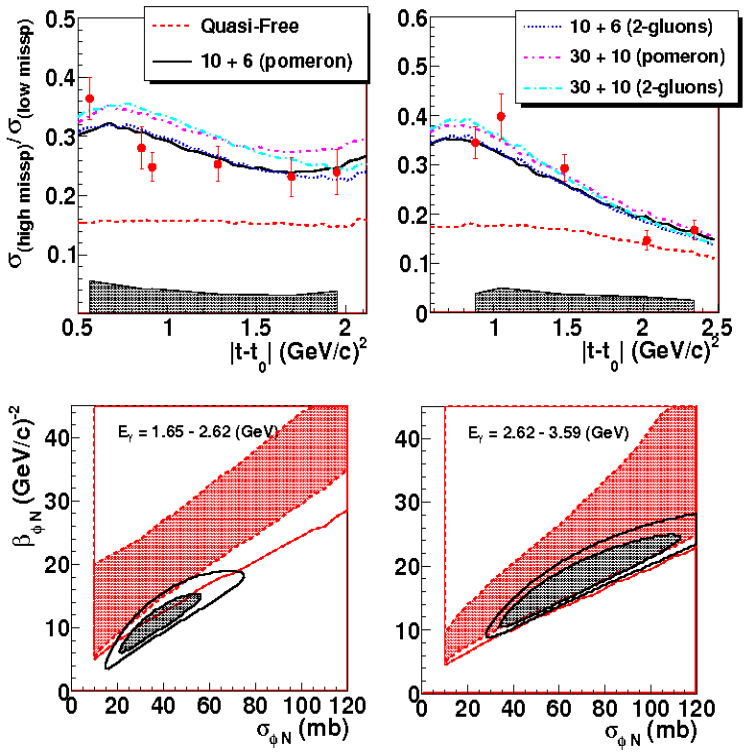

FIGURE 1.8: Cross section ratios between the high and the low missing momentum regions for photon energies of 1.65-2.62 GeV (top left) and 2.62-3.59 GeV (top right). The results of this work are shown in red solid circles. The black bands represent the systematic uncertainties. The label "30 + 10" indicates the calculation from Laget with $\sigma_{tot}^{\phi N} = 30$ mb and $\beta_{\phi N} = 10$ GeV^{-2}. The legend for the calculations applies to both top panels. The 70% (shaded area) and the 95% (open area) confidence level plots shown for the $\gamma + d \rightarrow \phi + p + (n)$ channel (red), the $\gamma + d \rightarrow \phi + d$ coherent channel (black) for photon energies of 1.65-2.62 GeV (bottom left) and 2.62-3.59 GeV (bottom right).

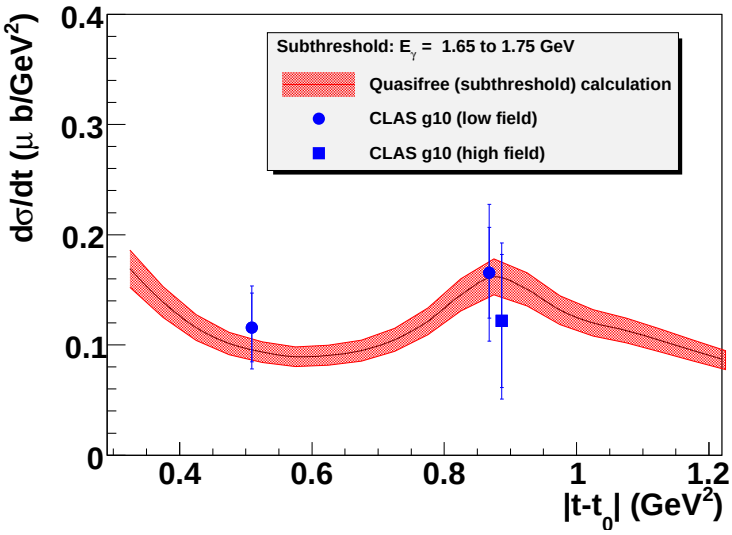

FIGURE 1.9: Sub-threshold ϕ Production Cross Sections. The red curve is a simple theoretical calculation for the photon energy in the same range. The error bands show the estimated uncertainties for the calculation.

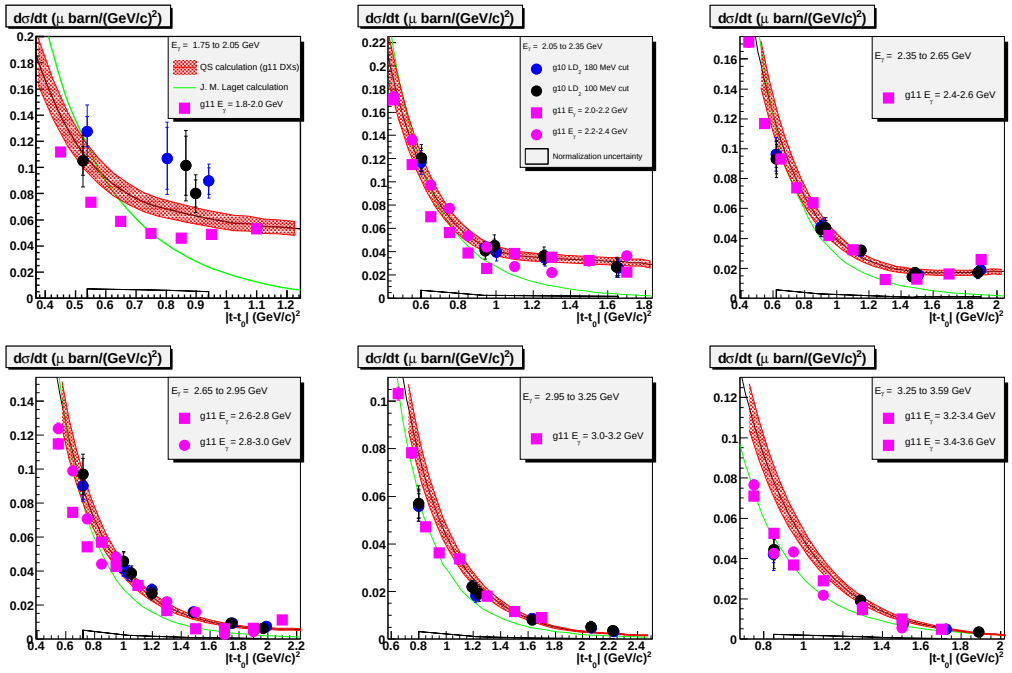

FIGURE 1.10: ϕ photo-production cross sections on "proton" are plotted. The inner error bar of the data points is the statistical uncertainty, the outer error bar is the square root of the quadratic sum of point-to-point systematic uncertainty and statistical uncertainty. The normalization uncertainties are plotted as a black band.

2

Introduction

The strong interaction, one of the four fundamental interactions, is responsible for 99% of all visible matter in the universe [54] [1]. Quantum Chromodynamics (QCD), which treats quarks and gluons as the fundamental degrees of freedom, is regarded as the accepted description of strong interactions. Carrying "color charges", quarks and gluons are bounded inside colorless hadrons, namely baryons ($|qqq>$) and mesons ($|q\bar{q}>$). Of all baryons, nucleons (protons/neutrons) are the most fundamental ones that form all atomic nuclei. Nucleon-nucleon interactions, often mediated by meson exchange, are in essence the residual strong interactions leaked from within the nucleons. One central quest of nuclear physics is to employ QCD, or quark/gluon degrees of freedom, to understand the nucleon structure. In the next section, we will briefly review the history and general features of QCD, in particular, the asymptotic freedom and the confinement.

[1] More than 99% of the visible matter is made up of proton and neutron. Only a few percent from quark masses and the rest are from the kinetic energy and interactions of quarks and gluons. Such findings are confirmed with the lattice calculation [54].

2.1 A Brief History of QCD

The history of QCD dates back to 1964, when Gell-Mann [55] (1969 Nobel Laureate) and Zweig [56] independently proposed the quark model in order to categorize hadrons. A recent review of the quark model can be found in Ref. [57]. Before the establishment of the quark model, physicists classified various hadrons into octets according to their charges, masses, and other physical properties, which is referred to as the "eightfold way" [58, 59, 60]. With the quark model, hadrons are no longer treated as the fundamental building blocks of the strong interaction. Instead, three flavors of quarks, up (u), down (d), and strange (s), are introduced to describe the observed structure groups in "eightfold way" [2].

Despite its success in hadron categorization, the quark model could not explain the existence of some "exotic" baryons, such as Δ^{++} and Ω^{-}. The Δ^{++}, carrying two positive charges, is a particle with spin $\frac{3}{2}$. Therefore, according to the quark model, it consists of three u quarks with the same spin orientation. Similarly, Ω^{-} was interpreted as three s quarks with the same spin orientation. Given that there were no other quantum numbers available at the time, the existence of such "exotic" baryons was forbidden by the Pauli exclusion principle. The paradox was solved by Han with Nambu [61] and Greenberg [62] by introducing into the quark model an additional SU(3) gauge degree of freedom, which was later named color charge. In addition, Han and Nambu [61] also introduced an octet of particles (gluons) as the mediator of the interaction between the quarks.

In 1969, Feynman proposed the parton model [63], an analogue to the quark model in hadron spectroscopy, to study hadron collisions at high energies. The idea of "parton" was subsequently adopted by Bjorken and Paschos [64] in inelastic electron-proton and γ-proton scattering. The predicted "Bjorken Scaling" [64] was

[2] Later, three additional quark flavors, c, b, and t were found.

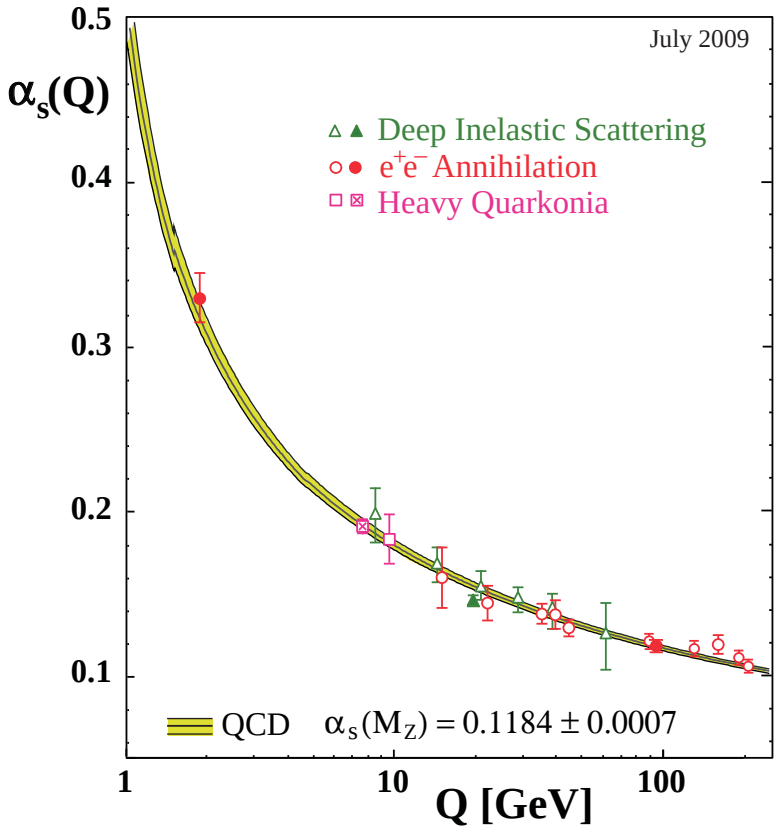

FIGURE 2.1: The strong interaction coupling constant, measured from Deep Inelastic Scattering, e^+e^- annihilation, and heavy Quarkonia, is plotted as a function of 4-momentum transfer Q. The yellow band represents the first principle calculation based on the QCD renormalization group equation. Figure is from Ref. [57].

confirmed in experiments at SLAC by Friedman, Kendall and Taylor *et al.* [65, 66]. This was the first evidence of the existence of quarks, for which Friedman, Kendall and Taylor were awarded Nobel Prize in 1990.

In 1973, Gross, Politzer and Wilczek [67, 68] demonstrated that a wide class of non-Abelian gauge theories (Yang-Mills theories) all exhibited asymptotic free behavior, leading to the eventual discovery of QCD. They were awarded Nobel Prize in 2004.

QCD is a non-abelian gauge theory with local SU(3) gauge group of phase transformations on the quark color fields. In comparison, quantum electrodynamics (QED) is an abelian gauge theory based on the U(1) gauge group. The photons,

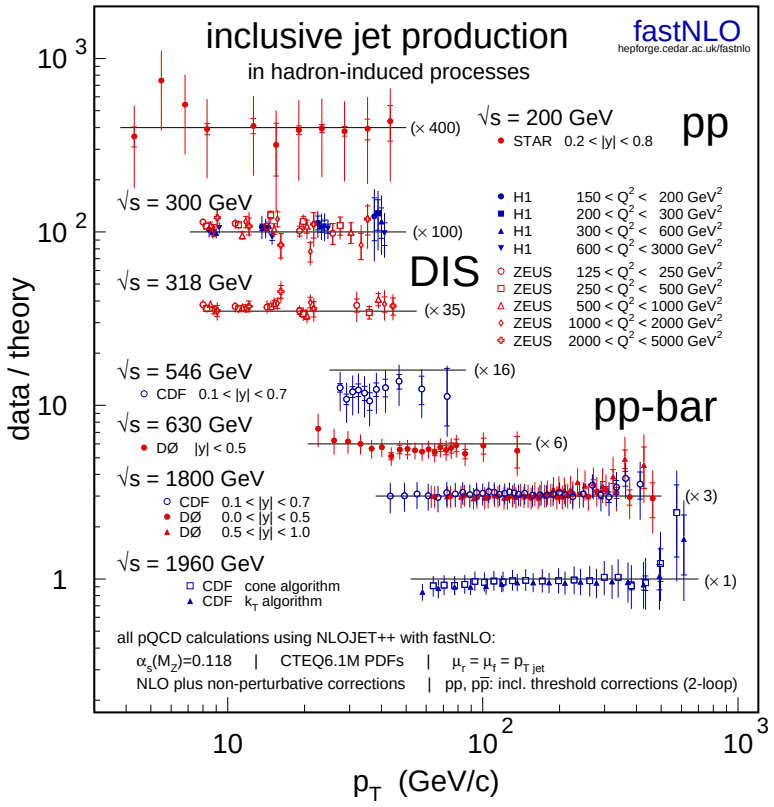

FIGURE 2.2: The data of inclusive jet production cross sections, measured in different hadron-induced processes and DIS at different center-of-mass energies, are plotted as a function of jet transverse momentum (p_T) in arbitrary scales. For comparison, the corresponding next leading order (NLO) theoretical predictions are also plotted. Different parameters, including coupling constant, PDFs, renormalization, and factorization scales, are illustrated at the bottom of the figure. Figure is from Ref. [57].

which are the mediators of the electromagnetic force, do not carry electric charge, and thus can not couple to themselves. However, due to the non-abelian nature of QCD, the gluons, which are the mediators of the strong force, carry color charges and thus interact with themselves. This special feature of the strong interaction leads to two famous phenomena of QCD: the asymptotic freedom and the color confinement.

Asymptotic freedom describes the observation that the interaction between two color objects is weak at high energy (short distance), and strong at low energy (long distance). Fig. 2.1 [57] shows the strong interaction coupling constant, calculated

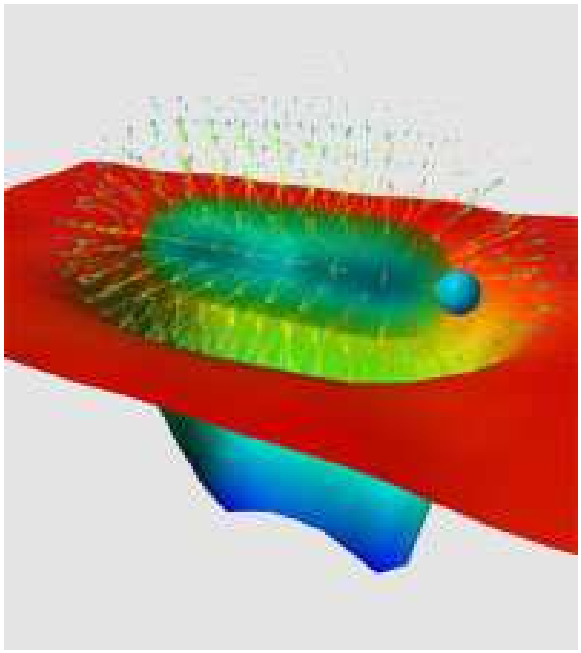

FIGURE 2.3: An illustration of the gluon flux tube between a heavy quark and its antiquark. Figure is from `http://dustbunny.physics.indiana.edu/HallD/GlueX/Home.html`.

through the renormalization group equation, as a function of the 4-momentum transfer Q. At infinitely large Q, the strong interaction coupling constant α_S approaches zero, and the quarks/gluons behave like free particles. Thus, in the circumstances of large Q, perturbative calculations together with the input of the nucleon structure, particularly parton distribution functions (PDFs), can be used to provide first-principle predictions for experimental observables[3]. For example, Fig. 2.2 [57] shows the agreement between data and theory for the inclusive jet cross sections as a function of the jet transverse momentum p_T. However, the perturbative calculations do not apply at small Q due to the significant increment of the strong interaction coupling constant and contributions from higher twist [4].

Color confinement refers to the observation that quarks/gluons, which carry color

[3] Based on the QCD factorization theorem (Sec. 2.3.5), the PDFs should be universal and process independent.

[4] See more discussions in Sec. 2.3.5.

charges, can not be singularly isolated or directly observed. For heavy quarks (c, b, and t), confinement has been verified in the quenched lattice QCD calculation of the static quark anti-quark potential [69], whose linearly rising behavior over distance has been established. One intuitive way to understand the color confinement is in the model of the Lund string fragmentation [70]. In this picture, the interaction between quarks and anti-quarks can be modeled as narrow tubes or strings (See Fig. 2.3), which are formed by gluon fields. As the quark and anti-quark move apart, the energy stored in the string will increase until it is large enough to produce a new quark-antiquark pair from the QCD vacuum. Consequently, the original quark (anti-quark) will be neutralized by the newly created antiquark (quark) from the QCD vacuum, and remain bound in the colorless hadron. Although color confinement has been established through lattice QCD for heavy quarks and is well recognized to be responsible for the fact that no free quarks have been observed in experiments, it has neither been mathematically proven, nor been experimentally demonstrated for the light quarks (u, d and s) on the lattice.

2.2 Nucleon Structure

In the real world, where quarks/gluons are confined in nucleons, the energy scale, Λ_{QCD}, is about 200 MeV, resulting in a large α_S and the breakdown of perturbative QCD calculations. Therefore, nucleon structure can not be directly calculated by first principles of QCD. Nevertheless, understanding the nucleon structure in terms of quark and gluon degrees of freedom, is not only very important by itself, but will also provide important information about QCD in the confinement region. In this section, we will briefly introduce theoretical descriptions, together with definitions of some important concepts concerning the structure of the nucleon.

The most fundamental element that describes nucleon structure with parton de-

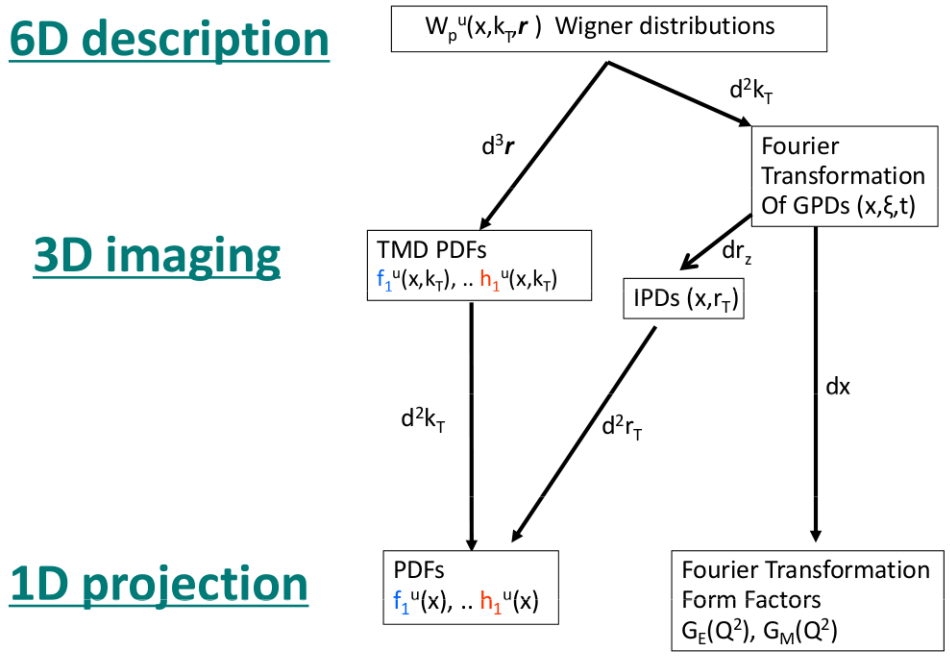

FIGURE 2.4: An illustration of how the Generalized Parton Distribution Functions (GPD), the Impact Parameter Distribution Functions (IPD), the Transverse Momentum Distribution Functions (TMD), the Form Factor, and the normal Parton Distribution Functions (PDF) are deduced from the mother Wigner distributions.

grees of freedom is called the Wigner-type parton distribution function $W_\Gamma(\vec{r},\vec{k})$ [71][5], where $\vec{r}$ is the 3-vector of parton position in the coordinate space and $\vec{k}$ is the 3-vector parton momentum in the momentum space. For any fixed parton $\vec{k}$ and $\vec{r}$, the Wigner distribution does not convey a probability interpretation, but gives a full-3D nucleon picture at every fixed momentum $\vec{k}$.

By integrating over the parton transverse momentum $\vec{k}_T$, the $W_\Gamma(\vec{r},\vec{k})$ is converted into the Fourier transformation of the Generalized Parton Distributions (GPD) $F_\Gamma(x,\xi,t)$ [72, 73, 74], which contains the information of parton distribution both in

[5] In Ref. [71], the Wigner-type PDF is defined as $W_\Gamma(\vec{r},k)$. By integrating over the $k^- = (k^0 - k^z)/\sqrt{2}$, the $W_\Gamma(\vec{r},k)$ becomes the reduced Wigner distribution $W_\Gamma(\vec{r},\vec{k})$.

the transverse plane and longitudinal direction:

$$f_\Gamma(\vec{r}, k^+) = \int \frac{d^2\vec{k}_T}{(2\pi)^2} W_\Gamma(\vec{r}, \vec{k}) \sim \int \frac{d^3\vec{q}}{(2\pi)^3} e^{-i\vec{q}\cdot\vec{r}} F_\Gamma(x, \xi, t). \tag{2.1}$$

Here $q = p - p'$ is the t channel momentum transfer between the initial nucleon momentum p and final nucleon momentum p', $\xi = q^z/2\sqrt{M^2 + \vec{q}^2/4}$ and $t = -\vec{q}^2$. If one subsequently integrates $f_{\gamma^+}(\vec{r}, k^+)$ over r_z (replacing Γ with γ^+), the impact parameter space distributions (IPDs) [75, 76] are obtained, providing the 2-D density distribution of the parton inside the nucleon at fixed x. Moreover, integrating IPDs over r_T will give rise to the normal parton distribution functions (PDFs), which are interpreted as the probability of finding a parton, within the nucleon, with momentum fraction x_{bj} in the light-cone frame. On the other hand, if one integrates $f_{\gamma^+}(\vec{r}, k^+)$ over k^+, then the Fourier transformation of the electric G_E and magnetic G_M form factors are obtained, describing the charge and current distribution of nucleon.

Integrating $W_\Gamma(\vec{r}, \vec{k})$ over $\vec{r}$ gives rise to the transverse-momentum dependent parton distributions (TMD) $f(\vec{k}_T, x_{bj})$, which will be discussed in more details in Sec. 3.2. Subsequently, the normal parton distribution functions are then obtained by further integrating TMD over $\vec{k}_T$. The discussions above are summarized and illustrated in Fig. 2.4.

To fully comprehend the nucleon structure in terms of QCD, one must understand two basic properties of the nucleon: mass and spin. The nucleon mass consists of the quark and gluon kinematic and potential energies, quark masses, and the trace anomaly. A detailed QCD analysis of the nucleon mass structure can be found in Ref. [77]. In the next section, we will focus on the decomposition of the nucleon spin.

2.2.1 Nucleon Spin Structure

The study of the proton spin structure started with the pioneer work of the EMC collaboration at CERN [78, 79], which measured the proton's g_1 spin dependent structure function through polarized deep inelastic muon-proton scattering. Their data suggested that, contrary to the prediction by the quark model, all quark spins did not add up to the entire nucleon spin ($\frac{1}{2}$). This surprising result subsequently drew an explosion of theoretical interest and experimental efforts at CERN, SLAC, DESY, JLab and RHIC. Recent reviews can be found in Ref. [80, 81, 82, 83].

In the simple parton model, the nucleon spin carried by quarks ($\sum_q \Delta q$) equals $g_A^{(0)}|_{pDIS}$, the flavor singlet axial charge, which can be extracted from the inclusive g_1 data. The recent COMPASS data [84] shows:

$$g_A^{(0)}|_{pDIS,Q^2\to\inf} = 0.33 \pm 0.03(stat) \pm 0.05(sys.), \tag{2.2}$$

which is significantly lower than the predicted values (0.75) from simple relativistic quark models [85, 86, 87, 88, 89, 90, 91][6].

In the QCD improved parton model, the $\sum_q \Delta q$ is expressed as:

$$\sum_q \Delta q = g_A^{(0)}|_{pDIS} + 3\frac{\alpha_s}{2\pi}\Delta G \tag{2.3}$$

by including the QCD axial anomaly. Here ΔG is the amount of nucleon spin carried by the gluons. In the past 15 years, ΔG has been accessed by many experiments, including COMPASS, SMC, HERMES, and RHIC. For example, the ΔG value extracted from the PHENIX $\sqrt{s} = 200$ GeV data [92] is:

$$\Delta G_{GRSV}^{[0.02,0.3]} = 0.2 \pm 0.1(stat..) \pm 0.1(sys.)^{+0.0}_{-0.4}(shape) \pm 0.1(scale) \tag{2.4}$$

at $Q^2 = 4$ GeV^2. However, this value still fails to fully reconcile the discrepancy

[6] The other 25% is attributed to the quark orbital angular motion.

between the measured $\sum_q \Delta q$ and the expectation from the simple relativistic quark model.

The modern understanding of the nucleon spin is expressed by a set of nucleon spin sum rules. The first sum rule was derived by Jaffe and Manohar [93] in the Light-cone gauge ($A^+ = 0$):

$$\frac{1}{2} = \Delta L_q + \frac{1}{2}\Delta\Sigma + \Delta L_g + \Delta G. \tag{2.5}$$

Here, ΔL_q and ΔL_g represent the total orbital angular momentum of quarks and gluons, respectively. $\Delta\Sigma$ is the contribution from intrinsic quark spin, and ΔG is the contribution from gluon spin. They are expressed as matrix elements [93].

Later, Ji [94, 95] discovered a new nucleon spin sum rule, which is gauge invariant:

$$\frac{1}{2} = J_q + J_g = \frac{1}{2}\Delta\Sigma + L_q + J_g, \tag{2.6}$$

where J_q and J_g are the total angular momentum of quarks and gluons, respectively. In addition, J_q can be further decomposed into $\Delta\Sigma$ and the total quark orbital angular momentum L_q. J_q and J_g can be accessed through the measurement of the GPDs [94, 95], which is also referred to as the Ji's sum rule.

Recently, a transverse spin sum rule has been derived by Bakker, Leader and Trueman [96]:

$$\frac{1}{2} = \Delta\Sigma_T + L_q^T + L_g^T, \tag{2.7}$$

where $\Delta\Sigma_T$ is the total contribution from the quark transverse spin. L_q^T and L_g^T are the total transverse orbital angular momentum from quarks and gluons, respectively[7]. The underline physics interpretations of this transverse spin sum rule are still under debate.

[7] In the transverse spin sum rule, the total contribution from gluon transverse spin is zero, which will be discussed in detail in Sec. 3.2.2. The validity of the transverse spin sum rule is still under debatable.

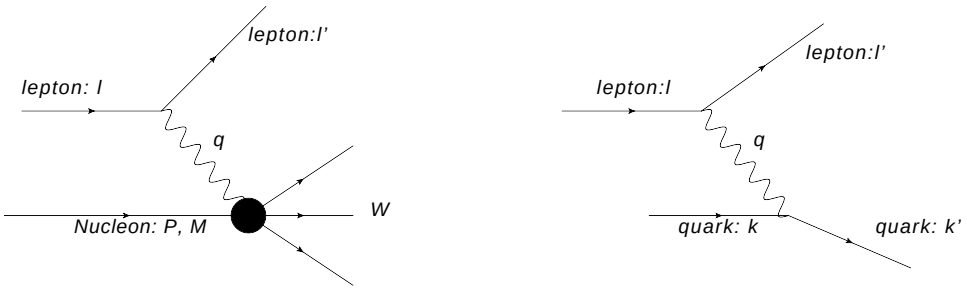

FIGURE 2.5: Kinematic variables of the DIS are shown in the left panel. l and l' are the 4-momentum of the incoming and outgoing leptons, respectively. P is the 4-momentum of the nucleon with mass M, and W is the invariant mass of the recoiling system X. The exchange is a virtual photon, whose 4-momentum is $q = l - l'$. The right panel shows the fundamental process, where the lepton is interacting with a quark inside the nucleon. The quark's original 4-momentum is $k = x_{bj} \cdot P$ in the light-cone frame.

2.3 Probing the Nucleon Structure – Experimental Methods With Electromagnetic Probe

The electromagnetic probe is one of the most important tools to study the nucleon structure. In particular, the high-energy lepton-nucleon deep inelastic scattering (DIS) plays an essential role in revealing the partonic degrees of freedom of the nucleon.

2.3.1 Deep-Inelastic Scattering

The DIS process is illustrated in Fig. 2.5. The filled circle represents the internal nucleon structure. The kinematic variables are defined as the following:

- The lepton's energy loss in the nucleon rest frame, or the energy it transfers into the nucleon system:

$$\nu = E_l - E_{l'} = \frac{q \cdot P}{M} \tag{2.8}$$

- 4-momentum transfer squared of the virtual photon. [8]

$$Q^2 = -q^2 \tag{2.9}$$

- x_{bj} is the fraction of the nucleon's momentum carried by the struck quark $k = x_{bj} \cdot P$ in the parton model and in the light-cone frame.

$$x_{bj} \equiv x = \frac{Q^2}{2M\nu} \tag{2.10}$$

- The fraction of the lepton's energy transfer in the nucleon rest frame.

$$y = \frac{E_l - E_{l'}}{E_l} = \frac{q \cdot P}{l \cdot P} \tag{2.11}$$

- W is the mass of the recoiling system.

$$W = \sqrt{(P+q)^2} \tag{2.12}$$

- The center-of-mass energy squared of the lepton-nucleon system.

$$s = (l+P)^2 \tag{2.13}$$

Fig. 2.6 shows the differential cross section spectrum of a typical inclusive lepton scattering off a light nuclear target. The spectrum includes elastic scattering $e+A \rightarrow e+A$, quasi-elastic scattering $e+N \rightarrow e+N$, the resonance $e+N \rightarrow e'+N^r$, where the N^r represents one of the resonance states of nucleon, and finally the DIS $e+q \rightarrow e+q$, where q represents the struck quark.

[8] Intuitively, it sets the energy scale of the process and designates the spatial resolution of the virtual photon.

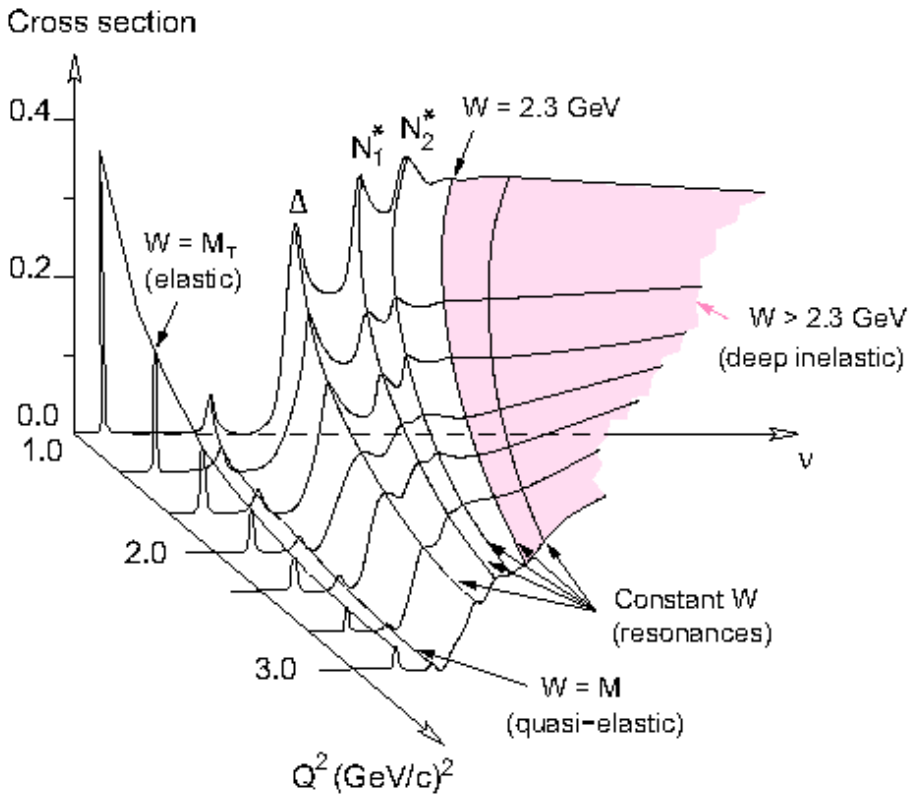

FIGURE 2.6: Differential Cross section (in arbitrary units) of inclusive lepton scattering off a light nuclear target. M_T is the target mass, and M is the nucleon mass. Figure is obtained from Ref. [97].

Structure Functions

In the DIS region, the differential cross section can be expressed by a set of structure functions with the assumption of one-photon exchange between the lepton and the struck quark (lowest order perturbation theory). In this section, we will review the formalism, adopting the conventions in Ref. [57]. The differential cross section of polarized lepton-nucleon scattering can be formulated as the product of leptonic and hadronic tensors:

$$\frac{d^2\sigma}{dxdy} = \frac{2\pi y\alpha^2}{Q^4} L^{\mu\nu} W_{\mu\nu}. \tag{2.14}$$

The leptonic tensor is

$$L_{\mu\nu} = 2(l_\mu l'_\nu + l'_\mu l_\nu - l \cdot l' g_{\mu\nu} - i\lambda\epsilon_{\mu\nu\alpha\beta} l^\alpha l'^\beta), \tag{2.15}$$

and $\lambda = \pm 1$ is the electron helicity. The hadronic tensor is

$$W_{\mu\nu} = \frac{1}{4\pi} \int d^4 z e^{iq\cdot z} < P, S|[J^\dagger_\mu(z), J_\nu(0)]|P, S >, \tag{2.16}$$

where S is the nucleon-spin 4-vector, with $S^2 = -M^2$ and $S \cdot P = 0$. The hadronic tensor can be expressed in terms of the structure functions F_1, F_2, g_1, and g_2:

$$\begin{aligned} W_{\mu\nu} &= (-g_{\mu\nu} + \frac{q_\mu q_\nu}{q^2}) F_1(x, Q^2) + \frac{\hat{P}_\mu \hat{P}_\nu}{P \cdot q} F_2(x, Q^2) \\ &+ i\epsilon_{\mu\nu\alpha\beta} \frac{q^\alpha}{P \cdot q} [S^\beta g_1(x, Q^2) + (S^\beta - \frac{S \cdot q}{P \cdot q} P^\beta) g_2(x, Q^2)]. \end{aligned} \tag{2.17}$$

Plugging Eqn. (2.15) and Eqn. (2.17) into Eqn. (2.14), one obtains:

$$\begin{aligned} \frac{d^2\sigma}{dxdy} &= \frac{4\pi\alpha^2}{xyQ^2} \{ y^2 x F_1 + (1 - y - \frac{x^2 y^2 M^2}{Q^2}) F_2 \\ &+ \lambda[-y(2 - y - 2x^2 y^2 \frac{M^2}{Q^2}) x g_1 + 4x^3 y^2 \frac{M^2}{Q^2} g_2] \}. \end{aligned} \tag{2.18}$$

The two unpolarized structure functions F_1 and F_2 satisfy:

$$F_1 = \frac{F_2(1 + \gamma^2)}{2x(1 + R)} \tag{2.19}$$

$$\gamma = \frac{Q^2}{\nu^2} = \frac{(2Mx)^2}{Q^2} \tag{2.20}$$

and $R = \frac{\sigma_L}{\sigma_T}$ is the ratio of the longitudinal to transverse virtual photon cross-sections[9]. In addition, the longitudinal structure function is usually defined as:

$$F_L = F_2 - 2xF_1. \tag{2.21}$$

In the simple quark-parton model, the Callan-Gross relation [98] defines: $F_L = 0$.

[9] The definition of the σ_L and σ_T can be found in Eqn. (1.5). In the parton model, the longitudinal DIS cross section is predicted to be zero ($R = 0$).

Structure Functions in Quark Parton Model

In the simple quark-parton model [63, 64], the structure functions,

$$F_1 = \frac{F_2}{2x} \tag{2.22}$$

$$F_2 = x\sum_q e_q^2(f_1^q + f_1^{\bar{q}}) \tag{2.23}$$

$$g_1 = \frac{1}{2}\sum_q e_q^2(g_{1L}^q + g_{1L}^{\bar{q}}) \tag{2.24}$$

$$g_2 = -g_1 + \int_x^1 \frac{dy}{y} g_1(y), \tag{2.25}$$

are expressed by the normal parton distribution functions $f_1(x, Q^2)$, which denotes the probability of finding a parton with certain momentum fraction x of the nucleon.

$g_{1L}^q = f_1^{q\uparrow} - f_1^{q\downarrow}$ is called the longitudinal parton distribution function, which represents the probability of finding a longitudinal polarized parton with x_{bj} inside a longitudinal polarized proton. e_q is the charge of the struck quark. Here the longitudinal direction is defined as the direction of the virtual photon 3-vector momentum. Eqn. 2.25 is also referred to as the Wandzura-Wilczek relation [99].

PDFs and QCD

At the Bjorken limit, where Q^2 and ν approach infinity and x_{bj} stays fixed, the PDF $f_1^q(x, Q^2)$ becomes $f_1^q(x)$. This feature, referred to as the Bjorken scaling [64], is based on the collinear approximation, where the quark transverse momenta are assumed to be small compared to Q^2 [10]. However, since a quark can radiate a hard gluon to gain large transverse momentum, the collinear approximation is partially violated in QCD. Therefore, the PDFs are associated with Q^2, and the PDFs at different

[10] More generally, the Bjorken scaling is based on the assumption that all other scales are small comparable to the Q^2.

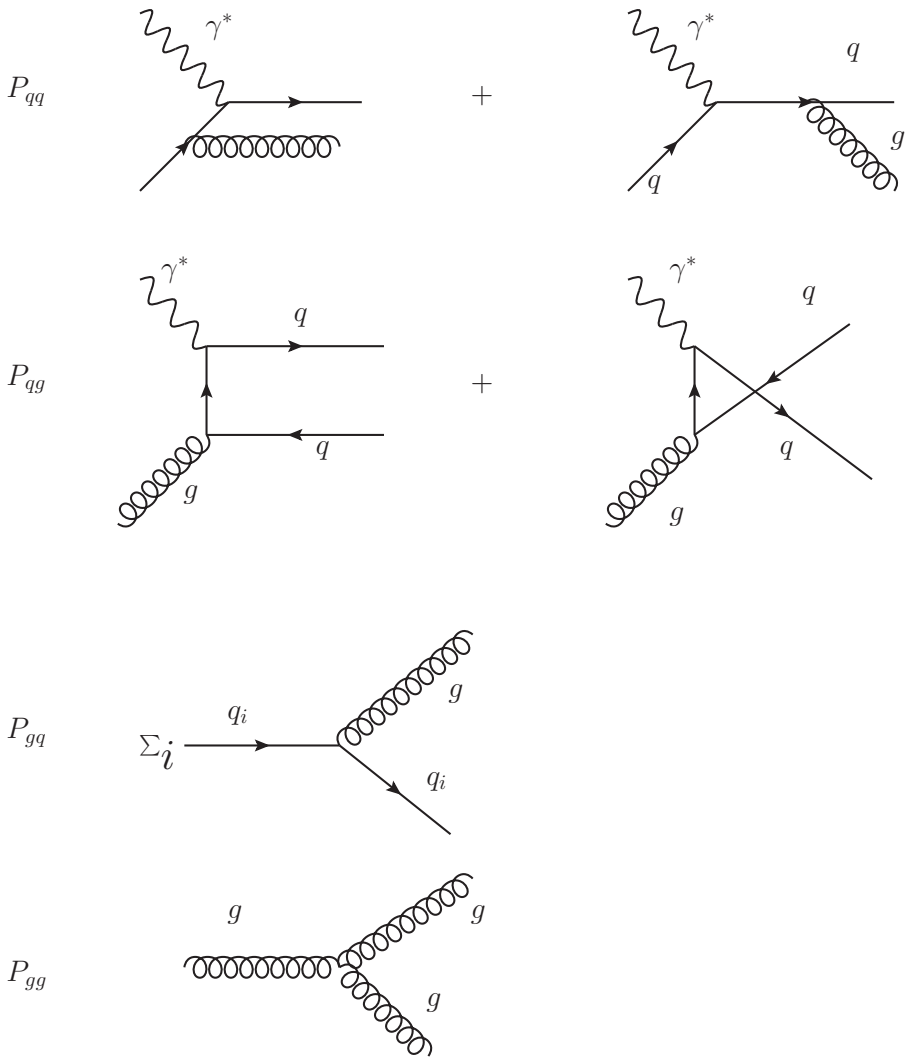

FIGURE 2.7: The splitting function Ps and their corresponding Feynman diagrams in QCD. The γ^* is the virtual photon emitted from the scattered lepton. q and g represent the quark and gluon, respectively.

Q^2 values can be connected through the Dokshitzer-Gribov-Lipatov-Altarelli-Parisi (DGLAP) evolution equations [100, 101, 102, 103].

$$\begin{aligned} \frac{\partial f_1^{qNS}}{\partial \ln Q^2} &= \frac{\alpha_s(Q^2)}{2\pi} P_{qq} \otimes f_1^{qNS} \\ \frac{\partial}{\partial \ln Q^2} \begin{pmatrix} f_1^{qS} \\ f_1^{g} \end{pmatrix} &= \frac{\alpha_s(Q^2)}{2\pi} \begin{pmatrix} P_{qq} & 2n_f P_{qg} \\ P_{gq} & P_{gg} \end{pmatrix} \otimes \begin{pmatrix} f_1^{qS} \\ f_1^{g} \end{pmatrix}. \end{aligned} \tag{2.26}$$

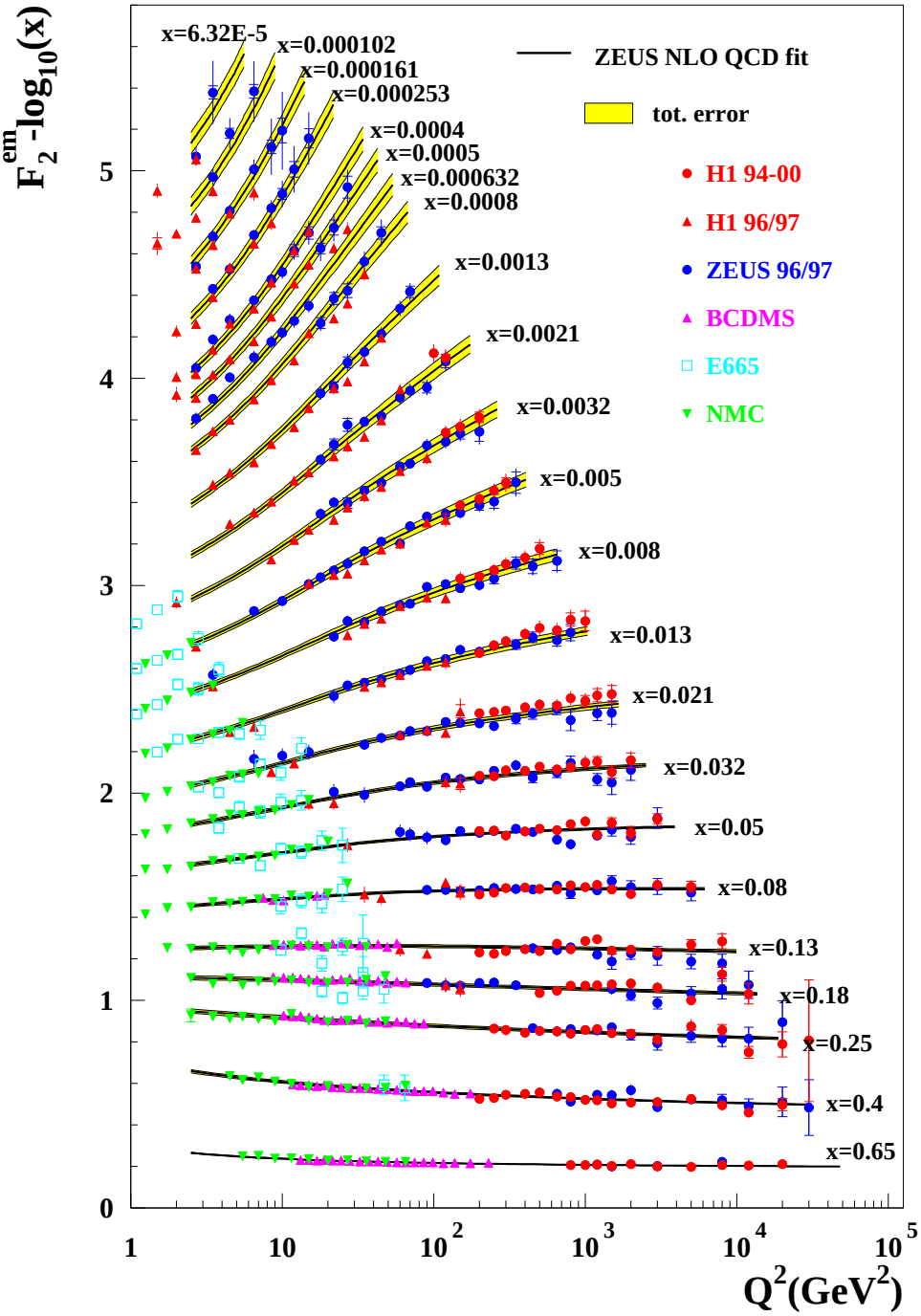

FIGURE 2.8: The measured F_2 structure functions from HERA collider and fixed-target experiments compared with the ZEUS NLO QCD fit [1]. Figure is from Ref. [4].

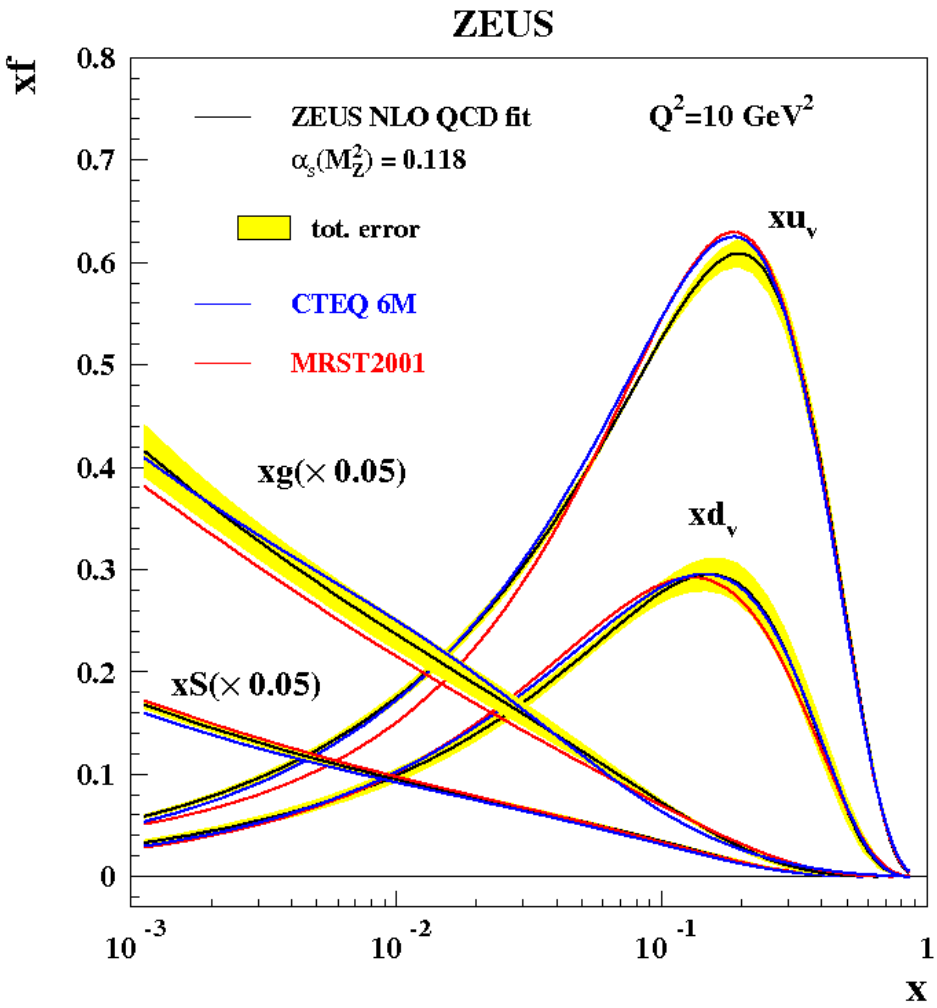

FIGURE 2.9: The ZEUS fit [1] compared with the global analyses CTEQ6M [2] and MRST2001 [3]. Figure is from Ref. [4].

Here, the flavor non-singlet (f_1^{qNS}) and singlet f_1^{qS} quark distributions in flavor $SU(3)_F$ group [80] are defined as:

$$f_1^{qNS} = f_1^q - f_1^{\bar{q}} \tag{2.27}$$

$$f_1^{qS} = \sum_q (f_1^q + f_1^{\bar{q}}). \tag{2.28}$$

$\alpha_s(Q^2)$ represents the strong interaction coupling constant. The P_{ij} are the splitting functions illustrated in Fig. 2.7.

Experimental Data and PDFs

The F_2 structure function has been measured extensively at HERA (H1 and ZEUS), SLAC, CERN, and BCDMS. Data from these experiments with the Electromagnetic (E&M) probe are shown in Fig. 2.8 in comparison to the ZEUS NLO QCD fit [1]. The Q^2 dependence of the F_2 structure function at fixed x_{bj} violates the Bjorken scaling, implying the existence of the gluons. The resulting PDFs from the fits are compared in Fig. 2.9. Recently, a combined fit including both ZEUS and H1 data was performed [104].

The g_1 structure function has also been measured in SLAC, CERN, DESY, and JLab over the past twenty years. The left panel of Fig. 2.10[11] shows xg_1 from different experiments for proton, deuteron and neutron. The right panel of Fig. 2.10 shows the Q^2 dependence of the g_1^p at different x values. Compared to F_2^p, which has been mapped in a wide range of Q^2 and x (both covering 4 orders of magnitude) (Fig. 2.8), the g_1^p has only been mapped in a much more limited range (2 orders of magnitude each) due to the limitations of the polarized experiments.

2.3.2 Drell-Yan Process

In addition to the DIS, the Drell-Yan [106] (DY) process is also a very powerful tool that utilizes the E&M probe to study the nucleon structure. In the DY process, the quark and the anti-quark from two initial hadrons electromagnetically annihilate and subsequently generate a pair of leptons. Fig. 2.11 shows the fundamental processes of the DY and the DIS. The differential cross section of the DY process can be expressed as products of PDFs in the simple parton model:

$$\frac{d^2\sigma}{dM^2 dx_F} = \frac{4\pi\alpha^2}{9M^2 s}\frac{1}{x_1 + x_2}\sum_q e_q^2 \left[f_1^q(x_1) f_1^{\bar{q}}(x_2) + f_1^{\bar{q}}(x_1) f_1^q(x_2)\right]. \tag{2.29}$$

[11] Recently, the COMPASS collaboration released their results on g_1^p [105], which are not included in Fig. 2.8.

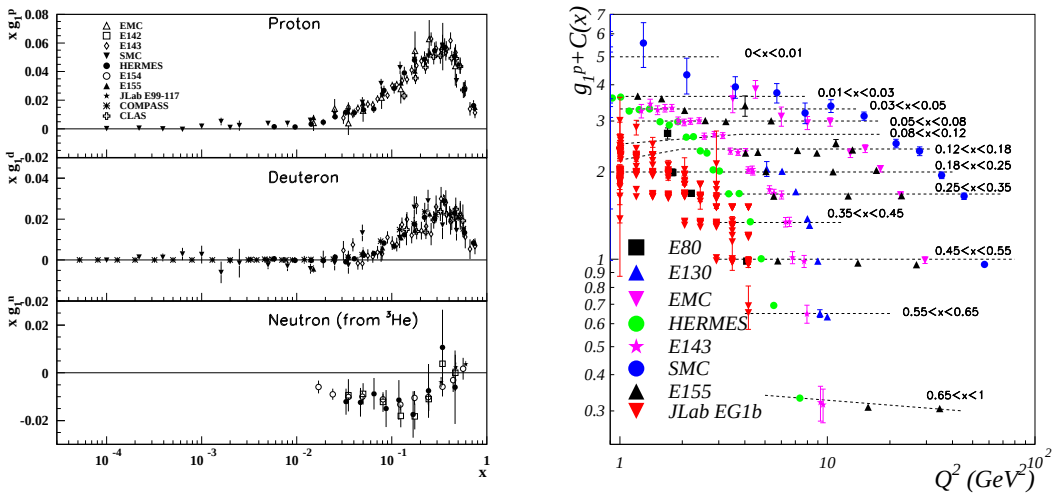

FIGURE 2.10: Left panel: World data on the polarized structure function $xg_1(x)$ for the proton, deuteron and neutron in the DIS region ($W > 2$ GeV), taken by different experiments, at several different values of Q^2, as compiled by the Particle Data Group [57]. Right panel: The proton data are also shown versus Q^2, for several bins in x. Figures are from Ref. [80].

Here x_1 and x_2 (or x_2 and x_1) are fraction of the two colliding hadrons carried by the quark and antiquark, respectively. f_1^q and $f_1^{\bar{q}}$ are the PDFs, and M is the invariant mass of the lepton pairs. Other kinematic variables include:

$$\tau \equiv x_1 \cdot x_2 = \frac{M^2}{s} \tag{2.30}$$

$$x_F = x_1 - x_2, \tag{2.31}$$

where s is the square of the center-of-mass energy of the two initial hadrons. Fig. 2.12 shows the scaling behavior of the DY process. A recent review of the DY process with nucleon and nucleus collision can be found in Ref. [107]. The latest measurement of the absolute DY di-muon cross section is from E866 [108], which agrees well with the expectation based on global PDFs.

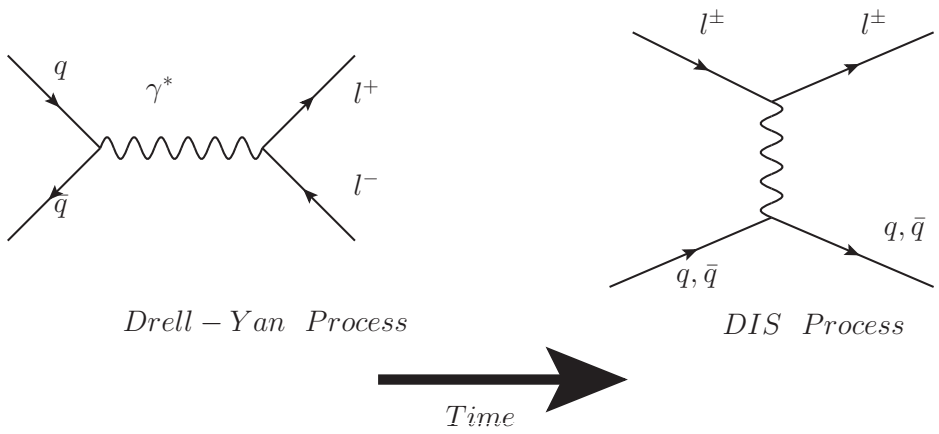

FIGURE 2.11: Left Panel: Drell-Yan Process with quark-antiquark E&M annihilation; Right Panel: DIS Process.

2.3.3 Semi-Inclusive Deep Inelastic Scattering

Compared to the inclusive DIS, where only the scattered lepton is detected, the semi-inclusive DIS (SIDIS) detects both the scattered lepton and the leading hadron simultaneously. Although the fundamental scattering process of the SIDIS is the same as that of the DIS, the detection of the leading hadron offers additional insights into the nucleon structure that are otherwise unattainable. High momentum fragments of the deep-inelastic nucleon breakup may statistically tag the underlying quark flavor structure. Fig. 2.13 shows the comparison between the DIS and SIDIS processes.

In addition to the kinematic variables defined in Sec. 2.3.1, the following variables are also needed to describe the SIDIS process in the rest frame of the nucleon:

- Transverse momentum of the detected hadron P_T:

$$P_T = \frac{\vec{q} \cdot \vec{P_h}}{|\vec{q}|} \tag{2.32}$$

- Ratio of the energy carried by the detected hadron and the energy of the virtual

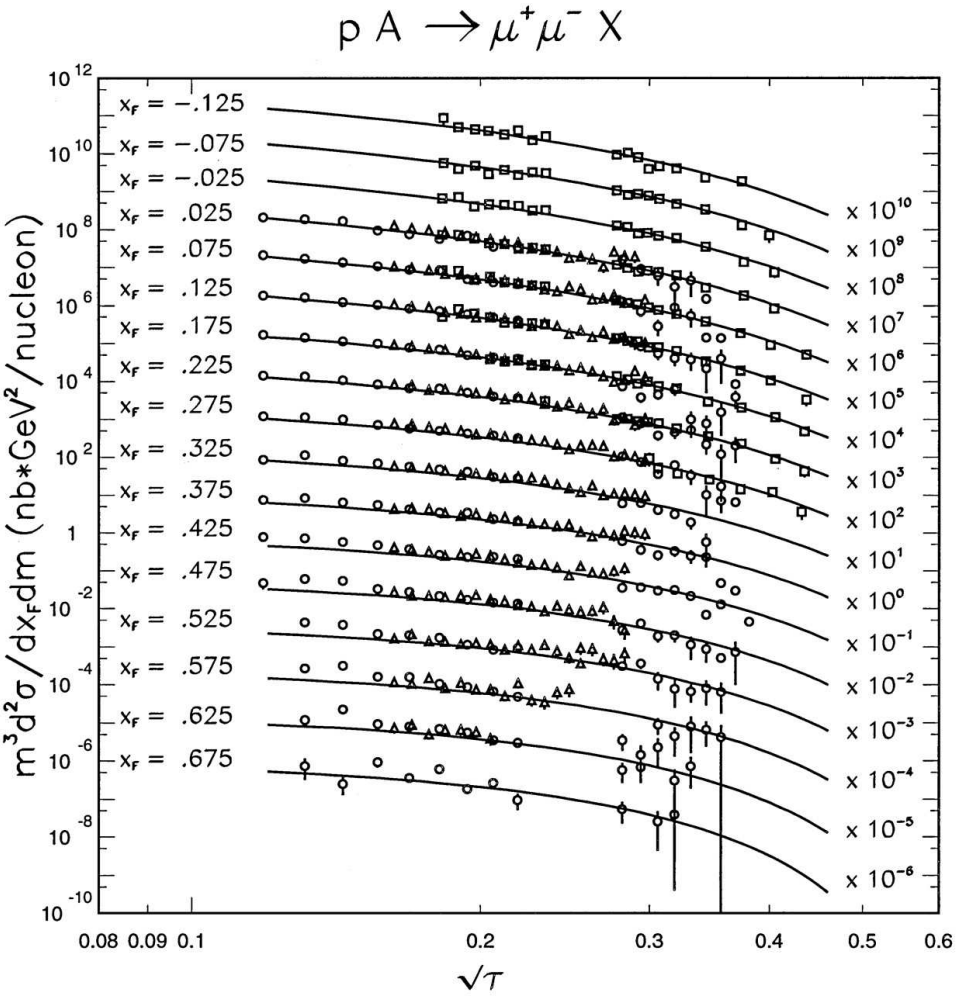

FIGURE 2.12: Proton-induced Drell-Yan production from experiments NA3 [109] (triangles) at 400 GeV, E605 [110] (squares) at 800 GeV, and E772 [111] (circles) at 800 GeV. The lines are absolute NLO order calculations for p + d collisions at 800 GeV using CTEQ4M PDFs [112]. Figure is from Ref. [107].

photon in the rest frame of the nucleon:

$$z = \frac{P \cdot P_h}{P \cdot q} \tag{2.33}$$

- Missing Mass W':

$$W' = \sqrt{(q + P - P_h)^2} \tag{2.34}$$

- ϕ_h (Fig. 2.14) is the angle between the scattering plane and the hadron plane.

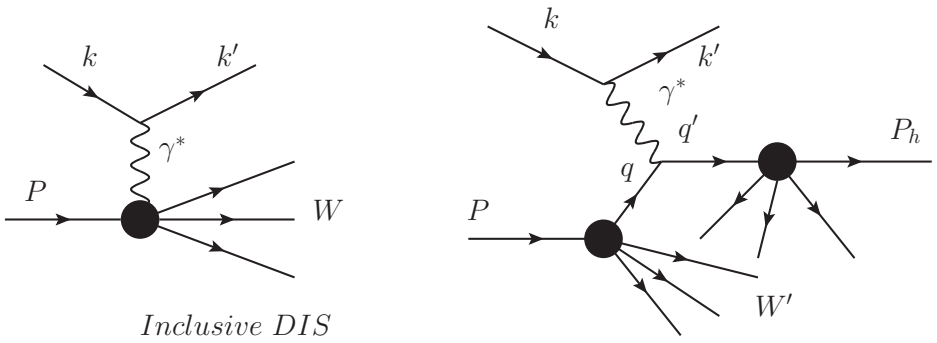

FIGURE 2.13: Illustration of the DIS and SIDIS processes. In SIDIS, the leading hadron is detected in addition to the scattered lepton. The fundamental scattering processes $l + q \rightarrow l + q$ are the same.

ϕ_h and ϕ_S

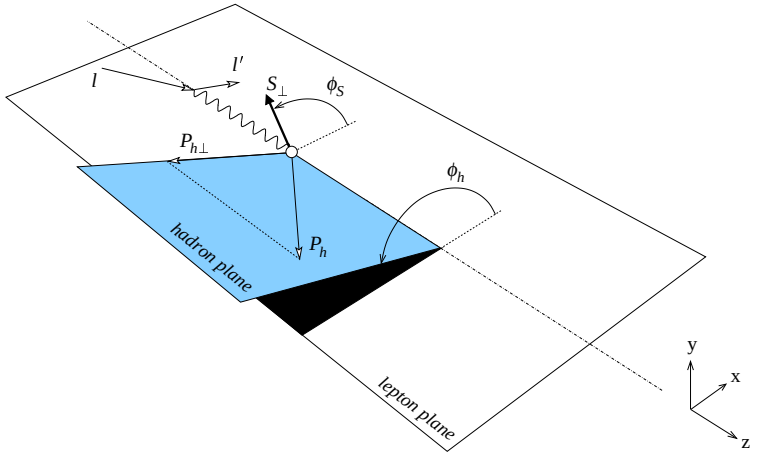

FIGURE 2.14: The definitions of ϕ_h and ϕ_S according to the Trento conventions [113].

The scattering plane is defined by the scattered lepton's 3-vector momentum and the virtual photon's 3-vector momentum. The hadron plane is defined by the detected hadron's 3-vector momentum and the virtual photon's 3-vector momentum.

- ϕ_S (Fig. 2.14) is the angle between the scattering plane and the spin plane, when the target is polarized. The spin plane is defined by the target's 3-vector spin and the virtual photon's 3-vector momentum.

- θ_S is the angle between the spin 3-vector and the virtual photon's 3-vector momentum $\vec{q}$:

$$\cos(\theta_S) = \frac{\vec{S} \cdot \vec{q}}{|\vec{S}| \cdot |\vec{q}|} \tag{2.35}$$

SIDIS in the Simple Quark/Parton Model

In the simple quark/parton model, the cross section of the SIDIS process can be expressed as:

$$\frac{d\sigma^h}{dxdydz} = \frac{4\pi\alpha^2 s}{Q^4}(1 - y + \frac{y^2}{2}) \sum_q e_q^2 [f_1^q(x) \cdot D_1^{qh}(z)]. \tag{2.36}$$

The function $D_1^{qh}(z)$ is called the fragmentation function, which represents the probability of a quark q fragmenting into a hadron h. In comparison, the inclusive DIS cross section is

$$\frac{d\sigma^h}{dxdy} = \frac{4\pi\alpha^2 s}{Q^4}(1 - y + \frac{y^2}{2}) \sum_q e_q^2 \cdot f_1^q(x). \tag{2.37}$$

Therefore, the fragmentation function $D_1^{qh}(z)$ will offer additional information about the struck quark. For example, the inclusive DIS can not differentiate the u quark and the $\bar{u}$ quark, since

$$(e_u)^2 = (\frac{1}{3})^2 = (-\frac{1}{3})^2 = (e_{\bar{u}})^2. \tag{2.38}$$

However, the SIDIS can differentiate them by detecting the leading hadron. The probability of u quark fragmenting into a π^+ ($u\bar{d}$) is expected to be larger than that of $\bar{u}$ quark fragmenting into the π^+. The former probability is categorized as a favored fragmentation function, since the final state hadron contains the original quark flavor in its quark model composition. Conversely, the latter is categorized as an unfavored fragmentation function. The SIDIS process will be further discussed in Sec. 3.

Fragmentation Functions

The fragmentation function $D_1^{qh}(z)$, which represents the probability that the parton q fragments into a hadron h with the parton's momentum fraction z, is an analogue to the PDFs. In the simple quark/parton model, $D_1^{qh}(z)$ needs to satisfy the following momentum sum rule:

$$\sum_h \int_0^1 dzz \cdot D_1^{qh}(z) = 1. \tag{2.39}$$

Similar to the PDFs, $D_1^{qh}(z)$ also depends on the scale Q^2, thus becoming $D_1^{qh}(z, Q^2)$. It can be measured through the e^+e^- annihilation, ep scattering, or pp collisions processes. A review of the fragmentation function can be found in Ref. [57].

In the SIDIS process, two regions of the fragmentation are defined:

- Current fragmentation region:

  The hadrons in this region originate from the struck quark. Therefore, the final state hadrons will carry the information of the struck quark.

- Target fragmentation region:

  The hadrons in this region originate from the rest of the target quark/gluon system[12]. Therefore, the final state hadrons will not directly carry the information of the struck quark.

For example, in the right panel of Fig. 2.13, the filled circle on the right (left) represents the current (target) fragmentation. Most of the experiments using SIDIS to explore the nucleon structure focus on the current fragmentation, which can be described using Eqn. (2.36). In experiment, the two fragmentation regions can usually be separated by a rapidity gap, and the Berger's criterion [114, 115] is in generally

[12] The initial nucleon is a color-neutral object. Both the struck quark and the rest of the nucleon system carry color charges, and will fragment into colorless objects in the final state due to confinement.

used to qualitatively define the two fragmentation regions. Due to the complexity in theoretical interpretations, the target fragmentation is generally less explored. For more information on target fragmentation, we refer to Ref. [116].

Experimental Data on SIDIS

The earliest data on SIDIS were from electron-proton scattering in Cornell Wilson Synchrontron Laboratory [117, 118] in the 1970s. These data indicated the simple scaling behaviors of both parton distribution function and fragmentation function, which were predicted by the simple quark/parton model (Eqn. (2.36)). Around 1995, the HERMES experiment at DESY laboratory in Hamburg, Germany, started taking data with longitudinal polarized 27.5 GeV e^-/e^+ beam and an internal gas target. At CERN, the COMPASS experiment started taking data in 2001 at Super Proton Synchrotron (SPS) with a high energy muon beam. The SIDIS process was one of the major programs in both experiments. At Jefferson lab, all three experimental halls carried out experiments with SIDIS processes. In Hall C, the E00-108 experiments [119] aimed to study the quark-hadron duality with the SIDIS process. In Hall B, the CLAS collaboration reported the first evidence for a non-zero beam-spin azimuthal asymmetry [120]. In Hall A, experiment E06-010 was performed using a longitudinal polarized electron beam and a transversely polarized ^{3}He target.

2.3.4 Experimental Methods with Non-E&M Probe

Besides the E&M probe, both strong and weak interactions are used to provide information about the nucleon structure [57] in terms of light quarks and gluons. Three major experimental methods with non-E&M probe are listed below together with primary reaction channels and their fundamental physical processes:

- Neutrino DIS, where the charged W boson replaces the role of the virtual photon.

$$\nu(\bar{\nu}) + N \rightarrow \mu^-(\mu^+)X \tag{2.40}$$

$$W^* + q \rightarrow q \tag{2.41}$$

- Jet production in proton-antiproton collision

$$p + \bar{p} \rightarrow jet + X \tag{2.42}$$

$$g + g, q + g, q + q \rightarrow jet + jet \tag{2.43}$$

- W boson production in proton-antiproton collision

$$p + \bar{p} \rightarrow (W^{\pm} \rightarrow l^{\pm} + \nu) + X \tag{2.44}$$

$$u + d, \bar{u} + \bar{d} \rightarrow W \tag{2.45}$$

2.3.5 Related Theoretical Issues

In this section, we will briefly describe two important theoretical issues related to experimentally accessing the nucleon structure with different processes.

QCD Factorization Theorem and Universality of Parton Distribution Function

The basic idea of the QCD factorization theorem is that parton distribution functions (PDFs) or fragmentation functions (FFs) are independent of hard scatterings, which differ significantly in various processes, such as the aforementioned DIS, DY, e^-e^+ annihilation, or pp collision. It implies that the quark/gluon distribution and fragmentation functions in hard scattering processes and their scale dependence are universal. The QCD factorization theorem provides the fundamental theoretical basis for accessing the nucleon structure through hard scattering processes. The proofs of the QCD factorization theorem are reviewed in Ref. [121].

Operator Product Expansion and Higher-Twist Effect

As shown in Sec. 2.3.1, the nucleon structure functions can be expressed as the PDFs in the quark/parton model. This is valid in QCD at infinitely large Q^2. However, at finite Q^2, besides the DGLAP evolution of PDFs (which takes into account the NLO QCD corrections in the hard lepton-quark scattering process $l + q \rightarrow l + q$) the soft part of PDFs will also be subject to QCD corrections. Such corrections are described below in the formalism of operator product expansion (OPE).

The OPE was introduced by Wilson in 1969 [122]. It was developed to calculate the hadronic tensor:

$$W_{\mu\nu} = \frac{1}{4\pi} \int d^4z e^{iq\cdot z} < P, S|[J^\dagger_\mu(z), J_\nu(0)]|P, S > \tag{2.46}$$

by expanding the Fourier transformation of the $J^\mu(z)J^\nu(0)$ as a series of local operators:

$$i \int d^4z e^{iq\cdot z} J^\mu(z)J^\nu(0) = \sum_n C^{(d,s)}_{\mu\nu n} O^{(n)}. \tag{2.47}$$

Here $C^{(d,s)}_{\mu\nu n}$ are called the Wilson coefficients, which can be calculated perturbatively. The d and s label the dimension and the spin of the operator $O^{(n)}$, respectively. It is shown in Ref. [123] that $O^{(n)}$ can be expressed as:

$$O^{(n)} = x^s (\frac{M_p}{Q})^{d-s-2}, \tag{2.48}$$

or more generally as

$$O^{(n)} \sim (\frac{\Lambda_{QCD}}{Q})^{d-s-2} \tag{2.49}$$

in DIS. M_p is the mass of the nucleon and Λ_{QCD} is the QCD scale. Therefore, the contributions of different OPE operators to DIS cross section are decided by the twist $t = d - s$. For example, the contributions of twist-2 operators (the lowest twist) will

be $O(Q^0)$, and those of twist-4 operators will be $O(Q^{-2})$. At infinitely large Q^2, only contributions of twist-2 operators remains. while at finite Q^2, those of higher twists become visible. The PDFs defined in the quark/parton model, which can be interpreted as probabilities, are only related to twist-2 operators. However, the experimental data on structure functions, from which PDFs are extracted, usually contain contributions of all twists: $(\frac{M_p}{Q})^{t-2}$ and $(\frac{\Lambda_{QCD}}{Q})^{t-2}$. $(\frac{M_p}{Q})^{t-2}$, or the "Target Mass Correction" (TMC), is one kind of higher twist effects, representing the effect of the finite target mass. A recent review of TMC can be found in Ref. [124]. $(\frac{\Lambda_{QCD}}{Q})^{t-2}$, which represents the multi-parton correlations, is usually referred to as the dynamic higher-twist effect[13]. A recent study of high-twist effects [125] was carried out by the MRST collaboration on the F_2 structure function data. Their results show that a wide coverage of Q^2 is essential in order to extract the higher-twist contributions.

[13] For example, the g_2 spin structure function contain the twist-3 contribution of quark-gluon correlation.

3

Physics Motivation

In our long history of using QCD to understand the structure of the nucleon, the spin of the nucleon has played a key role and provided plenty of surprises and excitement. In particular, the measurement of the longitudinal spin structure has revealed that the sum of all quark spins only contribute a small portion of the total nucleon spin. In the past twenty years, while the longitudinal spin structure of the nucleon has been relatively well elucidated, our understanding of its transverse spin structure is far from being satisfactory. Recently, the observation of non-zero single spin asymmetries (SSAs) with transversely polarized proton beams or targets from different laboratories around the world prompted an outburst of theoretical and experimental efforts, including this thesis experiment JLab E06-010, to study the transverse spin physics.

3.1 Semi-Inclusive Deep Inelastic Scattering

3.1.1 Unpolarized SIDIS in Simple Quark/Parton Model (Leading Order)

In the simple quark/parton model, the SIDIS process is factorized into a hard quark scattering followed by a quark hadronization, as shown in the upper-left diagram of

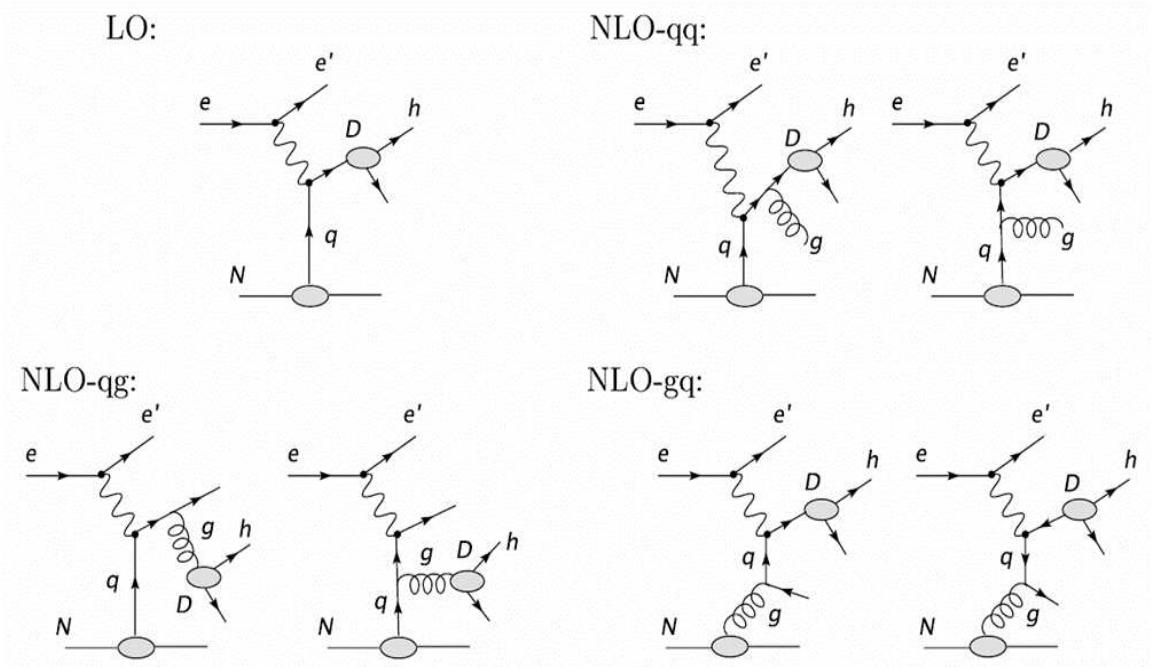

FIGURE 3.1: Semi-inclusive deep inelastic scattering diagrams at leading order (LO) and next-to-leading order (NLO).

Fig. 3.1. The unpolarized cross section can then be written as [126]:

$$\frac{d\sigma^h}{dxdydzd^2\mathbf{P_T}} = \frac{4\pi\alpha^2 s}{Q^4}(1 - y + \frac{y^2}{2}) \sum_q e_q^2 [f_1^q \otimes D_{1q}^h], \tag{3.1}$$

where $f_1^q(x)$ is the quark distribution function of light flavor q ($q = u, \bar{u}, d, \bar{d}, s, \bar{s}$) and x, y, z, and P_T are defined in Sec. 2.3.1. The function $D_{1q}^h(z)$ represents the probability that a quark q fragments into a hadron h ($\pi^{\pm}$, π^0 or $K^{\pm}$). The convolution in Eqn. (3.1) represents an integration over transverse momentum of initial (k_T) and final quark (p_T) with proper weighting [127, 126]:

$$[... \otimes ...] = \int d^2p_T d^2k_T \delta^{(2)}(\mathbf{p_T} - \frac{\mathbf{P_T}}{z} - \mathbf{k_T})[...]. \tag{3.2}$$

Gaussian Approximation

In order to realize the integral in Eqn. (3.2) theoretically, certain assumptions of the transverse momentum dependence have to be made for parton distributions and

fragmentation functions. One widely used assumption is the Gaussian approximation:

$$f_1^q(x,k_T^2) = f_1^q(x)\frac{1}{\pi\mu_0^2}\exp(-\frac{k_T^2}{\mu_0^2}) \tag{3.3}$$

$$D_{1q}^h(z,q_T^2) = D_{1q}^h(z)\frac{1}{\pi\mu_D^2}\exp(-\frac{q_T^2}{\mu_D^2}), \tag{3.4}$$

where the μ_0^2 is the average quark transverse momentum squared and the μ_D^2 is the average leading hadron transverse momentum squared.

Anselmino *et al.* [128] studied the dependence of the unpolarized SIDIS cross section on the azimuthal angle ϕ_h, also referred to as the Cahn effect. Their work suggests [128]:

$$\mu_0^2 = < k_T^2 > \approx 0.25 \text{ GeV}^2, \tag{3.5}$$

$$\mu_D^2 = < P_T^2 > \approx 0.2 \text{ GeV}^2. \tag{3.6}$$

Collins *et al.* [129] studied SIDIS SSAs data from HERMES, and found:

$$\mu_0^2 = < k_T^2 > \approx 0.33 \text{ GeV}^2 \tag{3.7}$$

$$\mu_D^2 = < P_T^2 > \approx 0.16 \text{ GeV}^2. \tag{3.8}$$

Recently, Schweitzer *et al.* [130] summarized the present knowledge of k_T. They showed that current SIDIS data from JLab Hall C, Hall B (CLAS), HERMES, COMPASS and EMC, and DY data from Fermilab are all consistent with the Gaussian model of k_T. In addition, they suggest that the intrinsic transverse parton momenta in the hadron h depends on the energy s [130]:

$$< k_T^2(s) >_h \approx < k_T^2(0) > + C_h \cdot s \tag{3.9}$$

$$< k_T^2(0) > = 0.3 \text{ GeV}^2, \tag{3.10}$$

and $C_h = 2.1 \times 10^{-3}$ for pions and 0.7×10^{-3} for protons. In addition, the recent results [131] from CLAS suggest that the width of k_T distribution for longitudinal PDF g_1 may be different from that of unpolarized PDF f_1.

Eqn. (3.1) is then simplified as the expression in Eqn. (2.36):

$$\sigma^h(x,z) \sim \sum_i e_f^2 f_1^q(x) \cdot D_{1q}^h(z), \tag{3.11}$$

which is often called the naive $x - z$ separation in the simple quark-parton picture.

3.1.2 Unpolarized SIDIS in Improved Quark/Parton Model (Next to Leading Order)

The naive x-z separation is violated at next-to-leading order when one-gluon diagrams in Fig. 3.1 are taken into account. The origin of this violation, same as in the DGLAP evolution equation of PDFs [132], is also responsible for the observed P_T dependence of SIDIS cross sections at large P_T ($P_T > 1$ GeV) [133]. At NLO, terms of $f_1^q(x) \cdot D(z)$ are added with the double convolutions of $f_1 \otimes C \otimes D$, in which the Cs are the Wilson coefficients [134]:

$$[f_1 \otimes C \otimes D](x,z) = \int_x^1 \frac{dx'}{x'} \int_z^1 \frac{dz'}{z'} f_1(\frac{x}{x'}) C(x',z') D(\frac{z}{z'}). \tag{3.12}$$

With the following short-hand notation

$$f_1 D + \frac{\alpha_s}{2\pi} f_1 \otimes C \otimes D = f_1[1 + \otimes \frac{\alpha_s}{2\pi} C \otimes] D, \tag{3.13}$$

we have

$$\begin{aligned} \sigma^h(x,z) &= \sum_f e_f^2 f_1^q [1 + \otimes \frac{\alpha_s}{2\pi} C_{qq} \otimes] D_{1q}^h \\ &+ (\sum_f e_f^2 q_f) \otimes \frac{\alpha_s}{2\pi} C_{qg} \otimes D_{1g}^h + G \otimes \frac{\alpha_s}{2\pi} C_{gq} \otimes (\sum_f e_f^2 D_{1q}^h). \end{aligned} \tag{3.14}$$

For any given form of PDFs, the SIDIS cross sections can be calculated numerically. Therefore, the NLO QCD corrections can be performed in extracting the PDFs with

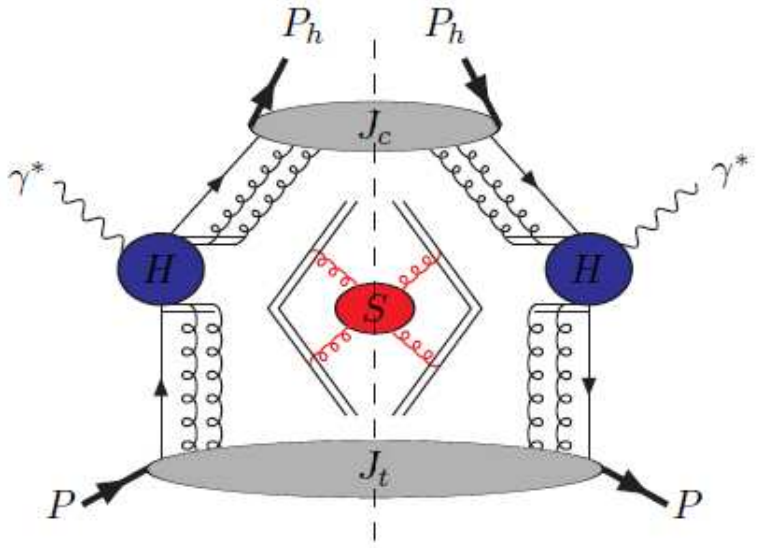

FIGURE 3.2: QCD Factorization Theorem of SIDIS Cross Sections with TMDs at Low P_T. H labels the hard scattering part, which can be calculated in pQCD. J_t and J_c are the TMD and transverse momentum dependent fragmentation function, respectively. S represents a soft contribution, which can be calculated at $P_T >> \Lambda_{QCD}$. Figure is from [138].

the equations above. Several global fits of longitudinal double-spin asymmetries have been carried out in recent years since the SIDIS data have became available [135, 136, 137]. Such fitting procedures have yet to be applied to the cross section.

3.1.3 Factorization Theorem of SIDIS

The factorization theorem of the SIDIS cross section integrated over hadron transverse momenta P_T has been established [139] with the collinear approximation. However, the general theorem for fixed P_T has not been demonstrated. Recently, Ji *et al.* [138] proved that a QCD factorization theorem exists at low hadron transverse momenta ($P_T << Q$). This new development, illustrated in Fig. 3.2, is based on transverse momentum dependent parton distribution functions (TMDs), which can be connected to the normal Feynman parton distribution functions by integrating

over the internal quark transverse momentum. At such low P_T, the differential cross sections of the SIDIS process are factorized into a TMD J_t, a fragmentation function J_c, a hard scattering part H, and a soft part S. At high P_T ($P_T >> Q$), the QCD factorization theorem has been proven for the Drell-Yan process [140], and a similar theorem for the SIDIS process is expected to exist as well.

3.1.4 Experimental Evidence for SIDIS LO $x - z$ Separation

The SIDIS process has been used by a number of collaborations (SMC, HERMES, JLAB, etc.) to extract parton or fragmentation functions in the relatively low Q^2 regime ($Q^2 \approx 1 - 4.5\text{GeV}^2$), assuming the validity of the LO naive $x - z$ separation. This assumption can be directly tested with the data. The HERMES collaboration reported evidence for the z independence of the measured ratio of $(\bar{d} - \bar{u})/(u - d)$ in the range of $0.3 < z < 0.8$ [141][1]. The data from the JLab Hall C E00-108 [119] experiment are consistent with a Monte-Carlo simulation adopting the LO $x - z$ separation in the region of $0.35 < z < 0.65$ [143] (Fig. 3.3). Recently, the JLab CLAS collaboration [120] reported the first evidence for a non-zero beam-spin azimuthal asymmetry in the semi-inclusive production of positive pions in the DIS region. Furthermore, their data are consistent with the $x - z$ separation in region of $0.1 < x < 0.4$ and $0.5 < z < 0.8$.

3.2 Transverse Momentum Dependent Parton Distributions (TMDs)

As discussed in Sec. 2.2, TMDs originate from the Wigner distributions $W_\Gamma(\vec{r}, \vec{k})$ upon integration over $\vec{r}$. At leading twist, there are in total eight TMDs [127, 144]. They are categorized by their target nucleon and quark spin, as illustrated in Fig. 3.4. The f, g , and h represent the TMDs of unpolarized, longitudinally polarized, and transversely polarized partons, respectively. The superscripts L and T denote that

[1] Later analysis [142] suggests that the z-independent observation may not be conclusive.

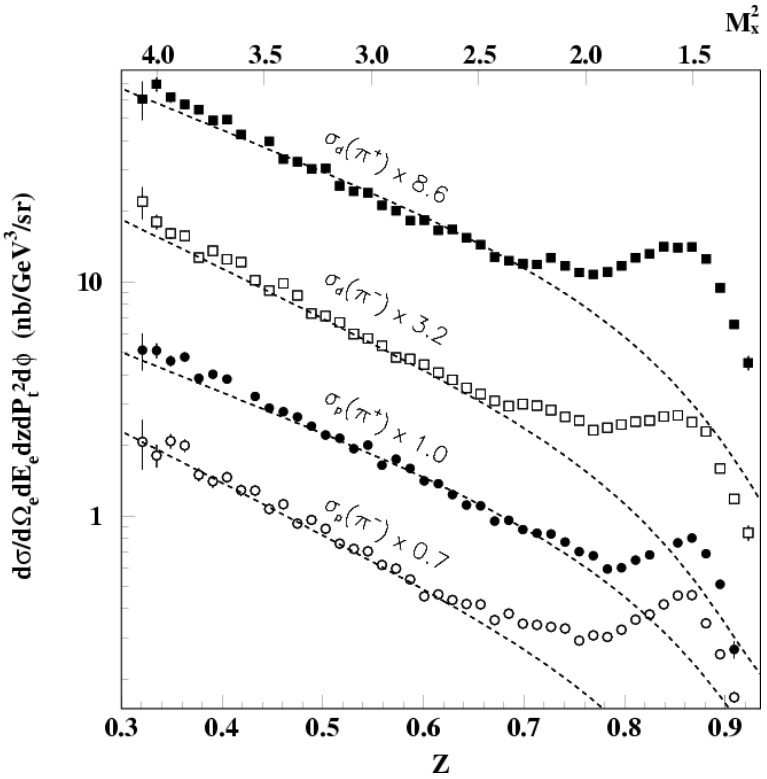

FIGURE 3.3: E00-108 semi-inclusive $\pi^{\pm}$ production cross sections on hydrogen and deuterium target (points) at $x = 0.32$ as a function of z in comparison with a Monte Carlo simulation (solid curve) starting from a factorization and fragmentation ansatz. Figure is from Ref. [143].

the nucleon is longitudinally and transversely polarized, respectively. In the following discussion, we will follow Ref. [145] to introduce leading twist TMDs within the simple quark/parton model.

3.2.1 TMDs in the Simple Quark/Parton Model

In the simple quark/parton model, the hadronic tensor introduced in Sec. 2.3.1 can be expressed as:

$$W^{\mu\nu} = \sum_q e_q^2 \int \frac{d^4k}{(2\pi)^4} \delta((k+q)^2) \mathrm{Tr}[\Phi \gamma^\mu (\not{k} + \not{q}) \gamma^\nu], \tag{3.15}$$

where k and q are the parton and virtual photon four-momentum (Fig. 2.5), respec-

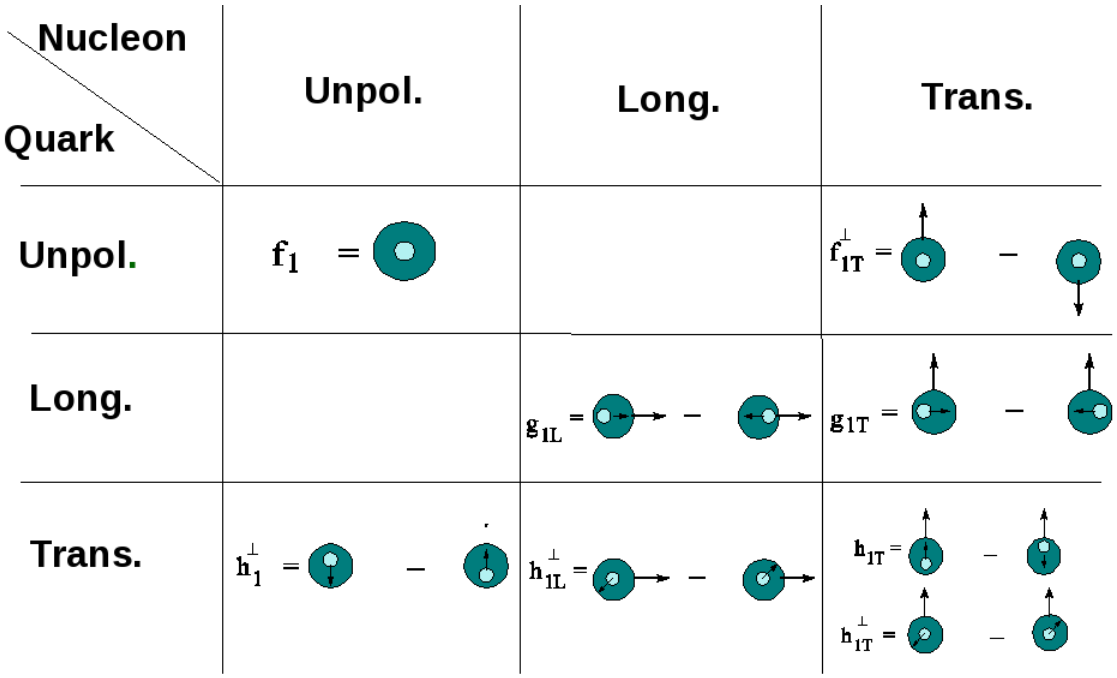

FIGURE 3.4: All eight TMDs at leading twist are categorized by their nucleon and parton spin.

tively, and $\not{k} = k^\mu \gamma_\mu$. Φ is the quark-quark correlation matrix:

$$\Phi_{ij}(k, P, S) = \int d^4\zeta e^{ik\cdot\zeta} \left\langle PS|\bar{\psi}_j(0)\psi_i(\zeta)|PS\right\rangle, \tag{3.16}$$

where S is the spin of the nucleon with momentum P. The Φ matrix is required to satisfy certain basic physical relations, such as hermiticity, parity invariance, and time reversal invariance [127, 144]. We then have

$$\Phi^{[\gamma^+]} = f_1(x, k_\perp) - \frac{\epsilon_\perp^{ij} k_{\perp i} S_{\perp j}}{M} f_{1T}^\perp(x, k_\perp) \tag{3.17}$$

$$\Phi^{[\gamma^+\gamma_5]} = \lambda_N g_{1L}(x, k_\perp) + \frac{\mathbf{k}_\perp \cdot \mathbf{S}_\perp}{M} g_{1T}(x, k_\perp) \tag{3.18}$$

$$\begin{aligned}\Phi^{[i\sigma^{i+}\gamma_5]} &= S_\perp^i h_{1T}(x, k_\perp) + \frac{\lambda_N}{M} k_\perp^i h_{1L}^\perp(x, k_\perp) \\ &- \frac{1}{M^2}(k_\perp^i k_\perp^j + \frac{1}{2}\mathbf{k}_\perp^2 g_\perp^{ij}) S_{\perp j} h_{1T}^\perp(x, k_\perp) - \frac{\epsilon_\perp^{ij} k_{\perp j}}{M} h_1^\perp(x, k_\perp).\end{aligned} \tag{3.19}$$

Here λ_N and $\mathbf{S}_\perp$ are the helicity and transverse component of the nucleon spin respectively, and

$$\Phi^{[\Gamma]} \equiv \frac{1}{2}\int \frac{dk^+dk^-}{(2\pi)^4}\mathrm{Tr}(\Gamma\Phi)\delta(k^+ - xP^+). \tag{3.20}$$

Among the eight leading twist TMDs, $h_1^\perp$ and $f_{1T}^\perp$ are naive T-odd[2]. They emerge after the requirement of time reversal invariance on Φ is removed. The other six TMDs are T-even.

TMDs provide the description of the parton distribution beyond the collinear approximation. They depend not only on the longitudinal momentum fraction x, but also on the transverse momentum k_T, thus providing a 3-D description of the nucleon structure. If we integrate TMDs over the transverse momenta of quarks, only three of them survive: the unpolarized parton distribution f_1, the longitudinal polarized parton distribution g_{1L}, and the quark transversity distribution h_{1T}. Here, the longitudinal direction is along the virtual photon momentum. In the quark/parton model, these three PDFs can be interpreted as following:

- The unpolarized PDF f_1 gives the probability of finding a parton with momentum fraction x in an unpolarized nucleon.

- The longitudinally polarized PDF g_{1L} gives the probability of finding a longitudinally polarized parton with momentum fraction x in a longitudinally polarized nucleon. It describes the net quark longitudinal polarization in a longitudinally polarized nucleon.

- The quark transversity distribution h_{1T} is very similar to g_{1L}. Instead of longitudinal direction, it gives the probability of finding a transversely polarized quark inside a transversely polarized nucleon.

[2] Here, the naive T-odd means that the initial and final state do not inter-change during the time reversal operation (time $t \to -t$, momentum $\vec{p} \to -\vec{p}$, and spin $\vec{s} \sim \vec{r} \times \vec{p} \to \vec{r} \times (-\vec{p}) \sim -\vec{s}$).

As mentioned in Sec. 2.3.1, f_1 and g_{1L} can be extracted from the measurements of the unpolarized F_2 and longitudinal polarized g_1 structure functions, respectively. Both structure functions have been well measured through inclusive DIS. The transversity distribution h_{1T} is the least known among all three leading twist PDFs.

3.2.2 Transversity Distribution h_{1T}

Hidaka, Monsay and Sivers [146] first discussed the transversity distribution function in 1978, followed by Ralston and Soper [147] in 1979, and Jaffe and Ji in the early 1990s [148]. A recent review of the transversity distribution can be found in Ref. [145].

The transversity distribution carries the following important properties:

- In the non-relativistic limit, the boost operator commutes with the rotation operator, indicating that h_{1T} is the same as g_{1L} , after integrating the internal quark transverse momentum. Therefore, the transversity distribution functions probe the relativistic nature of the quarks inside the nucleon.

- There is no gluon transversity distribution in nucleon, since the transversity distribution is related to the helicity flip amplitude $A_{-+,+-}$ (helicity of parton and nucleon). The gluon is a spin-1 particle and the nucleon is a spin-$\frac{1}{2}$ particle. Therefore, the helicity flip amplitude $A_{-+,+-}$ for gluons and the nucleon can't fulfill the law of helicity conservation. The non-existence of the gluon transversity further leads to three important features. First, quark transversity possesses a valence-like nature [149], which means that $h_{1T} \to 0$, when $x \to 0$[3]. Second, the QCD evolution of transversity distribution is simpler [149]. As shown in Sec. 2.3.1, there are three splitting functions in the DGLAP evolution equation: P_{qq}, P_{gq} and P_{qg}. Since there is no gluon transversity, the contribution from P_{gq} and P_{qg} will be strictly zero. The third feature is the

[3] For the unpolarized PDF f_1, at small x, the PDFs are dominated by the gluons, which perturbatively generate the sea quarks.

absence of gluon contribution in the transverse spin sum rule [96], as discussed in Sec. 2.2.1.

- The transversity distribution is a chiral-odd quark PDF. Therefore, it is very difficult to access in polarized inclusive DIS, since perturbative QCD processes involving light quarks preserve helicity [150] and the contribution of the transversity distribution will be suppressed by $\frac{m_q}{Q}$. Here m_q is the current quark mass, which is only about several MeV. In order to probe the quark transversity distribution, an additional chiral-odd distribution or function is needed, such as the additional transversity distribution in the double polarized Drell-Yan process, or the Collins fragmentation function in measuring the single target spin asymmetry from SIDIS pion electroproduction. In addition to the SIDIS and DY processes, the transversity distribution can also be accessed through measuring double spin asymmetry in Λ production of e-p or p-p collisions and single-spin asymmetry from double pion production of e-p scattering [145].

- It is predicted that the Soffer's inequality [151],

$$|h_{1T}^q| \leq \frac{1}{2}(f_1^q + g_{1L}^q), \tag{3.21}$$

  is valid for the transversity based on unitarity and parity conservation arguments. NLO QCD evolution of transversity was studied in Ref. [152]. And it was shown that Soffer's inequality held up to NLO QCD corrections. However, doubts have been cast [153] recently on this inequality and it is of interest to test it experimentally.

- The lowest moment of h_{1T}^q, called the "tensor charge", is analogous to the axial charge g_a^0. It is a fundamental property of the nucleon. The tensor charge

has been calculated from lattice QCD [154] and various models [155, 156, 157, 158, 159, 160]. Due to the valence-like nature of the transversity distribution, probing transversity in the high-x region is crucial to determine the tensor charge of quarks.

A review of different model calculations of the transversity distribution or tensor charge can be found in Ref. [145]. In the following paragraphs, we will simply present some basic ideas of these models.

MIT Bag Models

In the MIT bag model [161, 162, 163], the quarks are confined in a region with a color dielectric constant approximately equal to one, while the dielectric constant outside the nucleon is assumed to be zero (the boundary condition of the bag). The energy associated with the excitation of non-perturbative gluonic degrees of freedom is described by the vacuum pressure. Then, the quark distributions can be expressed as single-particle wave functions with the mean-field approximation. In Ref. [155], the u and d quark tensor charges are estimated to be 1.17 and -0.29, respectively.

Color Dielectric Model (CDM)

The CDM is also a bag model, which shares many important features with the aforementioned MIT bag model. The major difference between these two models is the implementation of confinement. In the MIT bag model, confinement is implemented by the boundary conditions. In the CDM, confinement is implemented dynamically by modeling the non-perturbative gluonic degrees of freedom with the interaction between quarks and the phenomenological scalar fields. The u and d quark tensor charges computed in the CDM are 1.22 and -0.31, respectively, at $Q^2 = 0.16$ GeV^2 [156].

Chiral Quark Soliton Model (CQSM)

The CQSM is based on two principles [164]:

- The importance of the spontaneous chiral symmetry breaking in QCD vacuum:

  The QCD Lagrangian with N_f massless quarks should exhibit a chiral symmetry under $U(N_f)_L \times U(N_f)_R$. However, the chiral symmetry in the QCD Lagrangian can not explain why pions are much lighter than other mesons, and why the mass splitting between two hadronic states with the same quantum numbers but opposite parities is, in general, very large. These puzzles were solved by Nambu *et al.* [165, 166], who introduced the concept of spontaneous chiral symmetry breaking. In this picture, the chiral symmetry in the QCD vacuum is spontaneously broken. Consequently, light Goldsone pseudoscalar hadrons (pions, kaons, etc.) are generated.

- Using the large N_c (number of colors in the theory) limit to model approximately the real world:

  At large N_c, QCD can be perturbatively expanded with $1/N_c$ in low energy region. As a result, QCD Lagrangian is reduced to the effective chiral Lagrangian:

  $$\mathcal{L} = \bar{\psi}(\imath\partial - MU^{\gamma^5})\psi. \tag{3.22}$$

  Here $U^{\gamma^5} = e^{\imath\lambda\cdot\pi/f_\pi}$. M is the dynamical quark mass. λs are the Hermitian generator of the $SU(N_f)$, and πs are the pseudoscalar field originating from the spontaneous chiral symmetry breaking. In this case, the solitonic solution of the effective chiral Lagrangian, a composite of N_c valence quarks and infinitely many Dirac sea quarks, can be viewed as the nucleon .

The CQSM has also been used to study the spin content of the nucleon by Wakamatsu and Yoshiki [167]. The u and d quark tensor charges are predicted to be 0.95 and -0.27, respectively, at $Q^2 \approx 0.6$ GeV^2 [157].

Quark-diquark Model

In the quark-diquark model, the nucleon is treated as a quark and a diquark, the latter of which groups the other two quarks together. The tensor charges of u and d quark can then be written as [159]:

$$\begin{aligned}
\Delta_T u(x) &= \Delta_T f^s_{q/N}(x) + \frac{1}{2}\Delta_T f^s_{q(D)/N}(x) + \frac{1}{3}\Delta_T f^a_{q/N}(x) \\
&+ \frac{5}{6}\Delta_T f^a_{q(D)/N}(x) + \frac{1}{2\sqrt{3}}\Delta_T f^m_{q(D)/N}(x) \qquad (3.23) \\
\Delta_T d(x) &= \frac{1}{2}\Delta_T f^s_{q(D)/N}(x) + \frac{2}{3}\Delta_T f^a_{q/N}(x) \\
&+ \frac{1}{6}\Delta_T f^a_{q(D)/N}(x) - \frac{1}{2\sqrt{3}}\Delta_T f^m_{q(D)/N}(x). \qquad (3.24)
\end{aligned}$$

Here, the s, a and m are the scalar, the axial vector, and the mixing terms, respectively. The q/N labels the quark and $q(D)/N$ represents the diquark, respectively. The nucleon wave-function was solved by the relativistic Faddeev equation in the Nambu-Jona-Lasinio (NJL) model [165, 166, 168] with the quark-diquark approximation [159]. The u and d quark tensor charges are predicted to be 0.69 and -0.16, respectively, at $Q^2 = 0.4$ GeV^2.

Light Cone Models

In the light cone models, the light front form dynamics introduced by Dirac [169] is used to transform the quark wave function from the rest frame to the infinite momentum frame. DIS processes probe the parton dynamics in the light cone frame (infinite momentum frame) rather than in the rest frame. Based on the experimental

data, as well as the relationship between the light front and rest frame dynamics, Ma and Schmidt [158] deduced that the u and d quark tensor charges are 0.84-1.09 and (-0.23-0.51), respectively. More recently, Pasquini *et al.* [160] used the nucleon wave function calculated in Constituent Quark Model (CQM), in which the nucleon is assumed to only contain three valence quarks, to deduce the lowest-order Fock-state components of the light-cone wave functions [170], which can then be used to predict the quark tensor charges. The u and d quark tensor charges are predicted to be 0.97 and -0.24, respectively, at $Q^2 \approx 0.8$ GeV^2 [160].

QCD Sum Rule

In order to estimate the tensor charges with QCD sum rules, He and Ji [155] considered the three-point correlation function:

$$W_{\mu\nu} \sim \int d^4x d^4z e^{iq\cdot z} < 0|T(j^{\mu\nu}(z)\eta(x)\eta(0))|0 >, \tag{3.25}$$

where $j^{\mu\nu}$ is the quark tensor current and $\eta(x)$ is the nucleon interpolating field. The correlation function was evaluated by employing the operator production expansion (OPE) and the resonance saturation method, in which the dispersion relation is used to link the correlation function with the resonances in the s-channel. The tensor charges were then extracted by comparing the results of the two methods. The leading order QCD sum rule suggests that u and d quark tensor charges are 1.0 ± 0.5 and 0.0 ± 0.5 [155], respectively, at $Q^2 \sim 1.0$ GeV^2.

Lattice QCD

Lattice QCD is currently the only non-perturbative method to solve QCD from first principles. It is based on Feynman's path integral formalism in Euclidean space approximated as discrete lattice points, between which the quarks and gluons only travel along lines. A Monte Carlo method is further adopted to simulate all possible

field configurations $\phi(x)$ in the lattice to calculate the n-point Green's function

$$\mathcal{G}^{(n)}(x_1, ...x_n) = \frac{\int [d\phi]\phi(x_1)...\phi(x_n)e^{iS(\phi)}}{\int [d\phi]e^{iS(\phi)}}, \tag{3.26}$$

from which all physical quantities are derived. Here, $\int [d\phi]$ represents the integral over all possible field configurations. $S(\phi)$ is the action formed by the Lagrangian $\mathcal{L}$:

$$S(\phi) = \int d^4x \mathcal{L}(\phi(x), \partial^\mu \phi(x)). \tag{3.27}$$

There are several important concepts in lattice QCD:

- Lattice spacing:

  The lattice spacing a is the distance between two adjacent lattice points. In the lattice calculation, the smaller a, the closer the results are to the continuum limit. In addition, the inverse of lattice spacing $1/a$ sets a natural momentum cut-off to regularize the theory.

- Lattice volume:

  The larger the lattice volume, the closer the calculation approaches the infinite-volume limit.

- The pion mass:

  The pion mass is directly linked to the quark mass on the lattice. In Quenched QCD, which neglects all the quark loops, a smaller pion mass[4] demands a larger number of field configurations to be simulated. Thus, the smaller the pion mass, the closer the calculation approaches the physical limit.

- Chiral Perturbation Theory:

  Since the simulated pion mass is larger than its physical value, chiral pertur-

[4] Currently, the pion mass used in lattice calculations is usually above its physical value ∼140 MeV.

bation theory is used to extrapolate the simulated results. It is important to control the systematic uncertainties in the extrapolation.

A recent lattice QCD calculation [154] indicates that the u and d quark tensor charges are 0.857 ± 0.013 and -0.212 ± 0.005, respectively, at $Q^2 = 4.0$ GeV^2. The predicted tensor charges are summarized in Table. 3.1.

Model	δu	δd	Q^2 GeV^2
MIT Bag Model [155]	1.17	-0.29	-
CDM [156]	1.22	-0.31	0.16
CQSM [157]	0.95	-0.27	0.6
Quark-diquark Model [159]	0.69	-0.16	0.4
Line Cone Models [158]	$0.84 \rightarrow 1.09$	$-(0.23 \rightarrow 0.51)$	-
CQM [160]	0.97	-0.24	0.8
QCD Sum Rule [155]	1 ± 0.5	0.0 ± 0.5	1.0
Lattice QCD [154]	0.857 ± 0.013	-0.212 ± 0.005	4.0

Table 3.1: The predictions of quark tensor charges from various models and lattice QCD.

3.2.3 Sivers Distribution $f_{1T}^{\perp}$

Besides the three parton distributions (f_1, g_{1L}, and h_{1T}) at the leading twist, which survive the integration over the quark transverse momentum, there are five more TMDs [127, 144] (see Fig. 3.4), including the naive T-odd Sivers distribution function $f_{1T}^{\perp}$ which describes the distribution of an unpolarized parton in a transversely polarized nucleon. The Sivers function was originally expected to be zero with time-reversal symmetry arguments [171]. However, in 2002, Brodsky *et al.* [172] showed that the single spin asymmetry (SSA), associated with the Sivers distribution, could arise in a spectator diquark model, where the struck quark interacts with the target remnants through QCD final-state interaction. The time-reversal arguments were

soon found to be incorrect, as the presence of gauge links, or Wilson lines,

$$\mathcal{L}(0,\zeta) = \mathcal{P}\exp\left(-ig\int_0^\zeta dsA^a(s)T^a\right) \tag{3.28}$$

was neglected. Here, $\mathcal{P}$ represents the path-ordering. T^a is the color matrices and g is related to the strong interaction coupling constant by $\alpha_S = g^2/(4\pi)$. $A^a(s)$ represents the gluon field. The gauge link is an essential piece of the quark-quark correlation function Φ, introduced in Sec. 3.2.1 within the simple quark/parton model, as it keeps Φ gauge invariant in QCD. In addition, it is predicted that the Sivers function extracted from the Drell-Yan process is the same as that extracted from the SIDIS, but with a different sign [173, 174]:

$$f_{1T}^{\perp}(x,k_\perp)|_{Drell-Yan} = -f_{1T}^{\perp}(x,k_\perp)|_{SIDIS}. \tag{3.29}$$

In the Drell-Yan process, it is the initial state interaction, rather than the final-state interaction (SIDIS), that generates the SSA. Such a prediction suggests that the Sivers function is not strictly universal. However, the fact that the QCD predicts the same magnitude of Sivers function in both processes implies that the Sivers function has a special "universality".

A non-zero Sivers function would imply that there is a correlation between the nucleon spin and the quark transverse momentum. This is consistent with the belief that the quark orbital angular momentum, which requires the existence of the quark transverse momentum, contributes significantly to the nucleon spin. Therefore, a non-zero Sivers function would indicate that the nucleon contains wave function components with nonzero orbital angular momentum. In addition, the gluon Sivers

function is connected to the quark Sivers function by the Burkardt sum rule [175]:

$$\sum_{a=q,\bar{q},g} < \vec{k}_T^a >= 0$$

$$\sum_{a=q,\bar{q},g} \int_0^1 dx f_{1T}^{\perp(1)a}(x) = 0, \tag{3.30}$$

where

$$f_{1T}^{\perp(1)a}(x) = \int d^2\vec{k}_T \frac{\vec{k}_T^2}{2M^2} f_{1T}^{\perp a}(x, k_T^2), \tag{3.31}$$

and k_T is the quark transverse momentum. Recently, Brodsky *et al.* [176] made a connection between the Sivers function and the nucleon anomalous magnetic moment in the light-cone frame, suggesting the possible absence of gluon orbital angular momentum in the nucleon. Such arguments are also supported by Skyrme models [177], which is closely related to CQSM. Therefore, it is interesting to test these model dependent arguments with future experiments.

In principle, the TMDs work only in the low P_T region ($P_T << Q$). At large P_T, the contributions of NLO QCD processes dominate the cross section in comparison to those of TMDs. It was recognized [178, 179, 180, 181, 182] that the collinear twist-3 quark-gluon correlation, also referred to as the ETQS effect, is responsible for the observed SSA at large P_T[5]. Nevertheless, recent theoretical development shows that the twist-3 quark-gluon correlation picture actually describes the same physics as in the TMD framework [183, 184, 185] in certain P_T ranges. In particular, Ji *et al.* [183, 184, 185] showed that the Sivers effect agrees with the ETQS effect in the regime $\Lambda_{QCD} << P_T << Q$, where the two formalisms are believed to be valid.

Recently, the Sivers distribution has been modeled in light-cone quark models [186] and diquark spectator model [187]. The results from both models are in reasonable agreement with the phenomenology fit from Anselmino *et al.* [188].

[5] We will review the existing data on SSA in Sec. 3.4.

3.2.4 Pretzelosity Distribution $h_{1T}^{\perp}$ and Other TMDs

Besides the transversity h_{1T} and Sivers function $f_{1T}^{\perp}$, the other TMD that can be obtained with a transversely polarized target and an unpolarized beam is the Pretzelosity distribution $h_{1T}^{\perp}$, which requires the interference between wave function components that differ by two units of orbital angular momentum (OAM; e.g. p-p or s-d interference). Avakian *et al.* [189] showed that the Pretzelosity distribution is a direct measurement of the quark relativistic effects. Another model calculation [190] showed that the Pretzelosity distribution directly measures the parton orbital angular momentum. In addition, the Pretzelosity distribution can be connected to the spin densities [191]. Recently, Pasquini *et al.* [192] also calculated the Pretzelosity distribution, and they showed that the contributions from different angular momentum components would lead to the deformation of the nucleon shape.

The Boer-Mulders function $h_1^{\perp}$ has very similar properties to those of the Sivers function $f_{1T}^{\perp}$. It is also a naive T-odd TMD, which describes the transversely polarized parton distribution in an unpolarized nucleon. Therefore, it also requires FSI in order to generate SSA in the SIDIS process. $h_1^{\perp}$ should provide important information about the correlation between the parton orbital angular momentum and the parton spin.

In contrast to the Sivers function $f_{1T}^{\perp}$ and the Boer-Mulders function $h_1^{\perp}$, the functions g_{1T} and $h_{1L}^{\perp}$ are (naively) T-even, and thus do not require FSI to be nonzero. Nevertheless, they also require interference between wave function components that differ by one unit of OAM and thus require OAM to be nonzero. The wealth of information combined from all these functions is instrumental in disentangling the spin orbit correlations in the nucleon wave function, thus providing important information about the quark orbital angular momentum. Furthermore, together with Generalized Parton distributions (or Impact Parameter Dependent distributions),

which describe the probability of finding a parton with certain longitudinal momentum fraction x at certain transverse position b, TMDs provide a complementary 3-D description of the nucleon structure.

3.3 Transverse Target Spin Related SIDIS Cross Sections

The differential cross section in a SIDIS $(e, e'h)$ reaction, in which the beam is not polarized and the target is transversely polarized, can be expressed as the sum of target spin-independent and target spin-dependent terms at leading twist:

$$\begin{aligned} \frac{d\sigma^h}{dx_B dy d\phi_S dz_h d\phi_h dP_{h\perp}^2} \equiv d\sigma^h &= d\sigma_{UU} + d\sigma_{UT}, \\ &= d\sigma_{UU} + d\sigma_{UT}^{Collins} + d\sigma_{UT}^{Sivers} + d\sigma_{UT}^{Pretzelosity}. \end{aligned} \tag{3.32}$$

Each term in Eq. 3.32 can be expressed as convolutions of transverse momentum dependent parton distribution functions (TMDs) and fragmentation functions [193]:

$$d\sigma_{UU} = \frac{\alpha^2}{xyQ^2}\frac{y^2}{2(1-\epsilon)}(1+\frac{\gamma^2}{2x})(F_{UU} + \epsilon\cos(2\phi_h)F_{UU}^{\cos 2\phi_h}), \tag{3.33}$$

$$d\sigma_{UT}^{Collins} = \frac{\alpha^2}{xyQ^2}\frac{y^2}{2(1-\epsilon)}(1+\frac{\gamma^2}{2x})|\mathbf{S}_T|\epsilon\sin(\phi_h+\phi_S)F_{UT}^{\sin(\phi_h+\phi_S)}, \tag{3.34}$$

$$d\sigma_{UT}^{Sivers} = \frac{\alpha^2}{xyQ^2}\frac{y^2}{2(1-\epsilon)}(1+\frac{\gamma^2}{2x})|\mathbf{S}_T|\sin(\phi_h-\phi_S)F_{UT}^{\sin(\phi_h-\phi_S)}, \tag{3.35}$$

$$d\sigma_{UT}^{Pretzelosity} = \frac{\alpha^2}{xyQ^2}\frac{y^2}{2(1-\epsilon)}(1+\frac{\gamma^2}{2x})|\mathbf{S}_T|\epsilon\sin(3\phi_h-\phi_S)F_{UT}^{\sin(3\phi_h-\phi_S)}. \tag{3.36}$$

Here,

$$\gamma = \frac{2Mx}{Q}, \tag{3.37}$$

$$\epsilon = \frac{1-y-\frac{1}{4}\gamma^2y^2}{1-y+\frac{1}{2}y^2+\frac{1}{4}\gamma^2y^2}, \tag{3.38}$$

$$x = \frac{Q^2}{2M\nu}, \tag{3.39}$$

$$y = \nu/E, \tag{3.40}$$

and ν is $E - E'$, where E' is the energy of the scattered electron.

The azimuthal angles are defined according to the Trento convention [113] as shown in Fig. 2.14. The "F" functions in Eq.3.33-3.36 are defined as:

$$F_{UU} = [f_1 \otimes D_1], \tag{3.41}$$

$$F_{UU}^{\cos 2\phi_h} = \left[-\frac{2(\hat{\mathbf{h}}\cdot\mathbf{k_T})(\hat{\mathbf{h}}\cdot\mathbf{p_T})-\mathbf{k_T}\cdot\mathbf{p_T}}{MM_h}h_i^\perp \otimes H_1^\perp\right], \tag{3.42}$$

$$F_{UT}^{\sin(\phi_h+\phi_S)} = \left[-\frac{\hat{\mathbf{h}}\cdot\mathbf{k_T}}{M_h}h_1 \otimes H_1^\perp\right], \tag{3.43}$$

$$F_{UT}^{\sin(\phi_h-\phi_S)} = \left[-\frac{\hat{\mathbf{h}}\cdot\mathbf{p_T}}{M}f_{1T}^\perp \otimes D_1\right], \tag{3.44}$$

$$F_{UT}^{\sin(3\phi_h-\phi_S)} = \left[\frac{2(\hat{\mathbf{h}}\cdot\mathbf{p_T})(\mathbf{p_T}\cdot\mathbf{k_T})+\mathbf{p}_T^2(\hat{\mathbf{h}}\cdot\mathbf{k_T})-4(\hat{\mathbf{h}}\cdot\mathbf{p_T})^2(\hat{\mathbf{h}}\cdot\mathbf{k_T})}{2M^2M_h}h_{1T}^\perp \otimes H_1^\perp\right]. \tag{3.45}$$

The definition of all TMDs can be found in Fig. 3.4. D_1 is the unpolarized fragmentation function and $H_1^\perp$ is the Collins fragmentation function. The unit vector $\hat{\mathbf{h}} = \mathbf{P}_{h\perp}/|\mathbf{P}_{h\perp}|$ and the convolution in Eq. 3.41-Eq. 3.45 represent an integration over transverse momentum of initial ($\mathbf{k_T}$) and final quark ($\mathbf{p_T}$) with proper weight-

ing [193], i.e.

$$[.. \otimes ..] = x \sum_q e_q^2 \int d^2\mathbf{p_T} d^2\mathbf{k_T} \delta^{(2)}(\mathbf{p_T} - \frac{\mathbf{P_{h\perp}}}{z} - \mathbf{k_T})[...]. \tag{3.46}$$

These convolutions can be reduced to simple products if the $|P_{h\perp}|$-weighted integrations cover to infinite $|P_{h\perp}|$ or explicit $\mathbf{p_T}$ and $\mathbf{k_T}$ dependencies (like Gaussian distributions) are introduced.

3.3.1 Transverse Target Single-Spin Asymmetry

The target SSA is defined as:

$$A_{UT} \equiv \frac{1}{|S_T|} \frac{d\sigma_{UT}}{d\sigma_{UU}} \tag{3.47}$$

The Collins, Sivers and Pretzelosity asymmetries have different angular dependence:

$$\begin{aligned} A_{UT}(\phi_h, \phi_S) &\equiv \frac{1}{|S_T|} \frac{d\sigma(\phi_h, \phi_S) - d\sigma(\phi_h, \phi_S + \pi)}{d\sigma(\phi_h, \phi_S) + d\sigma(\phi_h, \phi_S + \pi)}, \\ &= A_{UT}^{Collins} \sin(\phi_h + \phi_S) + A_{UT}^{Sivers} \sin(\phi_h - \phi_S) \\ &+ A_{UT}^{Pretzelosity} \sin(3\phi_h - \phi_S). \end{aligned} \tag{3.48}$$

where

$$A_{UT}^{Collins} = 2 < \sin(\phi_h + \phi_S) > \tag{3.49}$$

$$A_{UT}^{Sivers} = 2 < \sin(\phi_h - \phi_S) > \tag{3.50}$$

$$A_{UT}^{Pretzelosity} = 2 < \sin(3\phi_h - \phi_S) > \tag{3.51}$$

and

$$\langle \sin(\phi) \rangle = \frac{1}{\pi} \int_0^\pi A_{UT} \sin\phi d\phi. \tag{3.52}$$

As we will discuss in the following sections, the HERMES and COMPASS collaborations have done pioneering work in measuring SSA with SIDIS processes. The

HERMES [194] and the COMPASS [195] papers used the notations:

$$A_{UT}^{Collins} \equiv 2\langle \sin(\phi_h + \phi_S)\rangle_{UT} \cdot D_{nn}, \tag{3.53}$$

$$A_{UT}^{Sivers} \equiv 2\langle \sin(\phi_h - \phi_S)\rangle_{UT}, \tag{3.54}$$

where $D_{nn} \equiv (1-y)/(1-y+\frac{y^2}{2})$ for COMPASS. The HERMES definition of D_{nn} includes the longitudinal virtual photon effect $R = \sigma_L/\sigma_T$ and is expressed as $B(y)/A(x,y)$ where $B(y) = (1-y)$, $A(x,y) = \frac{y^2}{2} + (1-y)\frac{1+R(x,y)}{1+Q^2/\nu^2}$. The differences between the HERMES' and COMPASS' definition of D_{nn} are rather small and agree to a few percent.

From Eq. 3.33-3.36 we have:

$$A_{UT}^{Collins} \equiv D_{nn} \cdot 2\langle \sin(\phi_h + \phi_S)\rangle_{UT} = D_{nn} \cdot \frac{\left[-\frac{\hat{\mathbf{h}}\cdot\mathbf{k_T}}{M_h} h_1 \otimes H_1^\perp\right]}{[f_1 \otimes D_1]}, \tag{3.55}$$

$$A_{UT}^{Sivers} \equiv 2\langle \sin(\phi_h - \phi_S)\rangle_{UT} = \frac{\left[-\frac{\hat{\mathbf{h}}\cdot\mathbf{p_T}}{M} f_{1T}^\perp \otimes D_1\right]}{[f_1 \otimes D_1]}, \tag{3.56}$$

$$A_{UT}^{Pretzelosity} \equiv D_{nn} \cdot 2\langle \sin(3\phi_h - \phi_S)\rangle_{UT} \tag{3.57}$$

$$= D_{nn} \cdot \frac{[\frac{2(\hat{\mathbf{h}}\cdot\mathbf{p_T})(\mathbf{p_T}\cdot\mathbf{k_T}) + \mathbf{p}_T^2(\hat{\mathbf{h}}\cdot\mathbf{k_T}) - 4(\hat{\mathbf{h}}\cdot\mathbf{p_T})^2(\hat{\mathbf{h}}\cdot\mathbf{k_T})}{2M^2 M_h} h_{1T}^\perp \otimes H_1^\perp]}{[f_1 \otimes D_1]}$$

Although Eq. 3.55 and Eq. 3.56 are defined without any ambiguity, in reality, different experiments often cover different ranges in the convolution of Eq. 3.46 due to finite $P_\perp^h$ coverages, making it impossible to directly compare the A_{UT} results among different experiments. Such comparison becomes meaningful only after explicit $\mathbf{p_T}$ and $\mathbf{k_T}$ dependencies are introduced. For an ideal experiment with infinite $P_\perp$ coverage, SSA asymmetries can be weighted by $|P_\perp^h/z_h M_h|$ so that the convolutions in

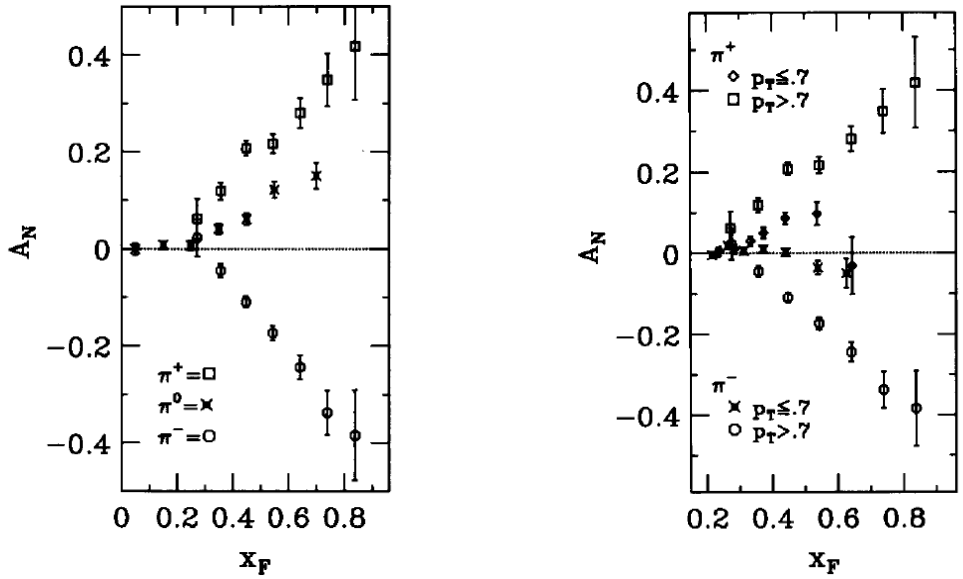

FIGURE 3.5: A_N observed in the E704 experiment. The results of π^+, π^- and π^0 are shown in the left panel. The results at different P_T bins are shown in the right panel. Figures are from Ref. [199].

Eq. 3.46 reduce to the products:

$$A_{UT}^{Collins} = \frac{(1-y)}{(1-y+\frac{y^2}{2})} \frac{\sum_q e_q^2 h_1^q(x) \cdot H_1^{\perp(1)q}(z)}{\sum_q e_q^2 f_1^q(x) \cdot D_{1q}(z)}, \tag{3.58}$$

$$A_{UT}^{Sivers} = \frac{\sum_q e_q^2 f_{1T}^{\perp(1)q}(x) \cdot D_{1q}(z)}{\sum_q e_q^2 f_1^q(x) \cdot D_{1q}(z)}. \tag{3.59}$$

A slightly different approach, based on an assumed explicit transverse dependence of the TMDs, follows from Refs. [196, 197, 198].

3.4 Review of the Experimental Data of Transverse SSA

In this section, we will review the existing experimental data of the transverse SSA.

3.4.1 Fermi-Lab E704

The first evidence of the SSA was from inclusive pion production at high $x_F = \frac{P_L}{P_L^{mas}} \approx \frac{2E_\pi}{\sqrt{s}}$ (center-of-mass frame) in proton-proton collisions. In Fermi-Lab E704

experiment [199], a 200 GeV polarized proton beam hit on a unpolarized one-meter-long liquid hydrogen target. The measured analyzing power is defined as:

$$A_N = -\frac{1}{P_B \cos(\phi)} \frac{N_\uparrow(\phi) - N_\downarrow(\phi)}{N_\uparrow(\phi) + N_\downarrow(\phi)}, \tag{3.60}$$

where ϕ is the azimuthal angle between the beam polarization direction and the normal to the pion production plane. P_B is the average beam polarization. The negative sign in front the equation is due to the fact that the spectrometer is on the right of the beam. $N_{\uparrow(\downarrow)}(\phi)$ is the number of events normalized to the luminosity.

The published results of the E704 experiment [199] are shown in Fig. 3.5. A large A_N was observed at large x_F for π^+, π^- ,and π^0. The π^+ and π^0 A_N are positive, while the π^- A_N is negative. In addition, the P_T dependence of the A_N was also studied. It was shown that A_N was reduced at lower P_T values. The observed large asymmetries were not consistent with the SSA prediction [200] based on the naive parton model where

$$A_N \sim \frac{\alpha_S \cdot m_q}{P_T} \sim 0.001. \tag{3.61}$$

Here m_q is the current quark mass and α_S is the strong interaction coupling constant. Three mechanisms, Collins [201, 173], Sivers [196], and twist-3 quark-gluon correlation (the ETQS effect) [178, 179, 180, 181, 182], were proposed to explain the observed azimuthal asymmetry.

3.4.2 RHIC – Relativistic Heavy Ion Collider

In the E704 experiment, a large A_N was observed, which clearly disagrees with the naive-parton model predictions. However, one may question whether the $\sqrt{s}$ in E704 is big enough for the pQCD, or the naive-parton model, to work. The RHIC $p - p^\uparrow$ collider provides a much higher $\sqrt{s}$ than the fixed target experiments. The measured cross sections at $\sqrt{s} = 200$ GeV agree very well with the NLO pQCD predictions for

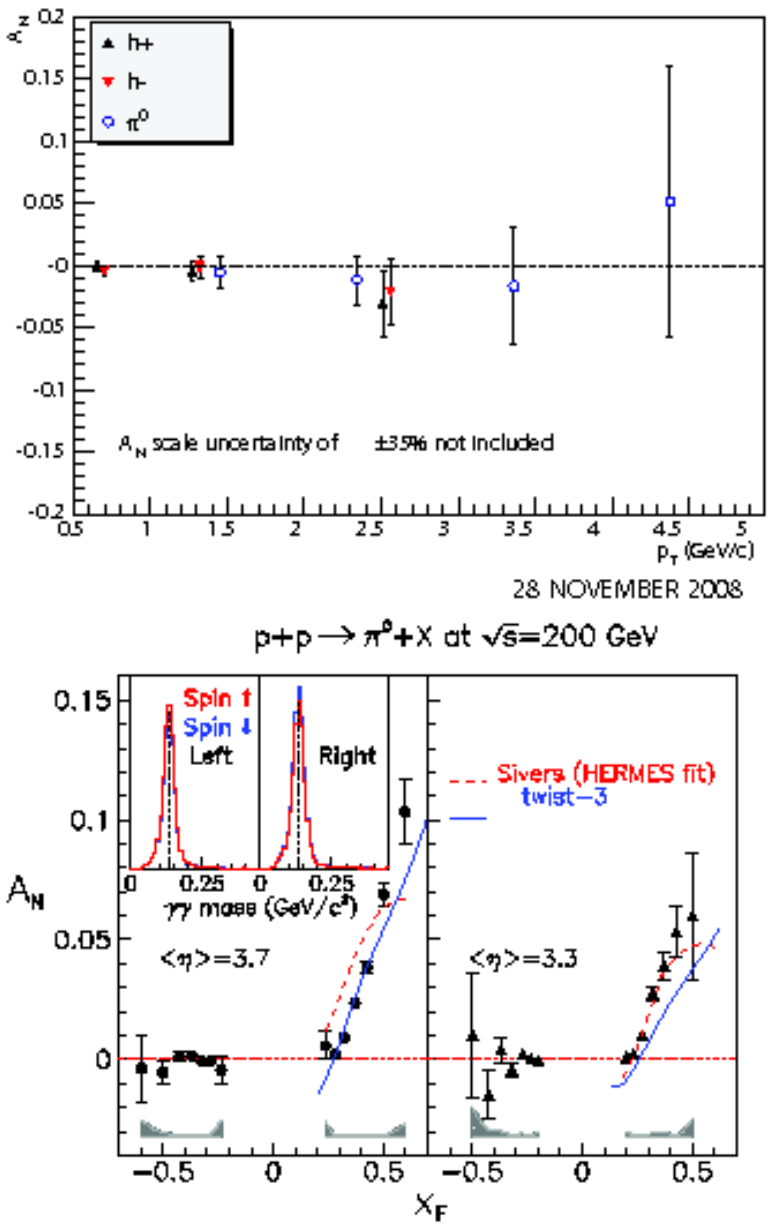

FIGURE 3.6: Top panel shows the A_N of π^0 and $h^{\pm}$ at mid rapidity, which are consistent with zero. Bottom panel shows the A_N of π^0 at forward rapidity. The top and bottom panels are from Ref. [202] and Ref. [203], respectively.

pion production with $P_T > 2.0$ GeV [202] and π^0 production in the forward region $\eta > 3.0$ [204]. Here η is pseudorapidity defined as

$$\eta = \frac{1}{2} ln \left(\frac{|\vec{p}| + p_L}{|\vec{p}| - p_L} \right), \tag{3.62}$$

where $\vec{p}$ and p_L are the particle momentum and its longitudinal component, respectively.

The observed π^0 and charged hadron SSAs at the $\sqrt{s} = 200$ GeV mid-rapidity region, which corresponds to $x_F \sim 0$, are consistent with zero [202] (top panel of Fig. 3.6). However, at forward rapidity ($x_F > 0$), a large π^0 SSA is observed [203] (bottom panel of Fig. 3.6), and has been compared with both Sivers [205, 206] and twist-3 calculations [207]. The results agree better with the calculations based on Sivers effect, but both calculations fail to describe the P_T dependence of the SSA. Meanwhile, the BRAHMS collaboration released the results of $\pi^{\pm}$ and $K^{\pm}$ SSAs at forward rapidity at $\sqrt{s} = 62.4$ GeV [208], which also showed large non-zero asymmetries. The signs of the asymmetries were consistent with the ones observed in E704 experiment. In addition, the observed A_N was also shown to reduce at smaller P_T [208], which was qualitatively consistent with the observation of E704.

In the p-p collision, Boer and Volgelsang proposed to utilize the back-to-back correlations in the azimuthal angle of jets to search for Sivers effect. In the presence of the quark transverse momentum in the initial state, it is expected that the two produced jets will have a kinematic distortion, which can lead to a SSA. However, the results from the STAR experiment were consistent with zero [209]. Later, it was found that both the initial-state interaction and the final-state interaction would contribute to the dijet-correlations in such process [210, 211, 212, 213, 214, 215], and the normal TMD factorization would break down [216].

3.4.3 HERMES

The first single target spin azimuthal asymmetry measurement of SIDIS process was from the HERMES collaboration [217], using a longitudinally internal polarized proton target and a 27.5 GeV $e^{\pm}$ beam. Their results showed significant non-zero asymmetries, which attracted much theoretical [218, 219, 220, 221, 222, 223, 224, 225, 172, 226, 175, 227, 173] and experimental interest. It is now apparent that such asymmetries are dominated by the twist-3 contribution, rather than the Collins or the Sivers effects [128].

Later, the HERMES Collaboration [194] reported results on the single-spin asymmetries from a transversely polarized proton target. The reported non-zero moments of the Collins asymmetry $< \sin(\phi_h + \phi_S) >$, which are products of the previously unmeasured quark transversity distribution and the unknown Collins fragmentation function, are shown in Fig. 3.7. While the HERMES π^+ data show positive Collins moments, the π^- data show rather large negative Collins moments. This surprising feature may be explained by the unexpected importance of the disfavored Collins fragmentation function, and that it is of the same magnitude as that of the favored Collins fragmentation function but with an opposite sign.

Furthermore, HERMES kaon Collins moments show interesting features. The K^+ moments are consistent with zero, and the K^- moments slightly favor positive values. The moment of Sivers asymmetry $< \sin(\phi_h - \phi_S) >$, which is due to the correlation between the target transverse polarization and quark transverse momentum, was also extracted for the first time from a transversely polarized proton target. A very interesting observation from the HERMES data is that the Sivers moments extracted from π^+ and π^0 are positive over the entire x and z range of the experiment, while the Sivers moment from the π^- appears consistent with zero. Recently, the HERMES Collaboration published data [228] on Sivers moments from charged kaon SIDIS

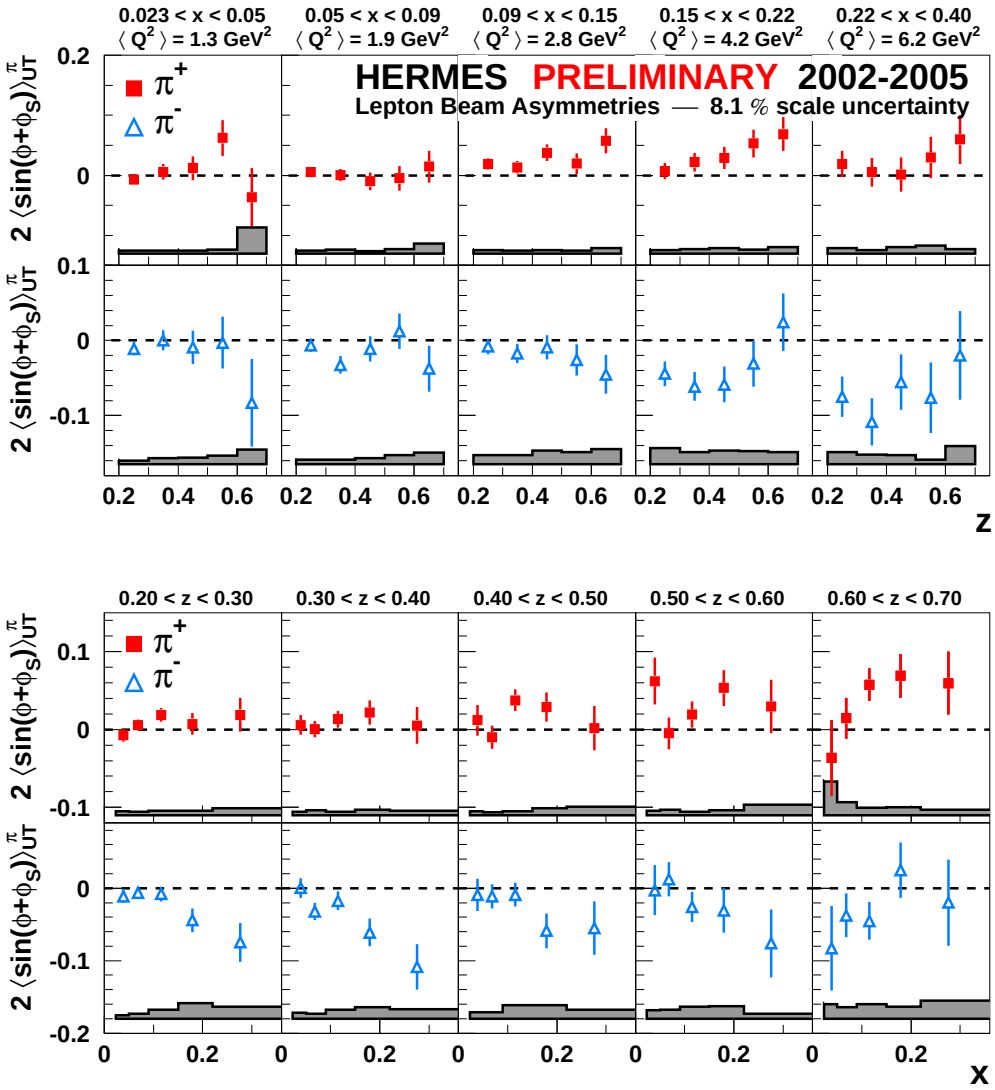

FIGURE 3.7: The HERMES results on the Collins moment in bins of x and in bins of z, separately for positively and negatively charged pions, for all transversely polarized hydrogen data from 2002-2005. The error bands display the respective total systematic uncertainty apart from the scale uncertainty due to the target polarization. For details, see Ref. [194].

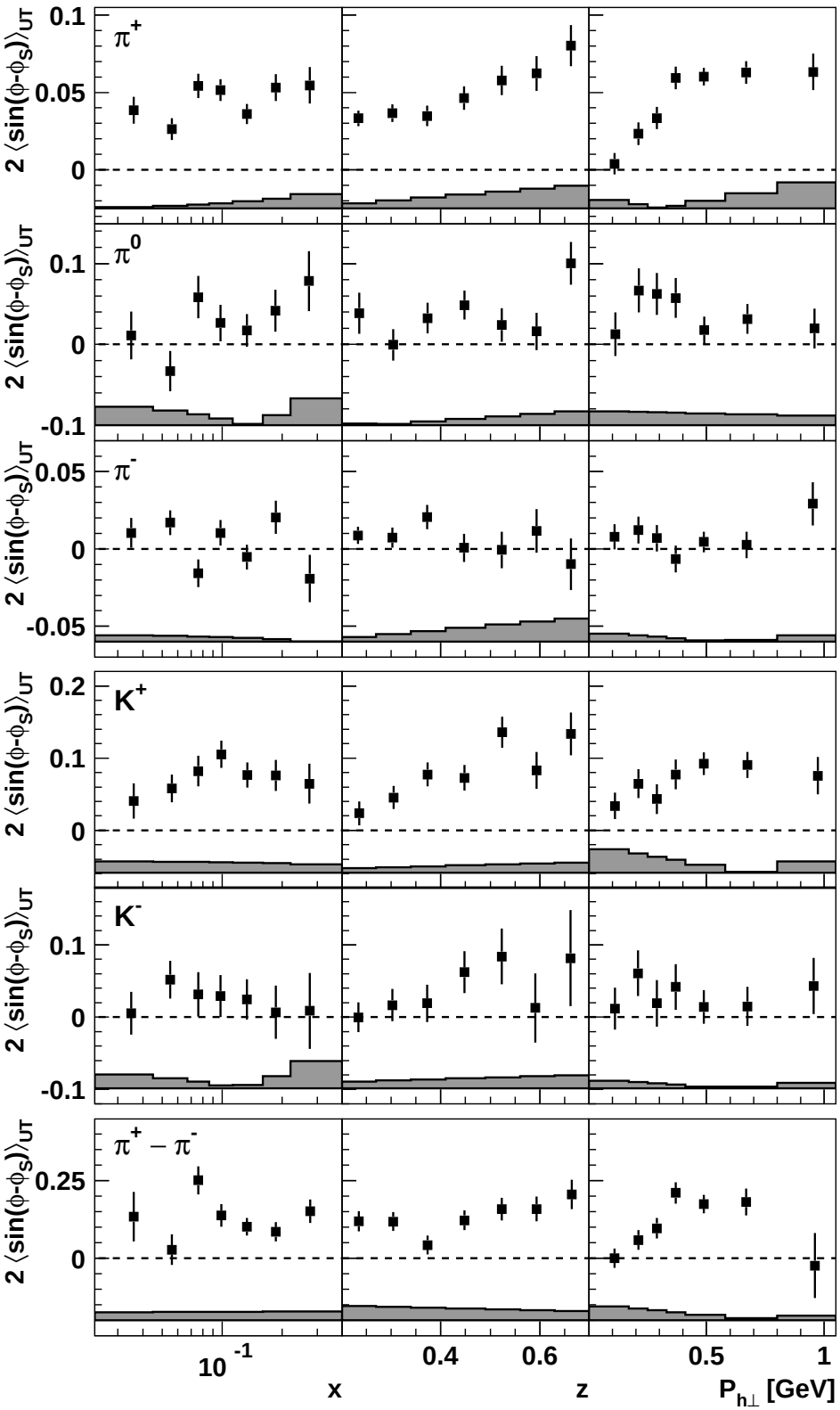

FIGURE 3.8: Sivers amplitude for pions, charge kaons and the pion-difference asymmetry as functions of x, z and $P_{h\perp}$. Figure is from Ref. [228].

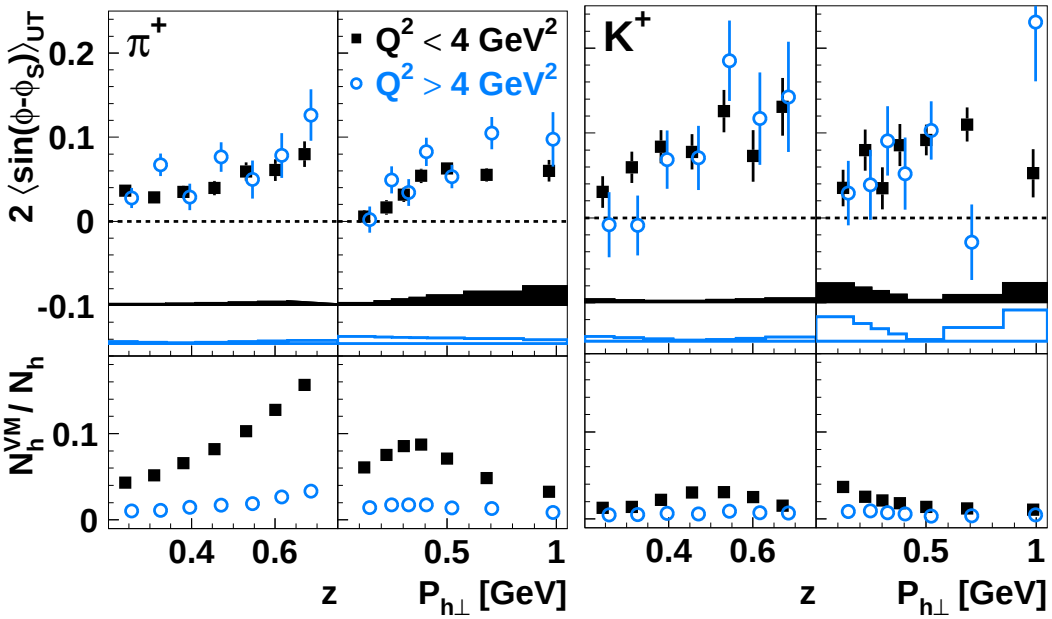

FIGURE 3.9: Sivers amplitude for π^+ and K^+. The results at different Q^2 range are shown in different colors. The contamination from vector meson diffractive scattering are shown at bottom panel. The Figure is from Ref. [228].

production in addition to pion production. The HERMES data provide evidence (See Fig. 3.8 and Fig. 3.9) for the existence of a naive T-odd, transverse-momentum-dependent parton distribution function from non-vanishing Sivers effects for π^+, π^0, and K^+.

3.4.4 COMPASS

The COMPASS collaboration reported first measurements [195, 197] of the Collins and Sivers asymmetries of charged hadrons for the deuteron from semi-inclusive scattering of 160 GeV μ^+ on a transversely polarized ^{6}LiD target in the deep-inelastic kinematic region. Both the Collins and the Sivers asymmetries are consistent with zero within the experimental uncertainties. One explanation is that the transversity distributions of u and d quarks have opposite signs. Therefore, some cancellations in single-spin asymmetries exist in measurements using a transversely polarized deuteron target, which may explain the smallness of the COMPASS Collins asym-

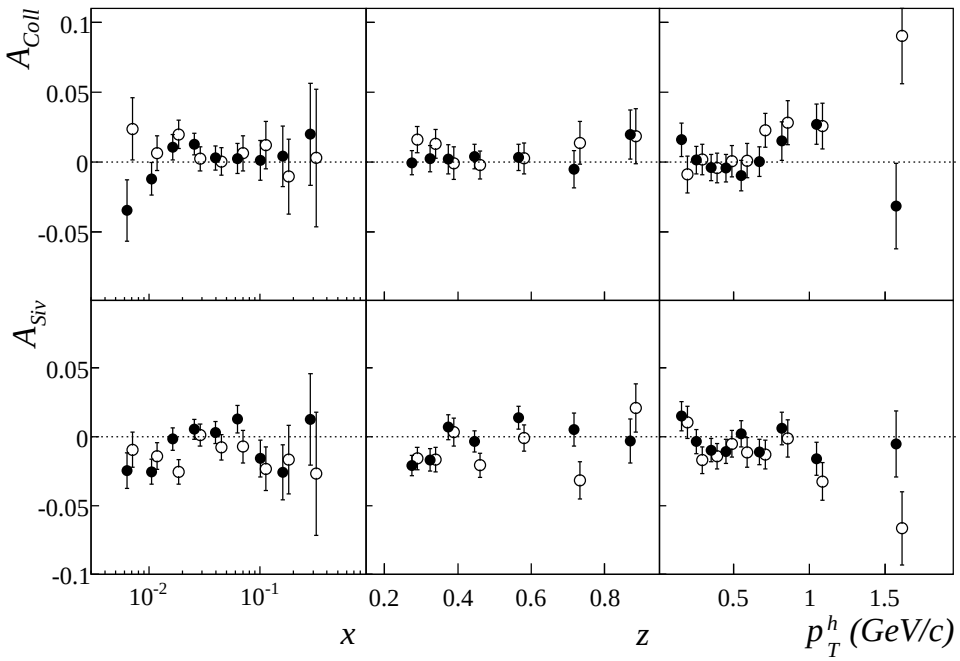

FIGURE 3.10: The COMPASS results on the deuteron Collins asymmetries (top) and the deuteron Sivers asymmetries (bottom) as a function of x, z, and p_T^h for positive leading hadrons (solid circles) and negative leading hadrons (open circles) with statistical errors only. Figure is from Ref. [197].

metry. A similar cancellation effect may also explain the smallness of the deuteron Sivers asymmetry. The COMPASS leading hadron results [197] with improved statistical errors by including the 2002, 2003 and 2004 data are shown in Fig. 3.10. Recently, the COMPASS collaboration published the Collins and Sivers asymmetries of $\pi^{\pm}$ and $K^{\pm,0}$, which are consistent with the previously published results of leading hadron without particle identification [229].

In 2010, the COMPASS collaboration [230] released the preliminary results on both the Collins (Fig. 3.11, top panel) and the Sivers (Fig. 3.11, bottom panel) asymmetries from a transversely polarized proton target. Also shown in Fig. 3.11 are the predictions of the Collins asymmetry from Anselmino *et al.* [231] based on the global analysis of the HERMES proton data, the previous COMPASS deuteron data, and

the BELLE e^+e^- collision data [232, 233][6], as well as the latest predictions for the Sivers asymmetry from Anselmino *et al.* [234] based on the global analysis of the HERMES proton data and the COMPASS deuteron data. The preliminary COMPASS proton data show that the Sivers asymmetries are statistically consistent with zero for the negatively charged hadrons and are positive for the positively charged hadrons. While the predictions agree with the COMPASS preliminary proton data for the Collins asymmetry [231], as well as for the Sivers asymmetry of the negatively charged hadrons [234], they possibly deviate from the data for Sivers asymmetry of positively charged hadrons [234].

3.5 Theoretical Parametrization

There have been significant theoretical efforts in understanding the quark transversity distributions and other TMDs in the last decade, perhaps more so in the last few years motivated by the experimental progress, particularly by the HERMES [217, 194, 228] and the COMPASS [195, 197, 229] results. Here we will briefly introduce two recent developments.

The role of the intrinsic quark transverse momentum, $\mathbf{k}_\perp$, in SIDIS has been studied [128] within QCD parton model at leading order. The resulting picture has been subsequently applied to describe the HERMES data on the weighted single-spin asymmetries in SIDIS, which allows for the extraction of the quark Sivers functions. Later, Anselmino *et al.* [188] extracted the Sivers functions of the u and d quarks by combining the HERMES results [194] from a transversely polarized proton target and the COMPASS results from a transversely polarized deuteron (^6LiD) target [195].

[6] As we discussed in Sec. 3.3, the Collins SSA measured in the SIDIS process involves both the transversity distribution and the Collins fragmentation function. BELLE Collaboration directly measured the Collins fragmentation function through the inclusive charged dihadron production $e^+e^- \to hhX$ at $\sqrt{s} = 10.52$ GeV.

Anselmino *et al.* [188] also made predictions of the Sivers asymmetries at JLab kinematics, as well as the SSAs in Drell-Yan processes at RHIC and GSI. Recently, Anselmino *et al.* [236] updated the global analysis of Sivers asymmetries by including the more recent SIDIS data from HERMES and COMPASS. The newly extracted Sivers functions $x\,\Delta^N f(x,k_\perp)$ and its first moment $x\,\Delta^N f^{(1)}(x) \equiv -x\,f_{1T}^{\perp(1)q}(x)$, which are defined as:

$$\Delta^N f_{q/p\uparrow}(x,k_\perp) = -\frac{2k_\perp}{m_p} f_{1T}^{\perp q}(x,k_\perp) \tag{3.63}$$

$$\Delta^N f^{(1)}_{q/p\uparrow}(x) \equiv -x\int d^2\mathbf{k}_\perp \frac{k_\perp}{4m_p}\Delta^N f_{q/p\uparrow}(x,k_\perp) = -f_{1T}^{\perp(1)q}(x), \tag{3.64}$$

are shown in Fig. 3.12.

Most recently, Anselmino and collaborators [231] carried out a global analysis of Collins fragmentation function and the quark transversity distribution from the SIDIS data of HERMES [194] on proton and COMPASS [197] on deuteron, as well as from the $e^+e^- \to h_1h_2X$ data of BELLE [232, 233]. The transversity distribution and Collins fragmentation function (Fig. 3.14) were extracted for the first time by these authors [237, 231]. Fig. 3.13 shows the fitting results from this global analysis together with the original HERMES data [194, 238] on the azimuthal asymmetry $A_{UT}^{\sin(\phi_S+\phi_h)}$ for $\pi^\pm$ production. The shaded areas represent theoretical uncertainties in this global analysis without the model uncertainties. The corresponding comparison between the global analysis [231] and the 2002-2004 COMPASS data [197] on positive hadron and negative hadron productions is shown in the lower panel of Fig. 3.13. Predictions for the COMPASS proton measurement as well as the JLAB "neutron" measurements have been made [231].

Vogelsang and Yuan [239] also studied SSAs from a transversely polarized target in SIDIS using the QCD factorization approach. Simple Collins and Sivers functions were obtained by fitting the HERMES data [194]. These functions were able to de-

scribe the COMPASS results reasonably well. Using this approach, Yuan [240] made predictions of SSAs for SIDIS pion electroproduction from a transversely polarized "neutron" (^{3}He) target at the JLab kinematics. The Collins asymmetry for the neutron is predicted to be smaller than that for the proton based on the HERMES data and charge symmetry:

$$u_p(x) = d_n(x) \tag{3.65}$$

$$d_p(x) = u_n(x), \tag{3.66}$$

where $u_p(x)$ ($u_n(x)$) represents the u quark PDF inside proton (neutron). The Sivers asymmetry of π^+ for the neutron is predicted to be as large as 40-50%. In order to fit the HERMES proton data, a large d quark Sivers function, with a sign opposite to that of the u quark Sivers function, is required. Therefore, based on charge , a large u quark Sivers function is expected in the neutron. Since the π^+ production is usually dominated by the u quark fragmentation process, such prediction of large π^+ asymmetry for neutron is reasonable. In understanding the nucleon structure, the information from proton and neutron are equally important. Since the proton results are usually expected to be dominated by the u quark, the neutron results can provide more information on the d quark. Therefore, the E06-010 and future SSAs measurement on the neutron using a polarized ^{3}He target at Jefferson Lab are very crucial and will provide unique information on transversity and other TMDs.

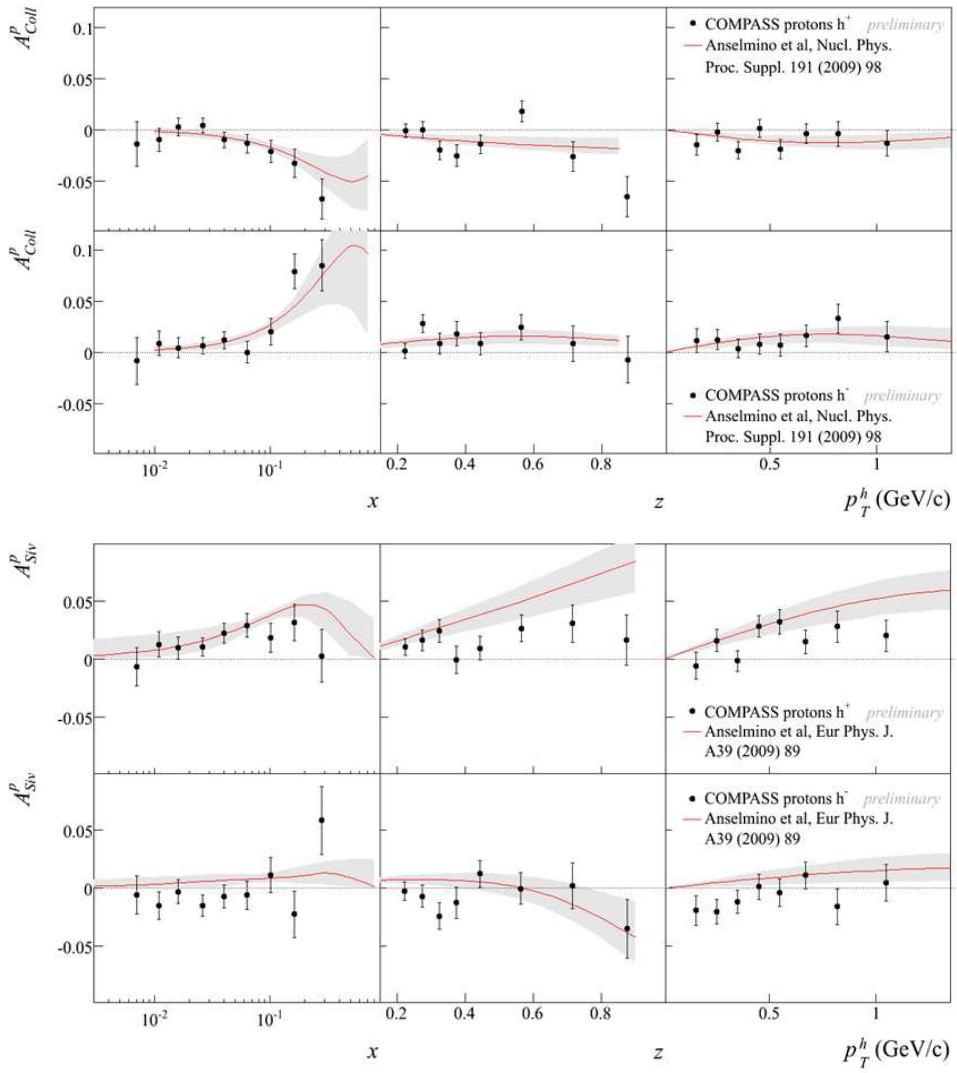

FIGURE 3.11: The preliminary COMPASS proton results [230] on the Collins asymmetries (top panel) and the Sivers asymmetries (bottom panel) as a function of x, z, and p_T for charged hadrons. Also shown are the predictions from Anselmino *et al.* [231] for the Collins asymmetry, and Anselmino *et al.* [234] for the Sivers asymmetry. The shaded areas represent the theoretical uncertainties in the predictions.

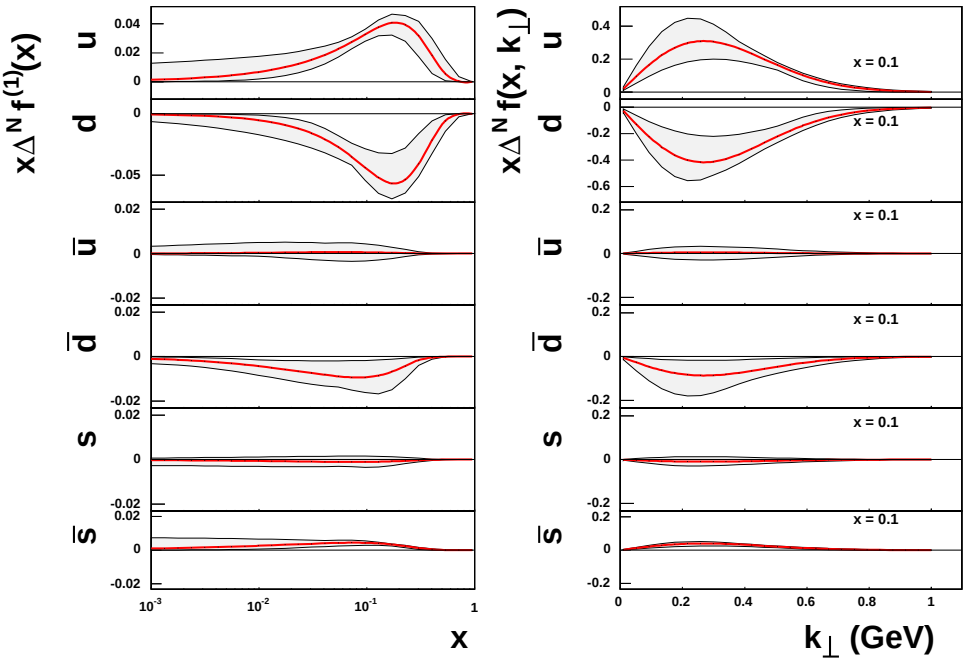

FIGURE 3.12: The Sivers distribution functions for u, d and s flavors from Ref. [235] On the left panel, the first moment $x\,\Delta^N f^{(1)}(x) \equiv -x\,f_{1T}^{\perp(1)q}(x)$ is shown as a function of x for each flavor. On the right panel, the Sivers distribution $x\,\Delta^N f(x, k_\perp)$ is shown as a function of $k_\perp$ at a fixed value of x for each flavor.

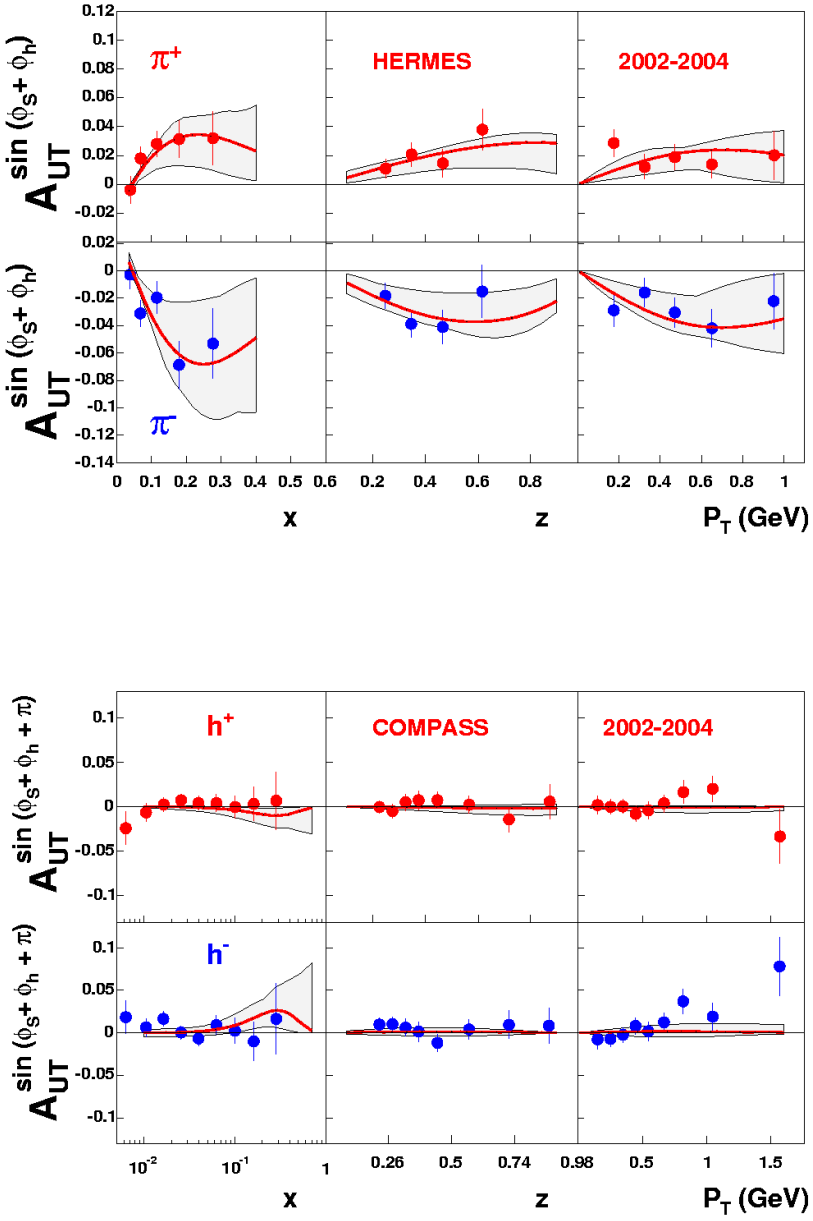

FIGURE 3.13: The comparison between the global analysis by Anselmino *et.* [231] and the results from the HERMES (top panel) and the COMPASS (lower panel) experiment on the Collins asymmetry as a function of x, z, and p_T for charged pions (charged hadrons for COMPASS). The shaded areas represent the theoretical uncertainties in the global analysis without the model uncertainties.

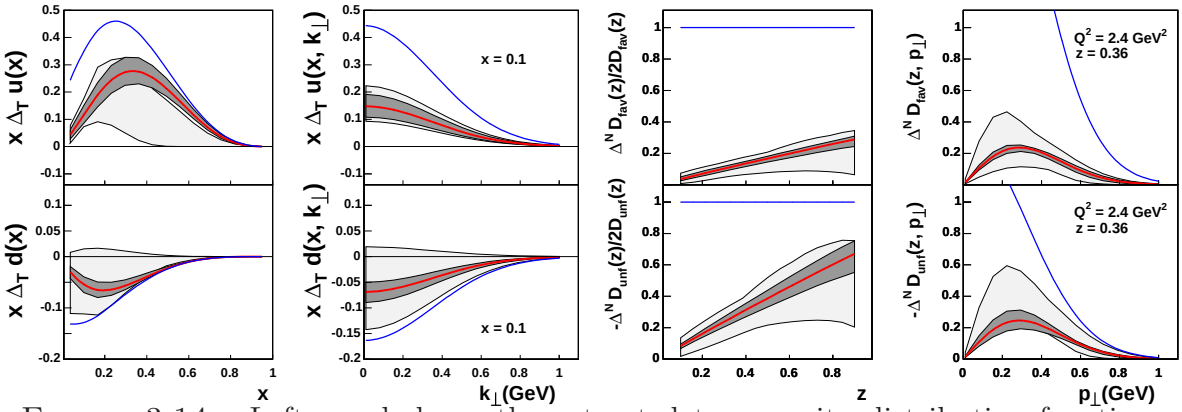

FIGURE 3.14: Left panel shows the extracted transversity distribution functions for u and d quarks from Ref. [231]. The Soffer bounds are shown as the highest or lowest blue lines. The wider bands are the transversity distribution extracted from Ref. [237]. Right panel shows the extracted favored and unfavored Collins fragmentation functions together with the positivity bounds. The wider bands are the extracted Collins fragmentation functions from Ref. [237]. The model uncertainties are not included. Figures are from Ref. [231]

4

Experimental Apparatus

Experiment E06-010 [241] started taking data near the end of October 2008 and completed in early February 2009 in Hall A at the Thomas Jefferson National Accelerator Facility (Jefferson Lab or JLab, formerly known as the Continuous Electron Beam Accelerator Facility, or CEBAF). The target single spin asymmetries (SSAs) of the neutron[1] were measured in the valence quark region, $x \sim 0.13 - 0.41$, at $Q^2 \sim 1.31 - 3.1$ GeV^2 through SIDIS pion electroproduction $e(n^\uparrow, e'\pi^\pm)X$ with a transversely polarized ^{3}He target.

4.1 Overview

The highest available beam energy, 5.89 GeV, was employed in taking the production data. Two lower beam energies, 1.2306 GeV and 2.3960 GeV, were utilized for calibration purposes. As illustrated in the left panel of Fig. 4.1, the BigBite spectrometer was positioned at 30 degrees to the right of the beam line facing downstream of the target for detecting electrons. The distance between the front face of the magnet and the center of the target was 1.5 m. The momentum coverage of the BigBite

[1] Neutron in the ^{3}He

was from 0.6 to 2.5 GeV. The solid angle acceptance was about 64 msr. The High Resolution Spectrometer (HRS) was located at 16 degrees to the left of the beam line for detecting the leading charged hadrons ($\pi^{\pm}$, $K^{\pm}$, and p) in coincidence to the electron detection in BigBite. The central momentum of HRS was set to 2.35 GeV. The solid angle of the HRS was about 6 msr, and the momentum coverage was about $\left|\frac{\delta p}{p}\right| < 5\%$. The standard Hall A 40 cm long polarized ^{3}He target was used as an effective polarized neutron target. The target cell was filled with about 10 amagats [2] of ^{3}He and small amount of N_2 mixture. As illustrated in the right panel of Fig. 4.1, three sets of coils were used to provide a magnetic field in any direction. During the production data taking, the ^{3}He nuclei were polarized in one of the two directions perpendicular to the initial electron beam: the vertical and transverse direction. The average polarization was about 60%, and the average beam current was about 12 μA with a maximum value of 14 μA reached near the end of the data taking. In the following, we will describe various experimental components used in this experiment.

4.2 The Accelerator

Jefferson Lab's electron accelerator consists of one injector, two super-conducting (temperature of 2 K) linear accelerators (linac), and two recirculation arcs (magnets). Electrons are accelerated through the linacs and circulated up to five times. There are three experimental Halls. The state-of-art photocathode gun system is used to deliver the continuous-wave (CW) beams of high polarization, high current to Hall A and C and low current to Hall B. The layout of the electron accelerator is shown in Fig. 4.2.

The polarized electrons are produced by shining the circularly polarized laser light on a strained gallium arsenide (GaAs) cathode. The electrons are then injected into

[2] One amagats is one atm at 0 degree.

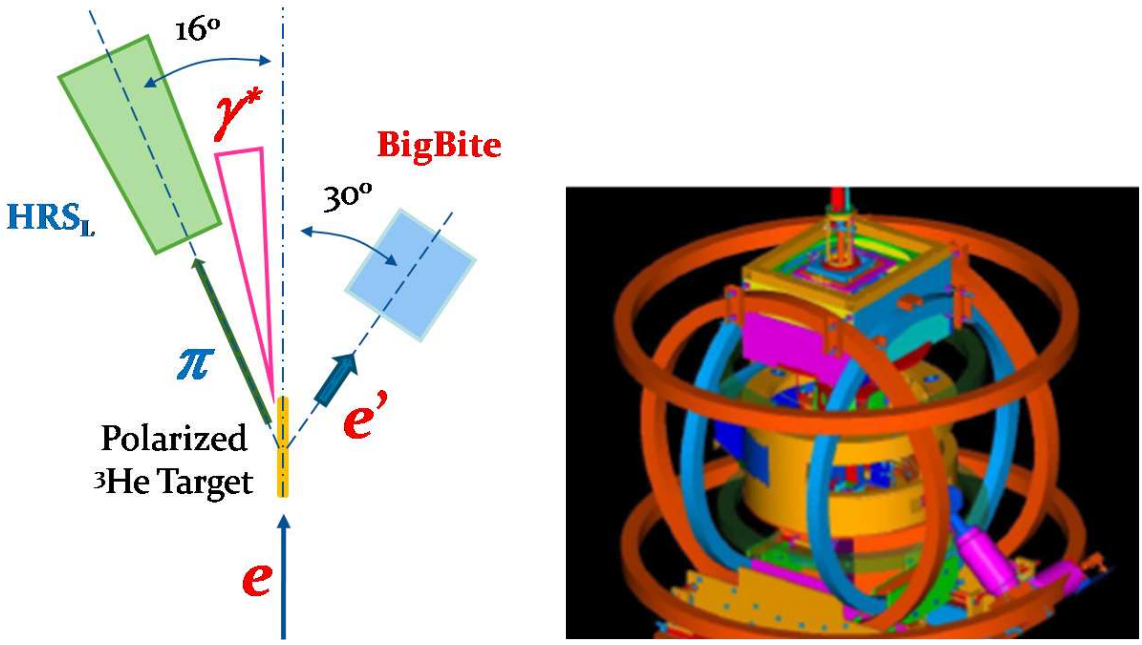

FIGURE 4.1: Left panel: Experimental layout of E06-010. Right Panel: Polarized ^{3}He target containing three sets of coils and the scattering chamber.

the accelerator after initial acceleration to 45 MeV. Each linac can further accelerate the electron by up to 570 MeV. With five rounds of circulation, the maximum beam energy is about 6 GeV. The entire accelerator is operated at an radio frequency (RF) of 1497 MHz, which is 499 MHz for the electron bunches (2 ns length) to each hall. The average beam polarization is about 85% and the maximum total beam current is about 200 μA.

4.3 Overview of Hall A

Hall A is the largest experimental Hall among the existing halls. It has two HRS with momentum resolution of 10^{-4}. The maximum momentum the HRS can reach is about 4.0 GeV. A large acceptance spectrometer, BigBite, can be installed upon the request of the experiment. Several pieces of equipment are built in the beam line in order to monitor the properties of the beam. The Compton and Moller polarimeters

g

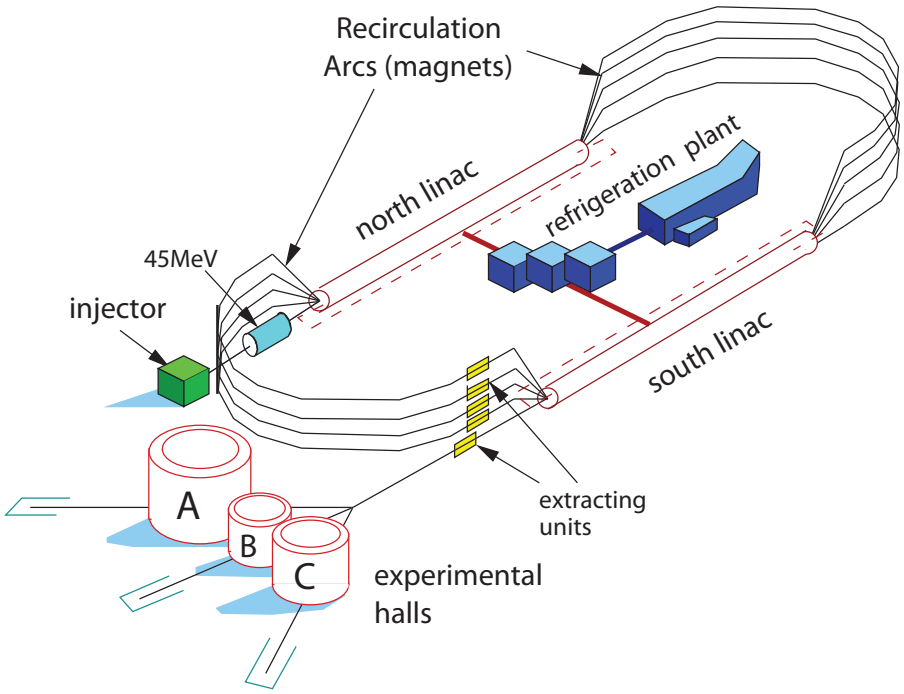

FIGURE 4.2: The Jefferson Lab Accelerator. Figure is from Ref. [97].

monitor the beam polarization. Other components include a beam current monitor (BCM), a beam position monitor (BPM), a beam raster, and a "eP" which measures the beam energy. Two pictures of Hall A are shown in Fig. 4.3.

4.4 Beam Energy Measurement

The electron beam energy in E06-010 was measured using the Arc energy method. The principle of this method is that the momentum of a charged particle is correlated to its bending angle as it moves through a magnetic field:

$$p = qB \cdot R = qB \cdot \frac{l}{\theta} = \frac{\int \vec{B} \cdot d\vec{l}}{\theta}. \tag{4.1}$$

p is the momentum of the particle. q is the charge of the particle. B is the strength of the magnetic field perpendicular to the particle's velocity direction. R is the

FIGURE 4.3: Two pictures of Hall A.

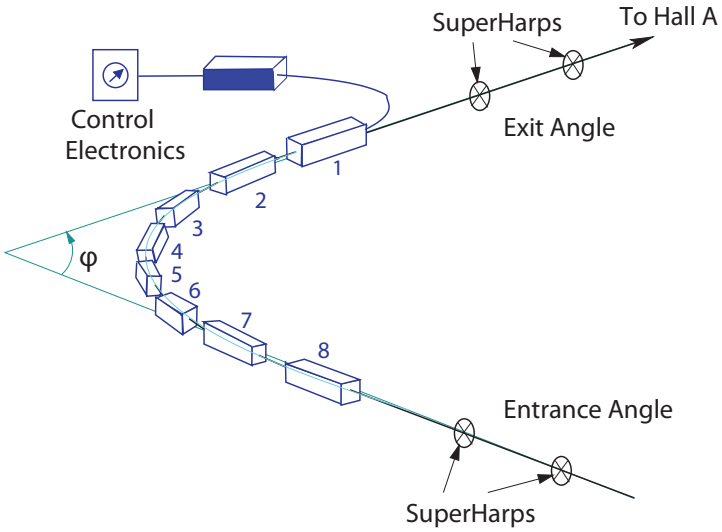

FIGURE 4.4: The schematic of the arc energy measurement. Figure is from Ref. [97].

radius of the trajectory. θ is the bending angle. Therefore, the momentum of a charged particle can be calculated using Eqn. (4.1) by measuring its bending angle θ after passing through a well determined magnetic field. As shown in Fig. 4.4, there are in total eight dipole magnets providing the magnetic field in the arc. The nominal bending angle θ is 34.3^o. Deviations from the nominal bending angle can be measured by the wire scanners, also referred to as the "SuperHarps", installed at both the entrance and exit of the arc. More details of the instrumentation can be

found in Ref. [242].

At the beginning of the experiment (Nov 17th, 2008), one full arc energy measurement was performed and the beam energy was determined to be $E_{arc} = 5889.4 \pm 0.5$ (stat.) $\pm$ 1.0 (sys.) MeV. During the experiment, the beam energy was continuously monitored by the Tiefenbach method, which uses the BPMs in the arc to provide the bending angles through the arc. The relative uncertainty of the Tiefenbach method is in general less than 5×10^{-4}.

4.5 Beam Position Monitor (BPM) and Raster

In Hall A, two BPMs are installed at about 1.1 (BMPA) and 7.3 (BPMB) meters upstream of the target. Each of them is a cavity with four wires placed at 45^o degrees from the horizontal and vertical planes. As the beam passes by, the wire will pick up the E&M signal, whose size depends on the distance between the beam and the wire. The Superharps are usually used to calibrate the BPMs.

The windows of the high pressure polarized ^{3}He target cell are very thin (thickness $\sim$ 0.1 mm) in order to reduce backgrounds. On the other hand, the electron beam profile, the size of the beam spot, is very narrow and current is relative high. Therefore, the beam is rastered by two sets of steering magnets, located about 23 meters upstream of the target. They can deflect the electron beam both in the vertical and horizontal directions. In E06-010, a 3×3 mm square raster was achieved by changing the frequency and magnitude of the magnetic field in the steering magnets.

4.6 Beam Current Monitors (BCM)

As illustrated in Fig. 4.5, the BCM consists of an Unser monitor and two cavities [243]. It is located at 25 meters upstream of the target. The Unser monitor is a Parametric Current Transformer, which provides an absolute measurement of the beam current. However, it is not able to provide a continuous and stable signal.

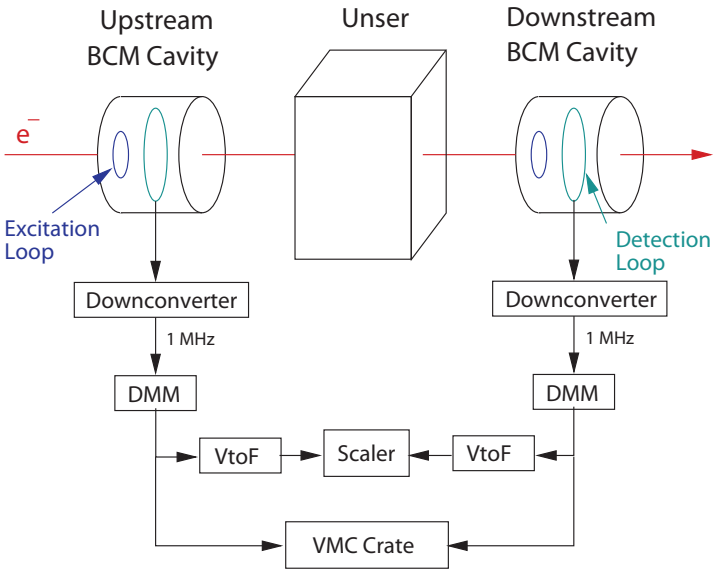

FIGURE 4.5: The schematic of the BCMs. Figure is from Ref. [97].

Instead, two RF cavities, placed in the front and the back of the Unser, also referred to as the upstream and the downstream BCMs, are usually used to provide the constant monitoring of the beam current. Each of the two RF cavities is a stainless steel waveguide tuned to the beam RF frequency of 1.497 GHz. The waveguide will pick up the signals proportional to the beam current as the electrons pass through the cavity.

The data from the RF cavities are split into two parts. The first part is the sampled signal processed by a Digital Multi-Meter (DMM), which sends out the RMS value of the input signal once per second. The second part is the integrated signal transformed by an RMS-to-DC converter into an analog DC signal, which is further converted to a frequency by a Voltage-to-Frequency converter. The output is then counted by the VME scalers, and thus provides a measure of the total accumulated charge. For the beam current from 5 to 200μA, the output of the RMS-to-DC converter is linear. Two additional amplifiers, $x3$ and $x10$, are used to extend the linear range to lower beam currents. As a result, there are in total 6 BCMs (u1, u3,

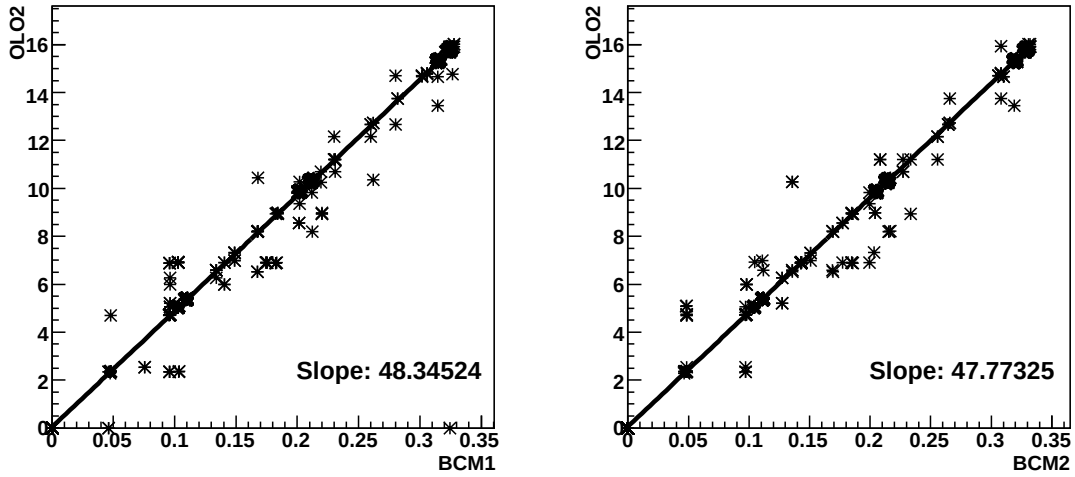

FIGURE 4.6: The calibration of the online beam current monitor BCM1 and BCM2 with the signal of "OLO2".

u10, d1, d3 and d10) recorded in the data.

In E06-010, a different approach to calibrate the BCMs was taken. The BCMs were calibrated by normalizing the RF cavities to the "OLO2" cavity which measures the beam current at the injector. During the calibration, the electron beam was only delivered to Hall A and the accelerator was operated in a "no electron loss" mode.

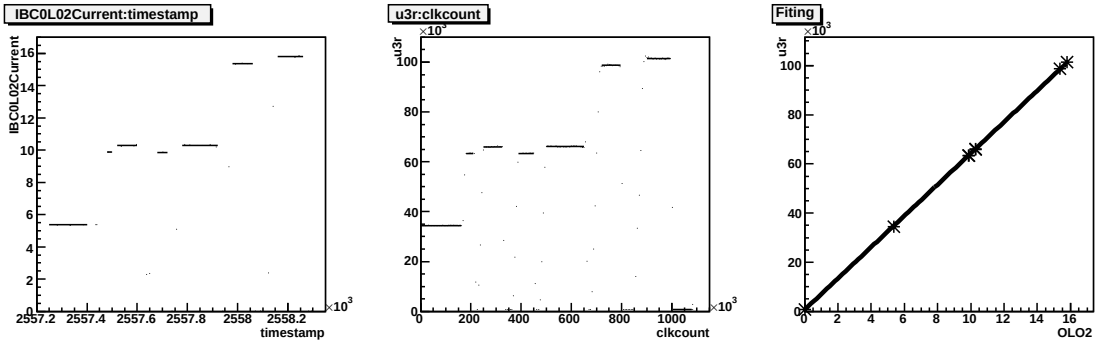

FIGURE 4.7: The calibration of the u3 BCM with the signal of "OLO2". The first panel shows the "OLO2" readings vs. the clock. The second panel shows the $u3_r$, rates of $u3$, vs. the clock in the scalers from data in the same period. Constant fits were used to determine the readings of "OLO2" and $u3_r$ at fixed beam currents. In the third panel, the results from the previous two fits were fitted with Eqn. (4.6).

The "OLO2" cavity was calibrated with a Faraday cup inserted after it. Fig. 4.6 shows the calibration of the online BCM readings with the signal from "OLO2". During the calibration run, the beam current was changed from 0 to about 16 μA. The BCM readings were fit to a linear line through the zero point. Fig. 4.7 shows the off-line calibration of the u3 BCM with the signal from "OLO2". The beam current I was calibrated using:

$$I = A_0 \cdot u3_r + A_1, \tag{4.2}$$

where A_0 and A_1 are constants. The same procedure was used in calibrating all six BCMs.

4.7 Beam Charge Asymmetry Feedback

The main goal of E06-010 is to measure the SSAs with a unpolarized beam and a transversely polarized target. However, the electron beam is in fact longitudinally polarized with a 30 Hz helicity flipping frequency. The polarized beam provided additional data on the double-spin asymmetries. The unpolarized beam was effectively achieved by summing the two beam helicity states together. During the experiment, the beam charge asymmetry between the two beam helicity states:

$$A_Q = \frac{Q^+ - Q^-}{Q^+ + Q^-} \tag{4.3}$$

was minimized by the beam charge asymmetry feedback system [244] between Hall A and the polarized electron source. This was realized by running the parity data acquisition system (DAQ) [245], which measures the charge asymmetry in Hall A, operated in parallel with the main DAQ. During the experiment, the beam charge asymmetry within a single production run was controlled to be less than 100 parts per million (ppm). However, this method has a shortcoming during beam trips, since the beam current asymmetry during the beam trips and ramping (recovering) was

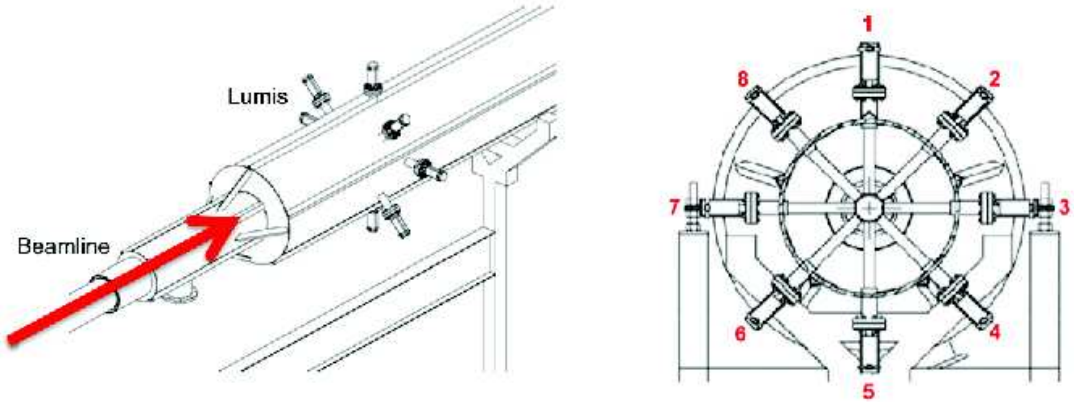

FIGURE 4.8: The Hall A luminosity monitor system. Right panel shows the numbering scheme, viewed from upstream.

large and could not be properly taken into account in the feedback system. Therefore, data associated with the beam trips were discarded during the offline analysis, which is described in Sec. 5.

4.8 Luminosity Monitors

During E06-010, target density fluctuations were monitored extensively by the luminosity monitors, which consist of 8 quartz bars oriented symmetrically around the electron beam pipe at 45^o intervals, and about 6.5 meters downstream of the target. The layout of the luminosity monitors is shown in Fig. 4.8. The scattering angles from target were between 0.5^o-0.7^o. The Cerenkov photons from the quarts were collected by a photo-multiplier tube (PMT). A separate parity DAQ was used to read the data from luminosity monitors. During the offline analysis, the lumi data were analyzed and the luminosity asymmetries were found to be negligible. Therefore, no correction from the luminosity monitor was made.

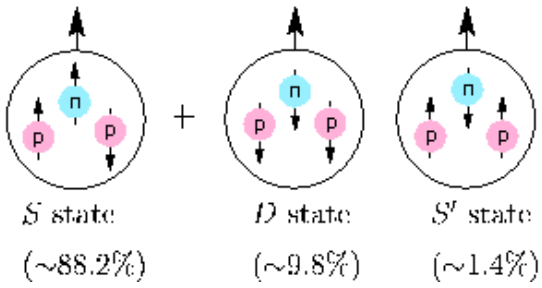

FIGURE 4.9: The ground state of ^{3}He as different wave functions. Figure is from Ref. [97].

4.9 Polarized ^{3}He target

4.9.1 Polarized ^{3}He as an Effective Polarized Neutron Target

Information from both the proton and neutron is essential to study the structure of the nucleon. However, experiments on neutron are always more difficult due to its short life time (885.7±0.8 s [57]). Therefore, one has to use stable light nuclei, such as deuteron or ^{3}He as effective neutron targets. The polarized ^{3}He, containing two protons and one neutron, is an effective polarized neutron target. The ground state of the polarized ^{3}He is dominated by the S state [246, 247], in which the two protons cancel their spins and the single neutron contributes the entire spin of ^{3}He. In addition, there are small portions of D-state and S' state in the ground state of ^{3}He as shown in Fig. 4.9. In experiment E06-010, we utilized polarized ^{3}He in order to probe the transverse spin structure of the neutron.

4.9.2 Spin Exchange Optical Pumping (SEOP)

The history of the nuclear spin polarization of ^{3}He via optical pumping dates back to 1960 [248]. Since then, there have been tremendous advances in polarization techniques [249, 250, 251, 252, 253], and in the production of highly polarized ^{3}He. During SEOP, the electrons in the Rb atoms are first polarized by optical pumping. Those electrons subsequently transfer their polarization to the ^{3}He via spin-exchange

collisions. In this experiment, a hybrid approach, which adds potassium into the system, was adopted in order to make the spin-exchange process faster and more efficient. In this section, we follow Ref. [254] to introduce the SEOP technique.

Polarizing Rubidium

Because of angular momentum conservation, circularly polarized laser light can excite valence electrons of alkali atoms to a specific spin state. For example in the case of rubidium, left circularly polarized 795 nm photons can be used to excite electrons of the m = $\frac{1}{2}$ (5S) state to the m = $-\frac{1}{2}$ (5P) state, while right circularly polarized light of the same wavelength can be used to excite electrons in the m = $-\frac{1}{2}$ (5S) state to the m =$\frac{1}{2}$ (5P) state.

The Rb atom excited by this process will decay, by emitting a photon, into either the m = $\frac{1}{2}$ or the m = $-\frac{1}{2}$ (5S) state. Since the left circularly polarized light is only exciting the electrons from the m = $\frac{1}{2}$ state, all the valence electrons of the exposed rubidium atoms will eventually occupy the opposite spin state. This process is commonly known as "optical pumping" and results in polarized rubidium atoms. A diagrammatic explanation of optical pumping is shown in Fig. 4.10.

The emitted photons from the Rb decays are unpolarized and can be re-absorbed by other rubidium atoms. This process makes high rubidium polarization impossible. Fortunately, this effect can be reduced by introducing nitrogen into the system, which allows for photon-less de-excitation by absorbing energy into its rotational and vibrational modes during a collision [255]. The amount of N_2 is chosen to be orders of magnitude less than the ^{3}He density and orders of magnitude more than the Rb density. Only about 5% of excited electrons decay by emitting a photon after introducing N_2.

The polarization of the rubidium vapor can be calculated via the following equa-

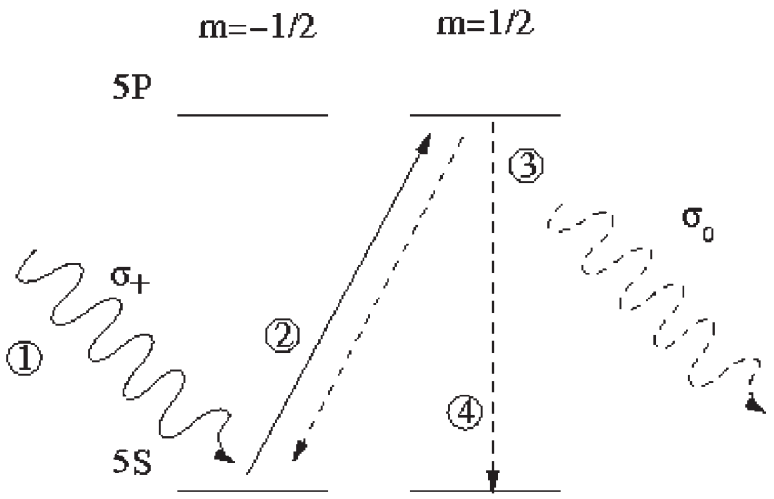

FIGURE 4.10: A diagram explaining optical pumping. (1) Rb atoms in a magnetic field are exposed to circularly polarized laser light; (2) the valence electron is excited from the $5S_{-1/2}$ state to the $5P_{1/2}$ state; (3) The Rb atom decays by emitting a photon into either the $5S_{-1/2}$ where it repeats steps (2) and (3) or into the $5S_{1/2}$ state where (4) it remains. Figure is from Ref. [254].

tion:

$$< P_{Rb} >= \frac{R}{R + \Gamma_{SD}}. \tag{4.4}$$

The quantity R is defined through

$$R = \int \Phi(\nu)\sigma(\nu)d\nu, \tag{4.5}$$

where $\Phi(\nu)$ is the photon flux per unit frequency emitted from the laser and $\sigma(\nu)$ is the light absorption cross-section. Γ_{SD} is the spin-destruction rate of the rubidium vapor.

From the polarization expression, it is easy to draw the conclusion that a high value of R and a small value of Γ_{SD} will lead to high rubidium polarization. While determining the laser flux as a function of laser power at the absorption frequency is straight forward, it is more complicated to determine the spin-destruction rate, since several factors need to be taken into account.

The primary reason is due to rubidium transferring spin angular momentum to the rotational angular momentum of other atoms. The three major rubidium collisions are: Rb-Rb, Rb-^{3}He and Rb-N_2, therefore it can be expressed as:

$$\Gamma_{SD} = k_{Rb-He}[^3He] + k_{Rb-N_2}[N_2] + k_{Rb-Rb}[Rb]. \tag{4.6}$$

Here, for each collision Rb-i, k_{Rb-i} denotes the spin destruction rate constant accordingly. Two points worth attention are: first, Rb-Rb collisions do not cause depolarization to the rubidium since spin is conserved in this process; second, Rb-^{3}He collisions which absorb the rubidium spin into their angular momentum are not the spin-exchange collisions with the ^{3}He nuclei which are needed for polarizing ^{3}He.

Polarized ^{3}He with Polarized Rubidium

Rubidium can transfer its electron polarization to the nucleus of an ^{3}He atom through a hyperfine-like interaction. The spin dependent interaction between an alkali atom and an inert gas atom can be written as [256]

$$V(\vec{R}) = \gamma(R)\vec{N}\cdot\vec{S} + A(R)\vec{I}\cdot\vec{S}, \tag{4.7}$$

where R is the interatomic separation. The first term describes the interaction between the electron spin $\vec{S}$ and the rotational angular momentum $\vec{N}$ of the Rb-^{3}He system. The second term stands for the hyperfine interaction between $\vec{S}$ and the inert gas nuclear spin $\vec{I}$. This spin-exchange process between Rb and ^{3}He has a small contribution compared to the total number of Rb-He collisions; consequently, only approximately 3% of polarized rubidium atoms lose their polarization through a spin-exchange process with ^{3}He. This makes the polarization of ^{3}He through rubidium spin-exchange an inherently inefficient process.

The time evolved expression of ^{3}He polarization is

$$P_{^3He}(t) =< P_{Rb} > \frac{\gamma_{SE}}{\gamma_{SE}+\Gamma}(1 - e^{-(\gamma_{SE}+\Gamma)t}), \tag{4.8}$$

where γ_{SE} is the Rb-^{3}He spin-exchange rate per ^{3}He nucleus, Γ is the ^{3}3He polarization destruction rate.

Γ is the quantity which best determines the ^{3}He polarization, and can be written into the following four terms:

$$\Gamma = \Gamma_{Dipole} + \Gamma_{Wall} + \Gamma_{\Delta B} + \Gamma_{Beam}. \tag{4.9}$$

Here, Γ_{Dipole} means depolarization rate from ^{3}He-^{3}He collisions, Γ_{Wall} is due to interactions with the glass walls, $\Gamma_{\Delta B}$ is depolarization from magnetic field gradients and Γ_{Beam} is due to the electron beam.

Γ_{Dipole} is the dominate factor in the high-density ^{3}He system. It is the result of spin-destructive ^{3}He-^{3}He collisions. Another important process in polarization relaxation is ^{3}He interactions with the glass cell walls. There are a few main reasons that the cell walls cause depolarization. First is the out-gassing of paramagnetic gases like O_2 from the walls when the cell is heated; second is paramagnetic materials like Rb_2O on the surface of the cell walls; and a third is the increased sticking time of ^{3}He to the surface of the walls due to microscopic fissures in the glass. For different cells, Γ_{Wall} varies significantly. A good cell can have a $\Gamma_{Wall} < \frac{1}{200}h^{-1}$, whereas a bad cell can have a $\Gamma_{Wall} > 1h^{-1}$.

Hybrid Approach

The hybrid approach to polarize ^{3}He atoms, by adding vaporized potassium to the pumping chamber, was first proposed by Happer *et al.* [257]. The Rb atom is polarized through the standard optical pumping, then it transfers the angular momentum to the potassium atom.

$$Rb(\uparrow) + K(\downarrow) \longrightarrow Rb(\downarrow) + K(\uparrow). \tag{4.10}$$

The spin-exchange collision between ^{3}He and K atoms will subsequently polarize ^{3}He atoms. The likelihood of potassium to ^{3}He spin-exchange is significantly higher than

that of rubidium to ^{3}He. The Princeton Group [258, 259] was able to extract γ_{SE} (Rb) to be around 2% at about 175^o, which is the typical pumping temperature for Rb. In contrast, the typical value of γ_{K-^3He} is around 25%. Therefore one would expect the SEOP process for hybrid cells to be more efficient than for a Rb-only-cell. This improvement has been demonstrated by an extensive study carried out by Chen *et al.* [260]. Direct spin-exchange between potassium and ^{3}He has also been realized by the Caltech Group [261].

4.9.3 Target System

The target system in E06-010 experiment was by far the most complicated system in the history of polarized ^{3}He experiments in Hall A. The system mainly consists of three pairs of Helmholtz coils, two pairs of RF coils, an oven with three pairs of pick-up coils, the ^{3}He cell, the target ladder with the empty target cell, reference target cell and the optics target (7 carbon foils and 1 BeO foil) and two pairs of pick up coils in the target chamber. A heater system together with an air flow system acted as an integral part of the target system in order to maintain the desired temperature of 230^{o}C inside the oven. Also, there were two pairs of correction coils to compensate for magnetic field gradients in the target region.

The ^{3}He cell

All three cells used in the experiment were hybrid cells. They were made at Princeton University by Mike Souza and filled at the University of Virginia and the College of William and Mary. A schematic diagram of the cell dimensions as well as the orientation with respect to the Hall system is shown in Fig. 4.11. The main characteristics of the cells used in this experiment are summarized in Table. 4.1.

As shown in Fig. 4.11, the target cell consists a 3-inch diameter pumping chamber and a 2-cm diameter target chamber that is about 40 cm long. The pumping chamber

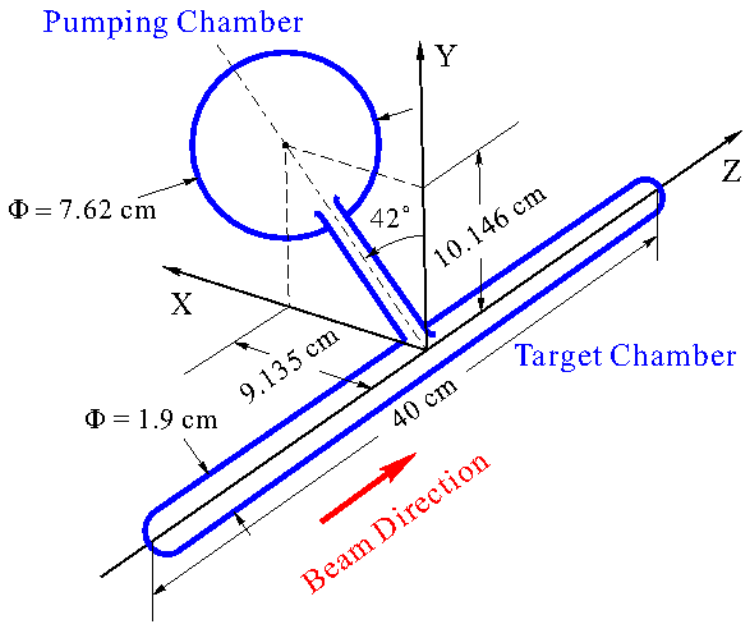

FIGURE 4.11: Orientation of the hybrid cell in the Hall.

Name	Filled at	V_p cm^3	V_t cm^3	V_{tt} cm^3	Filling Density amagats	Lifetime in hours (Raw/AFP corrected)
Astral	UVA	164.92	79.47	6.77	8.082	40/49
Maureen	W&M	180.75	89.05	4.15	7.23	26/29
Brady	UVA	169.27	74.57	5.98	7.87	31/36

Table 4.1: The numbers are from University of Virginia (UVA) and College of William and Mary (W&M) database. V_p is the volume of the pumping chamber, V_t is the volume of the target chamber and V_{tt} is the volume of the transfer tube.

and the target chamber are connected through a transfer tube of a known length. The target material is aluminosilicate glass (GE180). In addition to those numbers in Table. 4.1, the material of the glass, the thickness of the cell window and the cell walls, the length of the transfer tube and the ratio K/Rb are extremely important quantities for the polarimetry as well as other physics analyses.

Target Ladder

A target ladder, which has five different target positions, was used in experiment E06-010. The positions are shown in Fig. 4.12. The target ladder could be moved vertically to different positions using a stepper-motor-driven motion control system. A limit switch was located at each position and the motion was controlled remotely from the counting house. The pick up coil position shown in Fig. 4.12 was used for the NMR measurements. In the following, we briefly describe different components of the target ladder.

- **Polarized ^{3}He Cell**

  The polarized ^{3}He cell was replaced by the water cell during water calibrations.

- **A Solid BeO Target In-line with Seven Carbon Foils**

  The beryllium oxide (BeO) foil was used to align the beam on target. The seven carbon foils were used for the magnet optics calibration for both spectrometers.

- **An Empty Target**

  This position was mostly used for beam tuning and also used during the Moller measurement.

- **Reference Cell**

  The reference cell was used for different calibration processes, such as elastic calibrations, detector calibrations, background studies, etc. The reference cell was filled with either nitrogen, hydrogen or Helium-3 in accordance with the purpose of the studies.

Oven, Heater and Airflow System

The oven was used to keep the pumping chamber at 230^0C for hybrid optical pumping. It had an inlet and an outlet for the circulation of the compressed hot air; the

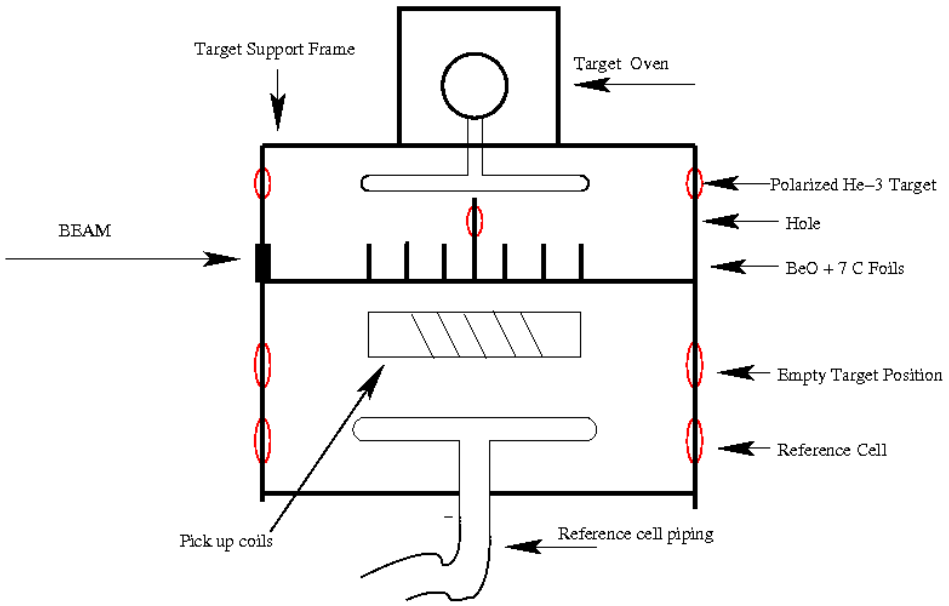

FIGURE 4.12: Schematic diagram of the target ladder system.

air was provided by a compressor in the Hall, which passed through two heaters. One of the two heaters was controlled by a variac in the Hall, and the other one was controlled by a feedback electronic control chassis. A Resistive Temperature Device (RTD) was attached inside the oven to read the inside temperature, and a thermocouple was inserted inside the insulation material near the second heater to measure the temperature of the hot air going into the oven.

Helmholtz Coils for the Holding Field

Three pairs of Helmholtz coils were used in the experiment for producing the magnetic fields in three mutually orthogonal directions. Two of them were used for providing the magnetic field in the longitudinal and the transverse directions with respect to the beam direction. The third pair was the largest one which encompassed the other two and was used to produce the vertical field. The schematic diagram of the Helmholtz coils system is shown in Fig. 4.13. Table 4.2 shows the basic characteristics of the three pairs of Helmholtz coils. The horizontal pairs of coils were

powered by two KEPCO BOP 36-12D power supplies while an Agilent 6675A was used to power the vertical pair.

Coil	Inner diameter meter	Number of turns	Resistance ohm
Small	1.27	256	3
Large	1.45	272	3
Vertical	1.83	355	4.4

Table 4.2: Dimensions of the Helmholtz coils used in the experiment.

$\vec{B}$	I_S Ampere	I_L Ampere	I_V Ampere
Transverse	6.234	-4.621	0.712066
Vertical	0.329	-0.358	14.0927

Table 4.3: Current settings for the three pairs of Helmholtz coils. $\vec{B}$ stands for the holding magnetic field direction, I_S for current in the small coils, I_L for current in the large coils and I_V for the current in the vertical coils.

4.9.4 Laser and Optical Fibers

During the E06-010 experiment, the previously used Coherent FAP (Fiber Array Package) system was replaced by the mixed spectra physics COMET and FAP laser system in order to provide the optical pumping. The difference between the COMET, also referred to as Narrow Bandwidth lasers, and the FAP systems is that the COMET lasers have a very narrow wavelength ($\sim$0.2 nm for FWHM) as compared to the 2 nm line-width of the FAP systems. As a result, there is a dramatic increase in the absorption of the laser light by the hybrid cells and hence better polarization can be achieved. The lasers were installed and interlocked in the laser building behind the Counting House. The fiber coming out of each COMET was connected to a 75 m long fiber that ran from the laser building into the Hall. As a

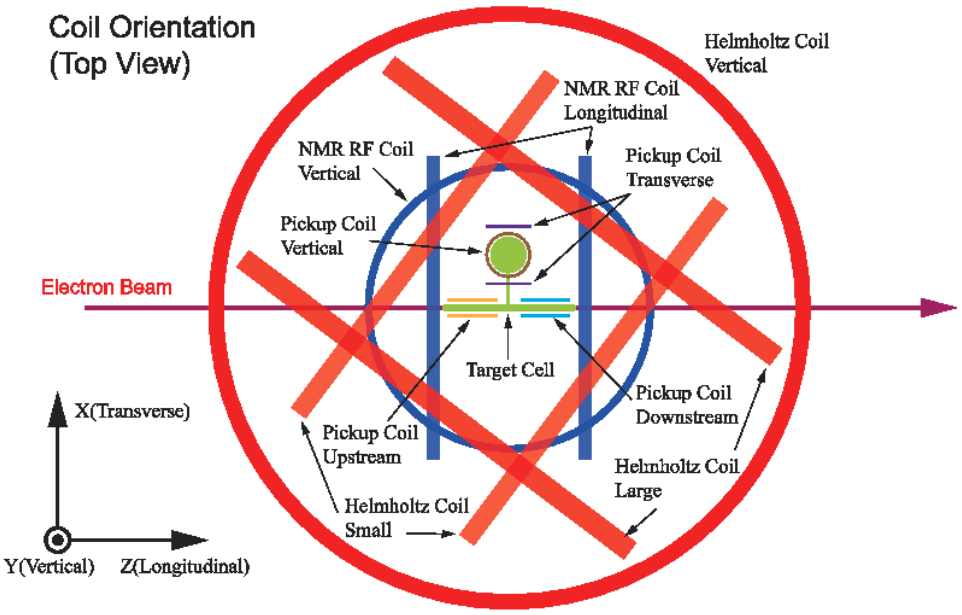

FIGURE 4.13: Schematic of the Helmholtz coils system in Hall A. The RF coils and the pick up coils are also shown.

result, there was a power loss of ∼6%. The 75 m long fiber was then connected to a 5-to-1 combiner, which has five inputs and one output. The output was the final input of the laser going into the optics assembly in the optics enclosure. During the experiment, three lasers were used for the optical pumping process.

4.9.5 Polarizing Optics

The laser light from the 5-to-1 combiner was then passed through the polarizing optics system before reaching the ^{3}He cell in the oven. The unpolarized laser light was allowed to pass through all the optical components so that a "well defined" light (either a left or a right circularly polarized) could be available at the output of the optics assembly in order to be absorbed by the Rb atoms in the cell. There were three optical lines in the optics enclosure in the Hall, and the setup of the optics component is shown in the Fig. 4.14.

The unpolarized and diverse laser light of 795 nm from the 5-to-1 combiner first

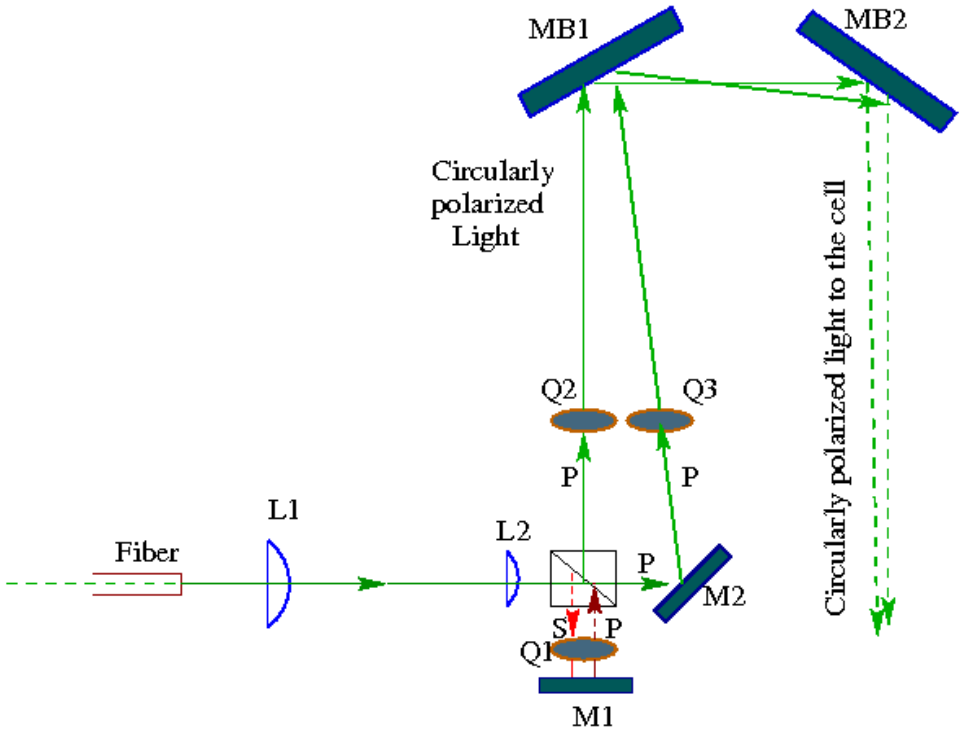

FIGURE 4.14: Schematic diagram of the optics setup for the Vertical pumping.

passes through the lens L1 (focal length 75 mm) and L2 (focal length 750 mm) before it reaches the beam splitter, which was used to separate S and P waves from the incident unpolarized light. The S wave was allowed to pass through the quarter wave plate Q1 and reflected back from the mirror M1 and passes through Q1 again; after passage the S wave became a P wave. On the other hand, the P wave was directly reflected by the mirror M2. Both the P waves were then allowed to pass through two quarter wave plates Q2 and Q3 so that the linearly polarized P waves became circularly polarized. The last two components in the path were two big mirrors MB1 and MB2 with a diameter of 6 inches. The two circularly polarized waves were reflected by MB1 (45^o) and subsequently MB2 (45^o) onto the pumping chamber.

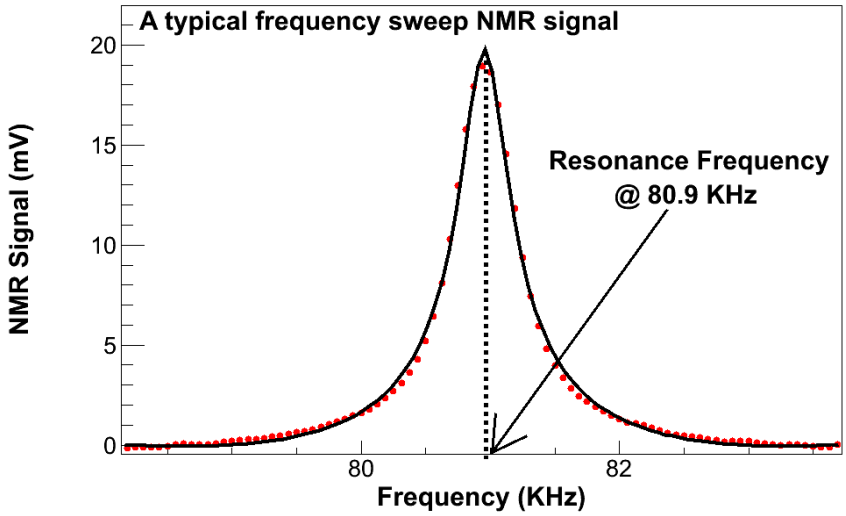

FIGURE 4.15: A NMR frequency sweep signal fitted to the square root of a Lorentzian.

4.9.6 Polarimetry

Two polarimetry techniques were employed during this experiment to measure the polarization of ^{3}He: Nuclear Magnetic Resonance under the Adiabatic Fast Passage condition (NMR-AFP) and Electron Paramagnetic Resonance (EPR), which are sensitive to different systematic uncertainties. During the experiment, the spin direction of the target was flipped every 20 mins, which generated a NMR signal and hence provided an instant polarization number. The NMR system was calibrated by water NMR measurements before the experiment. In addition, EPR was also employed to calibrate the NMR measurements during the experiment.

NMR-AFP

NMR is a phenomenon that happens when a nucleus with non zero spin is simultaneously subjected to both a static and an oscillating magnetic field. When a particle with spin $\vec{S}$ and magnetic moment $\vec{M} = \gamma\hbar\vec{S}$ is placed in a magnetic field $\vec{B}_H$, its

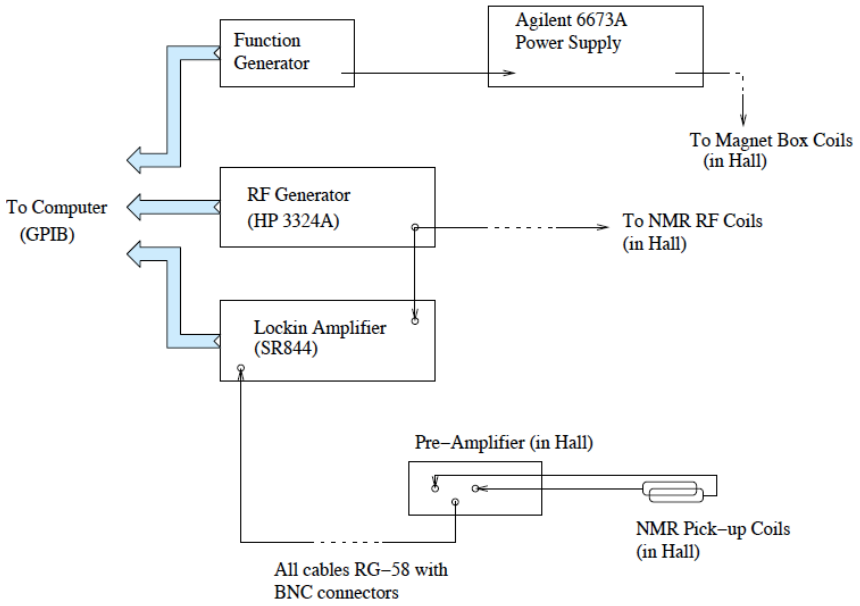

FIGURE 4.16: The electronic set up for the NMR measurements.

spin precession follows:

$$\frac{d\vec{M}}{dt} = \gamma \vec{M} \times \vec{B}_H, \tag{4.11}$$

where the γ is called the gyro-magnetic ratio ($\gamma = 3.24\,\mathrm{kHz/G}$ for ^{3}He). In a direction $\vec{x}$ perpendicular to the holding field direction $\vec{z}$, if a RF field is applied:

$$\vec{B}_{RF} = 2B_0 \cos(\omega_0 t)\vec{e}_x = B_0\vec{e}_+ + B_0\vec{e}_-, \tag{4.12}$$

where $\vec{e}_\pm = \cos(\omega_0 t)\vec{e}_x \pm \sin(\omega_0 t)\vec{e}_y$ are the two rotation vectors with frequency $\pm\omega_0$, then in the rotating frame with frequency $+\omega_0$, the effective magnetic field becomes [262][3]:

$$\vec{B}_{eff} = \left(B_H - \frac{\omega_0}{\gamma}\right)\vec{e}_z + B_0\vec{e}_+. \tag{4.13}$$

During the NMR measurements, one can either change the RF field frequency ω_0

[3] Here, the component with $-\omega_0$ frequency was neglected, since it is far from the resonance frequency.

or the holding field B_0 to pass the resonance condition $B_H = \frac{\omega_0}{\gamma}$. In addition, the entire change needs to satisfy the following AFP conditions:

- Fast Condition:

  The change should be fast enough so that the spin does not have time to relax.

- Adiabatic Condition:

  The change needs to be slow enough compared to $\omega_H = B_H\gamma$, so that the spin can follow the direction of the effective field.

In the case of frequency sweep NMR (changing the RF field frequency ω_0), the AFP condition can be expressed as:

$$\frac{1}{T_2} << \frac{1}{\gamma B_0}|\frac{d\omega_0}{dt}| << \gamma B_0, \tag{4.14}$$

where T_2 is the ^{3}He transverse relaxation time which refers to the spin dephasing time constant in the transverse plane. In the case of field sweep NMR (changing the holding field B_0), the AFP condition becomes

$$\frac{1}{T_2} << \frac{1}{B_0}|\frac{dB_H}{dt}| << \omega_0. \tag{4.15}$$

During each spin flip in E06-010, the RF field was swept from 77 kHz to 85 kHz (or from 85 kHz to 77 kHz) at a rate of 4 kHz/sec through resonance at $\omega_H = 81$ kHz inducing an electromotive force (EMF) signal, whose height is proportional to the polarization of the sample:

$$S \sim \frac{< \vec{M} > B_0}{\sqrt{(B_H - \frac{\omega_0}{\gamma})^2 + B_0^2}}. \tag{4.16}$$

The signal was collected by a pair of pick up coils, which were placed perpendicular to both the RF field and the holding field. The signal was then fed into a pre-amplifier SR620 (input A and input B), and the output (A-B) was connected to the

lock-in amplifier SR844, which was read by a computer via a GPIB (general purpose interface bus) interface. The electronics setup for the NMR measurements is shown in Fig. 4.16. A typical signal of the frequency sweep NMR is shown in Fig. 4.15. The spin direction of ^{3}He was reversed after each spin flip. During the experiment, field sweep NMR was also performed from time to time. For these measurements, the RF field was kept at a fixed frequency $\omega_0 = 91$ kHz, and the holding field was swept from 25 G to 32 G at a rate of 1.2 G/s. The resonance was at 28 G.

The NMR was calibrated by the measurement on water. The principle of water calibration is to calibrate the ^{3}He polarization with the thermal polarization of the protons. Therefore, a water cell (same geometry as the ^{3}He cell) needs to be mounted exactly the same way as the ^{3}He cell. Because of these constrains, only one water calibration was performed at the early stage of the experiment, during which, 2000 sweeps were performed to enhance the signal-to-noise ratio and to achieve a statistical uncertainty of less than 1%.

EPR

Another way of measuring the polarization of ^{3}He atoms is to measure the shift of the electron paramagnetic resonance frequency $\Delta\nu_{EPR}$ of the rubidium valence electron before and after AFP [263, 264, 265, 266]. In the EPR measurement, the splitting of different energy levels of the rubidium valence electron is measured in the presence of an external magnetic field due to the Zeeman effect. The $\Delta\nu_{EPR}$ is actually a combination of two terms:

$$\Delta\nu_{EPR} = \Delta\nu_{SE} + \Delta\nu_{He} = \frac{d\nu_{EPR}}{dB}[\Delta B_{SE} + \Delta B_{He}], \tag{4.17}$$

where $\Delta\nu_{SE}$ is the contribution from the alkali-^{3}He spin exchange and $\Delta\nu_{He}$ is the contribution from the classical magnetic field created by the polarized ^{3}He. The factor $\frac{d\nu_{EPR}}{dB}$ can be calculated with the Breit-Rabi formula [266]. The term ΔB_{SE}

corresponds to the small effective magnetic field that comes from the very short but frequent spin exchange collisions between the alkali atoms and the ^{3}He atoms and it can be written as:

$$\Delta B_{SE} = \left(2K_{He}\hbar/T_{He}g_e\mu_B\right)\langle K\rangle\,, \tag{4.18}$$

where K_{He} is the frequency shift parameter, $1/T_{He}$ is the alkali-^{3}He spin exchange rate per alkali atom, g_e=2.000232, μ_B=5.7884 $\times$ 10^{-11}MeV/T and $< K >$ is the average ^{3}He nuclear spin. The term ΔB_{He} corresponds to the classical magnetic field produced by the bulk magnetization of the polarized ^{3}He gas. The size of the classical magnetic field depends on the geometry of the target cell. It can be expressed as:

$$\Delta\vec{B}_{He} = C\eta_{He}\mu_{He}P_{^3He}, \tag{4.19}$$

where C is the dimensionless factor that depends on the geometry of the cell, η_{He} is the density of ^{3}He, μ_{He}=6.706984 $\times$ 10^{-14} MeV/T and $P_{^3He}$ is the polarization of ^{3}He in the cell. Therefore, one can write:

$$\Delta\nu_{EPR} = \frac{8\pi}{3}\frac{d\nu_{EPR}}{dB}\kappa_o\mu_{He}\eta_{He}P_{He}, \tag{4.20}$$

where κ_o is a dimensionless constant that parametrizes the spin-exchange "effective" field.

The setup of the EPR measurement is shown in Fig. 4.17. A small EPR-RF coil was placed on the side of the pumping chamber to induce the transition of rubidium atoms from a non-excitable state to an excitable state. The frequency of the resonance is affected by the ^{3}He polarization. The measurement of the EPR shift, $\Delta\nu$, was then performed by observing the $D2$ fluorescent light emitted by decaying rubidium atoms. The $D2$ light was collected by the photo-diode and filtered with $D2$ filters in order to remove the background from $D1$ light. A typical EPR-AFP spectrum is shown in Fig. 4.18.

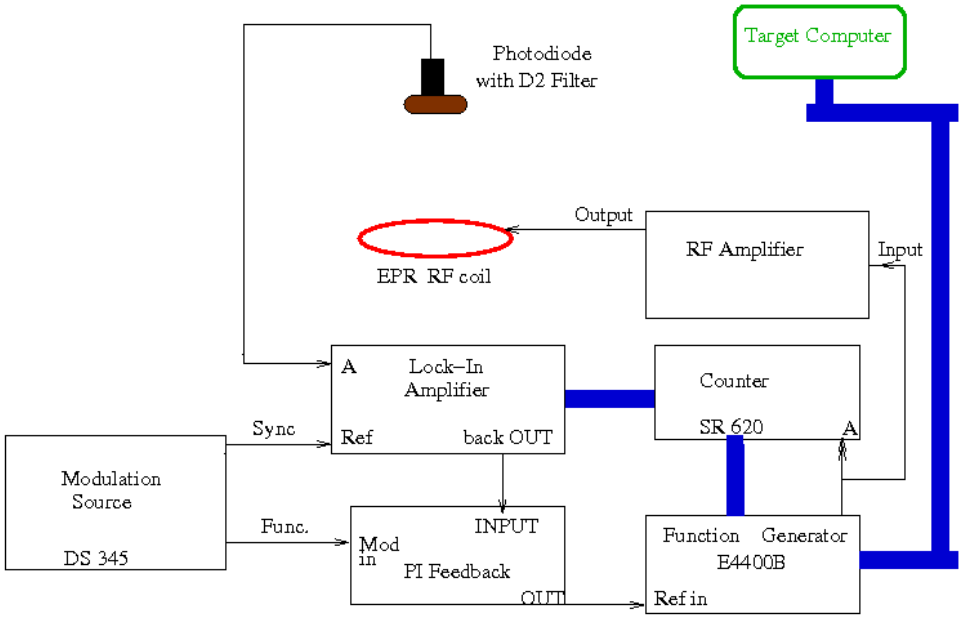

FIGURE 4.17: The schematic of the EPR setup in the experiment. The blue connections correspond to the GPIB controls and the others correspond to the BNC cables.

4.9.7 Magnetic Field Direction Measurement

Experiment E06-010 required polarizing ^{3}He in the vertical and the transverse directions. The holding field direction, which determines the ^{3}He polarization direction, was calibrated using two compasses. The transverse field direction was measured by a 40 cm iron bar, and the vertical field direction was measured by the vertical compass developed at the University of Kentucky. The vertical compass (Fig. 4.19) is a floating device in air with a magnetic cylinder and an optical encoder attached to it. The field directions were known to a level within 0.5^o for both orientations.

4.9.8 Target Spin Flip System

During E06-010, the ^{3}He target spins were flipped every 20 minutes through the AFP process to reduce possible false asymmetries. A faster spin flip would further reduce the possible systematic uncertainties or possible false asymmetries. However,

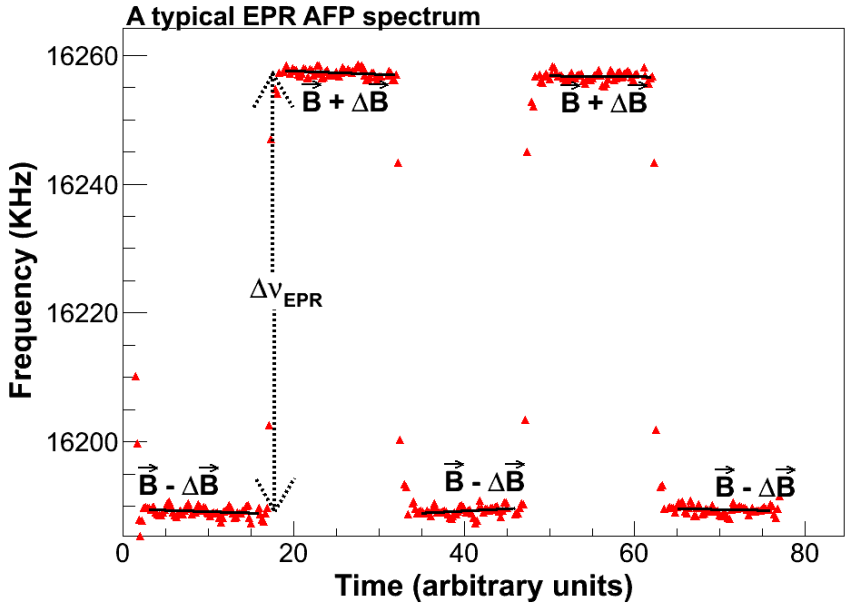

FIGURE 4.18: A typical EPR AFP spectrum. The higher frequency state corresponds to the initial state of ^{3}He spins being anti-parallel to the holding field. The lower frequency state corresponds to the flipped state of ^{3}He spins being parallel to the field. The difference between the frequencies in these two states is proportional to the ^{3}He polarization with a constant can be calculated through Eqn. (4.20).

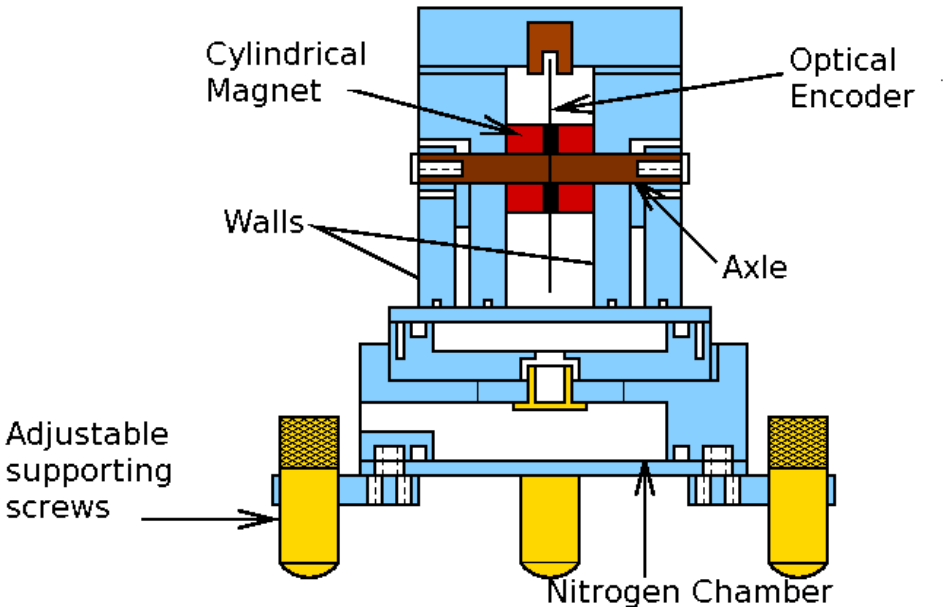

FIGURE 4.19: The side view of the vertical compass assembly.

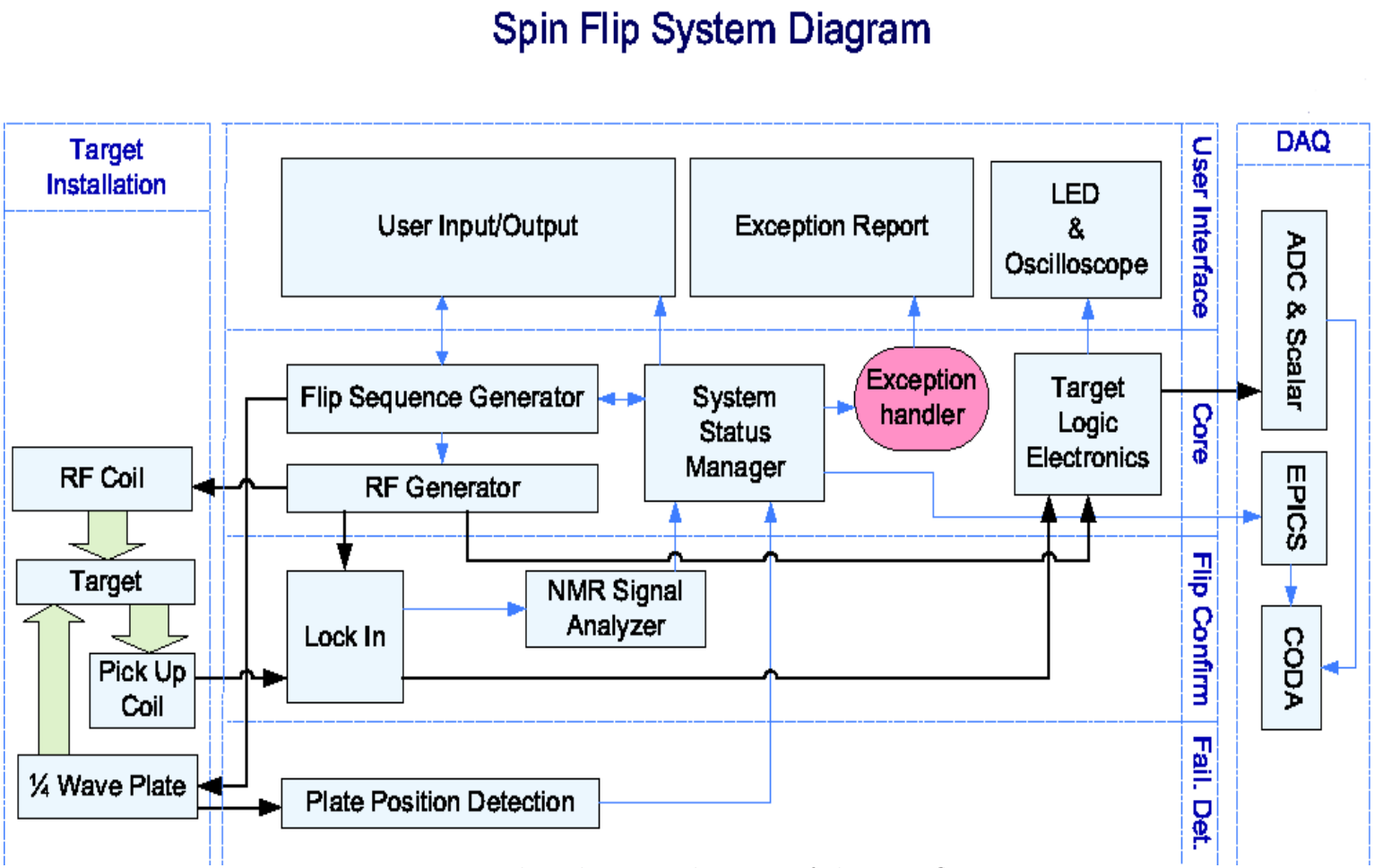

FIGURE 4.20: The schematic diagram of the spin flip system.

the ^{3}He polarization would get loss every time the target spin was flipped. In other words, a faster spin flip would reduce the average target polarization. Since the E06-010 is the first experiment of its kind, and the results are expected to be limited by the statistical uncertainties, the 20 mins spin flip time was adopted in the end in order to balance the statistical and systematic uncertainties. Meanwhile, when the ^{3}He spins were flipped from one spin state to another by 180^o, the polarization of the incoming lasers to the cell also needed to be reversed. This step was achieved by rotating all the quarter wave plates. The entire spin flip process was controlled by a LabView based target spin flip system. Once the spins were flipped, the information was collected and sent to the user interface. The spin state information was also sent to the main DAQ system in order to insert a target spin flag for every event and was used generate the gates for the scalers. In order to confirm the spin state, the system would also collect and process the NMR signal during the spin flip. To ensure the stability of the system, all the quarter wave plates were monitored in each spin flip. The summary of the system and its operation are illustrated in Fig. 4.20.

4.10 Hall A Spectrometers

For experiment E06-010, the BigBite spectrometer was used to detect electrons and the left HRS was used to detect leading charged hadrons simultaneously. In this section, we briefly describe the setup of both spectrometers.

4.10.1 High-Resolution Spectrometer (HRS)

The schematic layout of the Left HRS spectrometer is shown in Fig. 4.21 including the detector package. The magnet system includes two super-conducting quadruples, followed by a 6.6 m long dipole magnet and another quadruple magnet. The quadruple magnets are used to focus charged particles and the dipole magnet is used to bend particles vertically. More details can be found in Ref. [267].

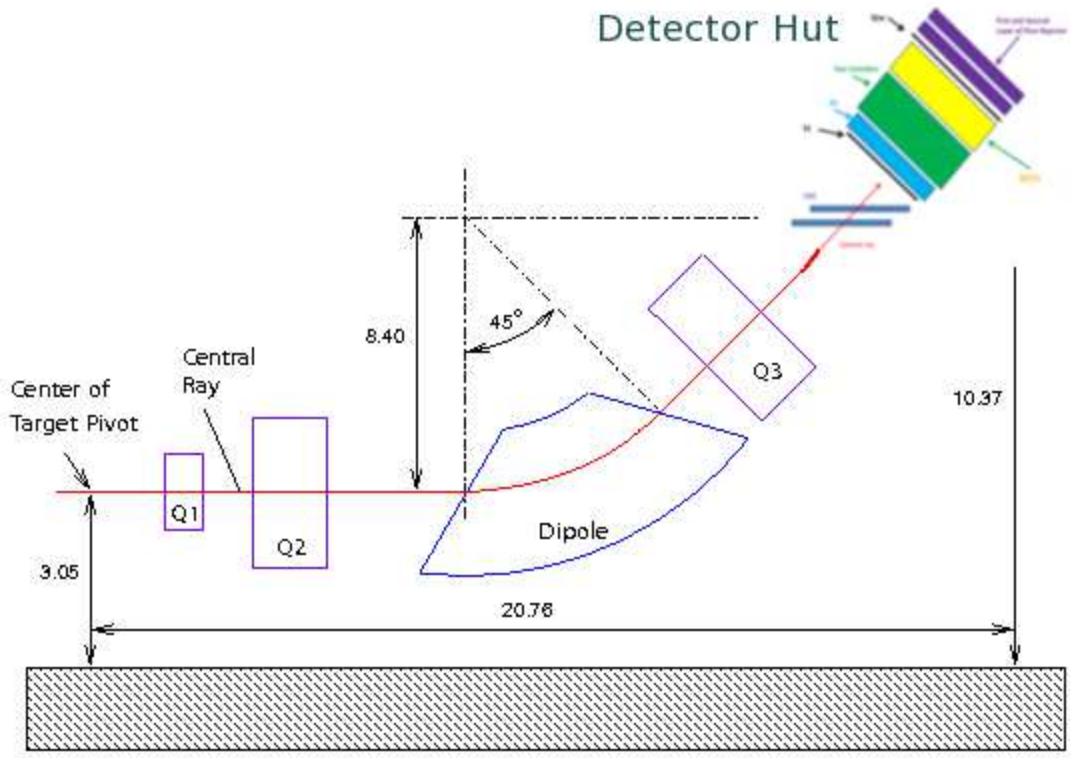

FIGURE 4.21: Schematic layout of the HRS spectrometer and the detector hut. Units are in meters.

Detector Package

The detector package [267] (left HRS) used in the E06-010 experiment is illustrated in Fig. 4.22, which include the following detectors:

- A pair of two Vertical Drift Chambers (VDCs) to provide the tracking information (positions and directions).
- S1 scintillator plane to provide the trigger.
- An aerogel Cerenkov counter to separate pions from kaons and protons.
- A light gas Cerenkov counter to separate pions from electrons and positrons.
- A ring imaging Cerenkov (RICH) detector to identify kaons.

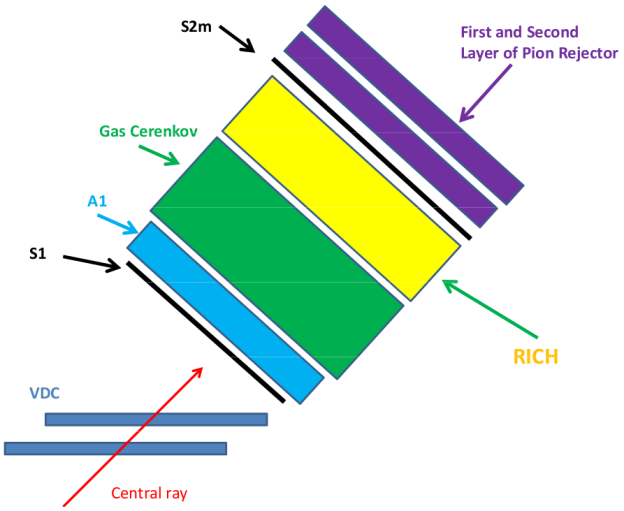

FIGURE 4.22: The Left HRS Detector Package.

- S2m scintillator plane to provide the trigger and the time-of-flight (TOF).
- Lead glass shower system to separate pions from electrons.

The entire detector package is enclosed inside a heavy steel and concrete detector hut above the magnet system as shown in Fig. 4.21.

Vertical Drift Chambers

Two Vertical Drift Chambers (VDCs) positioned 23 cm away from each other were used to provide the tracking information [268, 269]. Each VDC contains two wire planes, in U/V configuration, sandwiched between three high voltage (HV) planes. The "U" and "V" orientation are 45^o and -45^o, respectively, from the long edge of the plane. The VDCs lie in the horizontal plane, and particles cross the wire planes at nominal angle of 45^o as shown in Fig. 4.22.

During operation, a 62%/38% argon-ethane (C_2H_6) gas mixture was flowed into the VDCs. In addition, a HV of -4 kV was applied [267]. When a charged particle passes through the VDCs, it ionizes the gas and leaves a track of electrons and ions

along its trajectory. The ionized electron then drifts to the closest wires and the time it travels is proportional to the distance between the ionization point and the wire position. Combining the drift distance of all fired wires, the entire trajectory can be reconstructed.

Scintillators

Two scintillator planes (S1 and S2m), positioned about 2 m away from each other, were used to provide the trigger and TOF. The S1 plane contains 6 thin plastic scintillators. Each scintillator is read by two PMTs attached to both ends. The active volume of S1 is 36 cm (length) $\times$ 29.3 cm (width) $\times$ 0.5 cm (thickness). The S1 plane is designed to be thin in order to minimize particle absorption, and it also provides the first level trigger. The S2m plane is made of 16 fast scintillator bars with dimensions of 43.2 cm (length) $\times$ 14 cm (width) and 5.08 cm (thickness). The detector provides accurate timing for the charged particles passing through the bars. The calibration of S2m is one of the key components of the TOF particle identification (PID), which will be described in Sec. 5. The trigger logic of the HRS will be discussed in Sec. 4.11.2.

Gas Cerenkov Counter

A 80 cm long gas Cerenkov detector was mounted between the two scintillator planes. It was filled with one atmospheric pressure of CO_2, which allows a 99% electron identification with a pion momentum threshold of 4.8 GeV. The average number of photon electrons for this gas Cerenkov is about seven. The total amount of material in the particle path is about 1.4% radiation length. There are in total 10 mirrors used together with 10 PMTs to collect the signal. In experiment E06-010, the major goal for the gas Cerenkov was to separate negative pions from electrons.

Aerogel Cerenkov Counter

A diffusion-type aerogel counter A1 was installed in the HRS. There are 24 PMTs attached to A1. The 9 cm thick radiator used in A1 has an index of refraction of 1.015, which provides a threshold of 2.84 and 0.803 GeV for kaons and pions, respectively. The average number of photo-electrons for the GeV electrons in A1 is about eight. In experiment E06-010, the HRS momentum setting was 2.35 GeV. Therefore, the pions would fire the A1, while kaons and protons would not fire the detector. Together with the TOF, A1 provided a kaon rejection better than 10:1 for the pion identification, leading to less than 1% contamination in the pion sample.

Shower Counter System

The shower detectors consists of two layers, which were installed in the left HRS. Both layers were oriented perpendicular to the particle's velocity direction. The front layer was composed of 34 lead glass blocks (15 cm $\times$ 15 cm $\times$ 35 cm). The second layer also contained 34 such blocks. The goal of the the shower counter system was to complement and enhance the electron rejection capability of the gas Cerenkov counter.

The Ring Imaging Cerenkov Detector (RICH)

The Hall A RICH detector was upgraded, which was used in the hypernuclear spectroscopy experiment (E94-107) and installed to provide additional PID for the kaons. A detailed description of the original Hall A RICH can be found in Ref. [270]. The design of the Hall A RICH is identical to the CERN Alice HMPID detector [271]. It is based on proximity focusing, and is able to provide PID for protons, kaons and pions up to 2.5 GeV after the upgrade. The detector uses 15 mm thick C_6F_{14} liquid freon at standard temperature and pressure as a Cerenkov radiator. After traveling a proximity gap of 159 mm, Cerenkov photons in the ultraviolet region (160-220 nm,

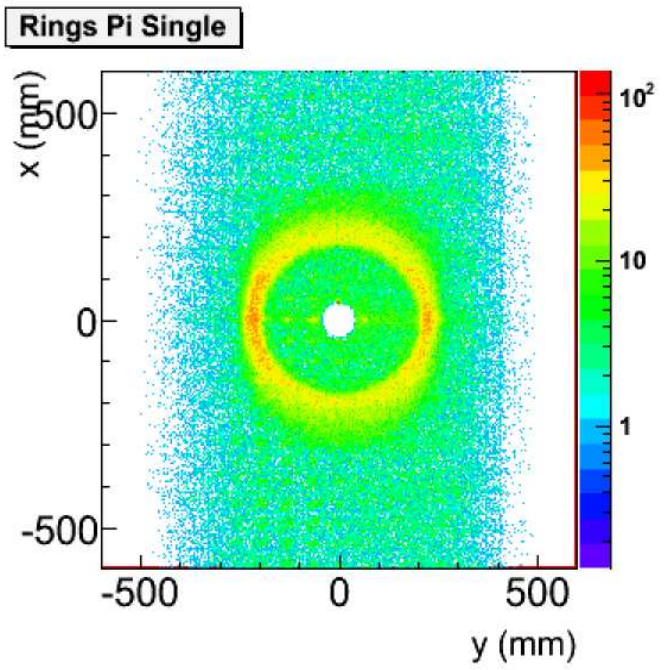

FIGURE 4.23: Simulated Cerenkov rings generated by charged pions at 2.35 GeV ±5%; the central region contains the intense signal produced by the charge particle (as minimum ionizing particle) which has been masked to enhance the ring pattern.

mean freon refractive index=1.287) are converted (with $\sim 25\%$ quantum efficiency) into electrons by a 300 nm layer of CsI. The CsI is deposited on top of the 19200 8×8.4 mm^2 pads of the 2×0.6 m^2 multipad proportional chamber, which is filled with CH_4 at the standard temperature and pressure. The positive ions, which are produced by the converted electrons and their secondaries in the electrostatic field ($10.5 - 11.5$ kV/cm) in the 2 mm chamber gap, are collected by the pads and read out by front-end electronics based on the Gassiplex chip. The chamber had been operated stably between 2100 and 2300 V with very marginal discharge events. At 2.4 GeV particle momentum, the expected Cerenkov angles for electron, pion, kaon and proton are 0.680, 0.678, 0.654 and 0.583 rad, respectively. The accumulated detected Cerenkov rings are shown in Fig. 4.23. The rings are represented by a circle, demonstrating the proper geometrical setup of the detector. The data from RICH

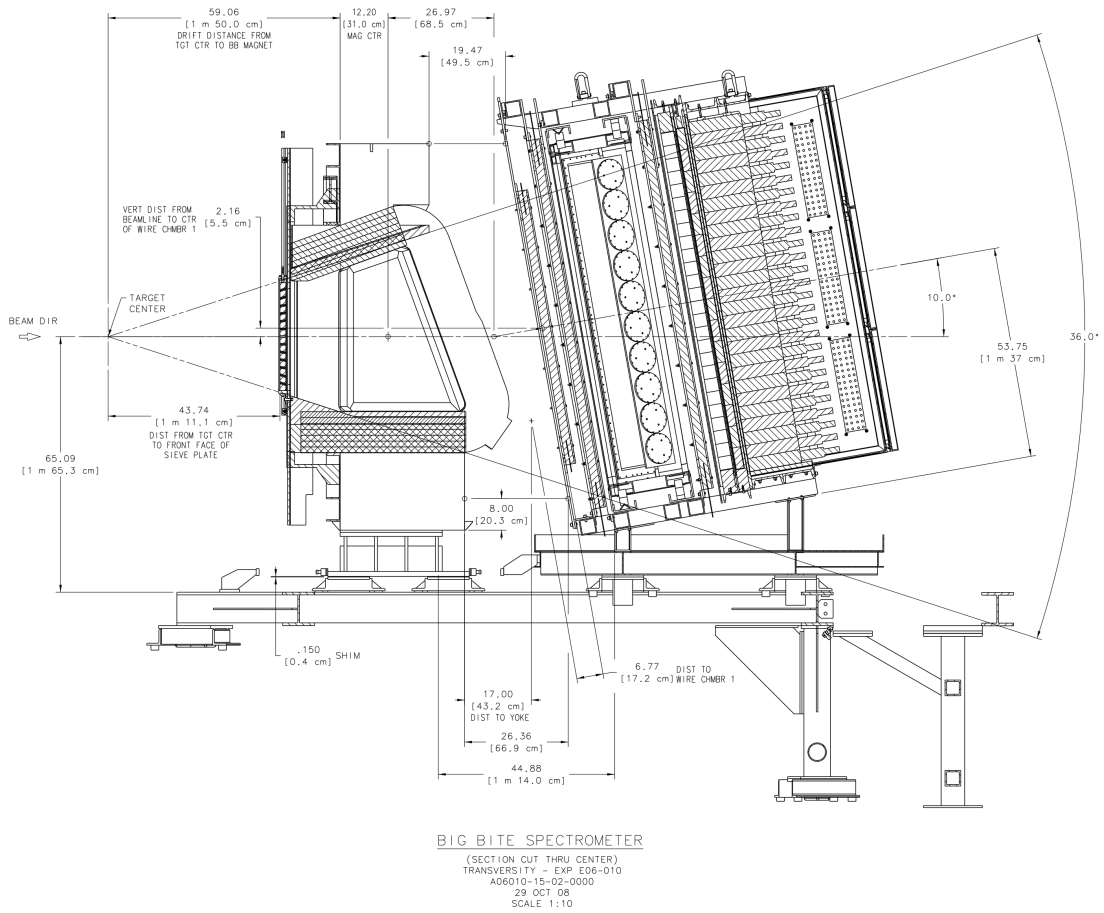

FIGURE 4.24: The engineering drawing of the BigBite spectrometer.

was essential for the kaon PID and the pion contamination study, but not essential for the pion PID. Therefore, it was not used in the data analysis for the pion channel.

4.10.2 BigBite Spectrometer (BigBite)

In experiment E06-010, the BigBite spectrometer was used to detect the scattered electrons. The momentum coverage was 0.6-2.5 GeV. The acceptance was about 64 msr for 1.0 GeV electrons. The large acceptance and the large coverage of the out-of-plane angle were essential in separating the different azimuthal asymmetries from

the measured raw asymmetries. An engineering drawing of the BigBite spectrometer can be found in Fig. 4.24, and a schematic view of the BigBite spectrometer can be found in Fig. 4.25. A field clamp (a large metal plate) was installed in front of the BigBite magnet during the experiment in order to shield the target from the fringe magnetic field from the BigBite magnet. The electron detection package included: three sets of multi-wire drift chambers (MWDC) to provide tracking information, a scintillator plane to provide the timing information, and a shower counter system including a preshower and a shower for PID. The scintillator plane was sandwiched between the layers of preshower and shower. During the experiment E06-010, a short gas Cerenkov counter, which is essential to experiment E06-014 (which ran after E06-010), was installed to take data for commissioning purposes. The data from this short gas Cerenkov were not used in the data analysis of this experiment. In addition, two target collimators were installed on the BigBite side to shield the high energy electrons/photons generated from the two endcaps of the target scattering chamber.

BigBite Magnet

The BigBox power supply was used to energize the BigBite magnet. The current was about 710 A, which is corresponding to a 1.2 T magnetic field inside the BigBite magnet. Field mapping of the BigBite magnet was performed before the experiment. The largest field component, B_y (detector coordinate system), at two current settings 710 A and 600 A is plotted against the z direction in the detector coordinate system, which is also the nominal particle's velocity direction, in Fig. 4.26.

Multi Wire Drift Chamber (MWDC)

Three sets of MWDCs including 18 wire planes were used in experiment E06-010 to provide the tracking information for the charged particles entering the BigBite

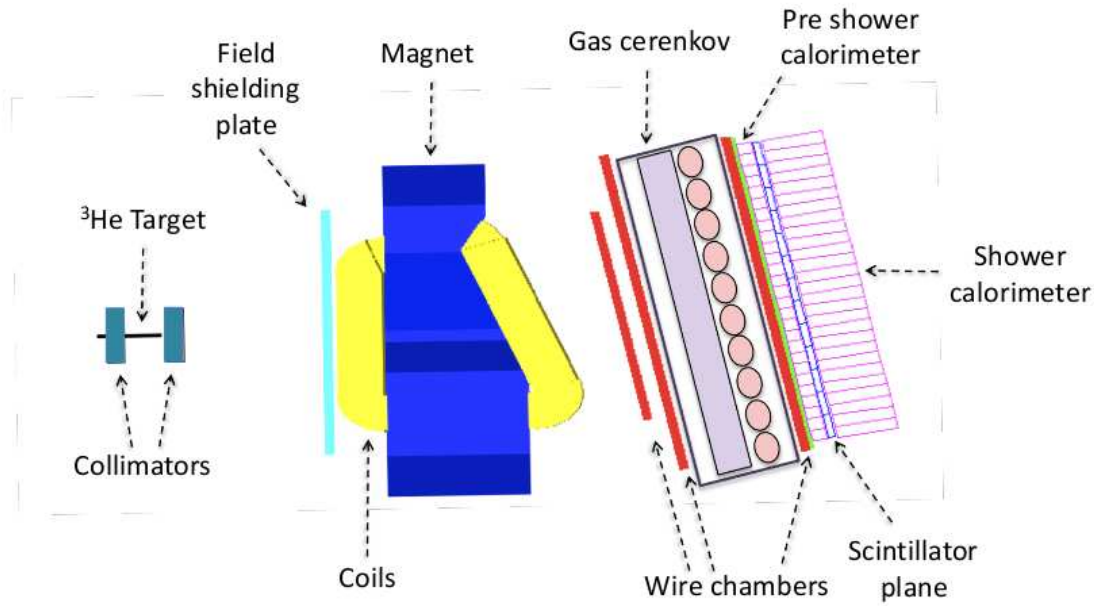

FIGURE 4.25: The schematic view of the BigBite spectrometer together with the target.

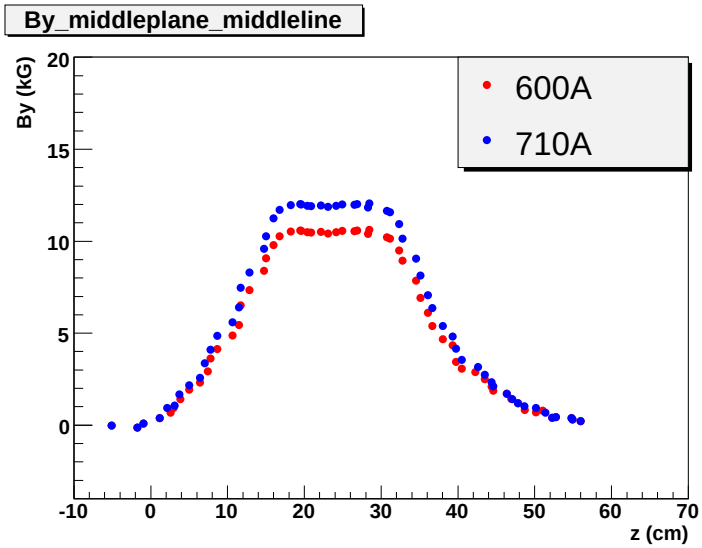

FIGURE 4.26: The field mapping of the BigBite magnet for two currents: 710 A and 600 A.

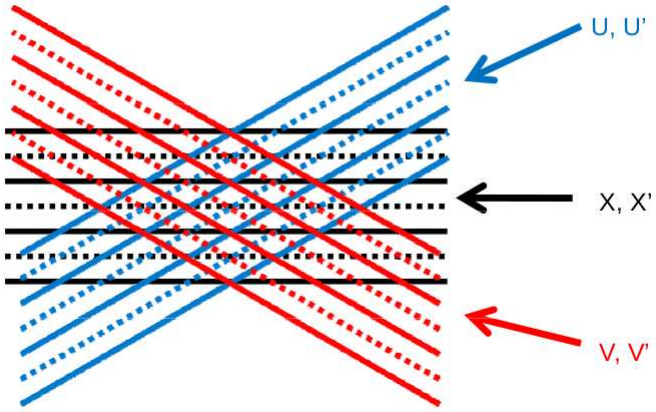

FIGURE 4.27: Illustration of the MWDC plane orientations: u, v and x. Each orientation contains two planes. The second plane is shifted by half the wire chamber cell.

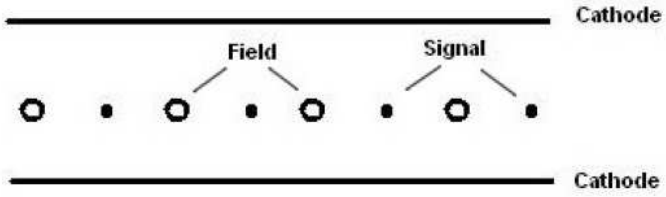

FIGURE 4.28: Side View of the MWDC Wire Plane.

detector system. They were constructed at the University of Virginia. The active area of the first chamber is about 140 cm $\times$ 35 cm. The active area of the second and the third chamber is the same, which is about 200 cm $\times$ 50 cm. Each wire chamber consists of six wire planes, which are divided into three groups with orientations of u (+30^o with respect to the horizontal direction), v (-30^o) and x (0^o), as illustrated in Fig. 4.27. The distance between two adjacent wires in a single wire plane is 1 cm. The second plane, usually labeled with prime (u', v' and x') is shifted by half of the wire cell (0.5 cm) to distinguish the left and right ambiguities.

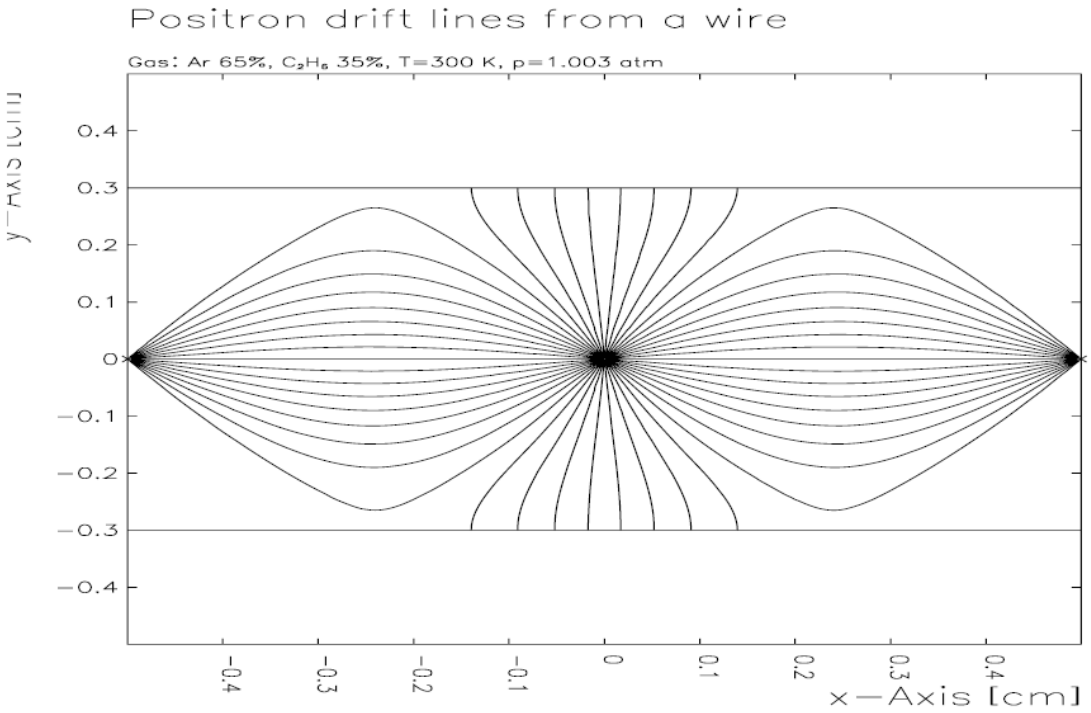

FIGURE 4.29: The example electric field inside a wire plane cell is shown when the HV is applied. Figure is from Ref. [272].

The principle of the MWDC is similar to that of the VDCs in HRS. However, the nominal direction for particles passing through the wire chamber is about 90^o instead of 45^o. Fig. 4.28 shows the side view of the MWDC wire plane. Each wire plane is sandwiched by two cathode planes, which were set to a HV about -1600 V during the experiment. The wire plane consists of signal and field wires. The field wires were also set to the same HV. The electric field diagram is shown in Fig. 4.29.

In the case of MWDC, only one wire can usually be fired when particles pass through the chamber. Therefore, the MWDC can handle much higher rates in comparison to the VDCs at the cost of recording more channels. Similar to the VDC, when a charged particles pass through the wire plane, tracks of electrons and ions will be ionized. The ionized electrons will drift to the closest wire. The time they take to reach the wire is proportional to the distance traveled. A gas mixture of

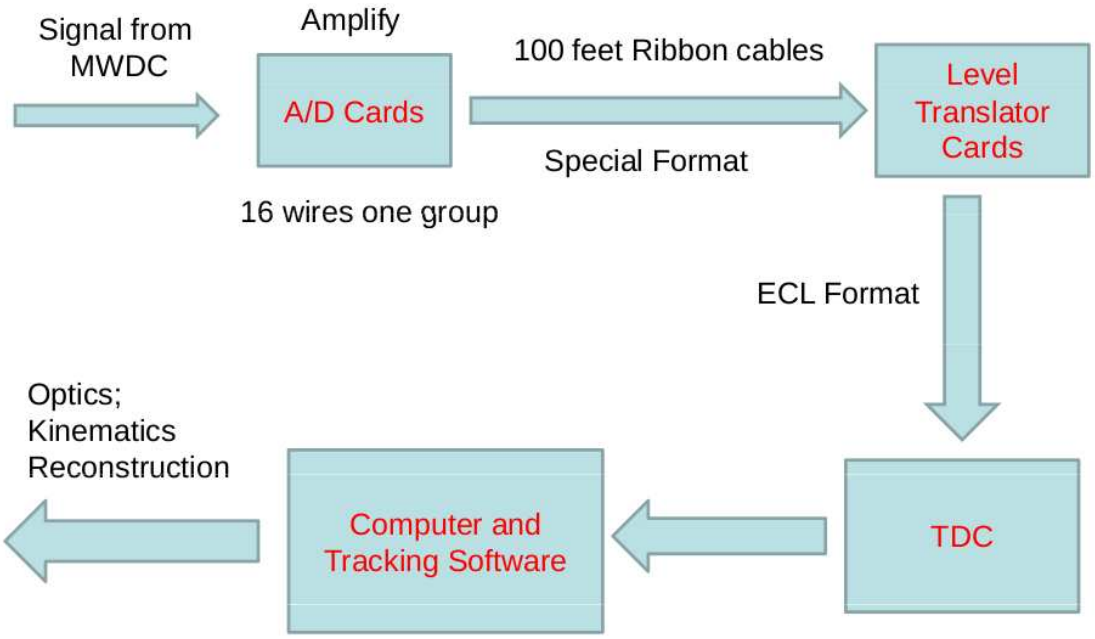

FIGURE 4.30: Illustration of the MWDC readout electronics.

50%/50% argon-ethane was kept flowing into the MWDC system, while the HV was applied.

In the readout electronics system, every sixteen wires, except for the wires located close to the edge of the chambers, were grouped together and read by an amplified A/D card. The A/D cards require a 6 V power supply and a floating ground power supply to provide the threshold. The output signals from A/D cards were then transported by about 100 feet long ribbon cables to the level translators, which transformed the signal from A/D cards to the standard ECL format[4]. The signals after the level translator cards were then fed into the Time-to-Digital Converters (TDCs). The entire diagram is shown in Fig. 4.30 for one A/D card.

[4] In the ECL level format, "0" = -1.75 V = Low - False and "1" = -0.9 V = High = True

Scintillator

The BigBite scintillator plane consists of 13 plastic scintillator bars as shown in Fig. 4.10.2. Two PMTs are connected to both sides of each scintillator bar in order to collect the signal. Each bar is 60 cm (length) $\times$ 17.5 cm (width) $\times$ 3.8 cm (thickness). The scintillator plane is placed between the preshower and shower and provides the timing information.

Preshower and Shower

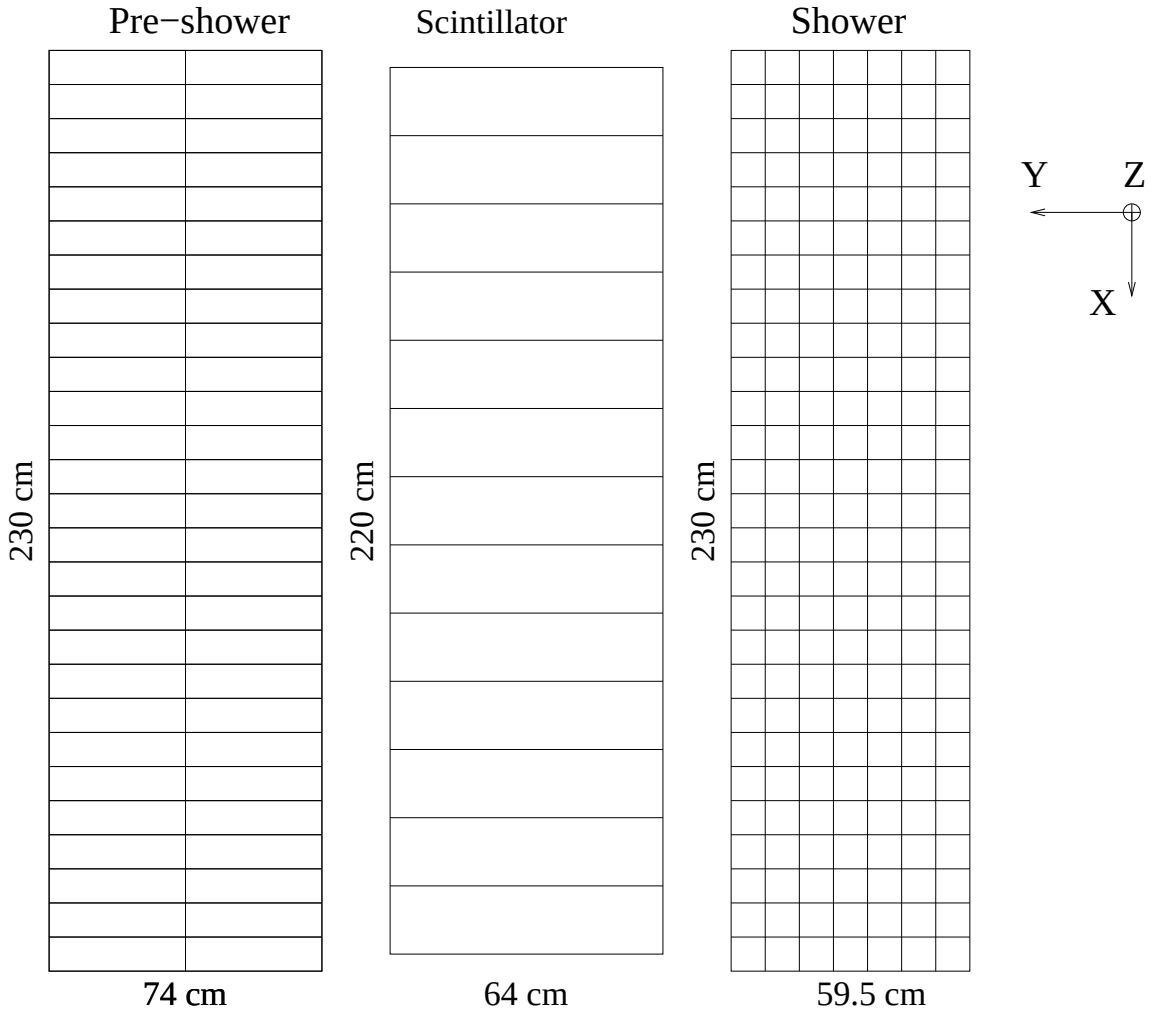

FIGURE 4.31: Geometry of BigBite Preshower, Scintillator and Shower detectors.

The preshower and shower detectors provide trigger and PID for electrons in the BigBite spectrometer. A detailed description of the BigBite trigger is given in Sec. 4.11.1. The preshower blocks are made of TF-5 lead-glass, each measuring 8.5cm $\times$ 34cm $\times$ 8.5cm in X, Y and Z directions, respectively. There are 54 preshower blocks arranged in two columns of 27 rows each. It has an active area of 210 $\times$ 74 cm^2, with 8.5cm (3 radiation lengths) along the particle's velocity direction. The shower blocks are made of TF-2 lead-glass material. They have the same dimensions as the preshower blocks, but with different orientation. It covers an active area of 221 $\times$ 85 cm^2, with 34cm (13 radiation lengths) along the particle's velocity direction. There are 189 shower blocks arranged in 7 columns of 27 rows each. The schematic layout of the preshower, scintillator and shower plane is illustrated in Fig. 4.10.2.

The electrons entering the lead-glass block generate electromagnetic showers and leave large signals in the PMTs, which are amplified and sent to the summing modules to form triggers. The signals are also recorded in the Analog-to-Digital Converters (ADCs). The combined ADC information from both the preshower and shower gives the total energy deposited by the particle in the detector. The reconstructed energy has a resolution of about $\sigma_{dE/E} = 8\%$. The signal generated by electrons are rather large compared to those of hadrons, which are heavier. Therefore, electrons can be separated from hadrons by combining the information from the preshower/shower system and the reconstructed momentum from the tracking information.

Target Collimator

During the experiment, target collimators were installed to shield the high energy electrons and high energy photons generated from the two endcaps of the target scattering chamber. Each collimator is made of Tungsten powder, and its thickness is about 10 cm in the nominal particle's velocity direction. The effect of the target collimator is shown in Fig. 4.32, where the reconstructed vertex from BigBite is

compared with that from the left HRS

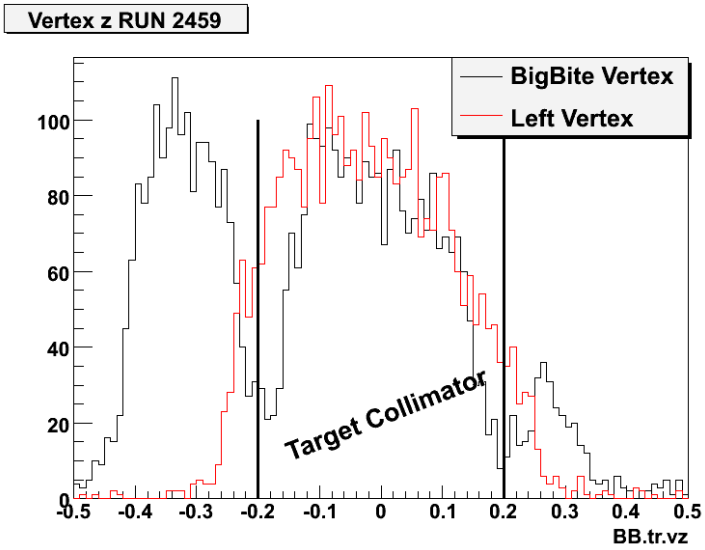

FIGURE 4.32: The effect of the BigBite target collimator. The red and black histograms show the reconstructed vertex from left HRS and BigBite, respectively.

4.11 Trigger and Data Acquisition System (DAQ)

The E06-010 DAQ setup included several important software and hardware components:

- **The Trigger Supervisor (TS)**:

  The TS, which was a 9U multi-functional VME board with several ECL inputs, was the brain of the entire DAQ for experiment E06-010. It linked the experiment trigger system with the read-out controllers (ROCs), which handled the event-by-event retrieval of the data recorded from the detectors. External triggers were accepted through the 8 inputs channels of the TS module , usually known as T1 to T8, with pre-set prescale factors. Each accepted trigger by the TS generated a signal, for gating and timing of the front-end electronics (ADCs and TDCs), known as level-1 accept (L1A). The status of the all ROCs were fed back to TS using a dedicated RS432 flat cable, which allowed TS to

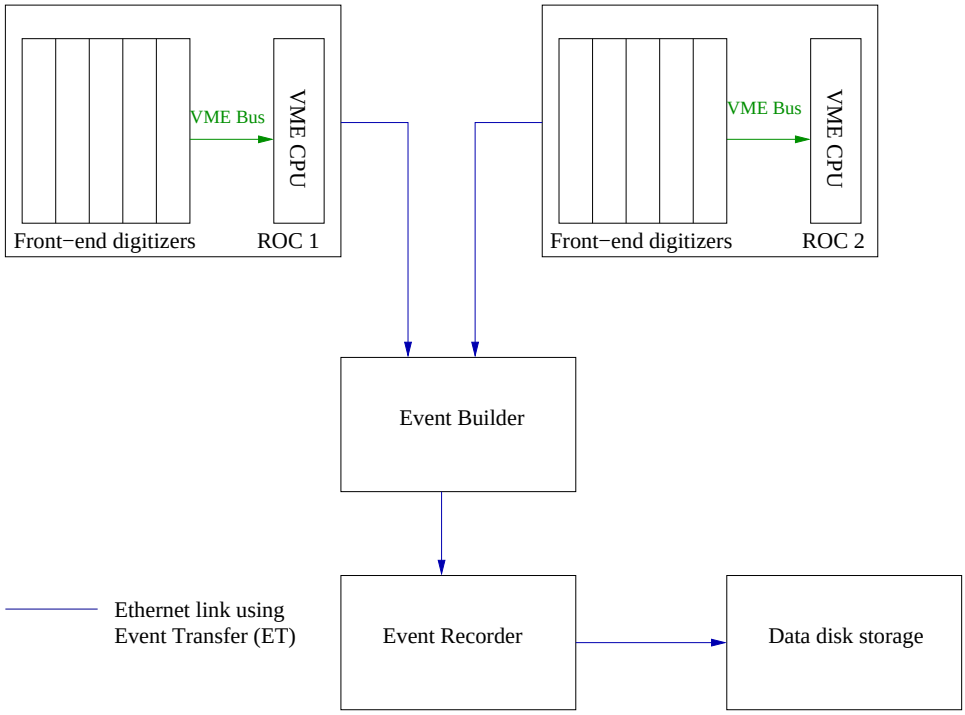

FIGURE 4.33: Example of CODA configuration using read-out controllers.

monitor whether the ROCs were busy. While a trigger was being processed, the system was maintained as "system busy", so that no additional triggers could be accepted until all the ROCs finished processing the current event. In this configuration, the TS effectively maintained synchronization among ROCs.

- **CODA (CEBAF Online Data Acquisition)**:

  CODA is the standard data acquisition software toolkit developed at Jefferson Lab and used by all experiments in the three existing Halls. It contains several software tools for monitoring and recording of the data. The main component is called the RcServer, which is responsible for storing and initializing the chosen configuration. It also periodically checks the status of all the components and ensures that the data are correct. In experiment E06-010, several CODA configurations using various combinations of the ROCs were created. All the configurations and the status of the components involved were stored in a

MiniSQL database server. Fig. 4.33 shows the general flow for an example CODA configuration. The L1A signal generated from the trigger supervisor as sent to the front-end electronics to trigger the digitization of the detector signals and readout of each ROC. The digitization and readout process were controlled by a set of C routines called CODA readout list (crl), which were programmed by the user. Data from each crate were then transmitted to the Event Builder (EB), which collected/sorted the data from different ROCs and recorded the data into the structured CODA events. The constructed event was then recorded on a computer disk by the Event Recorder (ER) in a CODA file. The transfer of the data from all the components was realized by the Event Transfer (ET) library.

- **EPICS**:

  Experimental Physics and Industrial Control System (EPICS) system is used to record information of the beam, magnets, power supplies and various other instruments in the accelerator and in the hall. These pieces of information can be accessed and written to the CODA data stream every few seconds. During experiment E06-010, it was also used to store the important information from the polarized ^{3}He target, such as the target oven temperature.

- **Slow Controls**:

  In E06-010, slow controls were used to set/adjust high voltages on the photo-multiplier tubes, MWDCs, VDCs, and RICH etc. For example, a LeCroy 1458 high voltage mainframe was used with a Ethernet connection to adjust the high voltages of PMTs and MWDCs.

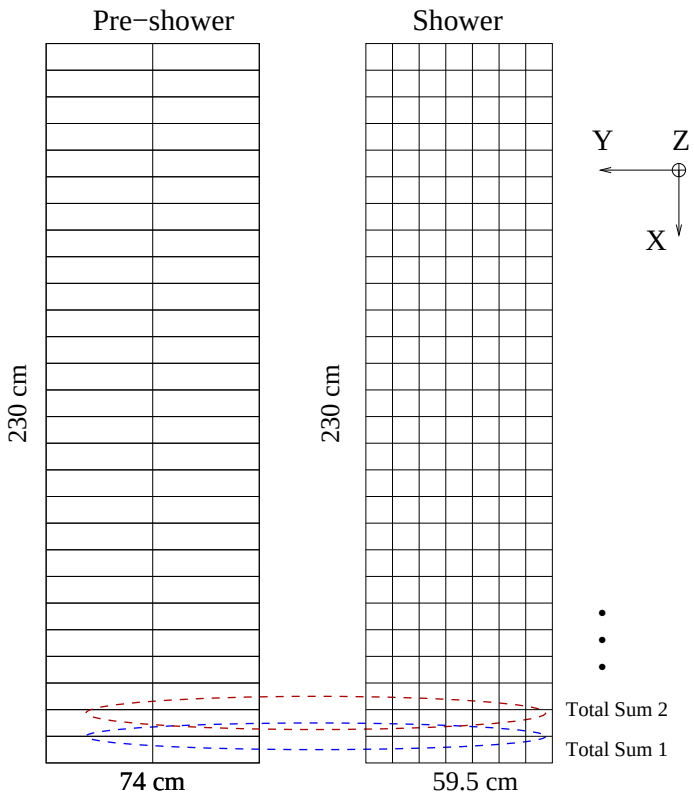

FIGURE 4.34: Total Sum of the preshower and shower.

4.11.1 Trigger and Electronics for BigBite Spectrometer

The trigger of the BigBite spectrometer was designed to select electrons and was implemented by effectively cutting on the signal of the total energy deposition in the calorimeter system made of lead-glass blocks. The detailed description of the calorimeter system is given in Sec. 4.10.2. The total energy deposited in the calorimeter was approximated with a total hardware sum (TSUM) formed by summing the two overlapping rows of preshower ($2\times2 = 4$ blocks) and shower ($2\times7 = 14$ blocks). The hardware sum as illustrated in Fig. 4.34 was performed by first summing the signals from two rows of preshower blocks together using a LeCroy 428F module and then further summing the signals from two rows of shower using custom built summing modules. The signal from preshower was amplified by 10 times, while

the signal from shower was amplified by 5 times before the total sum signal was formed. The analogue signal of TSUM then went through a discriminator, whose threshold could be controlled and adjusted remotely according to the experiment's requirements. The BigBite triggers were known as T1 and T6 (different thresholds). Fig. 4.35 shows the detailed trigger logic.

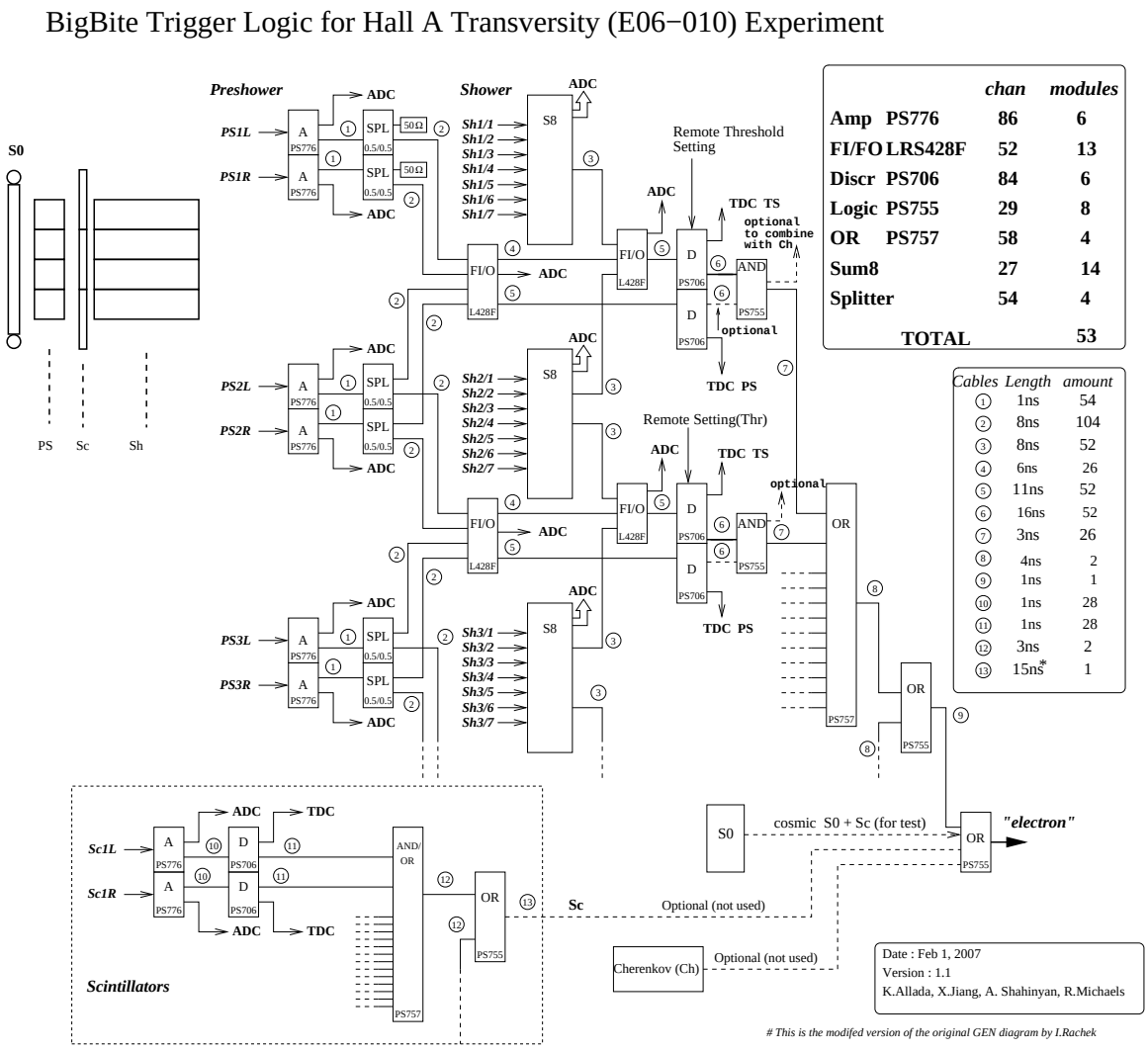

FIGURE 4.35: BigBite trigger logic diagram.

The signals of the BigBite detector were read using both FASTBUS and VME electronics. The timing information from the individual wires in MWDCs was read

using LeCroy 1877 TDCs. The timing information from the scintillators was recorded using Jefferson Lab made F1 TDCs, which are common-stop multi-hit TDCs with a resolution set to 60 ps. This high resolution is necessary in order to determine the coincidence TOF of the particle in the HRS to a high accuracy for PID. LeCroy 1881 ADCs were used to read all the PMT signals in the calorimeter and scintillators. The ADC gate width was set to 240 ns.

Retiming in the BigBite

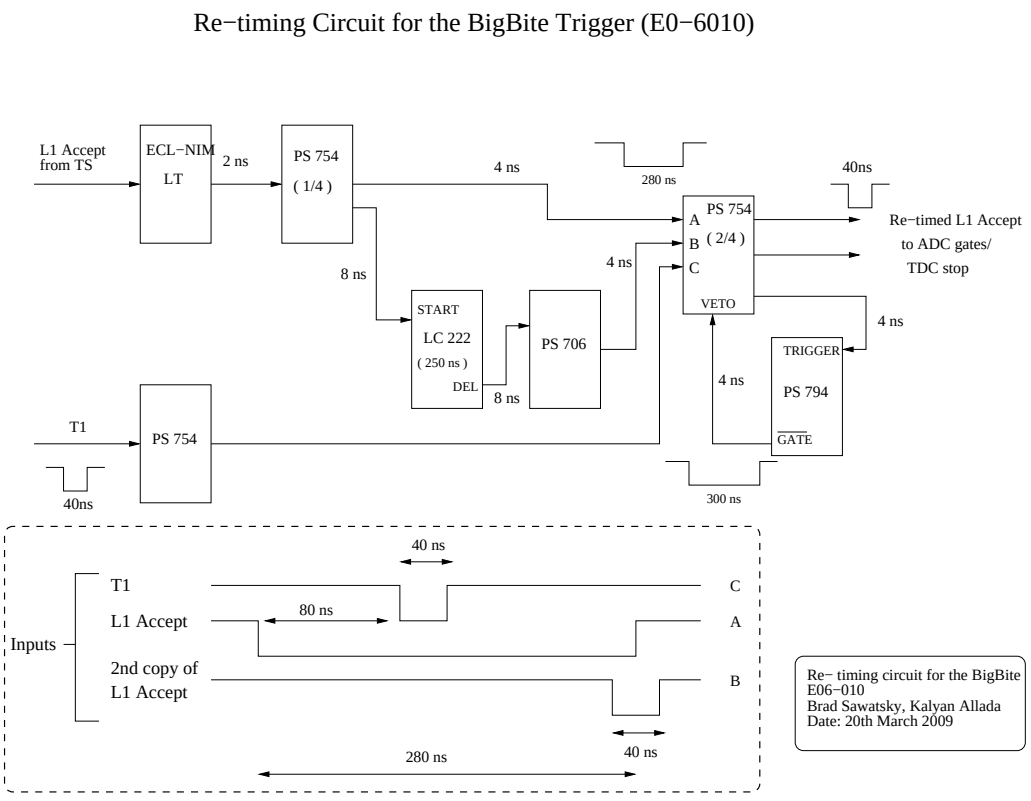

FIGURE 4.36: Retiming circuit for the BigBite trigger.

For the recorded TDC signals, it is necessary to keep the reference time constant with respect to the generated trigger in the spectrometer, which effectively is the time when particles pass through the spectrometer. When multiple triggers constructed from different spectrometers are used in the TS, this requirement becomes

problematic. A retiming circuit was employed in the BigBite trigger setup in order to achieve the previous requirement. The circuit was used to generate the gate for the ADCs and the common stop signal for TDCs. Fig. 4.36 shows the diagram of the retiming circuit. The principle of the retiming circuit in BigBite is to ensure that the L1A generated by the TS was regularized by the corresponding T1 trigger. This was realized by making a logical "AND" between the T1 and L1A signal, which effectively tied the reference time for ADCs/TDCs to the time of the T1 trigger. Since the timing of the coincidence trigger was given by the leading edge of the T1 trigger, the logical "AND" ensured that all the gates for the T5 trigger had the common reference time as the one for the T1 trigger. If there were no T1 signal for a particular L1A, for example the accepted trigger was from left HRS, then a delayed copy of the L1A provided the timing for ADCs/TDCs (Fig. 4.36).

4.11.2 Trigger and Electronics for left HRS

The trigger of the left HRS, also known as the T3 trigger, was formed by requiring that both S1 and S2m scintillator planes had a hit, i.e., one paddle in S1 and one paddle in S2m having a hit on both sides PMTs (total 4 PMTs). In addition to T3, there was a T4 trigger, an efficiency trigger, which was formed by requiring that 2 out of 3 detectors had a hit, by adding a third detector (Cerenkov) in addition to the S1 and S2m. The T4 further required that it was not a T3 trigger. A similar retiming circuit, as the one in BigBite, was realized by logical "AND" between the L1A signal and the strobe, where the strobe is the OR of the S1 and S2m signals, in order to gate the ADCs/TDCs. The trigger diagram for the left HRS is shown in Fig. 4.37.

The signals from the detectors in the spectrometer were also read using FASTBUS electronics. The timing information from S1 and S2m scintillator planes were recorded using high resolution common-start single-hit LeCroy 1875 TDCs with the

resolution set to 50 ps. The timing information of signals from individual wires in the VDCs, Aerogel (A1), Cerenkov, and two-layer lead-glass were recorded in common-stop multi-hit LeCroy 1877 TDCs, which have a timing resolution of 0.5 ns. The integrated charge of the signal coming out of the detectors was recorded in LeCroy 1881 ADCs.

4.11.3 Coincidence Trigger

The coincidence trigger, also known as T5, was formed with the BigBite single trigger T1 and the HRS single trigger T3 by overlapping the two triggers in time (logical "AND" as shown in Fig. 4.38). A sketch of coincidence trigger setup is shown in Fig. 4.39. The exact trigger formation time and the TOF of particles in both spectrometers are crucial in order to design the coincidence trigger. For experiment E06-010, the trigger formation time was measured by injecting an fake electronic pulse as a detector PMT signal into the trigger circuit. The exact TOF of the particles in both spectrometers was calculated by the momentum of the particles and distance that the particles traveled in the two spectrometers. Cable delays were then added in T1 and T3, so that there was an overlap between them. As illustrated in Fig. 4.38, the timing of the T5 was defined by the leading edge of the T1 trigger, which arrived about 40 ns after the T3 trigger for the real coincidence events. The coincidence window was defined by T3, whose width was set to 140 ns. The width of T5 was defined by T1. During the commissioning of the experiment, a full coincidence trigger was simulated using an electronic pulser with delays set close to situations in the real experiment. The T5 trigger was then sent to the TS, which generated the L1A signal and sent it to both spectrometers. The L1A signal was further retimed with the local trigger to form gates for the TDCs/ADCs.

Table. 4.4 describes all the triggers that were used during the experiment.

Table 4.4: Summary of Triggers in E06-010.

Trigger type	Description
1	Low threshold on BigBite lead-glass
2	BigBite gas Cerenkov singles
3	Left HRS singles (S1.AND.S2m)
4	Left HRS efficiency
5	Coincidence between BigBite and Left HRS (T1.AND.T3)
6	High threshold on BigBite lead-glass
7	BigBite Cerenkov and lead-glass overlap
8	1024 Hz clock

4.11.4 Scaler Setup

One major advantage of using scalers to read signals is the absence of dead time [5]. Therefore, in experiment E06-010, scalers were used to count and calculate rates for various triggers. In addition, scalers were also used for counting the signals from the BCMs, which was crucial in order to calculate the charge to properly normalize the number of recorded events. The scaler information was also very useful for the real time monitoring of the trigger rates, beam current, and raw rates on the individual PMTs. In the off-line analysis, the trigger scaler information was used to calculate the DAQ dead time, since the TS would reject all incoming triggers when it was processing the current trigger. The scaler setup is shown in the Fig. 4.40. A set of five SIS38xx VME modules were used. Each scaler has 32 inputs. The input signals, such as triggers, BCM signals, clock, etc., were daisy-chained using a RS-432 flat cable in order to provide identical signals to all five scalers. For redundancy and cross-checking purposes, two identical scaler setups were constructed in both the BigBite and the left HRS.

Four of the five scalers were gated by the beam helicity and target spin signal: Tar+ Hel+, Tar+ Hel−, Tar− Hel+, Tar− Hel−. All five scalers were further gated

[5] The dead time is the time when the electronic device is busy, and hence can not accept additional signals.

by the run gate formed by the TS, which allowed the scalers to count only between the run-start and run-stop. Fig. 4.40 shows the scaler gating scheme, which is formed by making a logical "AND" among three signals: run gate, target spin state, and beam helicity state. The gating signals were sent to the SIS3800 scaler.

There were three relevant signals associated with the helicity:

- Quartet trigger (QRT) defines when a new random sequence of four helicity states has begun.
- The micro-pulse trigger (MPS) at 30Hz defines the periods when the helicity is valid.
- The helicity sequence has quartet structure (either $+--+$ or $-++-$).

The beam helicity signals, Hel+ and Hel−, were constructed using MPS and helicity signals as illustrated in Fig. 4.41. For example, the logical "AND" between MPS and helicity gave Hel+ state, while logical "AND" between MPS and inverse of helicity gave Hel− state.

Two input signals were used to form the NIM level target spin signals. The first one is an analog NMR signal recorded in the lock-in amplifier. The second one is the status signal (TTL) from the function generator, which provided the RF field to the NMR. Target spin-flip took place every 20 mins, and there was an period about 5 secs with a unknown spin state after each spin flip. The target-spin timing sequence is shown in Fig. 4.42.

The scalers were read from the server in VME and were used for different purposes:

- Online GUI:

  The online GUI displayed the real time trigger rates, raw PMT rates, and beam current during the experiment.

- Event type 140:

  The integrated scalers were inserted into the data stream using Event Transfer (ET) functionality of the CODA.

- Scaler read from the ROC in-synch with CODA events:

  This type of readout was performed for every 100 CODA events.

- Event-by-event readout:

  Some of the most important signals, such as primary triggers and BCM signals, were read for every CODA event.

- Writing to Hall A log:

  At the end of each run, the final reading of the scalers were written to the Hall A log in order to provide an online summary.

4.11.5 Dead Time Measurement

In the data acquisition process, some events were lost due to the dead time in the DAQ system, which needs to be corrected in the data analysis. There are two types of dead time. The first one, also referred to as the electronic dead time (EDT), is from the front-end electronics like discriminators or other logic modules which may lose some events in high rate situations. The second one is called DAQ dead time, during which the DAQ rejects all incoming triggers, since the system is busy with recording the current trigger. The busy state can last anywhere between 300 μS to 500 μS, depending on the kind of modules used and the event size. In experiment E06-010, the DAQ dead time $f_{deadtime}$ dominated the electronic dead time, and can be expressed as:

$$f_{deadtime} = 1 - \frac{T_{recorded}}{T_{raw}} \tag{4.21}$$

where $T_{recorded}$ and T_{raw} are the number of recorded trigger and raw triggers, respectively. Both $T_{recorded}$ and T_{raw} are recorded by the scalers. The typical dead time for the coincidence trigger is about 10-15%. In order to measure the electronic dead time, a pulser of 12.5 Hz was sent to the front-end trigger electronics, which formed a fake electronic trigger. The electronic dead time was then estimated by comparing the number of pulses recorded by DAQ with the number of pulses sent to the entire system.

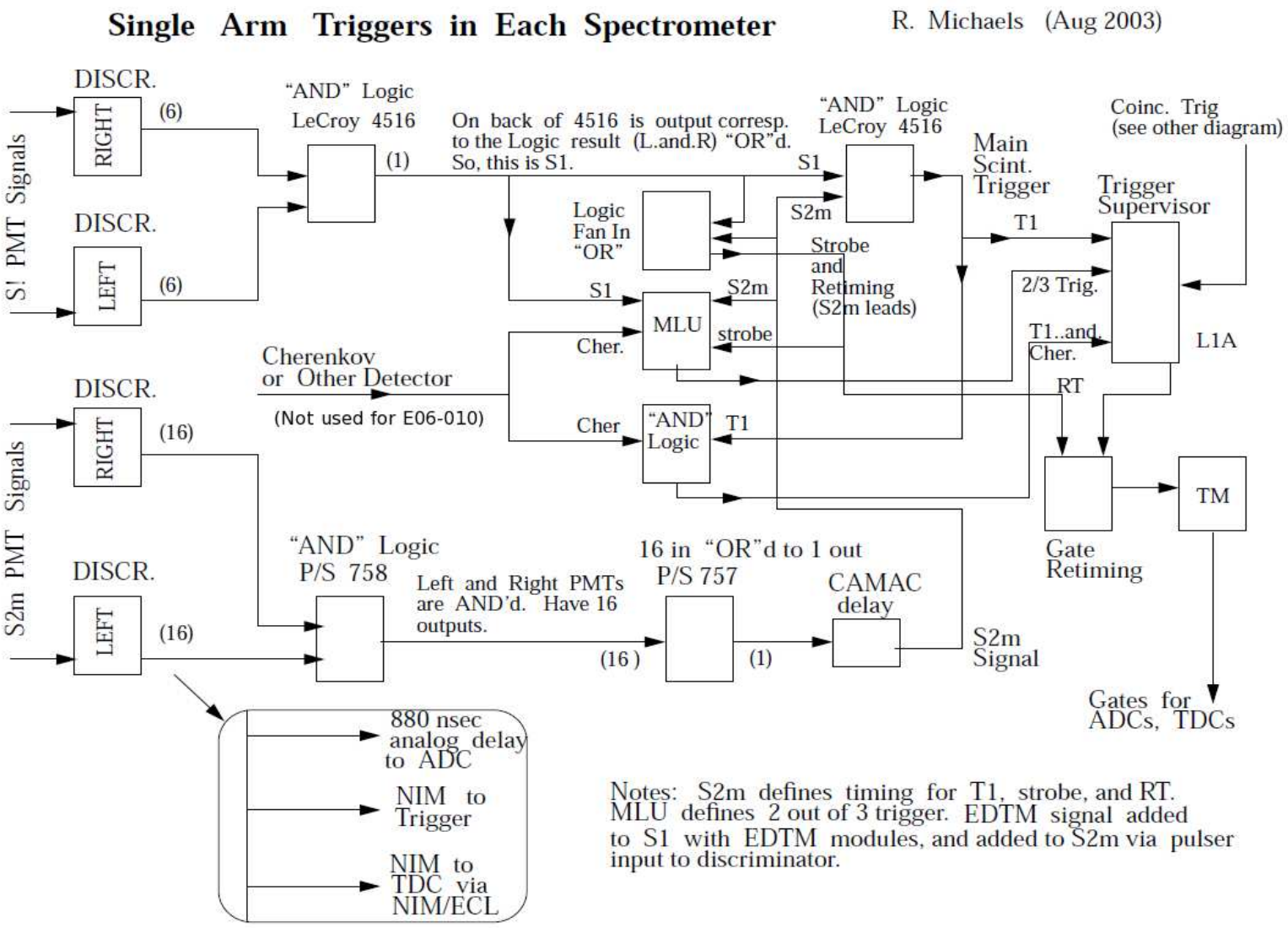

FIGURE 4.37: Trigger logic for left HRS.

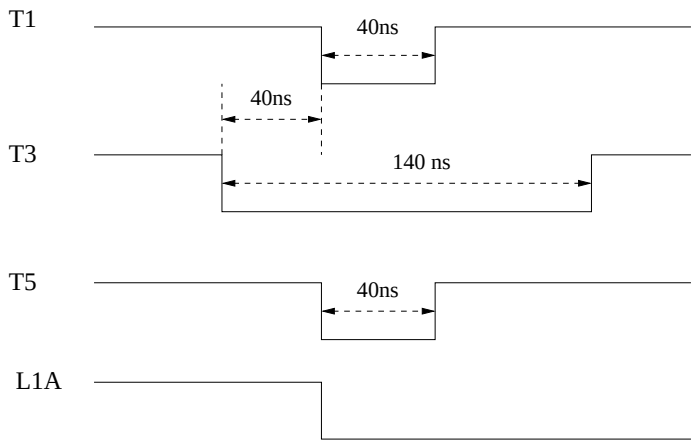

FIGURE 4.38: Coincidence timing between BigBite and left HRS.

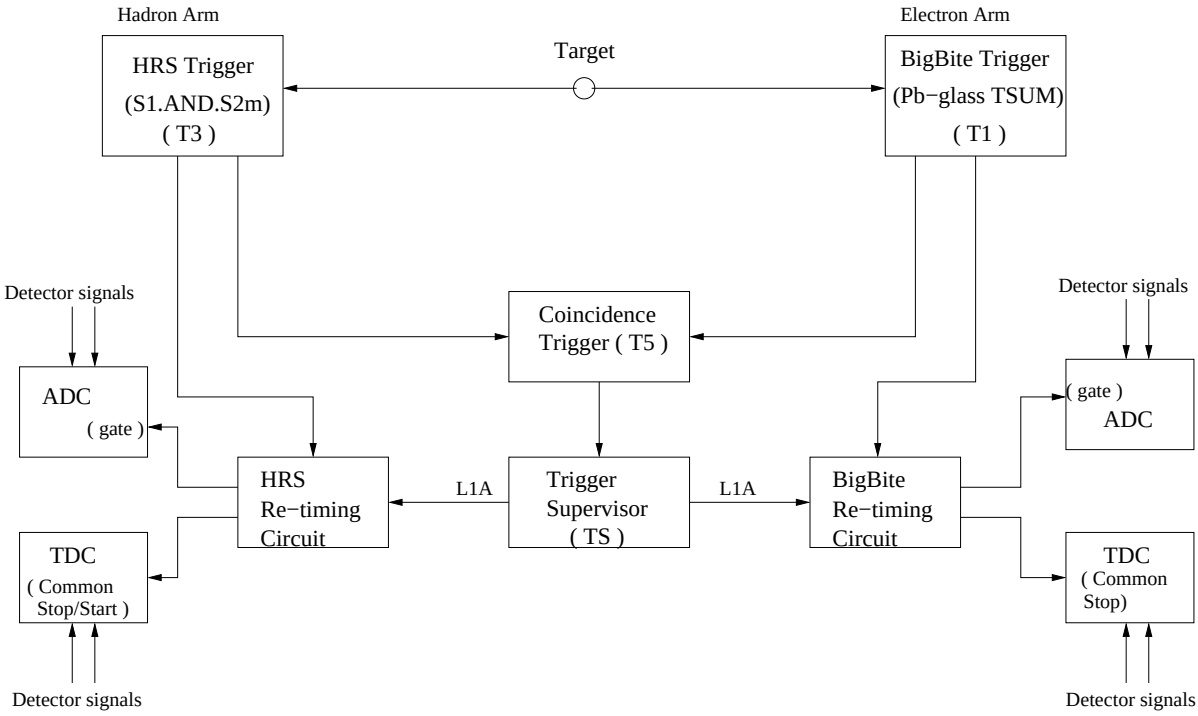

FIGURE 4.39: Schematic diagram of coincidence trigger setup between two spectrometers.

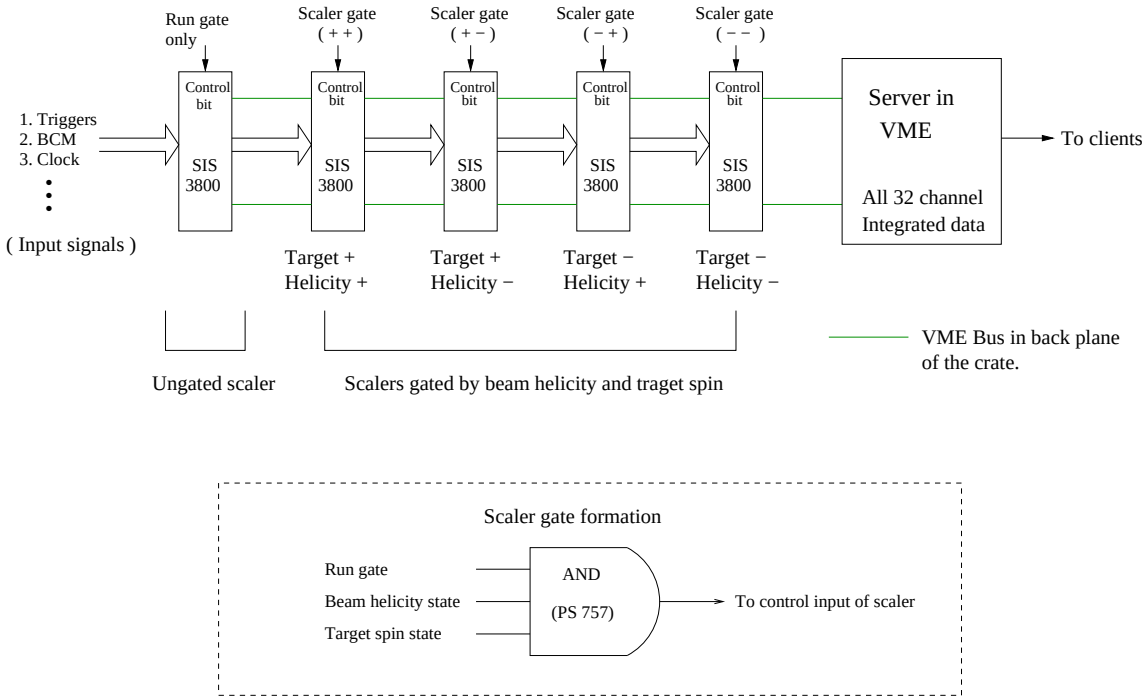

FIGURE 4.40: Scaler setup and gating scheme using target spin and beam helicity.

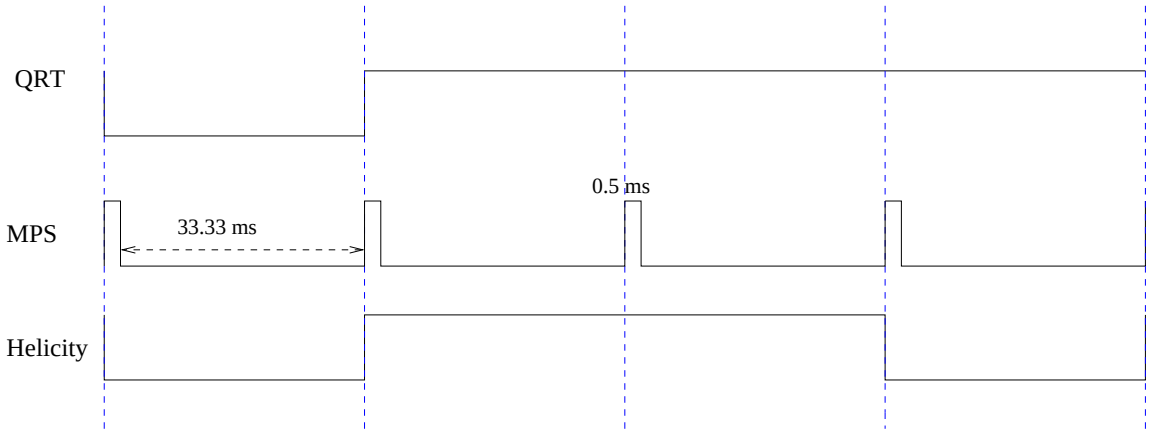

FIGURE 4.41: Beam helicity sequence during E06-010.

FIGURE 4.42: Timing sequence for the target spin state.

5

Data Analysis

The goal of the data analysis of the neutron transversity experiment is to extract the neutron Collins moment $A_{Collins}$ and Sivers moment A_{Sivers} from the ^{3}He single target spin asymmetry (SSA) by fitting the azimuthal angular dependence and correcting for the nuclear effects. The ^{3}He SSA was in turn measured in the Semi-inclusive Deep Inelastic Scattering (SIDIS) $^3\mathrm{He}^\uparrow(e, e'\pi^\pm)X$ process employing a vertically/transversely polarized ^{3}He target. The incident electron beam energy E is 5.89 GeV. The scattered electrons were detected with BigBite spectrometer at $\theta_e = 30^o$ and $p = 0.6 - 2.5$ GeV. The produced charged hadrons were detected with left HRS at $\theta_h = -16^o$ and $p = 2.35$ GeV. The corresponding $x \sim 0.13 - 0.41$, $Q^2 \sim 1.31 - 3.1$ GeV^2, $z \sim 0.4 - 0.6$, and $P_T \sim 0.1 - 0.6$ GeV. The entire data analysis procedure is illustrated in Fig. 5.1.

First, the detector raw data, supplemented with the detector calibrations, optics reconstructions, and coincidence timing calibrations, were processed through the standard Hall A analysis software "ANALYZER" in order to generate rootfiles containing event reconstructions. Meanwhile, the scalers were also calculated from the raw data by the same software. A special "skim" analysis was performed to

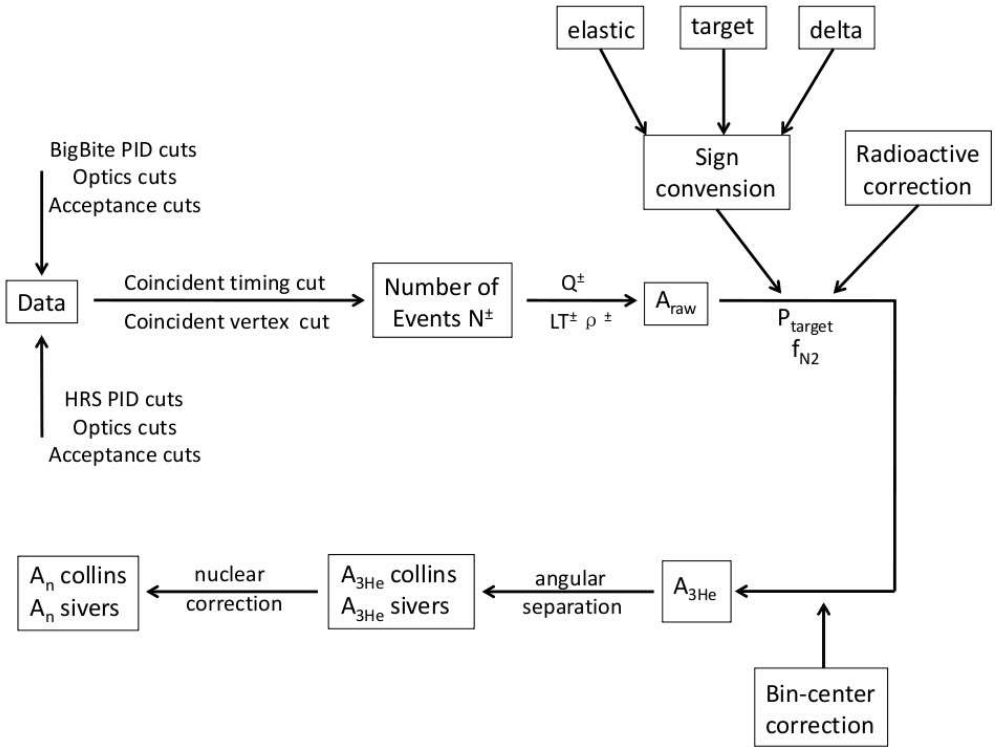

FIGURE 5.1: Illustration of the analysis procedure from raw data to the neutron Collins moment $A_{Collins}$ and Sivers moment A_{Sivers}.

discard data of the problematic regions (eg. beam trip, BigBite wire chamber trip, etc.), which were identified during the data quality check. Such "skimmed" rootfiles were then used to count the number of events $N^{\pm}$ in each target spin state after applying the detector cuts, particle identification cuts, and spectrometer acceptance cuts. The target spin dependent yields were then obtained by dividing $N^{\pm}$ by the accumulated charges, and further corrected by the livetime and target density. Subsequently, the raw asymmetry A_{raw} was deduced by taking the difference between the corrected yields of the opposite target spin states, and dividing it by the sum of these two yields.

Next, to calculate the ^{3}He physics asymmetries $A_{^3\mathrm{He}}$ from the raw asymmetries,

three factors were taken into account: the target polarization P_t, the direction of the target polarization, and the nitrogen dilution factor f_{N_2} which excluded the contribution from the unpolarized nitrogen nuclei mixed with the polarized ^{3}He. In addition, the radiative correction and bin-center correction procedures were followed to obtain the final $A_{^3\mathrm{He}}$.

Lastly, the ^{3}He Collins and Sivers moments ($A_{Collins}$ and A_{Sivers}) were obtained by fitting the azimuthal angular dependence of $A_{^3\mathrm{He}}$. In the final step, the neutron Collins and Sivers moments were extracted from the final ^{3}He Collins and Sivers moments by correcting the nuclear effects.

5.1 Detector calibration

The entire detector system was calibrated prior to replaying the raw data file through "ANALYZER", which is the standard Hall A analysis software based on C++/ROOT. The procedures involved in the calibration are discussed in this section.

5.1.1 BigBite Wire Chamber

BigBite wire chambers were used to reconstruct tracks of the charged particles falling into the acceptance of the BigBite spectrometer with the pattern match tree search tracking algorithm. The calibration of the BigBite wire chambers generally consists of four parts: examination of the detector map, calibration of t_0, calibration of the drift time to drift distance conversion functions, and the calibration of individual wire positions.

Examination of Detector Channel Map

Three sets of wire chambers, containing more than 3200 wires, were installed in experiment E06-010. Each wire was connected to one FASTBUS TDC channel as illustrated in Sec. 4.10.2. The timing information of the wire hits were recorded

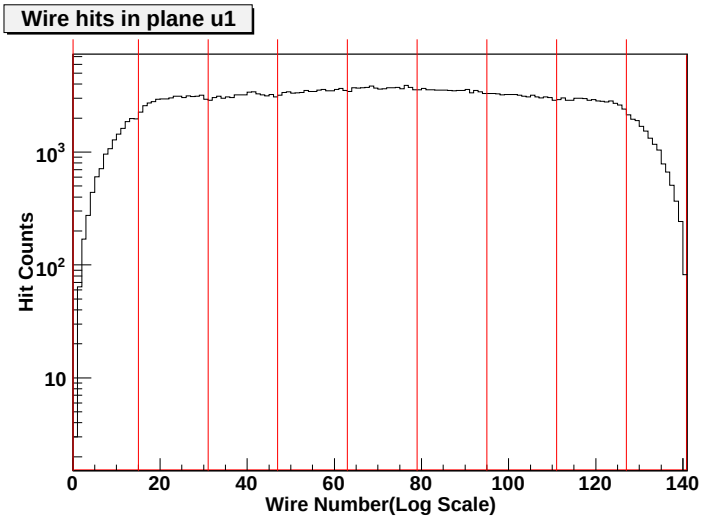

FIGURE 5.2: The distribution of the wire hits of the u plane in the first chamber. The red lines separate the different read-out amplified A/D cards which in general groups sixteen wires together.

by FASTBUS 1877 TDCs. During the track reconstructing process, each signal in the TDC channel needs to be projected to the corresponding wire in the wire chambers. The initial channel map was formed when different components of the wire chamber read out electronics were connected. However, given the enormous number of channels in the MWDC, it is essential to confirm the detector map with the experimental data. The distribution of the wire hit, shown in Fig. 5.2, can reveal many mapping problems, such as swap of cables, breakdown of the electronics, etc. If everything was connected correctly, the distribution of the wire hit in each wire plane should be smooth and reflect the physical geometry of the wire chambers. For example, for the wires in u and v orientations, the length of wire is shorter at the edge of the chamber, thus one expects to see fewer number of hits in those wires.

Inside each wire chamber, there are six wire planes, categorized into three groups with different orientations. Within each group, the second wire plane is shifted by about half of the wire cell in order to exclude the left/right ambiguities in the track reconstruction. Therefore, a correlation of the wire hits between two planes with

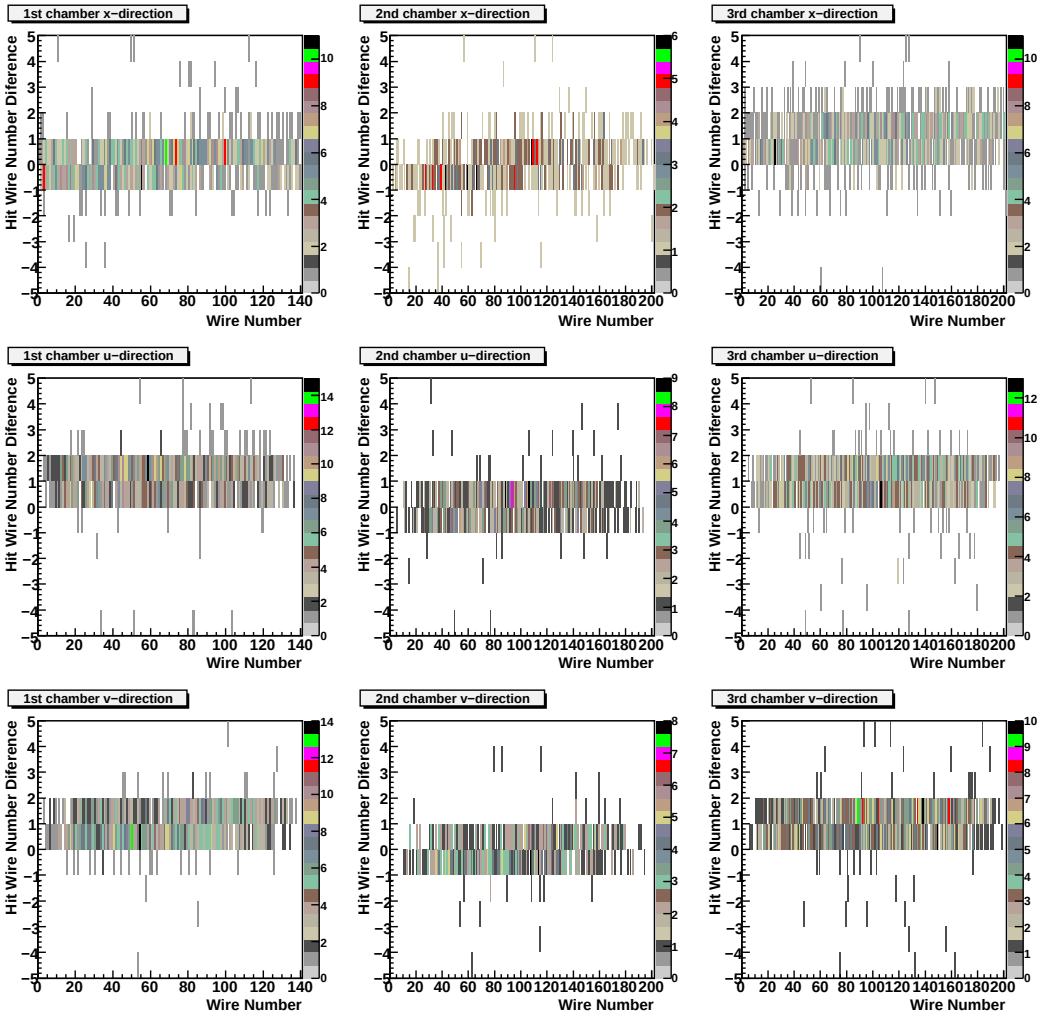

FIGURE 5.3: The correlations of the wire hits between two planes with the same orientation in each chamber are plotted with respect to the position of the hit.

same orientation inside each chamber (Fig. 5.3) is expected. Such exercise can reveal higher level mapping problems, such as cable swap between two planes with same orientations in each chamber, which can not be found out by examining the wire hit distributions.

In the end, one can further examine the detector map with the help of the reconstructed tracks. The track x vs. track y position distributions of all three wire chambers are shown in Fig. 5.4.

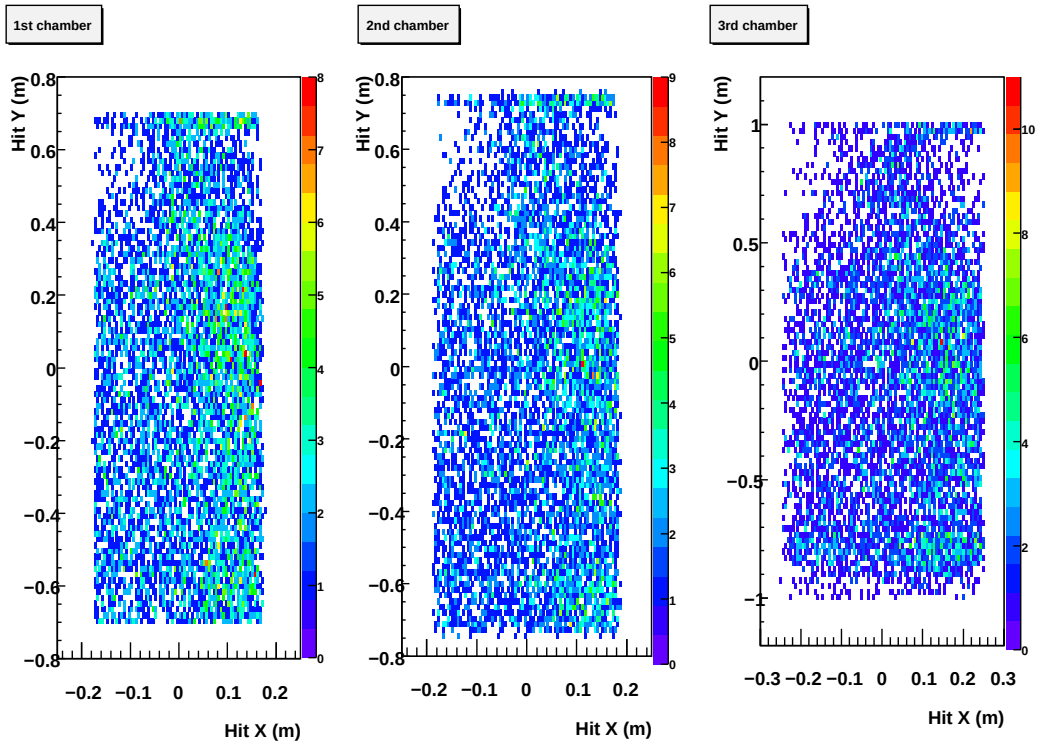

FIGURE 5.4: The reconstructed track projections in all three wire chambers are plotted. "X" ("Y") labels the horizontal (vertical) direction.

t_0 *Calibration*

The wire chamber DAQ is designed to record the difference between the time when the signal from one particular wire reaches the TDC (t_{signal}) and the time when the trigger signal arrives at the TDC ($t_{trigger}$). The t_{signal} is related to the time when the drifting electrons reach the hit wire (t_{drift}) by the following equation:

$$t_{signal} = t_{drift} + t^{a}_{propagate}, \tag{5.1}$$

where the $t^{a}_{propagate}$ is the time for the signal to travel from the hit wire to the TDC. The $t_{trigger}$ is related to the time when the particle reaches the wire chamber (t_{hit}) by the following equation:

$$t_{trigger} = t_{hit} + t_{travel} + t^{b}_{propagate} + t_{timewalk}, \tag{5.2}$$

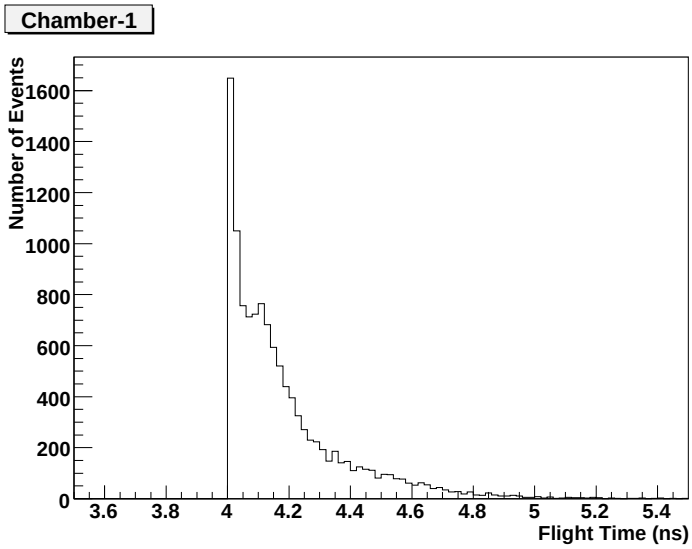

FIGURE 5.5: The flight time of a 1 GeV electron traveling from the first chamber to the calorimeter for all accepted events in BigBite.

where the t_{travel} is the time this particle travels between the hit wire chamber and the trigger detector (the BigBite calorimeter in this experiment). The $t^b_{propagate}$ is the time for the trigger signal to propagate from the trigger detector to the TDC. The $t_{timewalk}$ is the trigger time walk effect which has been corrected in the analysis. So the recorded time, after the time walk correction, $t_{signal} - t_{trigger} - t_{timewalk}$ is linked to the real drift time $t_{drift} - t_{hit}$ by

$$t_{signal} - t_{trigger} - t_{timewalk} = t_{drift} - t_{hit} + t^a_{propagate} - t_{travel} - t^b_{propagate} \approx t_{drift} - t_{hit} + t_0. \tag{5.3}$$

The last step is achieved by neglecting the differences of the t_{travel} among particles with different momenta and directions. Fig. 5.5 shows the flight time of a 1 GeV electron traveling from the first wire chamber to the calorimeter for all accepted events in BigBite. The differences are in general smaller than 1 ns. In comparison, the BigBite wire chamber TDC resolution is about 0.5 ns and the time walk correction is about a few ns. Therefore, it is safe to neglect the t_{travel} difference in Eqn. (5.3).

The t_0 is then extracted by identifying the rising edge of the drift time spectrum.

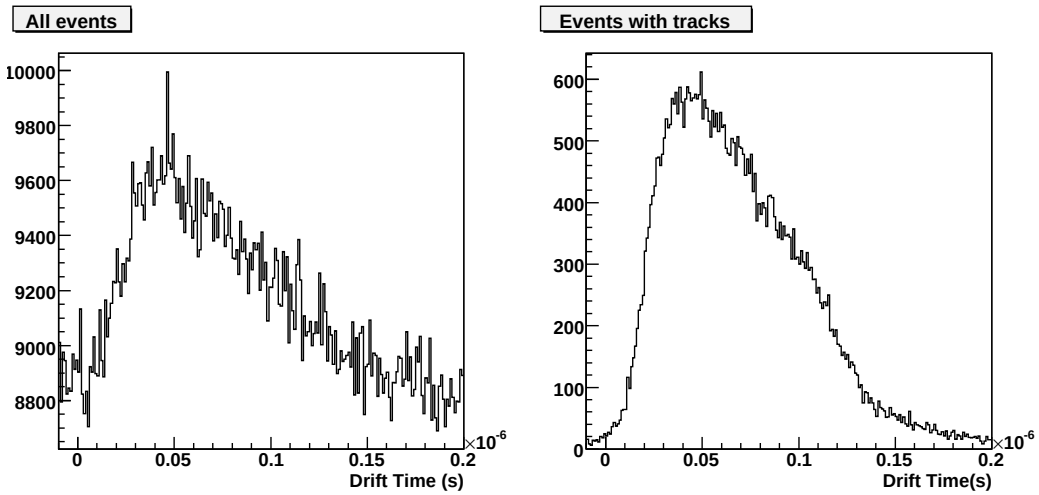

FIGURE 5.6: The drift time spectrum in x plane of the second chamber is shown for all events (left) and events in which a valid track is reconstructed (right). In the right panel, the background hits are strongly suppressed by requiring valid tracks.

Fig. 5.6 shows the drift time spectrum for all events (left panel) and events in which a valid track is reconstructed (right panel). A clear rising edge of the drift time spectrum can be seen in the right panel. During the t_0 calibration, the t_0 for each wire was calibrated individually by combining hundreds of runs together in order to collect enough number of hits on each wire. Fig. 5.7 shows the drift time spectrum for 100th wire in the x plane of the third chamber.

Drift Time to Drift Distance Conversion

The drift time for each hit was further converted to the drift distance. The conversion function was obtained using the reconstructed track. The drift distance is defined as the distance between track projection in the corresponding hit plane and the hit wire position. The drift distance was then plotted against the drift time in Fig. 5.8. The conversion function was parametrized as sectional continuous function of several polynomial functions through the entire drift time window from 0 to 200 ns.

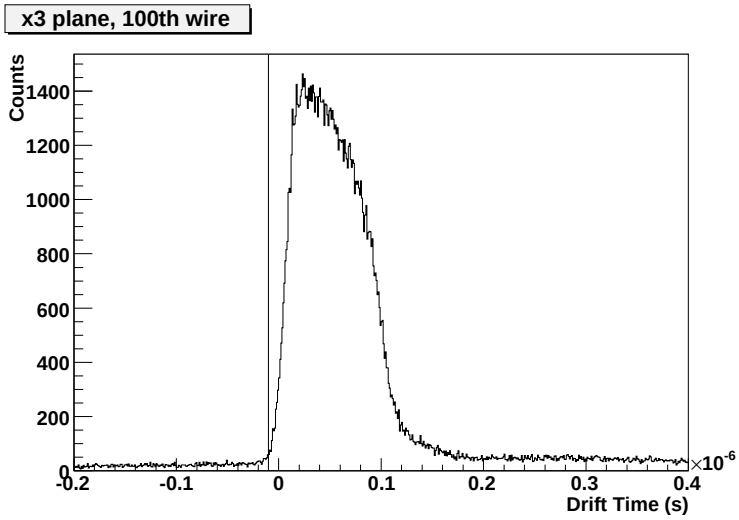

FIGURE 5.7: The drift time spectrum is shown for 100th wire in the x plane of the third chamber.

Wire Position Calibration

In the process of the track reconstruction, the precise knowledge of the wire position is very crucial. First, the position of each wire chamber was obtained by reading the survey report. The internal structure of each wire chamber was obtained by reading the wire chamber construction report. Next, the position of each wire was

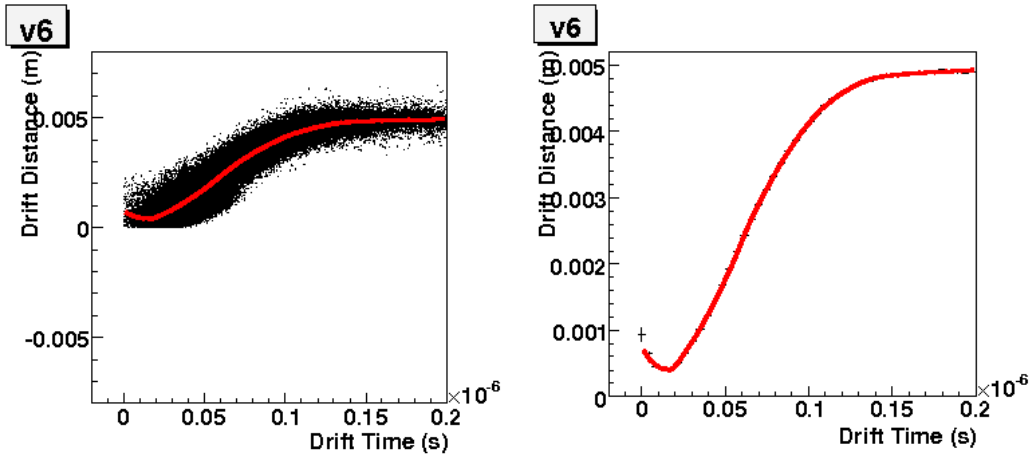

FIGURE 5.8: The drift distance is plotted against the drift time (left panel). The profile of the left 2-d histogram is plotted in the right panel.

calibrated with the information of reconstructed track. One important quantity in this calibration is the track residual, which is defined as the distance between track projections on the hit wire plane and the hit position (hit wire position corrected by the calculated drift distance after exclusion of left/right ambiguities). With the track residual spectrum, one can shift each wire position accordingly.

Iteration Procedure

The calibration of drift time to drift distance conversion function depends on the t_0 and the wire position for each wire and the information from the reconstructed tracks. Therefore, an iteration procedure is practically adopted. The iteration flow of the procedure is shown in Fig. 5.9. There are three iteration loops in this procedure. The first loop represents the global t_0 calibration for each readout card. The second loop represents the global calibration of the wire chamber vertical position for each plane. A low luminosity run was replayed multiple times in order to achieve this goal. The goal of the previous two loops is to tune the entire system to a reasonable starting point for the final iteration loop to converge. The final iteration loop represents the calibration of t_0 and wire positron for each wire. In order to collect enough number of hits in each wire, hundreds of runs were replayed and combined in this analysis.

Results

The average σ of the residual peak before the iterating calibration procedure is about 440 μm. After the iteration calibration procedure, the σ of the residual peak is below 200 μm (Fig. 5.10).

Hitting Efficiency

To evaluate the performance of the tracking, there are two important quantities, the hardware tracking efficiency, and the software tracking efficiency. When the tracking

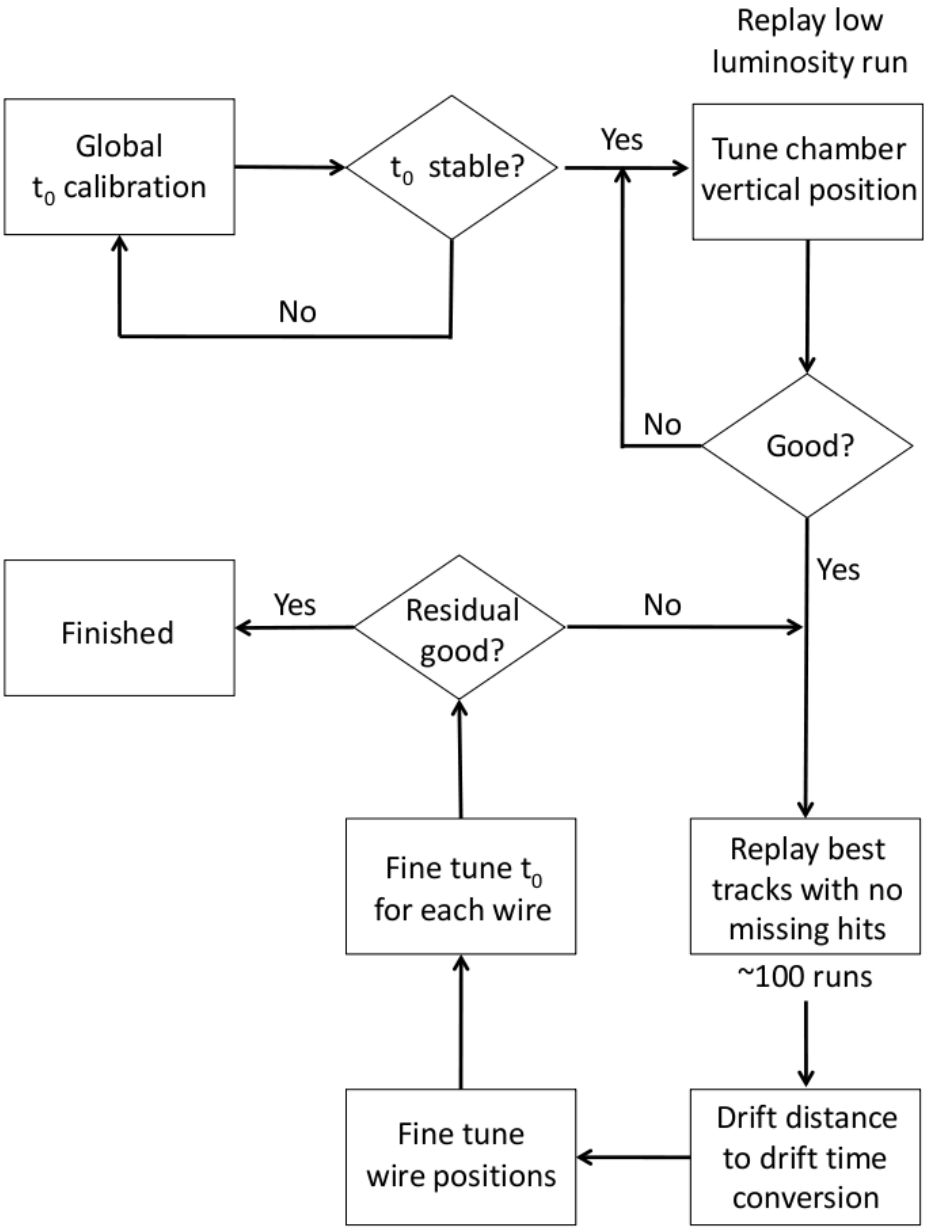

FIGURE 5.9: The off-line BigBite wire chamber calibration procedure is shown.

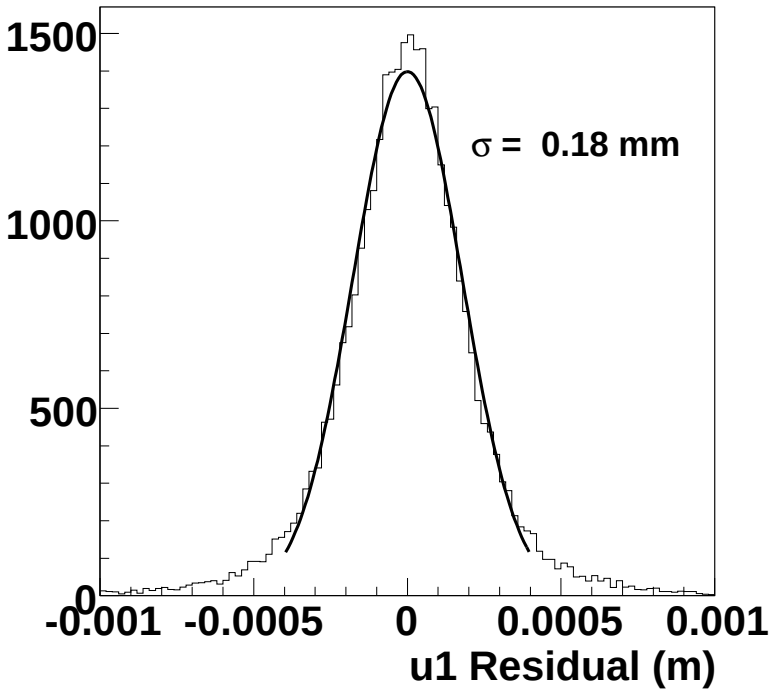

FIGURE 5.10: The residual peak of the u plane of the first chamber after the calibration is shown.

software is perfect, the hardware tracking efficiency can be expressed as

$$\epsilon_{hardware} = \frac{N_{tracks}^{found}}{N_{tracks}}. \tag{5.4}$$

It is usually determined by the wire hitting efficiency, which represents the probability of a wire to fire when a real charged particle passes by. For example, in experiment E06-010, there were 18 wire planes. If we assume the average hitting efficiency P = 95%, and we require at least 15 planes to fire in order to find a track, then the hardware tracking efficiency can be expressed as:

$$\begin{aligned} \epsilon_{hardware} &= C_{18}^{15}P^{15}(1-P)^3 + C_{18}^{16}P^{16}(1-P)^2 \\ &+ C_{18}^{17}P^{17}(1-P) + C_{18}^{18}P^{18} \\ &\approx 99\%, \end{aligned} \tag{5.5}$$

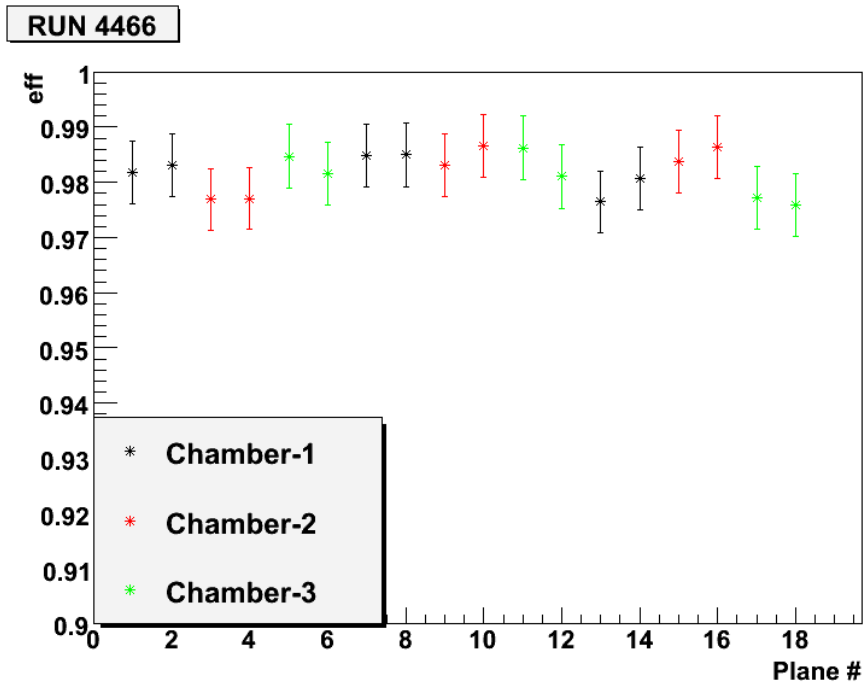

FIGURE 5.11: The MWDC hitting efficiency for run 4466.

where

$$C_m^n = \frac{m!}{n!(m-n)!}, \tag{5.6}$$

and $m! = m \cdot (m-1) \cdot ... \cdot 1$. In general, the inefficiencies of the hit wires are caused by wire chamber itself or its readout electronics, for example, the threshold applied on the A/D cards.

In the pattern match tree search tracking algorithm, the 18 planes were divided into three groups according to their orientations. Tracks were first searched within each group. Therefore the hardware tracking efficiency was written as

$$\epsilon_{hardware} = (C_6^6 P^6 + C_6^5 P^5 (1-P))^3 \approx 90\%, \tag{5.7}$$

if the tracking algorithm requires five out of six planes fired in order to define a valid track in each group.

In practice, the wire hitting efficiency was determined with the help of tracking

software. For example, to determine the wire hitting efficiency in the $u1$ wire plane, one needs to first exclude this plane in track reconstructions. For the tracks found, one can project them to the $u1$ wire plane to see if the corresponding wires are fired or not. The percentage of the firing probability represents the wire hitting efficiency. In order to obtain the wire hitting efficiency for all 18 planes, each run needs to be replayed by 18 times. One example plot of the hitting efficiency can be found in Fig. 5.11. This procedure was performed in the experiment from time to time to ensure the normal performance of the wire chamber. Throughout the entire experiment, the average wire hitting efficiency P was about 0.98, leading to a 98% hardware tracking efficiency.

BigBite Tracking Software

The software tracking efficiency represents the ability of the software to find a track from the hits recorded in the MWDC. Such efficiency is in general difficult to evaluate, since the number of events containing real tracks is unknown. We will further discuss this issue in Sec. 9.3. In this section, we briefly describe the tracking algorithm used in the BigBite Spectrometer.

The algorithm used in the BigBite tracking is "Pattern Match Tree Search". This algorithm uses templates to search for tracks. The schematic illustration of the tree-search algorithm can be found in Fig. 5.12. In the first step, the hit structure is viewed with a coarse resolution with some templates. Within the templates that matched the hit pattern, a set of daughter templates are then applied to further compare with the finer hit pattern. This procedure will continue until it reaches the desired matching resolution. The remaining hits are then fitted to reconstruct a track. A recent review of the modern pattern match tracking algorithm can be found in Ref. [273].

In the case of BigBite, the tracking software was developed by O. Hansen (Hall A

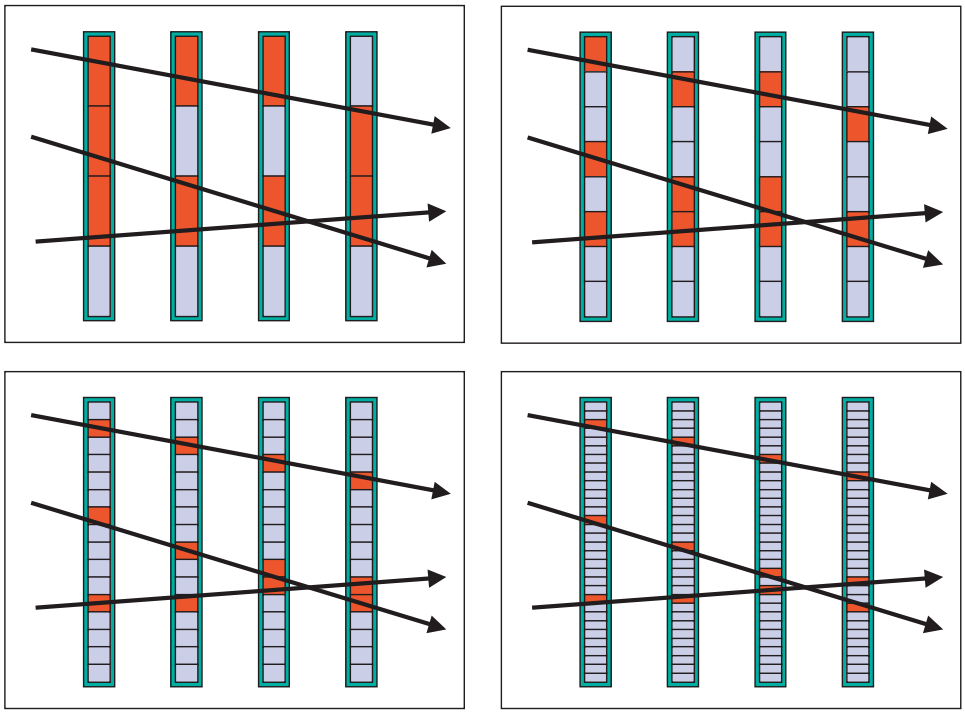

FIGURE 5.12: Schematic illustration of the tree-search algorithm in the case of four steps. The track is matched with templates of increasing granularity and resolution. Figure is from Ref. [273].

Staff Scientist). The total 18 wire planed were divided into three groups, also called "projections", according to their orientations. The tree-search was then used to find 2-D tracks, also called "Roads", within each group with the hits. Finally, the 2-D tracks were matched and a fitting procedure was used to reconstruct the 3-D tracks, also called "Tracks".

A few modifications were implemented with the help of the event-display when applying this set of software in analyzing the experiment E06-010 data:

- A special plane was added to include the calorimeter in the tracking:

  With the addition of the calorimeter, the speed of the tracking software was further increased. A flag was added into the database to turn on/off this feature.

- The "Roads" method in the tracking software was updated:

  In the updated "Roads" method, both left and right hits were saved in order to achieve more exclusive searches.

- Fit conditions for "Roads" were loosed:

  More "Roads" were saved for the final 3-D fit.

- Ghost track removing algorithm was updated:

  The algorithm was updated to remove the saved identical "Roads".

After the application of above modifications, more tracks can be found by the tracking software at the cost of reducing the speed of the tracking software. An example event display is shown in Fig. 5.13.

5.1.2 BigBite Optics

After each track was reconstructed with the MWDC and tracking software, the kinematic information of the particle, such as, the momentum, angles, and the interaction vertex when it left the target, needed to be determined by the BigBite optics module. The principle of the optics reconstruction is based on the fact that the trajectory of a charged particle moving in a known magnetic field is completely determined by its momentum and charge. Therefore, with the trajectory of the particle and magnetic field information, one can reconstruct all the kinematic information of the particle. However, in reality, the knowledge on the magnetic field is usually not precise enough to use the aforementioned method. Instead, a calibration of the optics module is performed. In this section, we describe the calibration of the BigBite optics in experiment E06-010.

BigBite spectrometer optics calibration was performed with two incident beam energies (1st pass beam: 1.2306 GeV and 2nd pass beam 2.3960 GeV). The quality of the optics reconstruction was further checked with data taken in 5th pass (beam

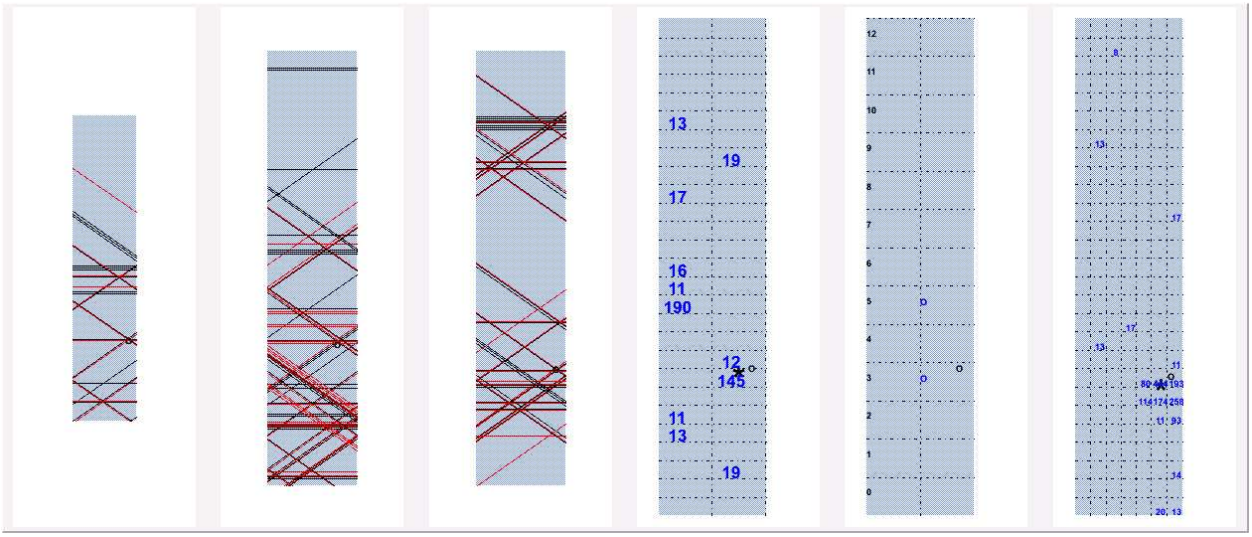

FIGURE 5.13: The first three panels shows the event display for the MWDC. The black lines represent hits in u, v, and x planes. The red lines represent hits in u', v', and x' planes. The reconstructed track is labeled as the black circle, which is the projected points on the corresponding plane from reconstructed tracks. The fourth and sixth panels are the event display for the preshower and shower, respectively. The fifth panel is the event display for the scintillator plane. The numbers represent the corrected ADC values for each block after pedestal subtraction. The stars represent the reconstructed cluster center for the calorimeter. The clustering in the calorimeter will be discussed in Sec. 5.1.3.

energy: 5.892 GeV). In Table. 5.1, we summarize all the data taken for the BigBite optics calibration. In general, the vertex reconstruction was performed with multi-foil carbon targets. The positions of the carbon foils are known accurately in order to calibrate the interaction vertex. The angles reconstruction was calibrated with a sieve slot which was placed in front of the magnet. The momentum reconstruction relied on the electron hydrogen elastic scattering. Two incident beam energies were used to cover the entire momentum range of interest from 0.6 GeV to 2.5 GeV.

The BigBite Optics strategy is summarized:

1. **Read Survey Report**: Find out the positions of targets, magnet (sieve slots), and MWDC.

Table 5.1: Data taken for the BigBite optics calibration.

Beam energy	Target	Sieve	Target Collimator	Magnet	Reason
1.2306 GeV	Multi-Carbon	in	in	off	Calibrate Chamber Positions
1.2306 GeV	Multi-Carbon	out	in	on	Calibrate Interaction Vertex
2.3960 GeV	Multi-Carbon	out	in	on	Calibrate Interaction Vertex
1.2306 GeV	Multi-Carbon	in	out	on	Calibrate Angles
1.2306 GeV	Multi-Carbon	in	in	on	Calibrate Angles
2.3960 GeV	Multi-Carbon	in	in	on	Calibrate Angles
1.2306 GeV	H2 reference	in	out	on	Calibrate Angles/Momentum
1.2306 GeV	H2 reference	in	in	on	Calibrate Angles/Momentum
1.2306 GeV	H2 reference	out	in	on	Calibrate Momentum
2.3960 GeV	H2 reference	in	out	on	Calibrate Angles/Momentum
2.3960 GeV	H2 reference	in	in	on	Calibrate Angles/Momentum
2.3960 GeV	H2 reference	out	in	on	Calibrate Momentum
5.892 GeV	Polarized ^{3}He	in	in	on	Check Angle Reconstruction
5.892 GeV	Multi-Carbon	out	in	on	Check Vertex Reconstruction
5.892 GeV	H2 reference	out	in	on	Check Momentum Reconstruction

2. **No-Field Runs**: Find out the locations of MWDC with data.

3. **Multi-Carbon Foils Runs**: Calibrate the interaction vertex with two incident beam energies.

4. **Sieve Runs**: Calibrate the angles with two incident beam energies and multi-foil carbon and hydrogen gas targets.

5. **Hydrogen Runs at Elastic Kinematics**: Calibrate the momentum with elastic data at two incident beam energies.

6. **Target Collimator**: Calibrate/check the effects of the extended target.

Survey Report and No-Field Run

To calibrate the BigBite optics, it is important to know the precise positions of the target foils and the magnet (or the sieve) as they are the basis of the calibration. Their positions were obtained from the survey report attached in Appendix. 9.2. Although the positions of the wire chambers were not required to build the BigBite optics model[1], they were still useful for a better first order optics model. No-field runs were used to calibrate the positions of the wire chamber. In this case, the reconstructed tracks from the MWDC were not bent by the magnetic field and the kinematics of the particle would not change. The quality of the no-field run after calibration can be found in Fig. 5.14. The left panel shows the reconstructed carbon foils. The middle panel shows the sieve used during the experiment. The right panel shows the reconstructed sieve pattern, where the red points were used to identify the center of the sieve holes/slots. One can clearly see the carbon foils as well as the sieve pattern.

[1] The positions of the wire chamber are by definition included as part of the optics

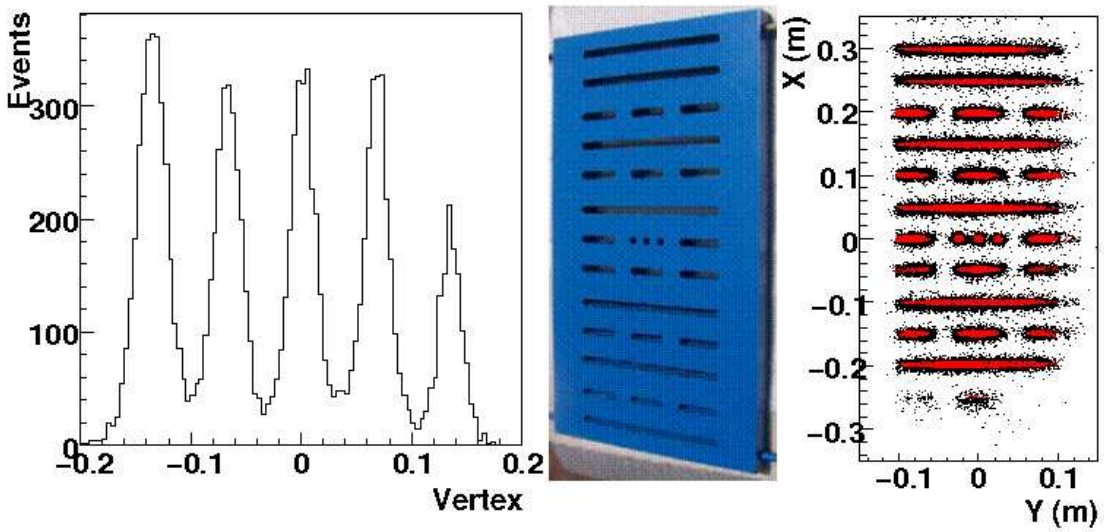

FIGURE 5.14: The left panel shows the reconstructed interaction vertex with BigBite no field configuration. The middle panel shows a real picture of the BigBite sieve slit. The right panel shows the reconstructed BigBite sieve pattern in the no-field configuration.

First Order BigBite Optics Model

The first order BigBite optics model treats the BigBite as a perfect dipole magnet. The angle ϕ between the particle momentum vector and the magnetic field vector then remains fixed as the particle travels through the magnetic field:

$$\cos\phi = \frac{\mathbf{B}\cdot\mathbf{p}}{|B|\cdot|p|}. \tag{5.8}$$

In addition, a virtual bending plane is assumed to be located in the middle of the BigBite magnet as illustrated in Fig. 5.15. Approximations about the boundary of the magnetic field are made. First, the reconstructed track from MWDC intercepts with the middle plane at the middle point. Next a cone is reconstructed by assuming the ϕ angle in Eqn. (5.8) is fixed. Such cone will intercept with the beam line. The resulting interception is the first order interaction vertex. The first order angles are subsequently determined by the vector which connects the first order interaction vertex to the middle point.

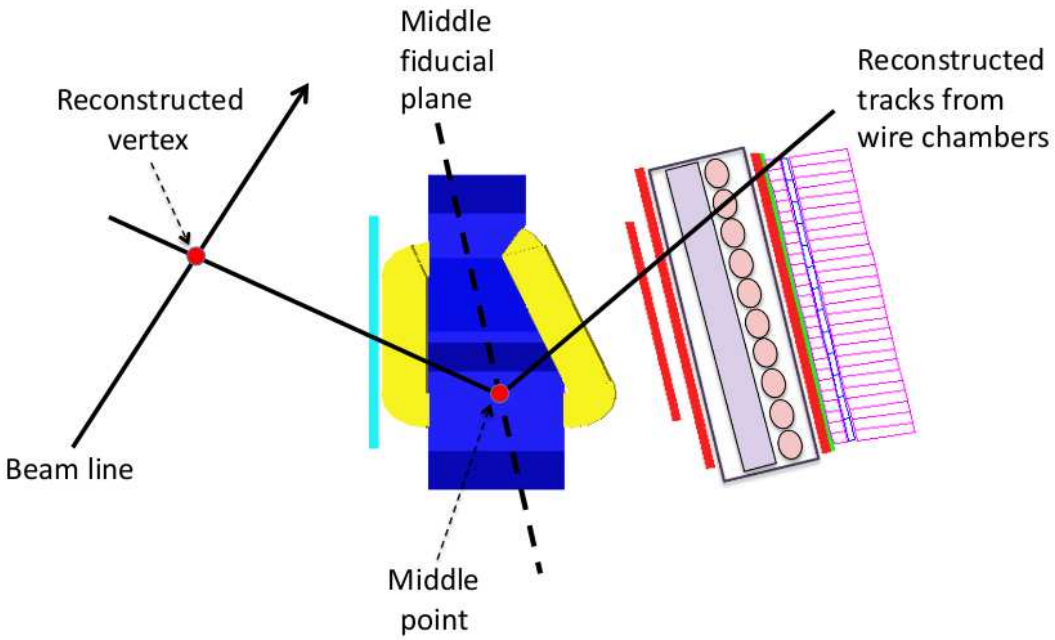

FIGURE 5.15: The first order model of the BigBite optics is shown. The definition of middle plane, middle point and the reconstructed first order interaction vertex is illustrated.

The first order momentum is expressed as:

$$p = \frac{L}{2 \cdot \tan\left(\theta_{bend}/2\right) \cdot \sin\left(\phi\right)}, \tag{5.9}$$

where the L is the distance the particle travels inside the magnetic field. The θ_{bend} is the bending angle for the particle in the plane perpendicular to the magnetic field. L is approximated as sum of the distance between the point the particle enters the magnetic field and the middle point and the distance between the middle point and the point the particle exits the magnetic field.

Vertex Reconstruction

Based on the first order vertex reconstruction $Z_v^{(0)}$, higher order corrections were added by plotting the difference between the reconstructed $Z_v^{(0)}$ and the expected Z_v from the multi-carbon foils vs. different tracking variables, such as tr_x, tr_y, tr_{xp}, tr_{yp}, $bend_x$ and $bend_y$:

$$Z_v^{(1)} = Z_v^{(0)} + a_1 \cdot tr_y + b_1, \tag{5.10}$$

$$\begin{aligned} Z_v^{(2)} &= Z_v^{(1)} + (a_{20} + a_{21} \cdot Z_v^{(1)}) + (b_{20} + b_{21} \cdot Z_v^{(1)}) \cdot tr_x + (a_{22} \\ &+ a_{23} \cdot Z_v^{(1)}) + (b_{22} + b_{23} \cdot Z_v^{(1)}) \cdot tr_y \\ &+ (a_{24} + a_{25} \cdot Z_v^{(1)}) + (b_{24} + b_{25} \cdot Z_v^{(1)}) \cdot tr_{yp} \\ &+ (a_{26} + a_{27} \cdot Z_v^{(1)}) + (b_{26} + b_{27} \cdot Z_v^{(1)}) \cdot tr_{xp} \\ &+ (a_{28} + a_{29} \cdot Z_v^{(1)}) + (b_{28} + b_{29} \cdot Z_v^{(1)}) \cdot bend_x \\ &+ (a_{30} + a_{31} \cdot Z_v^{(1)}) + (b_{30} + b_{31} \cdot Z_v^{(1)}) \cdot bend_y. \end{aligned} \tag{5.11}$$

The tr_x and tr_y indicate the hit position of the reconstructed track in the first chamber in the detector coordinate system. The tr_{xp} and tr_{yp} indicate the direction of the reconstructed track in the chamber coordinate system, which are defined as:

$$tr_{xp} = \frac{dtr_x}{dtr_z}, \tag{5.12}$$

$$tr_{yp} = \frac{dtr_y}{dtr_z}. \tag{5.13}$$

The $bend_x$ and $bend_y$ indicate the position of the middle point in the middle plane. Eqn. (5.11) was then repeated to obtain $Z_v^{(3)}$ from $Z_v^{(2)}$.

An approximate momentum reconstructed was used in order to obtain the momentum dependent correction on the interaction vertex. The first order momentum

$p^{(0)}$ was reconstructed from the $Z_v^{(3)}$ based on Eqn. (5.9). Then

$$\begin{aligned} p^{(1)} &= p^{(0)} \cdot (c_0 + c_1 \cdot bend_y + c_2 \cdot bend_y^2) \cdot (d_0 + d_1 \cdot bend_x) \cdot (e_0 + e_1 \cdot Z_v^{(3)}) \\ &\cdot (f_0 + f_1 \cdot tr_x + f_2 \cdot tr_x^2) \cdot (g_0 + g_1 \cdot tr_{xp} + g_2 \cdot tr_{xp}^2), \\ &\cdot (h_0 + h_1 \cdot tr_y + h_2 \cdot tr_y^2) \cdot (i_0 + i_1 \cdot tr_{yp} + i_2 \cdot tr_{yp}^2) \qquad (5.14) \\ p^{(2)} &= p^{(1)} \cdot (j_0 + j_1 \cdot bend_x + j_2 \cdot bend_x^2) \cdot (k_0 + k_1 \cdot bend_y + k_2 \cdot bend_y^2) \\ &\cdot (l_0 + l_1 \cdot p^{(1)}). \qquad (5.15) \end{aligned}$$

The momentum dependent vertex correction was obtained as:

$$\begin{aligned} Z_v^{(4)} &= Z_v^{(3)} - (Z_v^{(3)} \cdot (l_0 + l_1 \cdot p^{(2)}) \\ &+ ((m_0 + m_1 \cdot Z_v^{(3)}) \cdot (n_0 + n_1 \cdot p^{(2)}) \\ &+ exp((o_0 + o_1 \cdot p^{(2)}) \cdot (p_0 + p_1 \cdot V_z^{(3)}))) \cdot bend_x). \qquad (5.16) \end{aligned}$$

Eqn. (5.16) was then repeated to obtain $Z_v^{(5)}$ from $Z_v^{(4)}$.

There are two regions (one at the top and one at the bottom of the BigBite magnet) where the magnetic field is weaker than that in the center of the BigBite. Such a feature can lead to deviations of the reconstructed interaction vertex from the real one. The effect is presented in Fig. 5.16. A fiducial volume cut was added in the middle plane ($bend_x$ and $bend_y$) in order to exclude such extreme regions. In addition, based on several look-up tables, the following corrections were made to counteract such effects:

$$Z_v^{(6)} = f_1(bend_x, bend_y, Z_v^{(5)}), \qquad (5.17)$$

$$Z_v^{(7)} = f_2(bend_x, p^{(2)}, Z_v^{(6)}), \qquad (5.18)$$

$$Z_v^{(8)} = f_3(bend_y, p^{(2)}, Z_v^{(7)}). \qquad (5.19)$$

Each correction depends on the $bend_x$, $bend_y$, and Z_v. The entire 3-D phase space of $bend_x$, $bend_y$ and Z_v was divided into small regions. The functions in Eqn. (5.17)

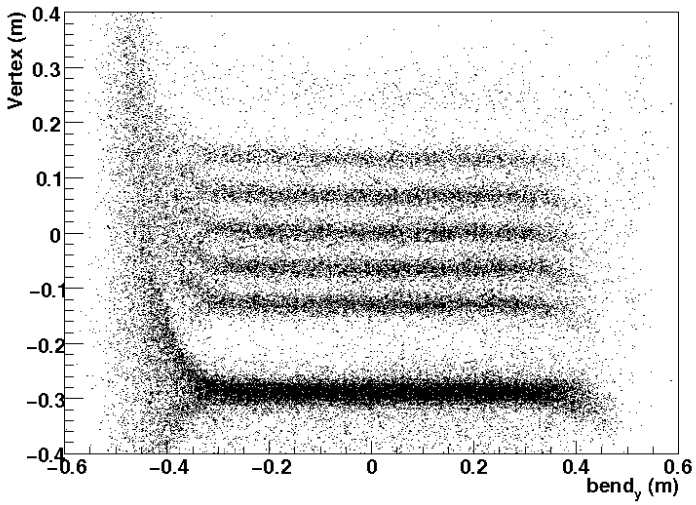

FIGURE 5.16: Reconstructed interaction vertex is plotted against the $bend_y$, which is the vertical position of the middle point. The left side is corresponding to the bottom region of the BigBite magnet. The extreme region can be found in the top and bottom of the magnet.

gave the interpolation and extrapolation results for any position in the 3-D phase space. For example, for any point inside the boundary of the phase space, there would be 8 points with different values of $bend_x$, $bend_y$ and Z_v around it. A simple linear interpolation method was adapted. In addition, the f_2 and f_3 took care of the momentum dependent corrections with additional look-up tables. The final vertex reconstruction is shown in Fig. 5.17. The vertex resolution is about 1 cm at a momentum of 0.95 GeV. The average resolution is about 0.8 cm from 0.8-2.0 GeV (Fig. 5.18).

Reconstruction of Angles

A sieve slit was used to calibrate the angles. In the first order model, all angles were determined by connecting the final vertex reconstruction and the middle point. The sieve pattern with the first order model can be seen in the left panel of Fig. 5.19. The middle panel shows the sieve pattern after adding offsets. The right panel shows

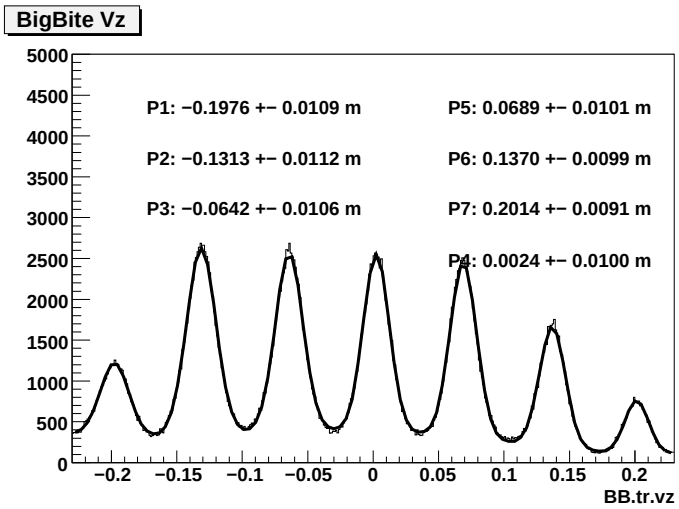

FIGURE 5.17: Final vertex reconstruction at momentum of 0.9 GeV for multi-carbon foils. The vertex resolution is about 1 cm.

the sieve pattern after applying the higher order corrections. The red points label where the sieve holes/slots should be. The similar procedure as the one used in the vertex reconstruction was adapted for the higher order corrections. Look-up tables were used for the extreme regions.

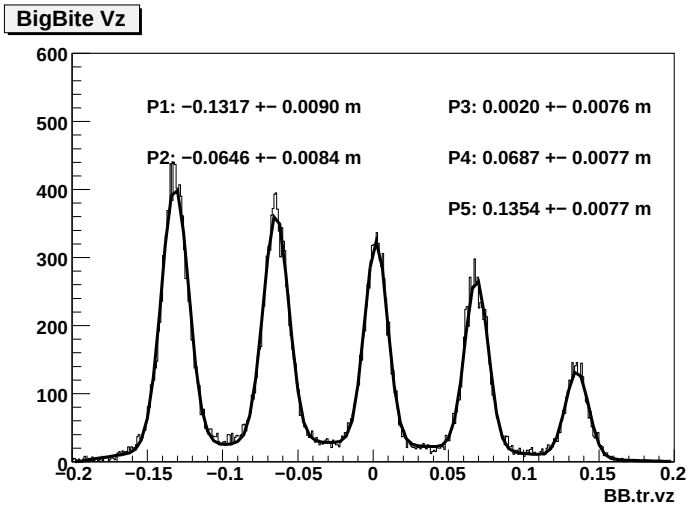

FIGURE 5.18: Vertex reconstruction at 1.2 GeV for multi-carbon foils. The vertex resolution is about 0.77 cm.

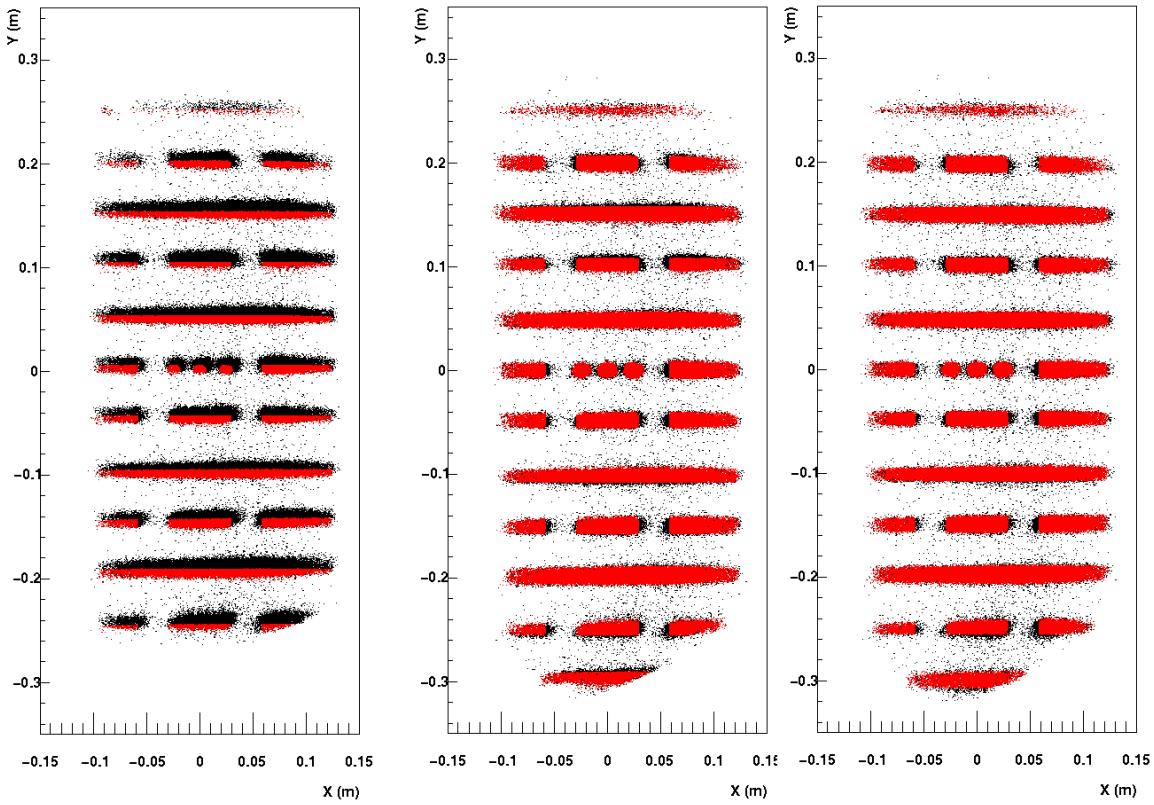

FIGURE 5.19: The left panel shows the reconstructed sieve pattern with first order optics model. The middle panel shows the sieve pattern after adding offsets. The right panel shows the sieve pattern after applying the higher order corrections. The red points label the location of sieve holes/slots.

The Procedure of Momentum Reconstruction

Elastic electron scattering from hydrogen target was used to calibrate the momentum. Two beam energies (1.2306 and 2.3960 GeV) were used to cover the entire momentum range of interest of the BigBite from 0.6 GeV to 2.2 GeV. The steps involved in calibrating the momentum are:

1. Global selection of electrons at hydrogen elastic kinematics.

2. The energy loss effect was taken into account for both incident electron beam

and the out-going electrons.

3. Obtain the first order momentum. See Eqn. (5.9).

4. Select electrons at hydrogen elastic kinematics with cut on the position of the middle point.

5. Use look-up tables to obtain final corrections on the momentum reconstruction depending on the position of the middle point.

Energy Loss for Electron Through Material

In experiment E06-010, materials along the beam line included: windows made by Be, ^{4}He gas, ^2H gas (20 cm long), and the front endcap glass wall. The total thickness L of materials is about 0.002473 of radiation length X_0. Thus the average energy loss was approximated as:

$$\frac{P_{loss}}{P_0} = 0.492 \cdot exp(-\frac{L}{X_0}), \tag{5.20}$$

where the factor 0.492 represents the difference between the average and peak values of a Landau distribution, which is usually used to describe the energy loss distribution.

The material on the way of outgoing electrons included: glass side wall, ^{4}He gas, yellow cover, and the air between the target hut and the first wire chamber. The window thickness was modeled as $0.0156/\sin(\theta_e)$ of radiation length X_0, where the θ_e is the polar angle of the outgoing electron. The air thickness depends on the path-length, which was modeled as $0.001685/(L_{path} - 0.8)$, where the 0.8 m is the distance between the target and the yellow cover.

Electron Selection at Elastic Kinematics

In order to select the electrons at elastic kinematics, the entire middle plane was divided into smaller regions in $bend_y$. The electrons at elastic kinematics were then selected with a 2-D graphic cut on the δp, the difference between the reconstructed momentum and the expected momentum, and the $bend_x$. Four plots are shown in Fig. 5.20. Top left panel shows the low field region at the bottom of the BigBite. Bottom left panel shows δ_p after the momentum correction for the same region. Top and bottom right panels show a region near the center of the magnet with two beam energies. The events inside the black loop, which is the graphic cut, were selected as the elastic electrons.

Momentum Reconstruction

Look-up tables were directly used after obtaining the first order momentum reconstruction. The correction was in a format of

$$p^{(1)} = z_0 \cdot p^{(0)} + z_1 + z_2 \cdot tr_x + z_3/\theta_{bend}, \tag{5.21}$$

where the z_0, z_1, z_2 and z_3 were all functions of $bend_x$ and $bend_y$ (position of the middle point):

$$z_0 = g_0(bend_x, bend_y), \tag{5.22}$$

$$z_1 = g_1(bend_x, bend_y), \tag{5.23}$$

$$z_2 = g_2(bend_x, bend_y), \tag{5.24}$$

$$z_3 = g_3(bend_x, bend_y) \tag{5.25}$$

Similar interpolation procedure as the one used in Eqn. (5.17) was adapted. The only difference is that 2-D phase space of $bend_x$ and $bend_y$ was used instead of the 3-D phase space of $bend_x$, $bend_y$ and Z_v. The effects of the momentum correction are shown in Fig. 5.21. The bottom panels show the δ_p vs. $bend_y$ together with the

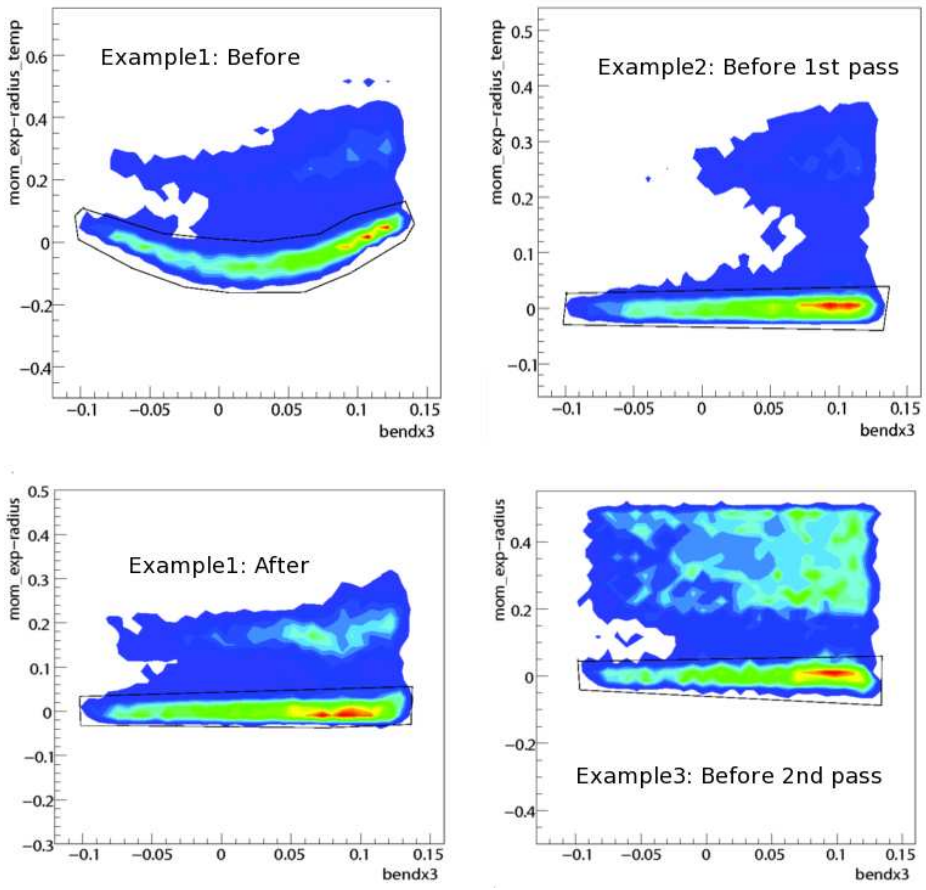

FIGURE 5.20: Selections of the electrons at elastic kinematics are shown for several sample regions of the BigBite magnet. The black loops represent the 2-D graphic cuts.

selected sample of elastic electrons at two incident beam energies. The top panels show the δ_p vs. $bend_y$ after applying the corrections at two incident beam energies. The final momentum resolutions are shown in Fig. 5.22. The average momentum resolution across the entire momentum coverage is about 1 %.

Optics Quality Check

The elastic scattered electrons from hydrogen at two incident beam energies were used to calibrate the momentum reconstruction. At 1.2306 GeV, the elastic electron momentum in the BigBite detector ranged from 0.95 GeV to 1.15 GeV. At 2.3960

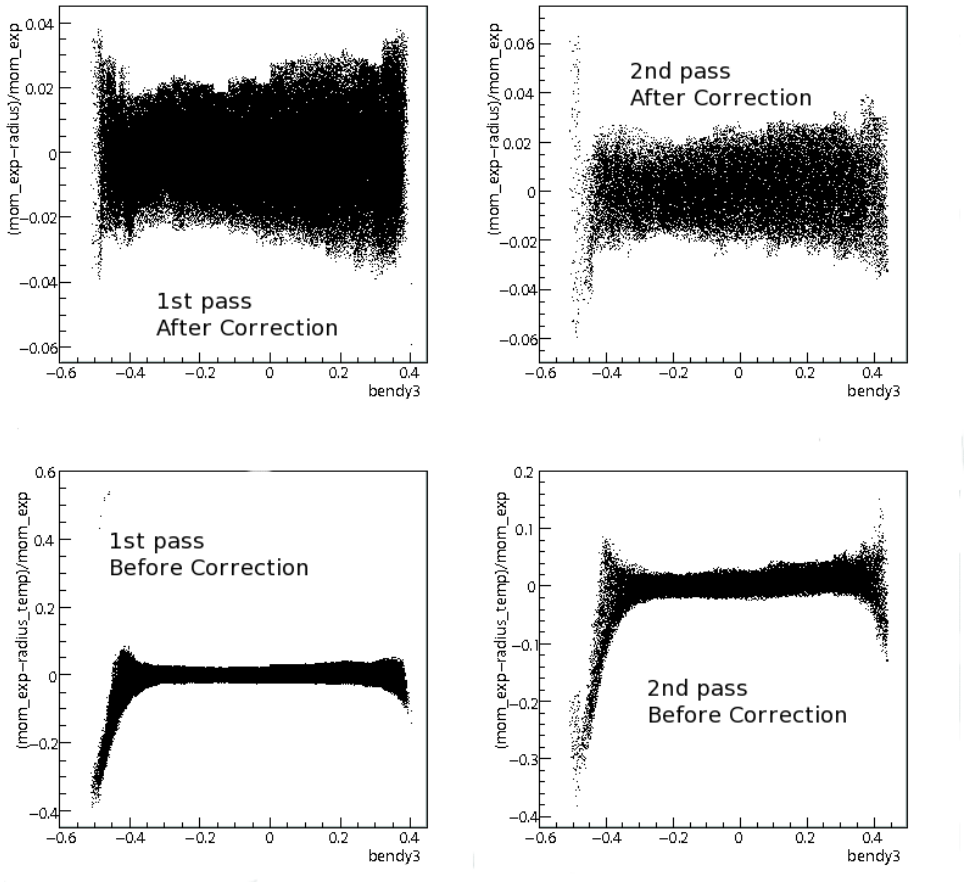

FIGURE 5.21: The effects of the momentum correction are shown here. The bottom left (right) shows the δp before the correction for beam energy of 1.2306 (2.3960) GeV. The top left (right) shows the δp after the correction for beam energy of 1.2306 (2.3960) GeV.

GeV, it ranged from 1.7 GeV to 1.9 GeV. Therefore, an important optics quality check was performed to examine whether the reconstruction was valid for the momentum region between the two calibration points and beyond the higher/lower calibration point. For the momentum region lower than 0.9 GeV, the Δ resonance was used. The top left panel of Fig. 5.23 shows the reconstructed missing mass at an incident electron beam energy of 1.2306 GeV. The top right panel shows the momentum vs. the lab polar θ angle. For the momentum range between the two calibration points, the Δ and other higher mass resonances were used to check the optics. The bottom

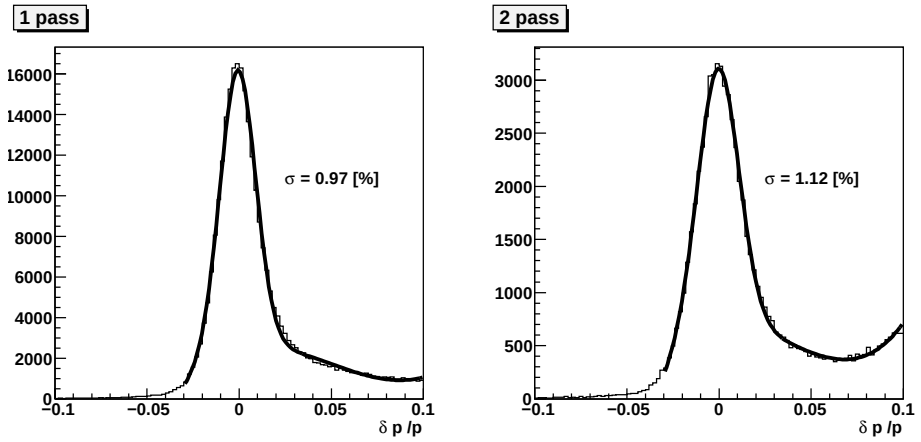

FIGURE 5.22: Final momentum resolutions after correction are shown for 1.2306 GeV (left) and 2.3960 GeV (right) beam energies.

left plot of Fig. 5.23 shows the reconstructed missing mass at 2.3960 GeV. The peaks of all visible resonances are located at the right positions. The bottom right panel shows the momentum vs. θ angle for the 2.3960 GeV incident beam energy. For the momentum range beyond 2.0 GeV, the elastic hydrogen scattering at 5th pass (5.892 GeV) beam was used to check the quality of the optics. The top left panel of Fig. 5.24 shows the δ_p defined as the difference between the reconstructed momentum and the expected electron momentum at 5th pass elastic kinematics. A small bump was observed around zero, which corresponds to the elastic events at 5th pass. These events can also be seen in the top right panel of the momentum vs. θ angle. The black line shows the correlation of the expected momentum and θ angle for the elastic scattering. The bottom left panel shows the reconstructed momentum vs. the energy deposited in the calorimeter. At high momentum, the calorimeter is not thick enough to contain the electron's energy. Therefore, the reconstructed energy is slightly lower than the reconstructed momentum. The bottom right panel shows the spectrum of the reconstructed mass. The black line shows the position of the proton mass.

The optics reconstruction was further checked with the production data. Fig. 5.25 shows the reconstructed interaction vertex of the multi-carbon foils at 5th pass. Near

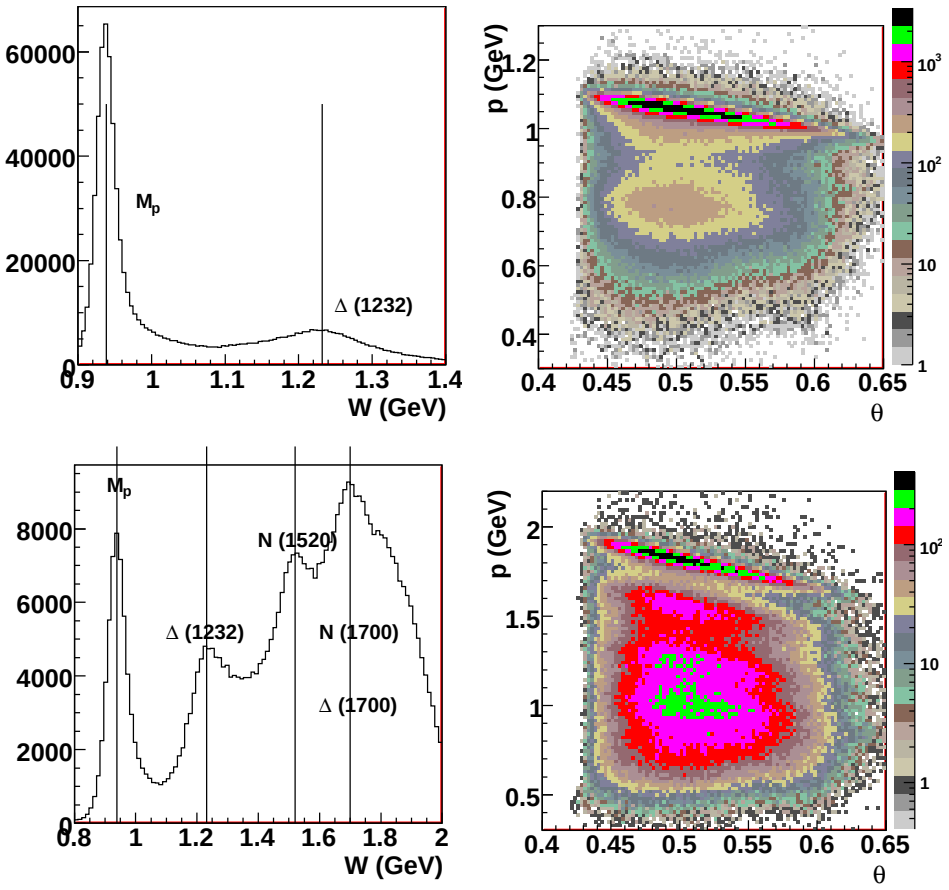

FIGURE 5.23: Momentum reconstruction is examined with positions of resonances. The top (bottom) left panel shows the reconstructed missing mass peaks for proton and resonances at an incident beam energy of 1.2306 (2.3960) GeV. The right two panels show the momentum vs. lab polar θ angle at two incident beam energies.

the end of the experiment, the sieve slot was placed in front of the BigBite magnet in order to check the reconstruction of the angles. Fig. 5.26 shows the sieve slot pattern for a production ^{3}He run at an incident beam energy of 5.892 GeV.

BigBite Positive Optics Model

BigBite spectrometer is an open geometry spectrometer. Both the negative and positive charged particles can reach the detector package. Thus, it is useful to work out the BigBite positive optics model. Since the calibration of the optics requires

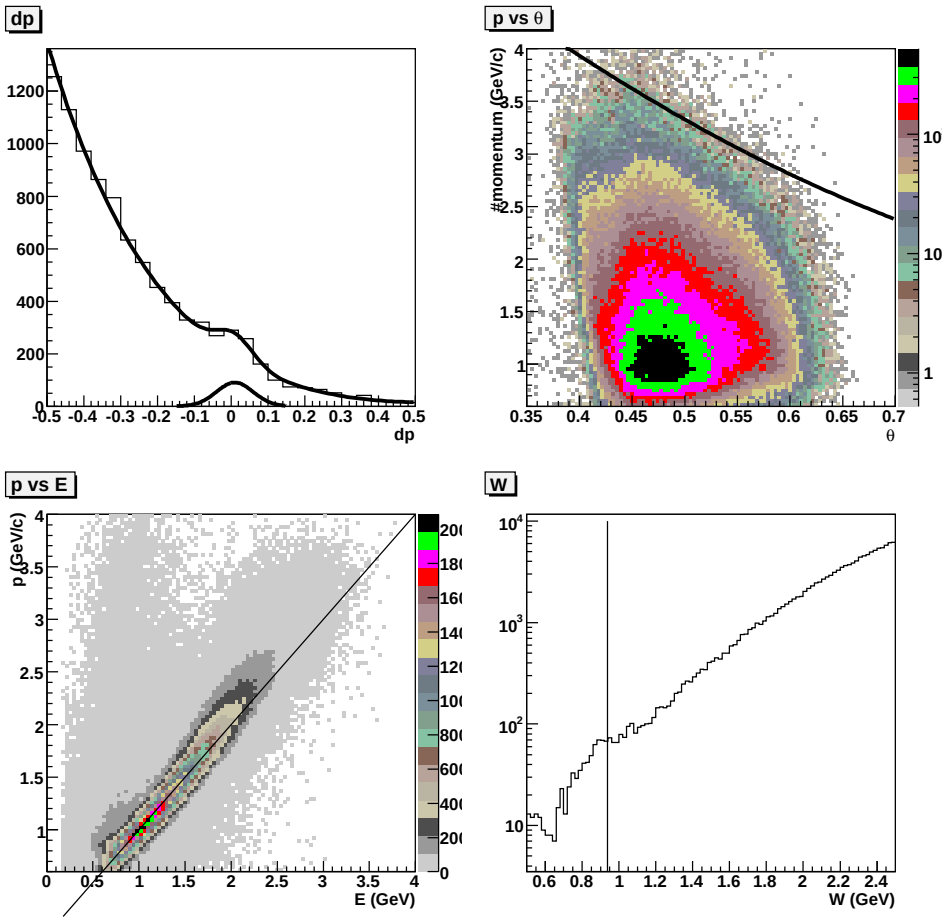

FIGURE 5.24: 5th pass electron hydrogen elastic scattering. Top left panel: δp; Top right panel: reconstructed p vs. reconstructed polar θ angle; Bottom left panel: reconstructed momentum vs. reconstructed energy in the calorimeter; Bottom right panel: reconstructed missing mass spectrum.

using scattered electrons from either the multi-carbon foil target or the hydrogen gas target, one has to reverse the BigBite polarity in order to calibrate the positive optics. During experiment E06-010, no such data were taken when the BigBite was positioned at 30 degrees. Instead, at the beginning of d2n experiment (E06-014), which ran following experiment E06-010, optics data were taken with BigBite in both negative and positive polarities. The BigBite spectrometer was positioned at 45 degrees in E06-014. The distance between the BigBite and the center of the target

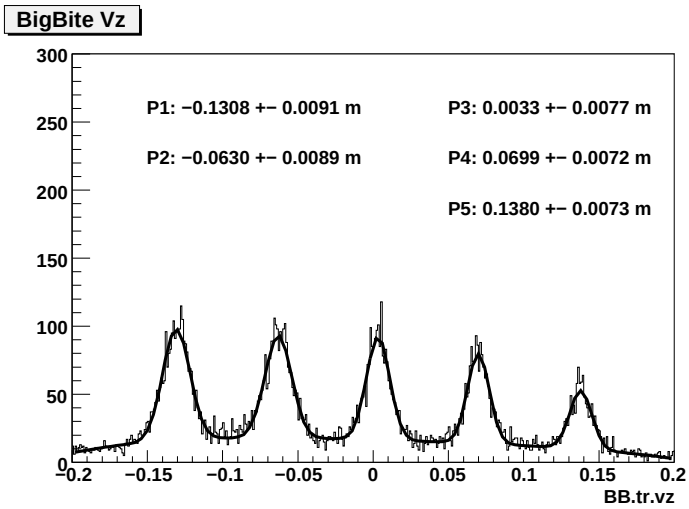

FIGURE 5.25: The reconstructed vertex for multi-carbon foil target at 5.892 GeV beam energy.

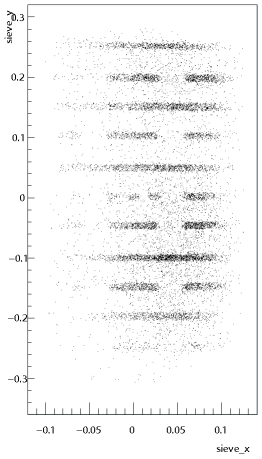

FIGURE 5.26: The reconstructed sieve pattern on a polarized ^{3}He target at 5.892 GeV beam energy.

in E06-014 was the same as that in experiment E06-010. Therefore, the positive optics of BigBite was calibrated using the data taken in E06-014 and was further implemented in the experiment E06-010 data analysis.

One major issue with the aforementioned method is the transformation of the BigBite optics model between 30 and 45 degrees. In practice, such transformation was only taken into account in the first order model. All the higher order corrections remained to be the same. This approach was checked with the negative optics model. More specifically, the negative optics model calibrated at 30 degrees was transformed to 45 degrees, by only changing the first order model. The transformed optics model at 45 degrees was then checked with the optics data taken in E06-014 including the 1st pass hydrogen elastic run, multi-carbon foils run, sieve slot run etc. Good descriptions for the reconstructed momentum, vertex and angles were observed, which demonstrated the validity of this approach.

The calibration of the positive optics model follows the approach in calibrating the negative optics model discussed in previous sections. Fig. 5.27 shows the resolution of the reconstructed momentum for the positive optics. The momentum resolution is about 1.2 % which is slightly worse than the 1.0% obtained in the negative optics. Fig. 5.28 shows the sieve pattern for the positive optics. Since the electrons were bent down when the BigBite polarity was positive, events were only observed on the top half of the BigBite acceptance. Fig. 5.29 shows the reconstructed interaction vertex for the multi-carbon foils for the positive optics. The vertex resolutions are comparable to those in the negative optics.

5.1.3 BigBite E&M Calorimeter

The BigBite calorimeter system consists of a preshower and a shower detectors, which are made of lead glass. The details are described in Sec. 4.10.2. It was used both for triggering the BigBite spectrometer and for PID of the scattered electrons. The

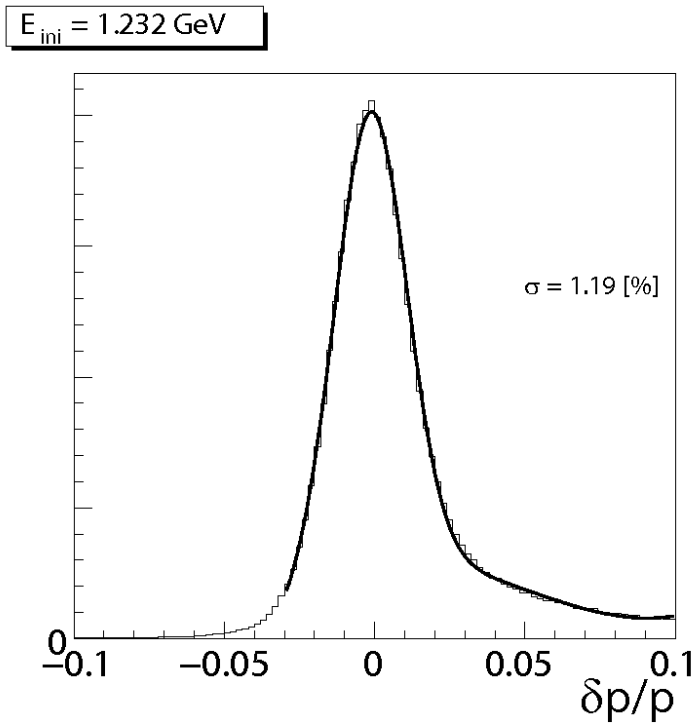

FIGURE 5.27: The momentum resolution for d2n positive optics data at 1.231 GeV. A 1.2% momentum resolution was achieved.

sum of the cluster energy deposition in the total shower for the incoming electron is expected to be proportional to its energy. Part of the resolution is intrinsic, and the rest is determined by how well the detectors are calibrated. In other words, the resolution is determined by how well the gains in different calorimeter blocks PMTs are aligned. In experiment E06-010, the shower calorimeter system was first calibrated with cosmic rays to match the gains for all PMTs by changing the HV settings. The electrons from the hydrogen elastic scattering at two incident beam energies, $E_0 = 1.231$ GeV and $E_0 = 2.306$ GeV, were then used to perform the fine calibration in matching the PMT gains in software. In this section, we will briefly describe the BigBite calorimeter calibration performed by K. Allada from University of Kentucky.

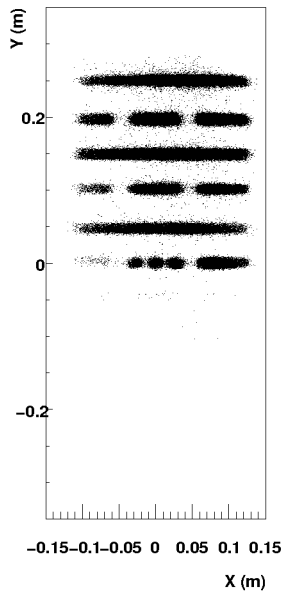

FIGURE 5.28: The reconstructed sieve pattern for d2n positive optics data at 1.231 GeV.

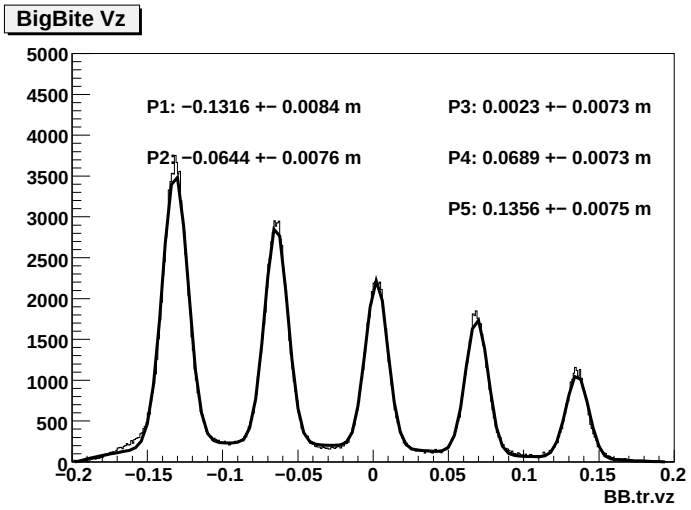

FIGURE 5.29: The reconstructed vertex for multi-carbon foils target for d2n positive optics data.

Calibration Using Cosmics

The shower calibration with cosmic rays utilizes the fact that high energy cosmics, mostly muons, would leave minimum ionization in all the blocks they pass by. Such a feature leads to a well defined energy deposition peak in the ADC. The calibration was then performed to align peaks in all PMTs by changing the HV with an iterative procedure. A scintillator trigger, containing two scintillator planes (one was mounted on the top of the calorimeter, the other one was mounted at the bottom of the calorimeter.), was chosen. Each scintillator plane had two PMTs, one on each side, and the trigger was constructed by making a logical AND of all four PMTs. Such trigger would select the cosmic rays passing vertically through the detector. Fig. 5.30 shows the event display of two cosmic events before and after the shower calibration. The minimum ionization peak in preshower in ADC was aligned to the channel 240 and the one in shower was aligned to the channel 120.

Shower Cluster Reconstruction

When an electron hits the shower, it usually leaves energies on a cluster of preshower/shower blocks. The total energy deposition in the cluster is essential in PID, and the position of the cluster provides additional information to reject false tracks. However, at high luminosities, more than one particle would reach the calorimeter in the same event, leaving more than one cluster. Therefore, a good cluster reconstruction algorithm is important in order to identify all the clusters properly. In experiment E06-010, a new shower cluster reconstruction algorithm was developed. The basic steps are described in the following:

- Search for the block with the largest energy deposition in the shower, known as central block.
- Sum over nine blocks surrounding this central block to form a cluster in the

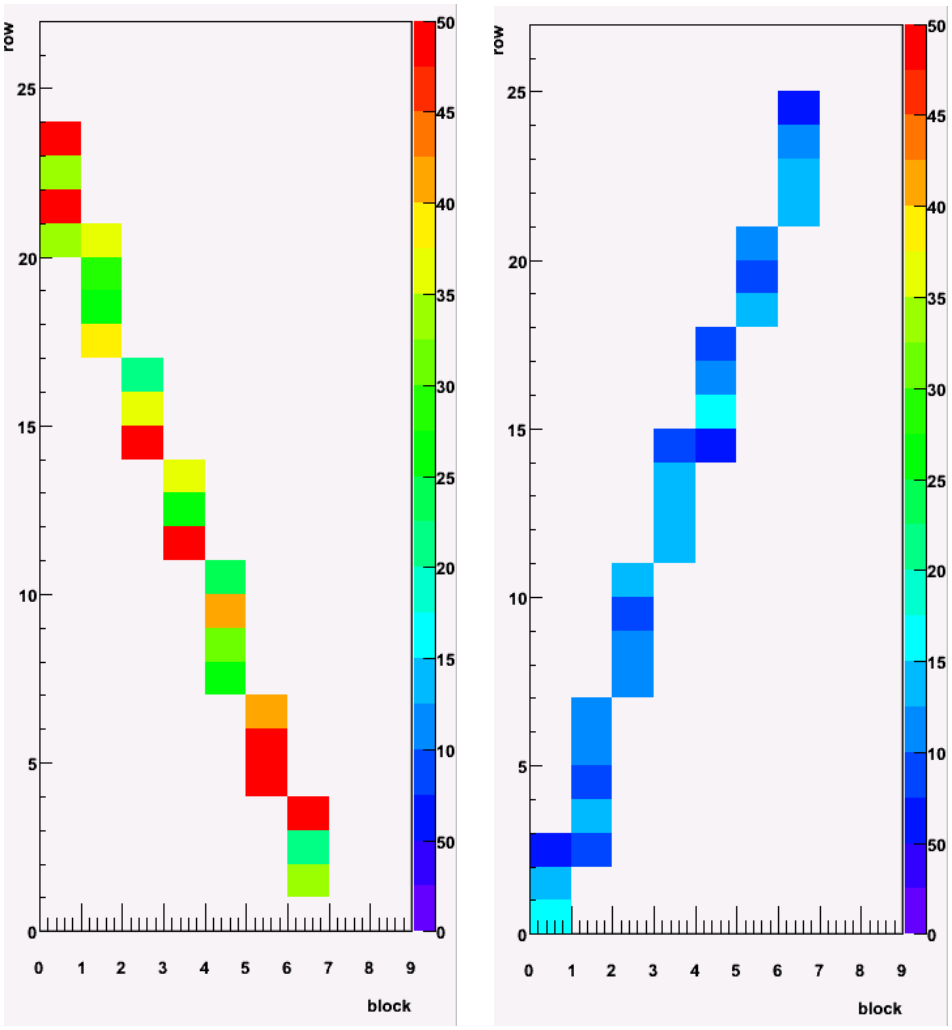

FIGURE 5.30: Event display for an uncalibrated and calibrated shower.

shower.

- All the blocks in the aforementioned cluster are then removed from this event. Next, the block with the largest energy deposition in the remaining blocks is chosen. The entire procedure is repeated until no blocks with energy deposition are left. The found clusters are then sorted in a decreasing order of the energy deposition.

- Similar procedure is applied to the preshower.

- The next step is to match the shower cluster with the preshower cluster. In practice, all clusters found in the shower are looped through one by one. For any given shower cluster, one searches for a preshower cluster within a certain distance (center-to-center). If no such preshower cluster can be found, the shower cluster is deemed invalid and the next one is considered. Otherwise, a cluster of total shower is obtained.

- This cluster of total shower is then matched with the reconstructed tracks. This is realized by comparing the track projections in the shower plane with the center of the total shower cluster. The distance between these two points is required to be smaller than twice the size of the shower block.

- If all of the above conditions are met, the position and energy information of the clusters in preshower and shower is stored for further analysis.

- Meanwhile, the first cluster, which has the highest energy deposition, together with its corresponding preshower cluster (if exists) is saved separately. These kinds of clusters, if no matching track is found, are likely to correspond to photons, which in general do not leave a track in the MWDC.

The above algorithm is optimized with the help of the event display. An example plot is shown in Fig. 5.13. The final energy E of the cluster is calculated as the sum of energy deposited in all the blocks in the cluster.

$$E = \sum_{i=1}^{N} E_i, \tag{5.26}$$

where N is the number of blocks in both the preshower and shower cluster. In addition, X, Y coordinates are calculated using the energy weighting method.

$$X = \sum_{i=1}^{M} E_i.X_i/E \quad , \quad Y = \sum_{i=1}^{M} E_i.Y_i/E, \tag{5.27}$$

where M is the number of blocks in the shower cluster.

Calibration of Calorimeter Using H_2 Elastics

After the initial gain match of all the BigBite calorimeter PMTs with the cosmic rays, the BigBite calorimeter was further fine tuned using singles electrons from the hydrogen elastic scattering at two incident beam energies $E_0 = 1.231$ GeV and $E_0 = 2.306$. The momentum (energy) of the scattered electrons at elastic kinematics can be calculated as:

$$E_e = \frac{M_p E_b}{(M_p + E_b(1 - cos\theta))}, \tag{5.28}$$

by neglecting the electron mass (0.511 MeV). Here, M_p is the mass of the proton, E_b is the incident beam energy, and θ is the scattered polar angle of the electron. As the momenta and angles of the charged particles are already determined by the BigBite optics module described in Sec. 5.1.2, one only needs to select the sample of elastic events and uses the reconstructed momentum to calibrate the calorimeter.

The principle of the calorimeter calibration is finding the coefficients C_i for every block which transforms the ADC amplitude to the energy deposited,

$$E_i = C_i.(A_i - P_i), \tag{5.29}$$

where A_i is the raw ADC amplitude, P_i is the value of the pedestal[2], and E_i is the energy deposited in the i^{th} block. The best coefficients are obtained by minimizing the χ^2. The χ^2 is defined as the square of the energy difference between the reconstructed energy from the optics module and the measured energy in the calorimeter,

[2] Even if there is no signal in PMT, the ADC will still give a non-zero value, which represents the electronic noise. Such non-zero value is called pedestal.

summed over a sample of elastic events:

$$\begin{aligned}\chi^2 &= \sum_{i=1}^{N}\Big(E_e^i - \sum_{j=0}^{M} C_j A_j^i\Big)^2 \\ &= \sum_{i=1}^{N}\Big((E_e^i)^2 + \Big(\sum_{j=0}^{M} C_j A_j^i\Big)^2 - 2E_e^i \sum_{j=0}^{M} C_j A_j^i\Big). \end{aligned} \tag{5.30}$$

The E_e is the reconstructed energy of the scattered electron from the optics module. C_k is the coefficient and A_k is the measured pedestal subtracted ADC amplitude for the k^{th} block. The M is the total number of the blocks in total shower cluster. The linear regression method is then used to calculate the coefficients.

$$\frac{\partial \chi^2}{\partial C_k} = 0, \tag{5.31}$$

The equations of this linear system can be expressed in the matrix form:

$$MC = B, \tag{5.32}$$

where

$$B = \begin{pmatrix} \sum_{i=1}^{N} E_e^i A_0^i \\ \cdot \\ \cdot \\ \cdot \\ \sum_{i=1}^{N} E_e^i A_M^i \end{pmatrix}, \tag{5.33}$$

$$B = \begin{pmatrix} \sum_{i=1}^{N} E_e^i A_0^i \\ \cdot \\ \cdot \\ \cdot \\ \sum_{i=1}^{N} E_e^i A_M^i \end{pmatrix}, \tag{5.34}$$

$$C = \begin{pmatrix} C_0 \\ \cdot \\ \cdot \\ \cdot \\ C_M \end{pmatrix}, \tag{5.35}$$

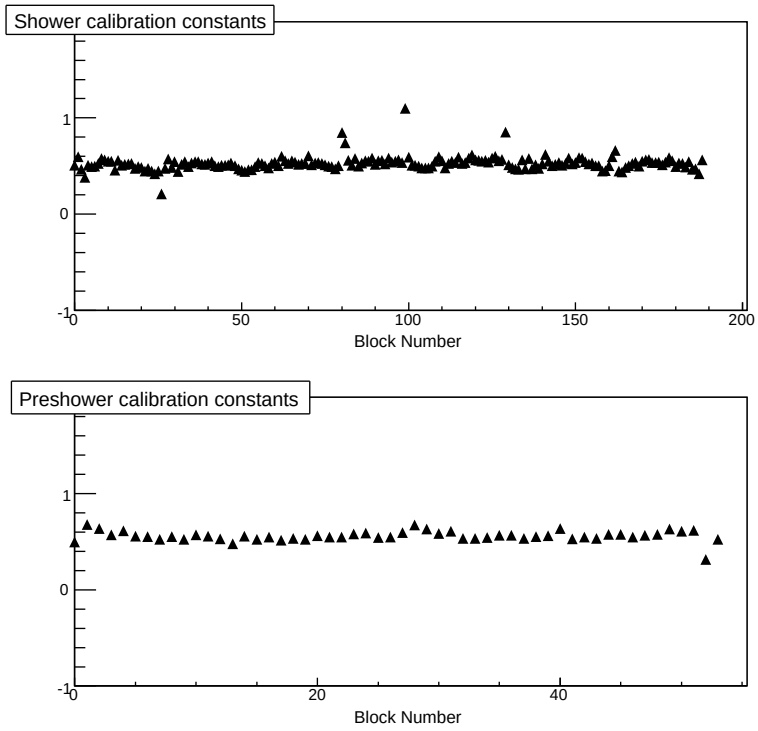

FIGURE 5.31: Preshower and shower calibration coefficients.

and the matrix elements of matrix M can be written as

$$M_{lm} = \sum_{i=1}^{N} A_l^i A_m^i. \tag{5.36}$$

The above linear system equations can be solved by inverting the matrix. Therefore, the coefficients in the matrix C are obtained. In total, there are 243 blocks, including 189 from the shower and 54 from the preshower, involved in the calibration process.

Such calibration procedure was implemented using the combined data from both incident beam energies. The momentum range of the scattered electrons was 0.8 - 2.0 GeV. The elastic events were selected by cutting on the momentum vs. scattered angle (θ) and selecting the elastic stripe (see Fig. 5.23). In addition, cuts were placed on the preshower energy deposition to remove the contaminated pions. The obtained set of coefficients were used for the entire data set of experiment E06-010.

Fig. 5.31 shows the ratio between the energy deposition in the shower system and

the reconstructed momentum for two incident beam energies. All the events shown in this plot passed the aforementioned cuts for selecting elastic events. An average energy resolution of about $\sigma_{E/p} = 8\%$ is achieved, while the energy resolution at high momentum is slightly better than that at low momentum.

5.1.4 Left HRS VDC

The left HRS VDC calibration was performed by C. Dutta from University of Kenkucky. The principle is very similar to the one discussed in Sec. 5.1.1 of the BigBite MWDC calibration. Since the HRS VDC is the standard Hall A equipment, the calibration only involved extracting t_0 for each wire. The rest of the procedure was not necessary. In practice, the t_0 of each wire was extracted by identifying the rising edge of the drift time spectrum.

5.1.5 Left HRS Gas Cerenkov

The principle of the gas Cerenkov calibration is similar to that of the BigBite calorimeter calibration, which is to align gains in all PMTs. In the case of gas Cerenkov, the calibration involved aligning the single photo-electron peak of each pedestal corrected ADC to channel 200. The purpose of this alignment was to make sure that all the events that were not electrons and assumed to be mostly pions were peaked at one specific ADC channel. The electrons, which were usually at high ADC channels, can then be cleanly separated from the non-electrons. In practice, the calibration procedure involved fitting each single photo-electron peak to a Gaussian shape. The mean of the Gaussian fit was then scaled to channel 200. Right panel of Fig. 5.32 shows the sum of the gas Cerenkov detector for a negative polarity run.

5.1.6 Left HRS Aerogel

The calibration of the HRS aerogel detector is similar to the calibration of the gas Cerenkov. Instead of channel 200 in the gas Cerenkov detector, the pedestal corrected

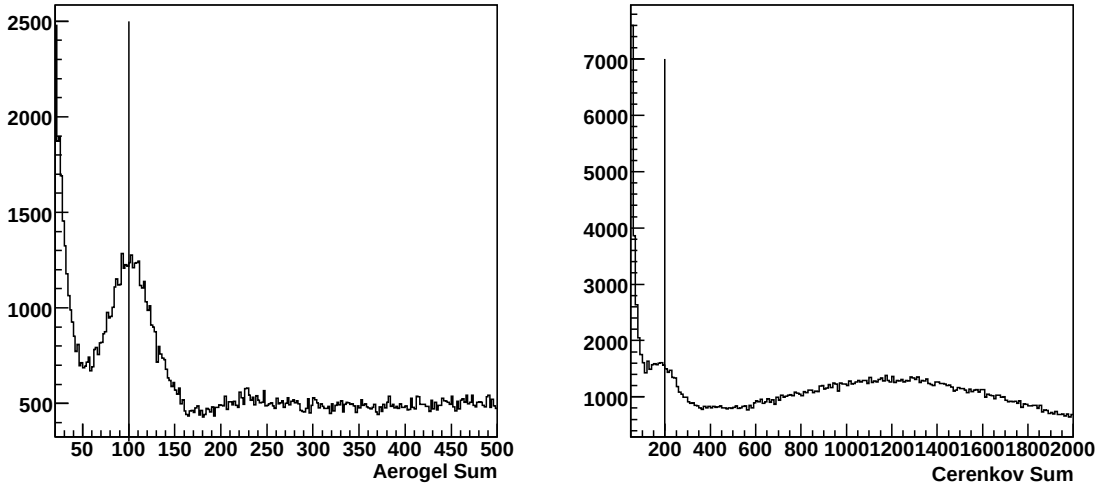

FIGURE 5.32: Left panel: Aerogel Sum; Right panel: Gas Cerenkov Sum.

single photo-electron peak for each aerogel PMT was aligned to channel 100. Left panel of Fig. 5.32 shows the sum of the aerogel detector for a positive polarity run.

5.1.7 Left HRS Calorimeter

The HRS calorimeter calibration was performed by D. Flay from Temple University. The calibration of the HRS calorimeter is similar to that of the BigBite Calorimeter, which is described in Sec. 5.1.3. Fig. 5.33 shows the ratio of the energy deposition to the reconstructed momentum. The electrons and pions are identified from HRS Cerenkov detector.

5.1.8 Left HRS Optics

The left HRS optics calibration was performed by J. Huang from M. I. T. The general procedure in Ref. [274] was followed. The goal of this calibration was to determine

- $y_{\rm tg}$ and $z_{\rm react}$: for vertex coincidence with BigBite spectrometer, suppressing the random coincidence background.
- $\theta_{\rm tg}$ and $\phi_{\rm tg}$: for reconstructing 3-vector momenta.

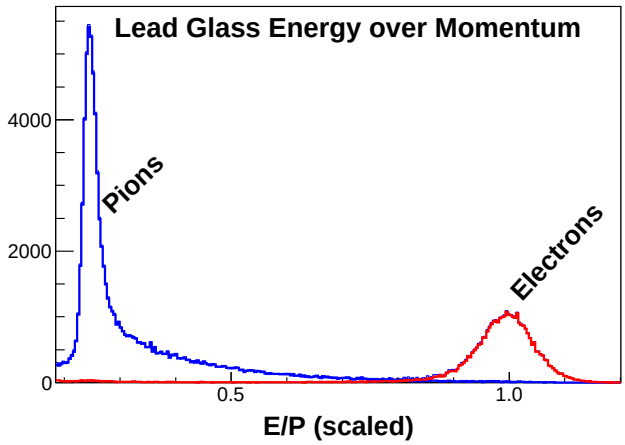

FIGURE 5.33: E/p plot for the left HRS calorimeter.

- $\delta_{\rm tg}$: for obtaining the absolute momentum value.

Due to the small momentum coverage of the HRS, the δ resolution is in general not crucial in experiment E06-010. The data used in calibration include the runs taken with the multi-carbon foils (sieve-slit plate in/out in Left HRS) and with elastic reference cell filled with ^{3}He, H_2, and N_2.

Similar to the BigBite Vertex reconstruction, the left HRS vertex was calibrated according to the locations of carbon foils. As shown in Fig. 5.34, all foil peaks were aligned to their actual positions. The average $z_{\rm react}$ resolution is 6 mm. The Left HRS and BigBite vertices are consistent to the level of 1 cm for coincidence events.

With carbon foil runs and the sieve-slit inserted, each good event corresponds to a specific carbon foil and one of the holes in the sieve-slit. By referencing to survey information [275], the actual angle of the vertex trajectory is known. The out-of-plane ($\theta_{\rm tg}$) and in-plane ($\phi_{\rm tg}$) angles were optimized by minimizing the difference between the calculated angle and the actual one. The final reconstructed sieve-slit is shown in Fig. 5.35

A set of runs similar to those used for the angular calibration was also used for the momentum calibration. The full momentum range of the spectrometer was covered

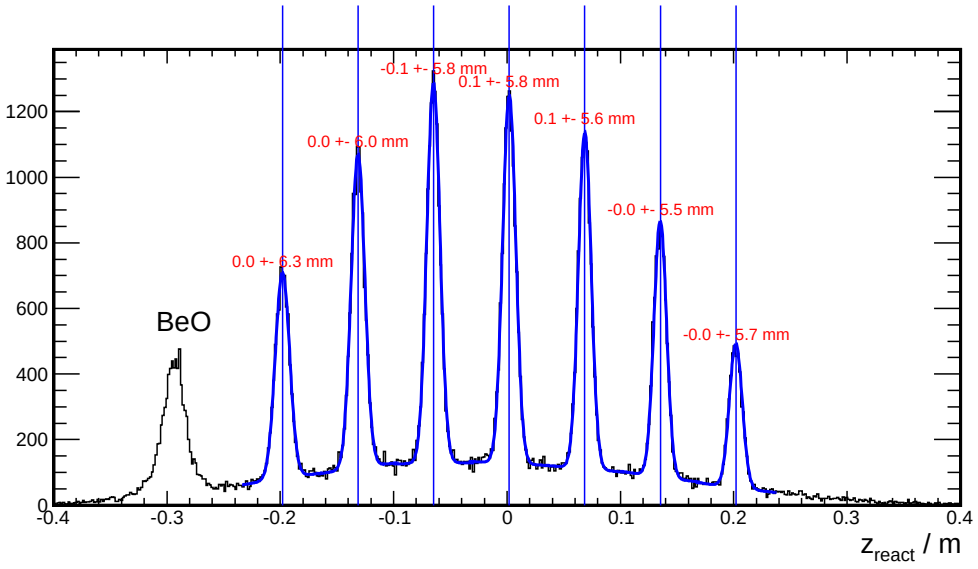

FIGURE 5.34: Reconstructed z_{react}: Each carbon peak is fitted and compared to its expected location. The left-most peak is the beryllium oxide foil.

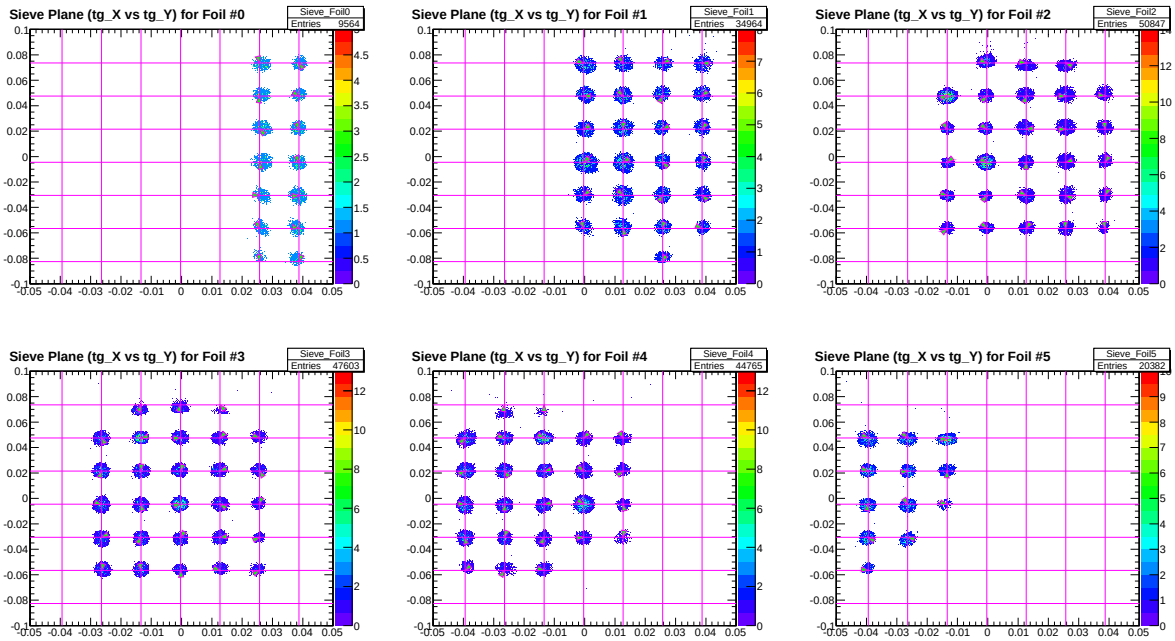

FIGURE 5.35: The reconstructed sieve-slit pattern (vertex trajectory projection at the sieve-slit plane): each plot is a single carbon foil; each crossing of pink lines represents the physical location of a sieve hole.

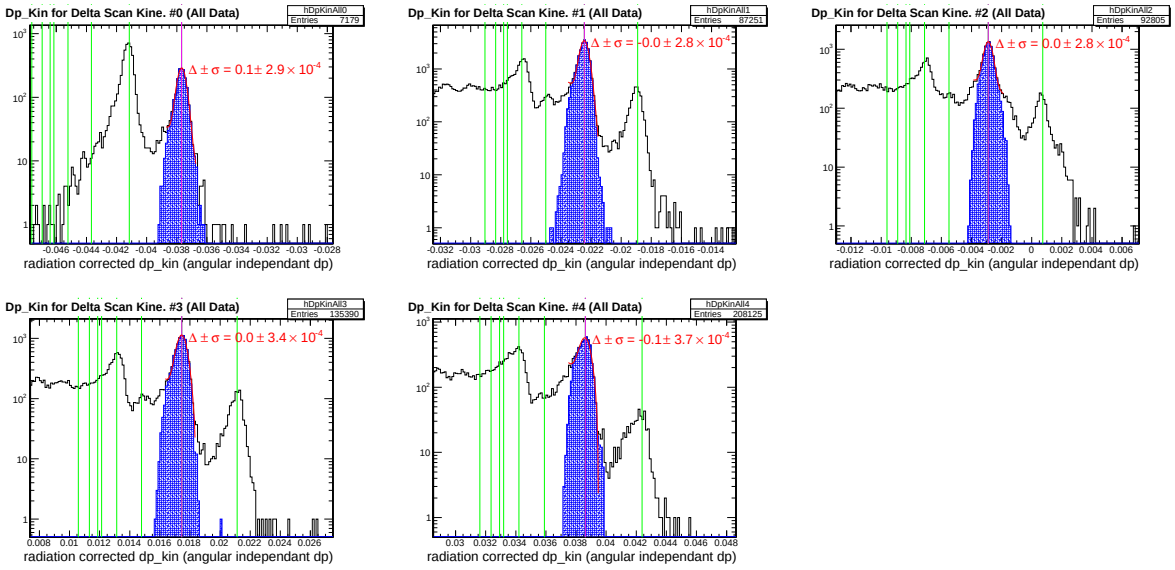

FIGURE 5.36: The reconstructed momentum of carbon elastic data for 5 momentum settings. The black curve is data, within which, the blue shaded area shows the data selected to be optimized toward the expected value (marked by magenta vertical lines). The blue areas are fitted and compared to the expectation, which are colored by red. The green lines mark out ground and other excitation states that were not optimized. These peaks also agree well with the reconstruction.

by moving the carbon elastic peak across the focal plane in a δ-scan: $p_0 = 0\%$, $\pm 2\%$ and $\pm 4\%$. For each momentum setting, a specific carbon ground state or excitation state was selected. An optimization was performed with all momentum settings simultaneously. The final results are shown in Fig. 5.36 with an achieved resolution better than 5×10^{-4}.

The optics matrix, calibrated as described earlier, is only applicable when the spectrometer angle is 90^o and the beam propagates along the center line of the hall. Therefore, in other conditions, a set of simple corrections, called "Extended Target Correction", need to be applied. Since the leading-order correction is linearly correlated with the vertical beam position, it is also called the raster correction. The extended target correction was applied to the production data with the information of the beam position.

5.1.9 Coincidence Timing

In each spectrometer, one can reconstructed the time when the corresponding particle leaves the target from the recorded time in the detector package. Such procedure is also referred to as the timing calibration. The left HRS timing calibration was performed by C. Dutta from University of Kentucky. The BigBite timing calibration was preformed by J. Huang from M. I. T. In general, the coincidence time is defined as the difference between the reconstructed time from the two spectrometers. Since the reconstructed time in the left HRS would depend on the particle species (π, K, or proton), three coincidence timings were calculated. The coincidence of different species of particle would appear at different locations in a coincidence timing spectrum. As a result, the coincidence timing can be used to do PID in the left HRS. For example, the kaon peak will be $\sim$ 1.8 ns apart from that of the pion, and the proton-pion peak separation is $\sim$ 6 ns. A smaller coincidence timing resolution will lead to a better kaon identification.

In the calculation, the coincidence timing is separated into three parts:

$$\text{CT} = \text{RF Time}_{\text{LHRS}} - \text{RF Time}_{\text{BigBite}} - \text{Trigger Time Difference}\,, \tag{5.37}$$

where "Trigger Time Difference" is the time difference between two single arm triggers, and RF $\text{Time}_{\text{Spectrometer}}$ [3] is defined as the amount of time between time of reaction and single arm trigger. RF $\text{Time}_{\text{Spectrometer}}$ includes contributions from

- TOF: amount of time for a particle to travel from the reaction point to the timing detector.
- Response time of timing detector including detector response time, cable delay, and electronic process time.

[3] Spectrometer can be BigBite or LHRS.

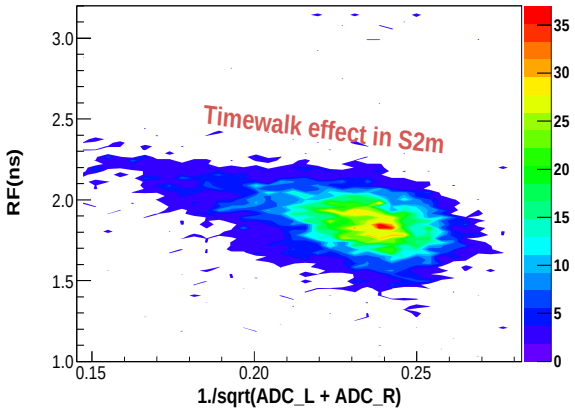

FIGURE 5.37: Time-walk effect for S2m.

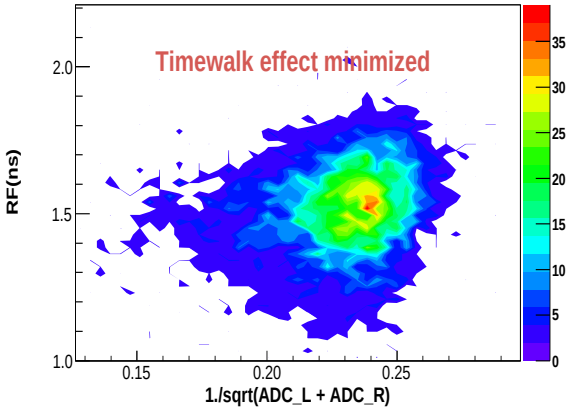

FIGURE 5.38: Time-walk effect corrected.

- Time difference between timing detector signal and trigger signal. These values are recorded using high resolution (60.2 ps on BigBite and 50.0 ps on Left HRS) TDCs.

The RF $\text{Time}_{\text{Spectrometer}}$ was named after its calibration procedures: during experiment E06-010, the beam RF signal, which characterizes the beam bunch time, was recorded in TDCs (noted as t_{RF}), relative to the single arm trigger signal. Therefore, when the spectrometer's angle is small, RF $\text{Time}_{\text{Spectrometer}} - t_{\text{RF}}$, also referred to as the RF or RF Structure for short in later section, would appear as sharp peaks every 2 ns (beam bunch spacing). By minimizing the width of these peaks, RF $\text{Time}_{\text{Spectrometer}}$ was calibrated separately for each arm.

Left HRS Single Arm Timing Calibration

In the Left HRS, the time reference was defined by the S2m scintillators. The 2 ns RF structure of the beam bunch was used as a reference for the analysis. In order to achieve a resolution at the level of a few hundred ps in the RF structure, various factors had to be corrected and implemented, which included the path-length corrections, time-walk corrections, and scintillator time offset corrections. The path-length corrections were performed paddle by paddle. Once it was finished for a simple

paddle, the timing structure would emerge for that particular paddle by plotting a quantity, RF, defined as:

$$\mathrm{RF} = t_{\mathrm{RF}} - \frac{(t_{\mathrm{Left}} + t_{\mathrm{Right}})}{2} + \frac{\text{path-length}}{c}\,, \tag{5.38}$$

where t_{Left} (t_{Right}) is the scintillator time from the left-side (right-side) of the paddle, and c is the speed of light. Such procedure was then extended to all 16 paddles of the S2m scintillator plane.

The time-walk correction for each paddle was evaluated by examining the dependence of the quantity RF as a function of the average of the left and right ADCs as shown in Fig. 5.37. Fig. 5.38 shows the time-walk effect corrected for that particular paddle. The time-walk correction was performed for pions. Even though the time-walk effect was considerably small, about 20 to 30 ps, the resolution could still be improved, and the tails of the spectrum were also reduced to some extent. Once the time-walk corrections were applied to all the paddles, a final alignment of the offsets was performed.

Finally when all these corrections were applied, the timing resolution from the Left HRS side was improved to ∼140 ps for the pions and ∼135 ps for the electrons as shown in Fig. 5.39 and Fig. 5.40, respectively.

BigBite Single Arm Timing Calibration

In the BigBite spectrometer, the timing detector is a scintillator plane inserted between the preshower and shower lead glass detectors. For an electron event, the primary electron, as well as secondary particles from electromagnetic shower inside the preshower detector, will fire at least one of the scintillator bars. The calibration of RF $\mathrm{Time}_{\mathrm{BigBite}}$ was simpler due to its shorter path-length and the similarity of speed of particles detected. Two series of RF times were generated for electron and photon candidates. The calibration procedure includes:

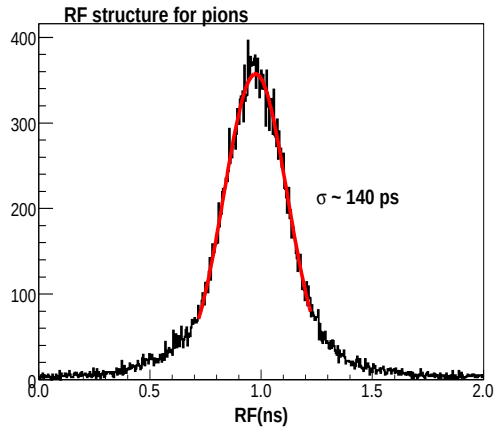

FIGURE 5.39: RF structure for pions

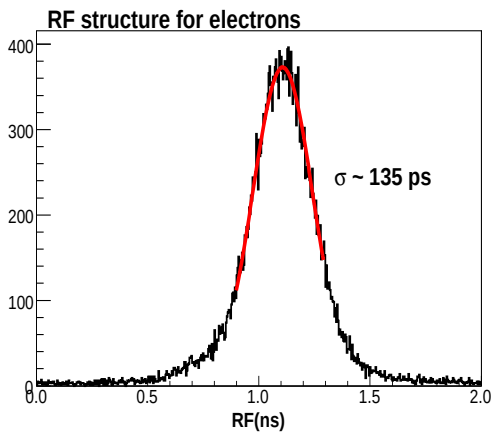

FIGURE 5.40: RF structure for electrons

- Scintillator bar time offset and time-walk effect correction:

  First, events firing only two neighboring scintillator bars were selected. The timing difference between these two bars were optimized toward zero by applying a time offset for each PMT as well as the time walk corrections. The time walk effect on each PMT was found to be similar so that a empirical formula, Eqn. (5.39) was used:

$$\Delta t_{\text{time walk}} = -17.9(\text{ADC} - \text{pedestal})^{-0.140}\text{ns}\,. \tag{5.39}$$

- path-length calibration:

  A simple linear correlation shown in Eqn. (5.40) was used to correct path-length differences:

$$\Delta L_{\text{time walk}}/c = 1.4 \cdot \theta_{\text{MWDC}}\,, \tag{5.40}$$

  Here, θ_{MWDC} is the tangent of the vertical track angle measured by the MWDC. It is also highly correlated with the vertical hit position on the chamber.

The final resolution of the RF time for the BigBite spectrometer was calibrated to ~ 270 ps, as shown in Fig. 5.41.

In a parallel study, the trigger detector (total shower detector) timing was also calibrated to achieve a better tracking performance in the drift chambers. The

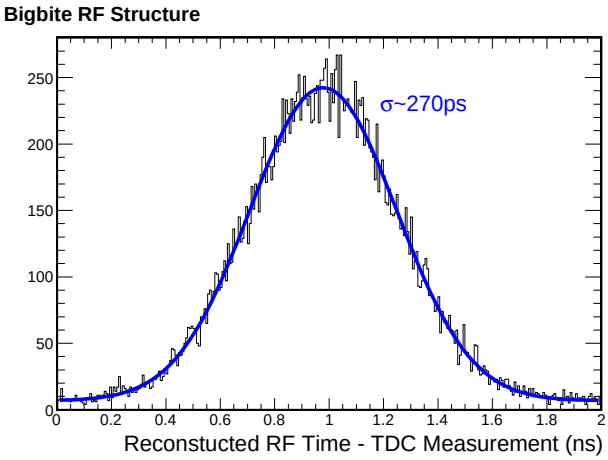

FIGURE 5.41: RF $\text{Time}_{\text{BigBite}} - t_{\text{RF}}$ for single arm electron events.

FWHM uncertainty of the trigger was reduced from ~ 8 ns down to ~ 4 ns, which is a $\sim 10\%$ improvement on the tracking quality χ^2/N_{dof}.

Two Arm Coincidence Time Calibration

The last term in Eqn. (5.37) was measured by a TDC with a resolution of 60.2 ps. A typical coincidence timing spectrum with the Left HRS detecting positive hadrons is shown in Fig. 5.42. Accounting for all the terms, the total coincidence timing reached a resolution of ~ 340 ps for $(e, e'\pi)$ reaction and ~ 400 ps for $(e, \gamma\pi)$ events. By cutting on the kaon coincidence timing with a window of ± 1 ns, pion rejection was better than $25:1$. Most of the pion leakage was from the non-Gaussian tails in the timing peaks.

5.2 Data quality check

During the three-month running of experiment E06-010, it was difficult to ensure all the detector components working perfectly all the time. Therefore, it is essential to perform a data quality check to exclude the bad data sections in order to reduce the possible systematic uncertainties. A complete list of studies performed in the data

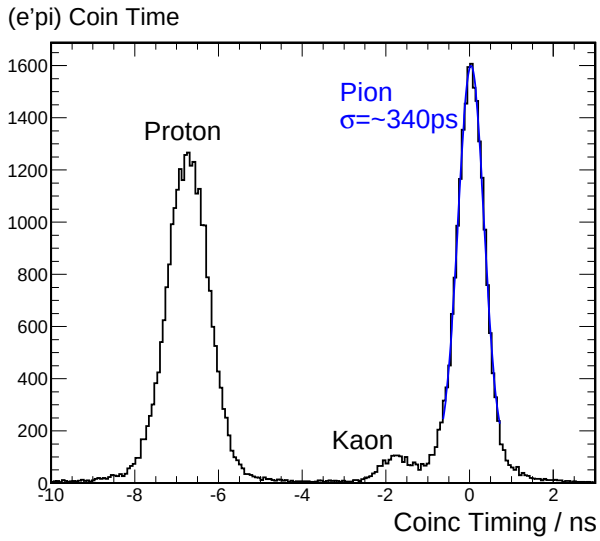

FIGURE 5.42: $(e, e'\pi)$ Coincidence timing spectrum for Left HRS at positive polarity.

quality check can be found in Sec. 9.6.

5.2.1 Run List

The run list of the transversity experiment was created with the information stored in the Hall A log book (`http://www.jlab.org/~adaq/halog/html/logdir.html`). It includes the following components:

- **General Run Information:**

  Such as the run time, beam current, beam energy, different detector configurations, and target name, etc.

- **Detailed Run Information:**

  This information including the collected beam charge, useful events in each trigger, etc., were obtained after replaying each run.

- **Labeling the Problems:**

  When the hardware problems happened during the experiment, shift crew would write down a log labeling the problems. Some of the problems would

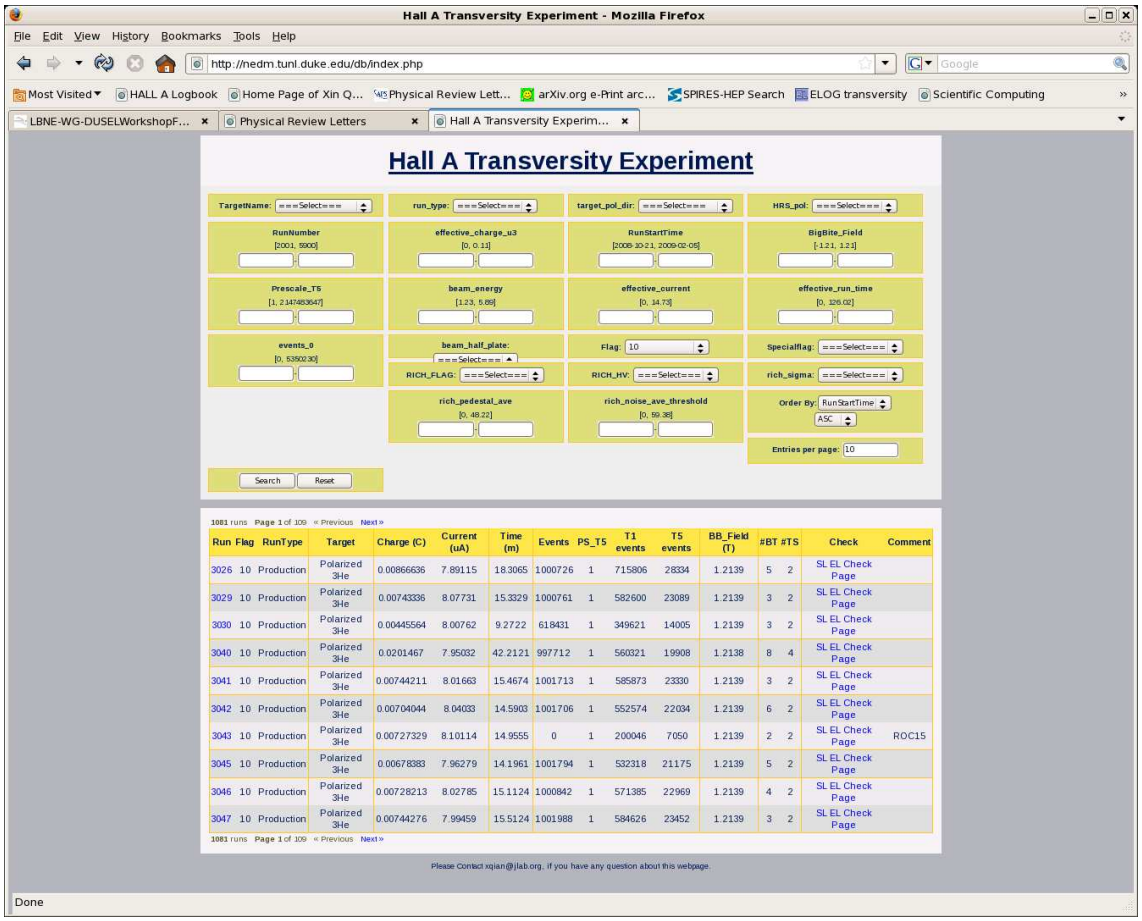

FIGURE 5.43: A screen shot of the transversity run list database.

lead to the corresponding data taken questionable. The log book was examined carefully and comments were added to the questionable runs. Meanwhile, the problems found during the data quality check procedure were also clearly labeled.

The run list was formed based on PHP/MYSQL. One can thus easily search/sort any run information. Fig. 5.43 shows a screen shot of the current run database. The website of the run list searching database is at `http://nedm.tunl.duke.edu/db/`.

5.2.2 Data Skim Process

During the data quality check, a set of software was developed to skim the rootfiles which were generated from the Hall A "ANALYZER". The goal of skimming the rootfiles are:

1. **Remove the bad regions from the data**:

   The bad regions including the beam trips, BigBite MWDC trips, trigger problems, dead time problem, etc., were removed from the data. In addition, the scalers were shifted accordingly.

2. **Calculate the kinematics**:

   In the BigBite side, about 10% of the events containing valid tracks had the more than one track. The current analyzer can not calculate the kinematics information for the second track. Therefore, all kinematics information were recalculated during the skim process.

3. **Reduce the rootfile size**:

   The rootfiles directly generated by the "ANALYZER" were usually several Gigabytes (GBs). Any analysis of such large rootfiles would be slow. In the skim process, only the essential variables were saved. The size of the skimmed rootfiles was only about 100 MBs, which significantly enhanced the speed of the analysis.

4. **Calculate the target spin-dependent scalers**:

   During the process of the scaler consistency check, which is discussed in Sec. 5.2.3, the ungated scalers were found to be the most reliable one. Therefore the target spin-dependent scalers were generated from the ungated scaler according to the spin state during the skim process.

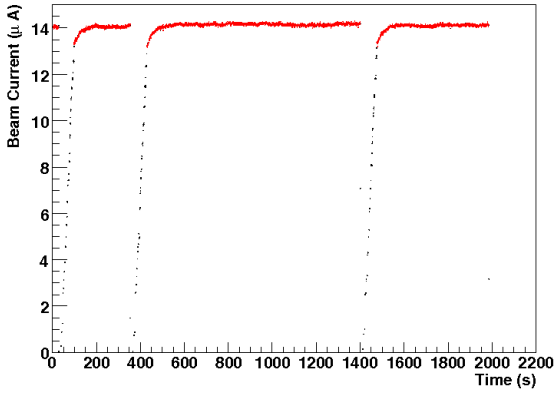

FIGURE 5.44: An example plot of the beam trips. The black points label the periods of data which were excluded in the analysis.

Beam Trip Cut

During experiment E06-010, the electron beam tripped from time to time due to various reasons. Fig. 5.44 shows the beam trips during one of the production runs. As discussed in Sec. 4.6, the BCMs only work accurately within certain ranges of beam current. Therefore, it is important to exclude the data when the electron beam tripped. Meanwhile, the scaler readings during the beam trip would also be excluded. In other words, the scalers were shifted accordingly. Since the scalers were read and stored in the data stream every 100 events[4], the smallest unit to remove the beam trip and to shift the scalers was 100 events. In order to label the period of data during the beam trips, the fast clock (103.7 kHz) readings at the start and end of the beam trips were recorded in order to perform the skim process for all the production runs. During the skim process, the events taken during the beam trips were labeled with a special flag. In addition, the scaler readings during this period were shifted. As a result, after the skim process, the scaler readings at the start and the end of each beam trip would be exactly the same.

[4] Every event within the 100 events has the same scaler reading.

BigBite Wire Chamber Trip Cut

During experiment E06-010, the load on the BigBite MWDC was very high, which was observed as a large current in the HV power supply[5]. A very high dark current is not healthy to the MWDC, and it increases the chances of breaking the MWDC or reducing the MWDC's lifetime. During experiment E06-010, the dark current in the HV power supply was set to $200\mu A$ to protect the wire chamber. At the 10^{37} nucleons/cm^2/s luminosity (15 μ A electron beam on a 40 cm long 10 amagats ^{3}He target with two target endcap windows), the dark current on the MWDC HV power supply was close to 180 μA, which was very close to the $200\mu A$ limit. Therefore, a small drift of the beam, such as hitting the glass wall of the target etc, would lead to a dark current higher than $200\mu A$. When it happened, the HV power supply will automatically shut down, leading to a trip of the BigBite MWDC. During those periods, the tracking information from MWDC would be lost. During the data quality check, periods of MWDC trips were also identified. In practice, the total number of hits for every 100 events were plotted against the fast clock. Each beam trip was identified by eye in the aforementioned plots. Similar to the treatment in removing the beam trips, the fast clock readings at the start and end points of the MWDC trip period were recorded.

DAQ Dead Time Cut

During one of the test in the data quality check procedure, the time to take every 100 events was plotted after removing the beam trips. Such time is directly linked to the overall event recording rate, and should be stable, since the beam trips were already removed. However, if there was some problems with the DAQ or computers, the rate

[5] When a charged particle passes through the MWDC, the electrons are ionized and drift to the signal wire. Meanwhile, in order to balance the charge, the electrons in the field wires or cathod planes will move and fill the position. Such movement forms a current, which is usually referred to as the dark current

would be reduced significantly. The data from such period were also removed in a similar manner as removing the beam and MWDC trips.

Other Cuts

Furthermore, a few other situations, such as Left HRS Q1 magnet trip, BigBite Calorimeter (trigger detector) trip etc. happened during experiment E06-010. The data taken in those periods were not useful. All those regions were identified during the data quality check, and removed from the data stream.

5.2.3 Scaler Consistency Check

The scaler consistency check was performed by M. Huang (Duke) under my guidance. In experiment E06-010, scalers were used to record the collected charges, the raw trigger counts, and the recorded trigger counts. The latter two were used to calculate the live time of the DAQ system. As described in Sec. 4.6, there are in total six BCM readings: u1, u3, and u10 for upstream BCMs, and d1, d3, and d10 for downstream BCMs. The difference between u3 (u10) and u1 is that the signal was amplified by 3 (10) times. In addition, as described in Sec. 4.11.4, each of the BCM scalers was recorded using one ungated scaler and four other scalers gated according to different target spin state and beam helicity states. Furthermore, as a redundancy check, each signal was split into two, one for each spectrometer. For the triggers, as illustrated in Table. 4.4, there were in total eight trigger channels, each for one trigger type. Each channel was also recorded by one ungated scaler and four gated scalers. The signal was also split to two spectrometers.

The following checks were performed in the scaler consistency check:

- **Left HRS vs. BigBite**:

  The scaler readings in Left HRS and BigBite should be exactly the same, since they were reading the same signal. However, after all, the signals were read by

different scalers. Therefore, such check is important for identifying problems with the scaler hardware.

- **Helicity - vs. Helicity +**:

  The beam helicity was flipped at a rate of 30 Hz, while the target spin was flipped every 20 mins. Thus, it was expected that the scaler readings of helicity + state were very close to those helicity - state.

- **Charges from different BCMs**:

  Assuming majority of the BCMs were good, the problems with BCMs could be identified by comparing the readings from different BCMs.

The results of the scaler consistency check are summarized in Table. 5.2. It was found that the ungated scaler was the most reliable one. Therefore, the ungated scaler was used to calculate the target spin dependent scalers according to the target spin state recorded in each event, which effectively synchronized the target spin state recorded in each event with the target spin dependent scalers. In this case, some data near the edge (generally fewer than 100 events at each spin flip) were thrown away, since the scalers were read every 100 events.

Table 5.2: The results of the scaler consistency check are summarized. "Left" labels the situation when there was a problem with the scaler on the Left HRS. 10^{-6} means that the asymmetry between the Left HRS and BigBite readings was on the order or 10^{-6}.

(Target,Beam)	u1	d1	u3	d3	u10	d10	t1	t3	t5	t6
Ungated	$\surd$	$\surd$	10^{-6}	10^{-6}	$\surd$	10^{-6}	$\surd$	$\surd$	10^{-4}	10^{-4}
–	Left	Left	Left	Left	Left	Left	Left	Left	Left	Left
-+	$\surd$	$\surd$	$\surd$	$\surd$	$\surd$	$\surd$	$\surd$	$\surd$	$\surd$	$\surd$
+-	$\surd$	$\surd$	$\surd$	$\surd$	$\surd$	$\surd$	$\surd$	$\surd$	$\surd$	$\surd$
++	$\surd$	$\surd$	$\surd$	Left	$\surd$	$\surd$	$\surd$	$\surd$	$\surd$	Left

5.2.4 Observed Problems and Solutions

Through the entire running period of experiment E06-010, there were a few major hardware problems. All of them were identified quickly and fixed in the experiment. In this section, we describe the problems and present the solutions used in the data analysis.

BigBite Retiming

As discussed in Sec. 4.11.1, a special BigBite retiming circuit was implemented in the trigger in order to fix the reference time for different trigger types. This was important, since the formation times for different trigger types were different. For example, the coincidence trigger T5 would take more steps in order to form coincidence signal than the singles BigBite trigger T1. As the BigBite retiming circuit was implemented after Nov 16th 2008, the data before suffered from the reference times for different trigger types were different. The problems include :

- BigBite Singles Trigger:

  There were two major BigBite singles trigger: T1 and T6. They had different thresholds on the TSUM. Since the T1 and T6 were formed from different trigger circuits, the T1 arrived about 6 ns later than the T6, when both of them were triggered by the same event. Such time difference led to a problem for all the T6 events in calculating the drift time of MWDC. In other words, the t_0 for T1 and T6 would be different, and the t_0 of the data was calibrated with the T1 events. In order to correct for this effect, a 6 ns time shift was added for all T6 events in the replay software.

- Coincidence Trigger:

  As discussed in Sec. 4.11.3, the time of the T5 was defined by the leading edge of the T1. Therefore, the majority of T5 events would not be affected by the

aforementioned retiming problem. However, this is not the case for the events when a T3 and a T5 trigger were accepted by the DAQ at the same time. Those events are referred to as the T3/T5 events. This is a problem for the T3/T5 events, because the T3 trigger arrived earlier than the T5 trigger. Therefore, the T3 trigger would steal the trigger timing from the T5 trigger. Fortunately, a large prescale factor was applied to the T3 trigger. Thus, the number of T3/T5 events was much smaller than that of the T5 events. In this period, all the T3/T5 events were discarded. The asymmetries:

$$A = \frac{N^+_{T3T5}/N^+_{T5} - N^-_{T3T5}/N^-_{T5}}{N^+_{T3T5}/N^+_{T5} + N^-_{T3T5}/N^-_{T5}} \tag{5.41}$$

are shown in Fig. 5.45 for all four states: V+, V-, T+, and T-. The false asymmetries are smaller than 10^-3. Combining this result with the fact that the T3/T5 events were about 14% of all T5 events, and the fact that the T3/T5 events were only removed in the period before the implementation of the BigBite retiming circuit, whose accumulated charge is about 1/10 of the total accumulated charge in the entire experiment, the final false asymmetry due to removal of the T3/T5 events in this period is less than 10^{-5}, which is negligible in comparison with the projected statistical precision of 10^{-3}.

- Random Coincidence Background Subtraction:

  The trigger times before and after the implementation of the hardware retiming were different, which led to a problem in selecting the side band in order to subtract the random coincidence background. In the first period of the data, a special side band cut was used in the analysis.

- Effect on LHRS retiming:

  During this period, it was also found that the retiming module on the left HRS was used on the edge of its safe zone. This was due to the incorrect delay

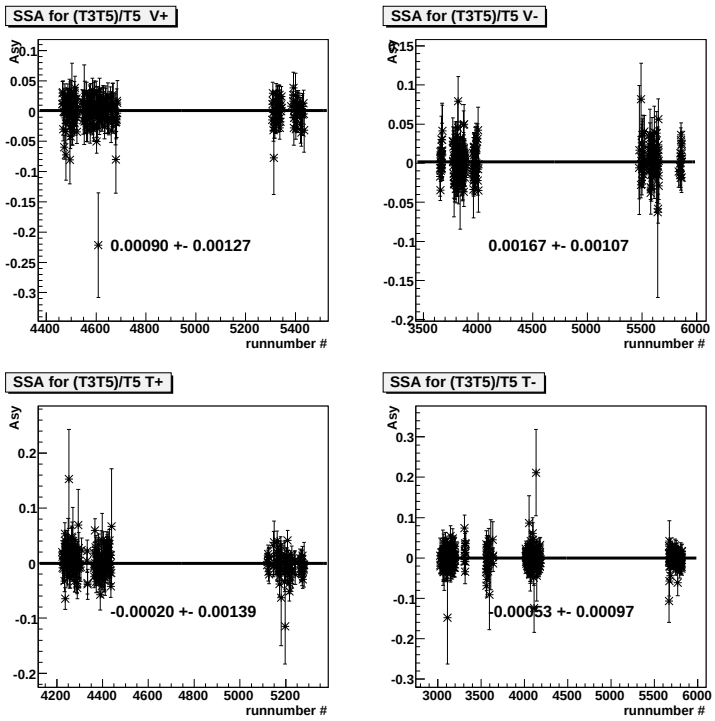

FIGURE 5.45: The false asymmetries due to BigBite retiming are plotted versus run number. The false asymmetries are fitted to a straight line.

of the T5 L1A signal. First graph of Fig. 5.46 shows various plots related to trigger timing for a problematic run. First panel shows the coincidence trigger time. Second panel shows the drift time in left HRS VDC v1 plane vs. the coincidence channel. The data between -120 and -110 were taken when the retiming completely failed. The data between -110 and -50 were taken when the retiming partially failed. In this case, the timing of the trigger was defined by the leading edge of the L1A signal, rather than the S2m signal in the Left HRS, since the L1A signal came too late. The third, fourth, and fifth panel shows the ADC readings of aerogel, gas Cerenkov and pion rejector respectively vs. the coincidence timing. Since the L1A signal defined the trigger time between -110 and -50, the ADC gates were also affected, leading to a shift in the ADC values. In the region between -110 and -120, the ADC gates were completely

off. The last panel shows the coincidence time vs. the coincidence trigger time. A shift in the slope was observed when the retiming module partially failed. The second graph shows the same plots for a good run after fixing this problem. Left (right) graph of Fig. 5.47 shows the related plots of S2m detectors for a problematic (good) run. The first and second panel show the S2m left and right ADC sum, respectively, vs. the coincidence timing. The ADC values were affected by the shift in the ADC gate. The third and fourth panel show the S2m left and right TDC, respectively, vs. the coincidence timing. The problem in the retiming module can be clearly observed. A software retiming module, developed by J. Huang from M. I. T., was added in the replay in order to correct this problem in this period for the offline analysis.

Trigger L1A Problem

During the January period of the data taking in experiment E06-010, a trigger L1A double pulsing problem occurred in the left HRS DAQ, which affected about 10% of events in about 56 runs. The problem was traced back to a bad cable. When the L1A was double pulsed in left HRS, multiple problems occurred:

- TDCs:

  When the L1A double pulsing problem occurred, the ROCs sometimes would miss the reference signal. In this case, the recorded time was incorrect. One could exclude these events by requiring the existence of the reference signal.

- ADCs:

  When the L1A double pulsing problem occurred, the ADC gates would sometimes be extended, which led to a shift of pedestal. When this happened, almost all the PMTs in different detectors would have a larger signal than the pedestal. In other words, almost all PMTs would be "fired". One thus could

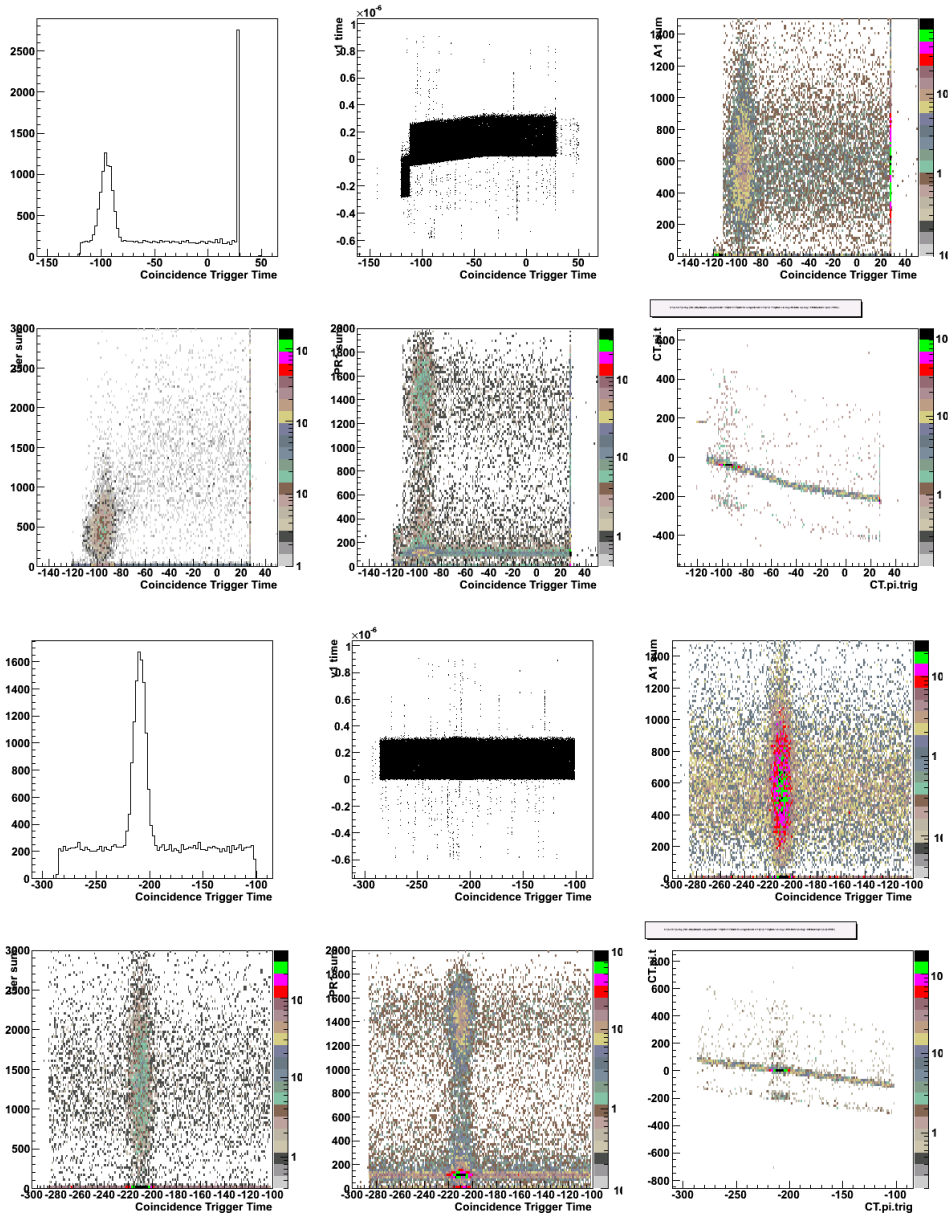

FIGURE 5.46: Left graph shows the various plots for a problematic run with the left retiming problem. The right graph shows the same plots for a good run after fixing this problem.

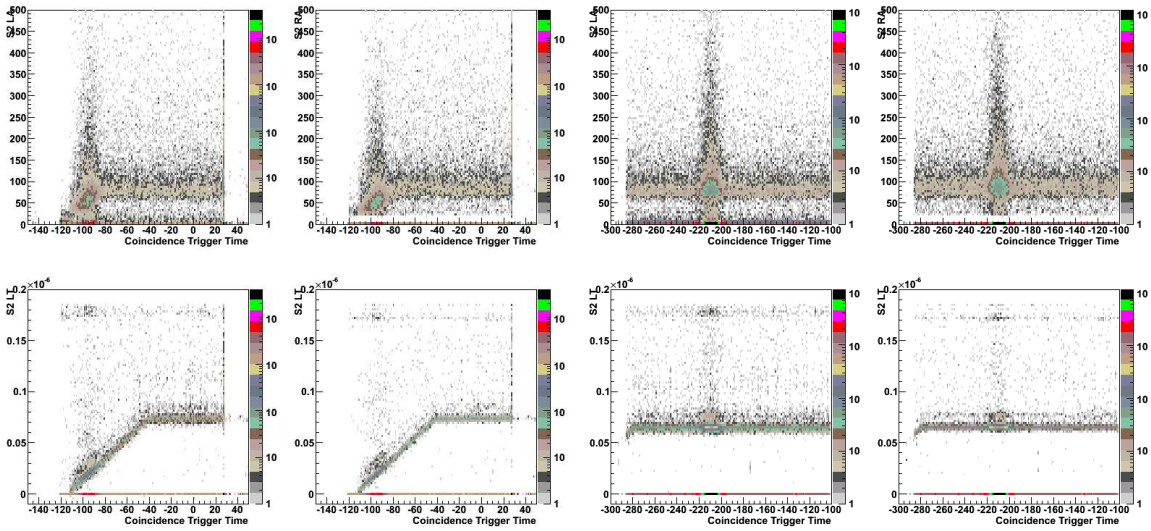

FIGURE 5.47: Left HRS retiming problem on S2m. Left graph shows various pots for a problematic run with the left retiming problem. The right graph shows the same plots for a good run after fixing this problem.

remove these events by adding a cut on the total number of channels fired in the system.

All the problematic L1A events were successfully identified and removed from data. Fig. 5.48 shows the comparison of a normal run (red) with a run with the L1A problem (black) before and after removing the L1A problematic events. In addition, the normalized yields and SSAs were checked with normal periods.

BigBite Calorimeter Radiation Damage

A gain drop was observed in the BigBite lead glass detector due to the radiation damage, especially in the preshower, from the background in experiment. There was about 15% drop the preshower and less than 5% drop in the shower. Since the threshold on the primary trigger T1 was set much lower ($\sim$ 300 MeV) than the energy of the scattered electron in which we were interested ($>$ 600 MeV), the effect was small. However, this issue severely affected the trigger T6 with a higher threshold.

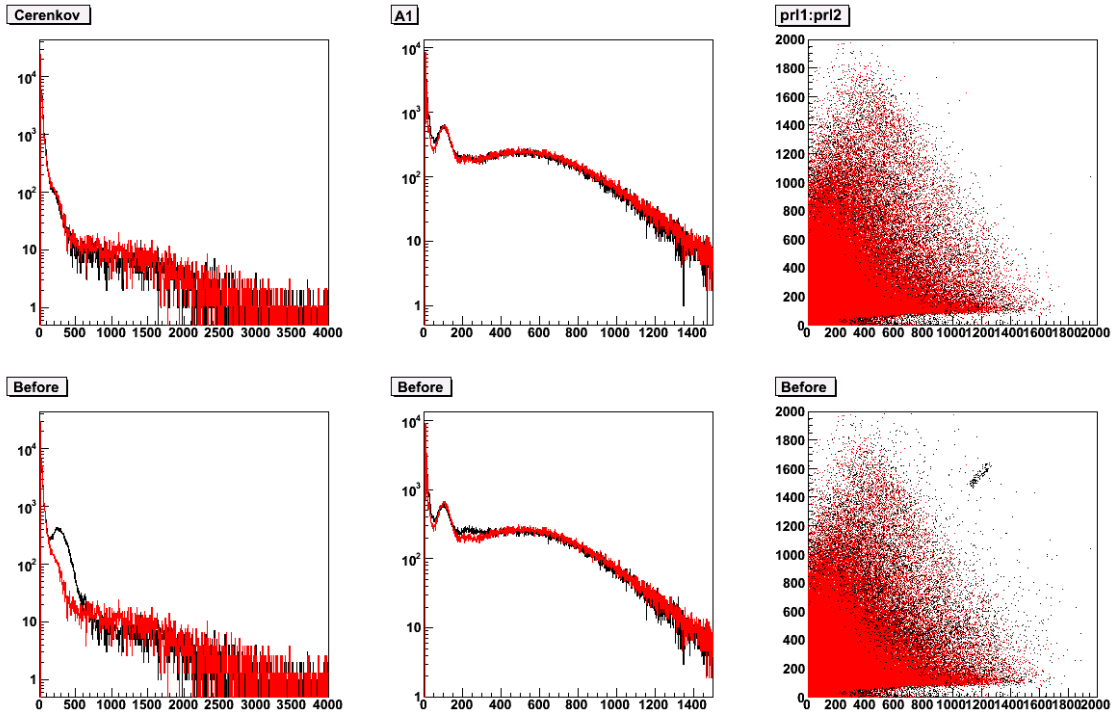

FIGURE 5.48: Red histograms/points are from a normal run. Black histograms/points are from a run with the L1A problem. The left panels show the left HRS Cerenkov ADC signal after subtracting the pedestal. The middle panels show the aerogel Cerenkov ADC signal after subtracting pedestal. The right panels show the ADC signal of the pion rejector layer-1 vs. the that of the layer-2. The top three panels show the comparison after removing the L1A problematic events. The bottom three panels show the comparison before removing them. The fact that distributions from the L1A run after removing the L1A events agree with those from a normal run demonstrates that the procedure of removing L1A events is successful.

Left panel of Fig. 5.49 shows the peak position of the minimum ionization energy deposition in the preshower vs. the accumulated charge in the experiment. The peak position clearly drifted to lower values as the accumulated charge increased[6]. In order to correct such a drift, a position and accumulated charge dependent correction with the following form:

$$E_{ps}^{cor} = E_{ps}^{raw}(a_0 + a_1 C) \tag{5.42}$$

[6] One expects the accumulated radiation level is proportional to the accumulated charge.

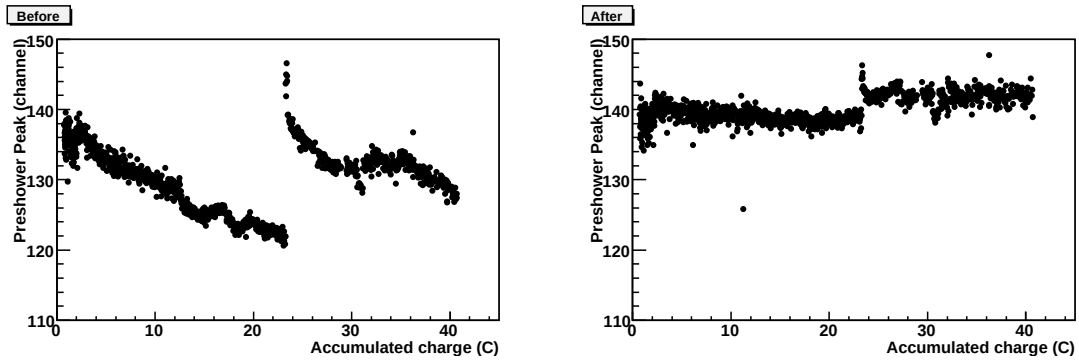

FIGURE 5.49: Radiation Damage on the BigBite Preshower Calorimeter. Left panel: peak positions of the minimum ionization in preshower are plotted against the accumulated charge before the software PMT gain correction. Right: same plot after the correction.

was applied to all the data. Here, E_{ps}^{raw} is the uncorrected preshower energy. a_0 and a_1 are fitting coefficients, which not only depend on different periods, but also depend on the position of the preshower block. C is the accumulated charge. The peak positions of all the runs were corrected back to the positions of runs taken at the beginning of the experiment. After the preshower correction, a similar procedure was used to correct the shower calorimeter. In this case, the same equation was used, except that the coefficients did not depend on the position of the shower blocks. The final E/p peak positions after corrections on preshower and shower are shown vs. the run number in Fig. 5.50.

5.3 Left HRS PID and Contamination Study

Three detectors were used to do PID in the left HRS. They were the pion rejector, gas Cerenkov, and the aerogel Cerenkov counter. Their responses to different particles are listed:

- Electrons and Pions fire aerogel Cerenkov counter. Thus, the cut is $A1 > 150$.

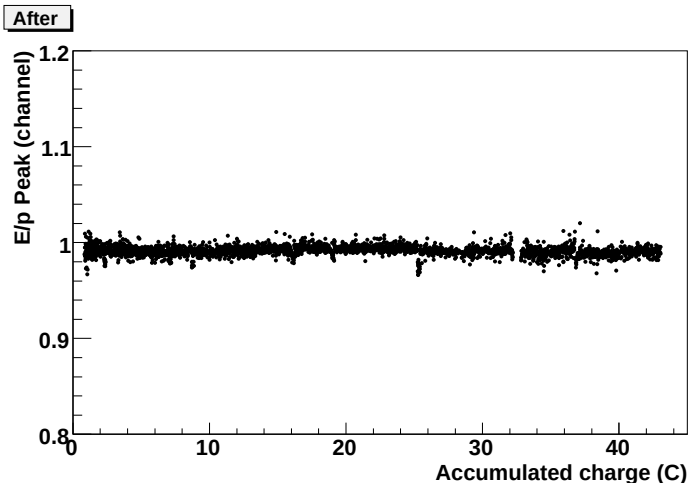

FIGURE 5.50: E/p peaks are plotted against run number after applying correction to both preshower and shower calorimeters.

- Electrons fire the light gas Cerenkov counter. Thus, the cut is $Cer > 300$.
- Pions and other hadrons do not fire the light gas Cerenkov counter. Thus, the cut is $Cer < 250$.
- Electrons result in a high E/p channel in the pion rejector. Thus, the cut is $E/p > 0.7$.
- Pions and other hadrons result in a low E/p channel in the pion rejector. Thus, the cut is $E/p < 0.6$.
- Kaons and protons (other hadrons) do not fire aerogel Cerenkov counter. Thus, the cut is $A1 < 150$.

In addition to these cuts, two acceptance cuts and an vertex cut were applied. The first acceptance cut is on the track projections on the pion rejector. The cuts are

$$-1.5 < \quad L.prl1.trx \quad < 1, \tag{5.43}$$

$$-0.2 < \quad L.ptrl1.try \quad < 0.2, \tag{5.44}$$

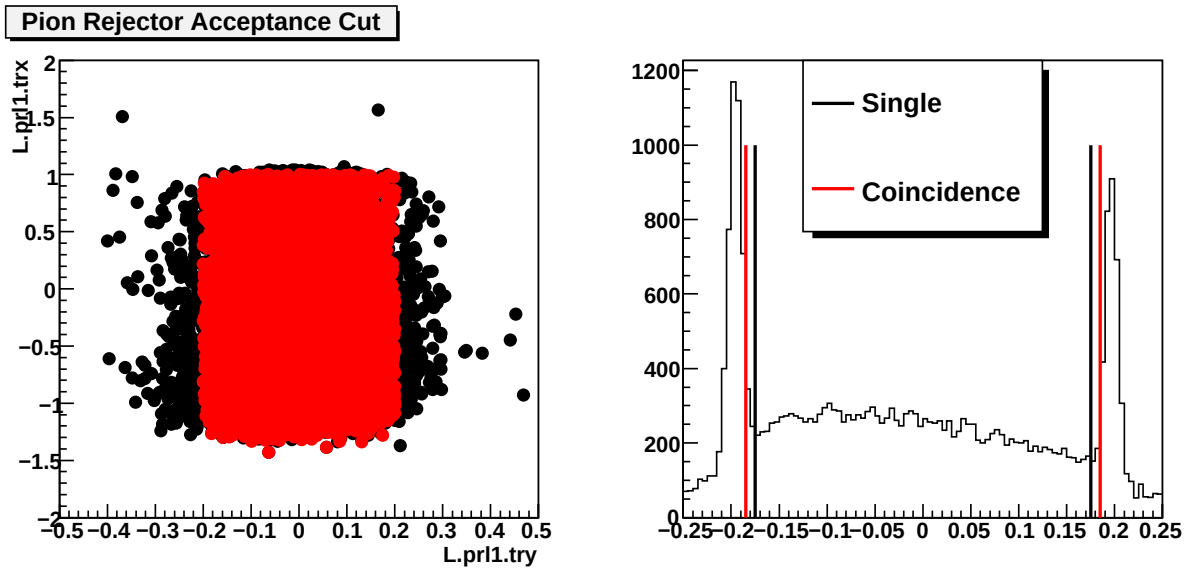

FIGURE 5.51: Left panel: Acceptance cut on calorimeter. Right panel: reaction vertex cut for single and coincidence events.

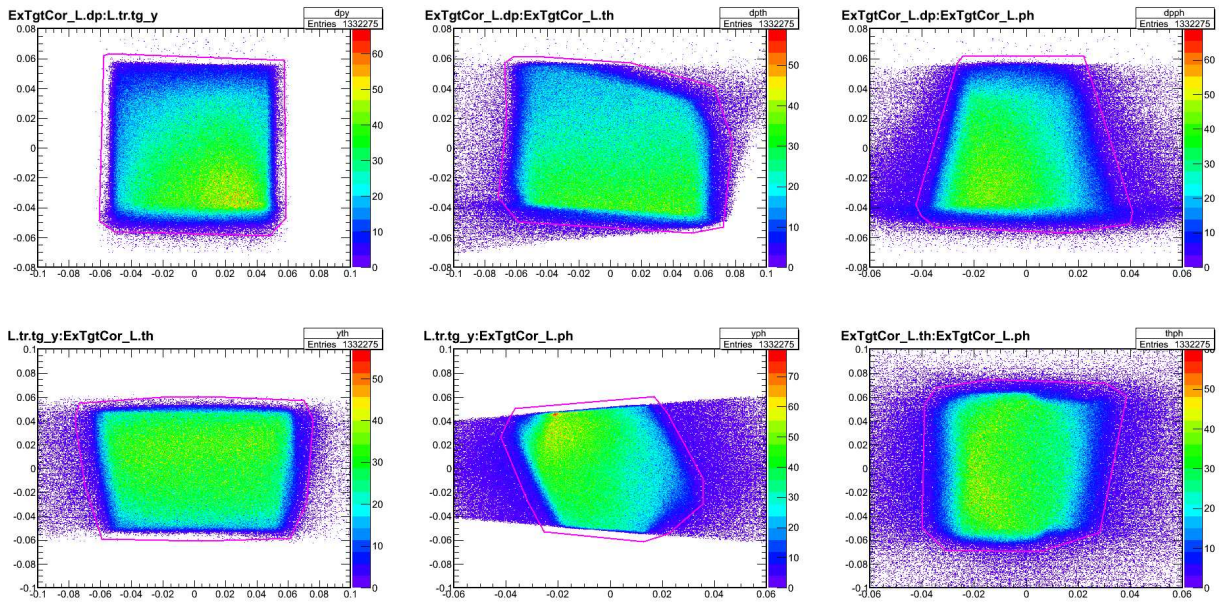

FIGURE 5.52: The six sets of 2-D graphic cuts were applied on two of four target kinematic variables: $target_y$, $target_\theta$, $target_\phi$, and δp.

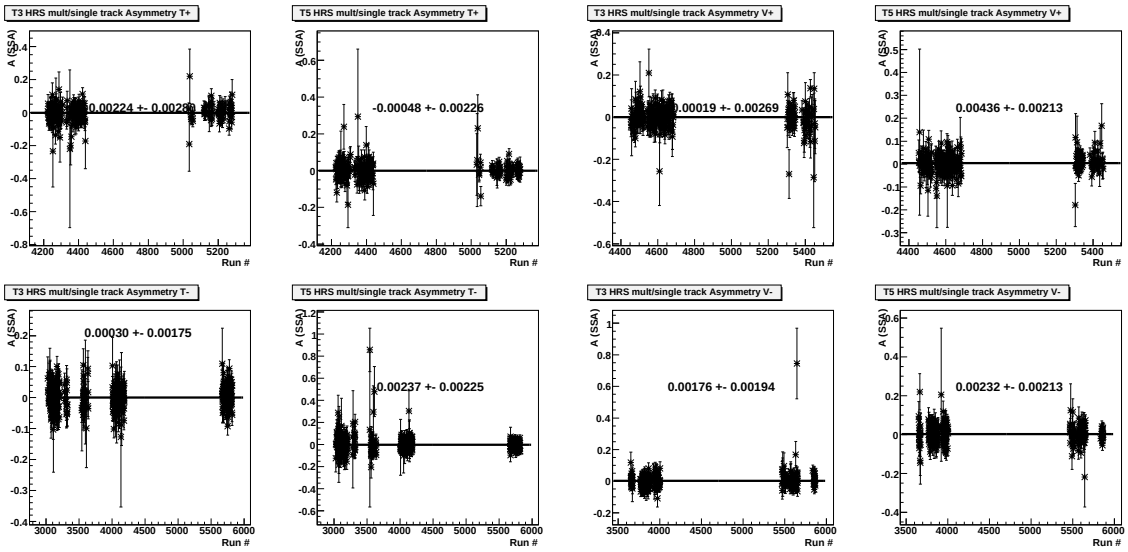

FIGURE 5.53: The false asymmetry due to the single-track cut in the left HRS for pions in T3 and T5 triggers for all four target spin states. The raw asymmetry is less than 5×10^{-3}.

where $L.prl1.trx$ is in the dispersive direction and $L.prl1.try$ is in the non-dispersive direction. The second acceptance cut includes six sets of 2-D graphic cuts applying on the two of four target kinematics variables: $target_y$, $target_\theta$, $target_\phi$, and δp. The third cut is the target vertex cut:

$$-0.175 < Vertex < 0.175. \tag{5.45}$$

The length unit is in meter. For coincidence events, the cut becomes:

$$-0.185 < Vertex < 0.185. \tag{5.46}$$

Fig. 5.51 shows acceptance cut on the calorimeter and the cut on vertex.

Furthermore, only events with single tracks were used in the analysis (ntrack == 1). The false asymmetry generated by this cut were studied by forming:

$$A = \frac{\frac{N^{\uparrow}_{mult}}{N^{\uparrow}_{single}} - \frac{N^{\downarrow}_{mult}}{N^{\downarrow}_{single}}}{\frac{N^{\uparrow}_{mult}}{N^{\uparrow}_{single}} - \frac{N^{\downarrow}_{mult}}{N^{\downarrow}_{single}}} \tag{5.47}$$

for pions in T3 left HRS single trigger and T5 coincidence trigger. Here, $\uparrow$ and $\downarrow$ in the superscript represent the events in two target spins states. The "single" and "mult" in the subscript represent the events with single-track and multi-tracks found, respectively. The results are shown in Fig. 5.53. The observed false asymmetry is less than 5×10^{-3}. Considering that the ratio of multi-track events to single-track events is in general less than 2%, the final false asymmetry due to the single track cut is less than 1×10^{-4}.

For the pion events, there are two sources of contamination. The first one is the electron and the second one is the kaons/protons. Gas Cerenkov and pion rejector gave a combined electron rejection factor better than $10^4 : 1$. The aerogel Cerenkov gave a kaon (proton) rejection factor better than $10 : 1$ estimated by the cross calibration of TOF. For kaons, the K^+/π^+ rate was about 6% and K^-/π^- is about 3% estimated from the E06-010 data. Therefore, the contamination of kaons into the pion sample was well below than 1%. The protons were completely rejected with the TOF cut in the coincidence channel (See TOF spectrum in Fig. 5.42).

5.4 BigBite PID

BigBite calorimeter system together with the reconstructed momentum information from MWDC were used to provide the PID. There are in total four categories including "electron-like", "negative-charged-hadron-like", "positive-charged-hadron-like", and "photon-like" events. In this section we describe the corresponding cuts used in each category.

5.4.1 General Cuts for Charged Particles

- Track Quality Cut:

  The quality of the reconstructed track is defined as χ^2/N_{dof}. Here N_{dof} is the number of degree of freedom, which equals to the number of planes used in the

tracking subtracts four, and

$$\chi^2 = \sum_i \frac{(x_{reconstructed} - x_{track})^2}{R_i^2}. \tag{5.48}$$

$x_{reconstructed} - x_{track}$, also called residual, is the difference between the reconstructed hit position ($x_{reconstructed}$) and the projected hit position by the reconstructed track (x_{track}). The R_i is the resolution assumed in the tracking software. Fig. 5.54 shows the χ^2/N_{dof} for the coincidence trigger (T5). P (N) represents the target spin 1/2 (-1/2) state. A cut of 2.4 was applied to remove the reconstructed tracks at high χ^2/N_{dof}. The false asymmetry introduced by this cut was estimated by comparing the mean of the χ^2/N_{dof} in the two spin states. We then scaled the mean value of χ^2/N_{dof} in T5N to the mean value of χ^2/N_{dof} in T5P. The number of events beyond the $\chi^2/N_{dof} < 2.4$ cut was counted. The false asymmetry was estimated with aforementioned numbers, and it was less than $1.5e^{-4}$.

- Track Matching Cut:

  As discussed in Sec. 5.1.3, the calorimeter provided the center position of the reconstructed shower cluster. For any charged particle, the position of the reconstructed cluster center (x and y) should match with the projected position from the reconstructed track on the shower. Since the energy deposition of electron and hadrons were quite different in the calorimeter, separate cuts were applied.

- Optics Validity Cut:

  As discussed in Sec. 5.1.2, at the very top and bottom of BigBite magnet, the magnetic field is weaker than that in the middle of the BigBite magnet. The optics reconstruction failed these extreme regions. Therefore a 2-D graphic cut was used to exclude these two regions. Fig. 5.55 shows the effect of this cut.

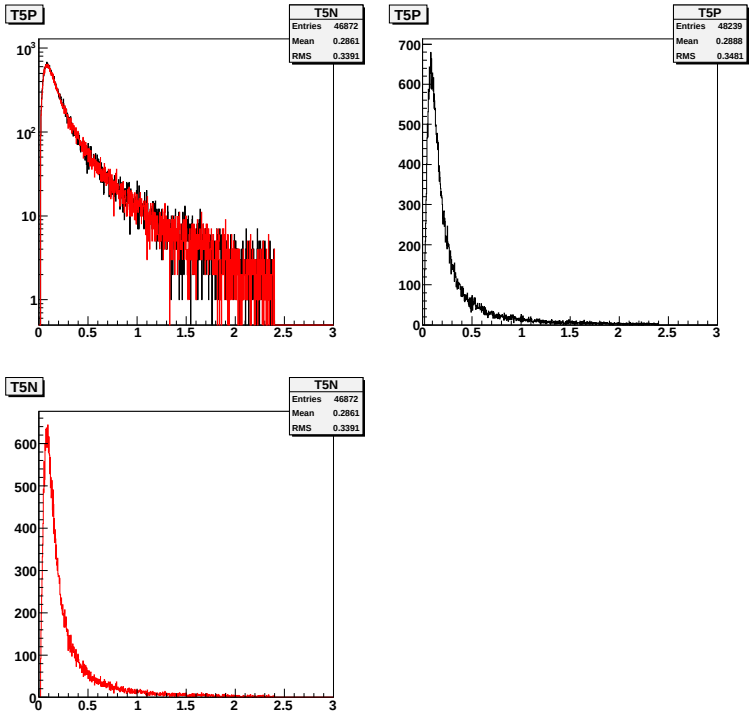

FIGURE 5.54: The track quality χ^2/N_{dof} was presented for the coincidence trigger T5. P (N) represents the target spin 1/2 (-1/2) state. The tracks with $\chi^2/N_{dof} > 2.4$ were removed.

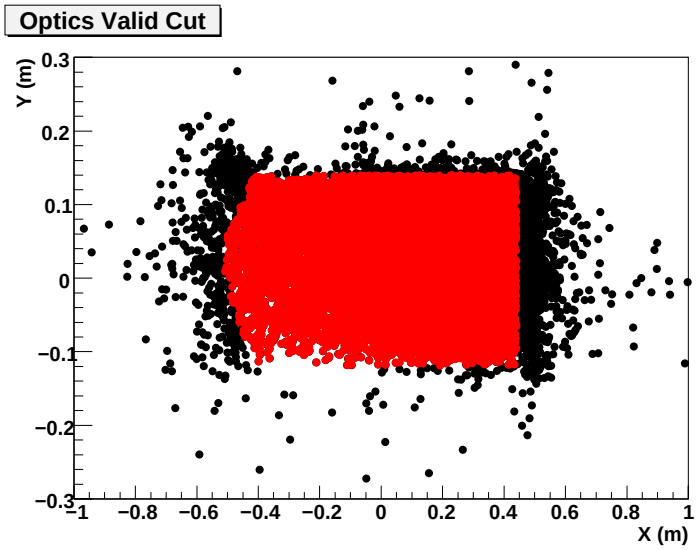

FIGURE 5.55: The black points represent all the tracks reconstructed in the BigBite. The red points represent the one pass the optics validity cut.

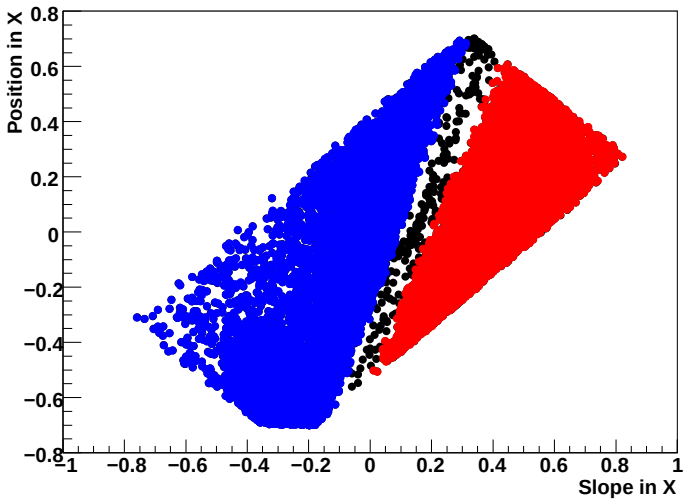

FIGURE 5.56: Vertical position (Position in X) vs. the vertical slope (Slope in X) in the first chamber. The blue points are the negative charged particle. The red points are the positive charged particles. The black points include everything.

- Charge Type Cut:

  The charges of the particles were identified from the reconstructed tracks. Since the BigBite magnet provide a simple dipole field, the negatively charged particles are bent up and the positively charged particles are bent down. Therefore, they are clearly separated in the plot of vertical position (Position in X) and the vertical slope (Slope in X) in the first chamber, as illustrated in Fig. 5.56.

- Calorimeter PID cut:

  The PID on the calorimeter system was performed with a 2-D cut on the energy deposited in preshower vs. the E/p, the ratio of the total energy deposited in the shower system to the reconstructed momentum. Fig. 5.57 shows a typical PID plot with T6 trigger. The corresponding regions for electrons and pions are labeled.

- Interaction Vertex cut :

  A cut was applied to the interaction vertex. Slightly different cuts were chosen

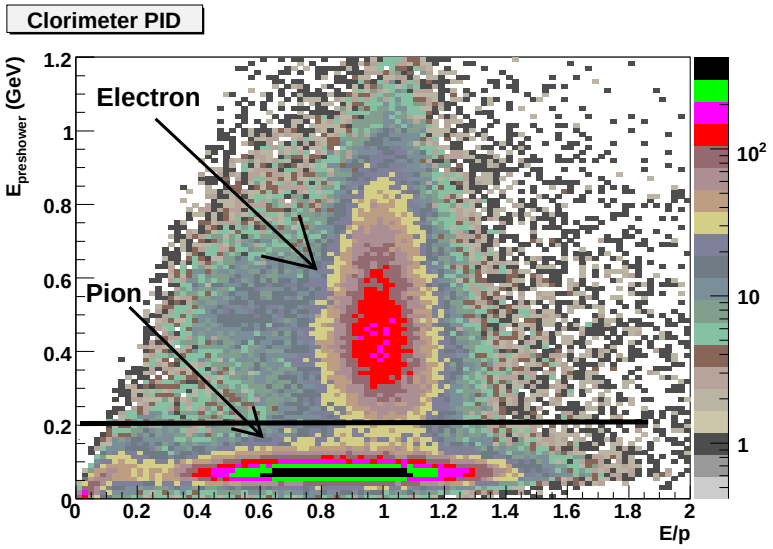

FIGURE 5.57: Energy deposition in the preshower vs. the E/p. Electrons and pions (hadrons) are labeled.

for the singles (T1 and T6) and coincidence (T5) events. Fig. 5.58 shows the cut positions.

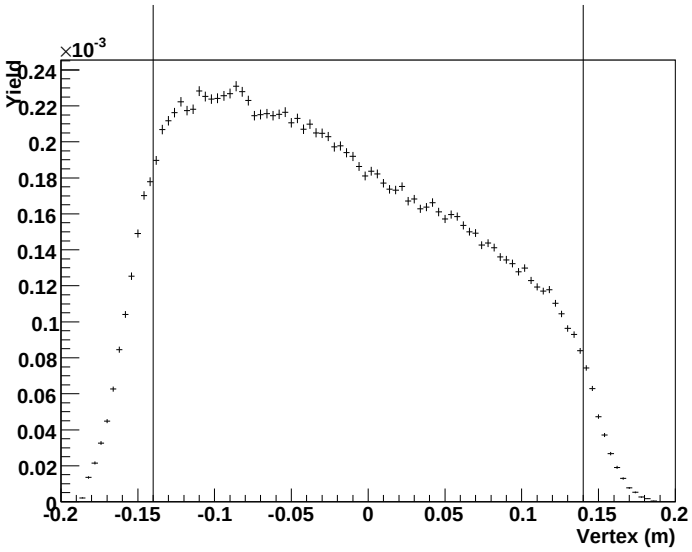

FIGURE 5.58: Reconstructed vertex is shown for electron-like events. The cut positions for coincidence and singles BigBite events are illustrated. The drops around ± 0.2 m in the reconstructed vertex are due to the BigBite target collimator.

5.4.2 Electron-Like Events

Most of the cuts for identifying electron in BigBite have been discussed in Sec. 5.4.1. Here we describe the additional cuts.

- Negatively Charged Particle Cut.
- Energy deposition in preshower: remove pions.

$$E_{preshower} > 0.2\ GeV \tag{5.49}$$

- Particle momentum cut:

$$0.6 < p < 2.5 \tag{5.50}$$

- E/p cut:

  An momentum dependent E/p cut was used to identify electron. Fig. 5.59 shows the distribution of E/p vs. the particle momentum after applying other cuts. The data were then binned into different momentum bins. Within each momentum bin, the E/p distribution was fitted with a Gaussian function. The center and σ of the fit are plotted in Fig. 5.60. A 2.5-σ cut was used as the standard cut.

- Position match cut:

  The center of the shower cluster was matched with the projected track position. A similar treatment as the one used in obtaining the momentum dependent E/p cut was used in obtaining the momentum dependent position match cut in both X and Y. Fig. 5.61 shows the center and σ of the Gaussian fit to the track match distribution, which is the difference between the projected track position and the center of shower cluster, for both directions. A 3-σ cut was used as the standard cut.

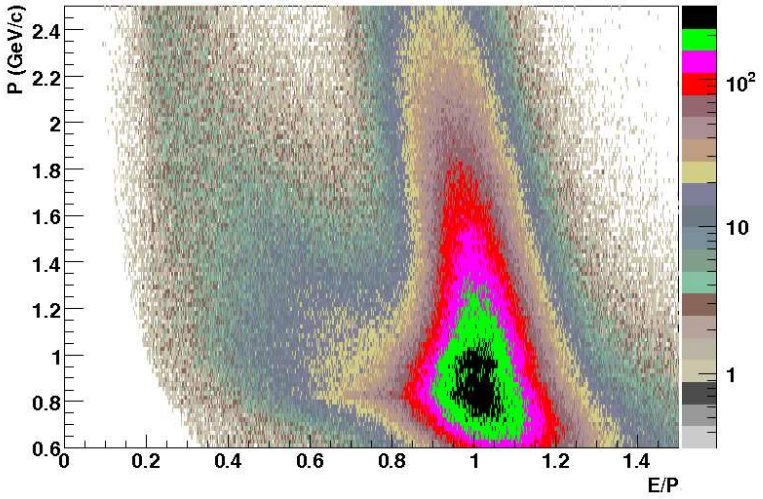

FIGURE 5.59: Distribution of E/p vs. P is plotted.

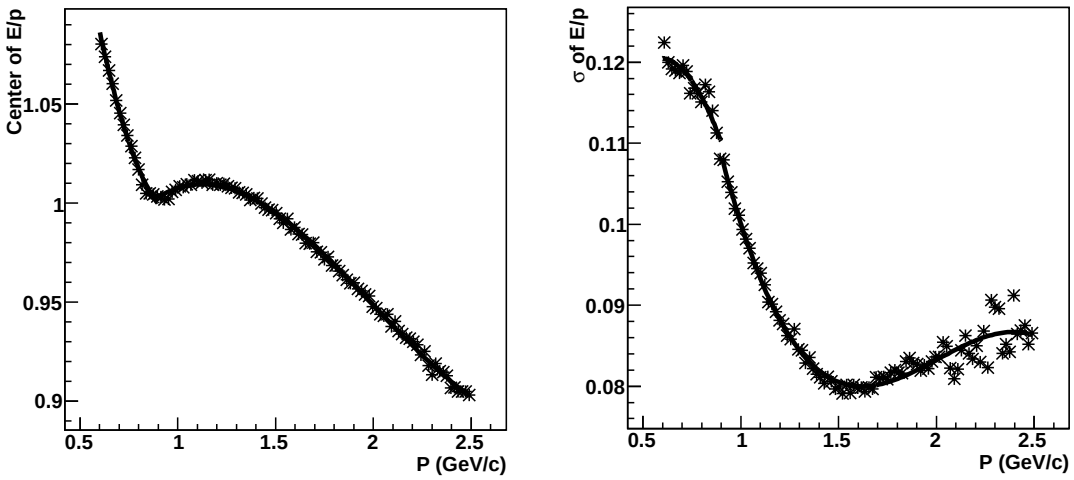

FIGURE 5.60: At different momentum bins, the E/p distribution were fitted with a Gaussian shape. Left panel shows the fitted center of E/p peak vs. the momentum P. Right panel shows the fitted σ of the E/p peak vs. the momentum P.

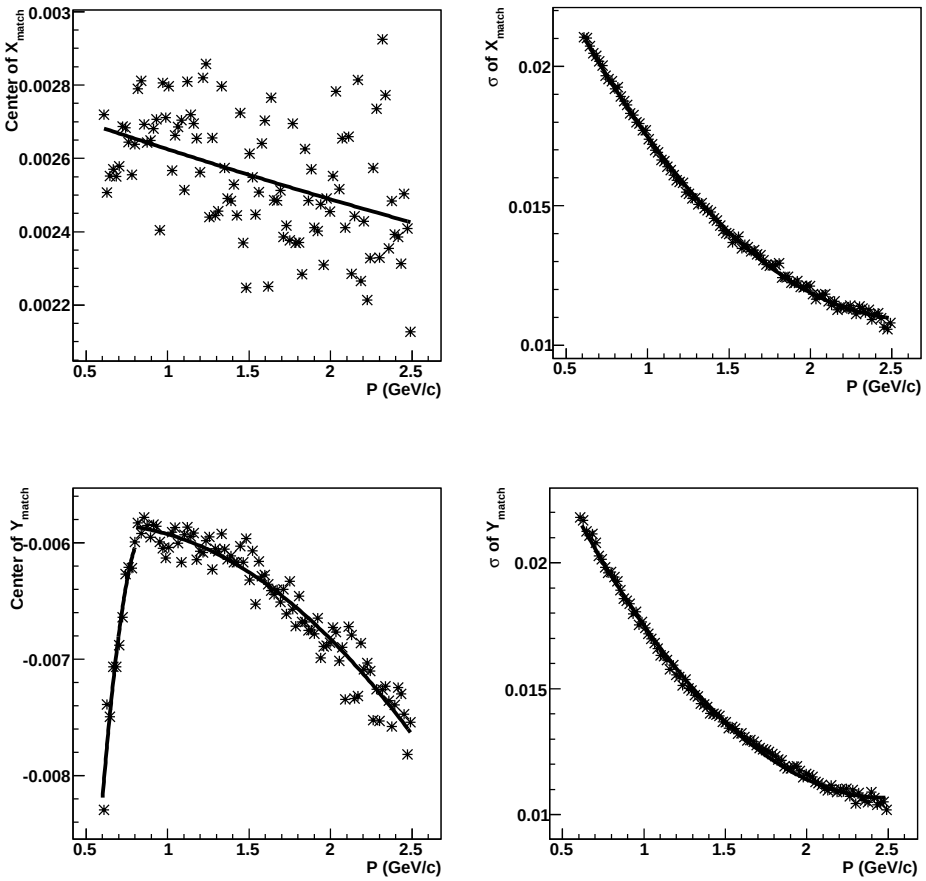

FIGURE 5.61: For different momentum bins, the track match X and Y distribution were fitted with an Gaussian shape. The mean and σ of the fitting distribution are plotted vs. momentum P.

5.4.3 Positron-Like Events

The cuts for selecting positrons are similar to those of electrons, except:

- Positively Charged particle Cut.
- Position match cut:

  A similar approach was used as the one used in obtaining the track match cut of electrons. A 2.5-σ cut was used.

- E/p cut: a 1.5-σ cut was used.

5.4.4 Negative-Charged-Hadron-Like Events

The negative charged hadrons were selected with

- Negative Charged Particle Cut.
- Energy deposition in the preshower less than 0.15 GeV.
- Track Match Cut:

  The approach is similar to the one of electrons. A 2-σ cut was used.

In BigBite, one can not differentiate the negative pions and negative kaons, so those events are called negative-charged-hadron-like events.

5.4.5 Positive-Charged-Hadron-Like Events

The positive charged hadrons were selected with

- Positively Charged Particle Cut.
- Energy deposition in the preshower less than 0.15 GeV.
- Track Match Cut:

  A 2-σ cut was used.

In BigBite, one can not differentiate the positive pions, positive kaons, and protons, so those events are called positive-charged-hadron-like events.

5.4.6 Photon-Like Events

The photon-like events in BigBite were selected with:

- Energy deposition in preshower higher than 0.2 GeV.

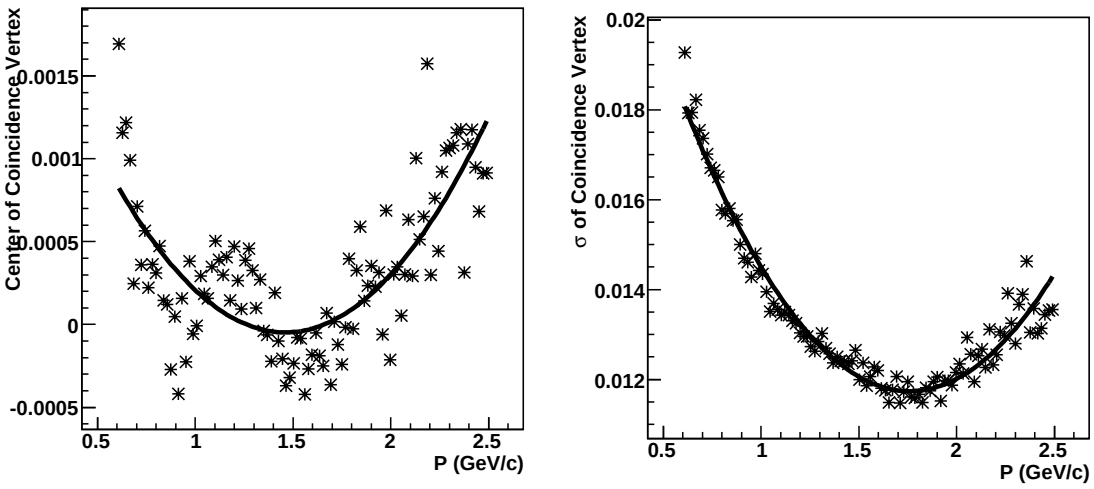

FIGURE 5.62: For different momentum bins, the coincidence vertex distribution (difference between the reconstructed vertex from left HRS and BigBite) was fitted to a Gaussian function. Left panel shows the fitted center vs. the momentum P. Right panel shows the fitted σ vs. the momentum P.

- No total shower cluster (requiring a match among preshower, shower and track) is found in BigBite
- The shower cluster is matched with the preshower cluster.
- The total energy deposition is between 0.6 and 2.5 GeV.

5.5 Coincidence PID

5.5.1 Coincidence Vertex

It is expected that the resolution on the reconstructed interaction vertex depends on the particle momentum. Therefore, a momentum dependent coincidence vertex cut between the reconstructed vertex from the left HRS and the BigBite was applied. A similar approach was used as the one in Sec. 5.4.2. Fig. 5.62 shows the center and σ of the Gaussian fits with momentum P.

5.5.2 Coincidence Time

In this section, we list the cuts on coincidence time for different channels. In addition, the coincidence time cuts for selecting the random coincidence background are also listed. For pions, kaons, and protons in left HRS, different variables pi_t, K_t, and p_t (or pi_photon_t, K_photon_t, and p_photon_t for photon in BigBite) are used.

- BigBite electron + Left HRS pion:

  Real coincidence 6 ns: -3 ns < pi_t < 3 ns

  Random coincidence 100 ns: 9 < pi_t < 59 or -69 < pi_t < -19

- BigBite electron + Left HRS kaon:

  Real coincidence 2 ns: -1 ns < K_t < 1 ns

  Random coincidence 80 ns: 9 < K_t < 59 or -73 < K_t < -43

- BigBite electron + Left HRS proton:

  Real coincidence 6 ns: -3 ns < p_t < 3 ns

  Random coincidence 100 ns: -73 < p_t < -23 or 11 < p_t < 61

- BigBite photon + Left HRS pion:

  Real coincidence 6 ns: -3 ns < pi_photon_t < 3 ns

  Random coincidence 100 ns: 9 < pi_photon_t < 59 or -69 < pi_photon_t < -19

- BigBite photon + Left HRS kaon:

  Real coincidence 2 ns: -1 ns < K_photon_t < 1 ns

  Random coincidence 80 ns: 9 < K_photon_t < 59 or -73 < K_photon_t < -43

- BigBite photon + Left HRS proton:

  Real coincidence 6 ns: -3 ns < p_photon_t < 3 ns

  Random coincidence 100 ns: -73 < p_photon_t < -23 or 11 < p_photon_t < 61

- BigBite hadron + Left HRS pion:

  Real coincidence 6 ns: -2.5 ns < pi_t < 3.5 ns

  Random coincidence 100 ns: 9.5 < pi_t < 59.5 or -69.5 < pi_t < -19.5

- BigBite hadron + Left HRS proton:

  Real coincidence 6 ns: -2.5 ns < p_t < 3.5 ns

  Random coincidence 100 ns: -73.5 < p_t < -23.5 or 11.5 < p_t < 61.5

5.6 Kinematic Settings and DIS Cuts

Experiment E06-010 measured the target SSAs at four x bins with a 5.89 GeV incident electron beam energy at deep inelastic kinematics. The DIS cuts includes:

- Q^2 cut:

$$1\ GeV^2 < Q^2 \tag{5.51}$$

- W cut to avoid the resonance region:

$$2.3 < W \tag{5.52}$$

- M_X (or W') cut to avoid the resonance region:

$$1.6 < W' \tag{5.53}$$

- z cut to ensure current fragmentation:

$$0.3 < z < 0.7 \tag{5.54}$$

The phase space plots after all the cuts for $N(e, e'\pi^{\pm})X$ process are shown in Fig. 5.63. The binnings of the data in terms of different variables are shown in Fig. 5.64. For each x-bin, the angular coverage of ϕ_h and ϕ_S are shown in Fig. 5.65

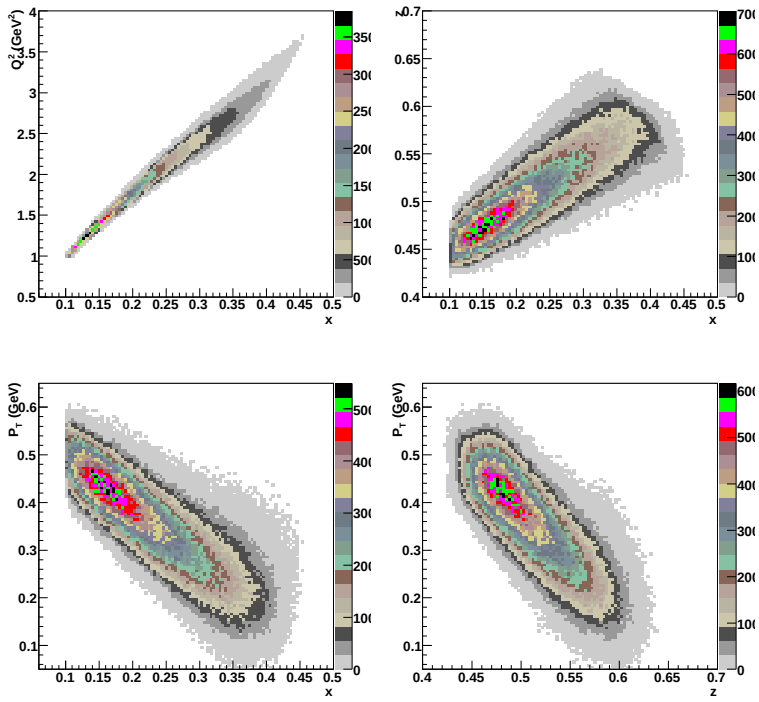

FIGURE 5.63: Phase space for $N(e, e'\pi^{\pm})X$ process after all cuts.

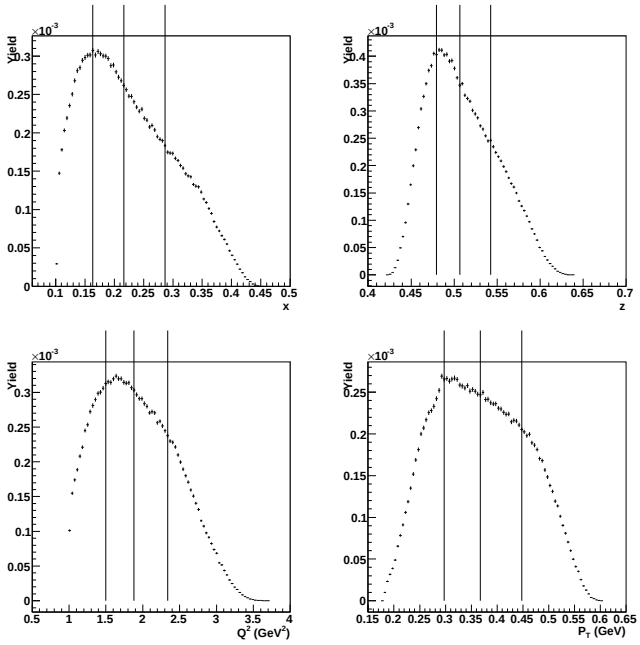

FIGURE 5.64: The binnings of the phase space were illustrated for different variables.

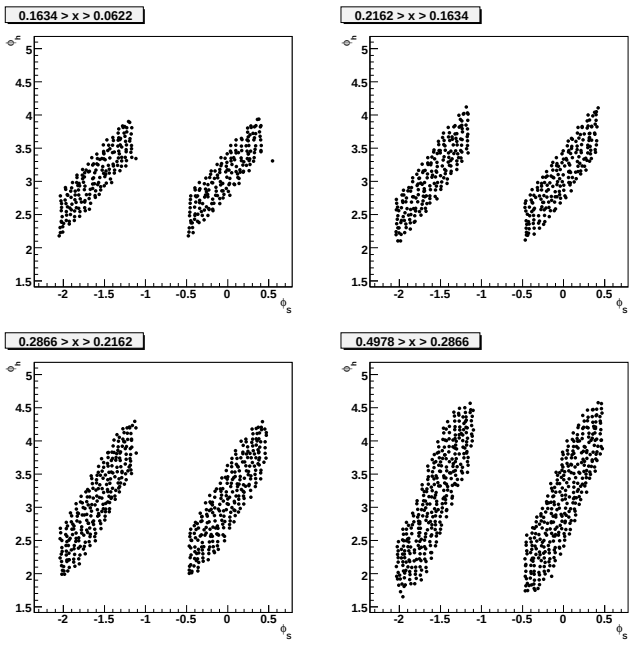

FIGURE 5.65: The angular coverages of ϕ_h and ϕ_S are shown for each x-bin.

5.7 Contamination Study for Identifying DIS Electrons in BigBite

5.7.1 Negative Pion Contamination

In the BigBite spectrometer, the main contamination to the electron sample was the negative pions. Since the calorimeter system was the only PID detectors, there was no direct way to extract the pion contamination. In this section, we use an indirect method to estimate the contamination by fitting the preshower energy deposition $E_{preshower}$ spectrum. In the Sec. 6.1, we revisit this issue with Monte-Carlo method. The difference between these two methods can be treated as the systematic uncertainties.

In practice, the energy deposition in the preshower was plotted after removing the $E_{preshower} < 0.2\ GeV$ (< 400 channels) cut. The minimum ionization peak around 200 channels was modeled as a Gaussian convoluted Landau function. The electron

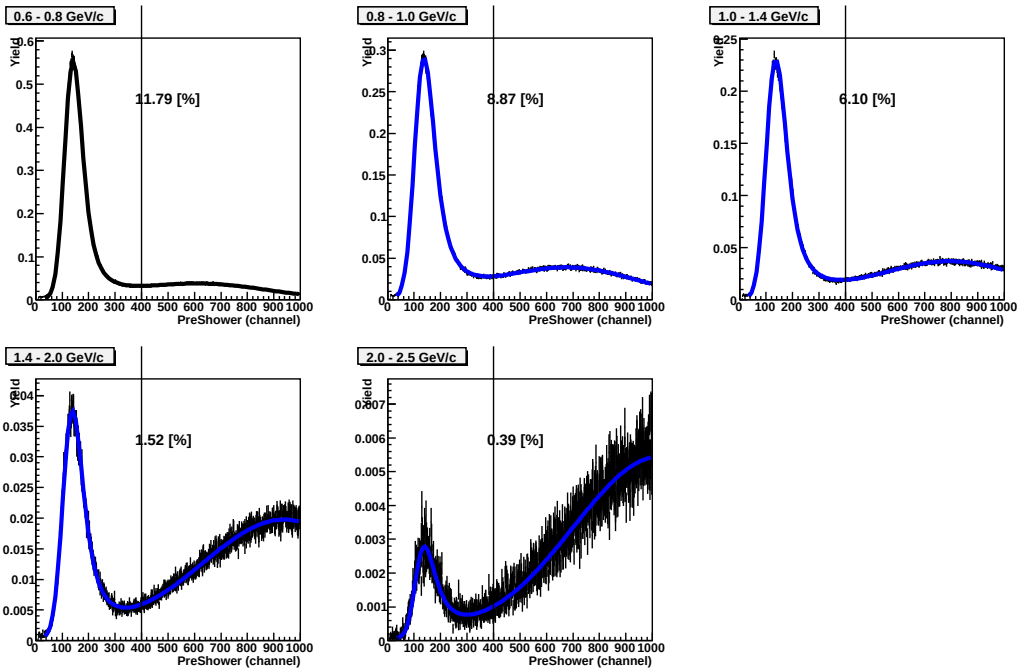

FIGURE 5.66: The pion contamination in the T1 trigger for different momentum bins.

peak above 400 channels was then modeled with a Gaussian function. The pion contamination f_{cont} was then obtained by:

$$f_{cont} = \frac{\int_{400}^{\infty} f_{gl}(x)dx}{N_{ele}^{>400 channels}}. \tag{5.55}$$

Here f_{gl} is the Gaussian convoluted Landau function obtained from the fitting procedure. x is the channel number of the preshower energy deposition. Fig. 5.66 and Fig. 5.67 show the pion contamination estimated for the T1 and T6 trigger, respectively. The fits including the Gaussian convoluted Landau function and the Gaussian function are plotted together.

In order to estimate the pion contamination in the T5 trigger, two methods were used. The first method is from the direct fitting, as that used in estimating the pion contamination in the T1 and T6 trigger. The second method takes the advantages that the T5 trigger was made from the T1 trigger. Therefore, the pion contamination

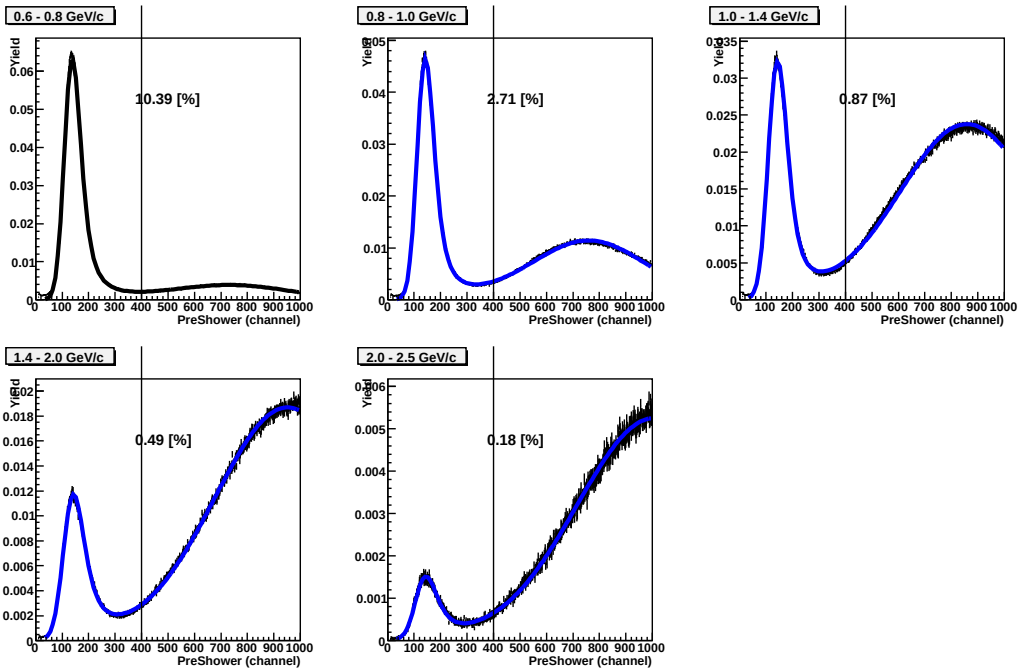

FIGURE 5.67: The pion contamination in the T6 trigger for different momentum bins.

was estimated by calculating the suppression factor f_{sup}:

$$f_{sup} = \frac{Y^{T5}_{\pi^-\pi^\pm}/Y^{T1}_{\pi^-}}{Y^{T5}_{e\pi^\pm}/Y^{T1}_{e}} = \frac{Y^{T5}_{\pi^-\pi^\pm}}{Y^{T5}_{e\pi^\pm}} \cdot \frac{1}{f^{T1}_{cont}}, \tag{5.56}$$

which is

$$f^{T5}_{cont} = f_{sup} \cdot f^{t1}_{cont}. \tag{5.57}$$

Fig. 5.68 shows the suppression factor f_{sup} vs. the BigBite momentum for positive and negative HRS polarities. The results from both methods are summarized in Table. 5.3. In both cases, the contamination of pions in the electron sample for the real coincidence $N(e, e'\pi^\pm)X$ process in the entire momentum range is less than 3%.

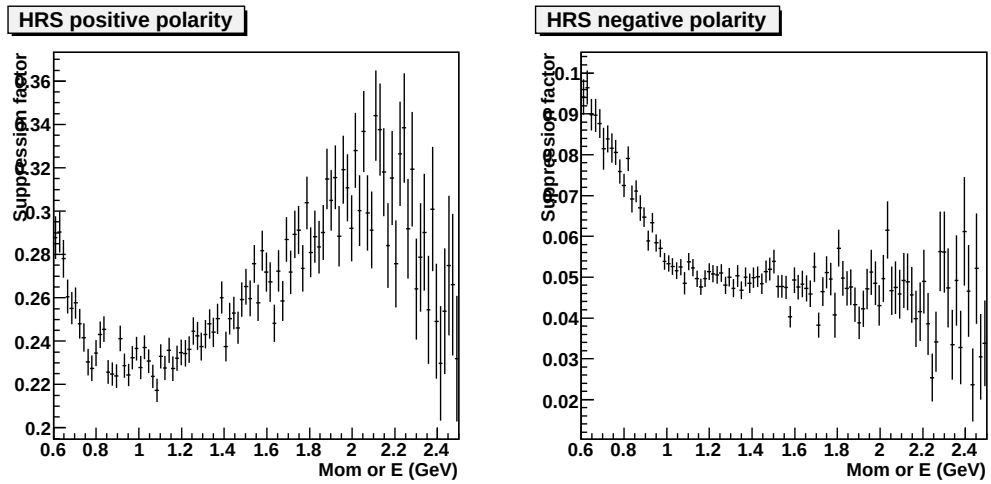

FIGURE 5.68: Super Ratio f_{sup} is plotted against the BigBite momentum for both the negative and positive HRS polarities.

Table 5.3: Pion contamination in the electron sample in the T5 trigger.

HRS polarity	Momentum Range GeV GeV	Contamination Method I %	Contamination Method II %
negative	0.6-0.8	1.2	0.83
negative	0.8-1.0	0.6	0.45
negative	1.0-1.4	0.11	0.3
negative	1.4-2.0	0.12	0.07
positive	0.6-0.8	3.1	2.87
positive	0.8-1.0	1.44	2.13
positive	1.0-1.4	1.25	1.7
positive	1.4-2.0	0.27	0.47

5.7.2 Photon Induced Electron Contamination

In experiment E06-010, more than 70% of the T1 triggers were identified as the photon-like events. These high energy photons were dominated by the decay products of π^o produced in the collision. The lifetime of π^o is short, such that it usually decays before it leaves the target region. When the photon passes through material, such as the target side wall, it has certain probabilities to produce a pair of electron and positron. In addition, the π^o has about 1% decay branching ratio to $(\gamma e^- e^+)$. In

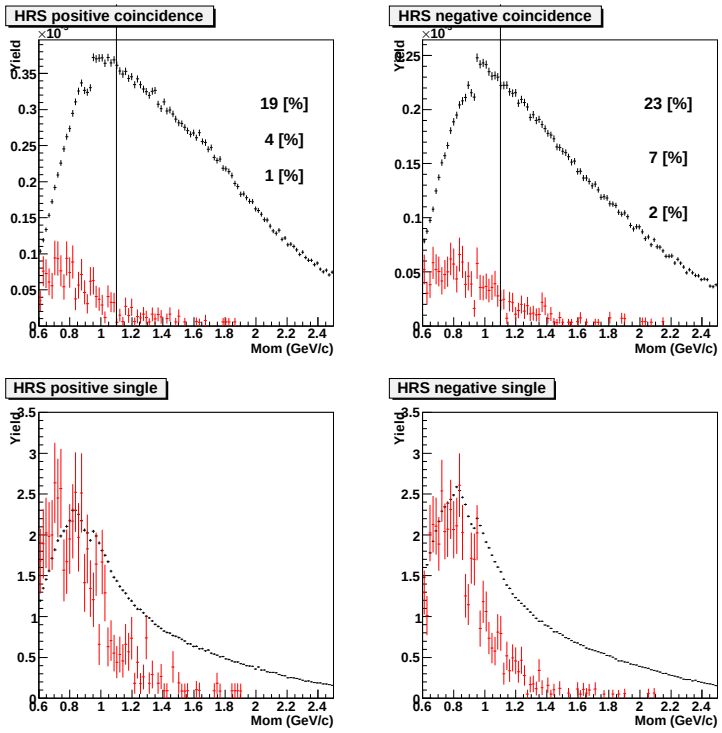

FIGURE 5.69: The yields of the electron-like events in BigBite negative polarity and the positron-like events in BigBite positive polarity are compared for both singles and coincidence triggers.

either case, an electron originated from π^o can end up in the BigBite spectrometer. Such electrons are referred to as the "photon-induced" electrons, and are a major contamination to the DIS electrons.

For each photon-induced electron, there is the corresponding photon-induced positron. The kinematics information for both of them is expected to be the same. Therefore, one can estimate the photon-induced electron yields by measuring the positron yields, which is expected to be dominated by the photon-induced positrons. This was realized in experiment E06-010 by reversing the BigBite polarity with the same magnetic field strength. In this case, the positrons were then bent up and had the same acceptance as the electrons with BigBite in its negative polarity. Fig. 5.69 shows the comparison of the yields of electron-like events in BigBite negative polarity

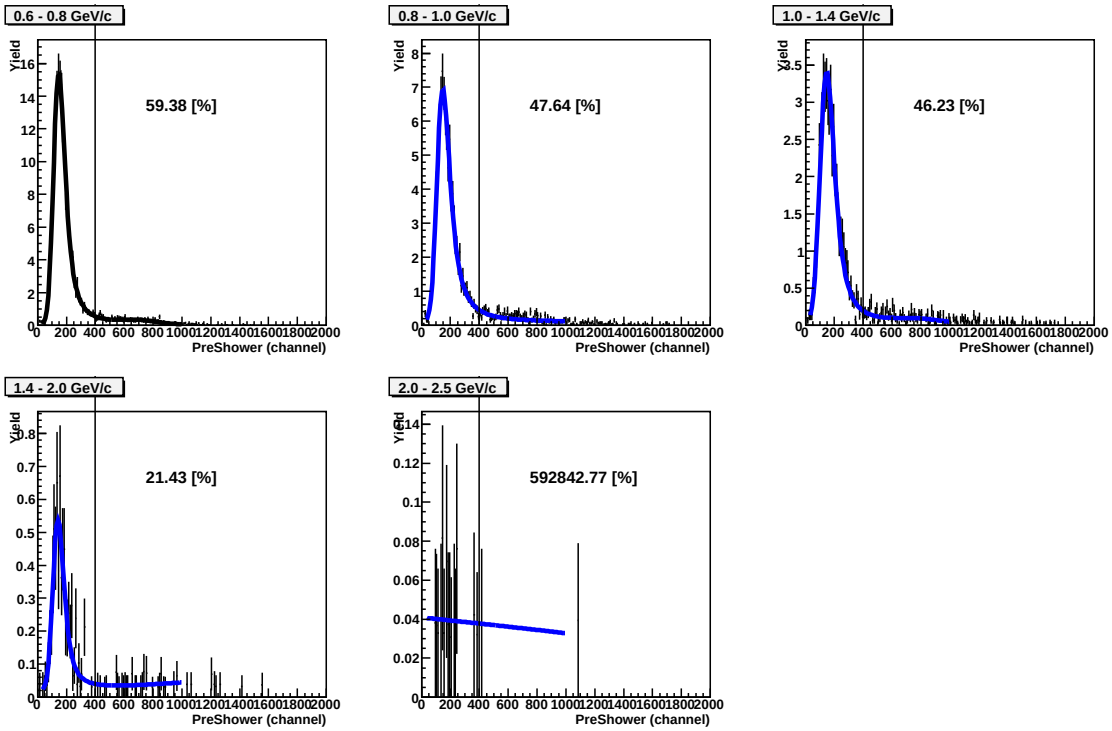

FIGURE 5.70: The π^+ contamination in the positron sample in the T1 trigger for different momentum bins.

and the positron-like events in BigBite positive polarity for both singles and coincidence triggers. As shown in the two lower panels of Fig. 5.69, the positron yields are comparable to the electron yields at low momentum. This is due to the large π^+ contamination in the positron sample. The π^+ contamination in the positron sample was estimated by the same method used in estimating the π^- contamination in the electron sample. The results are shown in Fig. 5.70. Combining all above information, the photon-induced electron contamination in the T1 single trigger was estimated to be 55.8 %, 48.5%, 24.2%, 9.5% for momentum range of 0.6-0.8 GeV, 0.8-1.0 GeV, 1.0-1.4 GeV and 1.4-2.0 GeV, respectively. The same method was used in estimating the photon-induced electron contamination in the coincidence channel. The results are listed in Table. 5.4.

HRS polarity	Momentum Range GeV GeV	Contamination %
negative	0.6-0.8	22
negative	0.8-1.0	6.9
negative	1.0-1.4	1.7
negative	1.4-2.0	1.6
positive	0.6-0.8	19.6
positive	0.8-1.0	3.8
positive	1.0-1.4	1.2
positive	1.4-2.0	0.6

Table 5.4: The photon-induced electron contamination in the coincidence channel are summarized in this table for both positive and negative polarities of left HRS.

5.8 Forming Asymmetries

Raw asymmetry is defined as:

$$A_{raw} = \frac{Y_+ - Y_-}{Y_+ + Y_-} = \frac{\frac{N_+}{C_+L_+} - \frac{N_-}{C_-L_-}}{\frac{N_+}{C_+L_+} + \frac{N_-}{C_-L_-}}, \tag{5.58}$$

where the N is the number of events in each states, C is the charge for each state, and L represents the possible corrections including live time, target density etc.

Assuming L is not statistically correlated with N and the target polarization, the uncertainty of the raw asymmetry is:

$$\begin{aligned} \delta_{A_{raw}} &= \frac{2C_+C_-L_+L_-(N_-\delta N_+ + N_+\delta N_-)}{(N_+C_-L_- + N_-C_+L_+)^2} \\ &= \frac{2Y_+Y_-}{(Y_+ + Y_-)^2}\sqrt{\frac{1}{N_+} + \frac{1}{N_-}}. \end{aligned} \tag{5.59}$$

With target polarization P and dilution factor f, the raw asymmetry is modified as:

$$A_{raw} = \frac{1}{P \cdot f} \cdot \frac{Y_+ - Y_-}{Y_+ + Y_-}, \tag{5.60}$$

and

$$\delta_{A_{raw}} = \frac{1}{P \cdot f} \cdot \frac{2Y_+Y_-}{(Y_+ + Y_-)^2}\sqrt{\frac{1}{N_+} + \frac{1}{N_-}}. \tag{5.61}$$

5.8.1 Livetime Corrections

The DAQ live time for each trigger is defined as:

$$l = \frac{N_{data}^{recorded}}{N_{scaler}^{trigger}}, \tag{5.62}$$

where $N_{data}^{recorded}$ is the number of events recorded for each trigger and $N_{scaler}^{trigger}$ is the number of raw triggers entered the DAQ system. Live time usually depends on the prescale factors of the trigger and the number of total rates recorded by the DAQ. In the trigger design of experiment E06-010, an electronic deadtime pulse (EDTP), which is 12.5 Hz, was plugged into each trigger type to mimic a real trigger. The goal of this EDT pulse was to monitor the electronics deadtime. Thus the livetime formula is modified as:

$$l = \frac{N_{data}^{recorded} - N_{EDTP}^{recorded}}{N_{scaler}^{trigger} - N_{scaler}^{EDTP}}. \tag{5.63}$$

In general, the livetime correction should be directly applied to the charge normalized yield before forming an asymmetry. However, after production run 5620, the EDT pulse, which went into the trigger system, failed, while the EDT pulse, which went into the scaler, was fine. Therefore, the effect of the EDT pulse could not be directly corrected in Eqn. (5.63). Instead, Eqn. (5.62) was used to calculate the live time for runs after 5620. This approach will lead to some false asymmetries. The following studies for the T5 coincidence trigger were performed to evaluate the false asymmetries due to this approximation.

Assuming there was an asymmetry in the live time,

$$\delta = \frac{l_+ - l_-}{l_+ + l_-}, \tag{5.64}$$

where + and − represent the target spin states.

The correction of live time to asymmetries is expressed as:

$$\begin{aligned} A_{real} &= \frac{\frac{Y_+}{(1+\delta)} - \frac{Y_-}{(1-\delta)}}{\frac{Y_+}{(1+\delta)} + \frac{Y_-}{(1-\delta)}} \approx \frac{Y_+(1-\delta+\delta^2) - Y_-(1+\delta+\delta^2)}{Y_+(1-\delta+\delta^2) + Y_-(1+\delta+\delta^2)} \\ &\approx \frac{(Y_+ - Y_-) - \delta(Y_+ + Y_-) + \delta^2(Y_+ - Y_-)}{(Y_+ + Y_-) - \delta(Y_+ - Y_-)} \\ &= \frac{A - \delta + \delta^2 A}{1 - \delta A} \approx (A - \delta + \delta^2 A) \cdot (1 + \delta A) \\ &\approx A - \delta + \delta A^2, \end{aligned} \tag{5.65}$$

where A is the asymmetry using the yields without the correction from the live time.

Therefore, the false asymmetry is $\delta - \delta'$, where δ is calculated from the live time calculation in Eqn. (5.63) and δ' is calculated from the live time in Eqn. (5.62). which is

$$\frac{\frac{a1}{b1} - \frac{a2}{b2}}{\frac{a1}{b1} + \frac{a2}{b2}} - \frac{\frac{a1+c1}{b1+d1} - \frac{a2+c2}{b2+d2}}{\frac{a1+c1}{b1+d1} + \frac{a2+c2}{b2+d2}}, \tag{5.66}$$

where $a1$, $b1$, $a2$, $b2$ are $N^+_{data} - N^{+edtpl}_{data}$, $N^+_{scaler} - N^{+edtpl}_{scaler}$, $N^-_{data} - N^{-edtpl}_{data}$, $N^-_{scaler} - N^{-edtpl}_{scaler}$, respectively. The $c1$, $d1$, $c2$, $d2$ are N^{+edtpl}_{data}, N^{+edtpl}_{scaler}, N^{-edtpl}_{data}, N^{-edtpl}_{scaler}, respectively. If we define

$$R_1 = \frac{1 + \frac{c1}{a1}}{1 + \frac{d1}{b1}}, \tag{5.67}$$

$$R_2 = \frac{1 + \frac{c2}{a2}}{1 + \frac{d2}{b2}}, \tag{5.68}$$

and

$$\epsilon = \frac{R_1 - R_2}{R_1 + R_2}, \tag{5.69}$$

then

$$A = \epsilon. \tag{5.70}$$

Fig. 5.71 shows the correction from the live time. Fig. 5.72 shows the size of A. Thus, the size of A is about 20% of the entire live time correction. Since only runs after 5620 received such approximation, only part of VN and TN settings were affected. Therefore, combining both facts, the effect of such treatment for runs after 5602 led to a false asymmetry less than 1e-4 in the worst scenario.

5.8.2 Asymmetries with Local Pairs

There are many reasons to form local pairs in extracting asymmetries. One of them is to search for unidentified experimental problems. For example, if one found out that certain local asymmetries behaved strangely, there might be some hidden experimental problems associated with those periods. Another reason is that the observed charged normalized yield in experiment E06-010 was drifting due to the radiation damage in the BigBite calorimeter system. In this case, the local pairs method becomes essential even if there is no hidden experimental problems. We can explain this with a simplified example.

A Simplified Example

If we assume that there are only two periods labeled as 1 and 2, then we have N_{1+}, N_{1-}, N_{2+}, N_{2-} which represent the number of events in each state. And L_{1+}, L_{1-}, L_{2+}, L_{2-} are the luminosities in each state. The yield is defined as $Y = N/L$. Since the yield is drifting, we can make the following assumptions:

$$\begin{aligned} A_1 = \frac{Y_{1+} - Y_{1-}}{Y_{1+} + Y_{1-}} \sim A_2 = \frac{Y_{2+} - Y_{2-}}{Y_{2+} + Y_{2-}}, \\ Y_{1+} \sim Y_{1-} = 2 \cdot Y_{2+} \sim 2 \cdot Y_{2-}, \\ L_{1+} = L_{1-} = 0.5 \cdot L_{2+} = 2 \cdot L_{2-}. \end{aligned} \tag{5.71}$$

The first equation tells us that the asymmetry is not drifting (local pairs). And the second equation tells us that the yield is in fact drifting. The yield in the second

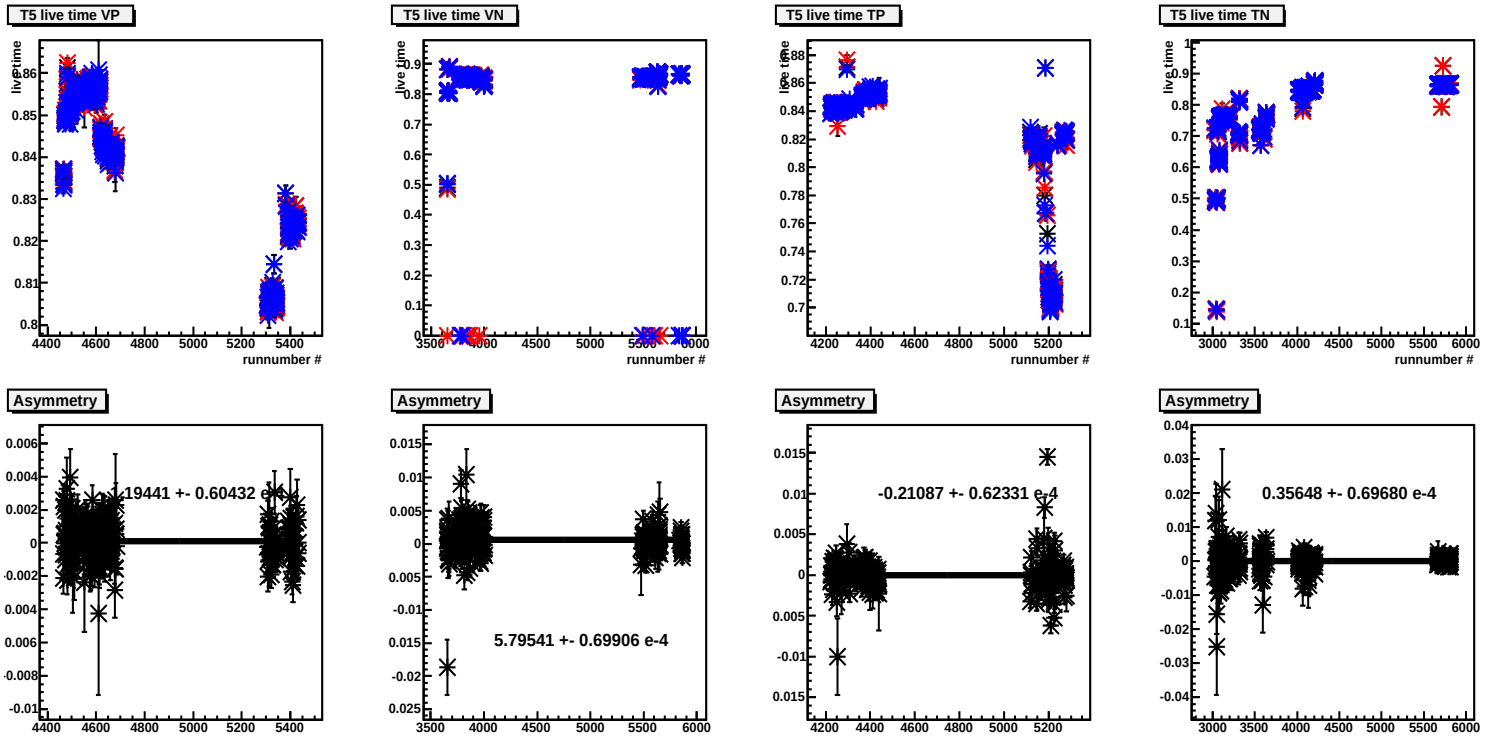

FIGURE 5.71: Live time asymmetry for T5 δ in Eqn. (5.64). The top four panels show the live time for four configurations (VP, VN, TP, and TN) and the bottom four panels show the asymmetry between the two target spin states in each configuration.

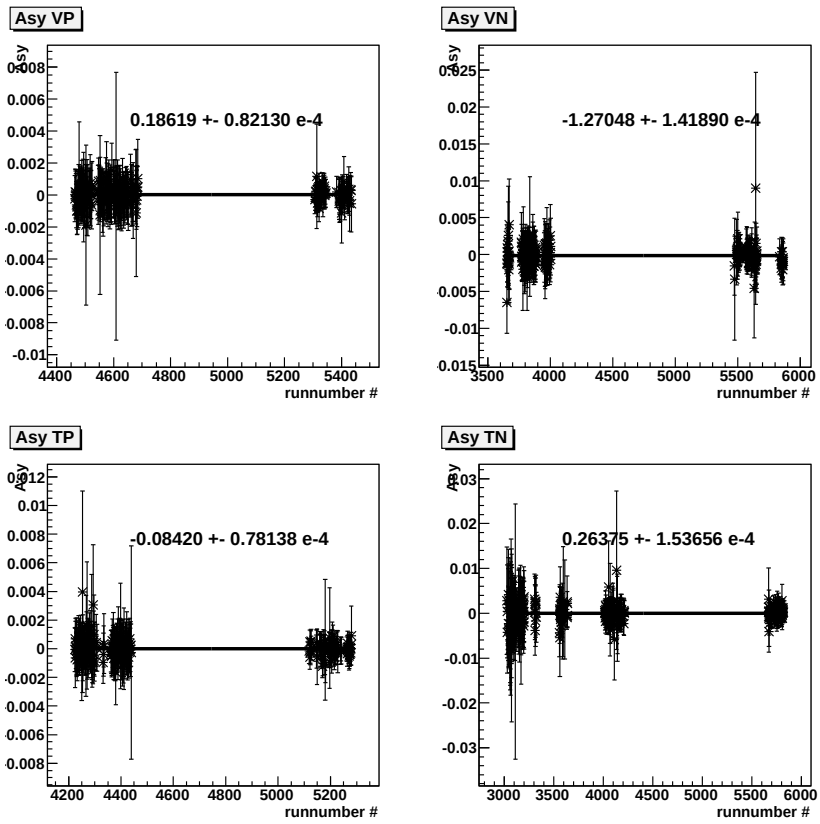

FIGURE 5.72: False asymmetry by EDT pulse.

period is about half of that in the first period. The third equation tells us that the luminosities in different states are different. The third equation reflects an important feature of the data, since the target spin flip in experiment E06-010 is independent of the beam and detectors. For example, if the beam was tripped in one of the spin states, but not in the other, the luminosities in two states would be quite different. With the second and third equations, one can calculate the number of events N in different states. If one directly combines the two periods together in the following

way:

$$A = \frac{\frac{N_{1+}+N_{2+}}{L_{1+}+L_{2+}} - \frac{N_{1-}+N_{2-}}{L_{1-}+L_{2-}}}{\frac{N_{1+}+N_{2+}}{L_{1+}+L_{2+}} + \frac{N_{1-}+N_{2-}}{L_{1-}+L_{2-}}} = \frac{\frac{N_{1+}+N_{1+}}{L_{1+}+2\cdot L_{1+}} - \frac{N_{1-}+0.25\cdot N_{1-}}{L_{1-}+0.5\cdot L_{1-}}}{\frac{N_{1+}+N_{1+}}{L_{1+}+2\cdot L_{1+}} + \frac{N_{1-}+0.25\cdot N_{1-}}{L_{1-}+0.5\cdot L_{1-}}}$$

$$= \frac{\frac{2\cdot N_{1+}}{3\cdot L_{1+}} - \frac{1.25\cdot N_{1-}}{1.5\cdot L_{1-}}}{\frac{2\cdot N_{1+}}{3\cdot L_{1+}} + \frac{1.25\cdot N_{1-}}{1.5\cdot L_{1-}}} \neq \frac{\frac{N_{1+}}{L_{1+}} - \frac{N_{1-}}{L_{1-}}}{\frac{N_{1+}}{L_{1+}} + \frac{N_{1-}}{L_{1-}}}, \tag{5.72}$$

a false asymmetry is generated.

Local Pair Method

Although the local pairs can minimize the possible systematic uncertainties caused by the yield drifting, it also has some disadvantages when the statistics are limited. For example, Eqn. (5.59) will fail when the number of events is zero in any one of the two spin states. In addition, if the charge asymmetry between the two spin states is large, forming local pairs will significantly reduce the statistical precision.

The first disadvantages can be avoided by combining the local pairs as:

$$A_{raw} = \frac{\sum a_i \cdot (Y_{i+} - Y_{i-})/P_i}{\sum a_i \cdot (Y_{i+} + Y_{i-})}. \tag{5.73}$$

Here P_i is the product of the target polarization and dilution, and a_i can be any number in principle. The best a_i can be obtained by solving the equation group:

$$\frac{\partial \delta A}{\partial a_i} = 0. \tag{5.74}$$

However, it is very hard to solve the equation groups. Instead we can do the following approximation:

$$A = \frac{\sum a_i \cdot (Y_{i+} - Y_{i-})}{\sum a_i \cdot (Y_{i+} + Y_{i-})} = \frac{\sum a_i A_i \cdot (Y_{i+} + Y_{i-})}{\sum a_i \cdot (Y_{i+} + Y_{i-})} \approx \frac{\sum b_i A_i}{\sum b_i}. \tag{5.75}$$

By solving Eqn. (5.74), the best b_i should be:

$$b_i \sim \frac{1}{\delta A_i^2} \sim \frac{1}{\frac{1}{N_+} + \frac{1}{N_-}} \sim \frac{1}{\frac{1}{Y_+ L_+} + \frac{1}{Y_- L_-}}, \tag{5.76}$$

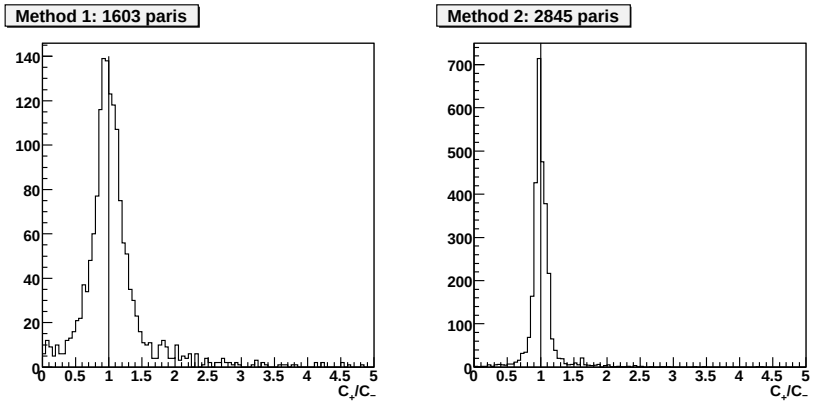

FIGURE 5.73: Left (right) panel shows the charge asymmetries with local pair (super local pair) method. There are in total 1603 (2845) pairs.

then

$$a_i = \frac{b_i}{Y_{i+} + Y_{i-}} \sim \frac{1}{\frac{1}{L_+} + \frac{1}{L_-}}. \tag{5.77}$$

The second disadvantage of using the local pairs can be reduced by using super local pairs method in experiment E06-010.

Local Pairs vs. Super Local Pairs

In experiment E06-010, there were two methods to combine the local pairs. In the first method, each target spin state was treated as half of one local pair. In the second method, each target spin state was further truncated into two, and each of the two would be half of one local pair. The second method was referred to as the "super local pair" method. The charge asymmetries in both methods are shown in Fig. 5.73. The super local pair method not only gives larger number of local pairs, but it also has smaller charge asymmetries. Both will reduce the systematic uncertainties. Therefore, in the experiment E06-010 analysis, the super local pair method is treated as the standard approach.

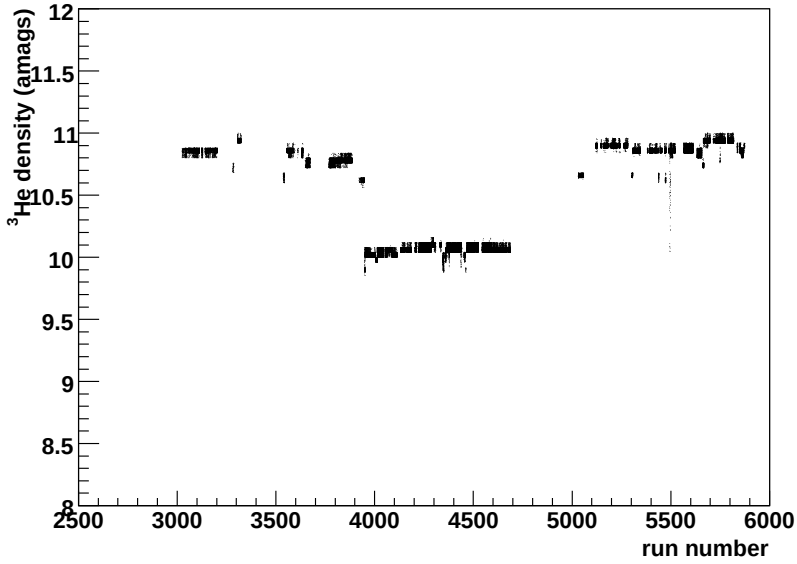

FIGURE 5.74: The calculated target densities are plotted vs. the run number.

5.8.3 Target Density Corrections

If the target density is assumed to be stable, the yield is defined as:

$$Y = \frac{N}{C \cdot l}. \tag{5.78}$$

Here N is the number of events, C is the total accumulated charge, and l is the life time correction. However, if the target density fluctuates with time, the yield definition should change to

$$Y = \frac{N}{C \cdot l \cdot D}. \tag{5.79}$$

D is the target density. Therefore, the target density corrections can be applied by calculating the average target density in one state.

Our target system is a two-cell system with a pumping chamber and a scattering chamber. The density in the scattering chamber was determined by the temperatures of the two chambers. The temperatures on various locations of both chambers are continuously monitored and recorded into the data stream. The target density can

then be calculated with the temperature readings. Fig. 5.74 shows the calculated target density vs. the run number. The calculated target densities were then inserted back into the rootfiles in the form of the charge weighted integral:

$$D = \int \rho dC \tag{5.80}$$

where ρ is the calculated target density and C is the beam charge. Therefore, the average target density between any two events can be calculated as:

$$\bar{\rho} = \frac{D}{C} \tag{5.81}$$

5.8.4 Prescale Factor Correction

In experiment E06-010, the singles triggers were taken with certain prescale factors. They would lead to a change in the statistical uncertainties of asymmetries. In this section, we will describe the correction due to the prescale factor. The derivation is introduced by Y. Qiang from Duke.

The primary inputs for this correction include:

- Total number of scalers: N
- Prescale Factor: P
- Acceptance for useful events: f
- Life time: L
- Total number of recorded events $D = N \cdot L/P$
- Total number of useful events $C = f \cdot D = N \cdot L \cdot f/P$

The origin of the fluctuation can then be separated into two sources. The first source is the fluctuation of the total number of events N:

$$\sigma_N = \sqrt{N}, \tag{5.82}$$

$$\Delta\sigma_N = \frac{1}{\sqrt{N}}. \tag{5.83}$$

The second source is the fluctuation of the acceptance $L \cdot f$. Here, as P is a fixed number, it would not introduce any fluctuations. The second fluctuation obeys Binominal distribution, and the effective possibility is $L \cdot f$. Assuming N is fixed, then we have:

$$\sigma_C = \sqrt{\frac{N}{P} L \cdot f(1 - L \cdot f)} = \sqrt{(}C(1 - L \cdot f)), \tag{5.84}$$

$$\Delta\sigma_c^* = \frac{\sigma_c}{C} = \sqrt{\frac{P(1 - L \cdot f)}{N \cdot L \cdot f}} = \sqrt{\frac{1 - L \cdot f}{C}}. \tag{5.85}$$

If we combine both $\Delta\sigma_N$ and $\Delta\sigma_C$, we have

$$\Delta\sigma_c = \sqrt{(\Delta\sigma_N)^2 + (\Delta\sigma_C^*)^2} = \sqrt{\frac{1}{C}(1 - L \cdot f(1 - \frac{1}{P}))}, \tag{5.86}$$

$$\sigma_c = \Delta\sigma_c \cdot C = \sqrt{C(1 - L \cdot f(1 - \frac{1}{P}))}, \tag{5.87}$$

so the prescale factor correction becomes

$$S = \sqrt{1 - L \cdot f(1 - \frac{1}{P})}. \tag{5.88}$$

5.9 Target Polarization Analysis

As discussed in Sec. 4.9.6, in experiment E06-010, two methods, EPR and NMR, were used to monitor/measure the target polarization. For each of the three polarized ^{3}He cells, Astral, Maureen and Brady, used in the experiment about 10 EPR

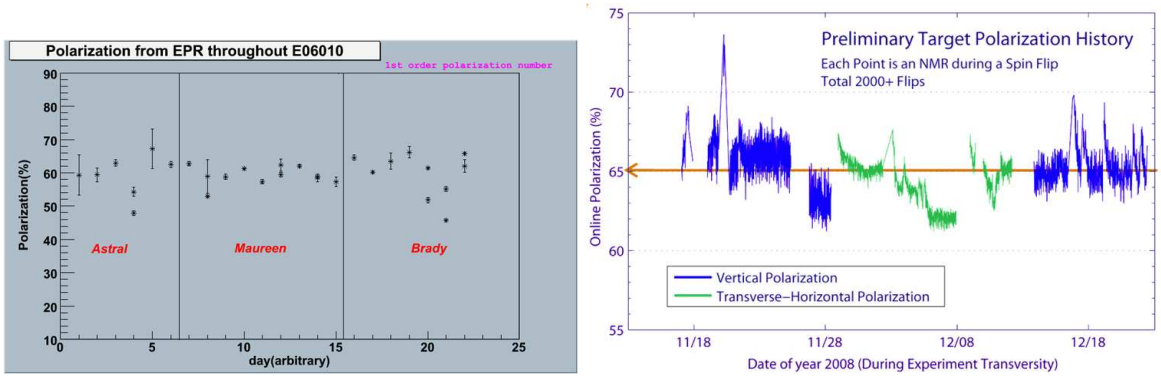

FIGURE 5.75: Left panel: preliminary target polarization from EPR. Right panel: preliminary target polarization from the NMR, which was measured every 20 mins during the target spin flip.

measurements were performed from time to time. The absolute ^{3}He polarization was extracted from EPR measurements by two methods, the "Direct method" and the "Derivative method", in order to cross check the polarization results. The "Direct method" evaluates directly the absolute holding field at each frequency states and uses the magnetization of ^{3}He to extract the polarization. The "Derivative method" uses the frequency difference between the two states (original and flipped) of the ^{3}He spins and the derivative of the frequency with respect to the holding field to calculate the polarization. The preliminary results from both analysis are consistent with each other. Left panel of Fig. 5.75 shows the preliminary polarization numbers from the EPR.

During experiment E06-010, the NMR measurement was taken every 20 mins, while the target spin was flipped. As discussed in Sec. 4.9.6, the height of the NMR signal is proportional to the target polarization with a calibration constant. This constant was calibrated to the obtained polarization in the corresponding EPR measurement. Furthermore, as a cross check the constant was also calibrated to the NMR water measurement. The principle of water calibration is to calibrate the

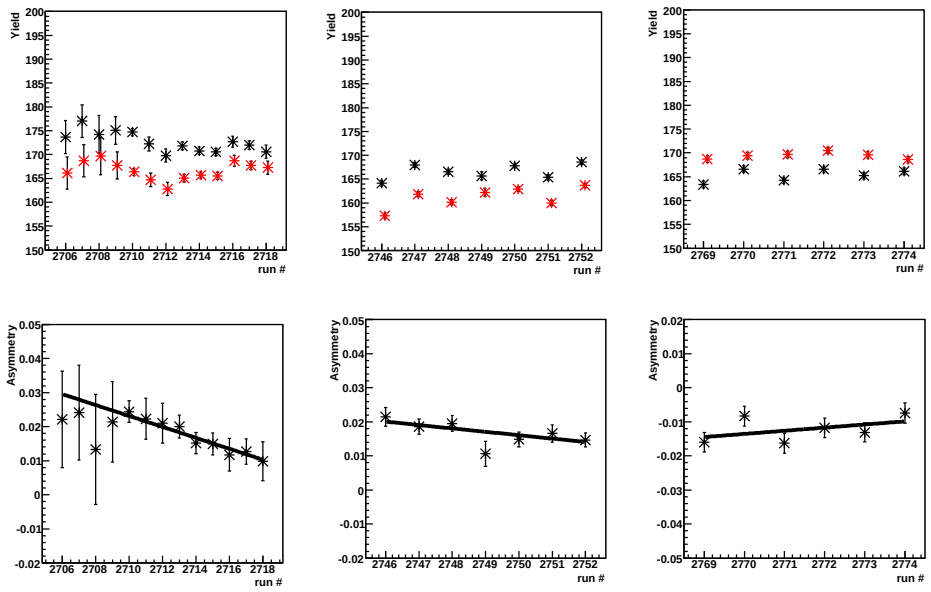

FIGURE 5.76: The online results of the elastic ^{3}He asymmetry from three periods of data taking. The black and red points represent the yields measured in beam helicity + and −, respectively. Since the SEOP can not be performed in the longitudinal direction, the target polarization was relaxing as time went. In the third period of data taking, the target spin was flipped, and the measured raw asymmetries also changed sign, which was consistent with the expectation.

^{3}He polarization with the thermal polarization of the protons. Therefore, a water cell (same geometry as the ^{3}He cell) needs to be mounted exactly the same way as the ^{3}He cell. Because of these constrains, only one water calibration was performed at the early stage of the experiment, during which, 2000 sweeps were performed to enhance the signal-to-noise ratio and to achieve a statistical uncertainty of less than 1%. The data from the water calibration are still being analyzed by Y. Zhang from Lanzhou University.

5.9.1 Sign of the Target Spin

The sign of the target spin was determined from the EPR measurement. As shown in Sec. 4.9.6, the EPR frequency ν is proportional to the effective magnetic field $B_H + B_{He}$. Since the directions of holding field B_H were determined, the direction of

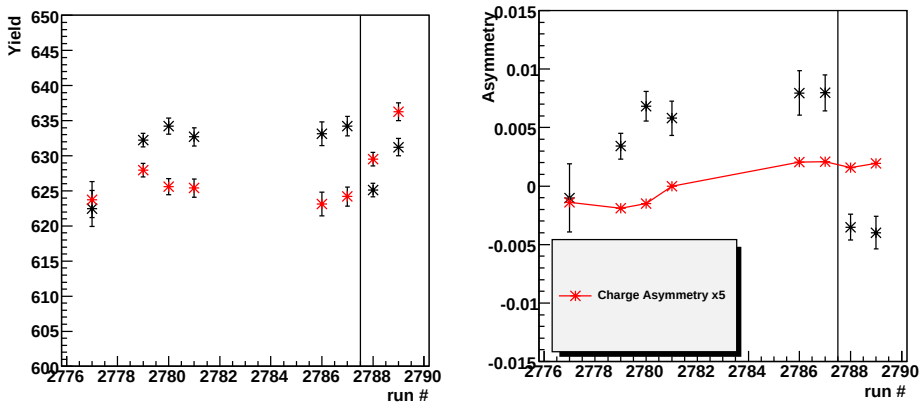

FIGURE 5.77: The online results of the ^{3}He asymmetry in the Δ resonance region. The black and red points represent the yields measured in beam helicity + and −, respectively. The black line represents the time when the target spin was flipped. The charge asymmetries were amplified by five times and plotted as the red line.

^{3}He spin was determined by its EPR frequency level (low or high). The sign of the ^{3}He spin was further confirmed by measuring double-spin asymmetries in two physics reaction channels, the ^{3}He elastic asymmetry with longitudinally polarized ^{3}He and the ^{3}He asymmetry in the Δ resonance region with transversely polarized ^{3}He. In both channels, the sign of the measured raw asymmetries was confirmed with that of the theoretical calculations [276, 277]. Fig. 5.76 shows the online results of the elastic ^{3}He yields/asymmetries. When the target spin was flipped (third column), the sign of the raw asymmetries were reversed. Fig. 5.77 shows the online results of the ^{3}He yields/asymmetries in the Δ resonance region with transversely polarized ^{3}He. The sign of the measured asymmetries changed when the target spin was flipped.

5.10 N_2 Dilution Factor

As discussed in Sec. 4.9.2, some amount of nitrogen was filled in the polarized ^{3}He cell, which allowed for photon-less de-excitation by absorbing energy into the nitrogen's rotational and vibrational motion during a collision [255]. Therefore, the

SIDIS pion electroproduction from nitrogen will dilute the ^{3}He asymmetry:

$$A_{raw} = f \cdot P_{^3\mathrm{He}} \cdot A_{^3\mathrm{He}}. \tag{5.89}$$

Here, $P_{^3\mathrm{He}}$ is the polarization of ^{3}He. $A_{^3\mathrm{He}}$ is the ^{3}He asymmetry, and f is called dilution factor defined as:

$$f = \frac{N_{^3\mathrm{He}}\sigma_{^3\mathrm{He}}}{N_{^3\mathrm{He}}\sigma_{^3\mathrm{He}} + N_{\mathrm{N_2}}\sigma_{\mathrm{N_2}}}. \tag{5.90}$$

Here $N_{^3\mathrm{He}}$ is the number of ^{3}He atoms in the target cell, and $N_{\mathrm{N_2}}$ is the number of N_2 atoms in the target cell. $\frac{\sigma_{\mathrm{N_2}}}{\sigma_{^3\mathrm{He}}}$ was measured through the reference cell runs filled with N_2 or ^{3}He. The density (or pressure) of N_2 and ^{3}He in the cell can be obtained by the filling density and cross-checked with the data taken at the beginning of the experiment. Table. 5.5 lists the filling densities of all three target cells.

Table 5.5: The filling densities of all three target cells. The "2 % (relative)" represents the 2% of the listed density.

Name	^{3}He (amg)	N_2 (amg)
Astral	8.08 ± 2% (relative)	0.11 ± 5% (relative)
Maureen	7.52 ± 2% (relative)	0.106 ± 5% (relative)
Brady	7.87 ± 2% (relative)	0.11 ± 5% (relative)

5.10.1 Pressure Curve of N_2 and ^{3}He

As introduced in Sec. 5.10, the dilution factor f is essential to extract the the ^{3}He asymmetry from the raw asymmetry which was obtained from the ^{3}He and N_2 mixture. The density of N_2 and ^{3}He were recorded when they were filled into the target cell. However, it is important to confirm them with the experimental data by measuring the yield of the ^{3}He or N_2 elastic scattering with electron detection.

The principle of using elastic scattering to confirm the N_2 density is by comparing the N_2 elastic signal from the target cell with that from a reference cell filled with

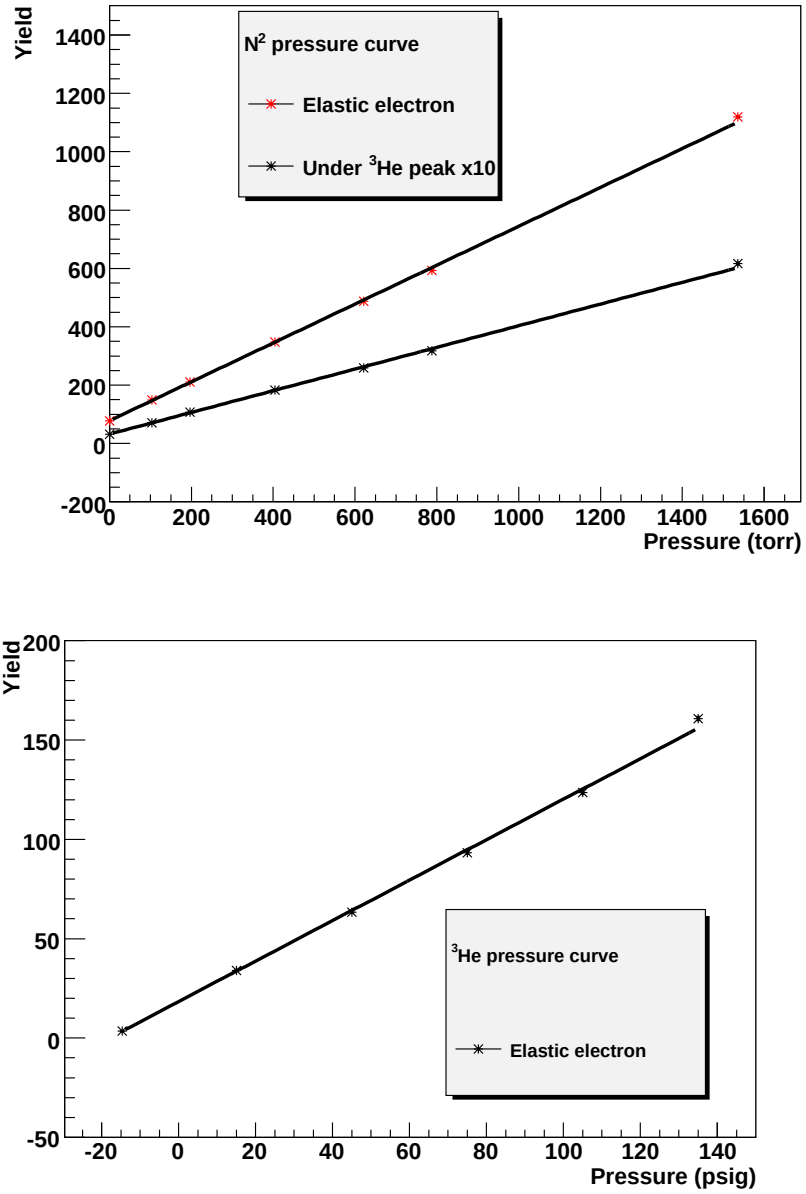

FIGURE 5.78: Left panel shows the online results of N_2 pressure curve. The red points represent the elastic N_2 scattering. The black points represent the events under the ^{3}He peak position and they are amplified by a factor of 10. Right panel shows the online results of ^{3}He pressure curve.

a known density of N_2. The systematic uncertainties in this analysis are further reduced by varying the density in the reference cell. Therefore, it is also called the "Pressure Curve" of N_2. The same procedure also applies to the extraction of ^{3}He density. The reference cell data are still being analyzed by Y. Zhang from Lanzhou University. The online results of the N_2 and ^{3}He pressure curve are shown in left panel and right panel of Fig. 5.78, respectively.

5.11 Nuclear Correction of ^{3}He

In the extraction of neutron double spin asymmetry from the measured ^{3}He asymmetry in the DIS region, the common approach is to use the effective nucleon polarization:

$$g_1^{^3He} = P_n g_1^n + 2P_p g_1^p, \tag{5.91}$$

where $P_n(P_p)$ is the effective polarization of the neutron (proton) inside ^{3}He [278]. These effective nucleon polarizations $P_{n,p}$ can be calculated using ^{3}He wave functions constructed from N-N interactions, and their uncertainties are estimated using various nuclear models [279, 278, 280, 281], giving

$$P_n = 0.86^{+0.036}_{-0.02} \;\; and \; P_p = -0.028^{+0.009}_{-0.004} \; . \tag{5.92}$$

Recently, Scopetta [282] performed a calculation of the neutron target SSA (Collins and Sivers) including the ^{3}He nuclear effects in the initial state. Fig. 5.79 shows the difference of Collins/Sivers moments between full calculation and the calculation using Eqn. (5.92). The full calculation utilized the AV18 interaction as a realistic description of the nuclear dynamics. It is shown that at our kinematics the average effect for Collins moment is less than 4% (relative) and about 5% (relative) for the Sivers moment. Furthermore, the small proton effective polarization (-2.8%) causes small offsets in the ^{3}He asymmetries, compared to that from a free neutron. The

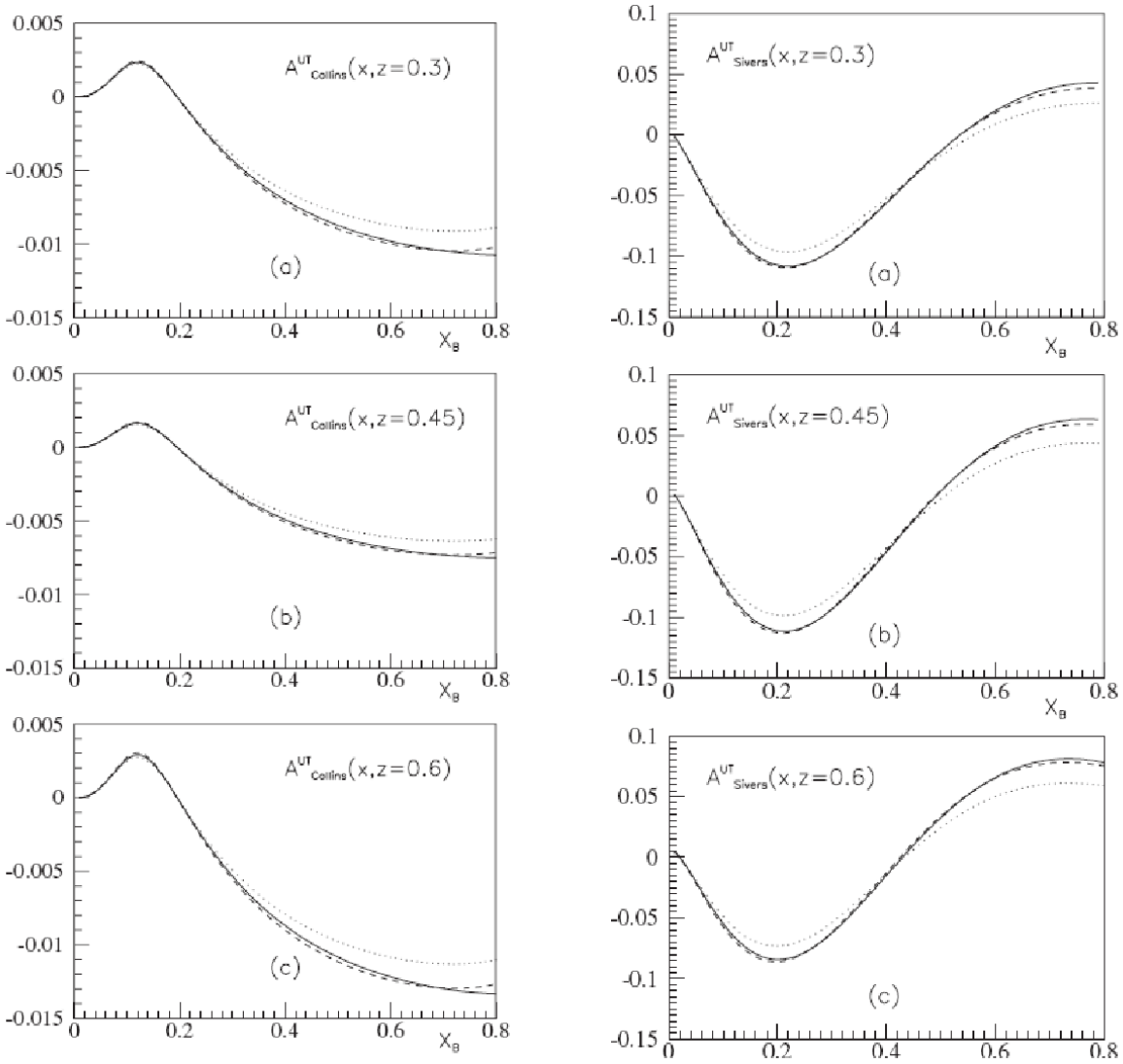

FIGURE 5.79: The left panel shows the calculation for Collins moment and the right panel shows the calculation for the Sivers moment. The solid curve shows the full calculation. The dashed and dotted curves show the calculation using Eqn. (5.92) and Eqn. (5.92) by neglecting the proton contribution completely. Figure is from Ref. [282].

uncertainties associated with this small offset are even smaller when considering that the corresponding proton asymmetries are relatively well known from the HERMES data.

The calculations in Ref. [282] are based on the impulsed approximation (IA). In principle, effects beyond IA, such as nuclear shadowing effects and final state interaction (FSI) could be relevant to the SSAs. In general, the shadowing effects are pronounced at small Bjorken x as shown in Fig. 9.1 (Appendix). In experiment E06-010, the probed x range is between 0.1 and 0.4, in which the effects caused by nuclear shadowing are less than 5%. Concerning the FSI of the produced π with the spectator nucleons, in principle the effect at low Q^2 can not be neglected. However, since the chosen π momentum is 2.35 GeV (z about 0.5), the effect of the FSI is expected to be small at such high momentum. Furthermore, in the asymmetry measurement the effects of any spin-independent interaction are expected to be canceled out in particular for the spinless π. Recently, another work [283] showed that the effect of finite-Q^2 on longitudinal structure functions g_1 and g_2 might also play an important role. The calculation on transverse SSA is expected to be performed in the near future.

6

Simulation of the Experiment

In the modern experimental data analysis, the role of Monte Carlo (MC) simulation is extremely important. First, MC can help understand many experimental factors, such as physics backgrounds, detector acceptance, etc. Second, MC can help to apply various corrections to the data, such as the bin centering correction, radiative correction, etc. Finally, MC can also help evaluate the systematic uncertainties of the experiments. In this section, two major simulations used in the experiment E06-010 data analysis are discussed. The SIMC (second part), which will be used for the coincidence channel, is still under developing.

6.1 GEANT3 Simulation of BigBite Spectrometer

During the preparation of experiment E06-010, a GEANT3 based BigBite spectrometer simulation code was developed. The motivation for developing such a MC was to understand the low energy background in the MWDC (more discussion in Sec. 9.4), to evaluate the tracking efficiency of the newly developed Pattern Match Tree Search tracking algorithm (more discussion in Sec. 9.3.2), to design the Big-

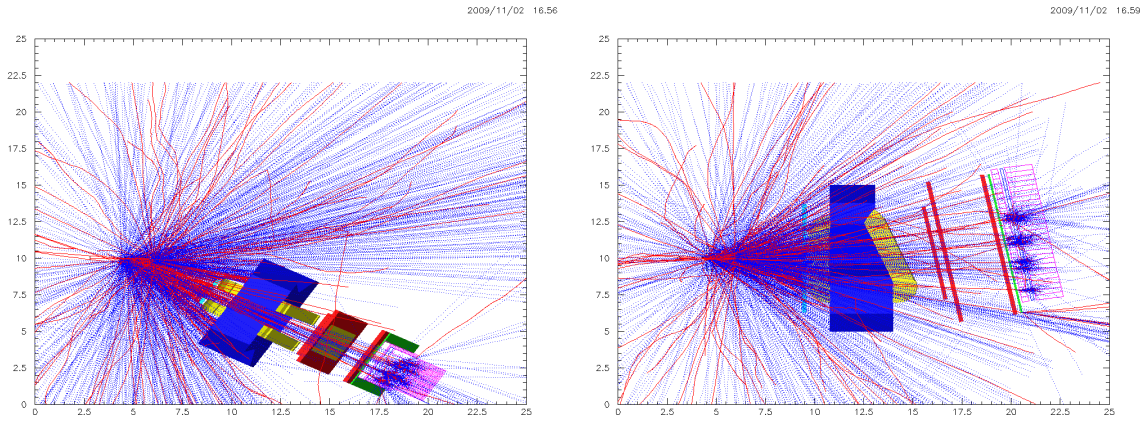

FIGURE 6.1: Left and right panel show the top and side view of one event simulated with the MC. Red lines represent the charged particles and the blue lines represent photons.

Bite optics slot slit, and to estimate the solid angle of BigBite. The software is based on "COMGEANT" [284], which is an interface to GEANT3.21 program. Data input files are used to define the detector geometry and all other parameters without recompiling the code. It also contains event generators for various hadron and lepton-induced interactions.

The initial BigBite Model was constructed by E. Chudakov (Staff Scientist of Jefferson Lab) based on BigBite engineering drawing (Fig. 4.24). The model was later updated in the data analysis of the experiment E06-010 in order to describe the distribution of the data. The BigBite magnetic field mapping was from SNAKE EMULATION from MAFIA by V. Nelyubin [285] from University of Virginia. A side view of the BigBite model is shown in Fig. 4.25. In the simulation, events were uniformly generated from the 40 cm long ^{3}He target according to the selected event generator. The interaction between the particle and the defined material was controlled by the standard GEANT3, including energy loss, particle decay, bremsstrahlung, etc. Each interaction could be turned on/off according to the requirement of the study. The magnetic field was parametrized in a file and the motion of a charged particle inside

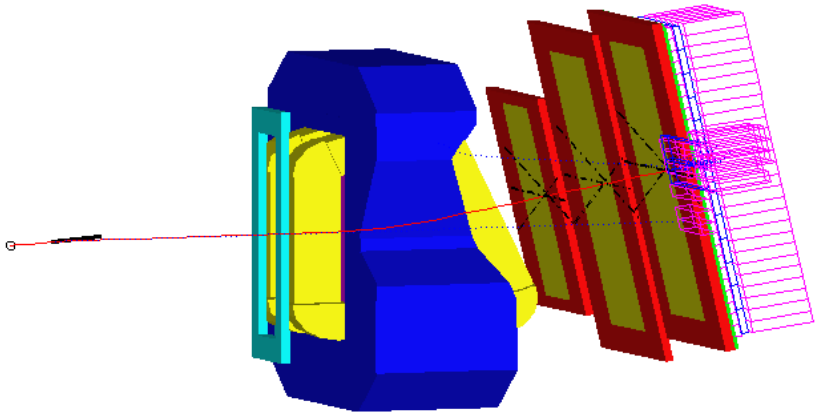

FIGURE 6.2: An event display of BigBite in COMGEANT. The fired wires are labeled by dashed lines. The hit preshower/shower blocks are illustrated.

the magnetic field was performed step-by-step. Fig. 6.1 shows the top and side view of one event simulated in the MC.

6.1.1 BigBite Model in COMGEANT

In the COMGEANT, all three MWDCs, preshower, scintillator and shower detectors of BigBite were modeled with the exact geometry and materials of those used in experiment E06-010. For MWDC, every chamber consisted of six wire planes with different orientations. The digitization included the number of the fired wires and the drift time. For preshower, scintillator and shower plane, the digitization included the energy deposition in each block. Fig. 6.2[1] shows an event display in COMGEANT. All the digitization from detectors and the kinematic information for the initial particle as well as the secondary particles were stored in a specialized ntuple file. In order to reduce the size of the ntuple file, the information was packed and needed to

[1] This plot was generated before the geometry of BigBite was finalized. In this case, the second chamber was assumed to be in the middle of the first and the third chamber.

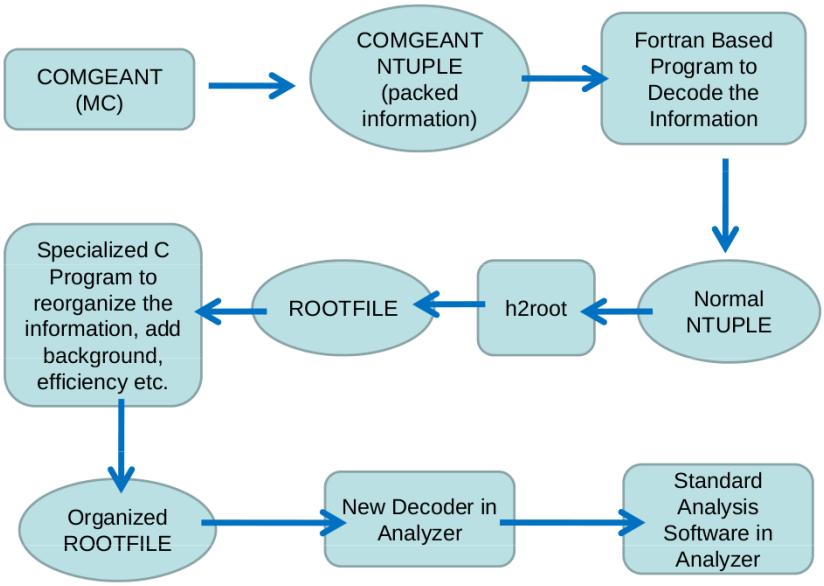

FIGURE 6.3: The procedure for analyzing the MC data.

be decoded before further analysis.

6.1.2 Interface to ANALYZER

In order to analyze the MC data with the same set of software developed in analyzing the experimental data, an interface was developed to convert the output of COMGEANT to the input of ANALYZER. The entire procedure is illustrated in Fig. 6.3. The COMGEANT ntuple is first generated by running the COMGEANT MC simulation. A FORTRAN based program is then used to decode the information in the COMGEANT ntuple and stores them in a normal ntuple, which is further converted into a rootfile with the standard root software "h2root". The converted rootfile is subsequently processed through a C based program in order to

- Reorganize the information.
- Add the background for MWDC.

- Add the detector efficiency.
- Add the effect of detector pileup.
- Add the extra detector resolution.

. An organized rootfile with the designed format was generated. Such organized rootfile could then be analyzed by the ANALYZER with a newly developed decoder "BBMWDC", which let the ANALYZER read the data from the rootfile instead of the raw experimental data file. In particular, the decoder of ANALYZER needs to map the information stored in the rootfile to the corresponding detector channels (ADC/TDC). With this decoder, the standard analysis software in the ANALYZER including the BigBite optics, tracking, shower clustering and etc. can be used to analyze the MC data. Therefore, the same cuts can be applied in both the MC data and experimental data.

6.1.3 Comparison of BigBite MC with Data

The forward transportation of the BigBite model in the MC was examined with the optics reconstruction used in the data analysis. In this case, electrons were generated in the entire acceptance and for momentum range of 0.5 GeV to 3.2 GeV. The simulated data were fed into the analysis code using the interface software. Fig. 6.4 shows the δVz, which is the difference between the generated and the reconstructed interaction vertex, and the $\delta P/P$, where δP is the difference between the generated and the reconstructed momentum. Both the δVz and $\delta P/P$ distribution peaked at zero. The resolution of δVz is about 1 cm, and the resolution of $\delta P/P$ is about 1.5 %. There are long tails on both sides of peaks, representing the effect of the fringe field, which is difficult to be taken into account in the MC.

Two target collimators, which were modeled according to their design, were added to shield the high energy electrons/photons generated from the two endcaps of the

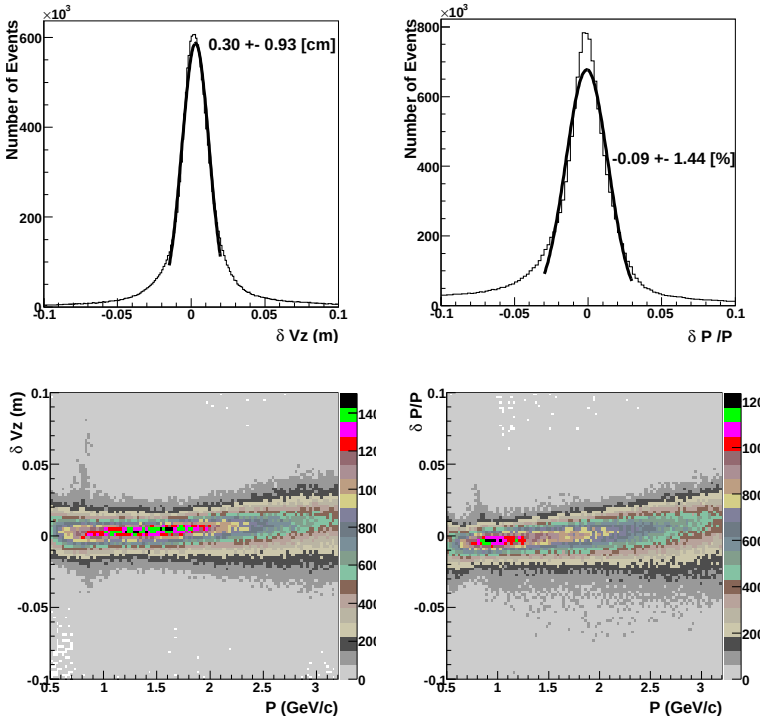

FIGURE 6.4: δVz and $\frac{\delta P}{P}$ of the MC data. The lower two panels show the δVz and $\frac{\delta P}{P}$ against the momentum P.

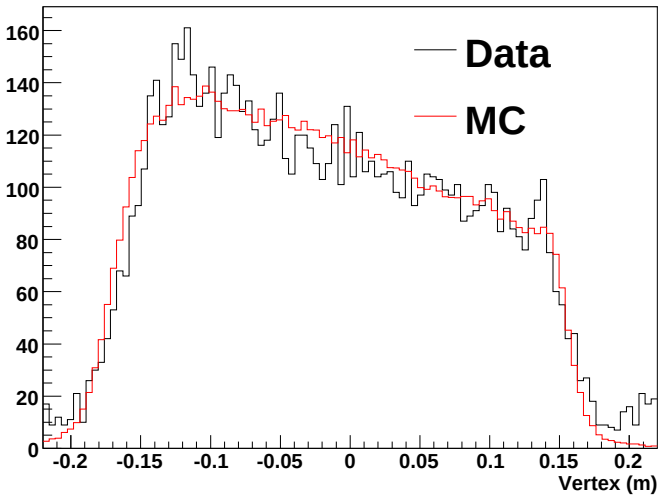

FIGURE 6.5: Interaction vertex comparison between MC and the data.

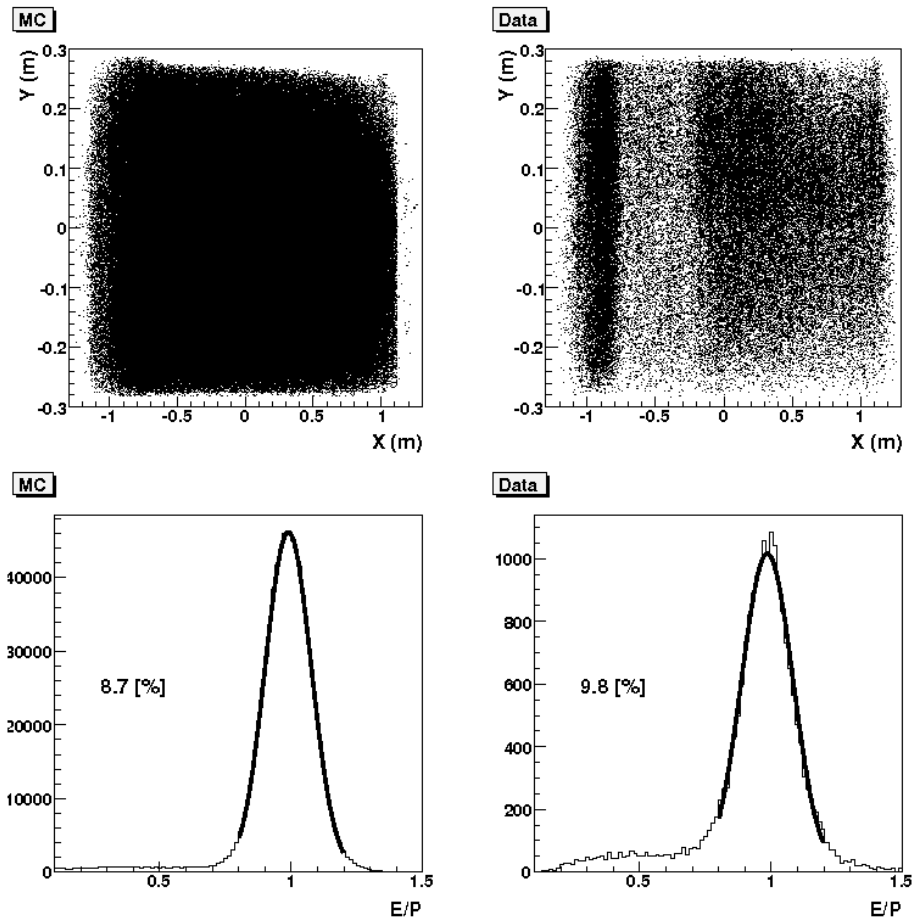

FIGURE 6.6: Comparisons of acceptance and energy resolution in the calorimeter between MC and the data.

target scattering chamber. The effect of the target collimators is compared with that of data in Fig. 6.5. The MC can reasonably describe both edges of the reconstructed vertex.

Finally, the acceptance of the calorimeter and the energy resolution in the calorimeter system were compared between the data and MC. The results are shown in Fig. 6.6. The top two panels show the track projection in the shower plane for MC and the data. The distribution observed in the data is due to the trigger of the BigBite. The bottom two panels show E/p peak for the MC and data. Each peak was fitted with a Gaussian function. The σ, representing the resolution of E/p, is

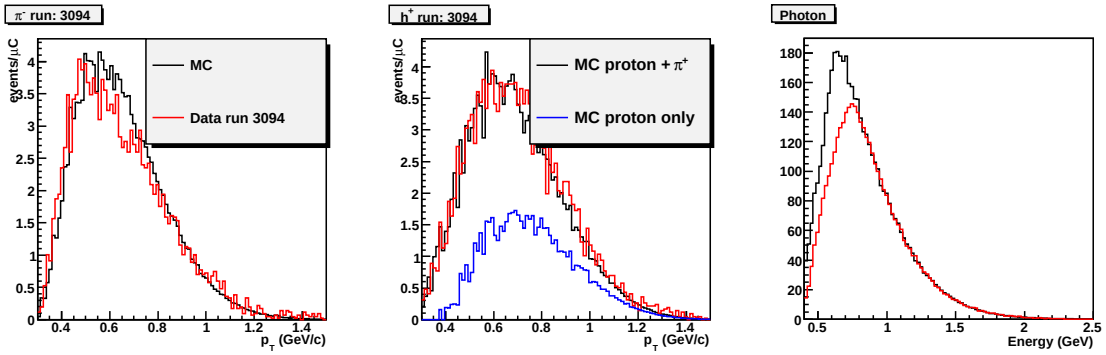

FIGURE 6.7: The yield comparison between the MC and data for π^-, positive hadrons and photons. The blue histogram in the middle panel shows the MC yield for the proton, and the red histogram in the middle panel shows the sum of proton and π^+.

shown in the plot. The fitted σ in the data is slightly worse than that in the MC, possibly due to the π contamination in the data.

6.1.4 Single Rate Comparison between Data and MC

The MC was used to understand the singles rate in BigBite. The main goal of this study was to provide an independent verification of the pion contamination and the photon-induced electron contamination in the sample of DIS electrons. In order to do so, one has to reasonably understand the singles rate for various particle types. This was realized by performing a MC to simulate particles of different types (protons, $\pi^{\pm}$ and π^o) in a flat phase space of lab polar angle θ, lab azimuthal angle ϕ, and the momentum p. Each event was then weighted by a cross section calculated outside the COMGEANT simulation. The cross sections of single hadron electroproduction including proton and $\pi^{\pm}$ were calculated by the Wiser code [286]. The π^o production cross section was assumed to be twice of the sum of π^+ and π^- cross sections calculated from the Wiser code. Since the Wiser code was a fit to the data [286], one does not expect it to describe the data in our kinematics perfectly. Therefore, transverse momentum P_T dependent corrections were applied to the cross section calculated from the Wiser code in order to match the distributions of data with those of MC.

	π^+	π^-	e-	p
Data	54.8	34	12.4	49.6
Corrected Calculation (Wiser&Whitlow)	62.6	37.2	-	51
Calculation (Wiser&Whitlow)	105	62.4	11.6	71

Table 6.1: The HRS rate comparison between the data and the calculation based on the Whitlow and the Wiser code. The units is in events/μC.

Here, $P_T = P \cdot \sin\theta$, where the θ is the lab polar angle, z axis is long the beam line, and P is the momentum of the particle. The P_T distributions of singles positive, negative charged hadrons, and photons between data and MC are compared in Fig. 6.7. The black histogram shows the yield from run 3904 in the data. The red histogram shows the MC results with the updated Wiser code. The blue histogram shown in the middle is for the proton only. The photons in MC are assumed to be from the decay of π^o. The π^o production cross section, after correcting for the $\pi^\pm$ production cross section, was further corrected by another P_T dependent term in order to describe the photon yields observed in the data. The discrepancy between the data and MC for the photon yield at lower energies is partly due to the trigger threshold effects.

The updated Wiser code was also compared with data from left HRS. The HRS solid angle is assumed to be 6.7 msr. The momentum acceptance is about $\pm$ 5%. The decay of hadrons was also taken into account with the average travel distance inside HRS. The comparisons are shown in the Table. 6.1. To compare the original calculation from the Wiser code without the correction are also presented. For pions, the original Wiser code over-estimates the data by about factor of 2. For photons, the original Wiser code over-estimates by about 40%. The electron rate calculated from the Whitlow code [287] can describe the data reasonably well.

In the HRS, the pion contamination and the photon-induced electron contamination are negligible for two reasons. First, there were two detectors, the gas Cerenkov

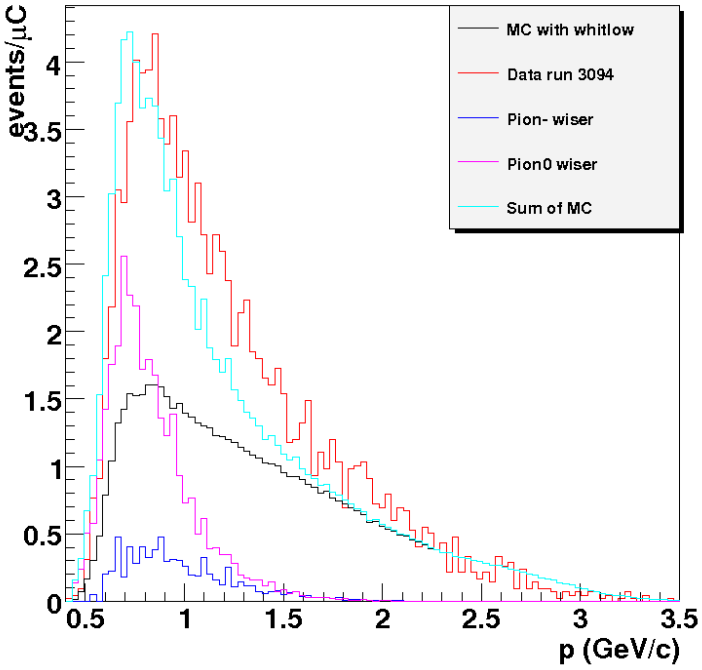

FIGURE 6.8: Electron yield comparison between data and MC.

counter and the pion rejector, which could provide the separation of electrons and pions. Second, the HRS central momentum setting was set at 2.35 GeV, at which the photon-induced electrons were negligible. However, this is not the case for the BigBite spectrometer. First, the only PID detector in the BigBite was the lead glass calorimeter. Next, the momentum coverage of the BigBite spectrometer was rather low, from 0.6 GeV - 2.5 GeV, at which the photon-induced electrons are expected to contaminate the DIS electrons severely. Fig. 6.8 shows the electron yield comparison between the data and MC. The red histogram is the yield from run 3094 of the data. The black histogram is the simulated DIS electrons based on the Whitlow cross section without any further correction. The dark blue histogram is the π^- contamination in the electron sample after applying the standard PID cuts as those used in the analysis. The magenta histogram shows the yield of photon-induced electrons from simulating π^o in the BigBite. The light blue histogram is the sum of

Mom. Bin GeV	π^- Cont. % MC	π^- % Data	Photon-induced e^- Cont. % MC	Photon-induced e^- Cont. Cont. % Data
0.6-0.8	8.7	13.8	54.8	55.8
0.8-1.0	10.7	10.5	42.0	48.5
1.0-1.4	9.5	6.8	21.2	24.2
1.4-2.0	4.0	1.7	4.6	9.5

Table 6.2: This table summarized the pion and photon-induced electron contamination in the DIS electron sample in the BigBite. In comparison, the results from Sec. 5.7 are also listed.

all the histograms from MC. The distributions of the blue histogram is reasonably in agreement with that of the data. Table. 6.2 summarizes the contamination results obtained in MC. In comparison, the results obtained in Sec. 5.7 are shown simultaneously. From Table. 6.2, one can see that the major contamination is actually from the photon-induced electrons. In addition, the results from MC agree very well with those directly obtained from the data. The MC study confirmed the observation in the data.

6.2 SIMC

In the previous section, we described the GEANT3 based MC simulation code, which played a major role in understanding both low energy backgrounds and physics rates, testing the software and studying the acceptance. However, in order to update it to accommodate the coincidence channels, such as $e(N, e\pi^{\pm})X$, a GEANT3 based HRS model needs to be constructed. Moreover, a GEANT3 based simulation is usually limited by its running speed. Instead, we decided to take another approach. The standard Monte Carlo simulation code for Hall C [288], called SIMC, was used to simulate the experimental data taken in experiment E06-010.

6.2.1 Features of SIMC

In SIMC, events are generated in the phase space larger than the acceptance of the spectrometer in order to take into account the offsets, radiation and energy loss that may smear the events. A forward particle transportation is then used to transport the simulated particles to the detector hut. In this process, cuts are applied to mimic the acceptance of the spectrometer. Many corrections, including pion decay, multiple scattering, energy loss, and radiative corrections have been built in the SIMC. Here, we will briefly describe the treatment of these effects in SIMC.

Pions $\pi^{\pm}$ may decay while traveling through the HRS magnets. At 2.35 GeV, the decay probabilities are calculated to be about 16% and 73% for pions and kaons, respectively, with the flight length L_{HRS} of 23.5 m and their lifetimes in the particle's rest frame. For example, the pion decay probability ϵ can be estimated as:

$$\epsilon = e^{-\frac{L_{HRS}}{T_{\pi} \cdot P/m_{\pi} \cdot c}}. \tag{6.1}$$

Here T_{π} is the pion lifetime in the pion rest frame; P is the momentum; m_{π} is the pion mass in its rest frame; and c is the speed of light. For asymmetry measurement in experiment E06-010, the decay of pions will reduce the number of events recorded, but it is not expected to affect the asymmetries.

When electrons and hadrons travel through materials, they may interact with the electrons inside the materials, thus changing the travel directions. Such behavior is usually referred to as multiple scatterings. In SIMC, a parametrization fitted to the theory of Moliére [57] was used. The width of the scattering angle is:

$$\theta_{rms} = \frac{13.6}{\beta p}\sqrt{t} \times (1 + 0.038 \cdot \log_{10} t), \tag{6.2}$$

where t is the thickness of material in radiation length, β is the particle speed and p is the particle momentum in MeV/c.

In addition to multiple scatterings, electrons and hadrons may also lose energies during ionization processes when they travel through materials. In the case of a thin layer of material, the Bethe-Bloch equation

$$E_{prob} = K\frac{Zl}{A\beta^2}[ln\frac{m_e}{I^2} + 2ln\frac{P}{M} + ln\frac{KZl}{A\beta^2} - \delta - U + 1.06] \tag{6.3}$$

is always used to calculate the most probable energy loss for a relativistic particle. Here $K = 0.15354$ cm^2/g, l is the material thickness in g/cm^2, and M is the mass of the particle. Z and A are number of protons and nucleons of the material, respectively. I is the mean ionization energy of the material, δ is the density correction, and U is the shell correction. The energy loss for each event is then modeled according to a Landau distribution with the most probable value at E_{prob}.

The radiative correction represents the correction from E&M interaction beyond the tree level to the interested process. For example, Fig. 6.9 shows the Feynman diagrams contributed in the radiative correction to the $e(N, e'\pi^{\pm})X$ processes. Fig. 6.9 a) is the tree level contribution. The rest are the diagrams contributing to the radiative correction. The radiative correction treatment in the SIMC is based on the formalism of Mo and Tsai [289], but updated for the use in the coincidence experiment [290]. In this approach, the extended peaking approximation, where the photons are only allowed to emit along the direction of incoming electrons, outgoing electrons and outgoing pions, is used. The non-peak part is evenly split between the incoming and outgoing electrons in order to preserve the entire radiation strength. In addition, the radiated photon energies are restricted to be much less than the energies of the particles (soft photon approximation). In practice, the radiative correction modifies both the cross section and the momentum of particles. The first

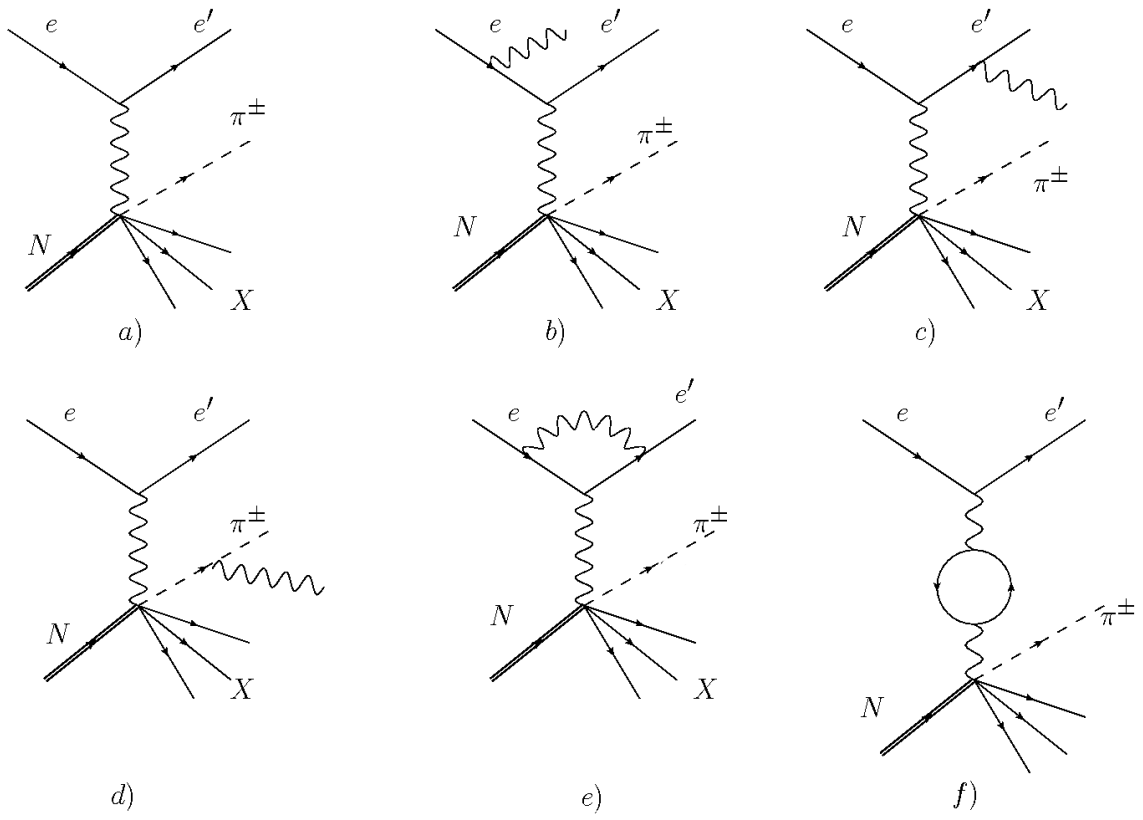

FIGURE 6.9: Radiative Correction to $e(N, e'\pi^{\pm})X$ Process. a) is the tree level diagram. The rest of the diagrams contribute to the radiative correction in SIMC.

order correction can be written as:

$$R_{corr} = (1 - \delta_{hard}) R_{soft} \Phi_e^{ext} \Phi_{e'}^{ext}, \tag{6.4}$$

$$R_{soft} = R^e R^{e'} R^{\pi}. \tag{6.5}$$

. Here, R^e, $R^{e'}$ and R^{π} are corresponding to the diagrams b), c) and d) in Fig. 6.9, respectively. In these cases, a soft photon was radiated by the incoming or outgoing charged particles. The $(1 - \delta_{hard})$ is the component due to the vertex corrections, which are corresponding to diagrams e) and f) in Fig. 6.9. Φ_e^{ext} and $\Phi_{e'}^{ext}$ are called the external radiation. They are corresponding to the E&M interaction between the incoming or outgoing particles with material in its path. In comparison, the R_{soft}

is called internal radiation, which is due to the E&M interaction between the target and the incoming or outgoing particle. In principle, Φ_π^{ext} also exists. However the contribution of Φ_π^{ext} is strongly suppressed in comparison to that of electrons by $\frac{m_e^2}{m_\pi^2} < 2 \times 10^{-5}$. Therefore, it is completely neglected.

In SIMC, the radiated photon energies along the incoming electron, the outgoing electron and the generated pion directions are generated randomly according to the energy distribution functional form $C \cdot E^{g-1} dE$. Here C and g are calculable constants. Once the energy of the radiated photon is fixed, it is used to modify the momentum of the incident and scattered particles which are initially generated using the MC method. The radiation weight in Eqn. (6.4) is then calculated and weighted to each event. In the measurement of SSAs, both the incoming and outgoing electrons are unpolarized. In addition, the π is a spinless particle. Therefore, according to Fig. 6.9, all the radiative corrections are expected to be spin-independent. In this case, the major effect of the radiative correction is the shift of kinematics. For example, the electrons in $e + N \rightarrow e' + \pi + N$ exclusive reaction channel can radiative a photon, and are then misidentified as a DIS electron.

In SIMC, after each event is generated, its corresponding cross section is calculated and saved as a weight, with which the MC equivalent yield can then be formed in order to compare with data.

6.2.2 Modification Plan

The modification of SIMC to suit the experimental setup of experiment E06-010 is currently working in progress. The planned modifications include:

- Construct BigBite spectrometer:

  The BigBite spectrometer model needs to be added into SIMC. The model includes a forward transportation, acceptance cuts (detector, magnet, target collimator), and backward transportation. Currently, the BigBite model is

under construction by A. Puckett, a postdoc from Los Alamos.

- Update the HRS spectrometer:

  There is an existing model of the HRS spectrometer in the SIMC. However, in experiment E06-010, the spectrometer collimator was removed. Therefore, the model in the HRS spectrometer needs to be examined. In addition, in experiment E06-010, the target is 40 cm long, rather than a short target. The forward/background reconstructions for the extended target effects need to be updated.

- Update the Target:

  The current target information in SIMC is based on the Hall C LH_2/LD_2 target. The target shape, target wall material, and other materials between the target and the detectors need to be updated.

SIDIS Cross Section and SSAs Calculation

In SIMC, the unpolarized SIDIS cross section $\frac{d\sigma^h_{UU}}{dx_B dy d\phi_S dz_h d\phi_h dP^2_{h\perp}}$ is calculated according to Eqn. (3.33) with the Gaussian ansatz. The PDFs are from the CTEQ parametrization [291], which can be replaced by other parametrization, such as MRST [292]. The FF parametrization is based on Kretzer's fit [293], and can be replaced by other parametrization. In order to use $\frac{d\sigma^h_{UU}}{dx_B dy d\phi_S dz_h d\phi_h dP^2_{h\perp}}$, a six-by-six Jacobian function needs to be calculated to transform the cross section into the lab frame $\frac{d\sigma^h_{UU}}{dP_e dCos\theta_e d\phi_e dP_h dCos\theta_h d\phi_h}$, since the events are generated in the lab frame. The derivation of the Jacobian functions can be found in Sec. 9.7. Similarly, the SSAs can be calculated in the SIMC for each event. In addition to the two parametrization discussed in Sec. 3.5, another model calculation [294] was used in generating prediction of SSAs in the data analysis. In this approach, the transversity distribution is based on Ref. [158]. The pretzelosity distribution is based on Ref. [295]. The quark

intrinsic transverse momentum k_T dependence and Collins fragmentation function are taken from parametrization of Ref. [296].

6.2.3 Goal of the Coincidence Simulation:

The coincidence simulation SIMC will be updated to the configuration in experiment E06-010, in order to perform a few corrections and study some of the systematic uncertainties. They are:

- Bin-Centering Correction:

  As shown in Fig. 5.64, data have to be binned into several finite-size bins in one kinematic variable, such as x. In order to disentangle different angular distributions inside each bin, the data are further binned into two dimensional bin in terms of ϕ_h and ϕ_S as shown in Fig. 5.65. A fitting procedure is then applied to extract the different components of SSAs, by assuming different components are the same in each small ϕ_h/ϕ_S bin. However, this assumption is not necessary to be true, since each small ϕ_h/ϕ_S bin can correlate to different central values of Q^2, x, z, and P_T, due to the correlations in the phase space. These correlations in the phase space normally come from the experimental limitations. Left panel of Fig. 6.10 shows the central x, Q^2, z, and P_T values for different ϕ_h/ϕ_S 2-D bins in the first x bin illustrated in Fig. 5.64. The right panel of Fig. 6.10 shows the predicted Collins asymmetries [294] for different ϕ_h/ϕ_S 2-D bins in four x bins, which clearly vary in different ϕ_h/ϕ_S 2-D bins. Therefore, a bin centering correction is necessary to be applied to each ϕ_h/ϕ_S bin to correct the measured asymmetry $A(Q^2_{ij}, x_{ij}, z_{ij}, P_{Tij}, \phi_{hi}, \phi_{Sj})$ (i and j denote bins in ϕ_h and ϕ_S, respectively) to $A(Q^2_0, x_0, z_0, P_{T0}, \phi_{hi}, \phi_{Sj})$ at a common point of Q^2_0, x_0, z_0, ad P_{T0} in the phase space:

$$A^{point}_{data} = \frac{A^{raw}_{data}}{A_{MC}} A^{point}_{MC} . \tag{6.6}$$

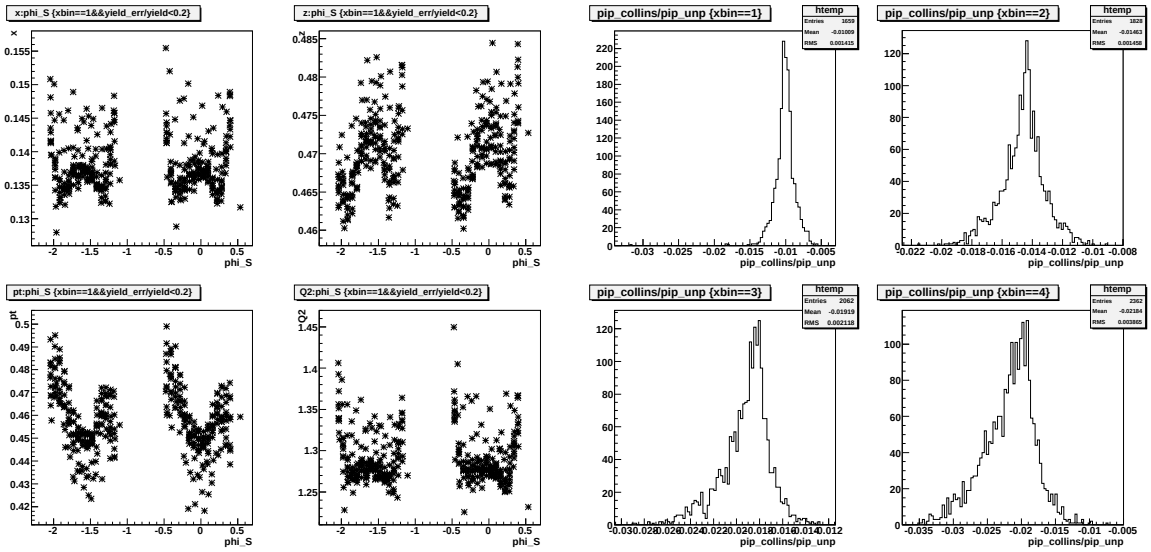

FIGURE 6.10: Left graph shows the central x, Q^2, z, and P_T values for different ϕ_h/ϕ_S 2-D bins in the first x bin shown in Fig. 5.64. Right graph shows the predicted Collins asymmetries [294] for different ϕ_h/ϕ_S 2-D bins in four x bins.

Clearly, such correction would require a good understanding of the acceptance, in other words, a good description of the spectrometer acceptance in the MC. In addition, a good theoretical parametrization is also necessary. Since the experiment E06-010 represents the first direct measurement of SSAs on the neutron, the knowledge of the theoretical parametrization is rather limited. Nevertheless, one can use the bin centering method to study the associated systematic uncertainties.

- Contamination from the diffractive ρ^0 Production:

  At HERA (the high energy collider), pomeron exchange interaction, which is interpreted as a type of multi-gluon exchange, can explain about 8-10% of the total virtual photon-proton interaction cross section [297]. In the case of ep scattering, the virtual photon may fluctuate into a vector meson (VMD) [34], followed by an elastic or inelastic scattering with the nucleon. Fig. 6.11 shows

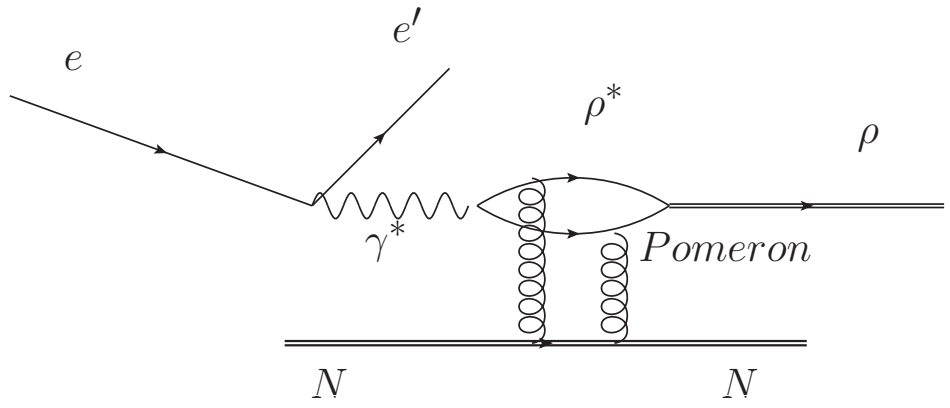

FIGURE 6.11: The diagram to illustrate the diffractive ρ^0 production in ep scattering.

an example diagram of the diffractive ρ^0 production in ep scattering. The ρ^0 subsequently decays into a pair of π^+ and π^-. One of the two pions can end up in the detector acceptance. Clearly the pions from the diffractive ρ^0 production do not belong to SIDIS pion electroproduction, since the pion does not tag the parton flavor information in the nucleon. Therefore, the diffractive ρ^0 production should be measured or estimated. In SIMC, a model of diffractive production based on parametrization of results of Pythia [298] was developed. Such model has been compared with data in CLAS and has been used in the HERMES SIDIS analysis [194, 299]. For the experiment E06-010 analysis, the SIMC will be used to estimate the contribution from diffractive ρ^0 events [2]. Furthermore, due to the symmetry of ρ^0 decays, one expects that the kinematics and cross section of π^+ should be the same as those of π^-. Therefore, the effect of diffractive ρ^0 production would be canceled in the combined π^+ and

[2] A quick estimation of the effect is about several percent.

π^- asymmetry:

$$A^{\pi^+-\pi^-}_{combined} = \frac{(\sigma^{\uparrow}_{\pi^+} - \sigma^{\uparrow}_{\pi^-}) - (\sigma^{\downarrow}_{\pi^+} - \sigma^{\downarrow}_{\pi^-})}{(\sigma^{\uparrow}_{\pi^+} - \sigma^{\uparrow}_{\pi^-}) + (\sigma^{\downarrow}_{\pi^+} - \sigma^{\downarrow}_{\pi^-})} = \frac{A_{\pi^+}\sigma_{\pi^+} - A_{\pi^-}\sigma_{\pi^-}}{\sigma_{\pi^+} - \sigma_{\pi^-}}, \quad (6.7)$$

$$A_{\pi^\pm} = \frac{\sigma^{\uparrow}_{\pi^\pm} - \sigma^{\downarrow}_{\pi^\pm}}{\sigma^{\uparrow}_{\pi^\pm} + \sigma^{\downarrow}_{\pi^\pm}}, \quad (6.8)$$

$$\sigma_{\pi^\pm} = \sigma_{\pi^+} + \sigma_{\pi^-}. \quad (6.9)$$

- Angular Resolutions:

  At low P_T, the angular resolution on ϕ_h will increase, since the virtual photon $\vec{q}$ vector will be close to the outgoing hadron momentum. This can lead to a problem in the angular separation of SSAs. With MC, one can easily calculate the angular resolution in ϕ_h with input of the detector resolutions. Thus, the MC can provide useful information about the low limit cutoff on P_T.

- Cross Section Analysis:

  With the development of MC, one can precisely understand the spectrometer acceptance, which is an important step in extracting the cross section from the data.

7

Results and Discussions

In this section, we present the preliminary results of experiment E06-010. Here, we do not show the target SSAs from the inclusive electron DIS process, since those will be included in the thesis of J. Katich from the College of William and Mary. In addition, as this thesis is focusing on the single target spin asymmetries, neither results from the double spin asymmetries including beam helicity nor the single beam spin asymmetries are discussed [1].

7.1 Single Hadron Target SSA

7.1.1 Left HRS

Fig. 7.1 shows the preliminary left HRS single hadron Target SSA results from polarized ^{3}He prior to corrections from the N_2 dilution and the target polarization. In the vertical case, the asymmetry is defined as:

$$A = \frac{Y_\uparrow - Y_\downarrow}{Y_\uparrow + Y_\downarrow}. \tag{7.1}$$

[1] The beam helicity related asymmetries will be presented in the thesis of J. Huang from M. I. T..

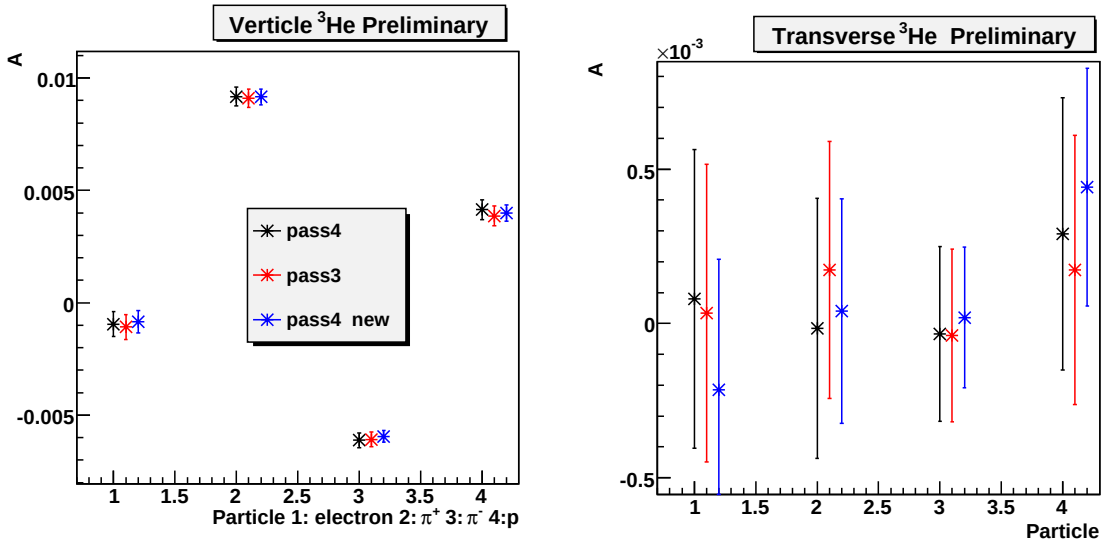

FIGURE 7.1: The preliminary left HRS single hadron Target SSA results from polarized ^{3}He before correction from the N_2 dilution, and the target polarization. The error bars represent statistical uncertainties only.

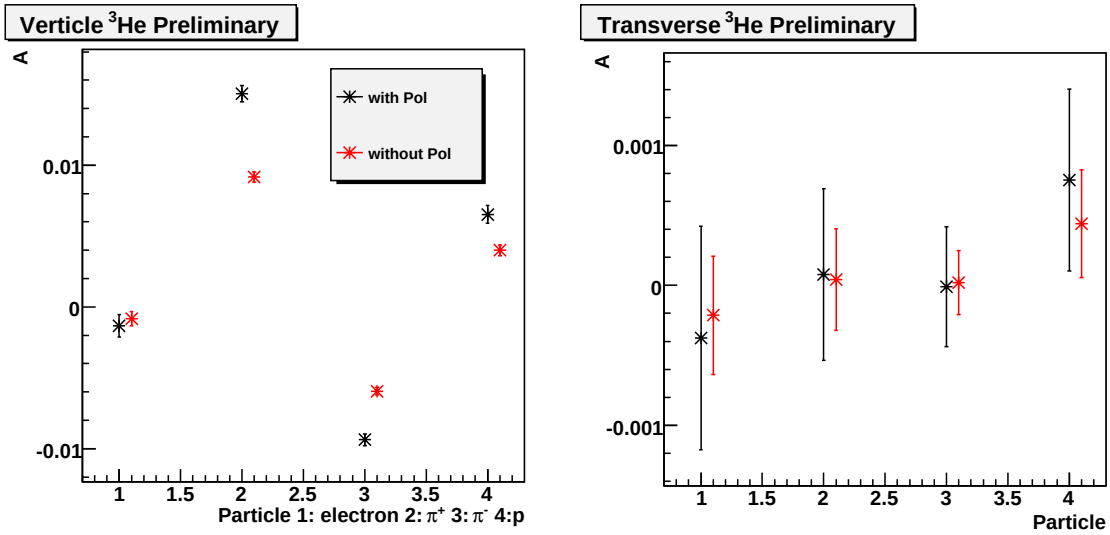

FIGURE 7.2: The preliminary left HRS single hadron Target SSA results from polarized ^{3}He before correction from the N_2 dilution. The black points include the correction from the target polarization. The error bars represent statistical uncertainties only.

In the transverse case, the asymmetry is defined as:

$$A = \frac{Y_{\rightarrow} - Y_{\leftarrow}}{Y_{\rightarrow} + Y_{\leftarrow}}, \tag{7.2}$$

and $\rightarrow$ is to the beam right (-x direction in the hall coordinate system). The points with different colors are from analysis of the same data set at different analysis periods. The error bars represent statistical uncertainties only. The blue points represent the latest results. The results from analysis of the data replayed in different passes are consistent with each other, demonstrating the stability of the analysis procedure. In the latest analysis (blue points), the super local pair method as discussed in Sec. 5.8.2 was used, which significantly improved the statistical precision. Fig. 7.2 shows the preliminary results including the target polarization correction. We observed a clear non-zero Target SSA for singles π^+, π^-, and proton production with a vertically polarized ^{3}He. The sign of proton and π^+ asymmetries are the same, which is different from that of π^-. In the transverse case[2], due to parity conservation, the Target SSAs are expected to be all zero, which is consistent with our observations.

7.1.2 BigBite

Fig. 7.3 and Fig. 7.4 show the preliminary BigBite singles hadron Target SSAs for negatively and positively charged hadrons, respectively [3]. The results are corrected by the target polarization, but prior to the N_2 dilution. The error bars represent the statistical uncertainties only. The black and red points represent the results from T1 and T6 triggers. The threshold on the T6 trigger was set higher than that of T1. The definition of the asymmetries are the same as the one in left HRS. However, since the BigBite was located to the beam right, while the left HRS was located to

[2] The acceptance of left HRS is small and the average ϕ_S angle is zero.

[3] Since BigBite spectrometer did not have any PID detectors to differentiate different hadron species. The sum of K^- and π^- is called negatively charged hadron and the sum of K^+, π^+ and p is called the positively charged hadron.

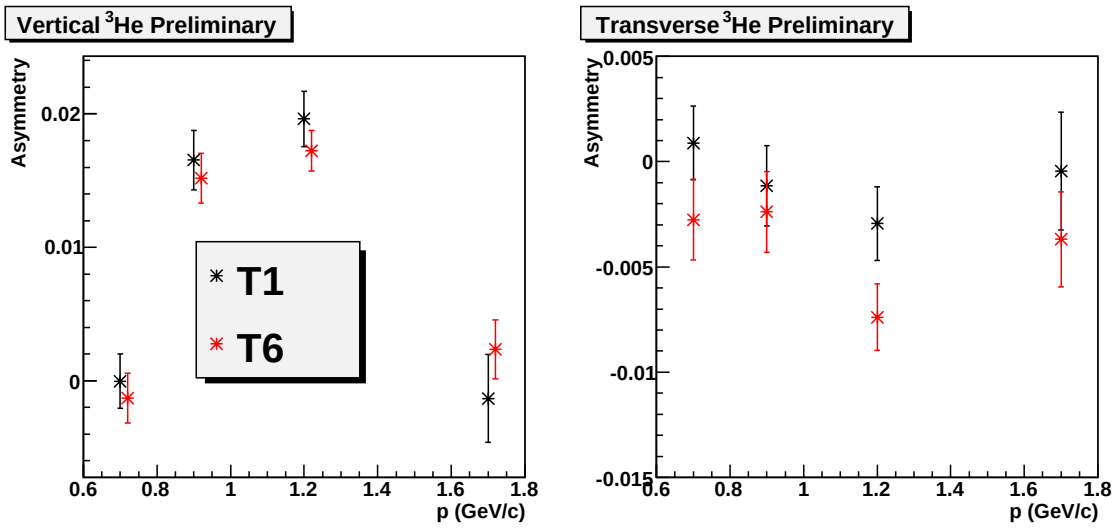

FIGURE 7.3: The preliminary BigBite single negatively charged hadron Target SSA results from polarized ^{3}He before correction from N_2 dilution. The positions of the T6 results were shifted slightly for clarity.

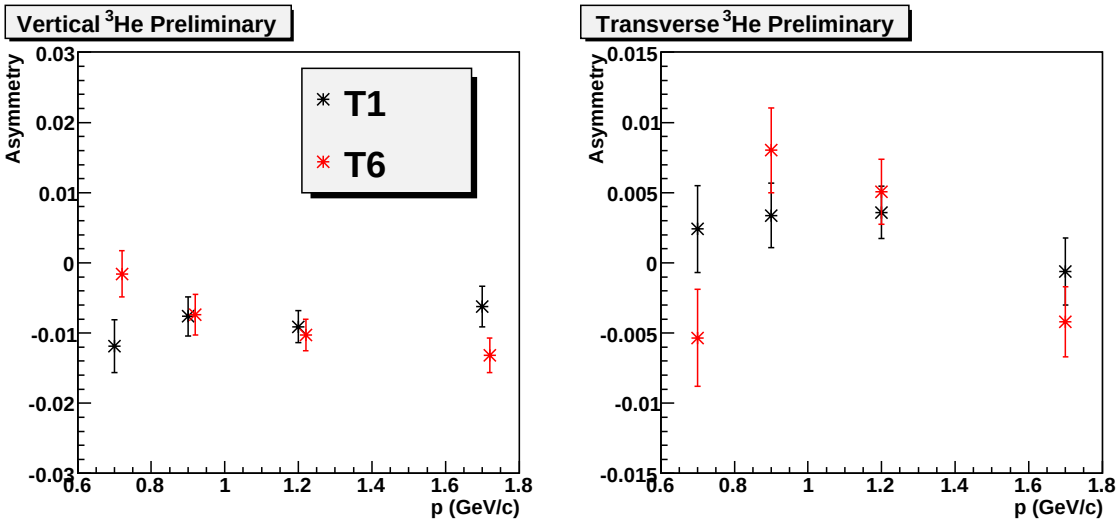

FIGURE 7.4: The preliminary BigBite single positively charged hadron Target SSA results from polarized ^{3}He before correction from N_2 dilution. The positions of the T6 results were shifted slightly for clarity.

the beam left, the expected asymmetries for BigBite and left HRS should have a different sign.

Similar checks of results with different analysis periods as the one performed with left HRS data were performed, and a consistency was observed. Although T1 and T6 were both single BigBite trigger, the threshold on them were different. In addition, the data were taken with high prescale factors (> 1000). There is almost no overlap between the data taken in T1 and those in T6. Therefore, they are totally statistical uncorrelated. The fact that the results in T1 are consistent with that of T6 confirm the reliabilities in the analysis procedure. In addition, since the data were taken with high prescale factors, the correction due to the prescale factors, as discussed in Sec. 5.8.4, was applied. The signs of the asymmetries with vertically polarized ^{3}He are consistent with those observed with left HRS. For example, a positive asymmetry was observed for negatively charged hadrons in the BigBite, while a negative asymmetry was observed for π^- in the left HRS. In the transverse case, the asymmetries are not consistent with zero, which is due to the non-symmetric acceptance of BigBite. In other words, the average ϕ_S is not zero for the BigBite spectrometer.

7.1.3 Angular Dependence

With the large acceptance of BigBite and data taken at two target spin states, one can study the angular dependence of the asymmetries. We fit our data with the form:

$$A(\phi_S) = a \cdot \sin(\phi_S) \ ^4 \tag{7.3}$$

Here, ϕ_S is the difference between the spin plane defined by the incident beam direction and spin direction and the scattering plane defined by the incident beam direction and outgoing electron direction. In addition, a is also referred to as $< \sin(\phi_S) >$.

[4] Other possible angular components may also contribute. The systematic uncertainties due to other possible components are still under investigation.

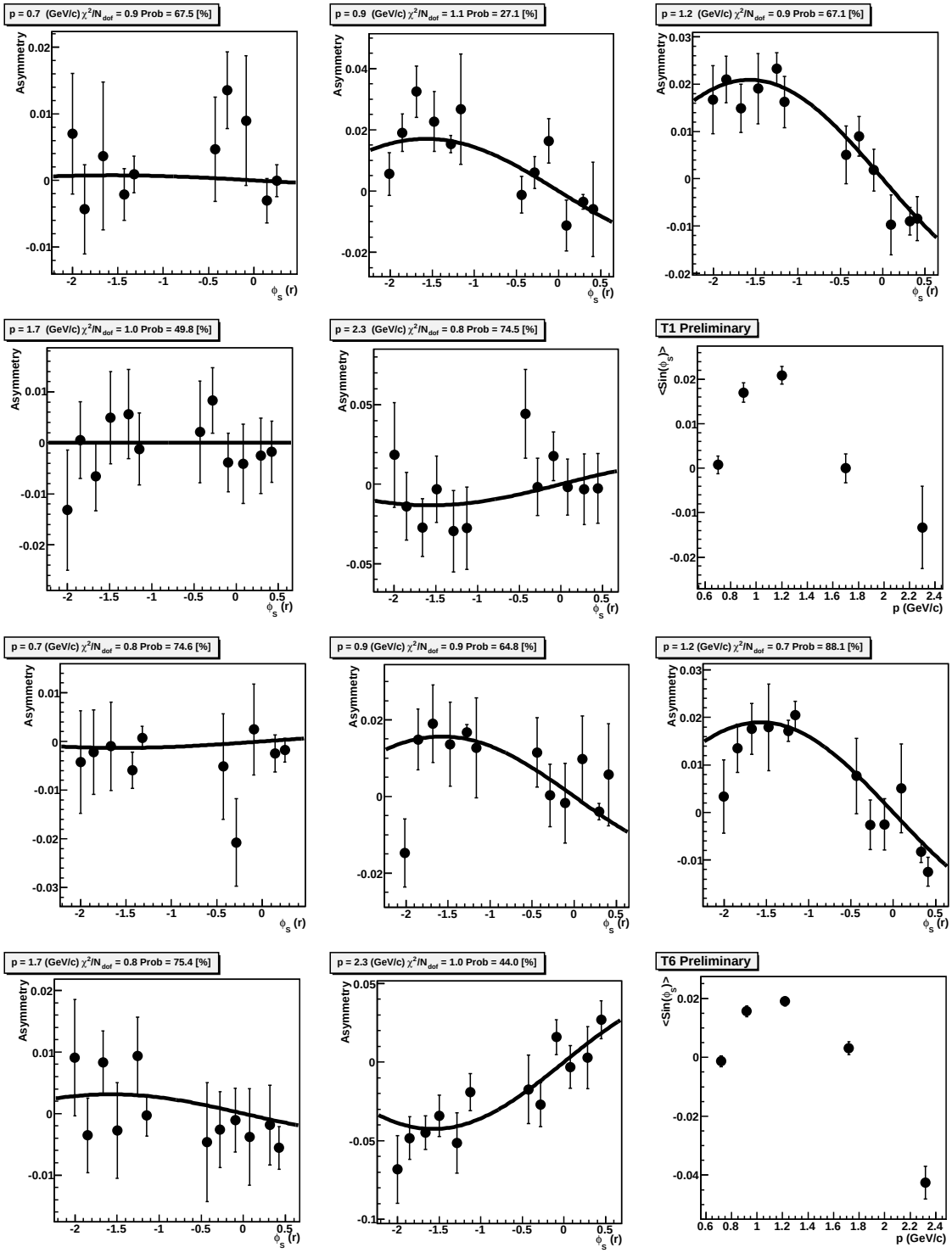

FIGURE 7.5: Angular modulation of h^- Target SSA for T1 (top) and T6 (bottom) triggers. The last panel in both plots show the extracted $< \sin(\phi_S) >$ value. The fitting quality χ^2/N_{dof} together with the probabilities of the fitting are listed. Only the statistical uncertainties are included.

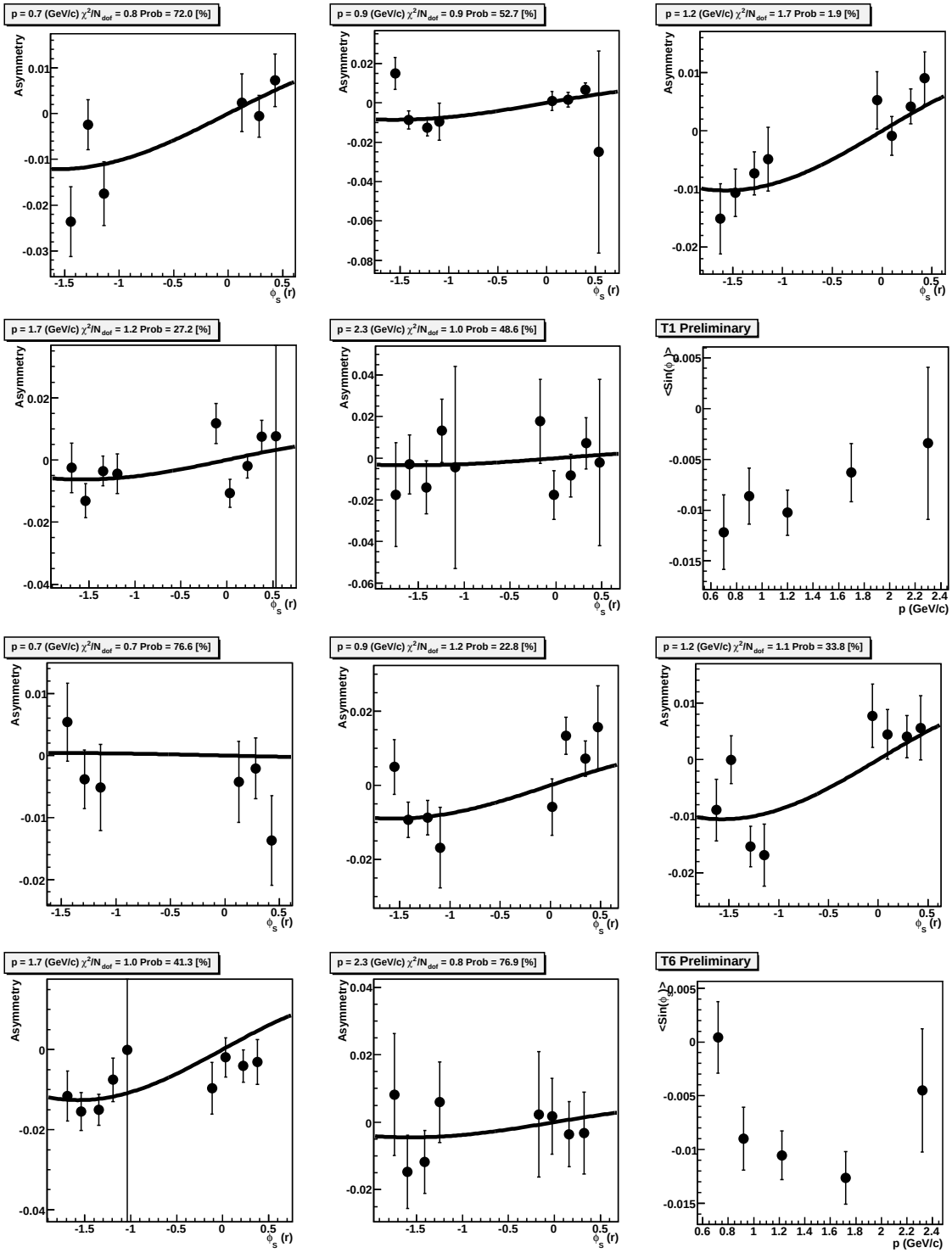

FIGURE 7.6: Angular modulation of h^+ Target SSA for T1 (top) and T6 (bottom) triggers. The last panel in both plots show the extracted $< \sin(\phi_S) >$ value. The fitting quality χ^2/N_{dof} together with the probabilities of the fitting are listed. Only the statistical uncertainties are included.

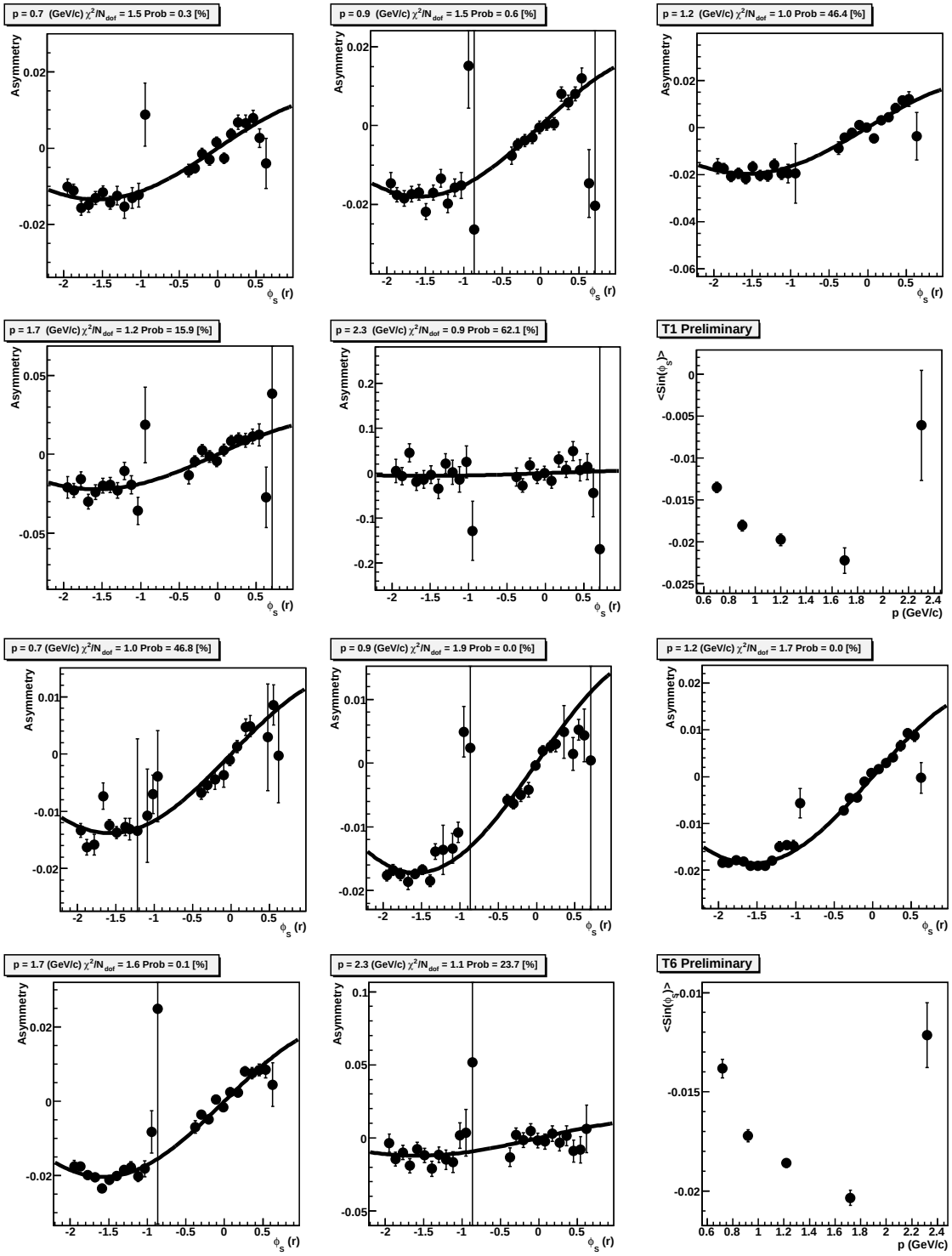

FIGURE 7.7: Angular modulation of γ Target SSA for T1 (top) and T6 (bottom) triggers. The last panel in both plots show the extracted $< \sin(\phi_S) >$ value. The fitting quality χ^2/N_{dof} together with the probabilities of the fitting are listed. Only the statistical uncertainties are included.

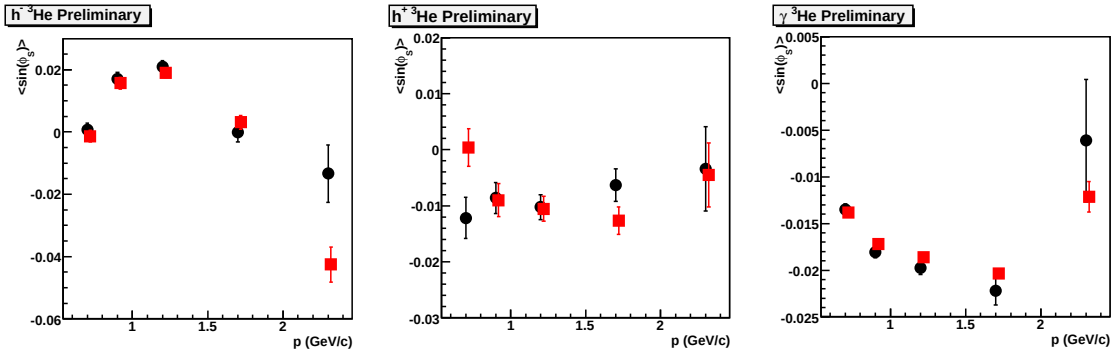

FIGURE 7.8: The extracted $< \sin(\phi_S) >$ for h^- (left), h^+ (middle), and γ (right) are shown for T1 (black) and T6 (red) triggers. The target polarization correction was included. The N_2 dilution correction was not applied. Only the statistical uncertainties are included.

Fig. 7.5, Fig. 7.6, and Fig. 7.7 show the fitting results to the singles h^-, h^+, and γ Target SSA, respectively, for T1 and T6 triggers. The extracted $< \sin(\phi_S) >$ together with the fitting quality χ^2/N_{dof} as well as the probabilities of the fitting are listed in the plots. From these plots, we can conclude that the data can be reasonably described with the functional form $\sin(\phi_S)$. Fig. 7.8 summarizes the extracted values of $< \sin(\phi_S) >$ for h^-, h^+, and γ from T1 and T6 triggers. The results from different triggers are consistent with each other within experimental uncertainties. Similar fits were performed for the left HRS side by combining the two target spin states. Fig. 7.9 shows the results.

7.1.4 Discussions

In order to discuss the meaning of these results, we generated the phase space plot of P_T vs. x_F for the inclusive hadron SSA for π^-, proton, π^+, and γ in Fig. 7.10. Here, P_T is defined as:

$$P_T = \sqrt{P_x^2 + P_y^2}, \tag{7.4}$$

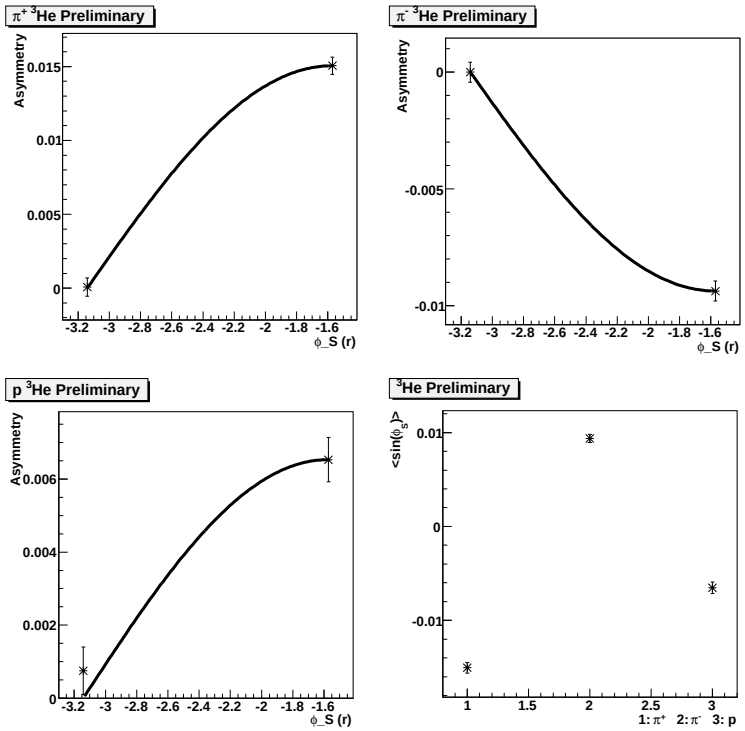

FIGURE 7.9: The fittings for π^+ (top left), π^- (top right), and p (bottom left). The extracted $< \sin(\phi_S) >$ for all three particles is summarized in bottom right panel. The results are prior to the N_2 dilution correction.

and z direction is along the incident electron beam. x-y plane is perpendicular to the z direction. x_F is defined as:

$$x_F = \frac{P_z}{P_z^{max}} = \frac{2 \cdot P_z^{CM}}{\sqrt{s}}, \tag{7.5}$$

where s is the center-of-mass energy squared of the electron-nucleon system:

$$s = M_N^2 + 2 \cdot M_N \cdot E_e^0, \tag{7.6}$$

and E_e^0 is the incident beam energy. P_z^{CM} is the longitudinal momentum in the center-of-mass frame:

$$P_z^{CM} = \gamma(P_z - \beta E). \tag{7.7}$$

Here, $\gamma = \frac{1}{1-\beta^2}$, $\beta = \frac{E_e^0}{E_e^0+M_N}$, P_z is the longitudinal momentum in the lab frame, and $E = \sqrt{P^2 + M_h^2}$, where M_h is the mass of hadron. Therefore, values of x_F depend

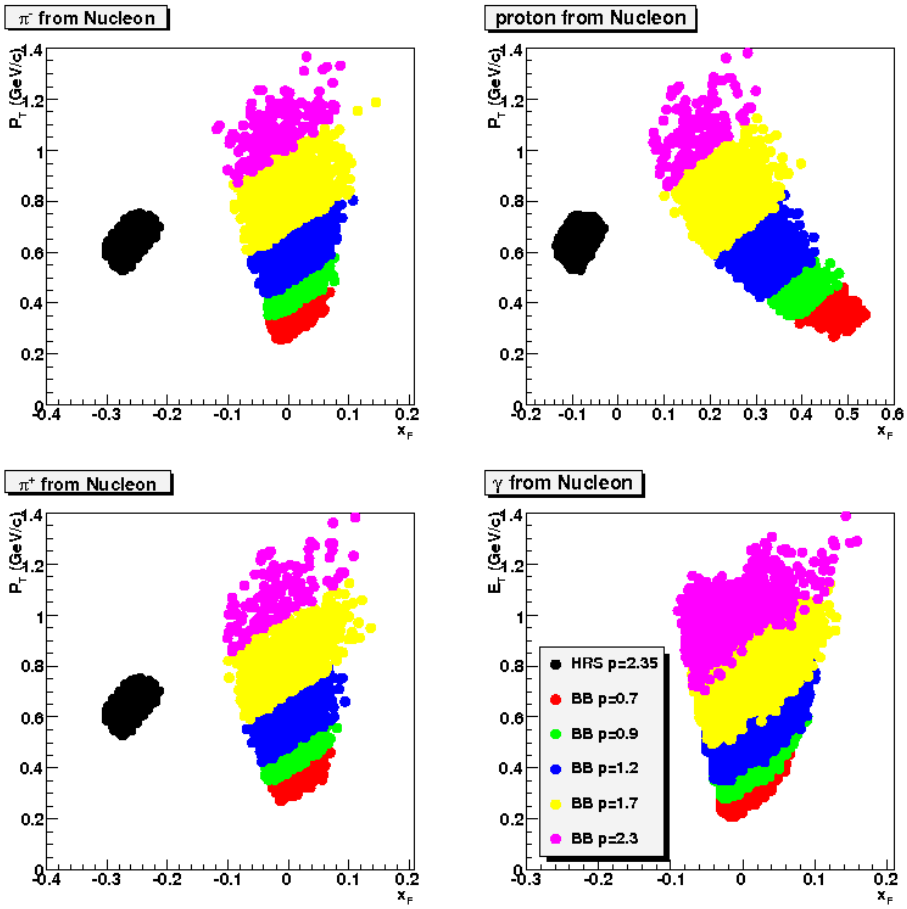

FIGURE 7.10: The phase space P_T vs. x_F are plotted for left HRS and different momentum bins in BigBite. Since the definition of x_F depends on the particle type. Four plots are presented for π^- (top left), proton (top right), π^+ (bottom left), and γ (bottom right).

on the mass of the detecting hadron.

The top and bottom left panels of Fig. 7.10 show the x_F and P_T bins for different momentum bins in the BigBite in detection of $\pi^{\pm}$. The average x_F values are almost the same, while the central P_T values of different momentum bins change dramatically. Therefore, the observed momentum-dependence of the asymmetries in BigBite is actually a transverse momentum dependence. Fig. 7.11 summarizes all the extracted $< \sin(\phi_S) >$ moments vs. the transverse momentum. We can conclude the following observations:

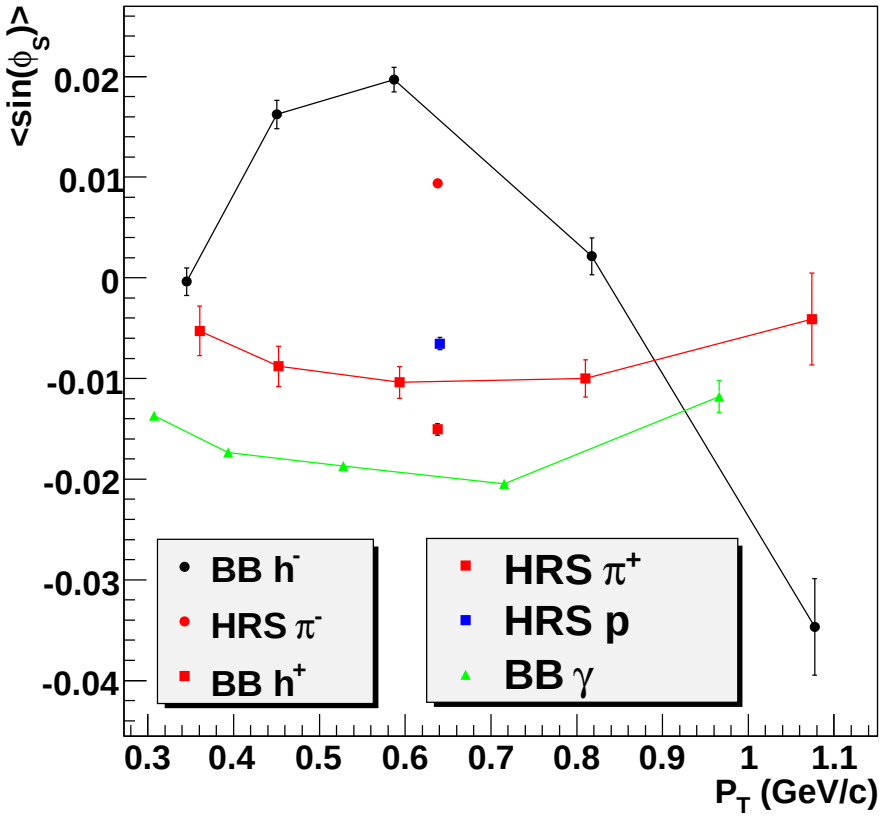

FIGURE 7.11: Summary of the (preliminary) extracted $\sin(\phi_s)$ moments from BigBite and left HRS for different particle types on ^{3}He prior to the N_2 dilution. Results are presented as a function of the transverse momentum P_T.

- The signs of moments extracted from left HRS are consistent with those extracted from BigBite. In particular, the π^- in left HRS and negatively charged hadrons in BigBite have a positive $< \sin(\phi_S) >$, except the highest P_T bin of BigBite. The π^+ and proton in left HRS and positive hadrons have a negative $< \sin(\phi_S) >$.

- As shown in Fig. 3.5 in $p^\uparrow p$ inclusive hadron production, the π^+ holds a positive A_N, and the π^- holds a negative A_N. The signs of asymmetries for proton are different from our results for ^{3}He ($n^\uparrow$) by -1.

- In addition, the A_N of π^o has the same sign as that of π^+ in E704 [199]. This is consistent with our results. As demonstrated in Sec. 6.1, the photons observed in BigBite are dominated by the decay products of π^0. Therefore, it is natural to assume that the photon inherits the asymmetries of π^o with some smearing due to decay process. The photon asymmetries have the same signs as those of positively charged hadron, which is consistent with the observation of negative asymmetries for π^+ and proton in the left HRS.

- As illustrated in Fig. 6.7, the positively charged hadrons in BigBite consist of proton and π^+. While the π^+ asymmetry in the left HRS is higher than the positively charged hadron asymmetry in BigBite, and the proton asymmetry in the left HRS is lower than the positively charged hadron asymmetry in the BigBite, the average of these two are close to the positively charged hadron asymmetry in BigBite. Similarly, the π^- asymmetry in the left HRS is close to that in the BigBite. These results suggest that $< \sin(\phi_S) >$ depends weakly on x_F.

- The P_T dependences of positively charged hadrons, negatively charged hadrons and γs are similar. The $< \sin(\phi_S) >$ increases with the increase of P_T. At large P_T, the $< \sin(\phi_S) >$ starts to decrease with increasing of P_T. In the negatively charged hadron case, the $< \sin(\phi_S) >$ changes sign at large P_T.

Recently, the HERMES Collaboration released the preliminary results of the inclusive hadron SSAs from a transversely polarized proton target. Fig. 7.12 shows the HERMES preliminary results [300]. While the π^+ shows large positive asymmetries, the π^- shows smaller asymmetries, which is negative at medium P_T region. Nevertheless, both π^+ and π^- asymmetry results decrease with increment of P_T at large P_T. The P_T dependence of asymmetry is consistent with our observation. Fig. 7.13 shows the P_T dependence of the asymmetries at different x_F bins. HERMES prelim-

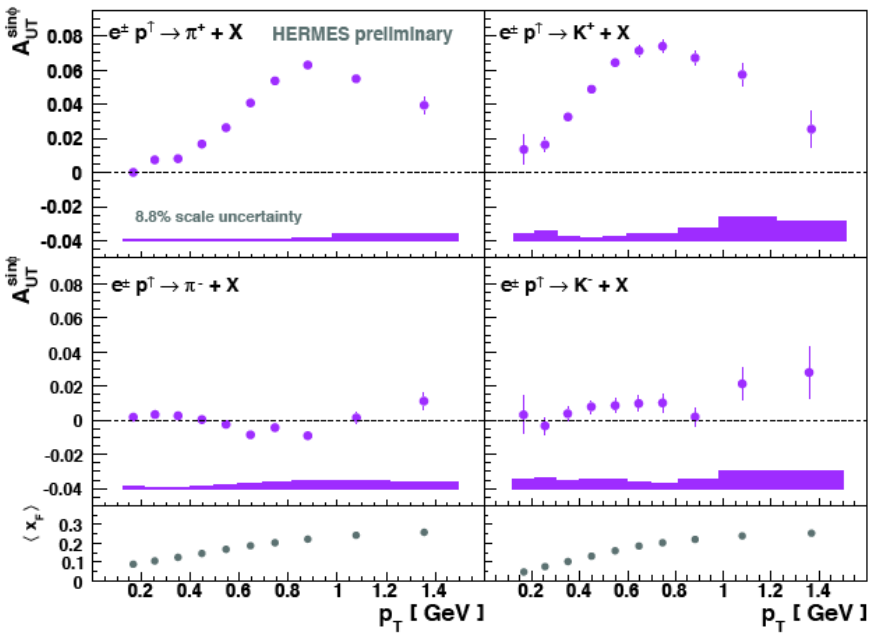

FIGURE 7.12: The HERMES preliminary results on inclusive hadron SSA for $\pi^{\pm}$ and $K^{\pm}$. A similar turn-over behavior at large P_T was observed.

inary results also suggest the small x_F dependence of $< \sin(\phi_S) >$. Moreover, the signs of $\pi^{\pm}$ asymmetries from proton target observed in HERMES are consistent with those observed in E704, but different from our results, which are from neutron. For example, the asymmetry of π^+ from proton of HERMES is positive; the asymmetry of π^+ from proton of E704 is positive; the asymmetry of the π^+ from neutron (this experiment) is negative.

The N_2 dilution, nuclear correction, and various systematic uncertainties are currently being analyzed.

7.2 Coincidence Channel Target SSA

7.2.1 Raw Asymmetries

The data were firstly binned in terms of the BigBite momentum. Fig. 7.14 shows the extracted raw asymmetries from the $^3\mathrm{He}(e, e\pi^{\pm})X$ process with different analysis software, cuts, and data from different replay passes. The stability of the results

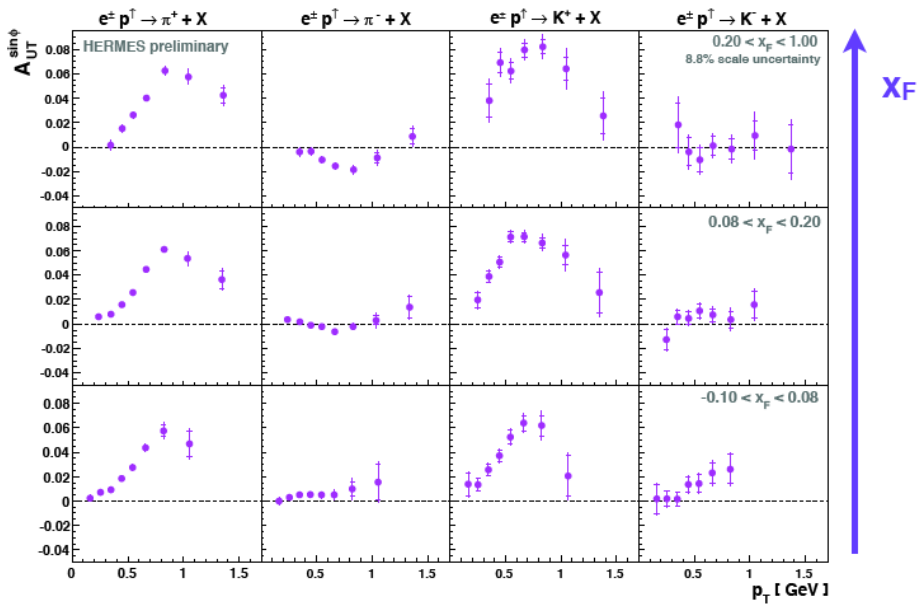

FIGURE 7.13: The HERMES preliminary results on inclusive hadron SSA for $\pi^{\pm}$ and $K^{\pm}$. Data were binned into different x_F bins. No clear x_F dependence of the asymmetry was observed.

was monitored during the entire analysis. Results were corrected by the target polarization. No additional corrections such as N_2 dilution were applied. Meanwhile, Fig. 7.15 and Fig. 7.16 show the extracted raw asymmetries from the $^3\mathrm{He}(e, \gamma\pi^{\pm})$ and $^3\mathrm{He}(e, \pi^{-}\pi^{\pm})$ processes, respectively. These two channels are the two major background contaminations in the BigBite spectrometer.

7.2.2 Separation of Collins and Sivers Moments

Different methods were used in separating Collins and Sivers moments from the measured raw asymmetries by their angular dependence. Fig. 7.17 shows the results from different methods. The various methods used in the analysis are:

- "S 1d Fit": The data were binned into the Sivers angle $\phi_{Sivers} = \phi_h - \phi_S$. The raw asymmetries were extracted in each angular bin, then the angular dependence of the raw asymmetries was fitted by the form of $A_{Siv}\sin(\phi_{Sivers})$. The Sivers moments were then extracted.

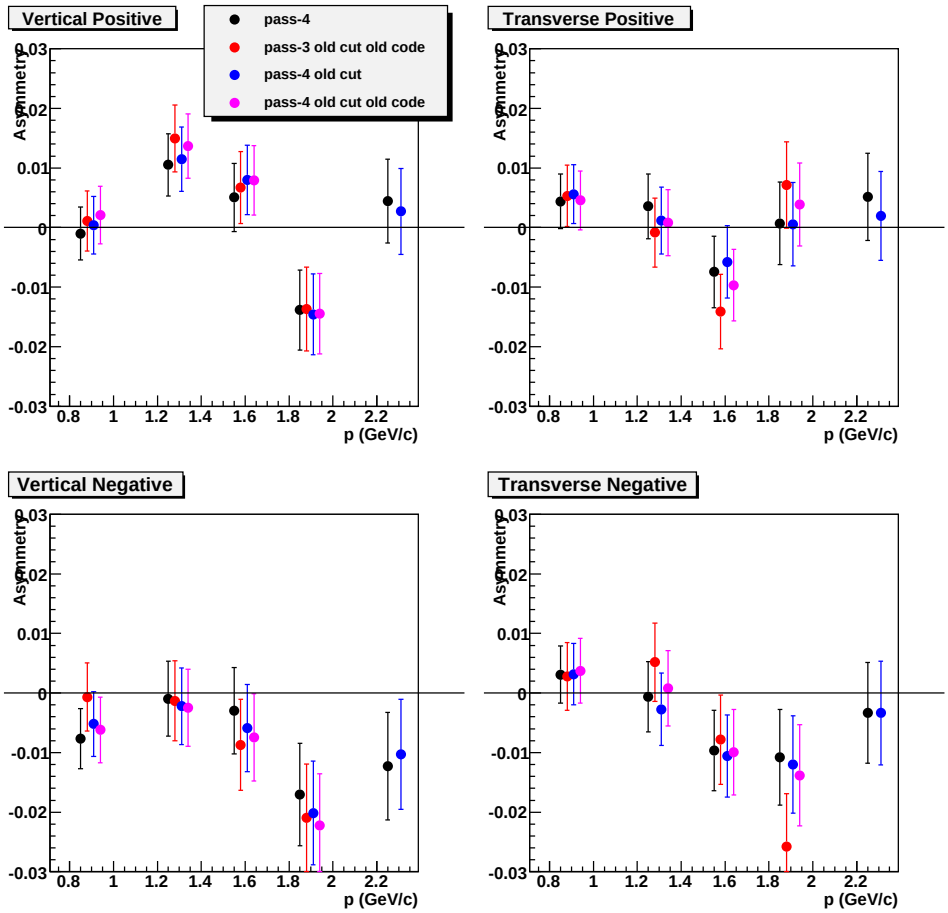

FIGURE 7.14: The raw asymmetries of the ^{3}He$(e, e\pi^{\pm})X$ process. Data from different passes are presented. The results are obtained with different sets of analysis software and different cuts. "old code" represents the online analysis software. "old cut" represents the online cuts. Here, the "Transverse" ("Vertical") represents the target polarization direction and the "Positive" ("Negative") represents the polarity of the left HRS.

- "C+S Fit (F)": The data were binned into 2-D ϕ_h and ϕ_S bins. The raw asymmetries were extracted in each angular bin, then the angular dependence of the raw asymmetries was fitted by the form of $A_{Col}\sin(\phi_{Collins}) + A_{Siv}\sin(\phi_{Sivers})$, where $\phi_{Collins} = \phi_h + \phi_S$.

- "... (M)": The analysis code is a stand-alone code which is based on "Minuit2". The angular bins with very poor statistics were excluded from the fitting proce-

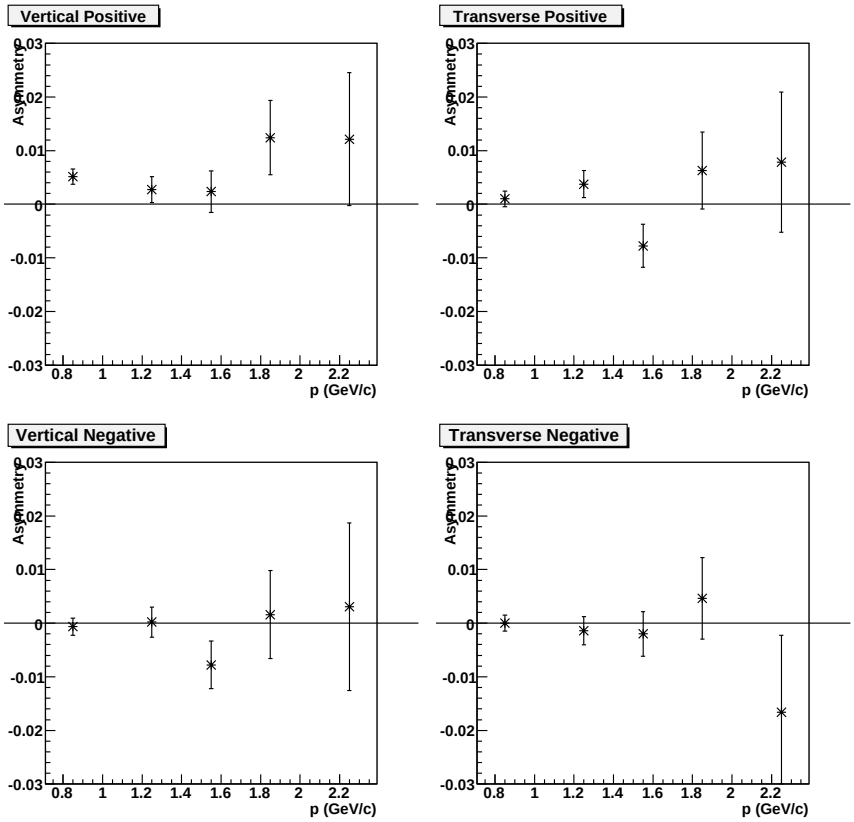

FIGURE 7.15: The raw asymmetries of the $^3\mathrm{He}(e,\gamma\pi^{\pm})X$ process.

dure. The central values of ϕ_h and ϕ_S for each angular bin were calculated based on the distribution of the data. Within the code, one can choose different fitting format to fit the data. For example, "S Fit" used the form of $A_{Siv}\sin(\phi_{Sivers})$, "C+S Fit" used the form of $A_{Col}\sin(\phi_{Collins}) + A_{Siv}\sin(\phi_{Sivers})$, and "C+S+P (Fit)" used the form $A_{Col}\sin(\phi_{Collins}) + A_{Siv}\sin(\phi_{Sivers}) + A_{Prez}\sin(3\phi_h - \phi_S)$ including the terms on Pretzelosity.

In the following, we refer to A_{Siv} and A_{Col} as Sivers and Collins moments, respectively.

From the comparison of results in Fig. 7.17, we can draw the following conclusions.

- Both methods ("M" and "F") yield the same results and statistical uncertainties. For example, one can compare the blue and green points in Fig. 7.17.

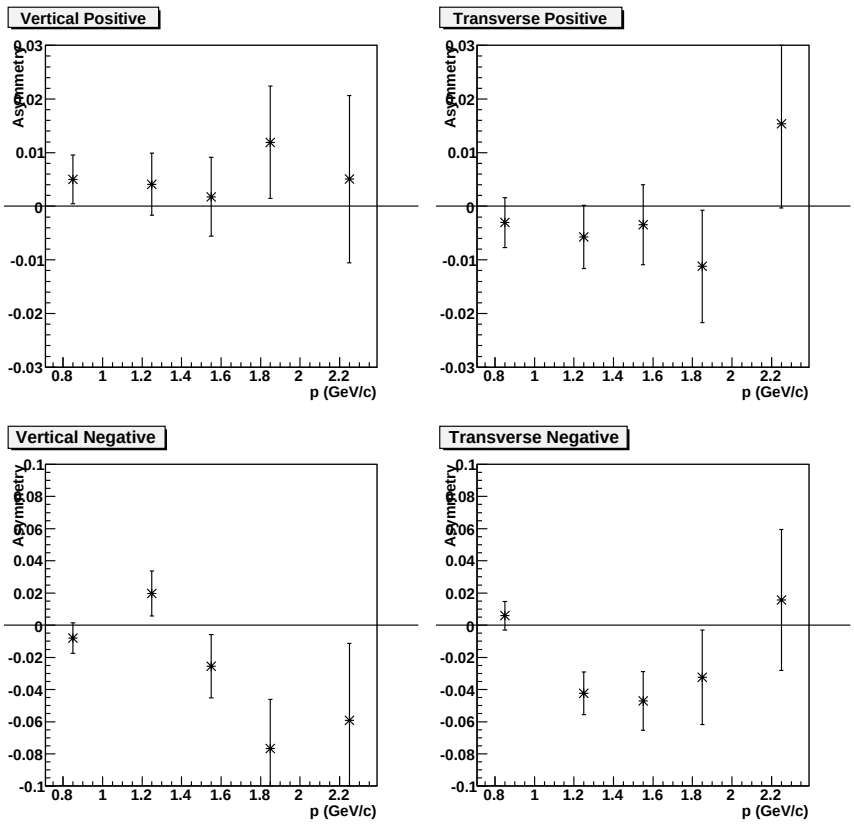

FIGURE 7.16: The raw asymmetries of the ^{3}He$(e, \pi^-\pi^\pm)X$ process.

One can also compare the magenta and red points in Fig. 7.17. The results are slightly different, since different angular bin centers are used in the two methods. In "F", the center of the angular bin is used as the bin center, while in "M", the weighted center (by the data distributions) is used as the bin center.

- The statistical uncertainties of the results increase with the number of terms included in the fitting process. Mathematically, one can prove when the angular coverages of ϕ_h and ϕ_S are complete, the statistical uncertainties of the results do not depend on the number of terms included in the fitting process. However, in experiment E06-010, we have limited coverage in terms of $\phi_h - \phi_S$, therefore the statistical uncertainties of the Collins and Sivers moments would depend on the number of terms included. Fig. 7.17 clearly shows this phenomenon.

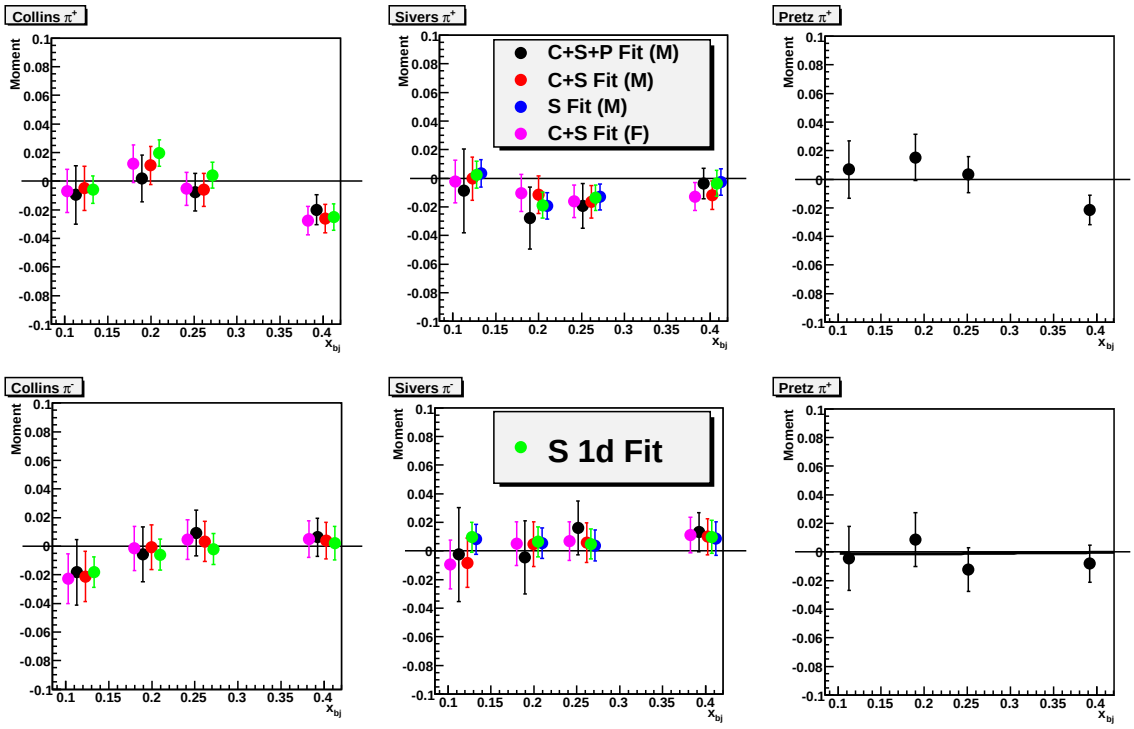

FIGURE 7.17: The results of Collins/Sivers Moments obtained by fitting the angular dependence of the ^{3}He raw asymmetries. Different methods are explained in the text.

7.2.3 N_2 Dilution

As discussed in Sec. 5.10, a small amount of nitrogen was filled in the polarized ^{3}He cell, which allowed for photon-less de-excitation by absorbing energy into the nitrogen's rotational and vibrational motion during a collision [255]. Therefore, the measured raw asymmetries need to be corrected by the N_2 dilution. Fig. 7.18 shows the charge and pressure normalized yield of the reference cell data. The top panel shows the results of nitrogen and the bottom panel shows the results of the ^{3}He.

The nitrogen dilution factor

$$f = \frac{N_{^3\mathrm{He}}\sigma_{^3\mathrm{He}}}{N_{^3\mathrm{He}}\sigma_{^3\mathrm{He}} + N_{\mathrm{N}_2}\sigma_{\mathrm{N}_2}} \tag{7.8}$$

was then calculated in each of the four x bins. The results are shown in Fig. 7.19. The systematic uncertainties include:

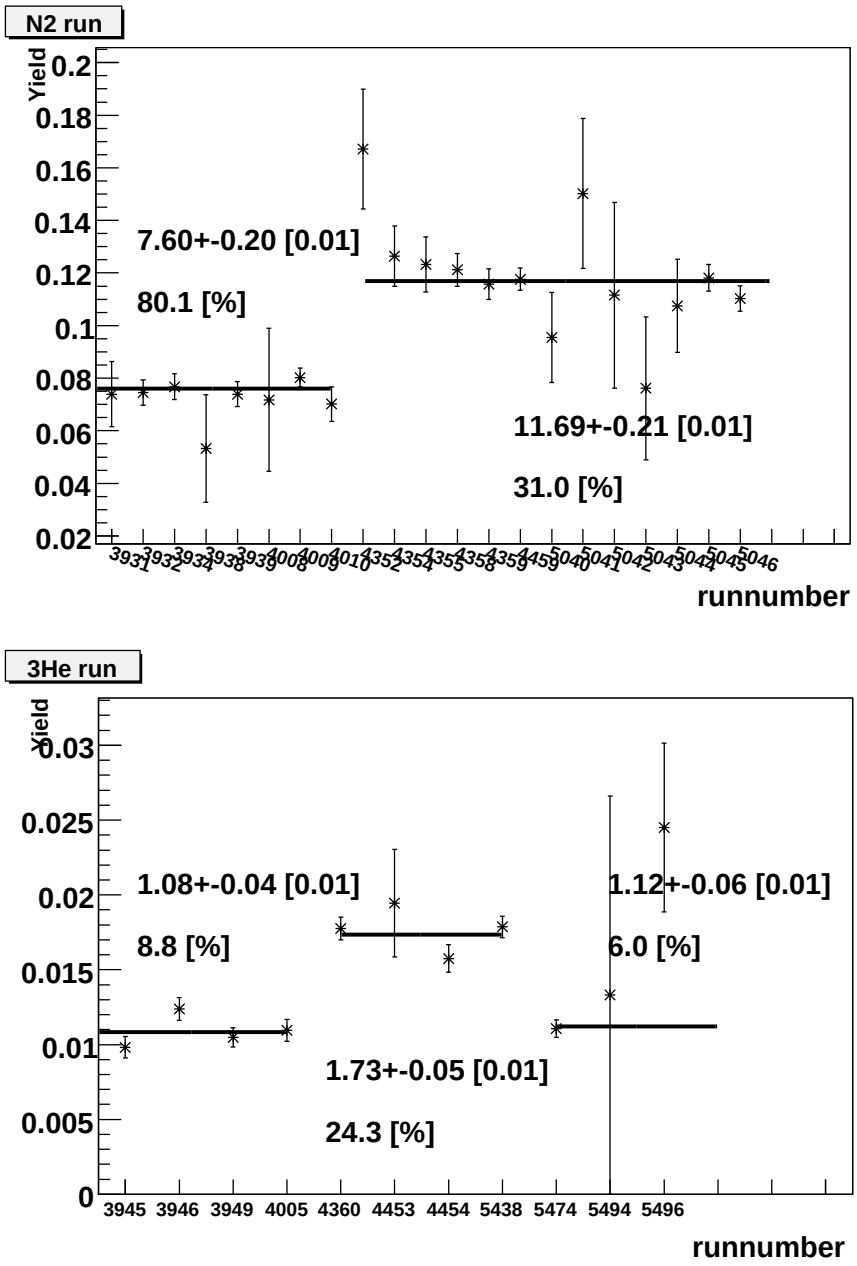

FIGURE 7.18: The charge and pressure normalized yield of the reference cell data. The top panel shows the results of N_2, and the bottom panel shows the results of ^{3}He. The yields are normalized to 135 psig pressure. The two periods of N_2 are corresponding to the negative and positive polarity of the left HRS setting. The middle section of the ^{3}He run is corresponding to the positive polarity of the left HRS, and the rest two sections are corresponding to the negative polarity of the left HRS. The yields are fitted with straight lines. The fit results together with the probability are listed in the plot.

- Uncertainties of the filling density in the target cells. The relative uncertainty of the ^{3}He density is about 2%, and that of the N_2 density is about 5%.

- The uncertainties of the filling pressure in the reference cell is 1 psig, which is the uncertainties of the pressure gauge.

- Radiative Correction. The wall thickness of the target cell and that of the reference cell are slightly different, which would lead to different effects of the radiative correction. In addition, the internal radiative correction of the target material is different. However, these effects are expected to be small in forming the cross section ratio $\sigma_{^3\mathrm{He}}/\sigma_{\mathrm{N}_2}$. For the preliminary results, the radiative correction is assumed to be 10% of the cross section ratio $\sigma_{^3\mathrm{He}}/\sigma_{\mathrm{N}_2}$.

- Yield Drift due to the Preshower Degrading. From Fig. 7.18, no clear sign of the yield drift is observed due to the limited statistics. Therefore, no additional uncertainties are added.

In summary, the nitrogen dilution factor is about 0.91 in experiment E06-010.

7.2.4 Systematic Uncertainties

In this section, we will discuss various systematic uncertainties in extracting the Collins/Sivers moments of ^{3}He from the experiment E06-010 data. In the previous section, we already discussed the systematic uncertainties in extracting the nitrogen dilution factor.

Yield Drift Due to BigBite Preshower Radiation Damage

As discussed in Sec. 5.2.4, the gains in the BigBite preshower PMTs were drifting in the experiment due to the radiation damage. The gains were corrected in the offline analysis. However, since the BigBite calorimeter also played a role as trigger, some data in the lowest x bin, which is corresponding to the lower momentum, were

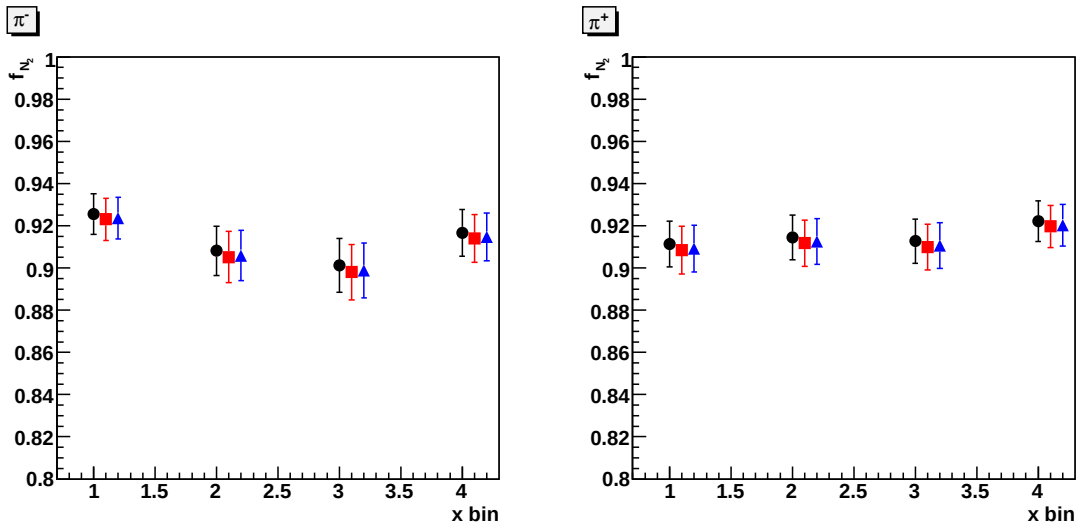

FIGURE 7.19: The preliminary nitrogen dilution factors are shown for four x bins for π^+ and π^-. The error bar represent the quadrature sum of the statistical uncertainties and systematic uncertainties. The three points represent the three target cells used in the experiment.

lost. Such effect was confirmed by looking at the yield vs. run number. Therefore, the drifts of the coincidence yield would lead to false asymmetries. In fact, other slow drift of the experimental conditions can also lead to drift of the yields. On the other hand, the target spin was flipped regularly throughout the entire experiment regardless of what happened on the detector side. To some extent, the target spin flip was "random" to the yield drift. Thus, the effect of the false asymmetries would be minimized by the "random" target spin flip.

In order to evaluate how much false asymmetry was introduced by the yield drifts, a dedicated study was carried out. In this study, the local yield of each spin section (half of each spin pair in the super local pair method) was fit as a linear line globally. In practice, the yield has to be fit section by section, since the yield can change dramatically when the major experimental conditions change. For example, the yield is directly linked to the target density. Thus, when the target cell was changed, the yield changed. Another example is the polarity of the left HRS. In this

case, the yield of π^+ was quite different from that of $\pi-$. For any spin pair (section 1 and section 2), one can calculate the expected yield with the fitting results Y_1 and Y_2. If the data in section 1 were taken earlier than those of section 2, one would expect that Y_1 is slightly higher than Y_2. In order to evaluate the effect, additional correction factors $\frac{Y_1+Y_2}{2Y_1}$ and $\frac{Y_1+Y_2}{2Y_2}$ were directly applied to the data before extracting the asymmetries. The changes of the central value of the extracted Collins and Sivers moments were in average 11% of the statistical uncertainties for the first x bin and 2% for the rest of the x bins. Therefore, those values are treated as systematic uncertainties due to the yield drift.

Cut Stability Studies

For every cut used in the analysis, we evaluated the associated systematic uncertainty. On the BigBite side, the systematic uncertainties on the PID cuts are the contamination in the DIS electron sample. On the HRS side, the systematic uncertainties on the PID cuts are the kaon contamination in the π sample. We will discuss the systematic uncertainties of contaminations in the following two sections. In addition, the acceptance cuts on the HRS and BigBite are quite tight, and one expects that the systematic uncertainties are negligible. The two additional types of cuts are the coincidence timing cut and the vertex related cuts. For coincidence timing, the random coincidence backgrounds were subtracted in each section of the spin pair directly. The statistical uncertainties of the backgrounds are included in the calculation of the statistical uncertainty of the yields. Thus, no additional systematic uncertainty is introduced. For the vertex related cut, the major source of the systematic uncertainties is associated with the BigBite target collimator. The target collimators were installed in experiment E06-010 on the BigBite side to exclude the high energy electrons/high energy photons generated in the target endcaps. They can significantly reduce the trigger rates and also reduce the background in the BigBite

detectors. The effect of target collimator has been discussed in Sec. 4.10.2. In addition, for all the empty reference cell runs taken during the experiment, zero number of coincidence pion events were observed. Although the target collimators are very effective, the electrons scattering from the ^{3}He atoms near the endcaps may hit the edge of the target collimator and continue falling into the acceptance. For those kind of events, they are not likely to have a correct optics reconstruction. Therefore, they have a great chance not passing the various optics cut and the coincidence vertex cut. Nevertheless, to be conservative, we study the possible systematic uncertainties by changing the vertex cut. Fig. 7.20 shows the position of vertex cut that we used in this study. The average effect is about 17% of the statistical uncertainties.

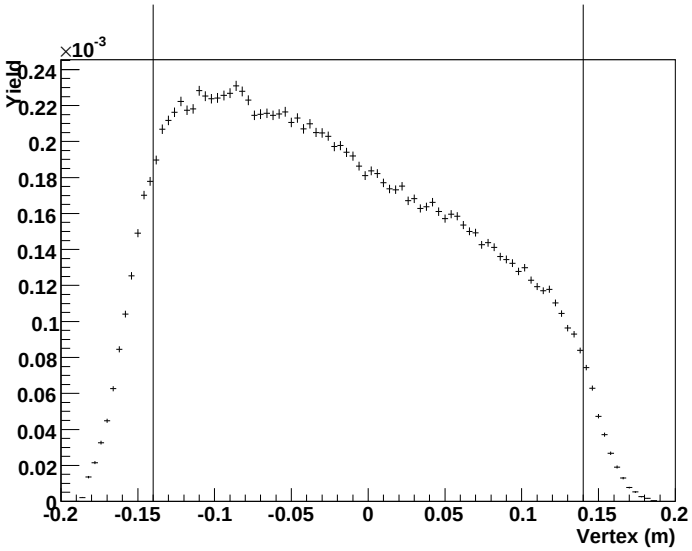

FIGURE 7.20: A tighter vertex cut was used in order to study the systematic uncertainties.

BigBite π^- and Photon-induced Electron Contamination

In Sec. 5.7, various contaminations in the BigBite spectrometer were discussed. The π^- contamination in the electron sample is about 0.1-3%, and the photon-induced electron contamination in the electron sample is about 1-20%. Therefore, the asymmetries of coincidence $\pi^-\pi^\pm$ and the photon-induced $e\pi^\pm$ channel would be false

asymmetries to the DIS coincidence $e\pi^{\pm}$ channel. In order to study these effects, we selected π^- in the BigBite for the coincidence events and extracted the "Collins" and "Sivers" moments by pretending they were electron events. The differences between the central values of the $\pi^-\pi^{\pm}$ "Collins" and "Sivers" moments and the central values of $e\pi^{\pm}$ "Collins" and "Sivers" moments are treated as the systematic uncertainties after weighting the corresponding contamination number. The effect is about 0.1-2.5% of the statistical uncertainties. The same approach was used to evaluate the false asymmetry due to the photon-induced $e\pi^{\pm}$ contamination. In this case, we selected the positron events in the BigBite under the assumption that the photon-induced electron and positron have the same kinematics and same asymmetries. The effects of the photon-induced $e\pi^{\pm}$ events are on average about 32%, 19%, 6%, and 6% of the statistical uncertainties [5].

Kaon Contamination

In Sec. 5.3, we discussed the kaon contamination in the pion sample for the coincidence events. The kaon yields are about 6% and 3% of the pion yields for the positive and negative polarities, respectively. With a better than 10:1 kaon rejection from the aerogel detectors, the kaon contamination in the pion sample is less than 0.6% and 0.3%. The extracted kaon Collins and Sivers asymmetries are shown in Fig. 7.21. The effect of the kaon contamination is less than 4% of the statistical uncertainties.

Bin Centering Correction

In extracting the Collins and Sivers moments from the the raw asymmetries, the data were first binned into 2-D ϕ_h and ϕ_S bins. The moments were then fitted from the angular dependence of the asymmetries. In this procedure, there is one important assumption that the Collins/Sivers moments are the same among all the

[5] The statistics in the highest x bin is so poor, so we used the number in the third x bin as an upper limit.

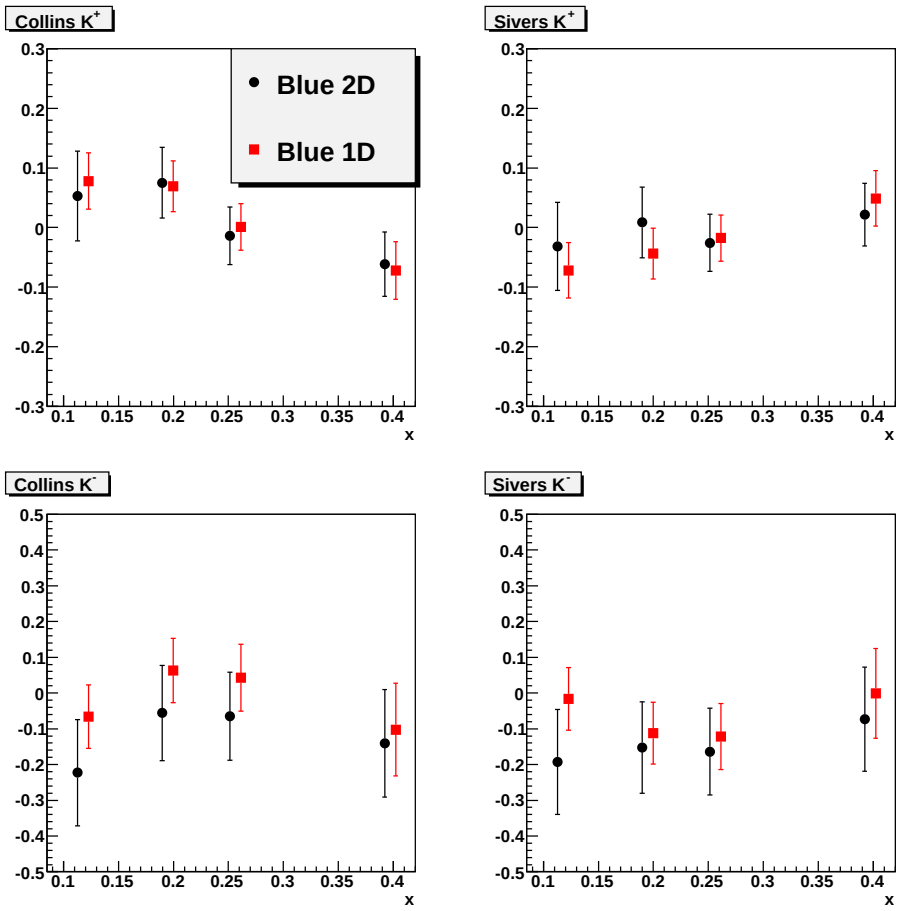

FIGURE 7.21: The preliminary extracted kaon Collins and Sivers asymmetries prior to the nitrogen dilution. The 2-D fit represents the fit including both the Collins and Sivers terms.

2-D angular bin. However, in the real experiment, the phase space in each x bin is usually irregular in the x, Q^2, z, P_T phase space. Therefore, there is no guarantee that the moments in all the angular bins are the the same. This assumption would lead to some false asymmetries. In order to study this effect, we used theoretical calculations (discussed in Sec. 9.8) to calculate the ^{3}He asymmetries A_{ij}^{ij} in the data weighted bin center (x_{ij}, Q^2_{ij}, z_{ij}, P_{Tij}) of each angular bin ϕ_{hi} and ϕ_{Sj}, and the ^{3}He asymmetries A_{ij}^0 in the data weighted bin center of this particular x bin (x_0, Q^2_0, z_0, P_{T0}) of this angular bin ϕ_{hi} and ϕ_{Sj}. The measured asymmetry in each angular

bin was then corrected by $\frac{A^0_{ij}}{A^{ij}_{ij}}$ before extracting the Collins/Sivers moments [6]. The average effect is about 13% of the statistical uncertainties.

High P_T Cut

At low P_T, the angular resolution of ϕ_h increases quite fast. In order to evaluate such effect, an additional cut $P_T > 0.1$ GeV was applied to the data. Such cut would only affect the highest x bin. The effect of such cut is negligible. Fig. 7.22 shows the comparison of the results with (red) and without (black) this cut. Since some Monte-Carlo related studies are still under going to investigate whether such a cut is really needed, no systematic uncertainties have been assigned for now.

Target Density Fluctuation

As discussed in Sec. 5.8.3, the target density would fluctuate due to the change of the temperatures. Therefore, the density related information was added into the rootfiles. Fig. 7.23 shows the extracted raw Collins/Sivers densities before and after applying the target density correction. The average change is about 2.1% of the statistical uncertainties.

Systematic Uncertainties due to Other Angular Dependent Terms

Besides the Collins and Sivers moments, Pretzelosity [193], which depends on the $\sin(3\phi_h - \phi_S)$, is another leading twist term which contributes to the Target SSA. In addition, there are two higher twist terms [193] (depending on $\sin(\phi_S)$ and $\sin(2\phi_h - \phi_S)$) contributing to the Target SSA. With a transversely polarized target with respect to the incident beam direction, there will be a small component of the longitudinal polarization [7]. With the small longitudinal polarization, the $\sin(\phi_h)$ and

[6] The $\frac{A^0_{ij}}{A^{ij}_{ij}}$ was limited between 0.8 and 1.2.

[7] The longitudinal and transverse direction are defined in the virtual photon nucleon system. The longitudinal direction is along the virtual photon direction.

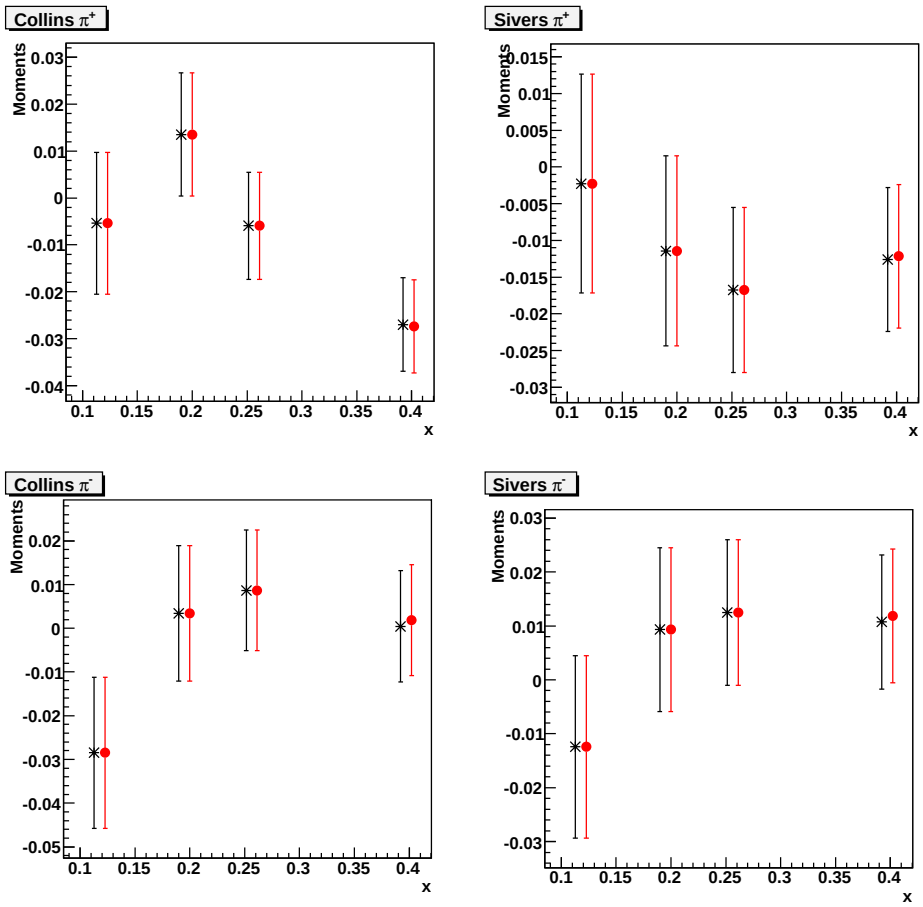

FIGURE 7.22: The effect of additional P_T cut in the separated raw asymmetries.

$\sin(2\phi_h)$ terms can also affect the fitting procedure of extracting the Collins and the Sivers moments. Moreover, the differential cross section with unpolarized beam and target also depends on the ϕ_h angle. They are the Cahn effect which depends on the $\cos(\phi_h)$ and the Boer-Mulder effect that depends on the $\cos(2\phi_j)$ [193]. Therefore, the non-zero $\cos(\phi_h)$ and $\cos(2\phi_j)$ terms would contribute in the denominator of the asymmetry.

As discussed in Sec. 7.2.2, the raw asymmetries were fitted with Collins/Sivers terms only in the standard fitting procedure. Therefore, it is important to evaluate the systematic uncertainties of the assumption for neglecting the other terms. The absolute size of each term discussed in the previous paragraph was estimated by

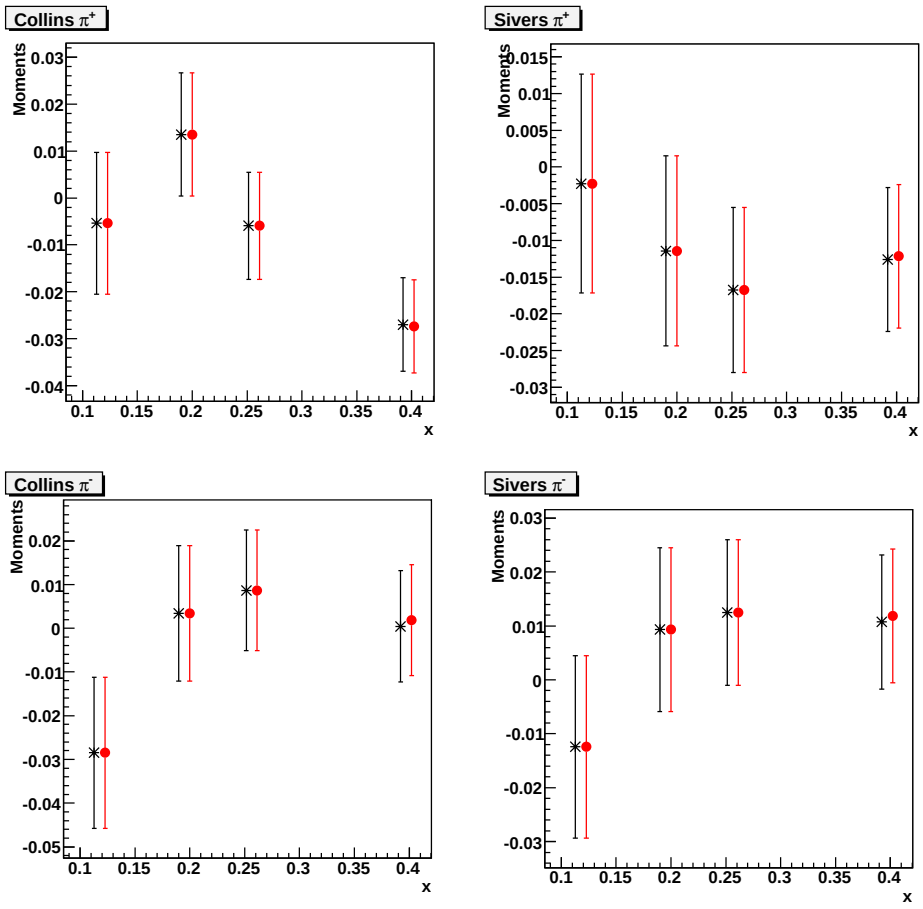

FIGURE 7.23: The effect of target density correction in the separated raw asymmetries.

the preliminary proton results from HERMES [300] except for the contribution from Pretzelocity term. Here, we made an assumption that the sizes of neutron asymmetries are similar to those of protons. Next, the asymmetries on neutron were further diluted by the proton, nitrogen unpolarized contributions and the neutron effective polarization in order to estimate the ^{3}He asymmetries. In this step, the small contribution from the polarized proton -2.8% was neglected. For the contribution from Pretzelocity term, we directly fit our data with Collins, Sivers and Pretzelocity. The differences between the results of three terms fit and two terms fit are treated as systematic uncertainties due to Pretzelocity now. Table. 7.1 summarizes our current

estimation of various terms for neutron and ^{3}He. The estimated moments for various terms are added in the fitting procedure in extracting the Collins/Sivers moments. The changes of the central values of Collins/Sivers moments in the four x bins are also listed in Table. 7.1 for $\pi^{\pm}$.

Other Systematic Uncertainties

Other sources of systematic uncertainties include:

- Target Polarization: 5% relative to the central value of asymmetries.
- Left HRS single-track cut: $1e^{-4}$ in the raw asymmetries which leads to about 1.5% of the statistical uncertainties.
- BigBite Tracking Quality cut: $1.5e^{-4}$ in the raw asymmetries which leads to about 1.5% of the statistical uncertainties.
- Livetime Correction: Discussed in Sec. 5.8.1. $1e^{-4}$ in the raw asymmetries which leads to about 1.5% of the statistical uncertainties for the HRS negative polarity only.

Table. 7.2 summarizes the current status of the systematic uncertainties. The systematic uncertainties due to other angular dependent terms are summarized in Table. 7.1. The systematic uncertainties not included are:

- Radiative Correction: The current results are prior to the radiative correction.
- Diffractive ρ Production.

They are still being studied now.

Terms	Neutron π^+	Neutron π^-	^{3}He π^+	^{3}He π^-	Collins π^+	Collins π^-	Sivers π^+	Sivers π^-
Pretzelosity $\sin(3\phi_h - \phi_S)$	-	-	-	-	14-68%	17-42%	24-124%	24-75%
$\sin(\phi_S)$	5%	5%	0.7%	1.0%	24-42%	30-47%	25-43%	32-49%
$\sin(2\phi_h - \phi_S)$	2%	2%	$2.8e^{-3}$	$4e^{-3}$	8-1[illegible]%	10-11%	23-28%	28-32%
A_{UL} leakage	3%	3%	$5.2e^{-3}$	$6e^{-3}$	<0.1%	<0.1%	<0.1%	<0.1%
Cahn $\cos(\phi_h)$	5%	5%	5%	5%	2-9%	1-7%	1-7%	1-4%
Boer-Mulder $\cos(2\phi_h)$	5%	5%	5%	5%	1-3%	1-3%	1-8%	1-3%

Table 7.1: The systematic uncertainties due to other angular dependent terms in extracting Collins/Sivers asymmetries from ^{3}He measured raw asymmetries. The estimated neutron asymmetries and the obtained the ^{3}He asymmetries are summarized in second to fifth column. The effects on the Collins/Sivers asymmetries are summarized in the last four panels. The unit is statistical uncertainty of the fitting results. The range of the effect represent the effect on the four x bins.

Source	Systematic Uncertainty	Type
N_2 dilution	0.3-0.6%	relative
Yield Drift	11%, 2%, 2%, 2%	absolute
Vertex Cut	17%	absolute
BigBite π^- Cont.	0.1-2.5%	absolute
BigBite Photon-induced electron Cont.	32%, 19%, 6%, 5%	absolute
HRS Kaon Cont.	4%	absolute
Bin Centering	13%	absolute
High P_T Cut	-	absolute
Target Density	2.1%	absolute
Target Polarization	5%	relative
Left HRS Single Track	1.5%	absolute
BigBite Tracking Quality	1.5%	absolute
Livetime Correction	1.5%	absolute

Table 7.2: Summary of the systematic uncertainties in the coincidence ^{3}He$(e, e'\pi^{\pm})X$ channel. Here "relative" represents the uncertainties are relative to the central value of the asymmetries. The "absolute" represents that the uncertainties are absolute, and presented in the unit of the statistical uncertainties.

7.2.5 Preliminary Results on ^{3}He

Fig. 7.24 shows the preliminary results of the Collins and Sivers moments ($2 < \sin(\phi_h + \phi_S) >$ and $2 < \sin(\phi_h - \phi_S) >$ as defined in Eqn. (3.49) of Sec. 3.3) on ^{3}He. The statistical uncertainties are plotted as the error bars. The systematic uncertainties are plotted as a red band. The magenta curve is the theoretical calculations from Anselmino *et al.* [237, 128] [8]. The detailed calculations is also discussed in Sec. 9.8.

Due to the limited/correlated angular coverages in ϕ_h and ϕ_S, the uncertainties in Sivers and Collins moments are larger in the 2-terms fit than the 1-term fit. Therefore, the contour confidence plots contain the most complete information. Fig. 7.25 and Fig. 7.26 show the contour confidence plot for π^+ and π^-, respectively. In the π^+ case, the second and fourth bin show non-zero target single spin asymmetries

[8] The calculation from Anselmino *et al.* gives the polarized and unpolarized cross sections for neutron and proton. The ^{3}He predictions are based on the effective polarization method as discussed in Sec. 5.11.

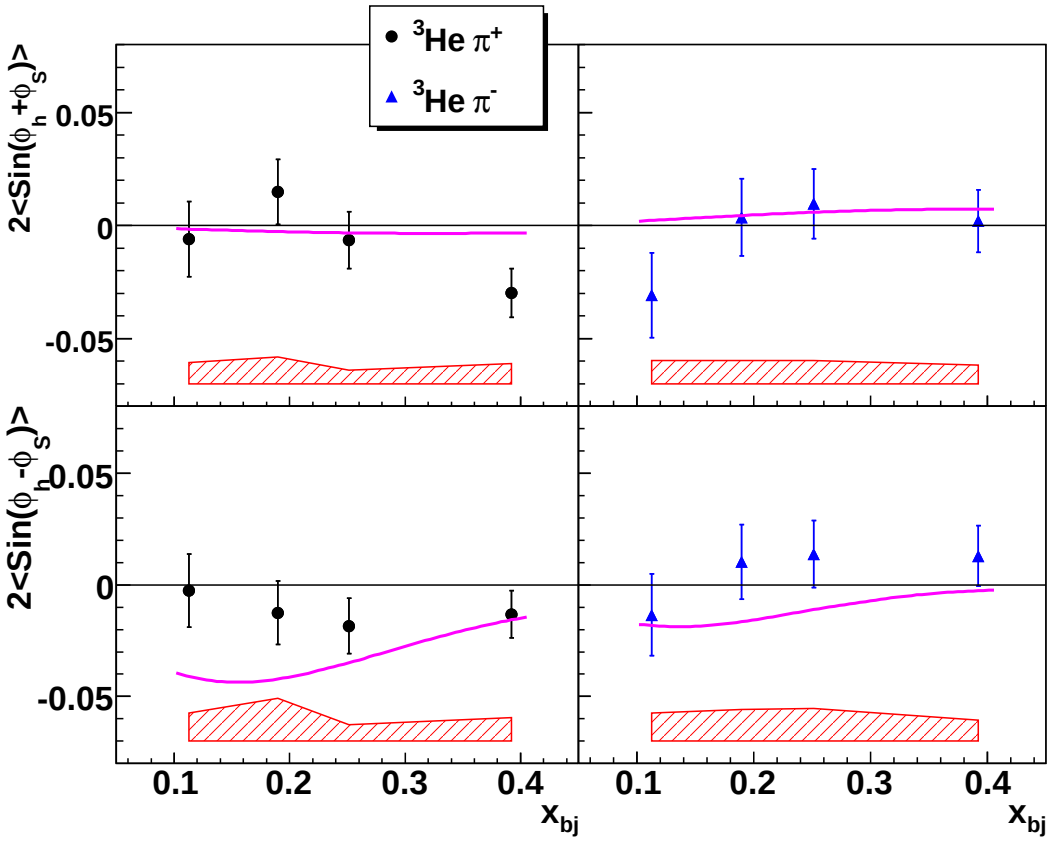

FIGURE 7.24: The preliminary results of Collins/Sivers Moments of ^{3}He are shown. The error bars represent the statistical uncertainties only. The different sources of systematic uncertainties are added in quadrature, which is plotted as a red band. The magenta curve is the theoretical calculations from Anselmino *et al.* [237, 128].

($> 2\sigma$ stat. only).

The observations from the ^{3}He preliminary results are listed:

- Except for the fourth x bin of π^+, the rest of the extracted Collins moments are consistent with theoretical predictions.
- Both the π^+ and π^- Sivers moments are systematically higher than the predictions. For the π^- Sivers moment, our data suggest that the asymmetry favors a positive value, while the calculation suggests a negative value.
- The second and fourth x bin of π^+ show non-zero target single spin asymmetries

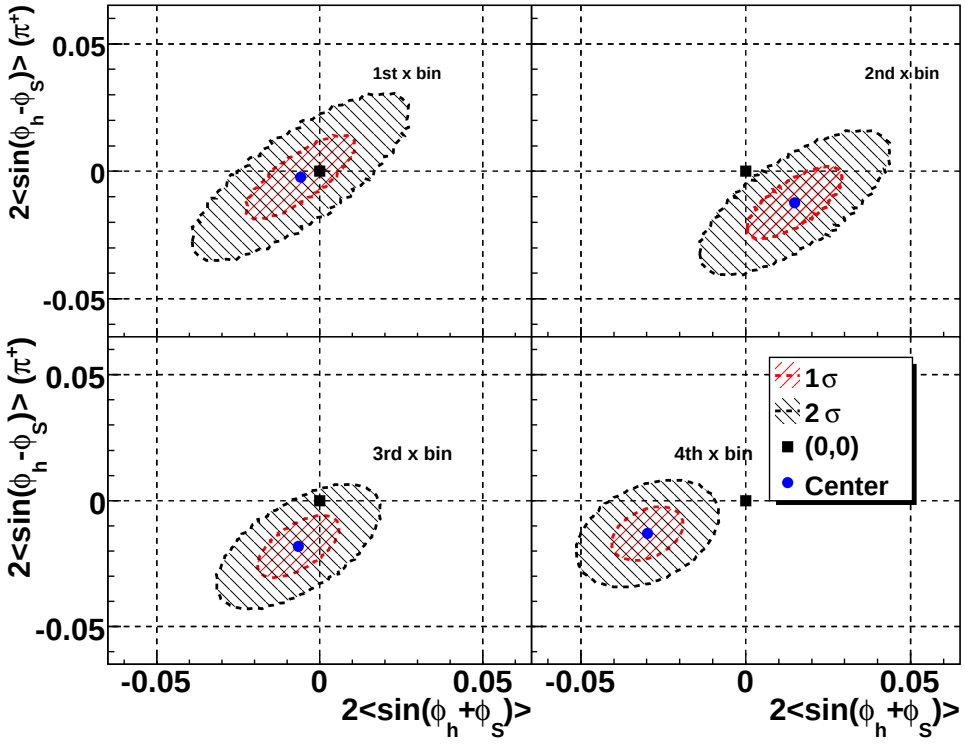

FIGURE 7.25: The contour confidence plot for ^{3}He Collins/Sivers moments for π^+. The 1σ, 2σ contour, origin point, and central point are shown. The four panels correspond to four x bins. The second and fourth x bin show non-zero target single spin asymmetries ($> 2\sigma$). Only statistical uncertainties are included in creating these contour confidence plots.

with more than two σ deviation from zero (stat. only).

In addition, we form $A_{combined}^{\pi^+-\pi^-}$ as in Eqn. (6.7) for ^{3}He. The results are shown in Fig. 7.27. Although both the Sivers moments on $^3\mathrm{He}(e,e'\pi^+)X$ and $^3\mathrm{He}(e,e'\pi^-)X$ channels are systematically higher than the prediction from Anselmino *et al.* [237, 128], our results of $A_{combined}^{\pi^+-\pi^-}$ are consistent with the prediction from Anselmino *et al.* [237, 128] within experimental uncertainties. In order to study whether such effect is due to the contribution of the pions decayed from the diffractive ρ production, we estimate the the diffractive ρ contamination at our kinematics based HERMES tuned

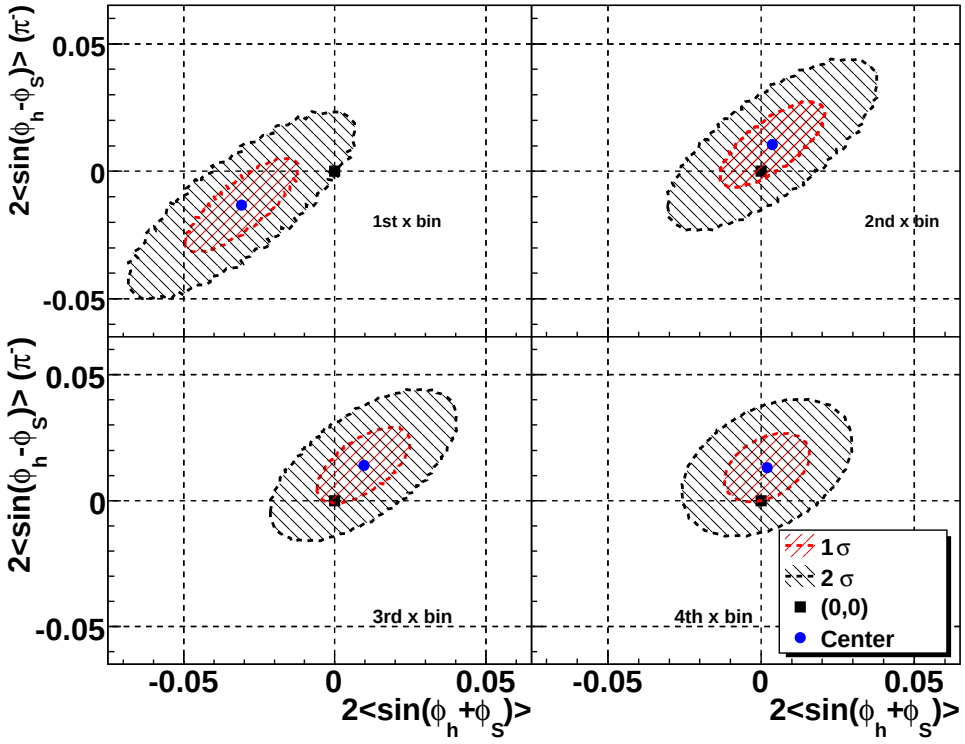

FIGURE 7.26: The contour confidence plot for ^{3}He Collins/Sivers moments for π^-. The 1σ, 2σ contour, origin point, and central point are shown. The four panels correspond to four x bins. Results from all four x bins are consistent with zero within 2σ. Only statistical uncertainties are included in creating these contour confidence plots.

Pythia [299] with simple models of BigBite and HRS acceptance [9]. The diffractive ρ contamination are estimated to be only 3-5% and 5-10% for $^3\mathrm{He}(e,e'\pi^+)X$ and $^3\mathrm{He}(e,e'\pi^-)X$, respectively. Therefore, the diffractive ρ is unlikely responsible for the differences between data and prediction observed in the ^{3}He Sivers moments.

7.2.6 Nuclear Correction: From ^{3}He to Neutron

As discussed in Sec. 5.11, the spin dependent cross section of ^{3}He can be written as the sum of spin dependent cross section of protons and neutron using the effective

[9] A full simulation is being developed to confirm these results.

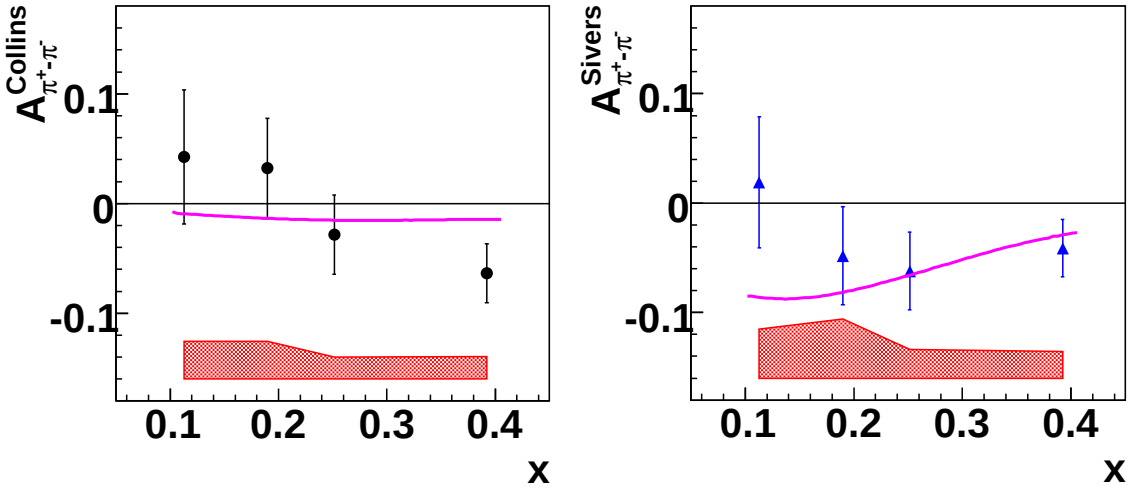

FIGURE 7.27: Preliminary Results of $A_{combined}^{\pi^+-\pi^-}$ on ^{3}He. The error bars represent the statistical uncertainties only. The different sources of systematic uncertainties are added in quadrature, which is plotted as a red band. The magenta curve is the theoretical calculations from Anselmino *et al.* [237, 128].

nucleon polarization:

$$\sigma_T^{^3\mathrm{He}} = P_n \sigma_T^n + 2P_p \sigma_T^p. \tag{7.9}$$

For unpolarized cross section, we have

$$\sigma_U^{^3\mathrm{He}} = \sigma_U^n + 2\sigma_U^p. \tag{7.10}$$

With the following definition:

$$A_p = \frac{\sigma_T^p}{\sigma_U^p},\ A_n = \frac{\sigma_T^n}{\sigma_U^n},\ f_{H_2} = \frac{\sigma_U^n}{\sigma_U^n + 2\sigma_U^p}, \tag{7.11}$$

we have

$$A_n = \frac{A_{^3\mathrm{He}} - (1 - f_{H_2}) P_p A_p}{f_{H_2} P_n}. \tag{7.12}$$

Therefore, we need the proton dilution f_{H_2} and the proton asymmetry A_p in order to extract the neutron asymmetry from the ^{3}He asymmetry.

The preliminary f_{H_2} is extracted from the reference cell data and model calculations based on PDF and FFs assuming leading order $x - z$ separation in the

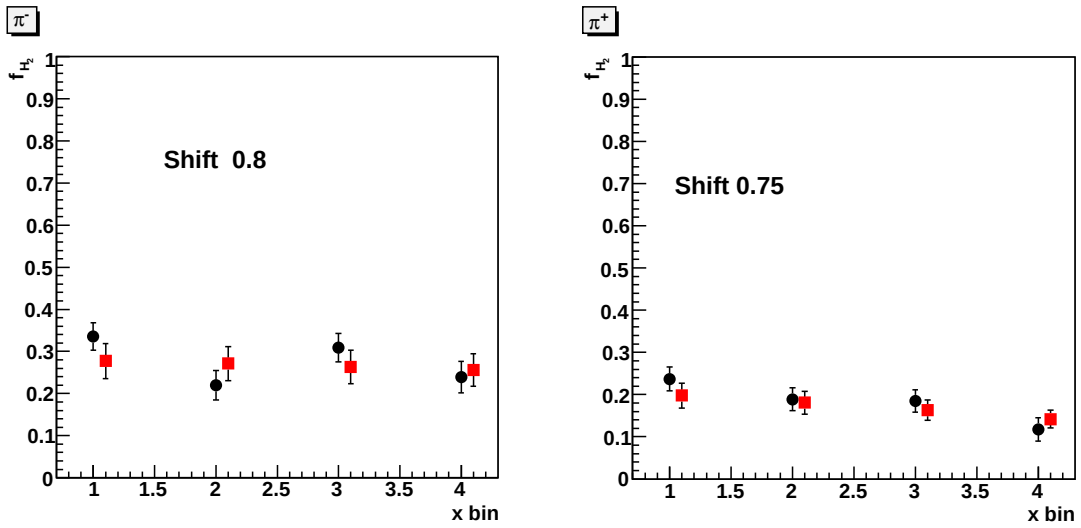

FIGURE 7.28: The proton dilution factors from the reference data (black) and model calculations (red). The model calculations are corrected by additional factors (0.8 for π^- and 0.75 for π^+) in order to obtain a better agreement with the data. A 15% relative uncertainty is assumed for the model calculations. The uncertainties of the black points include the statistical and systematic uncertainties.

SIDIS cross section. Fig. 7.28 shows the results from the data (black points) and the estimation from model calculations (red points). The red points are multiplied by additional factors (0.8 for π^- and 0.75 for π^+ [10]) in order to obtain a better agreement with the data. A 15% relative uncertainty is assumed for the model calculations. Currently, the red points are used for f_{H_2} in order to extract the neutron Collins/Sivers moments from ^{3}He results.

Fig. 7.29 shows the prediction of Collins and Sivers moments for proton and neutron from Anselmino *et al.* [237, 128]. The proton calculations are used to calculate A_p. The uncertainties of the calculation are treated as the systematic uncertainties of A_p. In addition, the effective polarization are

$$P_n = 0.86^{+0.036}_{-0.02} \quad \text{and} \quad P_p = -0.028^{+0.009}_{-0.004} \; . \tag{7.13}$$

[10] The current proton dilution factors used in presenting the experimental results are obtained from the data. Currently, the discrepancies between the data and model are under investigation.

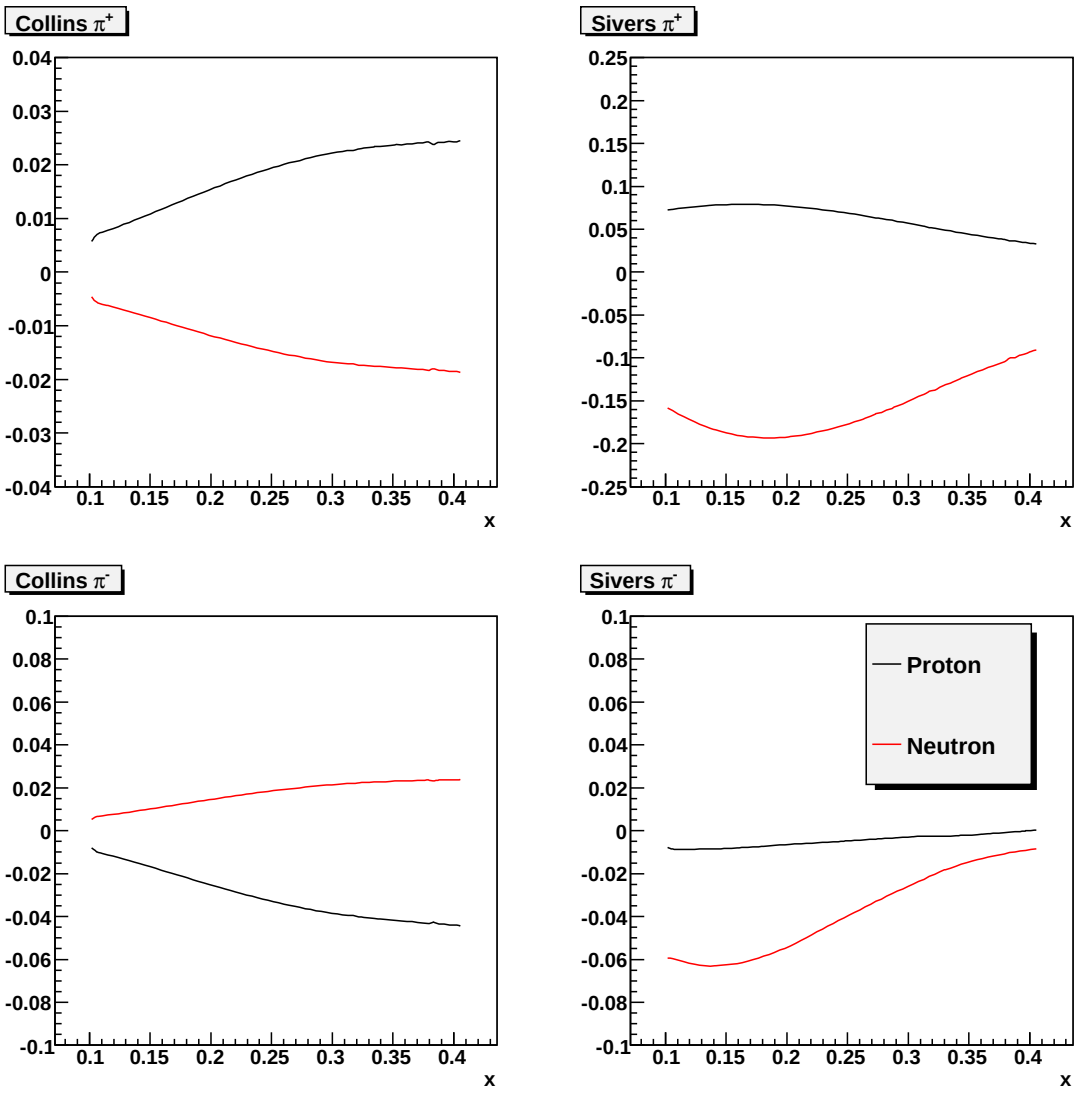

FIGURE 7.29: Predictions of Collins/Sivers moments for proton and neutron from Anselmino *et al.* [237, 128].

7.2.7 Preliminary Results on Neutron

The preliminary results of Collins/Sivers moments ($2 < \sin(\phi_h + \phi_S) >$ and $2 < \sin(\phi_h - \phi_S) >$ as defined in Eqn. (3.49) in Sec. 3.3) on neutron are shown in Fig. 7.30. The magenta curves are from Anselmino *et al.* [237, 128]. The black curves in Collins moments are from Ma *et al.* [158, 294]. The red curves are from Pasquini [301]. The blue curves and blue bands are from W. Vogelsang and F. Yuan [239, 240]. The

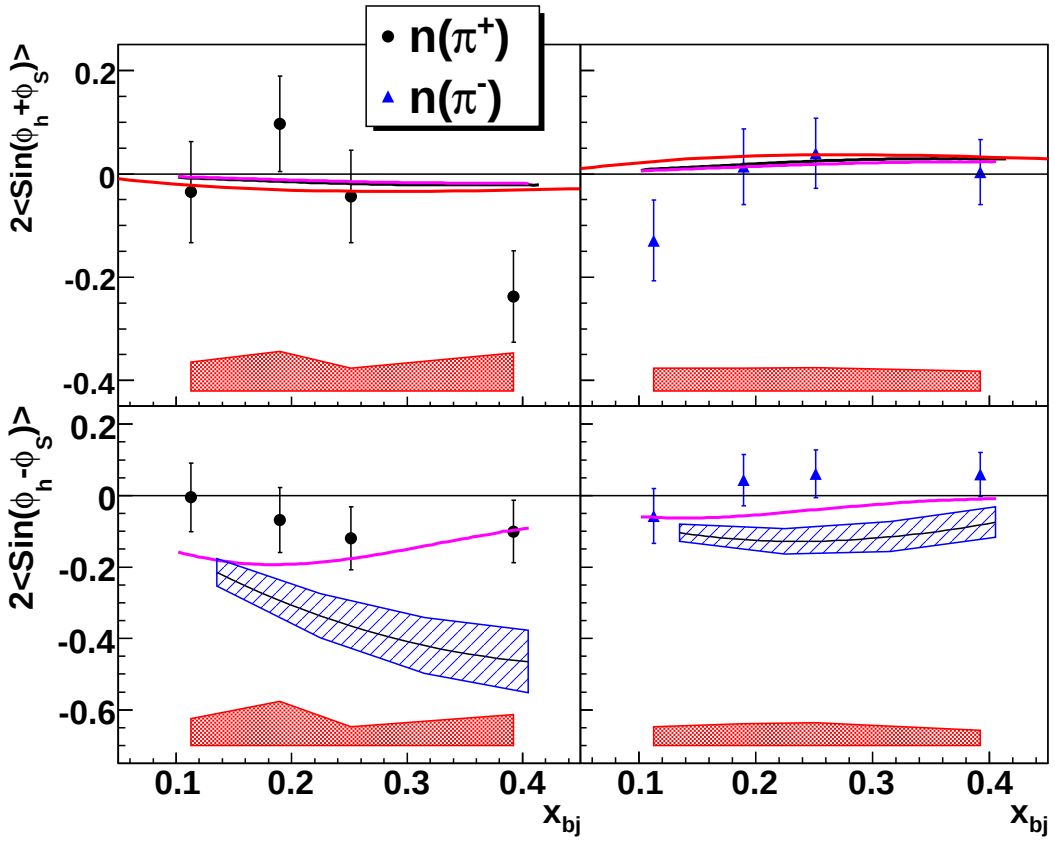

FIGURE 7.30: The preliminary results of Collins/Sivers Moments of Neutron are shown. The error bars represent the statistical uncertainties only. The different sources of systematic uncertainties are added in quadrature, which is plotted as a red band. The preliminary results are compared with calculations from different groups as described in the text.

observations of the preliminary neutron results [11] on Collins/Sivers moments are similar to those of ^{3}He. They are:

- Except the the fourth x bin of π^+, the rest of the extracted Collins moment are consistent with the theoretical predictions.

- Both the π^+ and π^- Sivers moment are systematically higher than the predictions. For the π^- Sivers moment, our data suggest that the asymmetry favors

[11] The impact of the preliminary results will not be discussed in this thesis in order to be cautious. The impact and final results will be presented in the future letter paper.

a positive value, while the calculation suggests a negative value.

- The second and fourth x bin of π^+ show non-zero target single spin asymmetries with more than two σ deviation from zero (stat. only).

- Our π^+ Sivers moments do not favor large negative values.

7.2.8 Future Studies

The coincidence Monte-Carlo simulation SIMC is currently being developed. With the MC, we will update the systematic uncertainties due to bin centering. In addition, effects of radiative correction and the contamination from the diffractive ρ production will be studied with the MC [12].

7.2.9 Summary

In summary, we have presented preliminary results on Collins/Sivers moments from ^{3}He and neutron through the SIDIS SSA measurement. Experiment E06-010 provides the first data in this channel. The kinematic coverage $x = 0.13 \sim 0.41$, at $Q^2 = 1.31 \sim 3.1$ GeV^2. While the preliminary Collins moments are in reasonable agreement with the prediction, the preliminary Sivers moments suggest possible deviations from the predictions. These data would significantly improve our knowledge of the transverse spin structure on neutron in the valence quark region. Together with the world data, one can extract the Transversity and Sivers distribution for different quark flavors.

In addition, the preliminary results of the inclusive hadron SSAs are presented. Large asymmetries were observed and the signs of the asymmetries are compared with preliminary proton results from HERMES.

[12] From the preliminary studies, all these effects are expected to be small.

8

Outlook of TMDs Measurements: From Exploration to Precision

The previous HERMES and COMPASS experiments, together with experiment E06-010, play important roles in exploring the nucleon TMDs, in particular the transversity and the Sivers distribution functions. They established some important features of the Sivers distribution, the transversity distribution, and the Collins fragmentation function for both the proton and neutron. However, compared to the unpolarized and the longitudinal polarized parton distributions, which depend on x and Q^2 only, the TMDs are much less understood since the observables in the SIDIS normally depend on four variables (x, z and p_T, 3-D nature and Q^2). In addition, the kinematics of x, z and p_T are always strongly correlated in all existing experiments, and the results are usually shown in one dimensional format (x, z or p_T) with integration over the other two variables. Furthermore, theoretical fittings [231, 234, 239] to these data usually make certain assumptions about TMDs in order to limit the number of parameters, which is essential considering the scarcity of the existing data. However, some of these assumptions may not be totally applicable. For instance, the

transverse momentum dependence of the parton TMDs is usually assumed to be a Gaussian function, which has been questioned by recent calculations [302]. Similarly, the Gaussian width of the transverse momentum dependence is usually assumed to be the same between the favored/unfavored fragmentation functions and among the parton distributions of different quark flavors. Yet, inconsistent with such assumptions, recent measurements from the JLab E00-108 [303] experiment suggests that the Gaussian width for the unfavored unpolarized fragmentation function may be smaller than that of the favored one. It also hints that the initial transverse momentum width of d quarks is larger than that of the u quark. Therefore, in order to improve our understanding on the TMDs and to resolve the aforementioned theoretical issues, it is important to perform precision measurements. In the following, we will discuss two future projects dedicated to the precision measurements of SSAs in SIDIS.

8.1 Neutron Transversity Measurement at JLab 12 GeV

With an incident electron beam energy up to 11 GeV (JLab 12 GeV upgrade), Jefferson Lab has unique advantages to carry out a measurement of semi-inclusive hadron yields from deep-inelastic scattering: fixed targets allow for a significantly higher luminosity compared with that of the HERMES experiment; and the kinematics allows for a probe of the interesting high x region, which is essential in determining the quark tensor charges.

Currently, in order to provide precision measurements for the neutron SSAs with 11 GeV electron beam, the E10-006 experiment [304], for which I serve as one of the spokespersons, has been proposed and approved at JLab. Similar to experiment E06-010, experiment E10-006 will also employ a high-pressure polarized ^{3}He as an effective polarized neutron target. Instead of the current BigBite and HRS spectrometers, a large acceptance solenoid spectrometer (SoLID) will be used to measure the single

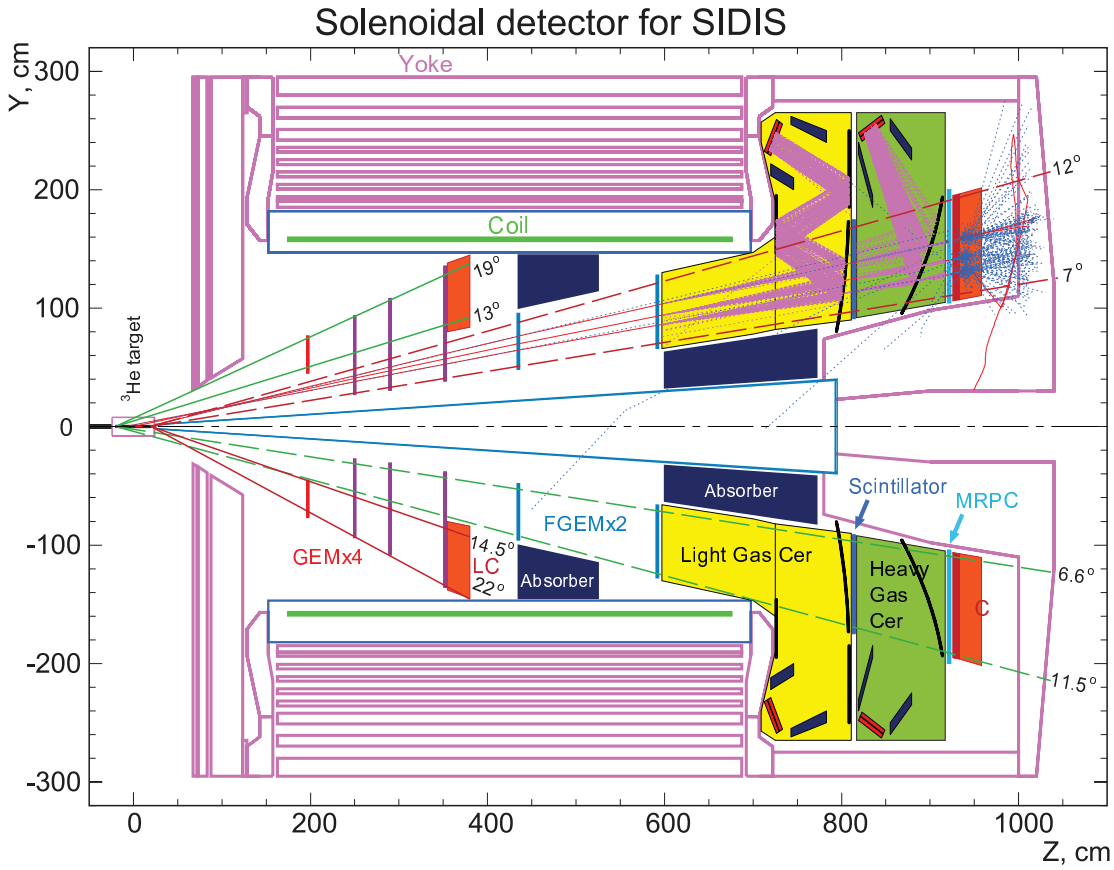

FIGURE 8.1: The experimental layout of the SoLID. At forward angle, there are five layers of GEM detectors inside the coils upstream of the gas Čerenkov (yellow), which excludes pions from electrons. The first three layers, in purple, are shared with the large-angle detectors. The other two layers are in blue. One layer of scintillator (dark blue) used in trigger is placed behind the light gas Čerenkov, followed by a 1 m long heavy gas Čerenkov (green), which excludes the kaons and the protons from the pions at high momentum. One layer of Multi-gap Resistive Plate Chamber (MRPC), in light blue, is placed behind the heavy gas Čerenkov to provide timing information. The calorimeter detectors, in orange, are used for electron/pion separation especially at high momentum. At large angle, four layers of the GEM detectors are placed inside the coils in front of a "shashlyk"-type calorimeter. One absorber is placed behind the large-angle calorimeter to absorb the low energy background, and another one is placed close to the beam line to protect the forward detectors from the low energy backgrounds.

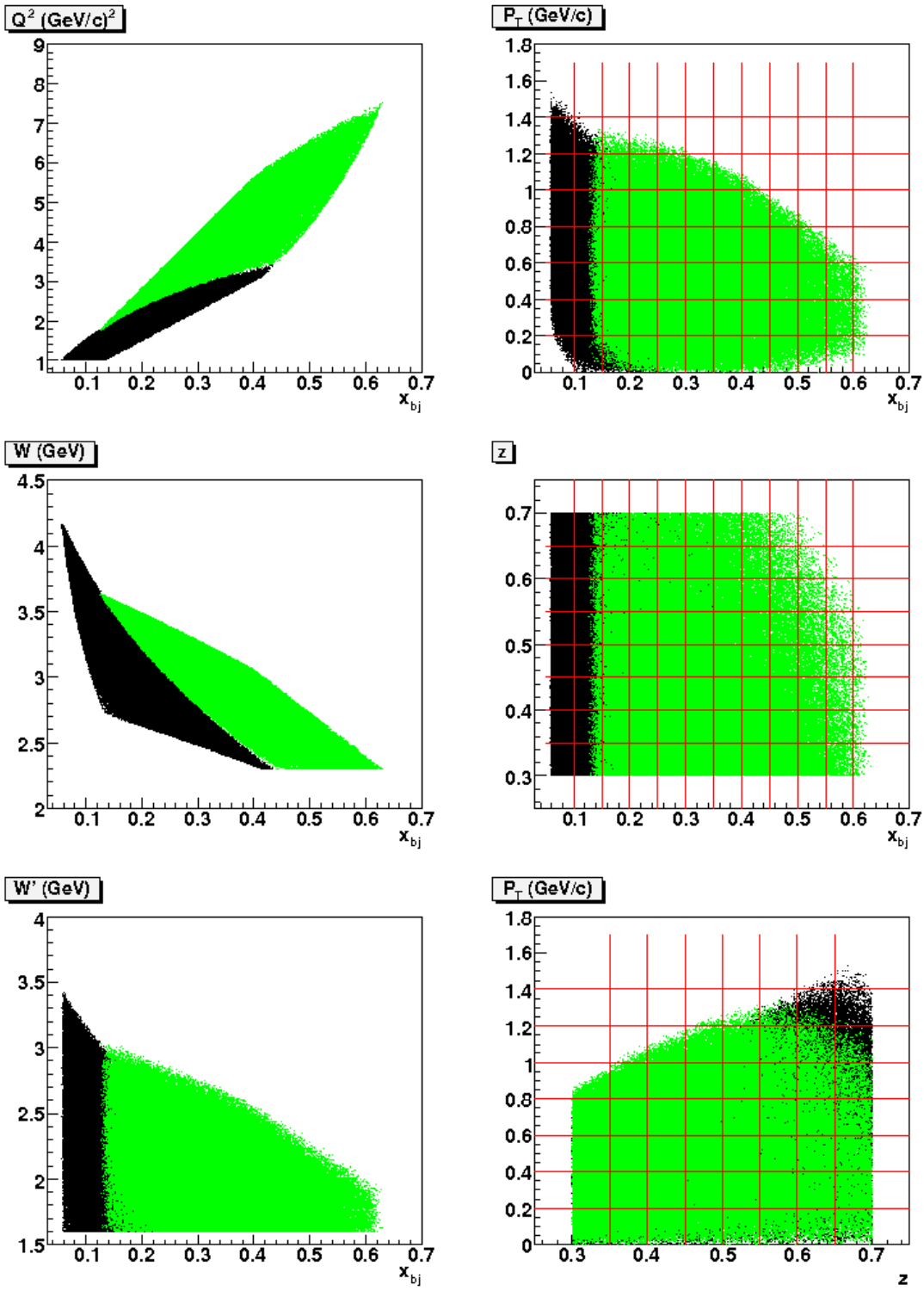

FIGURE 8.2: Kinematic coverage for the SoLID with a 11 GeV electron beam. The black points show the coverages for the forward-angle detectors and the green points show the coverages for the large-angle detectors.

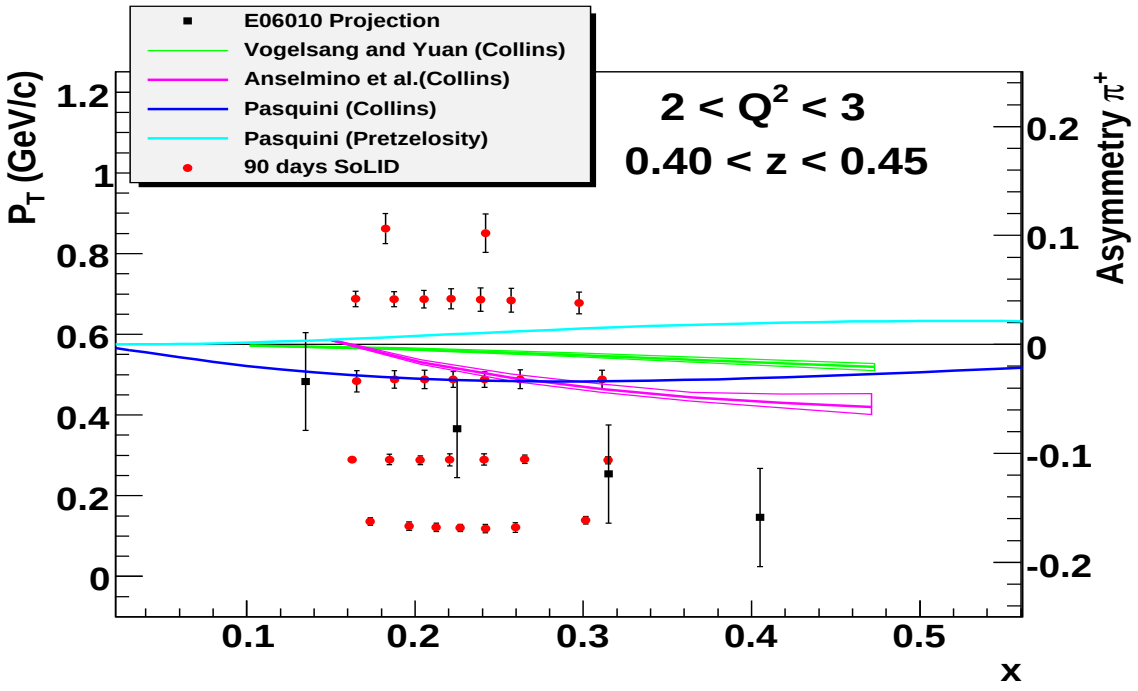

FIGURE 8.3: 12 GeV Projections with SoLID. π^+ Collins/Pretzelosity asymmetries at $0.3 < z < 0.35$, $2 > Q^2 > 1$.

target spin asymmetries with high precision at 8.8 and 11 GeV. The proposed setup of SoLID together with the location of the polarized ^{3}He target are illustrated in Fig. 8.1. The polar angles for electrons θ_e and pions θ_h coverage are from 6.6° to 22° and 6.6° to 12°, respectively. The momentum coverages for electrons and pions are from 1.0 GeV to 7.0 GeV. The kinematic coverages are shown in Fig. 8.2 with 11 GeV beam. The final coverage of x is 0.05-0.65, which covers most of the useful region of the d quark transversity distribution at Q^2 = 1.0-8.0 GeV^2. The coverage of $0.3 < z < 0.7$ is chosen to favor the detection of the leading pions in the current fragmentation region.

The projected results for π^+ Collins and Pretzelosity asymmetries including both 11 and 8.8 GeV data are shown in Fig. 8.3 for one typical kinematic bin, $0.45 > z > 0.4$, $3 > Q^2 > 2$. In addition, the theoretical predictions of Collins asymmetries from Anselmino *et al.* [198]and Vogelsang and Yuan [240], as well as the predictions

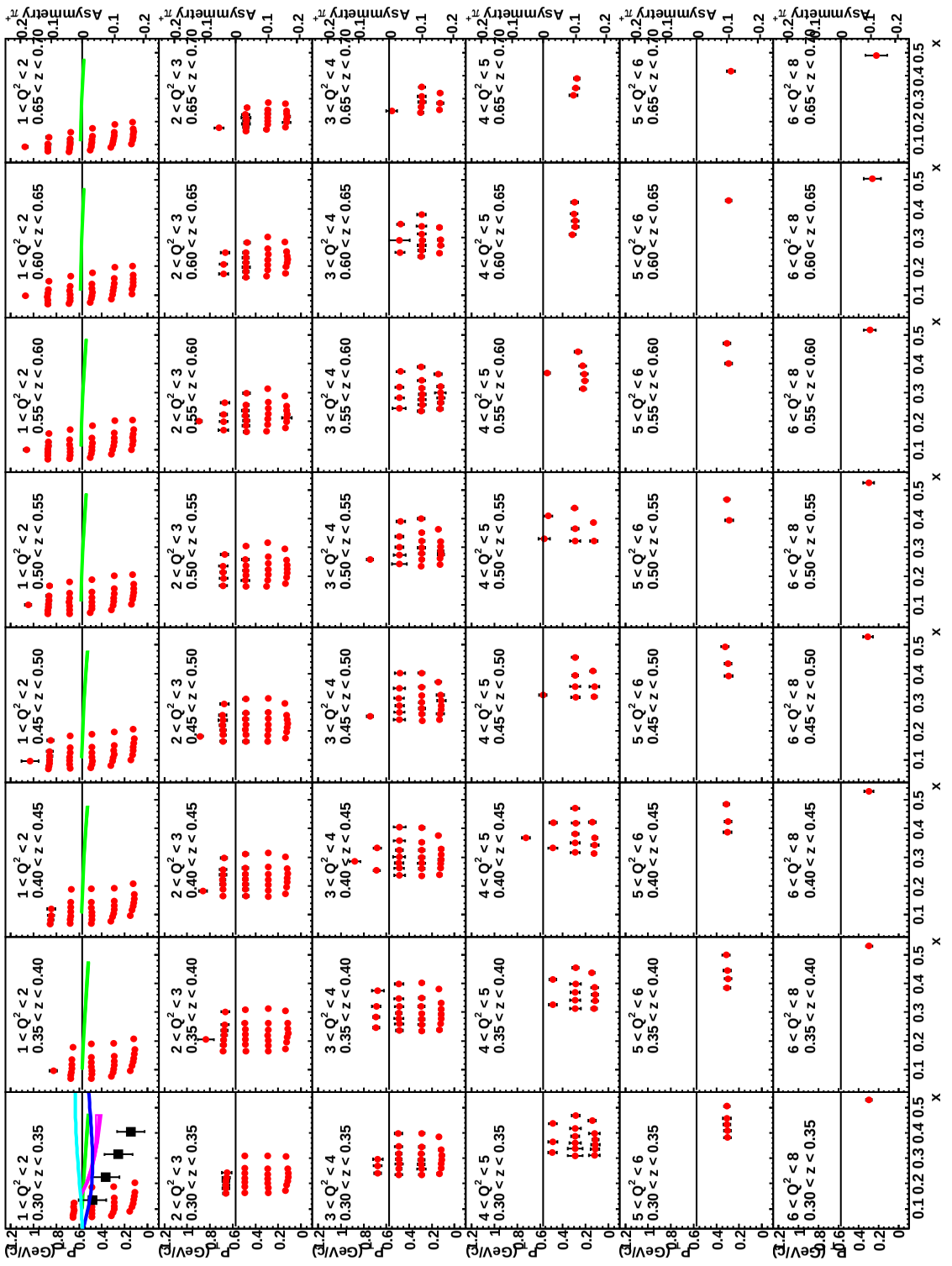

FIGURE 8.4: 12 GeV Projections with SoLID. π^+ Collins/Pretzelosity asymmetries for all kinematic bins in terms of different z and Q^2.

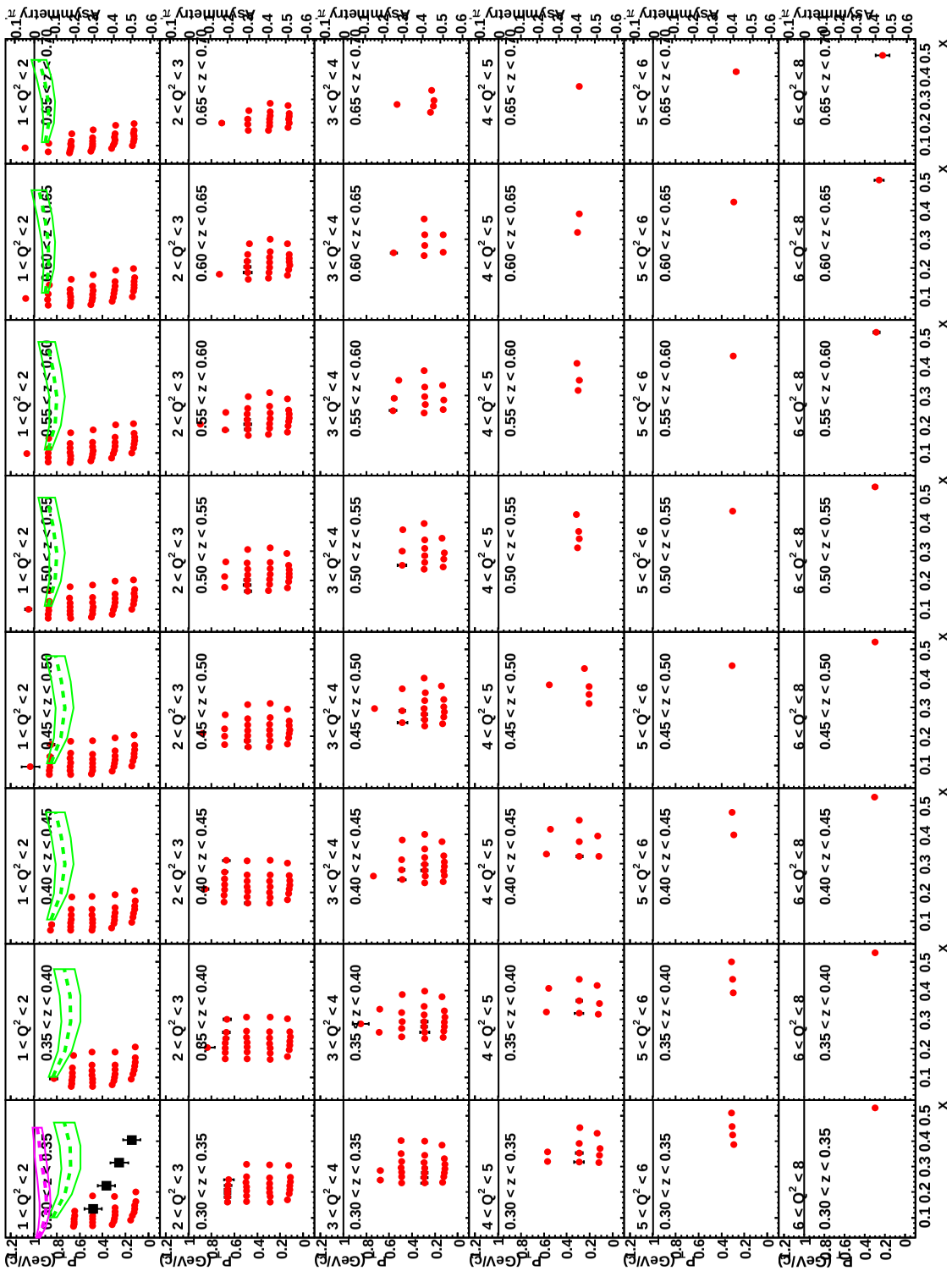

FIGURE 8.5: 12 GeV Projections with SoLID. π^- Sivers asymmetries for all kinematic bins in terms of different z and Q^2.

of Collins/Pretzelosity asymmetries from Pasquini [301], are plotted together. The projected results from experiment E06-010 are shown in black points. The position of each projected point on the left y-axis represents the average P_T value of the corresponding kinematic bin. The the statistical uncertainty of each project point and the theoretical calculations follow the right y-axis.

The complete projections for π^+ Collins/Pretzelosity and π^- Sivers asymmetries are shown in terms of 4-D (x, z, P_T and Q^2) kinematic bin in Fig. 8.4 and Fig. 8.5, respectively. Theoretical predictions of Collins asymmetries from Anselmino *et al.* [198], and predictions of Collins/Pretzelosity asymmetries from Pasquini [301] are shown in the first panel of Fig. 8.4. Theoretical predictions of Collins asymmetries from Vogelsang and Yuan [240] are shown in panels in the first row of Fig. 8.4. Theoretical predictions of Sivers asymmetries from Anselmino *et al.* [198] and Vogelsang and Yuan [240] are shown in Fig. 8.5. In this experiment, the full azimuthal angular coverage of SoLID plays a very important role in reducing the systematic uncertainties of luminosity, detection efficiency, etc., which is essential for such high precision measurement.

In summary, the E10-006 experiment will allow for the high-precision determination of the Collins, Sivers and Pretzelosity asymmetries, which is very important for testing theoretical predictions of TMDs and improving our understanding of TMDs ultimately from the first principles of QCD. In addition, the high precision will allow for a detailed study of the p_T dependence of the Collins, the Sivers, as well as the Pretzelosity asymmetries in fine bins of x, Q^2, and z, separately. Such a precise measurement of the "neutron" together with the precise proton SSA data in a wide kinematic range are essential for understanding the nature of the TMDs and carrying out the flavor decomposition.

8.2 TMD Measurements at Future EIC

Compared to the fixed target experiments, such as experiment E06-010 and the 12 GeV experiment E10-006, the future electron-ion collider (EIC) will be able to probe much larger phase space in x, Q^2 and P_T. In the fixed target experiments, the center-of-mass energy square of the electron-nucleon system is

$$s = 2P_e \cdot M_N + M_N^2. \tag{8.1}$$

For example, the s is about 12 GeV^2 in experiment E06-010 and 22 GeV^2 in experiment E10-006. In the collider environments, the s can be approximately written as:

$$s = 4P_e \cdot P_p. \tag{8.2}$$

For example, with 11 GeV electrons colliding with 60 GeV protons, the s is about 2640 GeV^2, which is equivalent to the s of a 1400 GeV electron beam in a fixed target experiment. The effect of s on the coverage of x and Q^2 is

$$s = Q^2 \cdot x \cdot y. \tag{8.3}$$

The highest achievable y is determined by the lowest detectable electron momentum. The lowest achievable y is usually determined by the experimental resolutions, since

$$\frac{\delta x}{x} = \frac{\delta P_e^f}{P_e^f} \cdot (\frac{1}{y}) + \frac{\delta \theta_e^f}{\tan\frac{\theta_e^f}{2}} \cdot (1 + \tan^2\frac{\theta_e^f}{2} \cdot (1 - \frac{1}{y})). \tag{8.4}$$

Here, the up-script 0 (f) labels the initial (final) detected particles. In addition, the final products of the collision are much easier to detect in a collider environment than in a fixed target environment, where the final products are concentrated at forward angles due to the Lorentz boost. In Fig. 8.6, we compare the Q^2 and x phase space coverage of the EIC with that of the 12 GeV E10-006 experiment. At EIC, one can reach much lower x and much higher Q^2, which are very important for studying the

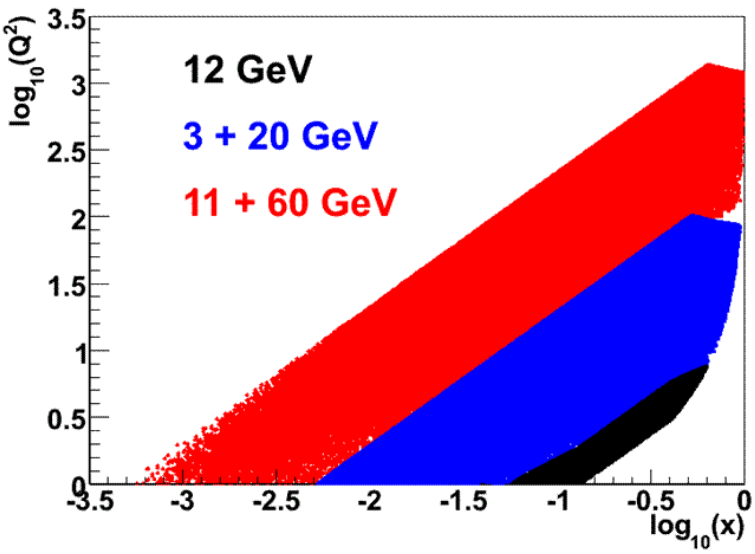

FIGURE 8.6: The EIC kinematics with two configurations (11+60 and 3+20) is compared with that of the 12 GeV E10-006. Here, the notation of "11+60" represents 11 GeV electrons colliding with 60 GeV protons.

TMDs of the sea quarks and gluons. Moreover, the large Q^2 coverage will allow a precise study of the higher twist effects, while the large P_T coverage will allow the study of the SSA phenomenon at high P_T, where the NLO QCD processes dominate.

In summary, the precision measurements at 12 GeV JLab and the future EIC on the TMDs will ultimately realize the multi-dimensional mapping of the TMDs, which will bring our current understanding of the nucleon structure from the one dimensional probability level to a new multi-dimensional amplitude level.

9

Appendix

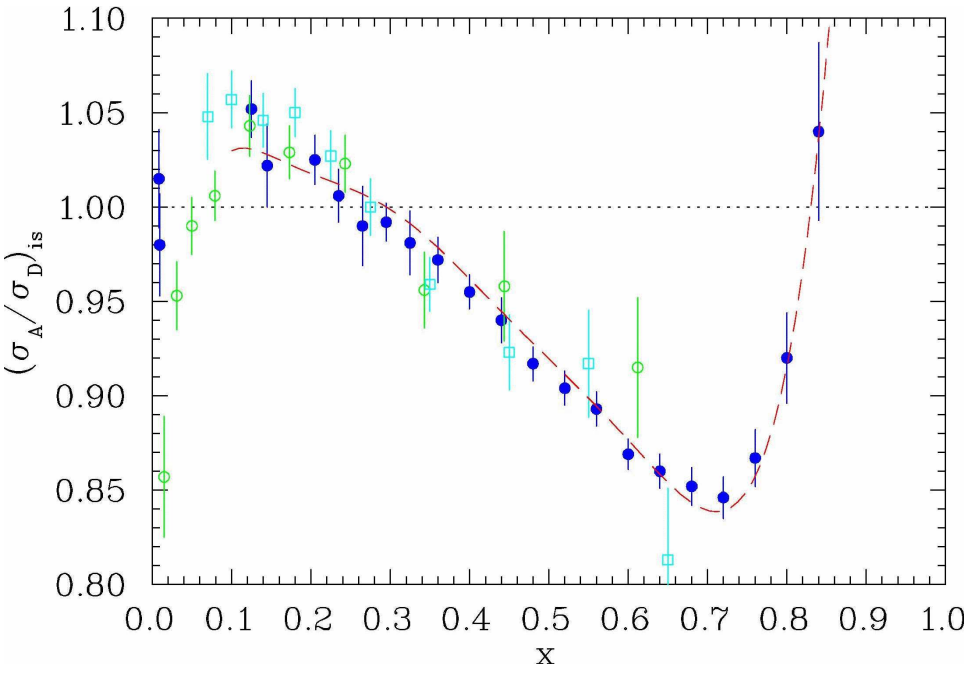

FIGURE 9.1: Ratios of the deep-inelastic cross sections of iron and coppers to those of deuterium. Filled blue circles represent data from Ref. [305] of Fe, open green circles represent data from Ref. [306] of Cu, and open blue squares represent the data from Ref. [307] of Fe. Figure is taken from Ref. [308]

9.1 Nucleon Structure in Nuclei – EMC effects

Another important question about the nucleon is whether it has the same structure in a bound state as in free space. In 1987, the EMC collaboration published the first measurement of normalized structure function ratio between Fe and D [309], which clearly deviated from one. Similar measurements have been carried out since then. Fig. 9.1 shows the ratios of the deep-inelastic cross sections of iron and copper to those of deuterium. These results reveal that the nucleon structure in a bound state is different from the one in free space. This phenomenon has since been referred to as the "EMC effect". There are two possible explanations for the EMC effect: a) nucleon structure is modified in the nuclear medium; b) nuclear structure is modified by the multi-nucleon effects, such as nuclear binding, pion exchange, and N-N short range correlations. Experimental results and different models explaining the EMC effect are reviewed in Ref. [310]. Recent results from JLab on D, ^{3}He ^{4}He, ^{9}Be and ^{12}C [311] show that the EMC effect may depend on the local nuclear environment, rather than mass number A or the nuclear density.

9.2 Survey Report

The survey report of BigBite, target, and sieve slit position is attached in Fig. 9.2.

9.3 Tracking Efficiency Study

In this section, we briefly summarize the evaluation of the BigBite MWDC tracking efficiency. In experiment E06-010, the main physics goal is to extract the SSAs. Therefore, the absolute tracking efficiency is not important. Nevertheless, a few

Jefferson Lab Alignment Group

Data Transmittal

TO: J. P. Chen, J. LeRose, D. Higinbotham		**DATE:** 28 Oct 2008
FROM: J. Dahlberg	**Checked:**	**# :** A1191

DETAILS: Data: Step2b\HallA\BigBite_Detector\080916A, 080916B

Below are the results from the survey performed on the BigBite detectors and sieve. The coordinates (in millimeters) are based on the ideal Hall A target center and straight ahead beam. A +X is to the beam left, a +Z is downstream, and a +Y is up. The corner points on the detectors are to the upstream of the detector frames. **Note:** The detector package was fiducialized in a vertical position on the floor. During this survey in the installed location, as much as 2 millimeters of deformation was seen on the fiducial points. The detector centers and corner points are derived from the fiducial points.

	LOCATION	Z	X	Y
	SIEVE	943.84	-555.84	0.65
DETECTOR CENTERS	**LOCATION**	**Z**	**X**	**Y**
	1CL	2472.12	-1401.24	68.02
	2CL	2583.87	-1465.18	80.59
	3CL	3176.39	-1806.91	219.00
DETECTOR CORNERS	**LOCATION**	**Z**	**X**	**Y**
	1TOPBR	2131.91	-1672.18	952.92
	1TOPBL	2536.33	-967.20	950.87
	1BOTBR	2407.86	-1835.29	-814.59
	1BOTBL	2812.39	-1130.29	-817.12
	2TOPBR	2146.70	-1792.30	1272.20
	2TOPBL	2650.24	-917.50	1269.77
	2BOTBR	2517.17	-2013.47	-1108.66
	2BOTBL	3021.39	-1137.42	-1110.96
	3TOPBR	2739.26	-2133.55	1409.74
	3TOPBL	3241.61	-1257.96	1408.73
	3BOTBR	3111.11	-2355.96	-970.74
	3BOTBL	3613.57	-1480.15	-971.74
DETECTOR FIDUCIALS	**LOCATION**	**Z**	**X**	**Y**
	HABBDTA	4008.92	-1267.36	1650.27
	HABBDTB	2953.59	-603.80	1431.14
	HABBDTC	3362.88	-846.39	-1180.33
	HABBDTD	4101.87	-1331.23	-1023.07
	HABBDTE	2028.62	-2209.90	1428.66
	HABBDTF	3132.90	-2786.91	1645.84
	HABBDTG	3232.47	-2854.95	-1018.89
	HABBDTH	2433.28	-2447.86	-1158.24

studies were performed to demonstrate that the tracking efficiency was acceptable. The tracking efficiency in MWDC was shown to be higher than 85% throughout the entire experiment.

9.3.1 Experience with Tracking During E06-010

With 1st pass beam (1.2306 GeV), the BigBite optics was calibrated with the hydrogen reference cell run at beam current of 1-2 μA. The principle is to utilize the single electrons at the hydrogen elastic kinematics to calibrate the momentum reconstruction. At such beam energy, it was expected that every valid trigger in the BigBite should contain a valid elastic electron, thus leaving a track in the MWDC. In order to select the valid triggers, we applied the following cuts:

- The energy deposition in the preshower was required to be higher than 150 MeV in order to remove pions.
- The energy deposition in the total preshower/shower calorimeter was required to be higher than 700 MeV in order to select high energy electrons. The top right panel of Fig. 5.23 shows the strong correlation between the reconstructed momentum and reconstructed polar angle of the elastic electron. The average of the momentum is about 1.05 GeV, while the lowest momentum is well above the 0.7 GeV.
- For each projections, u, v and x, a minimum of five out of six planes were required to be fired.
- If there was a track found, the χ^2/N_{dof} representing the track quality was required to be smaller than 2.4.

With the conditions above, about 86.5 % of events had valid tracks, representing a lower bound of the tracking efficiency, since there could be some high energy photons

Beam energy (GeV)	Run Number	Pressure (psig)
1.2306	2660-2664	100
2.3960	2892, 2893, 2896, 2897, 2903	135

Table 9.1: Data used in the hydrogen elastic cross section analysis at two beam energies are summarized in this table.

triggering the BigBite. Meanwhile, it was found that the MWDC hitting efficiency around this period was about 96%[1], leading to a hardware tracking efficiency of 93.5% as illustrated in Sec. 5.1.1. Therefore, the lower bound of the software tracking efficiency is about **92.5 %**.

9.3.2 BigBite Tracking MC

In order to predict the software tracking efficiency with the proposed MWDC setup, a BigBite tracking MC was developed. First, events were generated by a MC with the GEANT3 BigBite model, which digitized every hit in every wire in the MWDC. More details can be found in Sec. 6.1. Next, the output of the MC was analyzed by the same Hall A tracking software used in data analysis. Since the number of tracks simulated in the MC were known, the software tracking efficiency could be evaluated. With 100% hitting efficiency, the tracking efficiency was found to be about **95%**, which is consistent with the lower bound 92.5%.

9.3.3 Hydrogen Elastic Cross Section Analysis

The tracking efficiency was further verified by extracting the well known hydrogen elastic cross section from BigBite. The data used in this analysis are listed in Table. 9.1. A data quality check procedure, including removing the periods of beam trips, BigBite wire chamber trips, T1 trigger rates instability etc, was applied before extracting the cross sections. During this study, only data from the BigBite T1

[1] The HV on the MWDC was set to be low at the beginning of the experiment to be cautious. The HV was raised later and the corresponding hitting efficiency increased to about 98% during the production data taking.

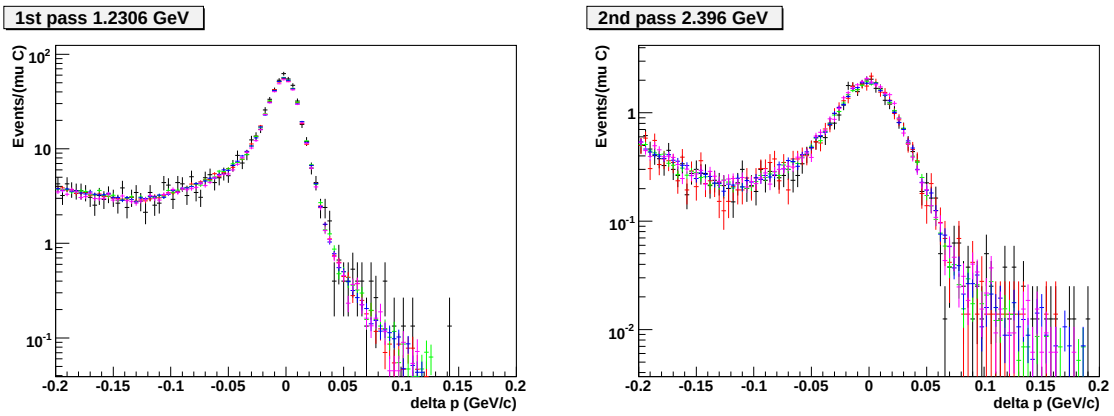

FIGURE 9.2: The stability check of normalized yield for the runs used in this hydrogen elastic cross section analysis. The x-axis, δp, is the difference between the reconstructed momentum and expected momentum at elastic kinematics. The histograms with different colors represent the data from different runs. Left and right panels show the data with incident beam energies of 1.2306 and 2.3960 GeV, respectively.

trigger were analyzed. The only correction included was the dead time correction in order to extract the normalized yield. Fig. 9.2 shows the stability check for the runs used at both incident beam energies.

The same GEANT3 BigBite MC as the one in tracking MC was used to generate the hydrogen elastic events with a flat distribution in the lab polar angle. The calculated cross sections [312, 313] with proper Jacobian transformation were then added as a weight for each generated events. The simulated events were then processed through the standard analysis software, and same cuts were applied in both MC and Data. Fig. 9.3 shows the absolute yield (number of events per μC) comparisons between the data and MC at two incident beam energies. The x-axis of Fig. 9.3 is the difference between the expected momentum and reconstructed momentum $\delta P = P_{exp} - P_{reconstructed}$. The width of the δP peak in the MC is slightly narrower than that of the data, as the position resolution of MWDC in MC did not get enough smearing, leading to a better momentum resolution. In order to minimize the effects due to different momentum resolutions in data and MC, the peaks of data

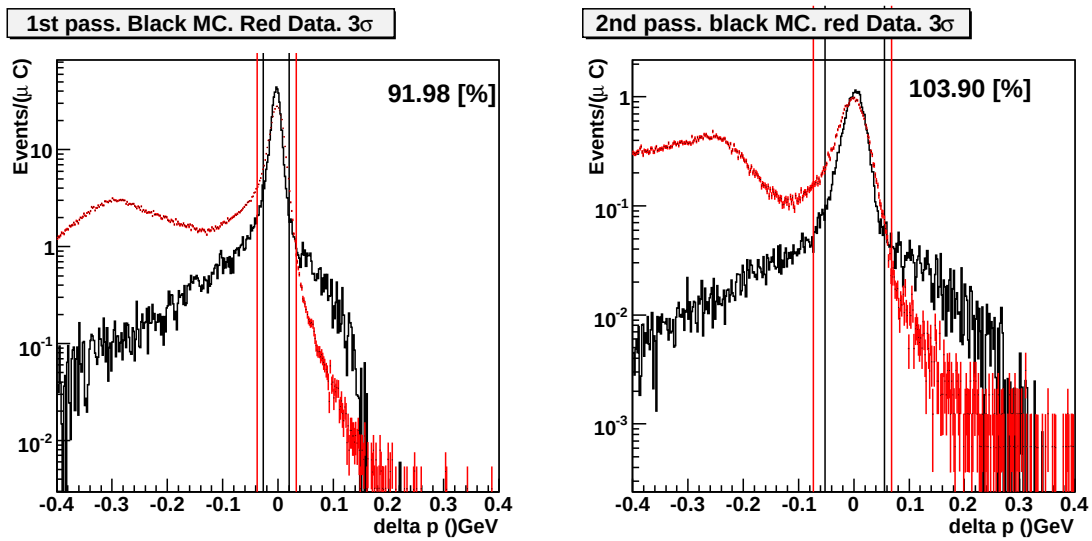

FIGURE 9.3: Absolute yields between data and MC in the hydrogen elastic cross section analysis are compared. The black and red histograms represent MC and data, respectively. The black and red lines represent the 3σ cut for MC and data, respectively. The x-axis, δp, is the difference between the reconstructed momentum and expected momentum at elastic kinematics. Left and right panels show the results with incident beam energies of 1.2306 and 2.3960 GeV, respectively.

and MC were fitted with a Gaussian shape and a 3-σ cut was applied on each peak. The yield within the 3-σ cut is defined as $Y_{3\sigma}$. In addition, events were observed on the right side of the elastic peak. Those events, also referred to as the super elastic events, were due to the tail of the momentum reconstruction (non-Gaussian tail). The yield in the super elastic region is defined as Y_{sel}. Therefore, the ratio of the elastic cross sections of data to MC can be expressed as:

$$\frac{\sigma_{data}}{\sigma_{MC}} = \frac{Y_{3\sigma}^{data} + 2 \cdot Y_{sel}^{data}}{Y_{3\sigma}^{MC} + 2 \cdot Y_{sel}^{MC}}, \tag{9.1}$$

which are 0.92 and 1.04, at incident beam energies of 1.2306 and 2.3960 GeV, respectively. The factor 2 in front Y_{sel} represents the fact that similar amount of events due to the non-Gaussian tail of momentum resolution is expected to be observed on the left of the elastic peak. However, they could not be obtained due to the contribution

from inelastic scattering. Therefore, the averaged cross section ratio of data to MC:

$$\frac{\sigma_{data}}{\sigma_{MC}} = 0.98 \pm 0.06, \tag{9.2}$$

which is consistent to one. In addition, as demonstrated in the previous section, the tracking efficiency shown with the tracking MC is about 95%. Combining both information, one can deduce that the tracking efficiency is about **95%** in the data.

Here, we also list a few possible improvements in this study:

- Radiative Correction and Cross Section Model:

  In the BigBite GEANT3 model, the external radiative correction due to the material that electrons pass through is naturally taken into account. However, the internal radiative correction, which is due to the interaction of electron with proton atom inside the hydrogen target, is not considered. The internal radiative correction can be viewed as a correction to the Cross Section Model.

- Momentum resolution:

  The smearing of the MWDC position resolution can be added to obtain a better match of the momentum resolution between MC and data.

9.3.4 Tracking Efficiency at High Background Rates

In the study with elastic hydrogen data, the beam current was usually about 1-2 μA. Therefore the background rates in the MWDC were lower than those of the polarized ^{3}He production data, which were taken with 8-14μA. Fig. 9.4 shows the normalized yield of electron defined as:

$$Y = \frac{N}{P \cdot C \cdot f} \tag{9.3}$$

vs. the beam current for the polarized ^{3}He cell. Here, N is the number of electrons; P is the pressure of the target cell (filling density); C is the accumulated charge;

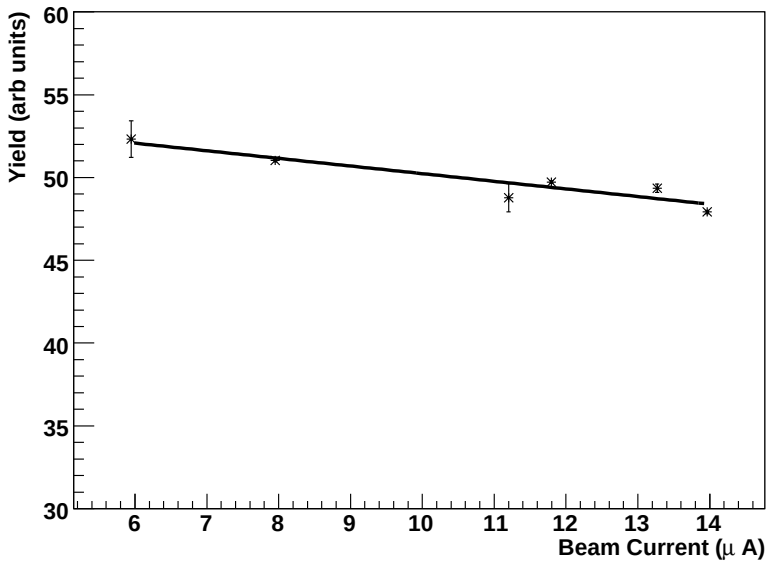

FIGURE 9.4: Normalized yields are plotted against the beam current. Only the statistical uncertainties are included. A linear fit is applied to extract the beam current (or background) dependence of the normalized yield, which effectively measure the tracking efficiency. The interception and the slope from the fit are listed in the plot.

and f is live time correction. Beside the cuts listed in Sec. 5.4.2, an additional cut for momentum larger than 1.0 GeV was applied to remove the effects due to the BigBite calorimeter radiation damage discussed in Sec. 5.2.4. Except the last point taken at $14\mu A$, which was the only point corresponding to the third target cell, the rest of the points are consistent with a flat line. In order to extract the background rates dependence of the yield, the data are fitted with a linear form. The effect of reduction in tracking efficiency at high background level can then be estimated as: (from 2 to 14 μA)

$$\epsilon = \frac{slope \cdot \Delta I}{Intercept} \approx 10\%. \tag{9.4}$$

Here the slope and interception are obtained by the linear fit in Fig. 9.4. The ΔI is 12 μA. The 10% (from $2\mu A$ to 14 μA) can be treated as a higher bound of the degradation in tracking efficiency at high background.

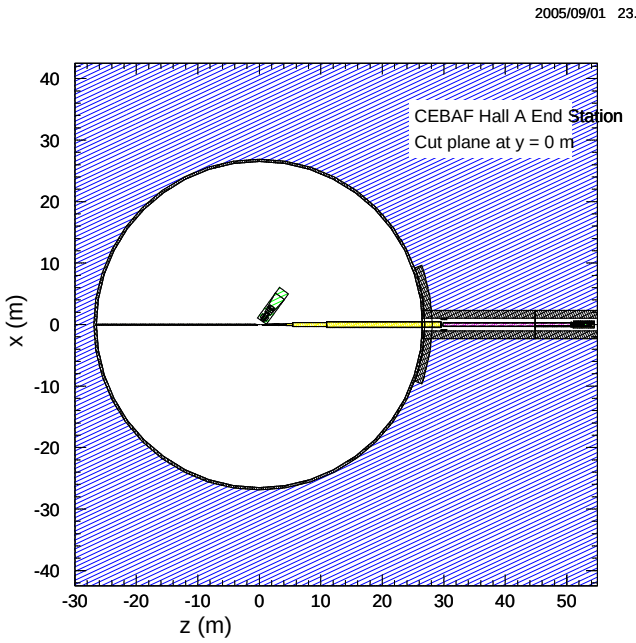

FIGURE 9.5: GEANT3 Model of the Hall A. Beam pipe, target, beam dump, and some other fine structures were also modeled.

In summary, the tracking efficiency in experiment E06-010 is higher than 85% throughout the entire experiments.

9.4 BigBite Background Estimation

In this section, we summarize our studies of the BigBite background simulation, which guided the design of the shielding of the BigBite spectrometer in experiment E06-010. The background simulation also played an important role in getting this experiment approved, since the program adviser committee (PAC) raised the question whether the BigBite MWDC would be able to handle the low energy background at the proposed running luminosity. A GEANT3 based simulation code [314] was used to study the background rates on the BigBite MWDC. An exclusive event generator, the photon-nuclear fragmentation package DINREG, was used to replace

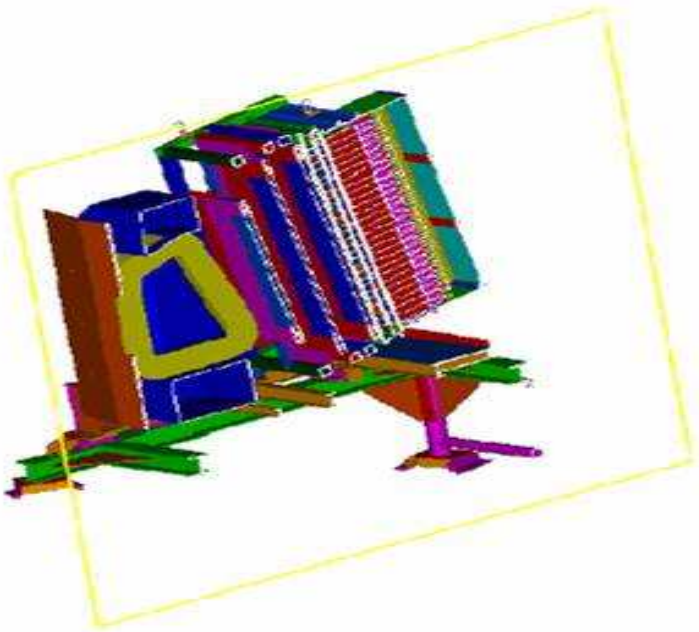

FIGURE 9.6: 3-D view of the BigBite magnet with a middle cut is shown. There are gaps with weaker field at the top and bottom of the BigBite magnet.

the old 'PFIS' mechanism in GEANT. In addition, the electron-nuclear interactions were modeled using the equivalent photon representation of an electron. Fig. 9.5 shows the geometry of the Hall A, together with beam pipe, target, and the beam dump modeled in the GEANT3. The BigBite geometry used in the simulation was modeled according to the BigBite engineering drawing, and is shown in Fig. 4.25 in Sec. 4.10.2[2]. The BigBite magnetic field mapping was from SNAKE EMULATION from MAFIA by V. Nelyubin [285] from University of Virginia.

9.4.1 BigBite Momentum Acceptance

During the simulation studies, it was found that there were gaps at both the top and the bottom of the BigBite magnet where the magnetic field was weaker. Fig. 9.6 shows the 3-D view of BigBite with a cut in the middle of the BigBite magnet in order to clearly illustrate the position of gaps. Charged particles with low momentum can

[2] The same BigBite model was used in all GEANT3 related MC.

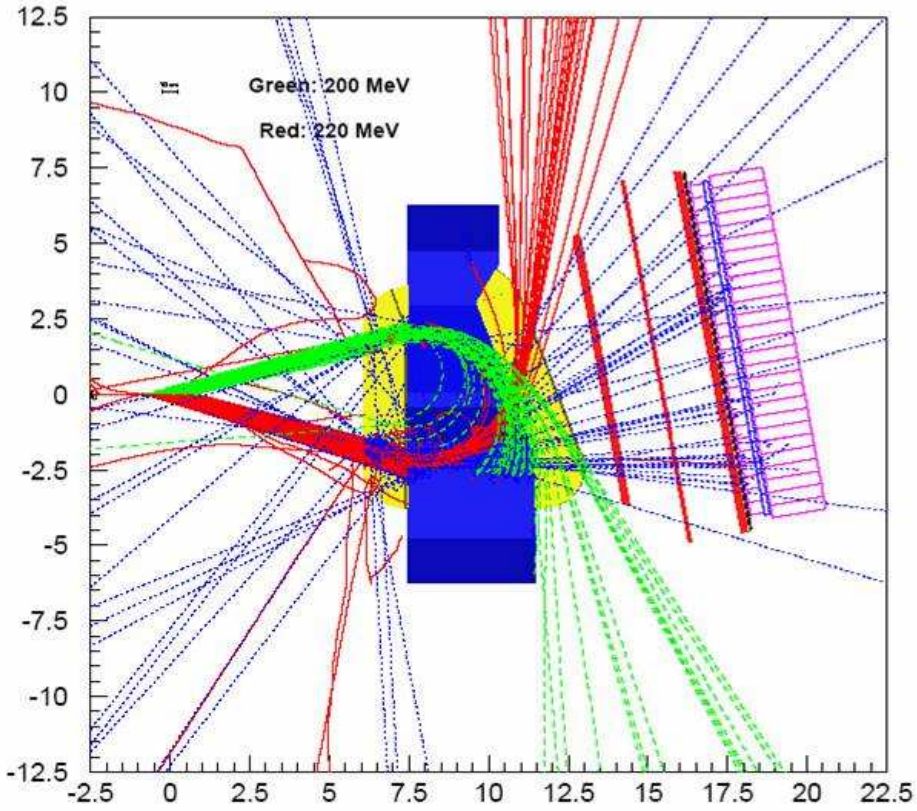

FIGURE 9.7: The low momentum charged particles were blocked by the additional shielding placed in the gaps of the BigBite magnet.

reach the detector package through those gaps. In experiment E06-010, the gaps were blocked by additional material. In this case, the BigBite spectrometer would only accept the charged particles with momentum higher than 200 MeV/c, as illustrated in Fig. 9.7.

9.4.2 Comparison Between MC and Data

In order to justify the simulation procedure, we compared the MC simulation with data from four experiments. The first one is a comparison with a test run taken during the Short Range Correlation (SRC) experiment in Hall A. The beam energy was 4.63 GeV, and the target was a 4 cm LD_2 target. The BigBite was located at 99 degrees with drift distance of 1 m. The magnetic field was about 0.986 T. The

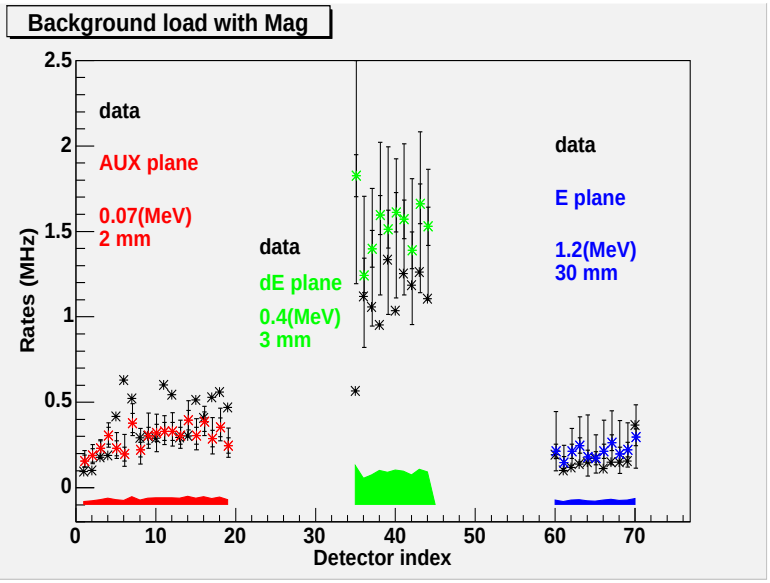

FIGURE 9.8: Rates comparison between the data and MC with magnetic field. For the MC results, the inner error bar is the statistical uncertainties and the outer error bar is the quadrature sum of the statistical and systematic uncertainties. Here the source of the systematic uncertainties include the threshold used in the data analysis. The color bands show the systematic uncertainties due to the geometry, beam current, beam energy, etc.

detector package consisted of three scintillator planes: auxiliary plane, dE plan, and E plane, made of standard plastic scintillator with an effective composition C_9H_{10} and density 1.032 g/cm^3. The auxiliary plane was placed just at the position of the first MWDC in experiment E06-010. The E plane was placed about 900 mm behind the auxiliary plane and dE plane was right in front of the E plane. The dimensions of the auxiliary plane, dE plane and E plan are 350×500×2.5 mm, 500×2064×3 mm and 500×2064×30 mm, respectively. The detector package was tilted at 25 degrees. The energy threshold was set to be 0.07 MeV, 0.4 MeV and 1.2 MeV for auxiliary plane, dE plane and E plane, respectively. Fig. 9.8 and Fig. 9.9 show the comparisons of the results between MC and data with and without the magnetic field, respectively. The difference between the data and simulation is within 50%.

The second comparison is with the SRC production data. The target was a

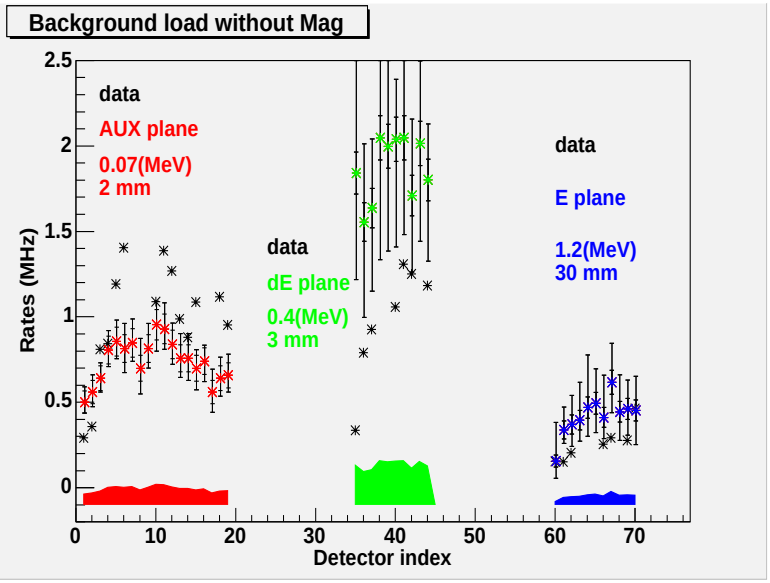

FIGURE 9.9: Rates comparison between the data and the MC without magnetic field. The rest of caption is the same as Fig. 9.8.

carbon foil (thickness of 42.3 mg/cm^2) tilted at 20 degrees. The rate of MC is 70 kHz, and the rate from data is $338 \pm 5.3(stat) \pm 57(sys)kHz$. The sources of systematic uncertainties include uncertainties in geometry, threshold cuts, etc. The MC overestimated the data by a factor of 4.

The third comparison is with data from the neutron detector in the N20 test run during the GEN experiment. The neutron detector layout is shown in Fig. 9.10, and the model of neutron detector was obtained from P. Degtiarenko [315], a staff scientist from JLab. The beam energy was 4.6 GeV. The target was a 15 cm long LH_2 target. The detector was located at 40 degrees and the distance was 15 m. The beam current was 9 μA. Fig. 9.11 shows the rate comparisons and the MC underestimated the data by about a factor of 2.

The fourth comparison is with a wire chamber test run during the HAPPEX experiment at Hall A. The beam energy was 2.75 GeV and the current was 8 μA. Only the first wire chamber was used in this test run. It was located at 70 degree

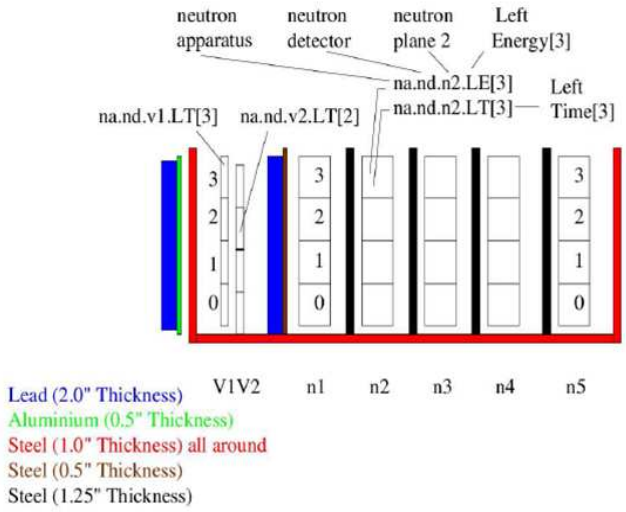

FIGURE 9.10: The layout of the neutron detectors during N20 test run.

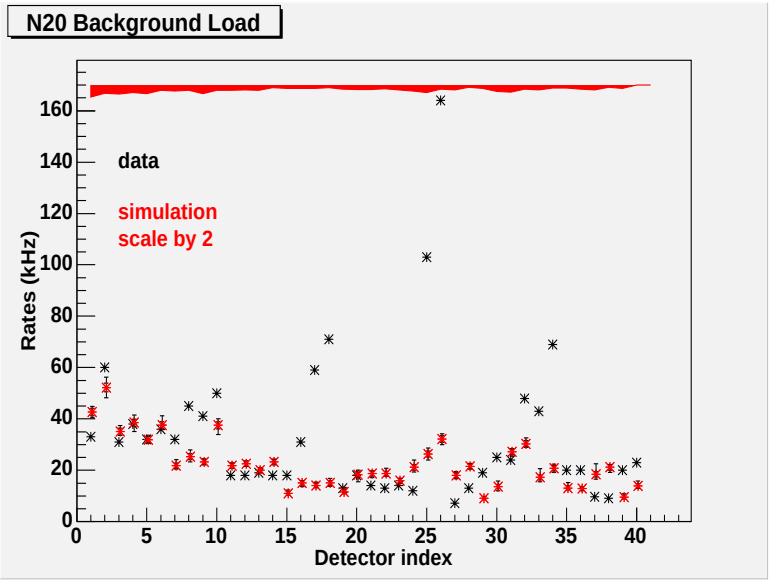

FIGURE 9.11: Rates comparison between the data and the MC for the N20 test run. For the MC results, the inner error bar is the statistical uncertainties, and the outer error bar is the systematic uncertainties. Sources of the systematic uncertainties include the threshold cut used in the data analysis. The color bands show the systematic uncertainties due to the geometry, beam current, beam energy, angle of detector, distance of detector etc. The MC results are scaled by a factor of 2.

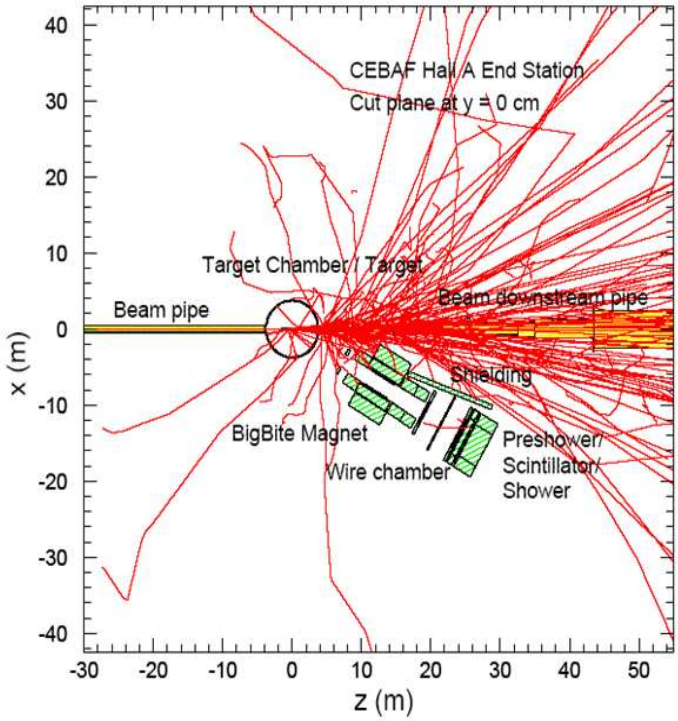

FIGURE 9.12: The shielding of the BigBite spectrometer is shown. The motivation of such shielding is to block the background originated from the beam line.

and the distance was 10 m. With 1 keV threshold cut (energy deposition inside the wire chamber), the MC overestimated the data by a factor of 5, and the MC agreed with the data with a 5 keV threshold cut.

9.4.3 Background on MWDC in GEN and Transversity Experiment

We further extended our studies to understand/predict the background on MWDC at experimental conditions of GEN (E02-013) and TRANSVERSITY (E06-010). Due to the large momentum acceptance of the BigBite spectrometer, the detector package had a direct view of the target in both experiments. The major background was the low energy electrons/photons from E&M processes, such as the Moller, Bremsstrahlung, Compton process, etc. The dipole magnetic field of the BigBite magnet would sweep the charged particles with momentum lower than 200 MeV.

Setting I	BD1 (MHz)	BD2 (MHz)	BD3 (MHz)
Data	14	7	5
MC	12[3]	4.07	3.41
Setting II			
Data	10.5	12.2	11.6
MC	7.2	12.7	11.0
Setting III			
Data	15.0	16.7	15.0
MC	8.48	16.7	15.0

Table 9.2: BigBite MWDC background simulation results were compared with the data in GEN experiment. Setting I is with run 2500 with 2 μA beam. The shielding modeled in the simulation was 3.15 inch lead, which was much thicker than the shielding used in the GEN experiment (1 in Aluminum). The threshold cut used in the MC was 1 keV. Setting II is with run 2812 with 5.0 μA beam. Setting III is with run 3463 with 7 μA beam. The target was the polarized ^{3}He cell. Here, BDi represents the predicted background rates on the ith chamber.

However, the low energy charged particles can still reach detector package through paths outside the magnet. For example, some charged particles will be generated along the downstream beam pipe. With the guidance of the simulation, additional shieldings were installed on both side of the BigBite magnet in experiment E06-010. Fig. 9.12 illustrated the designed shielding implemented in the experiment. In the following, we briefly summarize the comparisons between MC and data.

In the GEN experiment, the beam energy was 3.2 GeV. The BigBite spectrometer was located at 54 degrees with 1.1 m drift distance. The comparison of the background rates on chamber between the simulation and data is shown in Table. 9.2. The MC can describe the data with 50% precision except for the first chamber. The discrepancy in the first chamber might be due to fringe field of the BigBite magnet.

In TRANSVERSITY experiment, the beam energy was 5.89 GeV. The target was a 40 cm long 10 amagats ^{3}He target. The BigBite spectrometer was located at 30 degrees with 1.5 m drift distance. The predicted background rates on all

setting	Beam Energy GeV	Target	BD1 (MHz/μA)	BD2 (MHz/μA)	BD3 (MHz/μA)
MC	6	^{3}He	1	2.3	2.3
Data	5.89	^{3}He	3.5	4.5	4.2
Data	2.4	Single-Carbon	9.1	9.0	5.06
Data	5.89	Multi-Carbon	13.5	14.1	11
Data	2.4	Multi-Carbon	13	13	10
Data	1.23	Multi-Carbon	20	22	15
Data	5.89	H2 Gas	3.46	4.34	3.65
Data	2.4	H2 Gas	5.1	5.3	3.9

Table 9.3: BigBite MWDC background simulation results at transversity condition are compared with the data. Results are presented in the unit of $MHz/\mu A$. BDi gives the rates in the ith chamber.

three chambers are shown in Table. 9.3. The prediction on background rates is about factor of 2 lower than the data taken at same condition (first two lines of Table. 9.3). The background rates on the MWDC during the chamber threshold and high voltage scan are shown in Table. 9.4. In addition, a complete summary of the background rates study of BigBite wire chamber can be found in Halog Entry 215800 (`http://www.jlab.org/~adaq/halog/html/0812_archive/081203022504.html`). The background rates on the MWDC are well understood between different targets, luminosities, beam qualities, beam raster size, and the chamber running conditions in terms of threshold and high voltage.

In summary, the GEANT3 model successfully predicted the background rates on various detectors with various experimental conditions to about 50% level. The above studies built our confidence in this set of software in predicting background rates for the future experiments.

9.5 Maximum Likelihood Method

Maximum likelihood estimation (MLE) is a common method used for fitting certain statistical model to data. Meanwhile, MLE can provide estimates for all parameters

High Voltage (V)	Threshold (V)	BD1 (MHz/μA)	BD2 (MHz/μA)	BD3 (MHz/μA)
1650	3.5	12.2	13.3	9.5
1650	4.0	11.5	12.6	8.8
1650	4.5	11.1	12.1	8.5
1650	5.0	11	12.1	8.4
1550	5.0	8.9	9.4	6.6
1550	4.5	9.0	9.7	6.9
1550	4.0	9.4	10.2	7.1
1550	3.5	9.7	10.5	7.3
1550	3.0	10	10.8	7.6
1500	3.0	8.5	9.1	6.5
1500	4.0	7.7	8.0	5.8
1500	4.5	7.24	7.5	5.4
1500	5.0	6.9	7.1	5.0
1600	5.0	6.9	7.1	5.0
1600	4.5	10	10.9	7.7
1600	4.0	10.4	111.3	8.1
1600	3.5	10.6	11.5	8.1
1600	3.0	11.1	12.1	8.6

Table 9.4: This table summarizes the BigBite MWDC background rates during the threshold and HV scan in the transversity experiment. The data were taken from run period of 2662-2685.

in the model. The principle of the MLE is to find the probability function for one event to happen $f(x|\theta)$. The likelihood function can then be defined as:

$$\mathcal{L}(\theta, x_1...x_i...x_n) = \prod_{i=1}^{n} f(x_i|\theta) \tag{9.5}$$

by multiplying the probability function of all the events. Furthermore, the log-likelihood is defined as:

$$\hat{l}(\theta, x_1...x_i...x_n) = \frac{1}{n} ln\mathcal{L} = \frac{1}{n} \sum_{i=1}^{n} lnf(x_i|\theta) \tag{9.6}$$

One can then estimate the θ_0 by maximizing the log likelihood.

The MLE method was first introduced in the proposal of experiment E06-010 [241] in order to estimate the projections of this experiment. Later, it was further carefully derived by J. Huang from M. I. T. and Y. Qiang from Duke in the case of transversity analysis [316]. In the extraction of SSAs, the MLE method served as a cross-check to the local pair method discussed in Sec. 5.8.2. The results from MLE perfectly agreed with those extracted with the local pair method.

9.6 Data Quality Check

Here we summarizes the list of the studies performed in the data quality check. For many studies, no problems were found, which means that we could understand the changes in experimental observables based on the changes in the experimental conditions. However, although no problems were found, those studies were still very useful, since different periods with different configurations were identified, which was essential in forming local asymmetries.

- Left HRS Pion Rejector: Average energy deposition, average hit position in both dispersive and non-dispersive directions for both layer 1 and layer 2 were examined. No problems were observed.

- Left HRS VDC: Average drift time, hit position, and number of hits in all four planes were examined. Some problems related to the database were fixed.

- Left HRS Cerenkov and Aerogel Pedestal: A shift in the pedestal was observed. Such shift is related to the replacement of the power supply of left HRS detector ROCs, which was broken during the data taking. The shift in the pedestal was taken into account in the detector calibration for left HRS.

- Left HRS Cerenkov and Aerogel: Average values of ADC were examined. In the period when one PMT in aerogel was nearly broken, the response from

this PMT was fluctuating a lot. The PMT response from this PMT within this period was set to zero. Near the end of end of experiment E06-010, the response from one PMT in the gas Cerenkov was found to be fluctuating. A run-by-run correction, based on linear fits with run number, was applied for this PMT within that period. A database related problem was found for aerogel.

- Raw Trigger Rates vs. run number: No problems were found.
- Number of Events taken vs. run number: No problems were found.
- Scaler Consistency Check: See discussions in Sec. 5.2.3.
- BigBite Shower Counter: E/p peak positions/resolutions, preshower minimized ionization peak positions/resolutions, and cluster average positions were examined. The calorimeter radiation damage problem was found. More discussions can be found in Sec. 5.2.4.
- BigBite MWDC: Number of hits and average hit positions in all 18 planes were examined. Track qualities χ^2/N_{dof}, tracking residuals, number of tracks, average values of track positions, and average values reconstructed kinematics variables were examined. No problems were found after removing the MWDC trips.
- Yields of different particles: No additional issues were observed after fixing the problems related to the detectors.
- Coincidence Timing: The coincidence timing was examined against the run number. A period with DAQ problem was identified. During this period, the TDC readings on the BigBite scintillator were incorrect.
- Halog: Different run periods with different DAQ configuration, prescale factor, different experimental condition (beam current, HV on detectors) were iden-

tified. A period with the T2 and T3 trigger swapped was identified. All the short runs were identified and their corresponding reasons were listed in the MYSQL database. Major problems, such as failure of power supply, left HRS Q1 magnet quench, were identified. Beam fluctuation related issues were also identified.

9.7 Jacobian Matrix

In SIDIS, the cross section is usually presented in the form of $\frac{d\sigma^h}{dx_B dy d\phi_S dz_h d\phi_h dP_{h\perp}^2}$. However, it needs to be transformed in the $\frac{d\sigma^h}{dP_e d\cos\theta_e d\phi_e dP_\pi d\cos\theta_\pi d\phi_\pi}$ in lab frame in the simulation. The transformation between these two formats is the jacobian matrix. Using (x, y, z, m, n, l) to replace $(x, y, z, P_T^2, \phi_h, \phi_S)$ and (a, b, c, d, e, f) to replace $(P_e, \cos\theta_e, \phi_e, P_\pi, \cos\theta_\pi, \phi_\pi)$, the jacobian matrix J can be written as:

$$J = \begin{vmatrix} \frac{\partial x}{\partial a} & \frac{\partial x}{\partial b} & \frac{\partial x}{\partial c} & \frac{\partial x}{\partial d} & \frac{\partial x}{\partial e} & \frac{\partial x}{\partial f} \\ \frac{\partial y}{\partial a} & \frac{\partial y}{\partial b} & \frac{\partial y}{\partial c} & \frac{\partial y}{\partial d} & \frac{\partial y}{\partial e} & \frac{\partial y}{\partial f} \\ \frac{\partial z}{\partial a} & \frac{\partial z}{\partial b} & \frac{\partial z}{\partial c} & \frac{\partial z}{\partial d} & \frac{\partial z}{\partial e} & \frac{\partial z}{\partial f} \\ \frac{\partial l}{\partial a} & \frac{\partial l}{\partial b} & \frac{\partial l}{\partial c} & \frac{\partial l}{\partial d} & \frac{\partial l}{\partial e} & \frac{\partial l}{\partial f} \\ \frac{\partial m}{\partial a} & \frac{\partial m}{\partial b} & \frac{\partial m}{\partial c} & \frac{\partial m}{\partial d} & \frac{\partial m}{\partial e} & \frac{\partial m}{\partial f} \\ \frac{\partial n}{\partial a} & \frac{\partial n}{\partial b} & \frac{\partial n}{\partial c} & \frac{\partial n}{\partial d} & \frac{\partial n}{\partial e} & \frac{\partial n}{\partial f} \end{vmatrix}. \tag{9.7}$$

The four momentum vector of incoming electron, outgoing electron, incoming nucleon, and outgoing pion can be written as:

$$p_e = (0, 0, P_e^0, P_e^0), \tag{9.8}$$

$$p_p = (0, 0, -P_p, \sqrt{P_p^2 + M_p^2}), \tag{9.9}$$

$$p_e^f = (P_e \sin\theta_e, 0, P_e \cos\theta_e, P_e), \tag{9.10}$$

$$p_\pi = (P_\pi \sin\theta_\pi \cos\phi_\pi, P_\pi \sin\theta_\pi \sin\phi_\pi, P_\pi \cos\theta_\pi, \sqrt{P_\pi^2 + M_\pi^2}), \tag{9.11}$$

by neglecting the electron mass and assuming that scattered electron defines the zero point of the azimuthal angle ϕ_e. We also write $\sqrt{P_p^2 + M_p^2}$ as E_p. Therefore: x, y,

and z can be written as:

$$x = \frac{P_e P_e^0(1-\cos\theta_e)}{(P_e^0-P_e)E_p + P_p(P_e^0 - P_e\cos\theta_e)}, \tag{9.12}$$

$$y = \frac{(P_e^0-P_e)E_p + P_p(P_e^0 - P_e\cos\theta_e)}{P_e^0(E_p+P_p)}, \tag{9.13}$$

$$z = \frac{E_p\sqrt{P_\pi^2+M_\pi^2} + P_pP_\pi\cos\theta_\pi}{(P_e^0-P_e)E_p + P_p(P_e^0 - P_e\cos\theta_e)}, \tag{9.14}$$

and

$$\frac{\partial\phi_S}{\partial\phi_e} \approx -1, \tag{9.15}$$

as illustrated in Ref. [193]. Therefore, the jacobian matrix is simplified as:

$$J = \begin{vmatrix} \frac{\partial x}{\partial a} & \frac{\partial x}{\partial b} & 0 & 0 & 0 & 0 \\ \frac{\partial y}{\partial a} & \frac{\partial y}{\partial b} & 0 & 0 & 0 & 0 \\ 0 & 0 & \frac{\partial l}{\partial c} & 0 & 0 & 0 \\ \frac{\partial z}{\partial a} & \frac{\partial z}{\partial b} & 0 & \frac{\partial z}{\partial d} & \frac{\partial z}{\partial e} & 0 \\ \frac{\partial m}{\partial a} & \frac{\partial m}{\partial b} & \frac{\partial m}{\partial c} & \frac{\partial m}{\partial d} & \frac{\partial m}{\partial e} & \frac{\partial m}{\partial f} \\ \frac{\partial n}{\partial a} & \frac{\partial n}{\partial b} & \frac{\partial n}{\partial c} & \frac{\partial n}{\partial d} & \frac{\partial n}{\partial e} & \frac{\partial n}{\partial f} \end{vmatrix}, \tag{9.16}$$

and

$$\begin{aligned} J &= |(\frac{\partial x}{\partial a}\cdot\frac{\partial y}{\partial b} - \frac{\partial x}{\partial b}\cdot\frac{\partial y}{\partial a})\cdot\frac{\partial l}{\partial c}\cdot(\frac{\partial z}{\partial d}\cdot(\frac{\partial m}{\partial e}\cdot\frac{\partial n}{\partial f} - \frac{\partial n}{\partial e}\cdot\frac{\partial m}{\partial f}) \\ &- \frac{\partial z}{\partial e}\cdot(\frac{\partial m}{\partial d}\cdot\frac{\partial n}{\partial f} - \frac{\partial n}{\partial d}\cdot\frac{\partial m}{\partial f}))|. \end{aligned} \tag{9.17}$$

Since P_T and ϕ_h are both defined in the nucleon at rest frame or γ^*N center-of-mass frame[4], the 3-vector momentum of π in the nucleon at rest frame can be written as

$$(P_\pi^x P_\pi^y, P_\pi^z) = (P_\pi\sin\theta_\pi\cos\phi_\pi, P_\pi\sin\theta_\pi\sin\phi_\pi, \gamma\cdot(P_\pi\cos\theta_\pi - \beta\cdot\sqrt{P_\pi^2+M_\pi^2})), \tag{9.18}$$

[4] The Lorentz transformation between the nucleon at rest frame and γ^*N center-of-mass frame will leave P_T and ϕ_h unchanged.

with $\beta = -P_p/E_p$ and $\gamma = 1/\sqrt{1-\beta^2}$. In addition, the z component of the virtual photon 3-vector momentum can be written as

$$q_z = \gamma \cdot (P_e^0 - P_e \cos\theta_e - \beta \cdot (P_e^0 - P_e)). \tag{9.19}$$

We can then define the angle:

$$\alpha = \arctan(\frac{P_e \cdot \sin\theta_e}{q_z}) \tag{9.20}$$

in order to rotate the nucleon at rest frame to the frame where the virtual photon 3-vector momentum is at z-axis and the outgoing electron 3-vector momentum has zero azimuthal angle. We have

$$P_T^2 = \cos^2\alpha \cdot P_\pi^x P_\pi^x + P_\pi^y P_\pi^y + \sin^2\alpha \cdot P_\pi^z P_\pi^z + 2\sin\alpha \cdot \cos\alpha \cdot P_\pi^x P_\pi^z, \tag{9.21}$$

and

$$\phi_h = \arctan(\frac{P_\pi^y}{\cos\alpha \cdot P_\pi^x + \sin\alpha \cdot P_\pi^z}). \tag{9.22}$$

Therefore, one can easily derive all the derivatives in Eqn. (9.17) from expressions in Eqn. (9.12), (9.13), (9.14), (9.21), and (9.22) in order to calculate the Jacobian J.

9.8 Collins and Sivers Asymmetry Calculation in SIMC

In this section, we summarize the calculations of Collins and Sivers asymmetries in SIMC. The formalism of Collins and Sivers asymmetry calculation is based on Anselmino *et al.* [237] and Anselmino *et al.* [128], respectively.

9.8.1 Collins Asymmetry

With Gaussian ansatz, the transverse momentum dependent unpolarized parton distribution $f_{q/p}(x, k_\perp)$ and fragmentation function $D_{h/q}(z, p_\perp)$ can be expressed as:

$$f_{q/p}(x, k_\perp) = f_{q/p}(x) \frac{e^{k_\perp^2/<k_\perp^2>}}{\pi < k_\perp^2 >} \tag{9.23}$$

$$D_{h/q}(z, p_\perp) = D_{h/q}(z) \frac{e^{-p_\perp^2/<p_\perp^2>}}{\pi < p_\perp^2 >}, \tag{9.24}$$

and

$$< k_\perp^2 > = 0.25\ GeV^2 \tag{9.25}$$

$$< p_\perp^2 > = 0.2\ GeV^2 \tag{9.26}$$

[128] were used. The transversity distributions $\Delta_T q(x, k_\perp)$ were parametrized as:

$$\Delta_T q(x, k_\perp) = \frac{1}{2}[f_{q/p}(x) + \Delta q(x)] \mathcal{N}_q^T(x) \frac{e^{k_\perp^2/<k_\perp^2>}}{\pi < k_\perp^2 >}. \tag{9.27}$$

Here, $\Delta q(x)$ is the longitudinal polarized PDF, and

$$\mathcal{N}_q^T(x) = N_q^T x^\alpha (1-x)^\beta \frac{(\alpha+\beta)^(\alpha+\beta)}{\alpha^\alpha \beta^\beta}. \tag{9.28}$$

The Collins fragmentation function $\Delta^N D_{h/q^\uparrow}(z, p_\perp)$ were parametrized as:

$$\Delta^N D_{h/q^\uparrow}(z, p_\perp) = 2\mathcal{N}_q^C(z) D_{h/q}(z) h(p_\perp) \frac{e^{-p_\perp^2/<p_\perp^2>}}{\pi < p_\perp^2 >} \tag{9.29}$$

with

$$\mathcal{N}_q^C(z) = N_q^C z^\gamma (1-z)^\delta \frac{(\gamma+\delta)^{\gamma+\delta}}{\gamma^\gamma \delta^\delta} \tag{9.30}$$

$$h(p_\perp) = \sqrt{2e} \frac{p_\perp}{M} e^{-p_\perp^2/M^2}. \tag{9.31}$$

$N_u^T = 0.79 \pm 0.11$	$N_d^T = -1.00 \pm 0.15$	$\alpha = 0.62 \pm 0.18$	$\beta = 0.31 \pm 0.27$
$N_{fav}^C = 0.43 \pm 0.05$	$N_{unf}^C = -1.00 \pm 0.17$	$\gamma = 0.96 \pm 0.06$	$\delta = 0.01 \pm 0.03$
$M_h^2 = 0.91 \pm 0.46$ GeV^2			

Table 9.5: Best values of the free parameters for the u and d transversity distribution functions and for the favored and unfavored Collins fragmentation functions from Ref. [231].

The parameters used are listed in Table. 9.5 [231].

The Collins asymmetry can then expressed as:

$$A_{UT}^{\sin(\phi_S+\phi_h)} = \frac{2\frac{P_T}{M}(1-y)\sqrt{2e}\frac{<p_\perp^2>_C^2}{<p_\perp^2>}\frac{e^{-P_T^2/<P_T^2>_C}}{<P_T^2>_C^2}\sum_q e_q^2 \mathcal{N}_q^T(x)[f_{q/p}(x)+\Delta q(x)]\mathcal{N}_q^C(z)D_{h/q}(z)}{2\frac{e^{-P_T^2/<P_T^2>}}{<P_T^2>}(1+(1-y)^2)\sum_q e_q^2 f_{q/p}(x)D_{h/q}(z)} \tag{9.32}$$

where

$$< p_\perp^2 >_C = \frac{M^2 < p_\perp^2 >}{M^2 + < p_\perp^2 >}, \tag{9.33}$$

$$< P_T^2 > = < p_\perp^2 > + z^2 < k_\perp^2 >, \tag{9.34}$$

$$< P_T^2 >_C = < p_\perp^2 >_C + z^2 < k_\perp^2 > . \tag{9.35}$$

9.8.2 Sivers Asymmetry

The Sivers functions $\Delta^N f_{q/p^\perp}(x, k_\perp)$ were parametrized as:

$$\Delta^N f_{q/p^\perp}(x, k_\perp) = 2\mathcal{N}_q(x)h(k_\perp)f_{q/p}(x, k_\perp), \tag{9.36}$$

where

$$\mathcal{N}_q(x) = N_q x^\alpha (1-x)^\beta \frac{(\alpha+\beta)^(\alpha+\beta)}{\alpha^\alpha \beta^\beta} \tag{9.37}$$

$$h(k_\perp) = \sqrt{2e}\frac{k_\perp}{M}e^{-k_\perp^2/M^2}. \tag{9.38}$$

The values used are listed in Table. 9.6 [235].

$N_u = 0.35^{+0.08}_{-0.08}$ $N_{\bar{u}} = 0.04^{+0.22}_{-0.24}$ $\alpha_u = 0.73^{+0.72}_{-0.58}$ $\beta = 3.46^{+4.87}_{-2.90}$	$N_d = -0.90^{+0.43}_{-0.10}$ $N_{\bar{d}} = -0.40^{+0.33}_{-0.44}$ $\alpha_d = 1.08^{+0.82}_{-0.65}$ $M^2 = 0.34^{+0.30}_{-0.16}$ GeV^2	$N_s = -0.24^{+0.62}_{-0.50}$ $N_{\bar{s}} = 1^{+0}_{-0.0001}$ $\alpha_{sea} = 0.79^{+0.56}_{-0.47}$

Table 9.6:

Best values of the free parameters for the 'broken sea' ansatz from Ref. [235].

The Sivers asymmetry can then be expressed as:

$$A_{UT}^{\sin(\phi_h-\phi_S)} = \frac{(1+(1-y)^2)\frac{\sqrt{2e}zP_T}{M}\frac{<k_\perp^2>_S^2}{<k_\perp^2><P_T^2>_S}\frac{e^{-P_T^2/<P_T^2>_S}}{<P_T^2>_S}\sum_q e_q^2 2\mathcal{N}_q(x)f_{q/p}(x)D_{h/q}(z)}{2\frac{e^{-P_T^2/<P_T^2>}}{<P_T^2>}(1+(1-y)^2)\sum_q e_q^2 f_{q/p}(x)D_{h/q}(z)} \tag{9.39}$$

with

$$< k_\perp^2 >_S = \frac{M^2 < k_\perp^2 >}{M^2 + < k_\perp >^2} \tag{9.40}$$

$$< P_T^2 >_S = < p_\perp^2 > + z^2 < k_\perp^2 >_S . \tag{9.41}$$

The $< p_\perp^2 >$ and $< k_\perp^2 >$ are the same as those used in calculating Collins asymmetry.

Bibliography

[1] S. Chekanov *et al.* ZEUS Collab. *Phys. Rev.*, **D67**:012007, 2003.

[2] J. Pumplin *et al.* CTEQ Collab. *JHEP*, **0207**:012, 2002.

[3] A. D. Martin *et al. Eur. Phys. J. C*, **23**:73, 2002.

[4] J. Gayler, 2002. hep-ex/0211051.

[5] W. Bardeen *et al. Phys. Rev.*, **D18**:3998, 1978.

[6] B. Clasie. Measurement of nuclear transparency from a(e,e'π^+) reactions, 2006. Ph. D. thesis, M. I. T. `http://www.jlab.org/~clasie/bc_thesis.ps.gz`.

[7] B. Clasie and X. Qian *et al.* Measurement of nuclear transparency for the $A(e, e'\pi^+)$ reaction. *Phys. Rev. Lett.*, **99**:242502, 2007.

[8] `http://focus.aps.org/story/v20/st22#videos`.

[9] T. Horn and X. Qian *et al.* Scaling study of the pion electro-production cross section and the pion form factor. *Phys. Rev.*, **C78**:058201, 2008.

[10] X. Qian *et al.* "Study of the $A(e, e'\pi^+)$ Reaction on ^{1}H, ^{2}H, ^{12}C, ^{27}Al, ^{64}Cu and ^{197}Au" accepted by PRC, arXiv:0908.1616., 2009.

[11] A. Larson *et al. Phy. Rev.*, **C74**:018201, 2006.

[12] W. Cosyn *et al. Phys. Rev.*, **C74**:062201(R), 2006.

[13] M. M. Kaskulov *et al. Phys. Rev*, **C79**:0152007, 2009.

[14] A. S. Carroll *et al. Phys. Lett.*, **B80**:319, 1979.

[15] A. H. Mueller, in Proceedings of the Seventeenth Recontre de Moriond Conference on Elementary Particle Physics, Les Arcs, France, 1982 edited by J. Tran Thanh Van (Editions Fronriers, Gif-sur-Yvette, France, 1982); S. J. Brodsky, in Proceedings of the Thirteenth International Symposium on Multiparticle Dynamics, Volendam, The Netherlands, 1982, edited by W. Kittel et al. (World Scientific, Singapore, 1983).

[16] N. Makins *et al. Phys. Rev. Lett.*, **72**:1986, 1994.

[17] T. O'Neill *et al. Phys. Lett.*, **B351**:87, 1995.

[18] K. Garrow *et al. Phys. Rev.*, **C66**:044613, 2002.

[19] D. Abbott *et al. Phys. Rev. Lett.*, **80**:5072, 1998.

[20] J. M. Laget. *Phys. Rev.*, **C73**:044003, 2006.

[21] B. Blattel *et al. Phys. Rev. Lett.*, **70**:896, 1993.

[22] A. Airapetian *et al.* (HERMES). *Phys. Rev. Lett.*, **90**:052501, 2003.

[23] D. Dutta *et al. Phys. Rev.*, **C68**:021001(R), 2003.

[24] S. Nozawa and T. S. H. Lee. *Nucl. Phys.*, **A513**:511, 1990.

[25] A. S. Raskin and T. W. Donnelly. *Annals Phys.*, **191**:78, 1989.

[26] M. Diehl and S. Sapeta. *Eur.Phys.J.*, **C41**:515, 2005.

[27] M. Vanderhaeghen *et al. Phys. Rev.*, **C57**:1454, 1998.

[28] M. M. Kaskulov *et al. Phys. Rev.*, **D78**:114022, 2008.

[29] Spokesperson: H. Gao and D. Tedeschi. CAA proposal, CLAS password protected.

[30] X. Qian. *et al.* 152 pages. analysis note, CLAS password protected.

[31] X. Qian *et al.* The extraction of $\phi - N$ total cross section from $d(\gamma, pK^+K^-)n$. *Phys. Lett.*, **B680**:417, 2009.

[32] X. Qian *et al.* Subthreshold photoproduction of ϕ-meson from deuterium. to be submitted to PRC, 2010.

[33] X. Qian *et al.* ϕ-meson photoproduction from $\gamma(d, \phi p)n$ reaction. to be submitted to PRC, 2010.

[34] J. J. Sakurai, Currents and Mesons, University of Chicago Press, Chicago, 1969.

[35] T. Ishikawa *et al. Phys. Lett.*, **B608**:215, 2005.

[36] T. Mibe *et al.* CLAS Collab. *Phys. Rev.*, **C76**:052202(R), 2007.

[37] S. J. Brodsky *et al. Phys. Rev. Lett.*, **64**:1011, 1990.

[38] H. Gao *et al. Phys. Rev.*, **C73**:022201R, 2001.

[39] F. Huang *et al. Phys. Rev.*, **C73**:025207, 2006.

[40] M. Luke *et al. Phys. Lett.*, **B288**:355, 1992.

[41] S. Liska *et al. Phys. Rev.*, **C75**:058201, 2007.

[42] T. H. Bauer *et al. Rev. Mod. Phys.*, **50**:261, 1978.

[43] D. P. Barber *et al. Z. Phys.*, **C12**:1, 1982.

[44] H. J. Behrend *et al. Nucl. Phys.*, **B144**:22, 1978.

[45] H. J. Betsch *et al. Nucl. Phys.*, **B70**:257, 1974.

[46] J. Ballam *et al. Phys. Rev.*, **D7**:3150, 1973.

[47] H. J. Halpern. *Phys. Rev. Lett.*, **29**:1425, 1972.

[48] A. I. Titov *et al. Phys. Rev.*, **C60**:035205, 1999.

[49] Q. Zhao *et al. Nucl. Phys.*, **A660**:323, 1999.

[50] D. Tedeschi *et al.* "Electromagnetic Interactions in Nuclear and Hadronic Physics", M. Fujiwara and T. Shima (Eds.), World Scientific, 367 (2002).

[51] T. Mibe *et al. Phys. Rev. Lett.*, **95**:182001, 2005.

[52] J. Barth *et al. Eur. Phys. J.*, **A17**:269, 2003.

[53] W. Chen *et al.* CLAS Collab. *Phys. Rev. Lett.*, **103**:012301, 2009.

[54] S. Dürr *et al. Science*, **322**:1224, 2008.

[55] M. Gell-Mann. A schematic model of baryons and mesons. *Phys. Lett.*, **8**:214, 1964.

[56] G. Zweig, 1964. CERN Report TH 401.

[57] C. Amsler *et al.* (Particle Data Group). *Phys. Lett.*, **B667**:1, 2008.

[58] M.Gell-Mann, 1961. California Institue of Technology Synchrotron Laboratory Report CTSL-20.

[59] Y. Ne'eman. *Nucl. Phys.*, **26**:222, 1961.

[60] M. Gell-Mann. *Phys. Rev.*, **125**:1067, 1962.

[61] M. Y. Han and Y. Nambu. *Phys. Rev.*, **139**:1006, 1965.

[62] O. W. Greenberg. Spin and unitary spin independence in a paraquark model of baryons and mesons. *Phys. Rev. Lett.*, **13**:598, 1964.

[63] R. P. Feynman, 1969. Proceeding of the 3rd Topical Conference on High Energy Collision of Hadrons, Stony Brook, N. Y.

[64] J. D. Bjorken and F. A. Paschos. *Phys. Rev.*, **185**:1975, 1969.

[65] M. Breidenbach *et al. Phys. Rev. Lett.*, **23**:935, 1969.

[66] E. D. Bloom *et al. Phys. Rev. Lett.*, **23**:930, 1969.

[67] D. J. Gross and F. Wilczek. *Phys. Rev. Lett.*, **30**:1343, 1973.

[68] H. D. Polizer. *Phys. Rev. Lett.*, **30**:1346, 1973.

[69] G. S. Bali *et al. Phys. Rev.*, **D51**:5165, 1995.

[70] B. Andersson *et al. Phys. Rep.*, **97**:31, 1983.

[71] X. Ji. *Phys. Rev. Lett.*, **91**:062001, 2003.

[72] X. Ji. *J. Phys. G*, **24**:1181, 1998.

[73] K. Goeke *et al. Prog. Part. Nucl. Phys.*, **47**:401, 2001.

[74] A. V. Radyushkin. hep-ph/0101225.

[75] M. Burkardt. *Phys. Rev.*, **D62**:071503, 2000.

[76] M. Burkardt. *Phys. Rev.*, **D66**:119903(E), 2002.

[77] X. Ji. *Phys. Rev. Lett.*, **74**:1071, 1995.

[78] J. Ashman *et al.* EMC. *Phys. Lett.*, **B206**:364, 1988.

[79] J. Ashman *et al.* EMC. *Nucl. Phys.*, **B328**:1, 1989.

[80] S. E. Kuhn, J.-P. Chen, and E. Leader. *Prog. Part. Nucl. Phys.*, **63**:1, 2009.

[81] S. D. Bass. *Mod. Phys. Lett.*, **A24**:1087, 2009.

[82] S. D. Bass. *Rev. Mod. Phys.*, **77**:1257.

[83] B. W. Filippne and X. Ji. **26**:1, 2001.

[84] V. Y. Alexakhin *et al.* COMPASS Collab. *Phys. Lett.*, **B647**:8, 2007.

[85] N. N. Bogoliubov. *Ann. Inst. Henri Poincare*, **8**:163, 1968.

[86] F. E. Close. *Nucl. Phys.*, **B80**:269, 1974.

[87] A. LeYaouanc *et al. Phys. Rev.*, **D9**:2636, 1974.

[88] A. LeYaouanc *et al. Phys. Rev.*, **D15**:844, 1977.

[89] A. Chodos *et al. ibid.*, **10**:2599, 1974.

[90] M. J. Ruiz. *ibid.*, **12**:2922, 1975.

[91] C. Hayne and N. Isgur. *Phys. Rev.*, **D25**:1944, 1982.

[92] A. Adare *et al.* PHENIX Collab. *Phys. Rev. Lett.*, **103**:012003, 2009.

[93] R. L. Jaffe and A. Manohar. *Nucl. Phys.*, **B337**:509, 1990.

[94] X. Ji *et al. Phys. Rev. Lett.*, **76**:740, 1996.

[95] X. Ji. *Phys. Rev. Lett*, **78**:610, 1997.

[96] B. L. G. Bakker *et al. Phys. Rev.*, **D70**:114001, 2004.

[97] X. Zheng. Ph. D. Thesis, MIT, "Precesion Measurement of Neutron Spin Asymmetry A_1^n at Large x_{bj} Using CEBAF at 5.7 GeV".

[98] C. G. Callan and G. J. Gross. *Phys. Rev. Lett.*, **22**:156, 1969.

[99] S. Wandzura and F. Wilczek. *Phys. Rev.*, **B72**:195, 1977.

[100] V. N. Gribov and L. N. Lipatov. *Sov. J. Nucl. Phys.*, **15**:438, 1972.

[101] L. N. Lipatov. *Sol. J. Nucl. Phys.*, **20**:95, 1975.

[102] L. N. Lipatov. *Sov. J. Nucl. Phys.*, **20**:95, 1975.

[103] G. Altarelli and G. Parisi. *Nucl. Phys.*, **B126**:298, 1977.

[104] M. Wlasenko (H1 and ZEUS Collab.). *Nucl. Phys.*, **A827**:276, 2009.

[105] M. G. Alekseev *et al* COMPASS Collab., 2010. CERN-PH-EP/2010-001, arXiv:1001.4654.

[106] S. D. Drell and T. M. Yan. *Phys. Rev. Lett.*, **25**:316, 1971.

[107] P. L. McGaughey *et al. Annu. Rev. Nucl. Part. Sci.*, **49**:217, 1999.

[108] C. A. Gagliardi. *Nucl. Phys.*, **A 721**:344, 2003.

[109] J. Badier *et al. Z. Phys.*, **C 26**:489, 1984.

[110] G. Moreno *et al. Phys. Rev.*, **D43**:2815, 1991.

[111] P. L. McGaughey *et al. Phys. Rev.*, **D50**:3038, 1994.

[112] H. L. Lai *et al. Phys. Rev.*, **D55**:1280, 1997.

[113] A. Bacchetta *et al. Phys. Rev.*, **D70**:117504, 2004.

[114] T. Sloan, G. Smadja, and R. Voss. *Phys. Rep.*, **162**:45, 1988.

[115] P. Mulders, AIP Conf.Proc. 588 (2001) 75-88.

[116] M. Grazzini. *Nucl. Phys.*, bf B518:303, 1998.

[117] C. J. Bebek *et al. Phys. Rev. Lett.*, **30**:624, 1973.

[118] G. Drews *et al. Phys. Rev. Lett.*, **41**:1433, 1978.

[119] H. Mkrtchyan R. Ent and G. Niculescu. JLab E00-108 "Duality in Meson Electroproduction".

[120] H.Avakian *et al.* CLAS Collab. *Phys. Rev.*, **D69**:112004, 2004.

[121] J. C. Collins *et al. Adv. Ser. Direct High Energy Phys.*, **5**:1, 1988.

[122] K. Wilson. *Phys. Rev.*, **179**:1499, 1969.

[123] M. E. Peskin and D. V. Schroeder. *An Introduction to Quantum Field Theory.* Westview.

[124] I. Schienbein *et al. J. Phys.*, **G35**:053101, 2008.

[125] A. D. Martin *et al. Phys. Lett.*, **B 443**:301, 1998.

[126] A. Bacchetta *et al. Phys. Lett.*, **B574**:225, 2003.

[127] P. J. Mulders and R. D. Tangerman. *Nucl. Phys.*, **B461**:197, 1996.

[128] M. Anselmino *et al. Phys. Rev.*, **D71**:074006, 2005.

[129] J. C. Collins *et al. Phys. Rev.*, **D73**:014021, 2006.

[130] P. Schweitzer *et al.* arXiv:1003.2190 (2010).

[131] H. Avakian *et al.*, arXiv:1003.4549.

[132] D. Graudenz. *Nucl. Phys.*, **B432**:351, 1994.

[133] M. Anselmino *et al. Eur. Phys. J.*, **A31**:373, 2007.

[134] D. de Florian *et al. Nucl. Phys.*, **B470**:195, 1996.

[135] D. de Florian *et al. Phys. Rev.*, **D57**:5803, 1998.

[136] D. de Florian *et al. Phys. Rev.*, **D71**:094018, 2005.

[137] G. A. Navarro and R. Sassot. *Eur. Phys. J.*, **C28**:321, 2003.

[138] X. D. Ji *et al. Phys. Rev.*, **D71**:034005, 2005.

[139] R. K. Ellis *et al. Nucl. Phys.*, **B152**:285, 1979.

[140] E. L. Berger *et al. Phys. Rev.*, **D65**:034006, 2002.

[141] K. Ackerstaff *et al.* HERMES Collab. *Phys. Rev. Lett.*, **81**:5519, 1998.

[142] L. A. Linden-levy. Ph.D. Thesis UIUC "On Extracting Hadron Multiplicities And Unpolarized Nucleon Structure Ratios From SIDIS Data at the HERMES Experiment" 2008.

[143] T. Navasardyan *et al. Phys. Rev. Lett.*, **98**:022001, 2007.

[144] D. Boer and P.J. Mulders. *Phys. Rev.*, **D57**:5780, 1998.

[145] V. Barone *et al. Phys. Rep.*, **359**:1, 2002.

[146] K. Hidaka *et al. Phys. Rev.*, **D19**:1503, 1979.

[147] J.P. Ralston and D.E. Soper. *Nucl. Phys.*, **B152**:109, 1979.

[148] R.L. Jaffe and X. Ji. *Phys. Rev. Lett.*, **67**:552, 1991.

[149] C. Bourrely *et al. Phys. Lett.*, **B420**:375, 1998.

[150] D. Sivers. *Phys. Rev.*, **D79**:085008, 2009.

[151] J. Soffer. *Phys. Rev. Lett.*, **74**:1292, 1995.

[152] W. Vogelsang. *Phys. Rev.*, **D57**:1886, 1998.

[153] J. Ralston, *private communications.*

[154] M. Gockeler *et al. Phys. Lett.*, **B627**:113, 2005.

[155] H.-X. He and X. Ji. *Phys. Rev.*, **D52**:2960, 1995.

[156] V. Barone *et al. Phys. Lett.*, **B390**:287, 1997.

[157] M. Wakamatsu. *Phys. Lett.*, **B653**:398, 2007.

[158] B.-Q. Ma and I. Schmidt. *J. Phys.*, **G 24**:L71, 1998.

[159] I. C. Cloet *et al. Phys. Lett.*, **B659**:214, 2008.

[160] B. Pasquini *et al. Phys. Rev.*, **D72**:094029, 2005.

[161] A. Chodos *et al. Phys. Rev.*, **D9**:3471, 1974.

[162] A. Chodos *et al. Phys. Rev.*, **D10**:2599, 1974.

[163] T. DeGrand *et al. Phys. Rev.*, **D12**:2060, 1975.

[164] D. Diakonov. "Lectures at Advanced Summer School on Non-Perturbative Field Theory", Penisocola, Spain, June (1997) hep-ph/9802298.

[165] Y. Nambu and G. Jona-Lasinio. *Phys. Rev.*, **122**:345, 1961.

[166] Y. Nambu and G. Jona-Lasinio. *Phys. Rev.*, **124**:246, 1961.

[167] M. Wakamatsu and H. Yoshiki. *Nucl. Phys.*, **A524**:561, 1991.

[168] I. C. Cloet *et al. Phys. Lett.*, **B621**:246, 2005.

[169] P. A. M. Dirac. *Rev. Mod. Phys.*, **21**:392, 1949.

[170] S. J. Brodsky. SLAC-PUB-7870 hep-ph/9807212.

[171] J. C. Collins. *Nucl. Phys.*, **B396**:161, 1993.

[172] S. J. Brodsky *et al. Phys. Lett.*, **B530**:99, 2002.

[173] J.C. Collins. *Phys. Lett.*, **B536**:43, 2002.

[174] S. J. Brodsky *et al. Nucl. Phys.*, **B642**:344, 2002.

[175] M. Burkardt. *Phys. Rev.*, **D69**:091501, 2004.

[176] S. J. Brodsky and S. Gardner. *Phys. Lett.*, **B643**:22.

[177] J. Ellis and M. Karliner. *Phys. Lett.*, **B213**:73, 1988.

[178] A. V. Efremov and O. V. Teryaev. [Yad. Fiz. 36 242 (1982)].

[179] A. V. Efremov and O. V. Teryaev. *Phys. Lett.*, **B150**:383, 1985.

[180] J. Qiu and G. Sterman. *Phys. Rev. Lett.*, **67**:2264, 1991.

[181] J. Qiu and G. Sterman. *Nucl. Phys.*, **B378**:52, 1992.

[182] J. Qiu and G. Sterman. *Phys. Rev.*, **D59**:014004, 1999.

[183] X. Ji *et al. Phys. Rev. Lett.*, **97**:082002, 2006.

[184] X. Ji *et al. Phys. Rev.*, **D73**:094017, 2006.

[185] X. Ji *et al. Phys. Lett.*, **B638**:178, 2006.

[186] B. Pasquini and F. Yuan, arXiv:1001.5398 (2010).

[187] A. Bacchetta *et al.* arXiv 1003.1328 (2010).

[188] M. Anselmino *et al. Phys. Rev.*, **D72**:094007, 2005.

[189] H. Avakian *et al.* arXiv:0805.3355 (hep-ph).

[190] B.-Q. Ma and I. Schmidt. *Phys. Rev.*, **D58**:096008, 1998.

[191] G. A. Miller. *Phys. Rev.*, **C76**:065209, 2007.

[192] B. Pasquini *et al. Phys. Rev.*, **D78**:034025, 2008.

[193] A. Bacchetta *et al. JHEP*, 0702:093, 2007.

[194] A. Airapetian *et al.* HERMES Collaoration. *Phys. Rev. Lett*, **94**:012002, 2005.

[195] V. Yu. Alexakhin COMPASS Collab. *Phys. Rev. Lett.*, **94**:202002, 2005.

[196] D.W. Sivers. *Phys. Rev.*, **D41**:83, 1990.

[197] E.S. Ageev *et al.* COMPASS Collab. *Nucl. Phys.*, **B765**:31, 2007.

[198] M. Anselmino and A. Prokudin, private communications. Predictions are based on the extractions of Ref. e-Print: arXiv:0807.0173.

[199] D. L. Adams *et al.* FNAL E704 Collab. *Phys. Lett.*, **B264**:462.

[200] J. Pumplin G. L. Kane and W. Repko. *Phys. Rev. Lett.*, **41**:1689, 1978.

[201] J.C. Collins. *Nucl. Phys.*, **B396**:61, 1993.

[202] S. S. Adler *et al.* PHENIX Collab. *Phys. Rev. Lett.*, **95**:202001, 2005.

[203] B. I. Abelev *et al.* STAR Collab. *Phys. Rev. Lett.*, 101:222001, 2008.

[204] J. Adams *et al.* STAR Collab. *Phys. Rev. Lett.*, **97**:152302, 2006.

[205] U. D' Alesio and F. Murgia. *Phys. Rev.*, **D70**:074009, 2004.

[206] U. DAlesio M. Boglione and F. Murgia. *Phys. Rev.*, **D77**:051502, 2008.

[207] C. Kouvaris *et al. Phys. Rev.*, **D74**:114013, 2006.

[208] I. Arsene *et al.* BRAHMS Collab. *Phys. Rev. Lett.*, **101**:042001, 2008.

[209] B. I. Abelev *et. al.* STAR Collab. *Phys. Rev. Lett*, **99**:142003, 2007.

[210] J. W. Qiu *et al. Phys. Lett.*, **B650**:373, 2007.

[211] J. W. Qiu *et al. Phys. Rev.*, **D76**:074029, 2007.

[212] W. Vogelsang and F. Yuan. *Phys. Rev.*, **D76**:094013, 2007.

[213] C. J. Bomhof *et al. Phys. Lett.*, **B596**:277, 2004.

[214] A. Bacchetta *et al. Phys. Rev.*, **D72**:034030, 2005.

[215] C. J. Bomhof and P. J. Mulders. *Nucl. Phys.*, **B795**:409, 2008.

[216] J. Collins and J. W. Qiu. *Phys. Rev.*, **D75**:114014, 2007.

[217] A. Airapetian *et al.* HERMES Collab. *Phys. Rev. Lett.*, **84**:4047, 2002.

[218] M. Boglione and P.J. Mulders. *Phys. Lett.*, **B478**:114, 2000.

[219] M. Anselmino and F. Murgia. *Phys. Lett.*, **B483**:74, 2000.

[220] A.V. Efremov *et al. Eur. Phys. J*, **C24**:407, 2002.

[221] B.-Q. Ma *et al. Phys. Rev.*, **D66**:094001, 2002.

[222] A.V. Efremov *et al. Eur. Phys. J.*, **C32**:337, 2003.

[223] P. Schweitzer and A. Bacchetta. *Nucl. Phys.*, **A732**:106, 2004.

[224] A. Bacchetta *et al. Phys. Lett.*, **B574**:225, 2003.

[225] L.P. Gamberg *et al. Phys. Rev.*, **D68**:051501, 2003.

[226] M. Burkardt. *Phys. Rev.*, **D69**:057501, 2004.

[227] X. Ji and F. Yuan. *Phys. Lett.*, **B543**:66, 2002.

[228] A. Airapetian *et al.* HERMES Collab. *Phys. Rev. Lett.*, **103**:152002, 2009.

[229] M. Alekseev *et al.* COMPASS Collab. *Phys. Lett.*, **B673**:127, 2009.

[230] A. Martin, talk in DIS 2010 (2010).

[231] M. Anselmino *et al.* e-Print: arXiv:0807.0173.

[232] R. Seidl *et al.* (Belle Collaboration). *Phys. Rev. Lett.*, **96**:232002, 2006.

[233] R. Seidl *et al.* (Belle Collaboration). *Phys. Rev.*, **D78**:032001, 2008.

[234] M. Anselmino *et al.* arXiv:0805.2677, to appear in EPJA.

[235] M. Anselmino *et al.* arXiv:0807.0166 (2008).

[236] M. Anselmino *et al. Eur. Phys. J.*, **A39**:89, 2009.

[237] M. Anselmino *et al. Phys. Rev.*, **D75**:054032, 2007.

[238] L. Pappalardo *et al.* HERMES Collab. in the proceedings of the XIV International Workshop on Deep Inelastic Scattering, Tsukuba city, Japan, April 20-24, (2006).

[239] W. Vogelsang and F. Yuan. *Phy. Rev.*, **D72**:054028, 2005.

[240] W. Vogelsang and F. Yuan, private communications.

[241] JLab Experiment E06-010, Spokespersons: X. Jiang, J. P. Chen, E. Cisbani, H. Gao and J. C. Peng.

[242] D. Marchand, Ph. D. thesis, Universite Blasie Pascal, Clermont-Ferrand, France 1997.

[243] T. H. A. Collaboration JLab Hall A General Operations Manual (205).

[244] B. Humensky, "General exam advanced project", Princiton University (1999).

[245] `http://hallaweb.jlab.org/experiment/HAPPEX/HAPPEXII/paritydaq/parity_daq.html`

[246] B. Blankleider and R. M. Woloshyn. *Phys. Rev.*, **C29**:538, 1984.

[247] J. L. Friar *et al. Phys. Rev.*, **C42**:2310, 1990.

[248] M. A. Bouchiat *et al. Phys. Rev. Lett.*, **5**:373, 1960.

[249] T. Walke and W. Happer. *REv. Mod. Phys.*, **69**:629, 1997.

[250] F. D. Colegrove *et al. Phys. Rev.*, **132**:2561, 1963.

[251] J. Becker *et al. Nucl. Instr. and Meth.*, **A346**:45, 1994.

[252] T. R. Gentile and R. D. McKeown. *Phys. Rev.*, **A 47**:456, 1993.

[253] G. Eckert *et al. Nucl. Instr. and Meth.*, **A320**:53, 1992.

[254] K. Kramer *et al. Nucl. Instr. and Meth.*, **A582**:318, 2007.

[255] W. Happer. *Rev. Mod. Phys.*, **44**:169, 1972.

[256] chiran 7 needed!

[257] W. Happer *et al.* U. S. Patent No. 6318092 2001.

[258] A. Ben-Amar Baranga *et al. Phys. Rev.*, **A58**:2282, 1998.

[259] A. Ben-Amar Baranga *et al. Phys. Rev. Lett*, **80**:2801, 1998.

[260] W. C. Chen *et al. Phys. Rev.*, **A75**:013416, 2007.

[261] G. Wang *et al. Phys. Rev.*, **A47**:468, 1993.

[262] W. Lorenzon *et al. Phys. Rev.*, **A47**:468, 1993.

[263] S. R. Scheafer *et al. Phys. Rev.*, **A39**:5613, 1989.

[264] R. Newbury *et al.* N. *Phys. Rev.*, **A48**, 1993.

[265] A. S. Barton *et al. Phys. Rev.*, **A49**, 1994.

[266] M. V. Romalis and G. D. Cates. *Phys. Rev.*, **A58**, 1998.

[267] B. D. Anderson *et al. Nucl. Instr. and Meth.*, **A522**:294, 2004.

[268] N. Liyangage, Ph. D. thesis, MIT Cambridge Massachusetts (1999).

[269] C. Grupen, Particle Detectors, Cambridge University Press, p. 193 (1996).

[270] F. Garibaldi *et al.* The Hall A RICH detector. Hall A Status Report 2001. `http://hallaweb.jlab.org/publications/StatusReports/StatusReport2001.pdf`.

[271] CERN-LHCC-98-19 S. Beole *et al.* Detector for high momentum PID. `http://consult.cern.ch/alice/Documents/1998/01/HMPID/tdr.html`.

[272] R. Chan, Master thesis, University of Virginia, 2002.

[273] R. Mankel. *Rep. Prog. Phys.*, **67**:553, 2004.

[274] N. Liyanage, Jefferson Lab Tech Note, **JLAB-TN-02-012**.

[275] C. Curtis *et al.*, Jefferson Lab Alignment Group Data Transmittal, **A1189, A1197, A1198 and A1208**.

[276] T. W. Donnelly and A. S. Raskin. *Anna. Phys.*, **169**:247, 1986.

[277] SAID model, `http://gwdac.phys.gwu.edu`.

[278] J.L. Friar *et al. Phys. Rev.*, **C42**:2310, 1990.

[279] A. Nogga, Ph. D. thesis, Ruhr-Universität Bochum, Bochum, Germany (2001), p.72.

[280] C. Ciofi degli Atti *et al. Phys. Rev.*, **C48**:968(r), 1993.

[281] F. Bissey *et al. Phys. Rev.*, **C64**:024004, 2001.

[282] S. Scopetta. *Phys. Rev.*, **D75**:054005, 2007.

[283] S. A. Sulagin and W. Melnitchouk. *Phys. Rev.*, **C78**:065203, 2008.

[284] E. Chudakov, "COMGEANT simulation" `http://www.jlab.org/~gen/simul/`.

[285] V. Nelyubin, University of VA, *private communication*.

[286] D. E. Wiser, Ph.D. thesis, Univ. of Wisconsin (1977).

[287] L. W. Whitlow, SLAC-Report-357 (1990).

[288] SIMC, `https://hallcweb.jlab.org/wiki/index.php/Monte_Carlo`.

[289] L. W. Mo and Y.-S. Tsai. *Rev. Mod. Phys.*, **41**:205, 1969.

[290] R. Ent *et al. Phys. Rev.*, **C64**:054610, 2001.

[291] The Coordinated Theoretical-Experimental Project on QCD, `http://www.phys.psu.edu/~cteq/`.

[292] MRS/MRST/MSTW PARTON DISTRIBUTIONS, `http://durpdg.dur.ac.uk/hepdata/mrs.html`.

[293] S. Lretzer *et al. Enr. Phys. J.*, **C22**:269, 2001.

[294] J. She, *private communication*, Peking University.

[295] J. She *et al. Phys. Rev.*, **D79**:054008, 2009.

[296] M. Anselmino *et al.* arXiv:0807.0173 (hep-ph).

[297] L. Favart. *Nucl. Phys.*, **A654**:571, 1999.

[298] Pythia, `http://home.thep.lu.se/~torbjorn/Pythia.html`.

[299] H. Avakian and E. Aschenauer *private communication*.

[300] N. Makins, *private communication*. Duke P_T Workshop, Durham, Mar 12-13, 2010.

[301] B. Pasquini, *private commuication*.
S. Boffi, A. V. Efremov, B. Pasquini and P. Schweitzer, Phys. Rev. **D79**, 094012 (2009) arXiv:0903.1271.

[302] A. Bacchetta. *private communications*.

[303] H. Mkrtchyan *et al. Phys. Lett.*, **B665**:20, 2008.

[304] JLab approved experiment E10-006, "An update to PR12-09-014: Target Single Spin Asymmetry in Semi-Inclusive Deep-Inelastic $(e, e'\pi^{\pm})$ Reaction on a Transversely Polarized ^{3}He Target at 8.8 and 11 GeV", Spokesperson: J.-P. Chen, H. Gao, X. Jiang, J.-C. Peng and X. Qian.

[305] J. Gomez *et al. Phys. Rev.*, **D49**:4348, 1994.

[306] J. Ashman *et al.* EMC Collab. *Z. Phys. C*, **57**:211, 1993.

[307] A. C. Benvenuti *et al.* BCDMS Collab. *Phys. Lett.*, **B189**:483, 1987.

[308] P. Solvignon-Slifer, *private communiation*.

[309] J. J. Aubert. *Phys. Lett.*, **B123**:275, 1983.

[310] D. F. Geesaman *et al. Annu. Rev. Nucl. Part. Sci.*, **45**:337, 1995.

[311] J. Seely *et al. Phys. Rev. Lett.*, **103**:202301, 2009.

[312] X. Jiang *private communication*.

[313] P. E. Bosted. *Phys. Rev.*, **C51**:409, 1995.

[314] P. V. Degtyarenko, "Applications of the Photonuclear Fragmentation Model to Radiation Protection Problems". Proceedings of the Second Sepcialist's Meeting on Shielding Aspects of Accelerators, Targets and Irradiation Facilities (SATIF2), 12-13 October 1995, CERN, Geneva, Switzerland, p. 67; P. V. Degtyarenko, M. V. kossov, H-P. Wellisch, Chiral Invariant Phase Space Event Generator, I. Nucleon-antinucleon annihilation at rest, Eur. Phys. J. **A 8**, p.217 (2000).

[315] P. V. Degtyarenko, *private communications*.

[316] J. Huang and Y. Qiang, Transversity Tech-note: "Maximum Likelihood Estimation of Asymmetry and Angular Modilation for Transversity" `http://www.jlab.org/~jinhuang/Transversity/MLE.pdf` (2010).

Biography

Personal Data

1. Xin Qian
2. Birth date: 07-02-1984
3. Birth place: Beijing, P. R. China
4. M.A. degree in Physics, Sep. 2005. Duke University.
5. B.S. degree in Physics, May 2003. (Age: 19)

Awards and Honors

1. 2010 Postdoctoral Prize Fellowship in Experimental Physics or Astrophysics, CALIFORNIA INSTITUTE OF TECHNOLOGY.
2. 2006 Southern Universities Research Association (SURA)/Jefferson Lab (JLab) Graduate Fellowship.
3. 2005 SURA/Jefferson Lab Graduate Fellowship.
4. 2002, T. D. Lee scholar (Jun Zheng), Peking University.
5. 2001, "Jun Zheng" Chinese Undergraduate Student Research Fellowship. The most prestigious award in Chinese Universities.

Refereed Journal Publications

1. "Study of the $A(e, e'\pi^+)$ Reaction on ^{1}H, ^{2}H, ^{12}C, ^{27}Al, ^{64}Cu and ^{197}Au," X. Qian *et al.* accepted by PRC, arXiv:0908.1616.

2. "Hard Photodisintegration of a Proton Pair" I. Pomerantz *et al.* Phys. Lett. **B684**, 106 (2010), arXiv:0908.2968.

3. "New measurements of the EMC effect in very light nuclei", J.Seely *et al.*, Phys. Rev. Lett. **103**, 202301 (2009), arXiv:0904.4448.

4. "The extraction of $\phi - N$ total cross section from $d(\gamma, pK^+K^-)n$" **X. Qian** *et al.* Phys. Lett. **B680**, 417 (2009), arXiv:0907.2668.

5. "Scaling study of the pion electro-production cross section and the pion form factor ". T. Horn, **X. Qian** *et al.*, Phys. Rev. **C78**, 058201 (2008), arXiv:0707.1794.

6. "Relaxation of spin polarized ^{3}He in mixtures of ^{3}He and ^{4}He below the ^{4}He lambda point", Q. Ye *et al.*, Phys. Rev. **A77** 053408 (2008), arXiv:physics/0603176.

7. "A high-pressure Polarized ^{3}He Gas Target for the High Intensity Gamma Source (HIGS) Facility at Duke Free Electron Laser Laboratory", K. Kramer *et al.*, Nuclear Inst. and Methods in Physics Research, **A582**, 318 (2007).

8. "Search for the ϕN bound state from ϕ meson subthreshold production", S. Liska, H. Gao, W. Chen and **X. Qian**, Phys. Rev. **C75**, 058201 (2007), arxiv:0707.1009.

9. "The proton elastic form factor ratio $\mu = G_E^p/G_M^p$ at low momentum transfer", G. Ron *et al.*, Phys. Rev. Lett. **99**, 202002 (2007), arXiv:0706.0128.

10. "Precision Measurements of the Nucleon Strange Form Factors at Q^2 $\tilde{0}$.1 GeV^2", A. Acha *et al.*, Phys. Rev. Lett. **98**, 032301 (2007), nucl-ex/0609002.

11. "Measurement of nuclear transparency for the $A(e, e'\pi^+)$ reaction" B. Clasie, **X. Qian** *et al.* Phys. Rev. Lett. **99**, 242502 (2007), arxiv:0707.1481.

12. "The Kaon Form Factor in the Light-Cone Quark Model", Bo-Wen Xiao, **Xin Qian**, Bo-Qiang Ma. Eur. Phy. J. A **15** 523-527 (2002).

Proceedings

1. "Study of Semi-inclusive Deep-Inelastic (e,e'$\pi^{\pm}$) production at 11 GeV in JLab with a polarized ^{3}He target", **X. Qian**, H. Gao, J.-P. Chen and E. Chudakov, AIP Conf. Proc. 1149, 457 (2009).
2. "Transversity and Transverse Spin in Nucleon Structure through SIDIS at Jefferson Lab" A. Afanasev *et al.* JLAB-PHY-07-620, Mar 2007. 7pp arXiv:hep-ph/0703288.
3. "Neutron transversity measurement at Jefferson Lab with a polarized He-3 target" H. Gao, **X. Qian** *et al.* Few Body Syst. **41**:43-52 (2007).

References

1. Dr. Jian-Ping Chen (JLab Supervisor)
   Jefferson Lab, Hall A
   12000 Jefferson Ave. MS 12H
   Newport News, VA, 23606 (USA).
   (757)269-7413; jpchen@jlab.org
2. Dr. Kees De Jager
   Jefferson Lab, Hall A
   12000 Jefferson Ave. MS 12H
   Newport News, VA, 23606 (USA).
   (757)269-5254; kees@jlab.org
3. Dr. Rolf Ent
   Jefferson Lab, Hall C
   12000 Jefferson Ave. MS 12H

Newport News, VA, 23606 (USA).

(757)269-7373l ent@jlab.org

4. Prof. Haiyan Gao (Thesis Advisor)

   Phys. Dept. Duke University, TUNL

   2313 FFSC, Duke University

   Durham, NC 27708 (USA).

   (919)660-2622; gao@phy.duke.edu

5. Prof. Jean-Marc Laget

   CEA, Centre de Saclay, Irfu/Service de Physique Nucléaire

   91191 Gif-sur-Yvette, France

   Jefferson Lab, Theory Group

   Newport News VA 23606 (USA).

   laget@jlab.org

6. Prof. Zein-Eddine Meziani

   Phys. Dept. Temple University

   Barton Hall A323, 1900 N. 13th Street

   Philadelphia, PA 19122 (USA).

   (215)204-5971; meziani@temple.edu

7. Prof. Jen-chieh Peng

   Phys. Dept. University of Illinois at Urbana-Champaign

   409 Loomis Laboratory University of Illinois at Urbana-Champaign

   Urbana, IL 61801 (USA).

   (217)244-6039; jcpeng@illinois.edu

8. Dr. Stepan Stepanyan Jefferson Lab, Hall B

   12000 Jefferson Ave. MS 12H

   Newport News, VA, 23606 (USA).

(757)269-7196; stepanya@jlab.org